Post-Synthetic Modification of Metal-Organic Frameworks (MOFs) and Polyhedra (MOPs)

Jorge Albalad Alcalá

Universitat Autònoma de Barcelona

Post-Synthetic Modification of Metal-Organic Frameworks (MOFs) and Polyhedra (MOPs)

Jorge Albalad Alcalá

Doctoral Thesis
PhD in Chemistry

Supervisors

Prof. Dr. Daniel Maspoch
Dr. Inhar Imaz
Dr. Arnau Carné

Catalan Institute of Nanoscience and Nanotechnology (ICN2)
Department of Chemistry – Faculty of Sciences

2019

Memòria presentada per aspirar al Grau de Doctor per Jorge Albalad Alcalá

Jorge Albalad Alcalá
Vist-i-plau

Prof. Dr. Daniel Maspoch
ICREA Research Professor & Group Leader
Supramolecular Nanochemistry and Materials Group
Institut Català de Nanociència i Nanotecnologia (ICN2)

Dr. Inhar Imaz
Senior Researcher & Division Coordinator
Supramolecular Nanochemistry and Materials Group
Institut Català de Nanociència i Nanotecnologia (ICN2)

Dr. Arnau Carné
JdlC Fellowship Researcher
Supramolecular Nanochemistry and Materials Group
Institut Català de Nanociència i Nanotecnologia (ICN2)

Bellaterra, 20 de novembre de 2019

Table of contents

The present PhD Thesis has been dedicated to the design and implementation of new post-synthetic modification techniques to porous metal-organic materials, namely Coordination Polymers (CPs), Metal-Organic Frameworks (MOFs) and Metal-Organic Polyhedra (MOPs), in order to modify their physicochemical properties to inaccessible levels by common direct synthesis methodologies.

Chapter 1 offers a brief bibliographic review of the evolution of metal-organic materials field, from their beginnings up to their actual applications and future perspectives. This chapter presents the most relevant concepts in their synthesis and their potential post-synthetic modification, both in the metallic nodes or in the organic linkers that assemble the framework; with particular emphasis on the post-synthetic methodologies exploited up to date.

In Chapter 2, the general and specific objectives of this Thesis are introduced.

Chapter 3 focuses on the post-synthetic modification of the metallic subunits of macrocycle-based coordination polymers. The presence of a second source of metal ions quelated inside the macrocyclic cavity induces a single-crystal to single-crystal phase transition in contact with water, obtaining a regular distribution of bimetallic paddlewheel subunits within the framework. Such transition is studied by single-crystal X-Ray diffraction techniques, as well as spectroscopic and magnetic characterization techniques.

Chapter 4 opens up an unexplored post-synthetic modification pathway in the MOFs field. Thanks to their nanoporous structure, MOFs can diffuse highly-reactive gases through their framework in order to modify their structure through solid-gas reactions in a matter of minutes. Specifically, an olefin-tagged MOF is post-synthetically modified by diffusing ozone gas through the porous channels of the material. The as-obtained reaction intermediate can be chemoselectively converted to either aldehyde or carboxylic acid groups without affecting the crystalline integrity of the material. The whole two-step process is characterized by Nuclear Magnetic Resonance (NMR) techniques, as well as single-crystal X-Ray diffraction.

In Chapter 5, the post-synthetic modification of metal-organic architectures is extended to zero-dimensional materials. Concretely, it is demonstrated how the surface functionalization of Rhodium-based Metal-Organic Polyhedra, both through coordination or covalent chemistries, is able to tune their solubility within a wide range of solvents, without affecting the scaffold's integrity. This post-modification opens up new pathways for exploiting these materials. Because of their finite structure, MOPs can be seen as stoichiometrically-functionalized nanoparticles with tunable solubility.

Finally, Chapter 6 focuses on expanding the available roster of Rh(II)-based MOPs, given the awaken potential aroused in Chapter 5. Through a two-step protection/deprotection strategy, two unprecedented Rh-MOPs with 24 free carboxylate or amino groups on their periphery are synthesized. Both groups arguably present one of the richest chemistries in coordination and covalent chemistry, respectively, thus opening new pathways and frontiers towards the application of these materials.

Resumen

La presente Tesis Doctoral está dedicada al diseño e implementación de nuevas técnicas de modificación post-sintética en materiales porosos metal-orgánicos, tanto polímeros de coordinación (CPs), redes metal-orgánicas (MOFs) o poliedros metal-orgánicos (MOPs), con el fin de modificar sus propiedades fisicoquímicas a niveles inaccesibles a través de síntesis directa.

En el Capítulo 1 se ofrece una revisión bibliográfica de la evolución del campo de los materiales metal-orgánicos, desde sus inicios hasta su actual aplicación y perspectivas de futuro. El capítulo presenta los conceptos más relevantes durante el diseño, síntesis y la potencial modificación post-sintética de dichos materiales, ya sea en sus nodos metálicos o en los ligandos orgánicos que unen la red; enfatizando en las metodologías post-sintéticas explotadas hasta la fecha y su potencial.

En el Capítulo 2 se introducen los objetivos generales y específicos de esta Tesis.

El Capítulo 3 se centra en la modificación post-sintética de los nodos metálicos de polímeros de coordinación basados en ligandos macrocíclicos. La presencia de una segunda fuente de iones metálicos quelatados en la cavidad del macrociclo induce una transición de fase de monocristal a monocristal en contacto con agua, obteniendo una distribución regular de nodos bimetálicos "*paddlewheel*" a en la red. Dicha transición se estudia a través de difracción de rayos-X de monocristal, así como técnicas espectroscópicas y magnéticas.

El Capítulo 4 abre una nueva vía de modificación post-sintética inexplorada en el campo de los MOF. Gracias a su estructura nanoporosa, es posible difundir gases altamente reactivos a través del interior del material y modificar su estructura a través de reacciones sólido-gas en cuestión de minutos. Específicamente, se modifica post-sintéticamente un MOF con grupos olefina distribuidos en sus canales porosos difundiendo gas ozono a través del material. El intermedio de reacción obtenido puede ser convertido quimioselectivamente a grupos aldehído o carboxilato sin afectar la integridad cristalina del material. Todo el proceso es caracterizado profundamente a través de técnicas de Resonancia Magnética Nuclear, así como con difracción de rayos-X de monocristal.

En el Capítulo 5, se extiende la modificación post-sintética de materiales metal-orgánicos a materiales cero-dimensionales. Concretamente, se muestra que la funcionalización superficial de poliedros metal-orgánicos de Rodio (II), tanto por química de coordinación como química covalente, es capaz de modificar su solubilidad a un gran abanico de disolventes sin afectar a su integridad. Esta post-modificación abre nuevas vías de explotación de estos materiales, ya que al

ser estructuras finitas, pueden ser utilizados como nanopartículas con funcionalización estequiométrica con solubilidad tuneable.

Finalmente, el Capítulo 6 se focaliza en expandir el catálogo de poliedros metal-orgánicos de Rodio disponibles, debido al gran potencial despertado en el Capítulo 5. Gracias a un proceso en dos pasos de protección/desprotección, es posible sintetizar poliedros de Rodio con 24 grupos carboxilato o amina disponibles en la superficie del material. Estos grupos presentan presumiblemente una de las químicas más ricas en los campos de coordinación y covalente, respectivamente, abriendo nuevos caminos y fronteras en la aplicación de estos materiales.

Acknowledgments

Durante los casi cinco años que he pasado en el grupo, he visto pasar a decenas de personas. Todas y cada una de ellas han influido a su manera en mí, tanto a nivel personal como profesional. Por ello, esta Tesis no puede empezar sin reconocer su parte del mérito, que no es poca.

En primer lugar, quiero agradecer al Prof. Daniel Maspoch por brindarme la oportunidad de crecer y madurar bajo su tutela y supervisión. Su constante dedicación, rigurosidad, exigencia y sobretodo su confianza consiguen que proyectos de investigación utópicos se conviertan en realidad. Esta Tesis no hubiera sido posible sin su guía.

Agradecer como no al Dr. Inhar Imaz su constante dedicación, supervisión y ayuda durante mis comienzos en el grupo. Agradecerte todas esas reuniones de pasillo, noches de sincrotrón interminables y tu constante apoyo y confianza en la época más oscura de esta Tesis. Gracias por levantarme cuando me veía incapaz de seguir, y por mantener mi cabeza en la tierra cuando algo increíble florecía de algún experimento. He aprendido más trabajando contigo que durante todos mis años de formación, y he podido llegar a ser el químico (y persona) que soy ahora gracias a ti. Toda tu contribución merece ser reconocida. GRACIAS!

Me gustaría también agradecer al Dr. Arnau Carné por su incansable pasión por la investigación, su apoyo, los paseítos por el gym y todas las discusiones políticamente incorrectas. Agradecerte también el abrirme la puerta al mundo de los Metal-Organic Polyhedra, donde verdaderamente he disfrutado llevando ideas estúpidas hasta una realidad. Espero que el campo crezca y que tu esfuerzo se reconozca.

Agradecer especialmente al Dr. Javier Aríñez su infinita paciencia y dedicación durante mis prácticas de master. La humildad que demostrabas hacia alguien tan inmaduro como yo y la pasión que demostrabas por tu investigación (aunque no quisieras reconocerlo) fue el motivo por el que decidí seguir con la Tesis, con la esperanza de llegar a ser algún día un investigador de tu nivel. Gracias por enseñarme todo lo que sabías, no hubiese podido terminar esta Tesis sin ello.

Como no, agradecer a mis compañeros de oficina, tanto del viejo NanoUP como de las nuevas generaciones: Abraham, Iván, Ceren, Amirali, Vahid, Luis Carlos, Jordi, Claudia, Blanca, Heng, Civan, Yang, Cris, Paula, Natalia, Najmeh, Anna, Xu, Borja, Yunhui y en especial a Gerard y Laura, por compartir conmigo tantos inolvidables años de cafés, discusiones, congresos, fiestas y sesiones de “rajómetro”. También al excelente surtido de PostDoc que han circulado por el laboratorio: Thais, Vincent, Sabina, Javier Pérez, Javier Troyano, Emi, Carles, Alex, Jorge Cruz,

Mateusz, Jordi, Sonia, Mary, Nereida y Nerea. Agradecer también a todo el departamento técnico y de “Project management”: Raquel, Jose, Marta y Rosa por hacer la vida en el laboratorio mucho más fácil, y por no machacarme (excesivamente) por no usar nunca una bata de laboratorio…

A mis padres y hermano, tíos, primos y abuela por no preguntar demasiadas veces cuándo dejaría de estudiar; y a mis amigos, por preguntar demasiadas veces cuándo dejaría de estudiar.

Y por último y sin lugar a dudas el agradecimiento más importante va para ti, Elena. Gracias por todos estos años compartiendo tu vida conmigo, por todo tu apoyo incondicional cuando decidí meterme en esta Tesis, por toda la motivación que me has dado para seguir día a día, sabiendo que al volver a casa me esperabas con una sonrisa. Gracias por querer compartir conmigo una nueva época en la otra punta del mundo. Esta Tesis es tan tuya como mía, porque has sufrido todos sus fracasos y has disfrutado más que yo los éxitos. Nunca podré compensarte todo lo que has hecho por mí. Te quiero.

Chapter 1

Introduction to Metal-Organic Frameworks: historical background, design principles, applications and their post-synthetic modification

1.1. Introduction

For centuries, humanity has been captivated by their surroundings, focused in understanding and taking benefit of all things in their vicinity. Such vivid curiosity and endless seek of wisdom, either for intellectual reasons or for selfish benefit, has motivated scholars and fanatics equally to a continuous competition in the manipulation, purification and sophistication of the 'useless' matter from their environments into something profitable. In this race, observation and knowledge proved to be the key to success. In the early Middle Age, alchemists spent hundreds of years chasing the dream of *Chrysopoeia* (that is, the art of converting heavy metals into gold) with exhaustive (and sometimes esoteric) efforts in bypassing the principles of mass conservation. Such narcissistic belief of breaking the 'laws' of Nature, while futile and utopic, ended up leading to the discovery of several elements, purification steps and chemical transformations that heavily contributed in developing the basis of what we know today as *Chemical Composition*.[1,2] Likewise, practical alchemy further proved how the modification of such chemical composition (or as they called, Transmutation) could densely influence the toughness, flexibility, colour or even flammability of every element and their alloys.

Nowadays, it is widely known that the physical properties of a molecule/material are directly correlated to its chemical structure; following the "function follows form" rule.[3] The more our knowledge expanded to the atomic level, the more plausible every chemical transformation became,[4] to the point of bringing dreams from another age to life.[5,6] For this, the way scientists can manipulate and control compositional outcomes on a small scale has unveiled an enormous range of exploitable physicochemical properties that permit the creation of smart materials with highly specific functions.[7] This has become more evident the more the knowledge of the nanoscaled world has advanced, where bulk properties become less relevant and surface phenomena arise in influence.[8,9] At this point, researchers observed that physicochemical properties are not only dependent on the chemical composition, but also on their conformational order within the material. Indeed, atomic rearrangement processes without altering the overall chemical composition can reveal structuration-directed physicochemical properties.[10,11]

One cannot address structuration-directed properties without talking about porous materials,[12,13] clearly a perfect example of the axiom "function follows form". Porous materials present intrinsic accessible cavities that gave them a spotlight in applications involving molecular separation, adsorption and capture of metal ions, among others.[14] Recently, a new trend has awakened in the porous materials field, as scientists developed rational design strategies for obtaining regular pore sizes, shapes and inner volumes.[15–18] Among them, the field of Porous Coordination Polymers (PCPs),[19–21] including Metal-Organic Frameworks (MOFs),[22] received particular interest as they blend the properties of inorganic ions/clusters and the rich chemistry of

organic linkers. Thus, their properties can be predicted and tuned by a careful selection of the building blocks used.[23–25] Such structural flexibility and their regularly-shaped pore channels confer MOFs with a virtually infinite range of physical and chemical properties, which makes them suitable candidates in myriad applications such as gas storage,[26] catalysis[27,28] or drug delivery,[29] among others.

1.2. Metal-Organic Frameworks

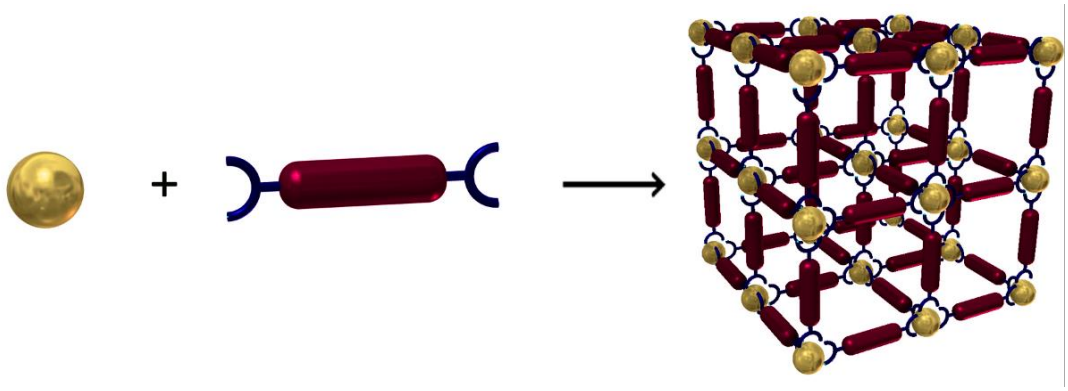

Figure 1.1. Schematic representation of the assembly of Metal-Organic Frameworks.

According to the official definition from the International Union of Pure and Applied Chemistry (IUPAC), a MOF is defined as follows: "*A metal–organic framework, abbreviated to MOF, is a coordination network with organic ligands containing potential voids*".[30] In other words, MOFs are porous materials assembled from inorganic ions or clusters and organic molecules linked by coordination bonds.[31,32] There is still nowadays strong controversy regarding this definition, as the words "coordination networks" do not imply three-dimensional extension, crystallinity, nor accessible voids. Nevertheless, a huge portion of the community agrees that MOFs represent a rather small section within the more general Porous Coordination Polymer field, that specifically englobes bi-dimensional (2D) and three-dimensional (3D) extended crystalline frameworks that present accessible microporosity upon evacuation of the inner cavities.[33] For this, this Thesis will explicitly use the acronym MOF to refer to such kind of materials, and will use PCPs accordingly when not every condition is fulfilled.

It is precisely this permanently accessible microporosity that has attracted several fields to MOF research.[34] Such interest can be perfectly embodied with the over 75,600 entries present in the Cambridge Structural Database (CSD) with the MOF tag over the last 20 years,[35,36] not including those without a properly refined crystalline structure. The crystallinity of MOFs arises from the dynamic nature of the coordination bonds that assemble the framework. Coordination

bonds present a dual behaviour where they are reversible enough to correct potential structural framework defects, but still robust to stand the porous framework upon desolvation. For this, MOFs are typically synthesised under aggressive solvothermal conditions (incorporating either acidic or basic agents accordingly) in order to awake the dynamic behaviour of their coordination linkages.[37]

1.2.1. Historical overview

The discovery of MOFs emerged as a direct consequence on the expansion of control and understanding of the synthesis of coordination polymers (CPs). In the early 90s, Robson and Hoskins pioneered the field by rationally designing the formation of extended networks by a careful assembly of what they referred as secondary units.[38] Taking into account common coordination environments adopted by metal ions and the directionality that organic linkers offer, both coworkers depicted a rational assembly of inorganic-organic subunits as long as the periodicity and symmetry of the final framework allows it. Like so, the first periodic 3D framework was successfully synthesised by mixing tetrahedral Cu(I) centers with the tetrahedral ligand tetra(4-cyanophenyl)methane. The as-obtained framework presented a diamond-like structure with large ordered adamantine-like cavities (Figure 1.2).[39] In the same decade, Yaghi and coworkers reported the first coordination framework to be called MOF in the literature by synthesising another diamond-like structure through the assembly of the rigid linker 4,4'-bipyridine (4,4'-bpy) with Cu(I) ions, with free NO_3^- ions accommodated within the porous cavities balancing the charge of the framework (Figure 1.3).[31]

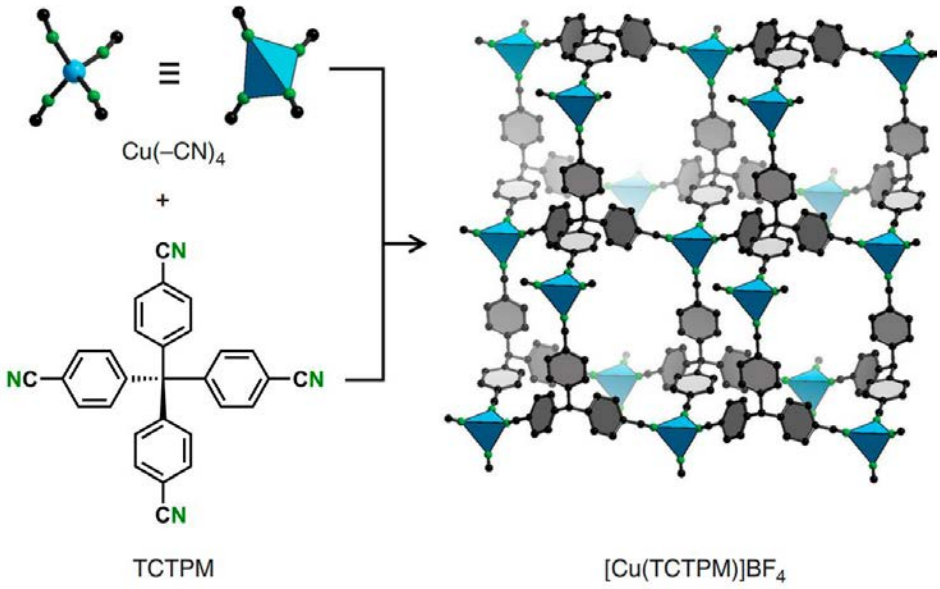

Figure 1.2. Diamond-like framework assembled through Cu(I) tetrahedral subunits linked by tetrahedral TCTPM Organic linkers. Colour code: Cu (blue), C (grey) and N (green).

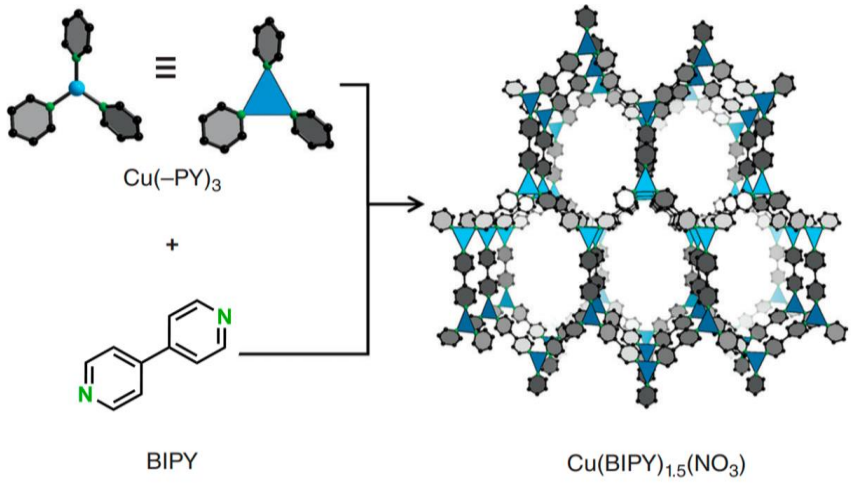

Figure 1.3. Schematic representation of MOF-1 ([$Cu(BIPY)_{1.5}(NO_3)$]). Colour code: Cu (blue), C (gray) and N (green).

Both works laid the foundation of a sequential discovery of several 3D coordination architectures by exploiting the rich chemistry both inorganic and organic subunits had to offer.[40] Not only the design of open-framework materials that could be predicted prior-synthesis was attractive, but also the physicochemical properties that aroused from such architectures. In this sense, Fujita and coworkers exploited for the first time the use of two-dimensional CPs with open channels as potential heterogeneous catalysts.[41] Through the assembly of the rigid 4,4'-bipyridine (BIPY) linker with Cd(II) ions, a new framework catalytically active to the cyanosilylation of aldehydes and chlatration of dihalobenzenes was reported (Figure 1.4).

In general, this first generation of "MOFs" shared a lack of permanent porosity due to poor stability on their evacuated state. The presence of charge imbalances within the framework's backbone, together with the fragility of the metal-linker bond did not afford successful surface area measurements until 1997, where the first evidence that MOF can indeed show permanent porosity was reported.[42]

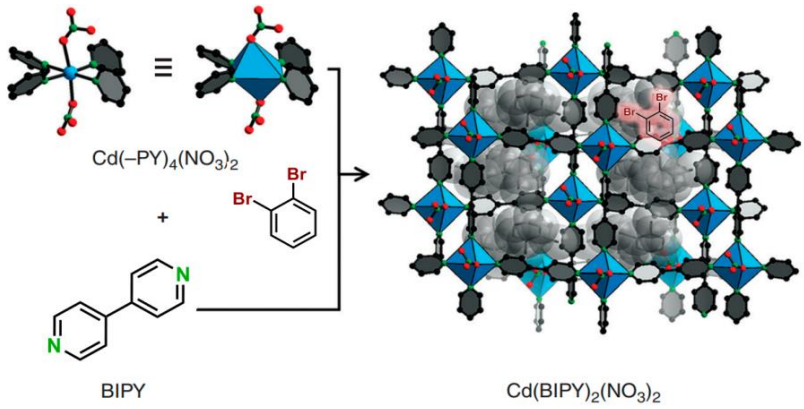

Figure 1.4. Schematic representation of [$Cd(BIPY)_2(NO_3)_2$] and how dihalobenzenes get accommodated within the porous cavities. Colour Scheme: Cd (blue), C (gray), N (green), O (red), Br (brown).

One year later, Yaghi and coworkers offered an alternative pathway to overcome the limitations of these first-generation materials by combining anionic deprotonated linkers with metallic ions, granting extra robustness to the bridging links. Thanks to the use of the polycarboxylic linker 1,4-benzenedicarboxylic acid (terephthalic acid, H_2BDC), a neutral framework of formula Zn(BDC)(DMF)(H_2O), named MOF-2, was obtained (Figure 1.5, top). The deprotonation of H_2BDC under basic solvothermal conditions allowed the network extension through bimetallic Zn-Zn paddlewheel subunits, without any counterions inside its cavities. Therefore, upon evacuation of the trapped solvent molecules, MOF-2 reported a specific Brunauer-Emmett-Teller (BET) surface area value of S_{BET} = 270 $m^2 \cdot g^{-1}$.[43]

The publication of MOF-2 was a huge milestone in the MOF field, as it showed how the use rigid coordination clusters, instead of simple metallic ions, was the ideal building strategy in MOF design with accessible porosity.[19] The majority of MOF papers reported afterwards followed the approach of using polycarboxylic linkers, and some of these structures are still relevant nowadays due to how their porous properties stand.[44] Specifically, two key porous MOFs were synthesised following Yaghi's path, known as HKUST-1 ([$Cu_3BTC_2(H_2O)_2$], where BTC= 1,3,5-benzenetricarboxylic acid), a 3D lattice assembled from Cu(II)-based paddlewheel clusters and a trigonal linker (Figure 1.5, bottom);[45] and MOF-5 ([ZnBDC(DMF)(H_2O)], where BDC = 1,4-benzenedicarboxylic acid), a 3D framework built through H_2BDC linkers combined with Zn(II) octahedral clusters (Figure 1.5, middle).[46] Surface area measurements of both HKUST-1 and MOF-5 greatly surpassed those given by the most prevalent competitors at the time, zeolites, with surface area values of 692 $m^2 \cdot g^{-1}$ (later increased up to 1,800 $m^2 \cdot g^{-1}$ under better activation conditions[47]) for HKUST-1 and 2,900 $m^2 \cdot g^{-1}$ for MOF-5.

Soon, it became clear how the complex inorganic clusters that could potentially extend MOF frameworks required rationalisation. Inspired by the work of Robson, Yaghi *et. al.* introduced the concept of Secondary Building Unit (SBU) in order to elucidate MOF topologies.[48] SBUs are defined as rigid directional clusters of metallic ions linked by rigid organic linkers (generally carboxylic acid linkers) that could potentially lead to extended MOF frameworks with structural stability and periodicity. A rational linkage of SBUs lead to the development of the Reticular Chemistry field, or "the chemistry of linking molecular building blocks by strong bonds intro crystalline extended structures".[49] In other words, reticular chemistry is a prediction science which aims to design, orient and interlink porous subunits by precisely arranging SBUs with linkers of predefined directionality and length. In practice, for any given structure, increasing the linker length (and therefore the distance between SBUs) should keep the same SBU (and hence

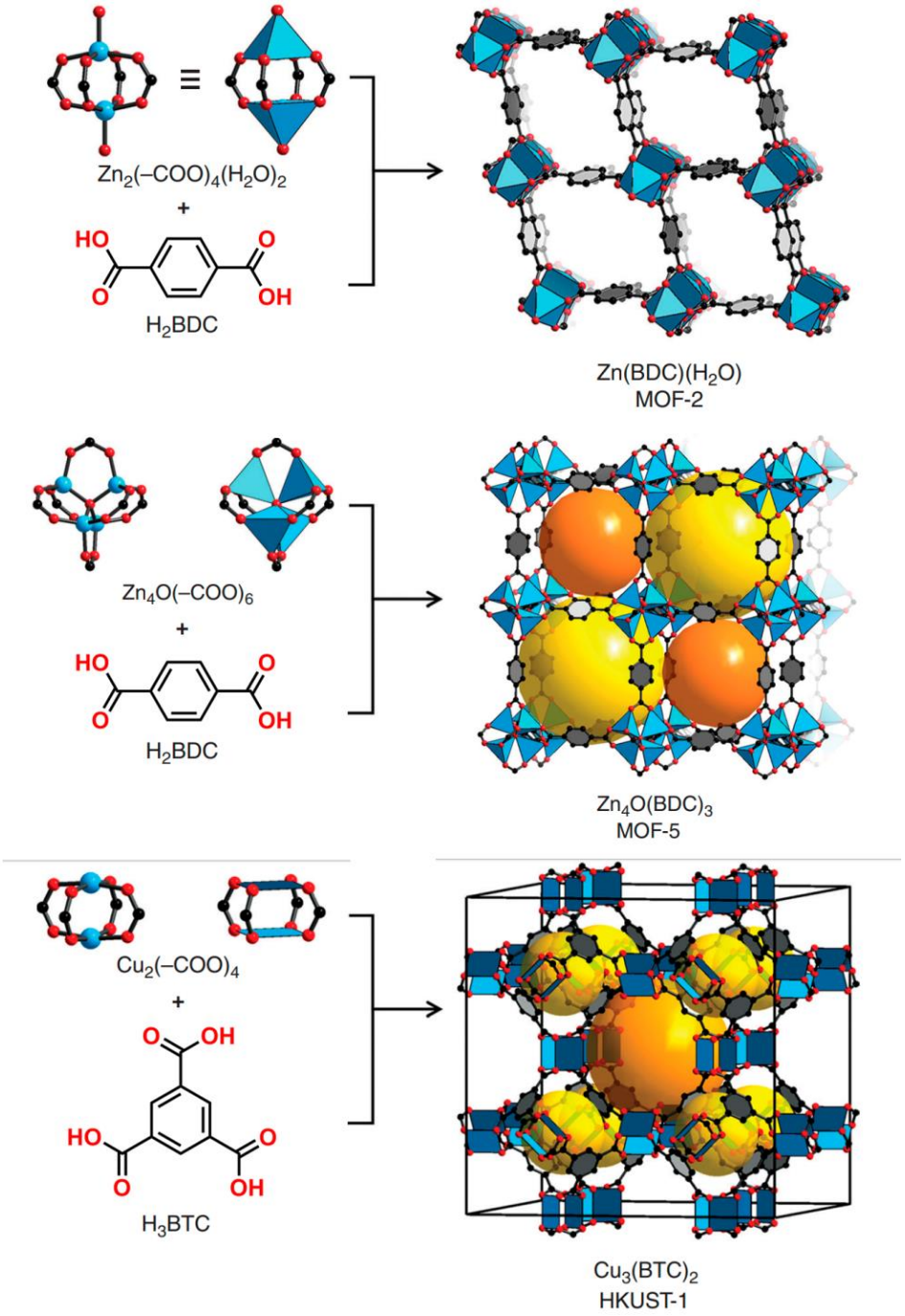

Figure 1.5. Schematic representation of the neutrally-charged MOF-2 (top), MOF-5 (middle) and HKUST-1 (bottom). Colour scheme: Zn/Cu (blue), C (gray), O (red). Hydrogen atoms omitted for clarity.

the structural topology of the framework) while expanding the free volume of its cavities. The first example of "Reticular Expansion" of MOFs was postulated by Yaghi and coworkers by reporting up to 16 isoreticular MOFs (IRMOF) that shared a common cubic topology. By alternating either the pendant functionalities or the length of the organic linker, the pore size of the framework could be increased from 3.8 to 28.8 Å without affecting the primitive lattice

(Figure 1.6). Additionally, the pores' functionality could be tuned by replacing BDC linkers with its functionalised counterparts.[50]

Reticular chemistry has proven to be one of the most powerful tools in the design and synthesis of new MOF frameworks, and it's still a relevant topic nowadays.[51–53] After bringing most of the regular (edge-transitive) possible topologies to life experimentally, researchers are moving to more unorthodox techniques for deepening the scope of reticular chemistry (bended ligands, merged frameworks, etc.) and expand the horizons for the application of these materials.[54]

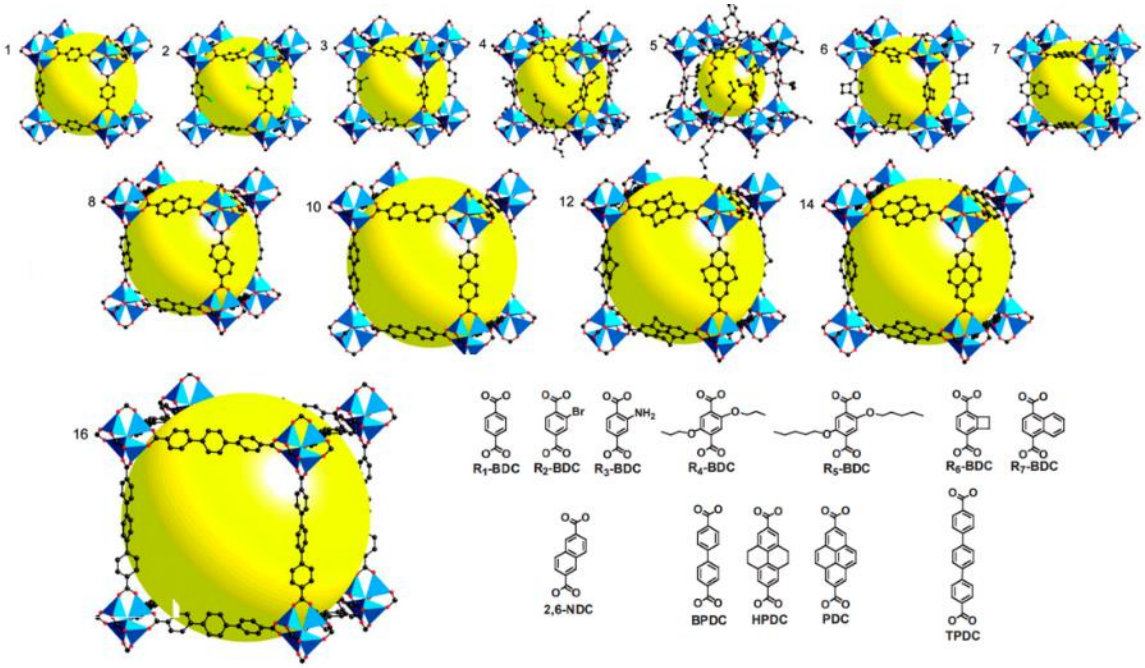

Figure 1.6. Schematic representation of the IRMOF series, obtained by Reticular Synthesis.

1.3. Applications of Metal-Organic Frameworks

MOFs have proven to be excellent candidates for multiple applications thanks to the exceptional properties they can intrinsically provide, such as microporosity, potential open-metal sites or structural/compositional flexibility, but also potential electronic,[55] magnetic,[56] optical[57] and hydrophobic/hydrophilic properties[58] derived from the building blocks used. The combination of these attributes opened up application pathways in the fields of gas storage/separation, catalysis, molecular separation, or drug delivery systems, among others (Figure 1.7). This section will provide a brief insight on the most relevant applications.

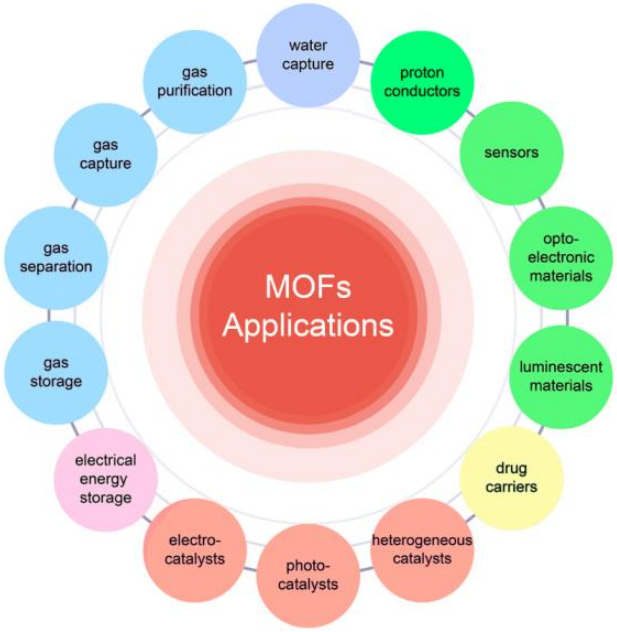

Figure 1.7. Applications of Metal-Organic Frameworks, ranging from energy storage, gas separation, catalysis, water capture and biomedical applications.[179]

1.3.1. Gas storage and separation

Energy management has become a global concern in the recent years. The inevitable drought of fossil fuels has made consumers to turn the gaze to other greener, exploitable energy resources. Among them, hydrogen and methane have aroused as the most attractive alternatives, but their exploitation demands herculean efforts on safe and efficient storage methodologies. In this sense, MOFs are very attractive adsorbents for many gas molecules due to their high specific surface area. Therefore, their potential has been thoroughly studied in the literature, and briefly explained in the sections below.

1.3.1.1. Hydrogen storage

Because of its abundance, non-hazardous combustion pathways (mostly forming water as byproduct) and high energy density, H_2 is an excellent replacement as an energy source for fossil fuels and coal. However, its major drawbacks derives from its extremely poor energy density on a volumetric mass (8.0 $MJ \cdot L^{-1}$ versus 32.0 $MJ \cdot L^{-1}$ from gasoline), which implies that 1 Kg of liquefied H_2 requires over 11,500 L at room temperature. To this end, hydrogen storage requires the use of pressurised tanks at the pressure range of 700 bar, thus being neither practical nor safe.[59] In these sense, MOFs can overcome this limitation due to their high intrinsic surface area and their ability to store pressurised gas through physisorption phenomena. Additionally, MOFs provide relatively fast adsorption/desorption cycles, drastically reducing the required pressure and

energy.[60] As mentioned in previous sections, the presence of open-metal sites within the MOF backbone also improves their H_2 storage capabilities, through dipole interactions.

As an example, the ultra-highly porous MOF NU-100 ($[Cu_3(L)(H_2O)]$, where L= 1,3,5-tris[(1,3-carboxylate-5-(4-ethynyl)phenyl))ethynyl]-benzene) and with SBET value of 6,143 $m^2 \cdot g^{-1}$, exhibits the highest H_2 storage at 77 K and 56 bar, with values of almost 100 $mg \cdot g^{-1}$ (Figure 1.8).[61] Later, Zhou *et. al.* proved how the presence of catenation within the organic linker can have strong synergy towards hydrogen storage within the MOF framework. As a proof of concept, they synthesised two isostructural MOFs (PCN-6, catenated and PCN-6', non-catenated; $[Cu_3(TATB)_2]$, where TATB= 4,4',4"-s-triazine-2,4,6-triyl-tribenzoic acid) and measured their sorption capabilities. As expected, the catenated PCN-6 exhibited almost a 72% increase on stored hydrogen (72 mg/g (6.7 wt %) at 77 K/50 bar or 9.3 mg/g (0.92 wt %) at 298 K/50 bar versus 42 mg/g (4.0 wt %) at 77 K/50 bar or 4.0 mg/g (0.40 wt %) at 298 K/50 bar).[62] Still, practical applications of MOFs in the field are almost inexistent due to not meeting the Department of Energy (DOE) storage targets (45 mg/g at ambient temperature (-20 ºC to 40 ºC, with a max. pressure of 12 bar[63]) and their elevated synthetic costs.

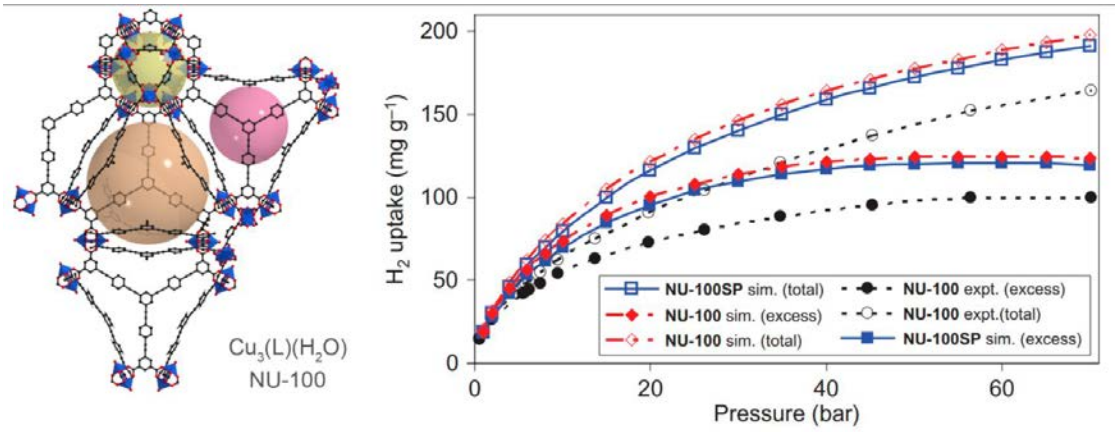

Figure 1.8. Schematic representation of the crystalline structure of NU-100 ($[Cu_3L(H_2O)]$) (left) and its experimental H_2 adsorption isotherms (black circles) at high pressure and 77 K (right).

1.3.1.2. Methane storage

Despite not being as eco-friendly as hydrogen combustion, methane is still considered a green energy source that could serve as replacement for fossil fuels, mainly because of its low CO_2 production during combustion. While not as extreme as H_2, CH_4 application gets hindered due to its low energy density. Therefore, adsorbent materials such as MOFs can provide storage conditions at room temperature and relatively low pressures, not possible to be achieved by common compressing methods.

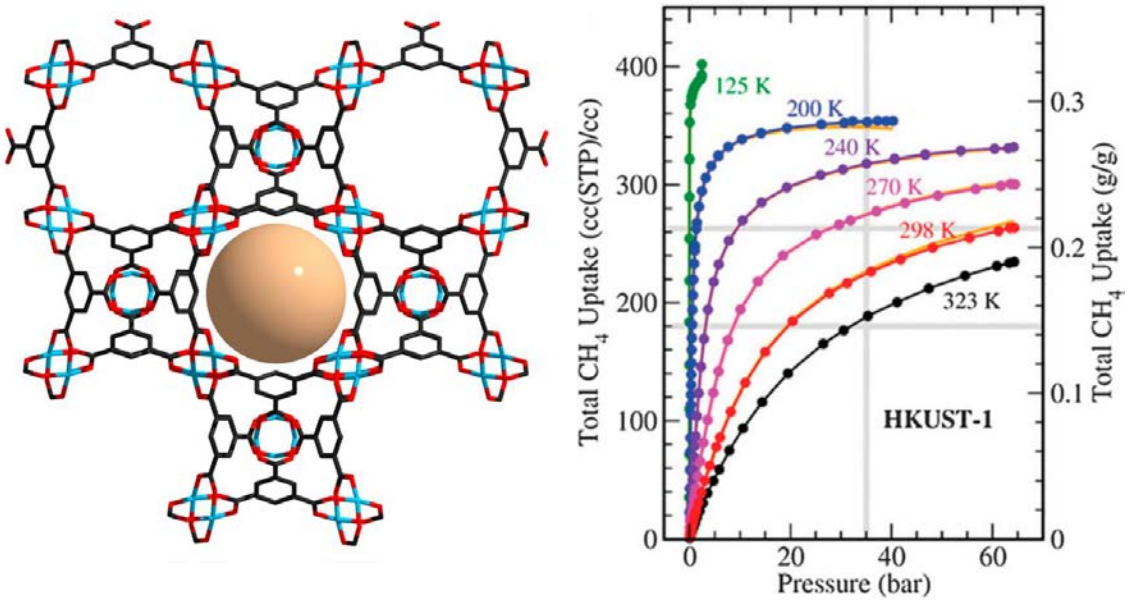

Figure 1.9. Schematic representation of the crystalline structure of HKUST-1 ($[Cu_3(BTC)_2]$) (left) and its experimental CH_4 adsorption isotherms at different temperatures (right).

MOFs have already proved their excellent capabilities in CH_4 storage in comparison with empty tanks.[64] Among many others, HKUST-1 ($[Cu_3BTC_2]$, where BTC = 1,3,5-benzenetricarboxylic acid) has been one of the most widely studied MOFs, showing exceptionally high volumetric methane storage that fulfils the requirements of DOE standards (35 bar, RT, 180 cm^3/ cm^3),[65] with values of up to 270 cm^3 CH_4/cm^3 at 65 bar and 298 K (Figure 1.9).[66,67] From a mechanistic point of view, the high uptake capabilities of HKUST-1 can be attributed to a synergistic effect with the unsaturated open metal sites and the strong interaction of CH_4 molecules with the oxygen atoms within the octahedral cages of the MOF.[68] Besides HKUST-1, several other MOFs have demonstrated outstanding storage capabilities, such as MOF-905 ($Zn_4O(BDC)(BTAC)_{4/3}$, BDC = 1,4-benzenedicarboxylic acid, and BTAC = benzene-1,3,5-tri-β-acrylic acid): 203 $cm^3 \cdot cm^{-3}$ at 64 bar; NOTT-100 (Cu_2BPTC, where BPTC= Biphenyl-3,3′,5,5′-tetracarboxylic acid): 230 $cm^3 \cdot cm^{-3}$ at 65 bar; and UTSA-20 (Cu_3BHB, where BHB= 3,3′,3″,5,5′,5″-benzene-1,3,5-triyl-hexabenzoic acid): 230 $cm^3 \cdot cm^{-3}$ at 65 bar.[69]

1.3.1.3. Carbon dioxide sequestration

Outside from storage opportunities on the energetic field, adsorbent materials have proven their strengths in atmospheric pollutant sequestration. In particular, MOFs have demonstrated to be efficient materials for carbon dioxide capture at both high and low pressure values. Yaghi and coworkers reported how the highly porous MOF-177 ($[Zn_3BTB_2]$, where BTB= 1,3,5-tris(4-carboxyphenyl)benzene) with BET surface area = 4,500 $m^2 \cdot g^{-1}$ is able to reversibly adsorb up to 33.5 mmol $CO_2 \cdot g^{-1}$ at 35 bar, thus meaning that its implementation to an empty storage cylinder

increases its capacity over 9 times.[70] Up to date, the highest reported CO_2 capture values are found on MOF-210 ([$Zn_4O(BTE)_{4/3}(BPDC)$], where BTE= 4,4′,4″-[benzene-1,3,5-triyl-tris(ethyne-2,1-diyl)]tribenzoate, BPDC= biphenyl-4,4′-dicarboxylate), with sorption capabilities up to 65.0 mmol $CO_2 \cdot g^{-1}$ at 50 bar, being the highest value reported at high pressures so far.[71]

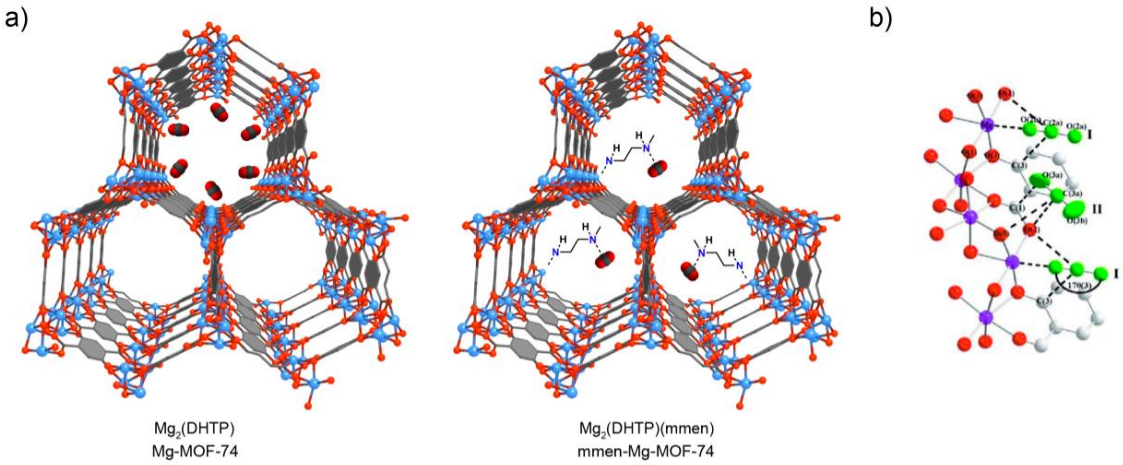

Figure 1.10. (a) Crystallographic structure of Mg-MOF-74, in which the interaction of CO_2 molecules with unsaturated Mg(II) ions is shown (left) and its covalent interactions with mmen molecules to enhance CO_2 sorption capabilities (center).[72] (b) Schematic of the interaction of CO_2 molecules with the unsaturated metal centers. Colour Scheme: Mg (purple), O (red) and CO_2 (green).[73]

At low pressures, the chemical composition of the framework gains significant importance, deeply relying on pore size and chemical affinity towards CO_2. One again, unsaturated Lewis sites play an important role in gas storage, as these coordination centers can act as binders through dipolar interactions. As an example, Mg-MOF-74 ([Mg_2(DHTP)], where DHTP= 2,5-dihydroxy-1,4-benzenedicarboxylic acid), reported by Deng *et. al.* presents up to 27.5 wt% at room temperature and 1 bar thanks to the unsaturated Mg ions in its channels.[74,75] Additionally, the chemical affinity of MOFs towards CO_2 can further be expanded by introducing functional groups or bonds amenable to H-bonding interactions. Like so, Hong, Long *et. al.* incorporated pendant dimethylethyldiamine (mmen) pending chains inside an isoreticular MOF-74 channelled structure (Figure 1.10). Through this, its CO_2 adsorption capacity skyrocketed up to 15 times its values without functionalisation. Remarkably, the material showed excellent selectivity and cyclable recovery towards CO_2, even under high humidity conditions.[72]

1.3.1.4. Molecular separation

The separation of hydrocarbon mixtures has traditionally been one of the most important processes in industry, as phase purity is essential in sophisticated chemical procedures. For example, most C_4 hydrocarbons are obtained as byproducts of ethylene production or oil refining, thus complex and energy-intensive separation schemes are required for their isolation. Recently,

MOFs have been presented as attractive alternatives in this process. Benefiting from the rational design and precise control over pore accessibility and polarisation that MOFs offer, the molecular separation field has advanced significantly in an energy efficient and green fashion. Several examples of MOF-based separation processes can be found in the literature, all of them appealing to rationalised size-exclusion, "clustering" and chemoselective pathways. Long *et. al.* examined recently this approach by examining the adsorption behavior of 1-butene, cis-2-butene and trans-2-butene in M-MOF-74 derivatives (M = Mn(II), Fe(II), Co(II), Ni(II)), which all contain high density of coordinatively-unsaturated M(II) sites. The authors spotted that both Co(II) and Ni(II)-based MOFs were able to separate 1-butene from the 2-butene isomers, a critical industrial process that until now relied largely on energetically demanding cryogenic distillation.[76] Presumably, 1-butene selectivity is traced to the high charge density retained by the M(II) metal centers.

1.3.2. Catalysis

The adjustable chemical composition that inorganic and organic subunits offer combined with the virtually infinite combinations available make MOFs attractive materials for catalytic applications.[27] In fact, MOFs have crossed a barrier in the field, as they essentially are able to combine multiple well-defined heterogeneous catalytic centers within a single material.[77] Additionally, the edge advantage of using MOFs over other non-structured catalytic supports is the size-exclusion phenomena derived from MOF pore windows, opening new size-dependant discrimination pathways.[78]

To date, several strategies have been employed to design MOFs as efficient catalysts, including unsaturated metal nodes, functionalised linkers, defective MOFs and using MOFs as inert supports for other active catalytic species.[79,80] The first and most forward approach consists on exploiting the unsaturated open-metal sites presents in several MOF clusters as potential Lewis acid catalysts. For this, reactions that require Lewis acid catalysts (*i.e.* acetylation of aldehydes, cyanosilylation reactions, oxidations or cycloadditions) are the most suitable for the exploration of MOFs in the field. For example, the open Cu(II) sites in HKUST-1 have proven to be excellent heterogeneous Lewis centers for several reactions, including isomerisation and cyclisation of terpenes.[81] Another example comes after exploiting Cr^{3+} or Fe^{3+} centers presents in MIL-101 ($[M_3O(BDC)_3(H_2O)_2]$, where M= Cr(III)/Fe(III)) in cyanosilylation pathways.[82] The more experience the field was getting, the more sophisticated this catalytic processes became, up to conversion levels of 98 % in relatively short reaction times (Figure 1.11, left). Additionally, researchers have developed alternative methodologies based on defect inductions in order to unveil open-metal sites in frameworks with saturated clusters. As an example, mono-coordinating acid agents such as trifluoroacetic acid have been used to partially remove the organic linkers on

USTC-253 ([Al(OH)(SBPDC)], where SBPDC= 4,4′-dibenzoic acid-2,2′-sulfone) generating open Lewis vacancies.[83]

The second alternative consists on taking advantage of the organic linkers to incorporate catalytic moieties in the MOF backbone, either by directly using catalytically active ligands during the synthesis, or by post-synthetic covalent anchoring (see Section 1.4.1.2). One smart example was presented by Zhou and coworkers, who structured porphyrin-based linkers into a 3D extended MOF, where the porphyrin moiety was able to coordinate metal species which proved to be catalytically active. Additionally, the structuration within a MOF framework hindered as well any potential pi-stacking quenching phenomena directly related to porphyrinic species, thus improving its catalytic activity.[84] Not only metal-supporting moieties have been introduced to MOFs, but also organocatalytic groups. Squaramide moieties, known to be amenable to self-quenching through H-bonding interactions,[85] have been structured in MOFs in two different fashions. Initially, Mirkin *et. al.* incorporated a bis-(trifluoromethyl)phenylsquaric acid into the Zr(IV)-based UiO-67 MOF ($Zr_6(O)_4(OH)_4(BPDC)_6$, where BPDC= biphenyl-4,4′-dicarboxylate) as a side-chain within the aromatic backbone (Figure 1.11, right). Even though porosity values were drastically reduced, this approach proved to dramatically increase Friedel–Crafts reaction yields between indole and β-nitrostyrene moieties, whereas free squaramide derivatives did not show catalytic activity.[86] Later, the same moiety was incorporated within the organic backbone of several MOFs, thus not partially blocking the porous channels and improving the overall catalytic activity.[87–89]

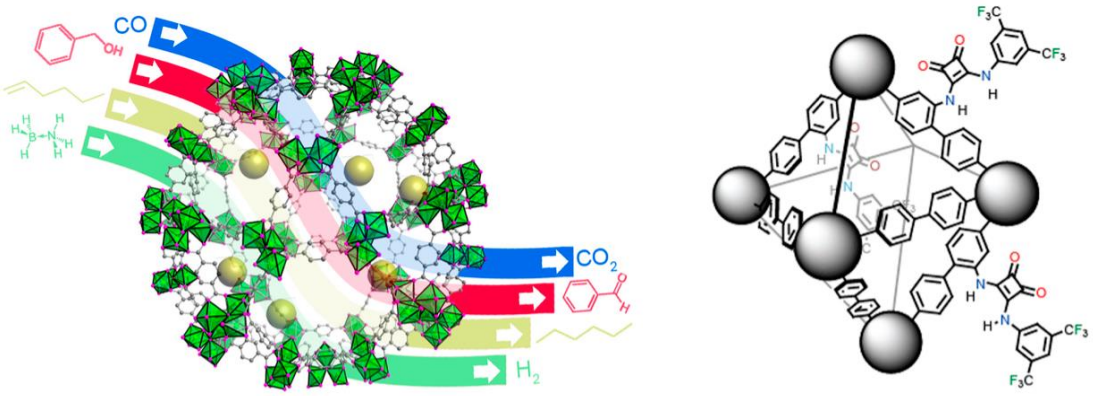

Figure 1.11. Schematic illustrations showing the two main approaches for exploiting MOFs in catalysis field: taking profit of unsaturated open-metal sites/embedded INPs as Lewis catalysts (left) and structuration of organic moieties within the MOF linkers (right).

Finally, MOFs can be used in catalysis as an inert support for highly-sensitive catalytic particles. Inorganic Nanoparticles (INPs) are well known catalytically active materials that suffer from major drawbacks;[90] (*i*) gradual decrease in their activity due to self-aggregation phenomena and irreversible precipitation; (*ii*) their nanoscopic size and homogeneous dispersion in practically

every solvent precludes the recovery of the catalyst from the reaction media and therefore their recyclability. For this, the practical use of INPs requires nanostructuration, typically achieved by anchoring on inert solid substrates.[91] To this end, MOFs represent robust candidates that offer high surface areas and discriminative pore-windows, boosting and complementing their catalytic properties. To date, several MOF@INP composites have been shown as efficient catalysts for key reactions, such as CO oxidation, hydrogenation, alcohol oxidation and even C-C couplings.[92] As an example, Xu and coworkers successfully immobilised active Pt nanoparticles within the cavities of Cr-MIL-101 by diffusing the precursor H_2PtCl_6 through the 1.2 and 1.6 nm pore windows, followed by *in situ* reduction with $NaBH_4$. The as-obtained composite proved to be active to CO oxidation, starting from 100 ºC up to quantitative conversions at 180 ºC.[93]

Remarkably, MOFs have recently become powerful tools in the catalysis field in a way completely different to the ones presented above. Due to their crystalline nature, MOFs have proven to be of invaluable help to elucidate catalytic reaction intermediates by single-crystal X-Ray diffraction (SCXRD). When a catalytic reaction (either intrinsically catalysed by the MOF itself or by external agents) is performed inside the pore channels of a MOF, either metastable reaction intermediates, products or unprecedented catalyst conformations can be kinetically trapped within the framework, and their crystalline structure can be elucidated at atomic level by SCXRD. Beautiful examples are included in recent work of Sumby, Doonan and coworkers (Figure 1.12). By using a low-symmetry Mn(II)-based MOF of formula $[Mn_3(L)_2(L')]$, where L = bis(4-(4-carboxyphenyl)-1H-3,5-dimethylpyrazolyl)methane and L′= bis(3,5-dimethylpyrazol-1-yl)methane. The same MOF platform, loaded with Mn(I) open metal sites to L' unsaturated centers, was used to register the atomic structure of both reagents and products of azide-alkyne cycloaddition reactions.[94,95]

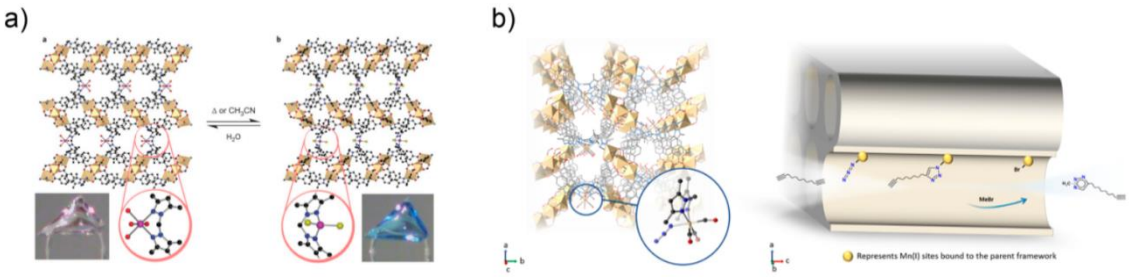

Figure 1.12. (a) View of Co-loaded $[[Mn_3(L)_2(L')]$ along the *c* axis showing the primary coordination sphere of the octahedral Co(II) centre (left) and structure of $[[Mn_3(L)_2(L')]$with a four-coordinate Co(II) centre composed of the di-pyrazole site of $[[Mn_3(L)_2(L')]$ and two chloride anions (one of two chemically identical but crystallographically independent centres shown (right). Inset: single crystal optical pictures. (b) Schematic showing the structural elucidation by SCXRD of click chemistry reagents, intermediates and products.

1.4. Post-synthetic modification of Metal-Organic Frameworks

Excluding applications related to gas sorption/separation, the application of MOFs in other fields of interest deeply relies on the development of MOFs with complex chemical functionalities that can transmit useable physical and chemical properties to the material.[23] While in principle a careful selection of the building blocks used may allow the introduction of virtually any functional group to the porous matrix, the preparation of MOFs with highly-complex chemical structure is harmfully hindered by the limited solvothermal conditions required for MOF synthesis. In practice, the theoretical catalogue of usable organic ligands cannot incorporate functionalities that are even moderately sensitive to temperature, pressure, strong acid or basic median and free metal ions. In any of these cases, the formation of a MOF will certainly get hindered, or even completely frustrated. Sadly, almost every "chemically-interesting" functionality will fall in at least one of these categories. Fortunately, older material fields suffered the same obstacles, and overcame these limitations by incorporating the target functionalities post-synthetically (that is, performing modifications to a pre-synthesised material) in a second step.[96] The post-synthetic modification (PSM) of MOFs could indeed offer an attractive alternative pathway to surpass exposing our target moiety to the aggressive MOF synthetic conditions. Unlike other porous materials, MOFs contain organic molecules as monomers, and those are still active towards organic chemical reactions.[97] Luckily, organic chemistry as a field has grown around exploiting these delicate functionalities, and thus developed mild reaction conditions for practically every coupling.

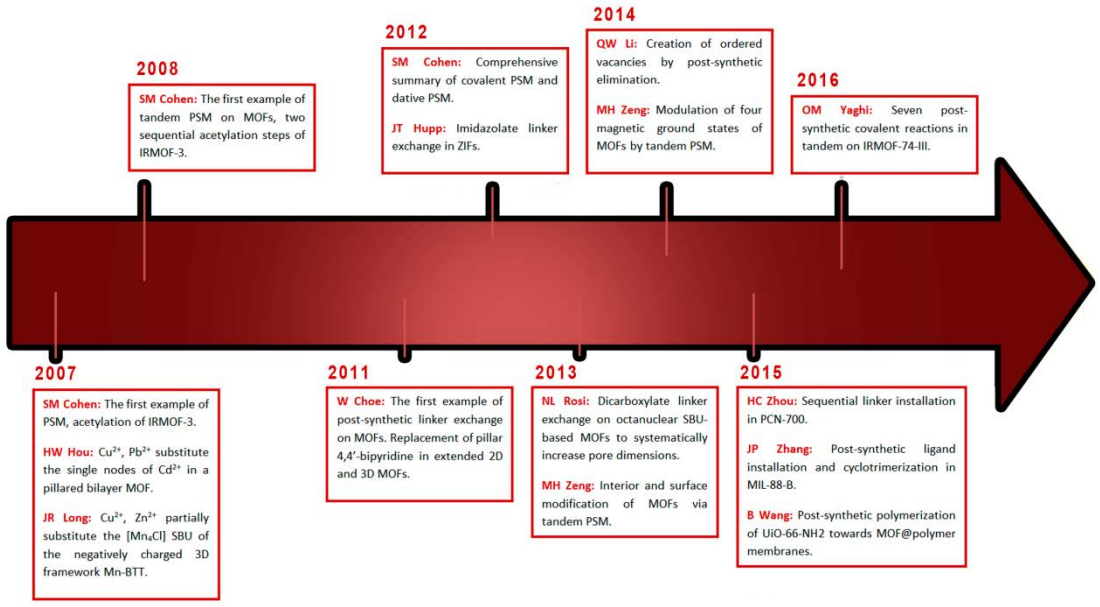

Figure 1.13. The history of development in PSM on MOFs with some representative works of the past decade.

In recent years, the field of PSM has gained a lot of attention within the MOF community. PSM is defined as a process by which a primitive preformed framework is transformed into a new MOF without affecting its crystalline integrity. Through this strategy, PSM allows the formation

of MOFs which cannot be obtained by direct synthesis. If robust functional groups (such as amines or phenols) that do not interfere in the MOF formation can be incorporated inside the pores during solvothermal synthesis, those can be later tagged by applying the principles of organic chemistry.[98] Not only can the organic linkers be modified, as the dynamic nature of MOFs coordination linkages allows the substitution of its metal ions/clusters.[99] PSM demonstrated to be an efficient and flexible tool to alter the structure and properties of MOFs, as MOFs that are obtained via PSM will typically present different physical/chemical properties from the starting parent material. These might include surface area, catalytic centers, hydrophobicity/hydrophilicity and selective affinity towards certain gases.[100,101] Thus, the properties of MOFs can not only be tuned during the initial selection of subunits, but it is also possible to tune their properties by introducing specific functionalities in sequential steps. A huge arsenal of characterisation techniques is available to follow the evolution of MOFs and their PSM (See Section 1.6) thanks to the hybrid nature of the materials and long-range structural order.

Post-synthetic modification methodologies can be divided into different categories, according to the chemistry by which the transformations take place. The most used methods are briefly described below.

- **Post-synthetic ligand modification (PSLig).** The focus of this pathway aims at exploiting the latent functionalised organic linkers within the framework, by means of organic chemistry. This pathway includes covalent anchoring (Dative PS) or thermal/photoinduced transformation of labile groups (PS Transformation).

- **Post-synthetic ligand exchange/insertion (PSLE/PSLI).** Another way of modifying the chemical composition of a MOF consists on exchanging its bridging ligands thanks to the dynamic behaviour of M-COO bonds. When the added linker does not displace any parent linker, but instead occupies defective vacancies, a ligand insertion step is produced.

- **Post-synthetic metalation (PSMet).** This methodology aims to introduce in a controlled manner metallic ions within the framework. PSMet can progress by several pathways: either by targeting the inorganic SBUs (Inorganic PSMet; metal exchange, metal insertion), by targeting coordination centers in the linkers (Dative PSMet; metal exchange, insertion) or by encapsulation within the pores (Ion exchange; metal substitution).

- **Post-synthetic macroscopic etching (PSEtch).** This methodology does not target the chemical structure *per-se*, but affects the macroscopic surface, shape and bulk

properties of the material. Brief sketches will be given in a later section, but this Thesis will focus mainly on functionalisation at molecular-level.

1.4.1. Post-synthetic ligand modification of Metal-Organic Frameworks (PSLig)

Since the majority of this Thesis will be deeply rooted on PSM via covalent chemistry, this Section will be dedicated to grant fruitful insight on the subject**,** including the most common experimental protocols and several examples on the chemistry employed in the field.

1.4.1.1. The dawn of post-synthetic ligand modification in MOFs

The earliest reports of post-synthetic modification in MOFs by means of chemical tuning of the linkers date from 2007. The term "post-synthetic modification" was first postulated by Wang and Cohen, after functionalising IRMOF-3 ([Zn(NH_2-BDC)(DMF)(H_2O)], where NH_2-BDC= 2-amino-1,4-benzenedicarboxylic acid) with acetic anhydride, analogously to how proteins are "post-translationally modified" after their synthesis. Here, the successful covalent anchoring not only on the external facets of the crystals, but also within the porous cavities was monitored by PXRD and digestion NMR experiments.[102]

Most of the early reports of covalent PSM experiments were based as well on amino-tagged MOFs, as it is the most abundant pendant functionality in the field.[103–107] Amino (NH_2-) groups are among the most exploited functional groups in the literature, owing to their basicity, dominant nucleophilicity and versatility, as they can be transformed into myriad products under diverse conditions. This has led to the generation of a rich catalogue of amine chemical reactivity. Moreover, amino-functionalized materials can exhibit enhanced physicochemical properties and have been thoroughly used in many applications, such as surface anchoring, carbon dioxide capture, water uptake and pollutant removal; hence their abundance within MOF pores.[108] As an example, in 2008 Rosseinsky *et. al.* reported the condensation coupling of 2-hydroxybenzaldehyde with IRMOF-3. The obtained product was tagged with salicylidene (imine) groups with a 40% yield. This new moiety, known to be a strong chelating agent, was then metalated with $VO(acac)_2$ (where acac = acetylacetonate) to produce a V(IV)-tagged IRMOF-3 variant.[109] This important project demonstrated that installation of metal chelators into the framework by PSM does not disturb the structural integrity of the MOF. Furthermore, these chelating agents are still accessible in further dative post-synthetic metalations (See Section 1.4.3.2), thereby generating metal centers within the MOF.

After these successful tests, the exploration of post-synthetic modification of MOF linkers grown exponentially in interest, becoming a powerful field that is still active nowadays.[110,111] Apart from classical condensation couplings, researchers developed several alternative techniques to overcome the limitations of the former, which will be presented in depth below.

1.4.1.2. Covalent post-synthetic ligand modification

Covalent PSM of the organic backbones evolves around the formation of strong covalent bonds (either dynamic or irreversible) to specific target functionalities within the linkers. As with common molecular chemistry, the degree of conversion of these processes is dictated by several factors. The first factor that affects conversion rates is the size of the anchored moiety. As expected, the bulkier the substituent is, the hardest is its diffusion through the porous MOF matrix. This was greatly evidenced by Cohen *et. al.,* who explored once again the functionalization of IRMOF-3 with several organic anhydrides (R-CO-O-OC-R; where R = alkyl chains from C_1 to C_{18}. The authors show how shorter chains produce yields over 90%, whereas longer, bulkier chains simply tag the external surface of the MOF crystals, reaching saturation yields below 10%.[112] To this end, MOFs with larger pore windows could theoretically allow bulkier reagents to diffuse through. Cohen *et al.* confirmed this hypothesis by comparing conversion ratios on

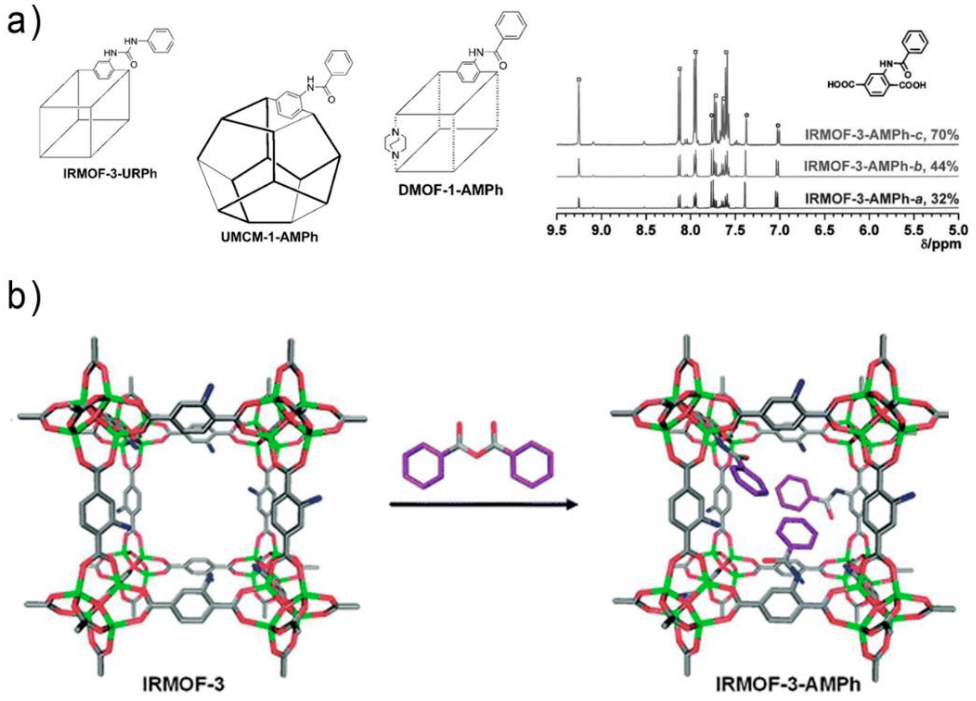

Figure 1.14. (a) Covalent PS anchoring on NH_2-tagged MOFs with different pore sizes and their overall conversion monitored by ^1H NMR analysis. (b) Insight on how anhydride molecules get anchored within IRMOF-3.[98]

NH_2-tagged MOFs with different aperture sizes (UMCM-1-NH_2 = 32 Å, IRMOF-3 = 9.6 Å, DMOF-1-NH_2 = 7.5 Å; UMCM= $(Zn_4O)_3(BTB)_4(BDC)_3$ and DMOF-1-NH_2= $[Zn_2(NH_2\text{-}BDC)_2(dabco)]$, where dabco= 1,4-diazabicyclo[2.2.2]octane). An expected trend was observed, as the highest conversions (monitored by digestion NMR) were achieved in the MOFs with wider pores (Figure 1.14).[113]

Nevertheless, poor conversion yields should not always be related with unsatisfying results. An attractive feature of PSM is the possibility of introducing multiple functional groups

in sequential steps. As so, partially unreacted MOFs can then be sequentially functionalised in further steps, thus achieving multivariate MOFs (MTV-MOFs). This process, generally referred as sequential PSM, involves performing second PSM reactions on a pre-modified MOF.[114] As an example, the incomplete reaction between IRMOF-3 and crotonic acid (*trans*-2-butenoic acid), which still contains unreacted NH_2 groups, was subsequently reacted with acetic anhydride to form a quantitatively-tagged framework with two different functionalities.[115]

When the second reaction step is not performed on the mother framework, but on the freshly anchored functionalities, we can refer to the process as tandem PSM.[116,117] One of the best examples representing tandem PSM was carried out by Yaghi and coworkers, who performed up to seven sequential covalent steps within an amino-tagged IRMOF derivative as a way to covalently incorporate tripeptide sequences that resemble the active sites of enzymes in their spatial arrangement and compositional heterogeneity (Figure 1.15).[118]

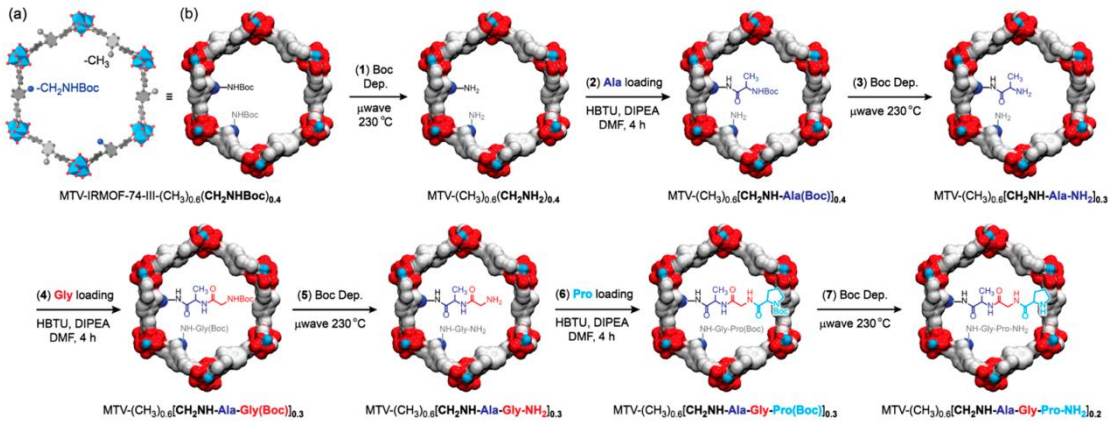

Figure 1.15. Illustration of seven post-synthetic reactions performed within the pores or MTV-IRMOF-74-NBoc to form the tripeptide Ala-Gly-Pro-NH_2.[118]

1.4.1.3. Post-synthetic ligand transformations and eliminations

This approach shares a common objective with the covalent anchoring PSM, but differs on the procedure. Ligand transformation does not introduce any external functionality during the post-synthetic step. Instead, an external stimulus (*i.e.* light, temperature, pH, redox, etc.) triggers a partial/total rearrangement on the chemical bonds of the organic linkers. Generally, post-synthetic transformations behave in a milder fashion, as only small fragments of the linkers are sensitive to the applied stimulus.[119,120] Taking advantage of the thermal robustness that MOFs display, most of these transformations generally evolve through a controlled thermal treatment. In particular, the groups of Telfer and Richardson contributed the most in exploring thermal deprotection (e.g. NBoc thermolysis, where NBoc= 4-*tert*-butyloxycarbonylamine) and rearrangements (e.g. allyl ester rearrangement) within MOF frameworks, respectively.[121–128]

Zhou and coworkers expanded the thermolytic approach recently, by targeting the organic backbone of the framework instead of the tagged functional groups. By applying a thermolytic treatment to Zr(IV) and Fe(III) MOFs (UiO-66 and PCN-250, respectively; UiO-66= $[Zr_6(O)_4(OH)_4(BDC)_6]$ and PCN-250 = $(Fe_3O)_2(AzTC)$, where AzTC= 3,3′,5,5′-azobenzenetetracarboxylate) the authors were able to controllably cleave a portion of the linkers through decarboxylation, which translated into the generation of hierarchical mesoporous cavities.[129,130]

1.4.2. Post-synthetic ligand exchange and insertion (PSLE/PSLI)

Another way to modify the composition of a MOF consists on exchanging its bridging ligands taking advantage of the dynamic nature of their linkages. Even though carboxylate struts are inherently difficult to exchange due to the strong and complex bonding with metal ions, Cohen *et.al.* showed that even some of the strongest MOF assemblies (*e.g.* UiO-66 and Al-MIL-53) can have their linkers partially or totally exchanged by simply soaking the pristine MOF onto saturated solutions of ligands with the same length and directionality. Neither the crystallinity nor the particle size were affected during the experiments, confirming the robustness of the approach.[131] Following the steps of Cohen, several reports demonstrated that the linker length and directionality could be tuned as well during linker exchange, creating hierarchically porous

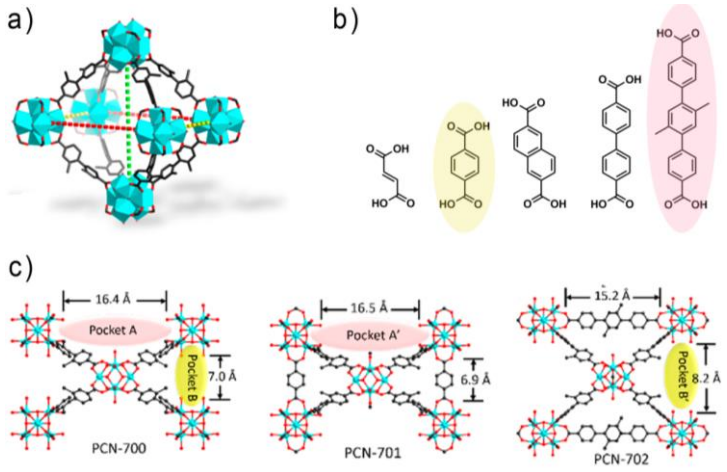

Figure 1.16. (a) Schematic of the crystalline lattice of PCN-700 ($[Zr_6(O)_4(OH)_8(H_2O)_4(Me_2\text{-}BPDC)_4]$). (b) Potential linker roster for the insertion process. (c) Scheme of the sequential PSLI process to form PCN-701 and PCN-702.[133]

architectures.[132]

Recently, a new class of post-synthetic methodology has emerged in the MOF field, based on the same approach as ligand exchange processes. In cases where MOF lattices present structural defects or uncoordinated metal sites, a second organic linker can be installed if the conditions of size, length and chemical affinity are accomplished. Zhou *et. al.* presented the most representative example of this approach. In their study, the Zr(IV)-based MOF PCN-700 ($[Zr_6(O)_4(OH)_8(H_2O)_4(Me_2\text{-}BPDC)_4]$, where Me_2-BPDC= 2,2′-dimethylbiphenyl-4,4′-

dicarboxylate), which presents equatorial "pockets" on its structure (that is, symmetrically localized linker vacancies) of 16.4 and 7.0 Å, was able to accept external dicarboxylate linkers upon soaking the crystals on saturated solutions of H_2BDC and H_2TPDC (TPDC = triphenyldicarboxylate) derivatives, which suitable fitted the pockets. The new MOFs, named PCN-701, PCN-702 and PCN-703, present such complex architectures that are impossible to obtain by direct synthesis (Figure 1.16).[133]

Another curious example of a two-step linker elimination/insertion was reported by Li and coworkers (Figure 1.17). There, they synthesized a Zn(II)-based MOF ($[Zn_4O(PyC)_3]$, where PyC= 4-pyrazolebenzoic acid) that was extended by two completely opposite coordination clusters (Zn_4ON_{12} and $Zn_4O(COO)_6$) due to the asymmetric nature of the used linker. Upon immersion of the MOF crystals in water, half of the linkers and Zn(II) ions were removed in a single-crystal to single-crystal fashion, revealing a hierarchical framework with rectangular-shaped pores. The latter MOF was able to insert secondary metal ions (Li(I), Co(II), Cd(II), La(III)) and linkers (CH_3 and NH_2-functionalised 4-pyrazolebenzoic acid) on its vacancies, thus achieving heterometallic and heterolinked architectures.[134]

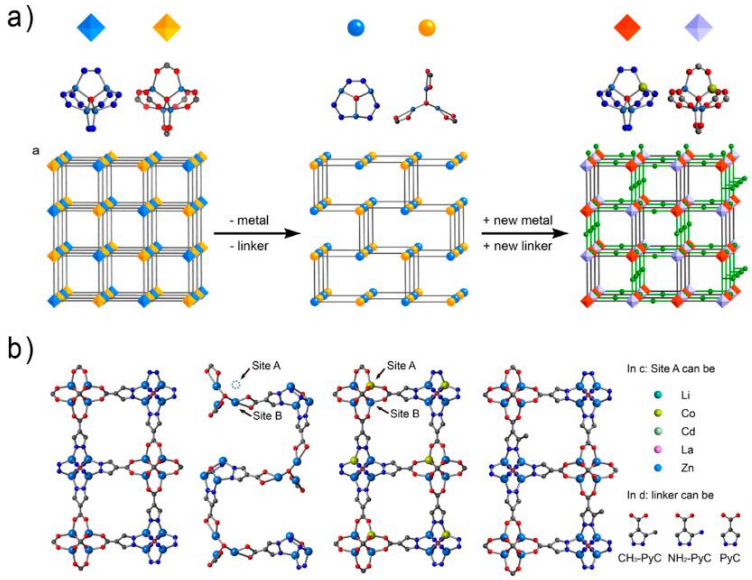

Figure 1.17. (a) Schematic elimination of ligands and metal ions from the original MOF ($[Zn_4O(PyC)_3]$ to generate ordered vacancies, followed by insertion of new metals and ligands into crystallographic defined positions. (b) Single-crystal insight of MOF ($[Zn_4O(PyC)_3]$ during the process.[134]

1.4.3. Post-synthetic metalation of Metal-Organic Frameworks (PSMet)

This Section will cover the most abundant post-synthetic metalation pathways found in the MOF literature. That is, Inorganic PSMet targeting metal exchange on the framework's SBUs; Dative PSMet, focused on anchoring metallic centers to coordination groups anchored within the organic backbone and encapsulation of metallic species within the MOF pores.[135]

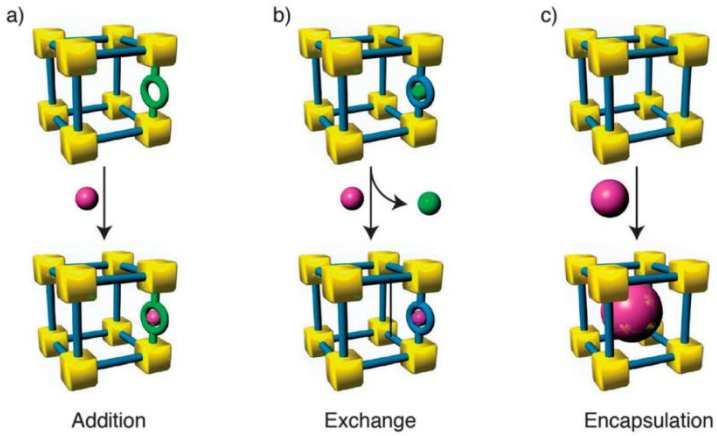

Figure 1.18. Schematic representation on the possible post-synthetic metalation (PSM) pathways.[135]

1.4.3.1. Inorganic post-synthetic metalation

Cationic exchange phenomena do not only happen by human intervention, but are also found in nature. In fact, field minerals are rarely ever found as pure phases. Instead, they crystalize as solid mixtures of equally sized and charged ions. Ion exchange techniques have always been a powerful tool in the design of new materials, and have been widely exploited in metallurgy, ceramics and zeolite fields for decades.[136,137] Briefly defined, these processes are based on partial or total substitution of labile metallic centers mildly accommodated in a material, thus modifying its atomic composition and therefore, tuning their inherent physicochemical properties.

The first documented cationic exchange in MOFs dates from 2007, in which the Mn(II) ions of the Mn-MOF $[Mn_3(Mn_4Cl)(BTT)_8(MeOH)_{10}]_2$ (where BTT= 1,3,5-benzenetristetrazole) were partially substituted by several other transition metals (Li(I), Fe(II), Co(II), Ni(II), Cu(I/II), Zn(II)), and their hydrogen storage capabilities were compared with that of the parent framework. In these materials, the exchange occurred at the inorganic clusters or SBUs and, even though the clusters were integral to the MOF structure, the metal ions were successfully replaced (sometimes even in a matter of hours) without compromising the structural integrity. Remarkably, some of these substitutions even altered the overall charge balance of the framework.[138]

The details of such transformations are still nowadays rather unknown, even with several mechanistic hypotheses around, and the bounty of MOF structures that can undergo metal substitution cannot be logically elucidated. Brozek and Dincă analyzed in-depth this subject in their review *Cation exchange at the secondary building units of metal–organic frameworks*.[139] There, the authors elucidate several common factors that govern every reported post-synthetic exchange, such as ionic diameter or preferential coordination geometries (the exchangeable metal ion in SBUs is often capable of higher coordination numbers than those observed in the X-ray

crystal structures). In some cases, the exchangeable metal ions that contain open sites within the framework become partially solvated when immersed in solution, completely changing its coordination environment and thus facilitating its replacements. Conversely, SBUs with fully-saturated metal sites that have no open centers or coordinated solvents typically do not undergo cation exchange. Remarkably, the M-COO bond strength does not affect the thermodynamic exchange process, but simply limits the kinetics of the substitution step. Still, these guidelines are pillared on experimental observation, and several exceptions are reported in which the organic linkers play a major role during the substitution. Nevertheless, even without full understanding, post-synthetic metal exchange processes in MOFs have been experimentally demonstrated to work, and thus have allowed the formation of various materials that could not be obtained by direct synthesis methods.[140]

Since 2007, hundreds of publications regarding Inorganic PSMet have been reported. Both subtle and total substitutions have been carried out in a myriad of MOFs and PCPs, each of them contributing heavily in expanding the knowledge and practical horizons of the approach. One of the most astonishing examples was carried out by Kin and coworkers, reporting a reversible quantitative substitution of the metallic clusters of a Cd(II) based-MOF by Pb(II) ions in a single-crystal to single-crystal fashion (Figure 1.19a). The MOF, with formula $[Cd_{1.5}(H_2O)_3[(Cd_4O)_3(HETT)_8 \cdot 6H_2O]$ (where HETT = ethyl-substituted truxenetricarboxylic acid) suffered a quantitative substitution of its square-planar Cd_4O SBUs by simply immersing the material in a saturated solution of Pb(II) ions for two weeks at room temperature. Likewise, the parent framework could be recovered by soaking the Pb(II)-based MOF in a saturated Cd(II) solution for five weeks. Both structures could be elucidated by SCXRD techniques, confirming the quantitative conversion in a single-crystal to single-crystal fashion, rather than a dissolution/precipitation step.[141]

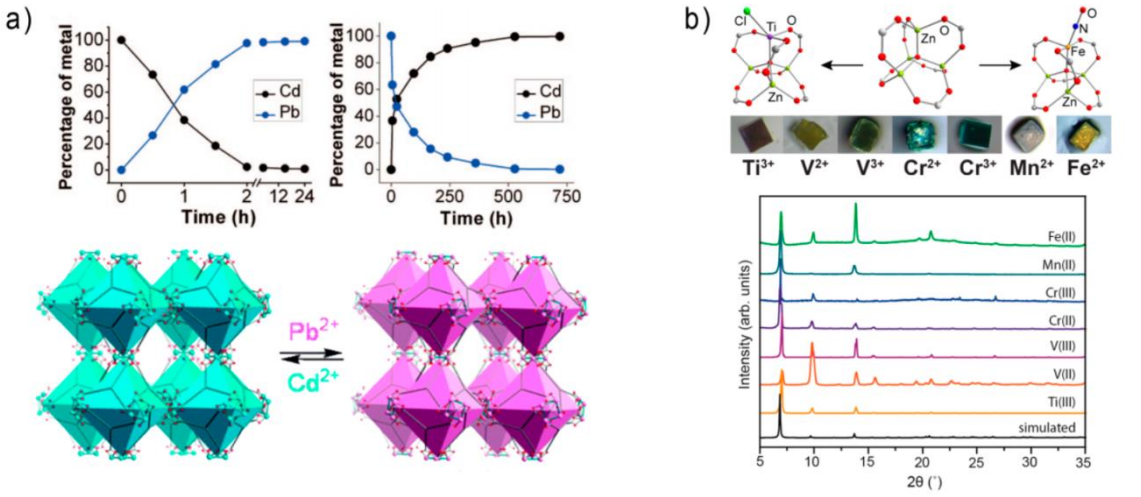

Figure 1.19. (a) Complete and reversible metal ion exchange between crystalline Cd(II) and Pd(II) MOF $[M_{1.5}(H_2O)_3[(Cd_4O)_3(HETT)_8 \cdot 6H_2O]$. [141] (b) Illustration showing how several metal ions can be inserted to the inorganic SBUs of MOF-5 analogues, featuring hetero-bimetallic metal clusters.[142]

Additionally, not only conveniently-shaped MOFs can be quantitatively substituted, but also some well-known materials can be decorated by PSMet. Dincă *et. al.* used MOF-5 as a sacrificial material to prepare several heterogeneous isostructural MOFs containing divalent (Cr(II), V(II), Mn(II) or Fe(II)) or trivalent (V(III), Ti(III)) transition metal ions (Figure 1.19b). Every transformation retained the powder X-Ray diffraction (PXRD) pattern of the original MOF-5 and the crystal size and morphology were not affected, thus denying potential dissolution/recrystallisation steps. Remarkably, when heterometallic SBUs were inserted to MOF-5, the obtained materials presented unique redox properties.[142]

1.4.3.2. Dative post-synthetic metalation

The second strategy to introduce external metal sources on MOFs is based on using free functional groups anchored to the organic backbone that are able to chelate or coordinate metallic ions, coordination clusters and organometallic complexes. During the process, certain considerations must be taken into account, such as the available free space that the new metallic entity will assume, as well as its associated ligands or anions. Nevertheless, unlike other porous materials, MOFs offer unparalleled opportunities in dative PSMet processes, as the availability of both inorganic and organic subunits opens up myriad pathways to anchor functional groups within the framework, either by direct synthesis or post-synthetic routes. Additionally, the crystalline behaviour of MOFs renders a highly ordered material, which translates on the ability to afford well-characterised PSM steps, up to the atomic level. Accordingly, ions can be post-synthetically incorporated into the framework at predefined positions throughout the backbone, precisely selected depending on the targeted applications.[143,144]

One of the first examples of this strategy was performed by Lin and coworkers, who took advantage of the relative affinity of functional groups towards certain metal ions to synthesise a Cd(II)-based MOF through the pyridine moieties of the linker (R)-6,6'-dichloro.2,2'-hydroxy-1,1'-binaphtalyl-4,4'-bipyridine, leaving two pendant OH groups per linker oriented towards the pore channels. Through those, the authors could successfully anchor the organometallic complex $Ti(O^iPr)_4$ (where O^iPr = isopropoxide) in almost 33% of the linkers. The metalated framework showed enantioselective catalytic activity towards diethylzinc addition reactions.[145] A similar example was reported in 2010 by Yaghi and coworkers. This time, the pyridine moieties of the linker 2,2'-bipyridyldicarboxylic acid (H_2BYPDC) were the ones left unreacted oriented towards the porous channels of the MOF when extended with Al(III) ions (MOF-253) (Figure 1.20). Pd(II) and Cu(II) ions could be then anchored post-synthetically by soaking MOF-253 in saturated solutions of the ions in acetonitrile.[146] Analogously, permanently porous MOFs composed of

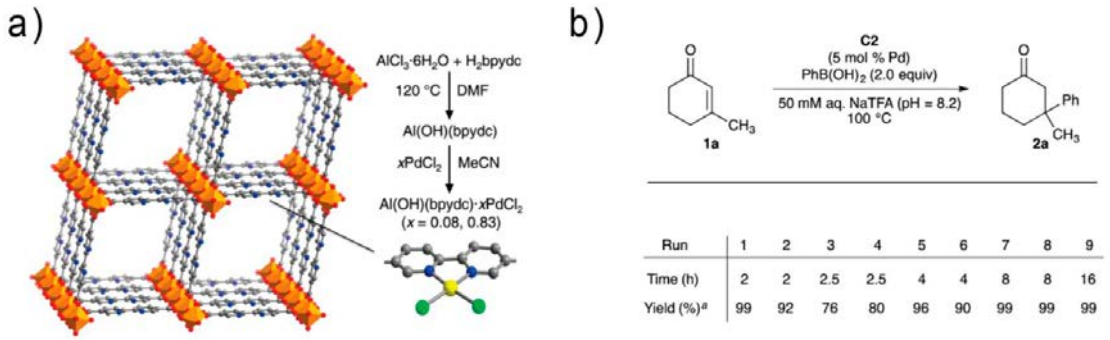

Run	1	2	3	4	5	6	7	8	9
Time (h)	2	2	2.5	2.5	4	4	8	8	16
Yield (%)[a]	99	92	76	80	96	90	99	99	99

Figure 1.20. (a) Schematic representation of Al-MOF-253, with metal-loaded bipyridine moieties oriented inwards towards the porous channels. (b) Catalytic activity of PSMet MOF-253, showing excellent cyclability towards Pd(II) catalysed α,β-Michael insertion.[180]

metal-free porphyrin units were synthesised by using oxophilic Zr(IV) ions, which preferentially bind the hard carboxylate donors of tetracarboxyphenylporphyrin linkers.[147–149] These porphyrin-based MOFs were highly robust and exhibited surface areas in excess of 2,000 $m^2 \cdot g^{-1}$, thus providing an excellent platform for further PSMet steps with N-affine cations.

However, as explained at the beginning of Chapter 2, sometimes the incorporation of highly-reactive functional groups within the MOF backbone tends to be incompatible with the aggressive conditions required for MOF synthesis. When preferential reactivity is not observed, alternative pathways should be taken. As so, some of the binding groups that could enable dative PSMet pathways need to be incorporated *a posteriori*. An obvious advantage of this approach is that the MOF synthesis can be performed without risking degradation of the target functional group. Some examples of the approach include (*i*) covalent anchoring at the linkers (Section 1.4.1.2); (*ii*) orthogonal deprotection of temporarily-blocked functional groups; and (*iii*) anchoring metal binding units to the MOF's SBUs. A representative example is found on the work

of Telfer *et. al.,* who used the Boc-protected linker (S)-2-(1-(tert-butoxycarbonyl)pyrrolidine-2-carboxamido)-[1,1′-biphenyl]-4,4′-dicarboxylic acid ((S)-pro-Boc) as a bridging ligand to synthesise an IRMOF derivative with protected Proline moieties accommodated in the pore cavities. IRMOF-pro-Boc was easily deprotected to form catalytically active IRMOF-pro by microwave irradiation heating, which proved to be an efficient catalyst on the asymmetric aldol reaction between acetone and 4-nitrobenzaldehyde.[127,128]

The post-synthetic anchoring of coordinative groups by any of these strategies has substantially amplified the scope of PSMet pathways. The ability to introduce fancier, more selective organometallic/coordination centers inside porous MOFs bypassing the aggressive solvothermal conditions is having real implications in many fields, particularly on heterogeneous catalysis.[96]

1.4.3.3. Encapsulation of metallic species within MOF pores

A more direct PSMet strategy for MOFs is to encapsulate metallic species (either in the form of free ions or structured into INPs, polyoxometalates, etc.) as guests within their porous cavities. Here, the MOF architecture will not accommodate the metals on their backbones, but simply act as a matrix to control the 3D structuration of metal compounds.[150] The nanometer-sized pore windows in MOFs allow metal species to diffuse into the pores both in solution and gas phase. In successive steps, adequate complexation agents, reductants or chelating agents can be diffused as well and react with the metallic species to form organometallic complexes inside the MOF channels. [151] Kim *et. al.* used vapor phase diffusion methods to impregnate the pores of MOF-5 with ferrocene complex. This method proved "too efficient", encapsulating seven ferrocene units per pore, only leaving around 1% accessible free volume and therefore leaving the catalytic compound unreachable.[152] Later, common metal precursors (Fe, Pt, Pd, Au, Cu, Zn, Sn) were deposited inside MOF-5 by chemical vapor deposition (CVD) without observing structural decomposition of the framework.[153] The efficiency of this methodology has pioneered a body of work that still nowadays investigates the *in situ* formation of organometallic entities within MOFs. Recent work by Ma and co-workers has demonstrated how MOF materials can not only accommodate inorganic species, but can as well encapsulate metal-loaded biomolecules. In their work, the authors show how the mesoporous MOF Tb(TATB) (,where TATB= triazine-1,3,5-tribenzoic acid) could be post-synthetically metalated with microperoxidase-11 (MP-11) under buffered conditions.[154]

Finally, several INPs have been formed *in situ* by loading MOF pores with metal ion solutions, followed by sequential reduction. Through this, important catalytic particles, such as Pt, Pd, Ru^0 and TiO_2 NPs have been structured inside MOFs without further aggregation. As an example, Jiang, Long and coworkers reported core–shell structured bimetallic NPs encapsulated

into Cr-MIL-101. $Pd(NO_3)_2 \cdot 2H_2O$ and $CoCl_2 \cdot 6H_2O$ were pre-incorporated in the pores of Cr-MIL-101 and were sequentially reduced *in situ* by the addition of NH_3BH_3 to yield ~2.5 nm Pd@Co core–shell NPs embedded inside the MOF. In this study, Pd NPs were formed first and served as cores for the subsequent reduction to yield Co shell NPs (Figure 1.21).[155]

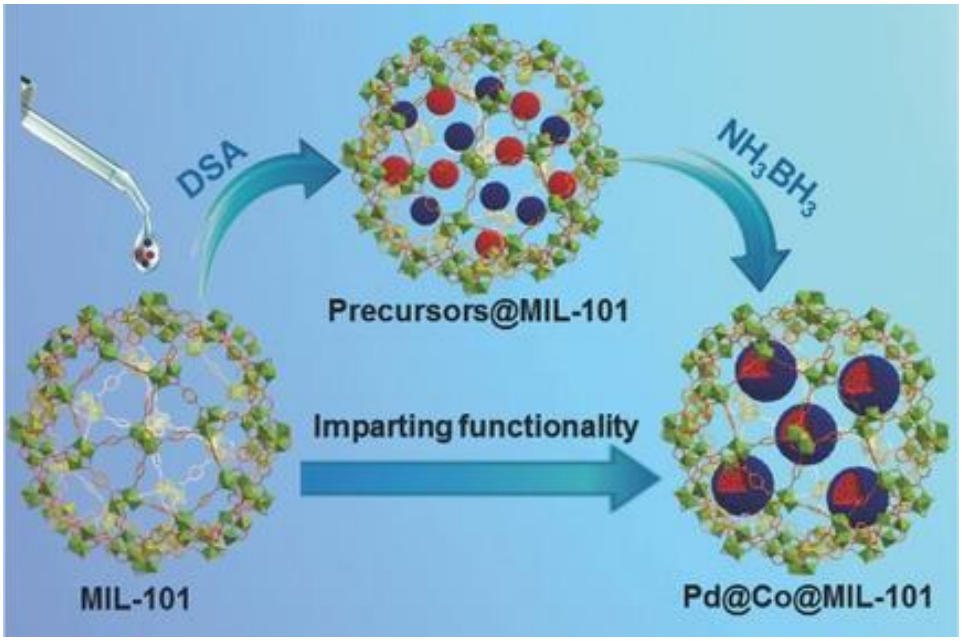

Figure 1.21. Representation of the Synthesis of core-shell Pd@Co@Cr-MIL-101 composite catalysts by sequential encapsulation/reduction with NH_3BH_3.

Both studies highlight the wide scope of this technique, acting as platforms that enable heterogeneous exploitation of nanoparticles.

1.4.4. Post-Synthetic macroscopic etching of Metal-Organic Frameworks

The post-synthetic modification of MOFs is not only limited to molecular-level chemical conversions. When the physicochemical properties of the material want to be preserved, but the practical application is limited due to its macroscopic properties *per se*, it is possible to chemically modify the crystal shape, morphology, size and even generate macroscopic holes on MOF crystals. This process, referred as chemical *etching* or shaping, has been gaining a lot of interest in the recent years, as the real applicability of MOFs is directly related with their processability into conveniently-structured materials. Chemical *etching* is not a new process, but an ancient fabrication method that was used by metal and glass craftsmen to obtain sophisticated surface designs. With the advent of controlling the etching process at the microscale and nanoscale, anisotropic chemical etching has become highly useful for shaping many materials for diverse applications.

Engineering the macroscopic surface of MOFs can afford to advantageously improve their performances in a myriad of fields. In a nutshell, macroscopic etching of MOF crystals has been used to improve the diffusion of substrates towards the inner core of microscopic crystals; improve their packing in membrane systems or facilitate their introduction in composite systems.[156–160] Remarkably, several studies have targeted the mechanism on these processes. As a general route, the chemical etching occurs preferentially of crystal facets with the higher density of metallic ions. There, the etching agent (acid, chelator, etc.) simultaneously breaks metal-ligand interactions and sequestrates the now-free metal ions in solution (Figure 1.22). Depending on the initial surface ratio of these metal-dense facets, the process will evolve differently, thus revealing a wide range of shapes, voids and structuration for the same material.

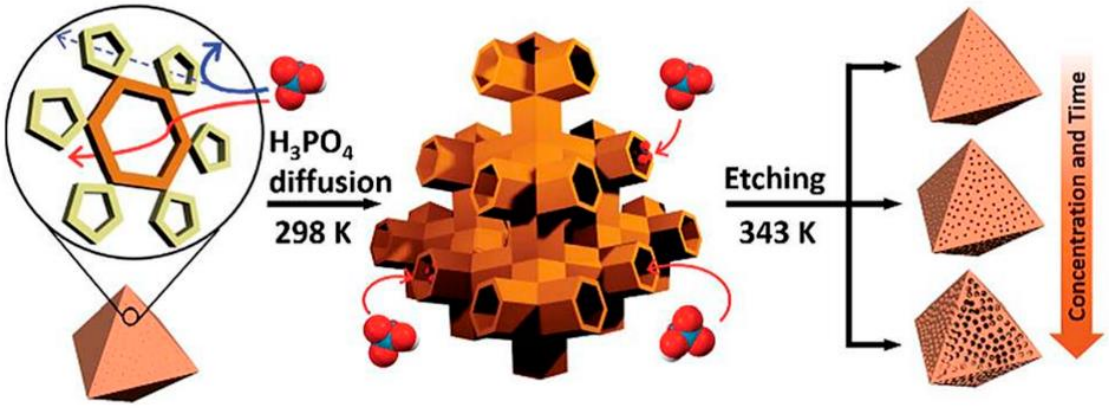

Figure 1.22. Illustration of the etching process of Fe-MIL-100. (Left) Fe-MIL-100 crystal with hexagonal and pentagonal windows; (middle) acid diffusion into tetrahedral channels through hexagonal windows; (right) resulting mesopores after etching.[161]

1.5. Limitation of the post-synthetic modification of Metal-Organic Frameworks

This Section will cover the future perspectives on the PSM field in MOF chemistry and what limitations are hindering the real-world application of such strategies. Particular emphasis will be made on intervoid diffusion phenomena and macroscopic influence, and how they affect these *a priori* intrinsic functionalisation steps.

1.5.1. Future perspectives

Inspiring advances have been made since the seeding that early covalent and inorganic PSMs achieved in 2007. The research of PSM of MOFs has matured to new levels driven by the combination of new post-synthetic methodologies and sequential tandem reactions. Additionally, sophisticated methodologies are arising by exploiting orthogonal reactivity within the frameworks. PSM provides new methods to access crystal engineering beyond standard synthetic methods. This Chapter exemplifies how PSM allows addressing early-career limitations that the MOFs field faced since the early 2000s, like the introduction of thermo- or coordinatively-active groups, creating atomically-defined catalytic centers, or improving framework stability. The latest major finding in tandem PSM combining subsequent reaction types integrate in MOFs unprecedented structural complexity and unveils the potential of MOFs as an ideal platform to realize multifunction. Nowadays, it is implicit that PSM will be absolutely necessary in the future research of MOFs.

However, several challenges are required to be solved prior to moving forward in the PSM field. Every post-synthetic pathway is just at the very early stages, mainly focused on singular MOFs specifically designed for the PSM to succeed. Little coverage on general strategies or mechanistic studies is being reported, greatly hindering real knowledge acquisition of the process (linker length/directionality influence, framework flexibility, crystal size, solvent influence, etc.). Additionally, even though the PSM of MOFs with multiple linkers can be operated orthogonally to different reactive positions,[162] the chemical disposition of these MTV-MOFs is structured in an inherently polydisperse fashion, thus limiting the study of such heterogeneous systems. Reagent diffusion within the porous channels, preferential pathways, and synergistic effects are excluded in most studies for a simpler justification of experimental evidence. Thus, advances in mechanistic studies and media influence evaluation are of great urgency to tie a new way to rational and precise PSM.

1.5.2. Gradient intervoid diffusion – Kinetic limitation

Loading porous frameworks with guest molecules is a crucial step for many applications.[163,164] Mass transfer of guest molecules is a critical parameter governing performance, for example, in gas separation processes, where poor transfer rates result in low efficiency. Theoretically, as long as the target guest is smaller than the average pore window diameter of the MOF, diffusion should occur smoothly in a continuous fashion. Unfortunately, diffusion phenomena in MOFs is not a regular process, and the experimentally-determined mass transfer ratios into the framework may vary by several orders of magnitude, even for different sample batches of the same material.[165] This limitation is particularly evident in post-synthetic methodologies, as the diffusivity of the target functionality within the porous cavities directly influences the final conversion yields.[166]

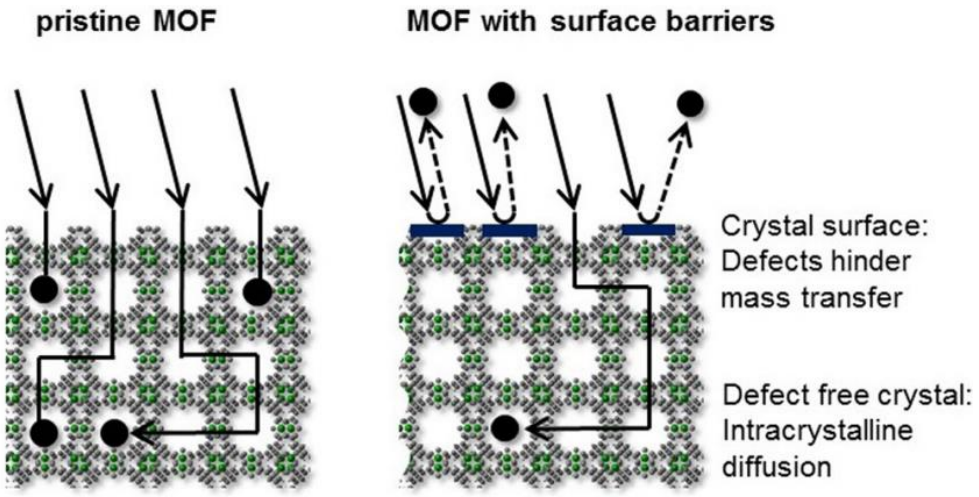

Figure 1.23. Model of the mass transfer in MOFs. (Left) unhindered mass transfer in the defect-free, nanopoorus crystal. (Right) Surface barriers, caused by a large amount of blocked pores, with very few accessible entrances, hinder the guest molecules.

There are several external factors (*i.e.* non-related to the MOFs chemical structure) that tremendously influence the degree of functionalisation obtained through PSM. Among them, physical parameters (temperature, pressure, relative humidity, etc.), solvent, reaction times and structural defects can easily be tuned and optimised. However, one of the most limiting factors, and one of the hardest to control, is the kinetic evolution of the reaction itself. Ironically, fast and quantitative reactions might end up performing awfully when used to functionalise the surface of MOFs, as the nimble functionalisation of the external surface obstructs the MOF windows, thus blocking the diffusion of reagents towards the crystal core (Figure 1.23). Additionally, the obstruction of external pore windows does not only happen due to partial covalent tagging on the surface. Lattice flexibility, partial collapse under ambient/solvent moisture or mechanical

obstruction due to solvent-filled pores are other parameters that avoid a precise control of diffusion, and therefore of post-synthetic functionalisation steps.

In order to overcome these sometimes arbitrary limitations, one could follow two logic strategies, (*i*) solvent-less strategies, in which the diffusion gets intrinsically dictated by the reactant's dynamic diffusion; and (*ii*) miniaturisation of crystal size, which translates to higher external surface/shorter diffusion gradients.

1.5.2.1. Solvent-less post-synthetic functionalisation of Metal-Organic Frameworks

The majority of PSM in MOFs, both to the inorganic clusters and to the organic ligands, is performed following solvent-immersion methodologies. Most of the time, these post-synthetic procedures end up deriving into long reaction times, achieving at best (excluding a few examples), moderate conversion yields.[97] This is because liquid phase reactions are limited by the gradual diffusion of solvated reagents into the MOF channels. As explained before, the nanosized windows in MOFs produce slower diffusion rates than the overall reaction rates, thus blocking access to the inner core of the MOF crystals. Additionally, solvent molecules need to be displaced from the free volume in order to properly access the reactive centers in the framework, again slowing the overall process.

To this end, a solvent-less methodology could overcome this limitation by partially or totally ignoring solvent diffusion phenomena. Solvent-less reactivity, particularly solid-gas phase reactivity, has been a widely explored approach in metallurgy and polymer science. Indeed, reactive gases (e.g. fluorine gas in steel industry) or liquid-state reagents have been used to quantitatively passivate, cleave or switch the hydrophobic behaviour of diverse materials.[167–169] For this reason, solvent-less PSM of MOFs has attracted much attention in the recent years as a quick, effective and simple method to overcome the aforementioned obstacles. Up to date, very few examples of solvent-less PSM of MOFs have been reported to be successful.

One of the first examples of solvent-less PSM was reported by Lobkovsky and coworkers, who reacted an Ag(I)-based CP which presented pending OH functionalities with vapours of trifluoroacetic anhydride.[170] High conversion yields were confirmed by IR and NMR analysis, demonstrating the latent potential of the strategy. Later studies, carried out by Wutke *et. al.* confirmed the faster dynamic behaviour of the solvent-less approach by performing imine condensation reactions with salicylaldehyde both in solid-solution and solid-vapour fashion. The authors functionalised a series of NH_2-tagged MOFs (Zr-UiO-66-NH_2, Al-MIL-153-NH_2 and Al-MIL-101-NH_2) by heating solid mixtures of MOF sample and the organic reagent of choice. Specifically, after reacting with a series of acyl chlorides, acid anhydrides and free carboxylic acids, the authors were able to tag the surface of every MOF with amide condensation reactions

in mere minutes. [171] Remarkably, the same strategy was exploited in a solid-gas fashion in 1999, taking advantage of the low boiling points of some acyl anhydrides. Under the same reaction conditions and reaction times, the solvent-less methodology presented an almost quantitative yield (>99% based on NH_2), whereas a conversion of only 13% was obtained under solution soaking. Additionally, the generality of this PSM approach was demonstrated by reacting the same amino-tagged MOFs with several carbonyl derivatives while always maintaining intact porosity and crystallinity values (Figure 1.24a).[171]

Not only covalent organic reactions can be performed in solvent-less fashion. Richardson and coworkers showed a solvent-less thermally induced transformation in an IRMOF-9-like MOF, which presented pending dimethylthiocarbamate groups. After heating at 285 ºC, a quantitative Newman-Kwat rearrangement took place without affecting the structural integrity of the material (Figure 1.24b).[172]

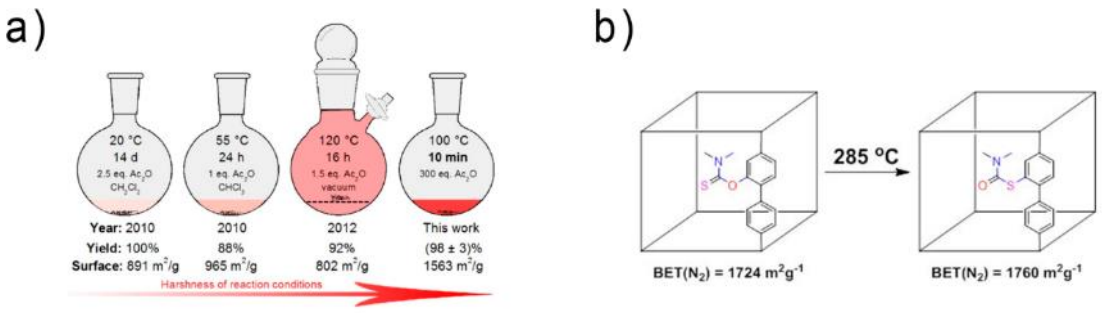

Figure 1.24. Representative examples of solvent-less PSM of MOFs. (a) quantitative covalent anchoring of carbonyl derivatives within the pores of IRMOF-3 by converting organic anhydrides to a vapour state. (b) Thermal Newman-Kwat rearrangement on the porous functionalities af an IRMOF-9-like MOF.

Beyond the covalent tagging of MOFs, solvent-less PSMet processes have been reported by loading MOF pores with metallic precursors through chemical vapour deposition (CVD). Typical metal-organic precursors (Au, Pd, etc.) have been inserted in MOFs through volatilization/absorption processes under elevated heat and vacuum, followed by a reduction step (*i.e.* hydrogenolysis, annealing treatments, etc.). Through this methodology, several MOFs have been loaded with INPs, but also with organometallic compounds amenable to sublimate. As an example, common metal precursors (Fe, Pt, Pd, Au, Cu, Zn, Sn) were deposited inside MOF-5 by chemical vapor deposition (CVD) without observing structural decomposition of the framework.[153]

1.5.2.2. Miniaturisation of Metal-Organic Frameworks

When comparing the physical properties of solid matter particles to those of samples that require an optical microscope to be regularly seen, only subtle differences are spotted. However, when operating at the nanoscale regime (between 1 – 100 nm), where the particles are only "visible" using powerful microscopes, the material's properties suffer drastic changes from those at larger scales. This is the size scale where quantum phenomena rule in the properties and behaviour of most materials. Here, physical properties tend to gain a size-dependant character, as the amount of atoms exposed in the surface increases drastically within the nanoscaled regime. The surface area to volume ratio for a particle with radius *r* can be calculated as follows:

$$\frac{Surface}{Volume} ratio = \frac{4\pi r^2}{\frac{4}{3}\pi r^3} = 3/r$$

In other words, as the radius decreases, the more atoms are exposed in the surface (10% for 50 nm, 20% for 10 nm and 50% for 3 nm). Exposed surface atoms or molecules are more amenable to react, as no diffusion phenomena are required to reach the inner material. MOFs are no exception to this rule. For any PSM process, given a given fixed reaction time, smaller crystals of the same MOF tend to present higher conversion yields, as more external surface is initially exposed. Maspoch *et. al.* demonstrated this phenomena by performing common covalent PSM to several MOFs with different particle sizes by using continuous flow spray drying technique. Here, the authors performed Schiff-base condensation reactions to nanoscaled structured MOFs at the droplet scale. The spray-dried superstructures of nanoscopic MOF particles exposed substantially more surface area to the reagents within the droplet than the macroscopic MOF crystals, obtaining higher conversion yields than common PSM methodologies in as short as a few seconds of reaction time.[173]

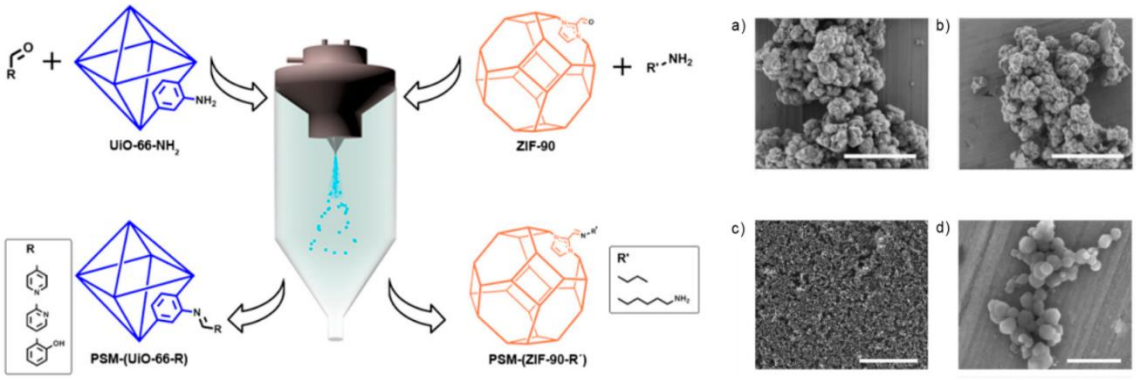

Figure 1.25. (Left) Illustration of the covalent PSM performed in UiO-66-NH_2 and ZIF-90 under Spray-Drying conditions. (Right) FESEM images of UiO-66-NH_2 ((a) before and (b) after) and ZIF-90 ((c) before and (d) after) Spray-Drying PSM. Inset: 2µm (a,b,c) and 200 nm (d).[173]

1.5.2.2.1. Metal-Organic Polyhedra (MOPs)

The miniaturisation process of porous frameworks can be further extended up to the point where only isolated pores are standing. In this case, the new material cannot be depicted as a framework *per se*, but as a supramolecular assembly of discrete zero-dimensional cages with polyhedral shapes. Following this thread, the field of Metal-Organic Polyhedra (MOPs)[174] has been gaining interest in the recent years, as these materials blend the properties of porous materials and molecular chemistry. MOPs can be described as "isolated MOF pores", assembled through a careful selection of metal ions/clusters and bended organic ligands.[175]

There is little information on when and why a bended linker will assemble into a discrete MOP or will periodically extend into a coordination polymer. Several factors such as the thermodynamic stability of every phase, favoured coordination clusters or supramolecular interactions can displace the equilibrium to one side or the other.[176] Still, there is no general strategy to avoid the formation of extended frameworks due to the inherent dynamic nature of coordination bonds. Generally, the formation of MOPs is favoured under slow diffusion systems at room temperature. Under these conditions, the formation of defect-free crystalline frameworks in thermodynamically unobtainable, therefore reagents tend to structure into zero-dimensional architectures. In systems where the MOP formation is not favoured, Yaghi *et. al.* demonstrated how the addition of bulky directing agents (*e.g.* Glycine *tert*-butyl ester) can impose the formation of discrete assemblies, as demonstrated in the synthesis of MOP-15 (Cu(II)-based 5-aminosiophtalic acid MOP).

A wide catalogue of MOP structures has been developed in the recent years. However, their physicochemical properties have not been properly exploited yet due to the fragile nature of their assembly. Even though MOPs have been successfully incorporated into matrix membranes,[177] or explored as potential delivery systems,[178] MOPs tend to collapse when their internal solvent gets evacuated. Additionally, the poor solubility that MOPs present in most solvents limits their competition in the solvated-state with other readily soluble porous cages (*i.e.* charged coordination cages, porous organic cages, cyclodextrins, etc.)

Still, once the fragile nature of MOPs is overcome, their molecular structure could potentially give MOPs an edge advantage over other porous cages. First, the neutrally-charged polyhedral nature of MOPs offers regularly distributed and oriented building blocks, with similar structuration patterns that those found in MOFs. For this, MOPs can be seen as molecular nanoparticles with well-defined coordination centers and oriented organic moieties. Therefore, their post-synthetic modification, by means of coordination or covalent chemistries, would be performed at a molecular level into the well-defined reactive centers at their periphery. Analogously to MOFs, the post-synthetic modification of MOPs should greatly tune their physicochemical properties (*i.e.* solubility, robustness, hydrophobicity), as the process will

essentially modify the whole chemical structure on the surface. Surface functionalisation has proven to be a powerful technique during the manipulation and process of nanoparticle, but unlike MOPs their surfaces are inherently polydisperse, which translates to poor structural information on how the surface is structured. However, despite the potential of the approach, there are little experimental data reports on the post-synthetic modification of these materials.

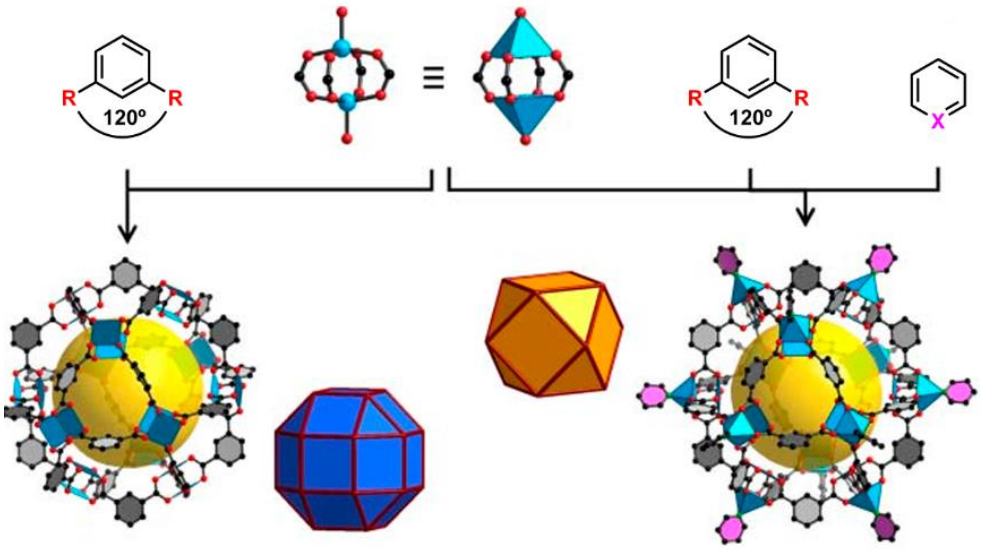

Figure 1.26. Schematic illustration on the assembly of zero-dimensional Metal-Organic Polyhedra (MOPs), highlighting in pink their directional coordination sites. Colour Scheme: Cu(blue), C (gray), O (red), pyridine-derivatives (pink).

1.6. Characterisation techniques

As briefly presented during the examples in Sections 2.1 – 2.4, there is a wide range of characterisation techniques that can be used to follow and quantify the evolution of PSM reactions in MOFs and MOPs, although not every technique will prove useful for every pathway. Depending on which subunit is targeted during PSM (*i.e.* inorganic SBU, organic linker, inner voids), one should make a precise selection in order to obtain the highest structural information without losing excessive sample in destructive techniques.

Most PSM pathways, excluding those focusing on phase transformations, are based upon the premise that the structural integrity (that is, crystallinity and porosity) of the mother framework is unaltered. To this end, X-Ray Diffraction (XRD) techniques (either powder or single-crystal measurements; referred as PXRD and SCXRD respectively) provide a fast analysis on the crystalline lattice and topology of MOFs. The PXRD pattern of a MOF after PSM should theoretically be identical to that of the starting MOF, where partial degradation can be spotted by comparing the intensity and width of the diffractograms peaks. Additionally, crystalline side-products, phase transitions or impurities of the PSM process can be spotted as well by this

technique. On the other hand, SCXRD offers richer structural information of the framework at atomic level, but is limited to single-crystal quality material and requires non-routine data treatment. Despite the power of these techniques, PXRD and SCXRD measurements provide little-to-no information of potential amorphous side-products, thus hindering the general scope of the technique.

The porous behaviour of MOFs, MOPs and their PSM products can be examined through gas sorption measurements. In MOF science, surface area values are calculated by Brunauer-Emmet-Teller (BET) physisorption measurements, which apply to systems of multilayer adsorption using probing gases that do not chemically react with the materials surface (typically N_2 at 77 K). Generally, the sample is exposed to strong temperature and vacuum conditions before the measurement in order to properly evacuate every solvent molecule from its porous cavities. This process, known as activation, is a clue step in order to fully unveil the porous potential of every sample. Partial or incomplete activation steps might lead to misleading porosity or surface area values. Therefore, activation temperatures, vacuum and time have to be properly optimised for every specimen.

Thermogravimetric Analysis (TGA) is an effective technique to characterise the thermal evolution/stability of MOF/MOP samples versus temperature. Through this technique, mass variations that happen to the sample at a given temperature range can be easily spotted and quantified, including solvent evacuation. TGA thermogram can be used as well to predict the thermal stability of a given MOF/MOP, as degradation steps can be spotted as drastic weight loss steps, typically between 30 and 60% depending on the material's chemical composition.

Nuclear Magnetic Resonance (NMR) spectroscopy has been employed by MOF scientists to follow the evolution of chemical transformations occurring in the linkers upon PSM. Routinely, ^{1}H NMR spectroscopy is used to gauge the percentage conversion of a functional group into a different group, or to spot the new signals attributed to the freshly-added pending functionality. Additionally, the wide arsenal of NMR techniques can provide powerful compositional information, including proton proximity, elucidation of solution entities, ^{1}H-^{13}C 2D analysis, etc. Prior to any NMR measurement, MOFs are typically digested in an acid or base solution together with the deuterated solvent of choice and heated for hours at high temperatures to ensure quantitative destruction of the lattice. Special care needs to be taken in order to ensure that no additional side-reaction occurs on the product during NMR digestion conditions (*e.g.* acid/base-induced hydrolytic cleavage of linker backbone). In cases where digestion conditions are not compatible, solid state NMR (ssNMR) is employed to address the issue. Nonetheless, solution NMR is generally preferred over ssNMR as the latter provides ambiguous information due to high signal/noise ratio or limitation to ^{13}C studies. On the other hand, the molecular behaviour of

MOPs allows their structural characterisation by solution ^{1}H NMR analysis without requiring digestion conditions, at the cost of getting broad hard-to-integrate signals due to their high molecular weight.

Unlike MOFs which require digestion conditions, the structural integrity of MOPs is maintained in solution. This processability of MOP samples in solution allows the use of Electrospray Ionisation coupled to Mass Spectroscopy (ESI-MS) or Matrix-Assisted Laser Desorption/Ionization coupled to Time-of-Flight detector (MALDI-TOF) as routine characterisation techniques. Through this, the molecular weight of post-synthetically modified MOPs can be spotted, as well as periodic mass losses attributed to the added fragments. Potential degradation of the MOP scaffold can be detected as well through these techniques.

Qualitative analysis of a PSM product can also be carried out by using Fourier Transform Infra-Red (FTIR) spectroscopy. Every target functional group has assigned several characteristic absorption bands that can be spotted with FTIR measurements. This technique is generally carried out on a solid sample, thus eliminating possible interferences due to solvent presence.

For PSM processes that involve the targeting of metallic centers or SBUs, various characterisation methods have been used to provide information of the metal ions and their environments. Most of these techniques are focused on quantification of metallic species, such as Atomic Absorption/Emission Spectroscopy (AAS/AES), Inductively-Coupled Plasma Optical Emission Spectroscopy (ICP-OES) and Energy-Dispersive X-ray spectroscopy (EDX). Other techniques focus on determining the structural disposition of these metallic species and their environments, such as Extended X-Ray Absorption Fine Structure (EXAFS) or X-ray absorption near edge structure (XANES). Finally, the magnetic properties and spin alignment can be followed by Magnetic susceptibility measurements and Electronic Paramagnetic Resonance (EPR), respectively.

1.7. References

(1) Schwartz, A. T.; Kauffman, G. B. *J. Chem. Educ.* **1976**, *53* (4), 235.

(2) Fabbrizzi, L. *J. Chem. Educ.* **2008**, *85* (11), 1501.

(3) Finn, M. G.; Fokin, V. V. *Chem. Soc. Rev.* **2010**, *39* (4), 1231.

(4) Ihde, A. J. *J. Chem. Educ.* **1956**, *33* (3), 107.

(5) Nagaoka, H. *Nature*. 1925, pp 95–96.

(6) Jacobson, D. M.; McKenzie, J. S. *Interdiscip. Sci. Rev.* **1992**, *17* (4), 326.

(7) Feynman, R. *Eng. Sci.* **1960**, *23* (5), 22.

(8) Hattori, G.; Takenaka, M.; Sawamoto, M.; Terashima, T. *J. Am. Chem. Soc.* **2018**, *140* (27), 8376.

(9) Chen, Q.-X.; Liu, Y.-H.; Qi, X.-Z.; Liu, J.-W.; Jiang, H.-J.; Wang, J.-L.; He, Z.; Ren, X.-F.; Hou, Z.-H.; Yu, S.-H. *J. Am. Chem. Soc.* **2019**, *141* (27), 10729.

(10) Rigling, C.; Kisunzu, J. K.; Duschmalé, J.; Häussinger, D.; Wiesner, M.; Ebert, M. O.; Wennemers, H. *J. Am. Chem. Soc.* **2018**, *140* (34), 10829.

(11) Chen, J. Z. Y. *Phys. Rev. Lett.* **2017**, *118* (24).

(12) Davis, M. E. *Nature* **2002**, 417, 813–821.

(13) Zhao, X. S. *J. Mat. Chem*. **2006**, 16, 623–625.

(14) Chae, H. K.; Siberio-Pérez, D. Y.; Kim, J.; Go, Y.; Eddaoudi, M.; Matzger, A. J.; O'Keeffe, M.; Yaghi, O. M. *Nature,* **2004**, *427*, 523.

(15) Serre, C.; Taulelle, F.; Ferey, G. *Chem. Commun.* **2003**, *3* (22), 2755.

(16) Rimer, J. D. *Nature Cat*., **2018**, 7, 488–489.

(17) Aulakh, D.; Islamoglu, T.; Bagundes, V. F.; Varghese, J. R.; Duell, K.; Joy, M.; Teat, S. J.; Farha, O. K.; Wriedt, M. *Chem. Mater.* **2018**, *30* (22), 8332.

(18) Yun, S.; Bak, S.; Kim, S.; Yeon, J. S.; Kim, M. G.; Yang, X.; Braun, P. V.; Park, H. S. *Adv. Energy Mater.* **2019**, *9* (6), 1802816.

(19) Kitagawa, S.; Kitaura, R.; Noro, S. I. *Angew. Chem. Int. Ed*., **2004**, 43 (18), 2334–2375.

(20) Kitagawa, S.; Matsuda, R. *Coord. Chem. Rev*. **2007**, 251, 2490–2509.

(21) Foo, M. L.; Matsuda, R.; Kitagawa, S. *Chem. Mater*. **2014**, 26 (1), 310–322.

(22) Zhou, H.-C.; Long, J. R.; Yaghi, O. M. *Chem. Rev.* **2012**, *112* (2), 673.

(23) Zhang, M.; Bosch, M.; Gentle, T.; Zhou, H. C. *CrystEngComm* **2014**, *16* (20), 4069.

(24) Cakici, M.; Gu, Z. G.; Nieger, M.; Bürck, J.; Heinke, L.; Bräse, S. *Chem. Commun.* **2015**, *51* (23), 4796.

(25) Hynek, J.; Brázda, P.; Rohlíček, J.; Londesborough, M. G. S.; Demel, J. *Angew. Chemie* **2018**, *130* (18), 5110.

(26) Alhamami, M.; Doan, H.; Cheng, C.-H. *Materials (Basel).* **2014**, *7* (4), 3198.

(27) Farrusseng, D.; Aguado, S.; Pinel, C. *Angew. Chemie Int. Ed.* **2009**, *48* (41), 7502.

(28) Ma, L.; Abney, C.; Lin, W. *Chem. Soc. Rev.* **2009**, *38* (5), 1248.

(29) Abánades Lázaro, I.; Forgan, R. S. *Coord. Chem. Rev*. **2019**, 380, 230–259.

(30) Batten, S. R.; Champness, N. R.; Chen, X. M.; Garcia-Martinez, J.; Kitagawa, S.; Öhrström, L.; O'Keeffe, M.; Suh, M. P.; Reedijk, J. *Pure Appl. Chem.* **2013**, *85* (8), 1715.

(31) Yaghi, O. M.; Li, H. *J. Am. Chem. Soc.* **1995**, *117* (41), 10401.

(32) Zaworotko, M. J. *Angew. Chemie - Int. Ed.* **2000**, *39* (17), 3052.

(33) Batten, S. R.; Champness, N. R.; Chen, X. M.; Garcia-Martinez, J.; Kitagawa, S.; Öhrström, L.; O'Keeffe, M.; Suh, M. P.; Reedijk, J. *CrystEngComm* **2012**, *14* (9), 3001.

(34) Long, J. R.; Yaghi, O. M. *Chem. Soc. Rev*. **2009**, 38 (5), 1213–1214.

(35) Moghadam, P. Z.; Li, A.; Wiggin, S. B.; Tao, A.; Maloney, A. G. P.; Wood, P. A.; Ward, S. C.; Fairen-Jimenez, D. *Chem. Mater*. **2017**, 29 (7), 2618–2625.

(36) Case: How many MOFs are there in the CSD? - The Cambridge Crystallographic Data Centre (CCDC) https://www.ccdc.cam.ac.uk/support-and-resources/support/case/?caseid=9833bd2c-27f9-4ff7-8186-71a9b415f012.

(37) Cheetham, A. K.; Kieslich, G.; Yeung, H. H.-M. *Acc. Chem. Res.* **2018**, *51* (3), 659.

(38) Hoskins, B. F.; Robson, R. *J. Am. Chem. Soc.* **1990**, *112* (4), 1546.

(39) Hoskins, B. F.; Robson, R. *J. Am. Chem. Soc.* **1989**, *111* (15), 5962.

(40) Abrahams, B. F.; Hoskins, B. F.; Michail, D. M.; Robson, R. *Nature* **1994**, *369* (6483), 727.

(41) Fujita, M.; Kwon, Y. J.; Washizu, S.; Ogura, K. *J. Am. Chem. Soc.* **1994**, *116* (3), 1151.

(42) Kondo, M.; Yoshitomi, T.; Matsuzaka, H.; Kitagawa, S.; Seki, K. *Angew. Chemie Int. Ed.* **1997**, *36* (16), 1725.

(43) Li, H.; Eddaoudi, M.; Groy, T. L.; Yaghi, O. M. *J. Am. Chem. Soc.* **1998**, *120* (33), 8571.

(44) Connolly, B. M.; Aragones-Anglada, M.; Gandara-Loe, J.; Danaf, N. A.; Lamb, D. C.; Mehta, J. P.; Vulpe, D.; Wuttke, S.; Silvestre-Albero, J.; Moghadam, P. Z.; Wheatley, A. E. H.; Fairen-Jimenez, D. *Nat. Commun.* **2019**, *10* (1).

(45) Chui, S. S. Y.; Lo, S. M. F.; Charmant, J. P. H.; Orpen, A. G.; Williams, I. D. *Science (80-.).* **1999**, *283* (5405), 1148.

(46) Li, H.; Eddaoudi, M.; O'Keeffe, M.; Yaghi, O. M. *Nature* **1999**, *402* (6759), 276.

(47) Kim, H. K.; Yun, W. S.; Kim, M.-B.; Kim, J. Y.; Bae, Y.-S.; Lee, J.; Jeong, N. C. *J. Am. Chem. Soc.* **2015**, *137* (31), 10009.

(48) Tranchemontagne, D. J.; Mendoza-Cortés, J. L.; O'Keeffe, M.; Yaghi, O. M. *Chem. Soc. Rev.* **2009**, *38* (5), 1257.

(49) Yaghi, O. M.; Kalmutzki, M. J.; Diercks, C. S. *Introduction to Reticular Chemistry: Metal-Organic Frameworks and Covalent Organic Frameworks.*; 2019.

(50) Eddaoudi, M.; Kim, J.; Rosi, N.; Vodak, D.; Wachter, J.; O'Keeffe, M.; Yaghi, O. M. *Science* **2002**, *295* (5554), 469.

(51) Kirchon, A.; Feng, L.; Drake, H. F.; Joseph, E. A.; Zhou, H. C. *Chem. Soc. Rev.* **2018**, 47 (23) 8611–8638.

(52) Guillerm, V.; Grancha, T.; Imaz, I.; Juanhuix, J.; Maspoch, D. *J. Am. Chem. Soc.* **2018**, *140* (32), 10153.

(53) Nguyen, T. T. M.; Le, H. M.; Kawazoe, Y.; Nguyen, H. L. *Mater. Chem. Front.* **2018**, *2* (11), 2063.

(54) Jiang, H.; Jia, J.; Shkurenko, A.; Chen, Z.; Adil, K.; Belmabkhout, Y.; Weselinski, L. J.; Assen, A. H.; Xue, D. X.; O'Keeffe, M.; Eddaoudi, M. *J. Am. Chem. Soc.* **2018**, *140* (28), 8858.

(55) Chidambaram, A.; Stylianou, K. C. *Inorg. Chem. Front*. **2018**, 5 (5), 979–998.

(56) Hu, P.; Yin, L.; Kirchon, A.; Li, J.; Li, B.; Wang, Z.; Ouyang, Z.; Zhang, T.; Zhou, H. C. *Inorg. Chem.* **2018**, *57* (12), 7006.

(57) Yang, Y.; Ishida, M.; Yasutake, Y.; Fukatsu, S.; Fukakusa, C.; Morikawa, M. A.; Yamada, T.; Kimizuka, N.; Furuta, H. *Inorg. Chem.* **2019**, *58* (7), 4647.

(58) Rodríguez-Hermida, S.; Tsang, M. Y.; Vignatti, C.; Stylianou, K. C.; Guillerm, V.; Pérez-Carvajal, J.; Teixidor, F.; Viñas, C.; Choquesillo-Lazarte, D.; Verdugo-Escamilla, C.; Peral, I.; Juanhuix, J.; Verdaguer, A.; Imaz, I.; Maspoch, D.; Giner Planas, J. *Angew. Chemie Int. Ed.* **2016**, *55* (52), 16049.

(59) Suh, M. P.; Park, H. J.; Prasad, T. K.; Lim, D.-W. *Chem. Rev.* **2012**, *112* (2), 782.

(60) Li, H.; Wang, K.; Sun, Y.; Lollar, C. T.; Li, J.; Zhou, H. C. *Mat. Today* **2018**, 21 (2) 108–121.

(61) Farha, O. K.; Yazaydin, A. Ö.; Eryazici, I.; Malliakas, C. D.; Hauser, B. G.; Kanatzidis, M. G.; Nguyen, S. T.; Snurr, R. Q.; Hupp, J. T. *Nat. Chem.* **2010**, *2* (11), 944.

(62) Ma, S.; Eckert, J.; Forster, P. M.; Yoon, J. W.; Hwang, Y. K.; Chang, J.-S.; Collier, C. D.; Parise, J. B.; Zhou, H.-C. *J. Am. Chem. Soc.* **2008**, *130* (47), 15896.

(63) U.S Deparment of Energy. DOE Technical Targets for Onboard Hydrogen Storage for Light-Duty Vehicles | Department of Energy https://www.energy.gov/eere/fuelcells/doe-technical-targets-onboard-hydrogen-storage-light-duty-vehicles.

(64) Peng, Y.; Krungleviciute, V.; Eryazici, I.; Hupp, J. T.; Farha, O. K.; Yildirim, T. *J. Am. Chem. Soc.* **2013**, *135* (32), 11887.

(65) Tsang, L. *EPA's Methane Regulations: Legal Overview*; 2018.

(66) Gallagher, J. *Nat. Energ.* **2018**, 3 (2), 86.

(67) Tian, T.; Zeng, Z.; Vulpe, D.; Casco, M. E.; Divitini, G.; Midgley, P. A.; Silvestre-Albero, J.; Tan, J. C.; Moghadam, P. Z.; Fairen-Jimenez, D. *Nat. Mater.* **2018**, *17* (2), 174.

(68) Wu, H.; Simmons, J. M.; Liu, Y.; Brown, C. M.; Wang, X.-S.; Ma, S.; Peterson, V. K.; Southon, P. D.; Kepert, C. J.; Zhou, H.-C.; Yildirim, T.; Zhou, W. *Chem. - A Eur. J.* **2010**, *16* (17), 5205.

(69) Jiang, J.; Furukawa, H.; Zhang, Y. B.; Yaghi, O. M. *J. Am. Chem. Soc.* **2016**, *138* (32), 10244.

(70) Millward, A. R.; Yaghi, O. M. *J. Am. Chem. Soc.* **2005**, *127* (51), 17998.

(71) Furukawa, H.; Ko, N.; Go, Y. B.; Aratani, N.; Choi, S. B.; Choi, E.; Yazaydin, A. Ö.; Snurr, R. Q.; O'Keeffe, M.; Kim, J.; Yaghi, O. M. *Science (80-.).* **2010**, *329* (5990), 424.

(72) McDonald, T. M.; Lee, W. R.; Mason, J. A.; Wiers, B. M.; Hong, C. S.; Long, J. R. *J. Am. Chem. Soc.* **2012**, *134* (16), 7056.

(73) Easun, T. L.; Moreau, F.; Yan, Y.; Yang, S.; Schröder, M. *Chem. Soc. Rev*. **2017**, 46 (1), 239.

(74) Dietzel, P. D. C.; Besikiotis, V.; Blom, R. *J. Mater. Chem.* **2009**, *19* (39), 7362.

(75) Dietzel, P. D. C.; Johnsen, R. E.; Fjellvåg, H.; Bordiga, S.; Groppo, E.; Chavan, S.; Blom, R. *Chem. Commun.* **2008**, 41, 5125.

(76) Barnett, B. R.; Parker, S. T.; Paley, M. V; Gonzalez, M. I.; Biggins, N.; Oktawiec, J.; Long, J. R.

J. Am. Chem. Soc. **2019**, *Accepted Manuscript* (DOI: jacs. 9b09942).

(77) Huang, Y. B.; Liang, J.; Wang, X. S.; Cao, R. *Chem. Soc. Rev*. **2017**, 46 (1), 126.

(78) Roberts, J. M.; Fini, B. M.; Sarjeant, A. A.; Farha, O. K.; Hupp, J. T.; Scheidt, K. A. *J. Am. Chem. Soc.* **2012**, *134* (7), 3334.

(79) Farrusseng, D.; Aguado, S.; Pinel, C. *Angew. Chemie Int. Ed.* **2009**, *48* (41), 7502.

(80) Dhakshinamoorthy, A.; Li, Z.; Garcia, H. *Chem. Soc. Rev*. **2018**, 47 (22), 8134.

(81) Alaerts, L.; Séguin, E.; Poelman, H.; Thibault-Starzyk, F.; Jacobs, P. A.; De Vos, D. E. *Chem. - A Eur. J.* **2006**, *12* (28), 7353.

(82) Liu, J.; Chen, L.; Cui, H.; Zhang, J.; Zhang, L.; Su, C. Y. *Chem. Soc. Rev*. **2014**, 43 (16), 6011.

(83) Jiang, Z.-R.; Wang, H.; Hu, Y.; Lu, J.; Jiang, H.-L. *ChemSusChem* **2015**, *8* (5), 878.

(84) Park, J.; Jiang, Q.; Feng, D.; Mao, L.; Zhou, H.-C. *J. Am. Chem. Soc.* **2016**, *138* (10), 3518.

(85) Ian Storer, R.; Aciro, C.; Jones, L. H. *Chem. Soc. Rev.* **2011**, 40 (5), 2330.

(86) McGuirk, C. M.; Katz, M. J.; Stern, C. L.; Sarjeant, A. A.; Hupp, J. T.; Farha, O. K.; Mirkin, C. A. *J. Am. Chem. Soc.* **2015**, *137* (2), 919.

(87) Cohen, S. M.; Zhang, Z.; Boissonnault, J. A. *Inorg. Chem.* **2016**, *55* (15), 7281.

(88) Jiang, M.; Li, P.; Wu, P.; Zhang, F.; Tian, X.; Deng, C.; Wang, J. *Chem. Commun.* **2018**, *54* (66), 9131.

(89) Vignatti, C.; Luis-Barrera, J.; Guillerm, V.; Imaz, I.; Mas-Ballesté, R.; Alemán, J.; Maspoch, D. *ChemCatChem* **2018**, *10* (18), 3995.

(90) El Badawy, A. M.; Luxton, T. P.; Silva, R. G.; Scheckel, K. G.; Suidan, M. T.; Tolaymat, T. M. *Environ. Sci. Technol.* **2010**, *44* (4), 1260.

(91) Awada, H.; Al Samad, A.; Laurencin, D.; Gilbert, R.; Dumail, X.; El Jundi, A.; Bethry, A.; Pomrenke, R.; Johnson, C.; Lemaire, L.; Franconi, F.; Félix, G.; Larionova, J.; Guari, Y.; Nottelet, B. *ACS Appl. Mater. Interfaces* **2019**, *11* (9), 9519.

(92) Falcaro, P.; Ricco, R.; Yazdi, A.; Imaz, I.; Furukawa, S.; Maspoch, D.; Ameloot, R.; Evans, J. D.; Doonan, C. J. *Coord. Chem. Rev*. **2016**, 307, 237–254.

(93) Aijaz, A.; Karkamkar, A.; Choi, Y. J.; Tsumori, N.; Rönnebro, E.; Autrey, T.; Shioyama, H.; Xu, Q. *J. Am. Chem. Soc.* **2012**, *134* (34), 13926.

(94) Bloch, W. M.; Burgun, A.; Coghlan, C. J.; Lee, R.; Coote, M. L.; Doonan, C. J.; Sumby, C. J. *Nat. Chem.* **2014**, *6* (10), 906.

(95) Huxley, M. T.; Burgun, A.; Ghodrati, H.; Coghlan, C. J.; Lemieux, A.; Champness, N. R.; Huang, D. M.; Doonan, C. J.; Sumby, C. J. *J. Am. Chem. Soc.* **2018**, *140* (20), 6416.

(96) Wu, C. De; Zhao, M. *Advanced Materials* **2017**, 29 (14), 1605446.

(97) Cohen, S. M. *Chem. Rev.* **2012**, *112* (2), 970.

(98) Tanabe, K. K.; Cohen, S. M. *Chem. Soc. Rev*. **2011**, 40 (2), 498.

(99) Smith, S. J. D.; Ladewig, B. P.; Hill, A. J.; Lau, C. H.; Hill, M. R. *Sci. Rep.* **2015**, *5*, 7823.

(100) Xu, L.; Luo, Y.; Sun, L.; Pu, S.; Fang, M.; Yuan, R. X.; Du, H. Bin. *Dalt. Trans.* **2016**, *45* (20), 8614.

(101) Yin, W.; Tao, C.; Zou, X.; Wang, F.; Qu, T.; Wang, J. *Nanomaterials* **2017**, *7* (9), 242.

(102) Wang, Z.; Cohen, S. M. *J. Am. Chem. Soc.* **2007**, *129* (41), 12368.

(103) Costa, J. S.; Gamez, P.; Black, C. A.; Roubeau, O.; Teat, S. J.; Reedijk, J. *Eur. J. Inorg. Chem.* **2008**, *2008* (10), 1551.

(104) Taylor-Pashow, K. M. L.; Della Rocca, J.; Xie, Z.; Tran, S.; Lin, W. *J. Am. Chem. Soc.* **2009**, *131* (40), 14261.

(105) Garibay, S. J.; Cohen, S. M. *Chem. Commun.* **2010**, *46* (41), 7700.

(106) Nguyen, J. G.; Cohen, S. M. *J. Am. Chem. Soc.* **2010**, *132* (13), 4560.

(107) Modrow, A.; Zargarani, D.; Herges, R.; Stock, N. *Dalt. Trans*. **2012**, 41 (28), 8690.

(108) Lin, Y.; Kong, C.; Chen, L. *RSC Adv*. **2016**, 6 (39), 32598.

(109) Ingleson, M. J.; Perez Barrio, J.; Guilbaud, J. B.; Khimyak, Y. Z.; Rosseinsky, M. J. *Chem. Commun.* **2008**, 23, 2680.

(110) Huangfu, M.; Tian, X.; Zhao, S.; Wu, P.; Chu, H.; Zheng, X.; Tang, J.; Wang, J. *New J. Chem.* **2019**, *43* (26), 10232.

(111) Segura, J. L.; Royuela, S.; Mar Ramos, M. *Chem. Soc. Rev*. **2019**, 48 (14), 3903.

(112) Tanabe, K. K.; Wang, Z.; Cohen, S. M. *J. Am. Chem. Soc.* **2008**, *130* (26), 8508.

(113) Wang, Z.; Tanabe, K. K.; Cohen, S. M. *Inorg. Chem.* **2009**, *48* (1), 296.

(114) Zwoliński, K. M.; Nowak, P.; Chmielewski, M. J. *Chem. Commun.* **2015**, *51* (49), 10030.

(115) Garibay, S. J.; Wang, Z.; Tanabe, K. K.; Cohen, S. M. *Inorg. Chem.* **2009**, *48* (15), 7341.

(116) Hindelang, K.; Vagin, S. I.; Anger, C.; Rieger, B. *Chem. Commun.* **2012**, *48* (23), 2888.

(117) Keenan, L. L.; Hamzah, H. A.; Mahon, M. F.; Warren, M. R.; Burrows, A. D. *CrystEngComm* **2016**, *18* (30), 5710.

(118) Fracaroli, A. M.; Siman, P.; Nagib, D. A.; Suzuki, M.; Furukawa, H.; Toste, F. D.; Yaghi, O. M. *J. Am. Chem. Soc.* **2016**, *138* (27), 8352.

(119) Gui, B.; Meng, X.; Chen, Y.; Tian, J.; Liu, G.; Shen, C.; Zeller, M.; Yuan, D.; Wang, C. *Chem. Mater.* **2015**, *27* (18), 6426.

(120) Pahari, G.; Bhattacharya, B.; Reddy, C. M.; Ghoshal, D. *Chem. Commun.* **2019**.

(121) Bryant, M. R.; Ablott, T. A.; Telfer, S. G.; Liu, L.; Richardson, C. *CrystEngComm* **2019**, *21* (1), 60.

(122) Ablott, T. A.; Turzer, M.; Telfer, S. G.; Richardson, C. *Cryst. Growth Des.* **2016**, *16* (12), 7067.

(123) Bryant, M. R.; Richardson, C. *CrystEngComm* **2015**, *17* (46), 8858.

(124) Tshering, L.; Hunter, S. O.; Nikolich, A.; Minato, E.; Fitchett, C. M.; D'Alessandro, D. M.; Richardson, C. *CrystEngComm* **2014**, *16* (39), 9158.

(125) Burrows, A. D.; Hunter, S. O.; Mahon, M. F.; Richardson, C. *Chem. Commun.* **2013**, *49* (10), 990.

(126) Gupta, A. Sen; Deshpande, R. K.; Liu, L.; Waterhouse, G. I. N.; Telfer, S. G. *CrystEngComm* **2012**, *14* (18), 5701.

(127) Lun, D. J.; Waterhouse, G. I. N.; Telfer, S. G. *J. Am. Chem. Soc.* **2011**, *133* (15), 5806.

(128) Deshpande, R. K.; Minnaar, J. L.; Telfer, S. G. *Angew. Chemie Int. Ed.* **2010**, *49* (27), 4598.

(129) Yuan, S.; Zou, L.; Qin, J.-S.; Li, J.; Huang, L.; Feng, L.; Wang, X.; Bosch, M.; Alsalme, A.; Cagin, T.; Zhou, H.-C. *Nat. Commun.* **2017**, *8*, 15356.

(130) Drake, H. F.; Day, G. S.; Vali, S. W.; Xiao, Z.; Banerjee, S.; Li, J.; Joseph, E. A.; Kuszynski, J. E.; Perry, Z. T.; Kirchon, A.; Ozdemir, O. K.; Lindahl, P. A.; Zhou, H.-C. *Chem. Commun.* **2019,** 55, 12769.

(131) Kim, M.; Cahill, J. F.; Su, Y.; Prather, K. A.; Cohen, S. M. *Chem. Sci.* **2012**, *3* (1), 126.

(132) Feng, L.; Yuan, S.; Qin, J.-S.; Wang, Y.; Kirchon, A.; Qiu, D.; Cheng, L.; Madrahimov, S. T.; Zhou, H.-C. *Matter* **2019**, *1* (1), 156.

(133) Yuan, S.; Lu, W.; Chen, Y. P.; Zhang, Q.; Liu, T. F.; Feng, D.; Wang, X.; Qin, J.; Zhou, H. C. *J. Am. Chem. Soc.* **2015**, *137* (9), 3177.

(134) Tu, B.; Pang, Q.; Wu, D.; Song, Y.; Weng, L.; Li, Q. *J. Am. Chem. Soc.* **2014**, *136* (41), 14465.

(135) Evans, J. D.; Sumby, C. J.; Doonan, C. J. *Chem.Soc. Rev*. **2014**, 43 (16), 5933.

(136) Sherry, H. S.; Walton, H. F. *J. Phys. Chem.* **1967**, *71* (5), 1457.

(137) Streat, M. *Hydrometallurgical Process Fundamentals*; **1984**; Section 2, 539–553.

(138) Dincă, M.; Long, J. R. *J. Am. Chem. Soc.* **2007**, *129* (36), 11172.

(139) Brozek, C. K.; Dincă, M. *Chem. Soc. Rev*. **2014**, 43 (16), 5456.

(140) Sun, D.; Sun, F.; Deng, X.; Li, Z. *Inorg. Chem.* **2015**, *54* (17), 8639.

(141) Das, S.; Kim, H.; Kim, K. *J. Am. Chem. Soc.* **2009**, *131* (11), 3814.

(142) Brozek, C. K.; Dincă, M. *J. Am. Chem. Soc.* **2013**, *135* (34), 12886.

(143) Aríñez-Soriano, J.; Albalad, J.; Vila-Parrondo, C.; Pérez-Carvajal, J.; Rodríguez-Hermida, S.; Cabeza, A.; Juanhuix, J.; Imaz, I.; Maspoch, D. *Chem. Commun.* **2016**, *52* (45), 7229.

(144) Sharma, N.; Dhankhar, S. S.; Nagaraja, C. M. *Microporous Mesoporous Mater.* **2019**, 372.

(145) Wu, C. De; Hu, A.; Zhang, L.; Lin, W. *J. Am. Chem. Soc.* **2005**, *127* (25), 8940.

(146) Bloch, E. D.; Britt, D.; Lee, C.; Doonan, C. J.; Uribe-Romo, F. J.; Furukawa, H.; Long, J. R.; Yaghi, O. M. *J. Am. Chem. Soc.* **2010**, *132* (41), 14382.

(147) Feng, D.; Chung, W. C.; Wei, Z.; Gu, Z. Y.; Jiang, H. L.; Chen, Y. P.; Darensbourg, D. J.; Zhou, H. C. *J. Am. Chem. Soc.* **2013**, *135* (45), 17105.

(148) Feng, D.; Gu, Z. Y.; Chen, Y. P.; Park, J.; Wei, Z.; Sun, Y.; Bosch, M.; Yuan, S.; Zhou, H. C. *J. Am. Chem. Soc.* **2014**, *136* (51), 17714.

(149) He, T.; Chen, S.; Ni, B.; Gong, Y.; Wu, Z.; Song, L.; Gu, L.; Hu, W.; Wang, X. *Angew. Chemie Int. Ed.* **2018**, *57* (13), 3493.

(150) Meilikhov, M.; Yusenko, K.; Esken, D.; Turner, S.; Van Tendeloo, G.; Fischer, R. A. *Eur. J. Inorg. Chem.* **2010**, *2010* (24), 3701.

(151) Chen, L.; Luque, R.; Li, Y. *Chem. Soc. Rev*. **2017**, 46 (15), 4614.

(152) Kim, H.; Chun, H.; Kim, G. H.; Lee, H. S.; Kim, K. *Chem. Commun.* **2006**, No. 26, 2759.

(153) Hermes, S.; Schröder, F.; Amirjalayer, S.; Schmid, R.; Fischer, R. A. *J. Mater. Chem.* **2006**, *16* (25), 2464.

(154) Lykourinou, V.; Chen, Y.; Wang, X. Sen; Meng, L.; Hoang, T.; Ming, L. J.; Musselman, R. L.; Ma, S. *J. Am. Chem. Soc.* **2011**, *133* (27), 10382.

(155) Chen, Y. Z.; Xu, Q.; Yu, S. H.; Jiang, H. L. *Small* **2014**, *11* (1), 71.

(156) Avci, C.; Ariñez-Soriano, J.; Carné-Sánchez, A.; Guillerm, V.; Carbonell, C.; Imaz, I.; Maspoch, D. *Angew. Chemie Int. Ed.* **2015**, *54* (48), 14417.

(157) Padmanaban, S.; Kim, M.; Yoon, S. *J. Ind. Eng. Chem.* **2019**, *71*, 336.

(158) Ou, Z.; Song, X.; Huang, W.; Jiang, X.; Qu, S.; Wang, Q.; Braun, P. V.; Moore, J. S.; Li, X.; Chen, Q. *ACS Appl. Mater. Interfaces* **2018**, *10* (48), 40990.

(159) Hu, M.; Ju, Y.; Liang, K.; Suma, T.; Cui, J.; Caruso, F. *Adv. Funct. Mater.* **2016**, *26* (32), 5827.

(160) Ye, Z.; Wu, S.; Zheng, C.; Yang, L.; Zhang, P.; Zhang, Z. *Langmuir* **2017**, *33* (45), 12952.

(161) Koo, J.; Hwang, I. C.; Yu, X.; Saha, S.; Kim, Y.; Kim, K. *Chem. Sci.* **2017**, *8* (10), 6799.

(162) Liu, C.; Luo, T. Y.; Feura, E. S.; Zhang, C.; Rosi, N. L. *J. Am. Chem. Soc.* **2015**, *137* (33), 10508.

(163) Gole, B.; Sanyal, U.; Banerjee, R.; Mukherjee, P. S. *Inorg. Chem.* **2016**, *55* (5), 2345.

(164) Seth, S.; Vaid, T. P.; Matzger, A. J. *Dalt. Trans.* **2019**, *48* (35), 13483.

(165) Heinke, L. *Journal of Physics D: Appl. Phys*. **2017**, 50 (19), 193004.

(166) Heinke, L.; Gu, Z.; Wöll, C. *Nat. Commun.* **2014**, *5*.

(167) Miki, N.; Maeno, M.; Maruhashi, K.; Nakagawa, Y.; Ohmi, T. *Corros. Sci.* **1990**, *31*, 69.

(168) Layer, R. W.; Lattimer, R. P. *Rubber Chem. Technol.* **1990**, *63* (3), 426.

(169) Harshé, G. *J. Mater. Eng. Perform.* **1992**, *1* (1), 83.

(170) Kiang, Y. H.; Gardner, G. B.; Lee, S.; Xu, Z.; Lobkovsky, E. B. *J. Am. Chem. Soc.* **1999**, *121* (36), 8204.

(171) Hintz, H.; Wuttke, S. *Chem. Mater.* **2014**, *26* (23), 6722.

(172) Ablott, T. A.; Turzer, M.; Telfer, S. G.; Richardson, C. *Cryst. Growth Des.* **2016**, *16* (12), 7067.

(173) Garzón-Tovar, L.; Rodríguez-Hermida, S.; Imaz, I.; Maspoch, D. *J. Am. Chem. Soc.* **2017**, *139* (2), 897.

(174) Eddaoudi, M.; Kim, J.; Wachter, J. B.; Chae, H. K.; O'Keeffe, M.; Yaghi, O. M. *J. Am. Chem. Soc*., **2001**, 18,4368–4369.

(175) Tranchemontagne, D. J.; Ni, Z.; O'Keeffe, M.; Yaghi, O. M. *Angew. Chemie Int. Ed.* **2008**, *47* (28), 5136.

(176) Furukawa, H.; Kim, J.; Ockwig, N. W.; O'Keeffe, M.; Yaghi, O. M. *J. Am. Chem. Soc.* **2008**, *130* (35), 11650.

(177) Liu, X.; Wang, X.; Bavykina, A. V.; Chu, L.; Shan, M.; Sabetghadam, A.; Miro, H.; Kapteijn, F.; Gascon, J. *ACS Appl. Mater. Interfaces* **2018**, *10* (25), 21381.

(178) Zhu, W.; Guo, J.; Ju, Y.; Serda, R. E.; Croissant, J. G.; Shang, J.; Coker, E.; Agola, J. O.; Zhong, Q.; Ping, Y.; Caruso, F.; Brinker, C. J. *Adv. Mater.* **2019**, *31* (12), 1970082.

(179) Rungtaweevoranit, B.; Diercks, C. S.; Kalmutzki, M. J.; Yaghi, O. M. *Faraday Discussions* **2017**

Chapter 2

Objectives

As presented in the previous Chapter, MOFs are an emerging class of porous materials which are gaining importance in several fields. Their notorious latent potential relies on the ability to rationally design the framework's dimensionality, porous distribution and physical properties through a judicious election of the building blocks used. Additionally, both the inorganic and organic subunits maintain a similar reactive behavior as if they were still isolated molecules, thus being amenable to post-synthetic modifications after the MOF has been formed. Thanks to the increasing efforts dedicated to Reticular Chemistry and post-synthetic modification strategies in MOFs, several reactions (*e.g.* covalent anchoring, metal exchange, and thermal rearrangements) have been successfully implemented in MOF chemistry in order to tune or improve their physicochemical properties or granting MOF crystals with unprecedented applications. However, this is yet the tip of the iceberg. The PSM of MOFs is still a relatively young field, and a huge amount of approaches are yet to be discovered, designed and exploited. Even though tens, maybe hundreds of different PSM strategies (each of them with their respective pros and cons) have been reported in MOFs, we have barely scratched the surface on how much variety inorganic and organic chemistries may put at our disposal.

In the above context, the main objective of this Thesis focuses on expanding the horizons on the post-synthetic field, moving forward from typical "wet" pathways (that is, soaking MOF crystals in saturated solutions of inorganic/organic reagents) and developing alternative methodologies, with particular emphasis on chemical transformations with well-defined mechanisms. More specifically, this thesis will be divided in three major milestones:

- Explore chemical transformations at the inorganic SBUs without the addition of external metal sources. Instead, the secondary metal source will be incorporated within macrocyclic cavities of the organic linkers, and structural rearrangements will be based on association constants and solvent-based dynamic equilibriums.

- Expand the solvent-less post-synthetic modification approach. Instead of preheating organic reagents up to their boiling points and work at high temperatures/vacuum, this milestone will focus on exploiting the intrinsic and chemoselective reactivity that some gas-phase molecules present. To this end, ozone-gas will be flowed through the porous cavities of MOFs tagged with unsaturated moieties, to which the gas is known to react chemoselectively. Such quantitative and chemoselective transformations might open up the use of single-crystal X-Ray diffraction to follow the evolution of the process, as quantitative yields are expected in mere minutes due to the removal of diffusion inconveniences within the solid-gas regime.

- Apply the gained knowledge in post-synthetic modification of MOFs to pioneer the post-synthetic modification of zero-dimensional Rh(II)-based Metal-Organic Polyhedra. MOPs can be depicted as "isolated MOF pores", in which their physical properties get dictated mainly by their external surface. Even though MOPs theoretically should present attractive features that MOFs cannot display (processability, supramolecular packing), their potential has never been fully exploited due to poor solubility and collapsing outside of solvent media. To this end, we aim to explore how the physicochemical properties of Rh(II)-based MOPs, known for their thermal and chemical robustness, get altered after an orthogonal or tandem covalent and coordination modification of their external surface. Additionally, we will explore the introduction of highly-reactive moieties (*i.e.* amino and carboxylic acid groups) into MOPs surface by sequential post-synthetic modification, as these moieties cannot withstand common MOP synthetic conditions. Expanding the available roster of active functional groups in MOPs surface could definitely open up new application paths for these relatively-new promising materials.

Chapter 3

Hetero-bimetallic paddlewheel clusters in coordination polymers formed by a water-induced single-crystal to single-crystal transformation

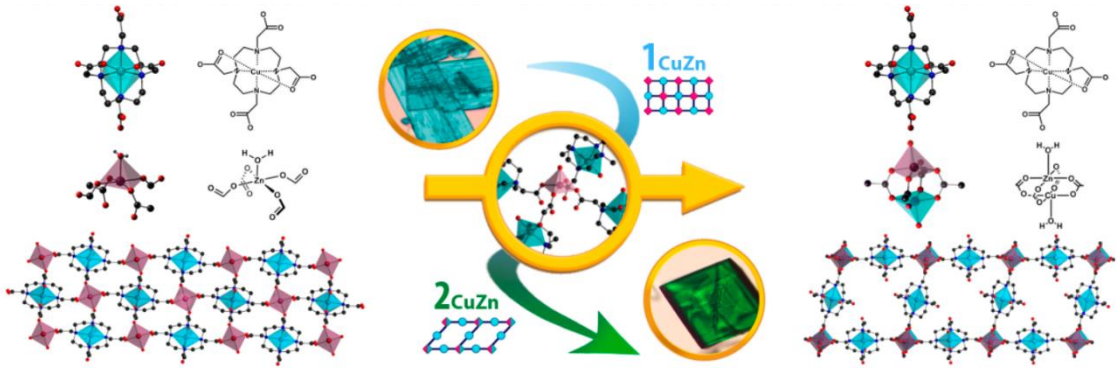

Abstract

Herein we report a water-induced single-crystal to single-crystal transformation that involves the formation of hetero-bimetallic paddlewheel clusters in coordination polymers. Through this transformation, which involves the cleavage and formation of different coordination bonds, two different Cu(II)–Zn(II) and Cu(II)–Ni(II) paddlewheel units exhibiting a 1 : 1 metal ratio were created.

This Chapter is based on the following publication:

Albalad, J.; Aríñez-Soriano, J.; Vidal-Gancedo, J.; Lloveras, V.; Juanhuix, J.; Imaz, I.; Aliaga-Alcalde, N.; Maspoch D.; *Chem. Commun.,* 2016, **52**, 13397-13400.

-

3.1. Introduction

Coordination polymers (CPs), including porous metal-organic frameworks (MOFs), exhibit a very rich organic-inorganic chemistry that makes possible their structural and compositional design for myriad applications.[1–4] This design is mostly succeeded through the careful choice of the building blocks[5–7] (that is, the organic linker and the metal ion), or by inducing macroscopic modifications onto pre-synthesized systems.[8] Recently, post-synthetic modifications (PSMs) at molecular level have been performed on the organic linkers of both CPs and MOFs (*i.e.* ligand exchange processes[9–11] or covalent reactivity[12–14]), inducing drastic changes on their physicochemical properties. However, an increasing interest is focused as well on exchanging/interconverting the metal ions in the inorganic units using post-synthetic metalation (PSM) pathways.[15–17] This latter strategy allows the creation of more "exotic" heterometallic inorganic units in CPs that can optimize, for example, their stability,[18] gas sorption properties,[19,20] catalytic activity,[21] luminescence[22] and/or magnetic behaviour.[23] Among all potential clusters present in the literature of CPs/MOFs,[24] the paddlewheel secondary building unit (SBU) is probably one of the best candidates for a precise study of the above-mentioned metalation processes due to its centrosymmetric character and structural simplicity. This cluster is relatively easy to synthesize using a wide range of metal sources, including Cu, Ni, Zn, Co, Mn, Cd, Ru, or even Bi-Rh,[25] among others. Additionally, the presence of (usually) uncoordinated axial sites allows sequential structuration of CPs built from this SBU.[26] Based on it, some advances have already been made on the PSM of paddlewheel units in CPs.[21,26,27] For example, as an early proof of concept, Cu(II) ions were introduced in the paddlewheel units of a pure Zn(II)-HKUST-1 sample by making PSM with $Cu(NO_3)\cdot 2.5H_2O$.[28] Several other metal ions, such as Cu(II), Ni(II) and Co(II), were exchanged in CPs made of Zn(II)-paddlewheel units.[26]

However, the governing factors of PSM are still uncertain and a successful insertion of a specific metal ion is usually achieved using empirical trial-and-error methodologies, provoking also uncontrolled substitutions in which the exact spatial disposition adopted by the new ions is generally unclear.[29] Another approach for designing novel heterometallic clusters (and in particular, hetero-bimetallic paddlewheel clusters) in a more controlled way should be their formation during the CP synthesis. Using this approach, an HKUST-1 analogue made of paddlewheel units containing Cu(II) and Ru(III) was synthesised.[27] However, the content of Ru(III) in this HKUST-1 was very low, meaning that only 9 % of the units should potentially be hetero-bimetallic units. Up to date, there are very few examples of pure hetero-bimetallic paddlewheel units with a 1:1 metal ratio done using this strategy. In 2016, the formation of discrete polyhedra made of Pd(II)-M(II) (where M is Zn, Cu and Ni) paddlewheel units starting from preformed bimetallic acetates as reagents was reported,[30] and more recently (in 2018) the same approach was used to develop 1:1 bimetallic versions of HKUST-1.[31]

This Chapter will show the formation of hetero-bimetallic Cu(II)-Zn(II) and Cu(II)-Ni(II) paddlewheel clusters exhibiting a 1:1 metal ratio in two isostructural CPs (hereafter called $\mathbf{2}_{\mathbf{CuZn}}$ and $\mathbf{2}_{\mathbf{CuNi}}$). These regular hetero-bimetallic CPs were not obtained by the beforementioned metal insertion techniques nor by direct synthesis, but through water-induced single-crystal to single-crystal (SC-to-SC) transformations of preformed macrocycle-based CPs (hereafter called $\mathbf{1}_{\mathbf{CuZn}}$ and $\mathbf{1}_{\mathbf{CuNi}}$) that incorporate the secondary metal source within the macrocyclic cavity of the linkers.

3.2. Results and Discussion

3.2.1. The "paddlewheel" Secondary Building Unit – Chemical properties

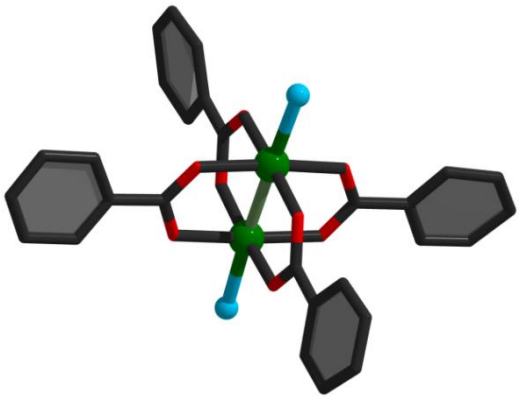

Figure 3.1. Schematic of a paddlewheel SBU.

Figure 3.1 depicts the atomic disposition of a bimetallic paddlewheel subunit. Paddlewheels are among the simpler neutral SBUs conformed by two symmetrical metallic centers bonded by four bridging carboxylic acid groups in an equatorial fashion. The axial positions of the metallic centers are crowned by two perpendicular axial linkers, granting a square-based pyramid coordination environment around the ions (octahedral environment when M-M bonds are present). Its molecular formula can therefore be expressed as $[M(II)_2(OOC\text{-}R)_4A_2]$ (where M(II) = any divalent metal ion; OOC-R = deprotonated carboxylate moiety; and A = axial linker). Initially found in the crystalline structure of Cu(II) and Zn(II) acetates, homometallic and heterometallic versions of this SBU can be commonly found in coordination clusters, discrete cages, Metal-Organic Polyhedra (MOPs) and Metal-Organic Frameworks (MOFs) due to its preferential formation over many chemical conditions.

The labile nature of the M-COO bond in paddlewheel SBUs, particularly with late transition metals, allows partial or total substitution of both the carboxylate linkers and the metallic ions within the cluster, opening up relatively simple post-synthetic pathways. Additionally, due to its thermodynamically favoured chemical state, several other more orthodox SBUs might end up transitioning to paddlewheels after being exposed to aggressive conditions.

3.2.2. Synthesis and characterisation of Phase 1

1_{CuZn} was initially obtained through a two-step synthesis.[32] In a first step, the macrocyclic H_2Cu-DOTA complex was precipitated by mixing $CuCl_2 \cdot 2H_2O$ and 1,4,7,10-tetraazacyclododecane-1,4,7,10-tetraacetic acid (H_4DOTA) in water under sonication for 5 min at room temperature

(Figure 3.2). In a second step, a N'N-dimethylformamide (DMF) solution containing the an equimolar amount of a second metal source (in this case $Zn(NO_3)\cdot 6H_2O$) was added into the aqueous solution containing the precipitated H_2Cu-DOTA complex under stirring. This mixture was then transferred to high temperature capped vials and allowed to react at 120 ºC, from which plate-shaped sky blue crystals of $\mathbf{1_{CuZn}}$ suitable for single-crystal X-Ray diffraction (SCXRD) were collected after 12 hours (yield: 66 %; obtained as a pure phase, as confirmed by elemental analysis (EA), energy-dispersive X-ray spectroscopy (EDX), inductively coupled plasma optical emission spectrometry (ICP-OES) and powder X-Ray diffraction (PXRD); See Section 3.3.4.; Tables 3.2, 3.3 and Figure 3.12).

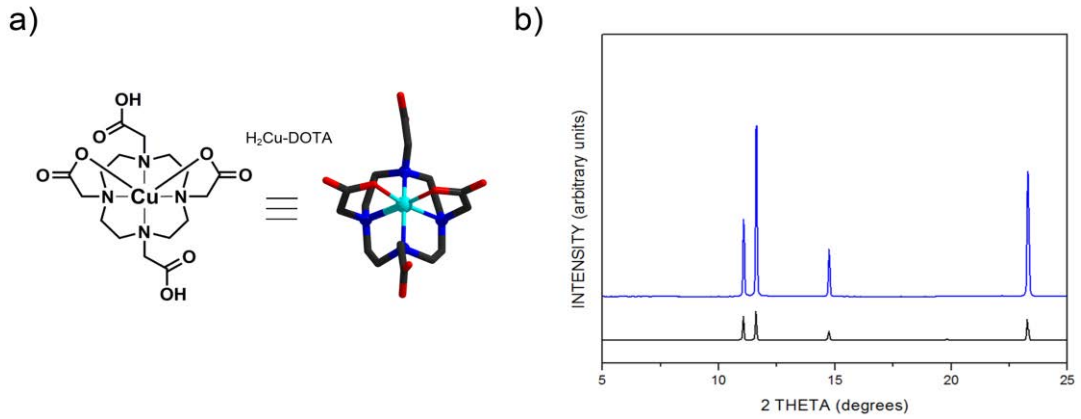

Figure 3.2. a) Schematic representation of the crystalline structure of the H_2Cu-DOTA complex. b) Experimental (blue) versus simulated (black) PXRD patterns of H_2Cu-DOTA.

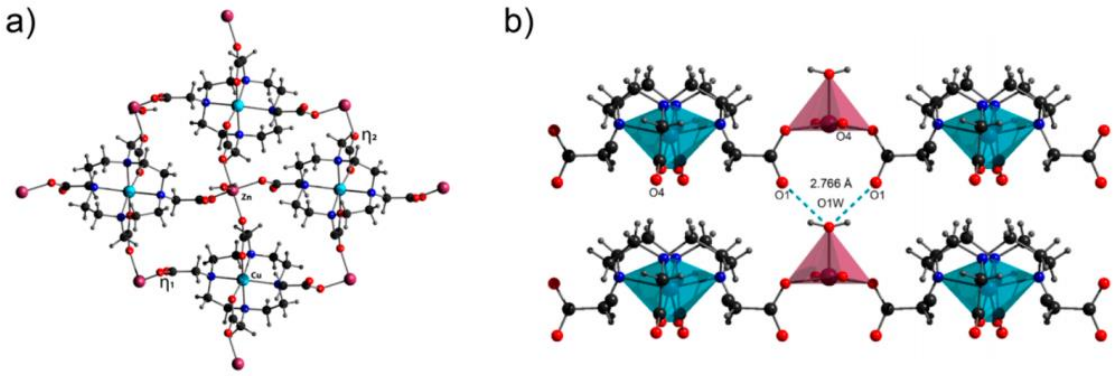

Figure 3.3. Crystal structure of $\mathbf{1_{CuZn}}$. (a) Coordination environment on the Cu-DOTA subunit and representation of the Zn(II) square-based pyramidal unit, with a view across the a crystallographic axis, showing both η2 and η1 acetate arms. (b) View of the hydrogen-bonded packing structure of 1CuZn. Hydrogen bonds are marked as sky-blue dash lines. Atomic color code: Zn, plum; Cu, sky blue; C, black, O, red, N, blue; H, light grey.

Crystals suitable for SCXRD analysis were tested in Alba Synchrotron, at the Xaloc beamline.[33] $\mathbf{1_{CuZn}}$ crystallized in the monoclinic P2/n symmetry group with formula $[ZnCu(DOTA)(H_2O)]$. A closer analysis on its structure revealed the formation of a 2-D framework extended along the *ac* plane (Figure 3.3a). In these layers, Cu(II) ions are

accommodated inside the macrocyclic cavity, adopting a distorted octahedral geometry coordinated to the cyclen subunit and to two of the acetate arms. These two arms act as bidentate bridges (η_2) between the Cu(II) and Zn(II) ions. On the other hand, Zn(II) ions extend the framework in a square-based pyramid motif (Figure 3.3b) using not only the two η_2 bridge carboxylate arms along the *a* axis, but also the open η_1 arms along the perpendicular *c* axis. The coordination environment around Zn(II) is completed with the presence of a water molecule (O_1W) crowning the axial position of the pyramid. Different layers of Phase 1 crystals are packed in an *AAA* sequence connected via hydrogen bonds between O_1W and the non-coordinated oxygen atoms in the η_1 carboxylate arms of a subsequent layer (Figure 3.3b). Remarkably, the resulting framework is compact, meaning that there are not guest solvent molecules in the structure.

Because the neighbouring Cu(II) and Zn(II) cannot be discriminated by SCXRD owing to their similar scattering power, the location of Cu(II) ions in $\mathbf{1_{CuZn}}$ was further investigated by electronic paramagnetic resonance (EPR) in collaboration with the *Institut de Ciència de Materials de Barcelona* (ICMAB-CSIC). To study the former, we performed measurements on 1_{CuZn} and compared with that of the discrete macrocyclic complex H_2Cu-DOTA.[34] As expected, H_2Cu-DOTA showed the characteristic EPR spectrum of a Cu(II) complex with an elongated octahedral geometry (Figure 3.4a). Its g_{II} and $g_{\perp}$ values were 2.290 and 2.083, respectively, matching accordingly with the simulated values (Figure 3.4a,b blue spectra). Importantly, the EPR spectrum of $\mathbf{1_{CuZn}}$ was very similar to that of H_2Cu-DOTA, with g_{II} and $g_{\perp}$ values of 2.240 and 2.085, respectively (Figure 3.4b).

This similarity confirmed that indeed the Cu(II) ions reside inside the macrocyclic cavities in 1_{CuZn}, and that the H_2Cu-DOTA units are bridged exclusively by Zn(II) ions. It is important to highlight here that this evidence is also in good agreement with the reported Cu/Zn association constants with H_4DOTA (Log K_d= 22.72 and 18.70 for H_2Cu-DOTA and H_2Zn-DOTA, respectively).[35]

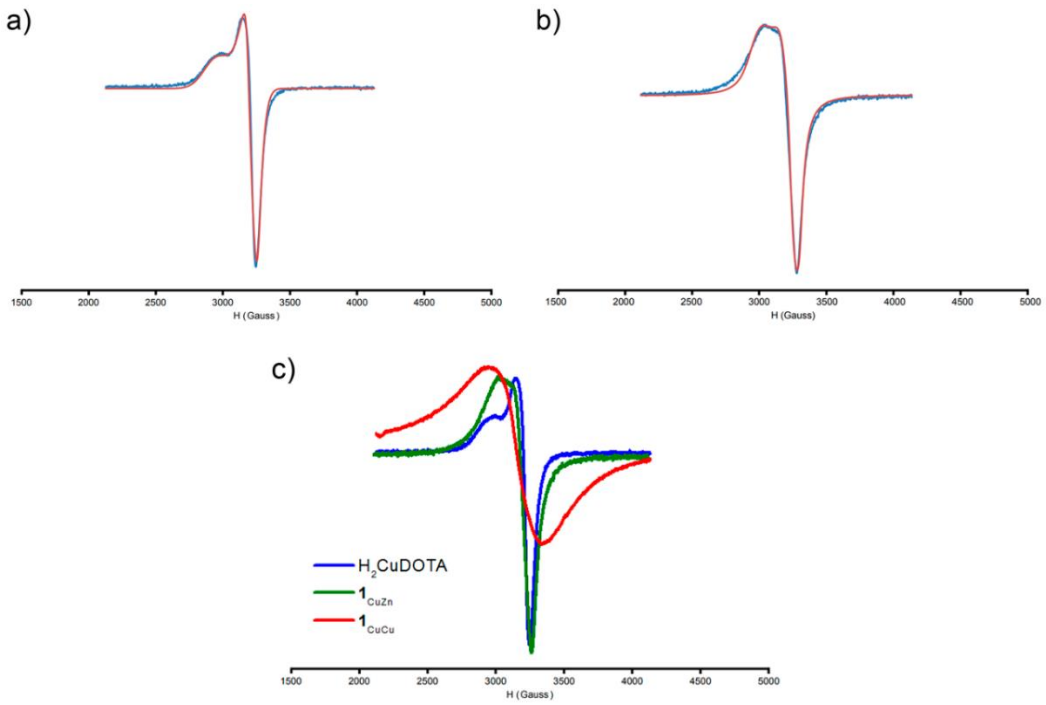

Figure 3.4. a) X-band EPR spectrum of Cu-DOTA, experimental (blue) and simulated (red). Simulation data: $g_{xx} = g_{yy} = 2.083$, $g_{zz} = 2.290$; $A_{xx}\{^{63,65}Cu\} = A_{yy}\{^{63,65}Cu\} = 20$ G, $A_{zz}\{^{63,65}Cu\} = 40$ G. b) X-band EPR spectrum of 1_{CuZn}, experimental (blue) and simulated (red). Simulation data: $g_{xx} = g_{yy} = 2.085$, $g_{zz} = 2.240$; $A_{xx}\{^{63,65}Cu\} = A_{yy}\{^{63,65}Cu\} = 20$ G, $A_{zz}\{^{63,65}Cu\} = 30$ G. c) Experimental X-band EPR spectra comparison between H_2CuDOTA (blue), 1_{CuZn} (green) and 1_{CuCu}(red).

Finally, to thoroughly discard the presence of Cu(II) ions in the metal positions bridging the macrocyclic complexes, the previously obtained spectra were compared with that obtained for the isostructural homometallic $\mathbf{1_{CuCu}}$ (note here that $\mathbf{1_{CuCu}}$ was prepared using the same conditions as for 1_{CuZn}, except that instead of $Zn(NO_3)\cdot 6H_2O$ in the second synthetic step, we used $Cu(NO_3)_2 \cdot 2.5H_2O$; yield: 87 %; obtained as a pure phase, as confirmed by EA and XRPD; See Section 3.3.4.; Figure 3.11). In this case, the EPR spectrum was quite different, exhibiting a broad band with a g value of 2.128 (Figure 3.4c). Since Cu(II) ions in $\mathbf{1_{CuCu}}$ adopt not only an elongated octahedral geometry but also a square pyramidal geometry, these results confirmed the absence of Cu(II) ions outside the macrocycle in 1_{CuZn}.

3.2.3. Water-induced SC-to-SC transformation to Phase 2

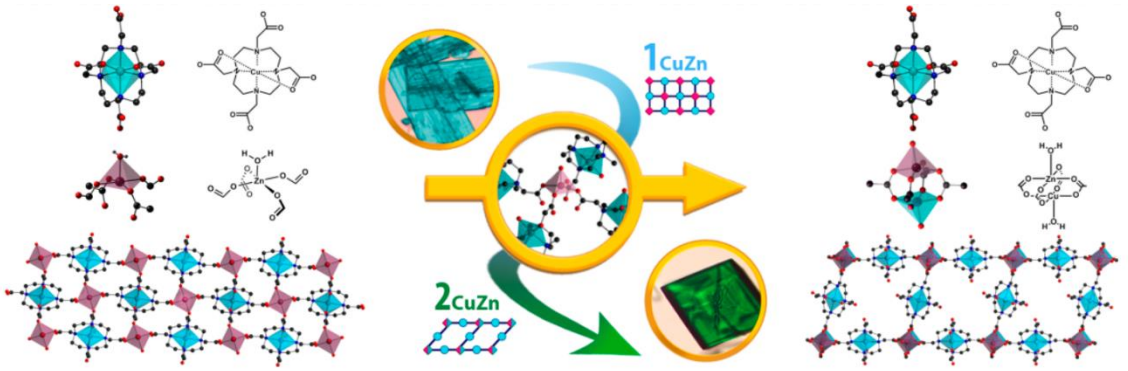

Figure 3.5. Schematic representation of the water-triggered transition from $\mathbf{1}_{\mathbf{CuZn}}$ to $\mathbf{2}_{\mathbf{CuZn}}$. For both sides: (top) Representation of the Cu–DOTA illustrating the octahedral coordination geometry (blue octahedron); (middle) representation of the square-based pyramidal coordination geometry of Zn(II) ions in $\mathbf{1}_{\mathbf{CuZn}}$ (purple tetrahedron), which is transformed to a hetero-bimetallic Cu(II)–Zn(II) paddlewheel unit in $\mathbf{2}_{\mathbf{CuZn}}$ (purple tetrahedron for Zn(II) and blue tetrahedron for Cu(II)); and (bottom) 2-D frameworks of $\mathbf{1}_{\mathbf{CuZn}}$ (left) and $\mathbf{2}_{\mathbf{CuZn}}$ (right).

Crystals of $\mathbf{1}_{\mathbf{CuZn}}$ (and also of $\mathbf{1}_{\mathbf{CuCu}}$) were thermodynamically unstable in their reaction media, undergoing a spontaneous SC-to-SC transition when left undisturbed for weeks. Moreover, this SC-to-SC transformation could be accelerated when dry crystals of $\mathbf{1}_{\mathbf{CuZn}}$ were soaked in pure distilled water without any addition of external metal sources for 72 hours (96 hours for 1_{CuCu}; Figure 3.6). Remarkably, the resulting prism-shaped green crystals of $\mathbf{2}_{\mathbf{CuZn}}$ were suitable for SCXRD. $\mathbf{2}_{\mathbf{CuZn}}$ crystallized in the $P2_1/c$ symmetry group showing a theoretical formula of $[Zn_xCu_{2-x}(DOTA)(H_2O)]\cdot 4H_2O$ (note here that Cu(II) and Zn(II) cannot be differentiated by SCXRD; Table 3.1). 2_{CuZn} shows a 2-D framework (Figure 3.5, right-bottom) in which the Cu(II) ions also reside in the macrocyclic cavity adopting the same distorted octahedral geometry (Figure 3.5, right-top). However, unlike in $\mathbf{1}_{\mathbf{CuZn}}$, the closed pendant arms do not contribute to extending the coordination layers. Instead, the coordination layers in $\mathbf{2}_{\mathbf{CuZn}}$ are expanded along the ab plane through the open arms forming $M_2(COO)_4$ paddlewheel clusters (Figure 3.5, right-middle). The different layers are then stacked in an ABA′B′ sequence forming 1-D channels along the *c* axis, which are filled with guest water molecules (Figure 3.7). Interestingly, $\mathbf{2}_{\mathbf{CuZn}}$ was stable in water for at least 6 months (See Section 3.3.4. Figure 3.13), and their guest water molecules could be removed and re-adsorbed without affecting the integrity of the open-framework (See Section 3.3.5. Figure 3.15). Indeed, water adsorption measurements showed a standard Type I isotherm with a water uptake of 0.12 $g_{water}\cdot g_{\mathbf{2CuZn}}^{-1}$ at 30% RH, which corresponds to 4.2 water molecules. The isotherm shows then a plateau from 25% to 65% RH and, after that, $\mathbf{2}_{\mathbf{CuZn}}$ gained hydrophilicity adsorbing up to 0.21 $g_{water}\cdot g_{\mathbf{2CuZn}}^{-1}$.

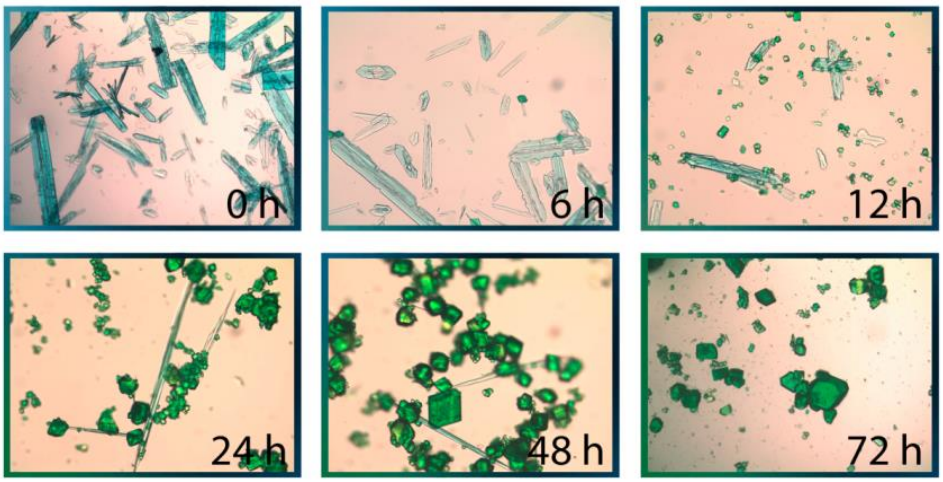

Figure 3.6. Optical microscopy images showing the evolution of the water-triggered transition from $\mathbf{1}_{\mathbf{CuZn}}$ to $\mathbf{2}_{\mathbf{CuZn}}$.

To obtain more details of the composition of $\mathbf{2}_{\mathbf{CuZn}}$, we then analyzed it using EDX and ICP-OES (See Section 3.3.4.; Tables 3.4 and 3.5). Surprisingly, the multiple measurements carried out using both techniques never suggested an equal proportion (x = 1) of Cu(II) and Zn(II) ions but always a precise 3:1 Cu(II) : Zn(II) ratio (or x = 0.5). These results lead to a final formula of $[Zn_{0.5}Cu_{1.5}(DOTA)(H_2O)]\cdot 4H_2O$ for $\mathbf{2}_{\mathbf{CuZn}}$. Thus, considering that the metal position inside the macrocycle is occupied by Cu(II), the two metal positions of the paddlewheel units must be occupied by a 1:1 mixture of Cu(II) and Zn(II) ions.

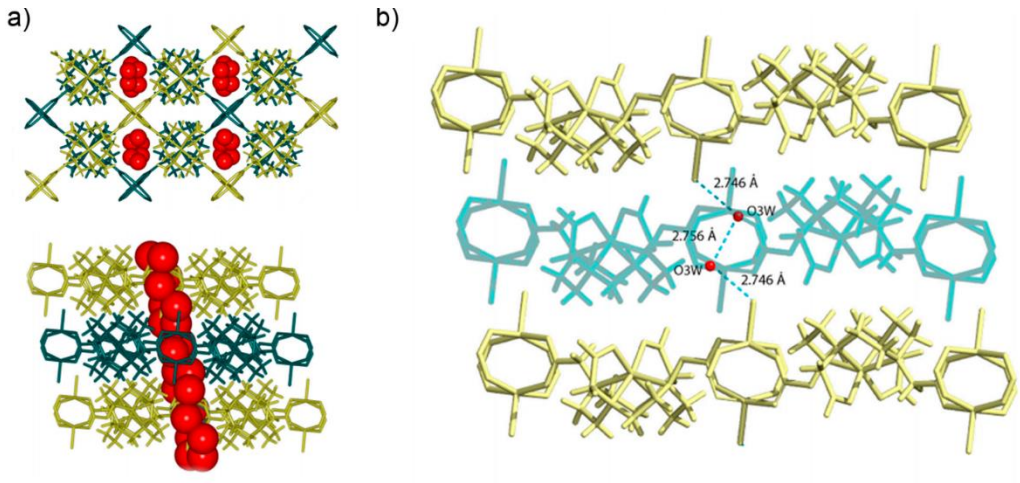

Figure 3.7. Crystal structure of $\mathbf{2}_{\mathbf{CuZn}}$ (a) View of the *ABAB* crystal packing across the b (top) and c (bottom) axis, highlighting the interlayer H-bonding water channels (represented as sky-blue dash lines). b) Views of the crystalline lattice, showing the water molecules (represented as red spheres) located in the channels.

To further confirm the formation of the bimetallic 1:1 Zn(II) : Cu(II) paddlewheel units, we performed magnetic susceptibility measurements in collaboration with ICMAB-CISC on both

2$_{CuZn}$ and **2**$_{CuCu}$ (Figure 3.8). If the hetero-bimetallic Cu(II)–Zn(II) units are formed, the paramagnetic Cu(II) ions located inside the macrocycles and those forming the paddlewheel units should be magnetically weakly coupled with only appreciable intermolecular magnetic interactions at the lowest temperatures. In contrast, strong antiferromagnetic interactions are expected if homometallic Cu(II)–Cu(II) paddlewheel units are present in **2**$_{CuZn}$. Indeed, homometallic Cu(II)–Cu(II) paddlewheel units display a rather strong antiferromagnetic behavior, providing exchange coupling constants of J values between −200 cm^{-1} and −1000 cm^{-1}.[36] With this in mind, solid-state variable-temperature (1.8–300.0 K) dc magnetic susceptibility data of polycrystalline samples of **2**$_{CuZn}$ and **2**$_{CuCu}$ using a 1.0 T field were collected. Their magnetic behaviors are depicted in Figure 3.8 as plots of $\chi_M T$ vs. T. In both cases, TIP corrections were performed by adding -60×10^{-6} cm^3 mol^{-1} K per Cu(II) unit. The $\chi_M T$ values at 300 K were 0.72 cm3 mol^{-1} K for **2**$_{CuCu}$ and 0.56 cm^3 mol^{-1} K for **2**$_{CuZn}$, which are in good agreement with those expected for one and a half independent Cu(II) centers in **2**$_{CuCu}$ (0.74 $cm^3 \cdot mol^{-1} \cdot K$) and for one Cu(II) center in **2**$_{CuZn}$ (0.55 $cm^3 \cdot mol^{-1}$ K); considering a g value of 2.00 in both cases. As expected, the $\chi_M T$ values of **2**$_{CuCu}$ rapidly decreased upon cooling, consistent with the presence of strong antiferromagnetic coupling between the two Cu(II) ions forming the homometallic paddlewheel units (J = −163 cm^{-1}, see fitting in Figure 3.8, red). In quite contrast, the $\chi_M T$ values for **2**$_{CuZn}$ remained almost constant all over the temperatures, and slightly decreased below 25 K. This behavior is characteristic of a system that is weakly coupled, as expected for a **2**$_{CuZn}$ system built up from hetero-bimetallic Cu(II)–Zn(II) paddlewheel units.

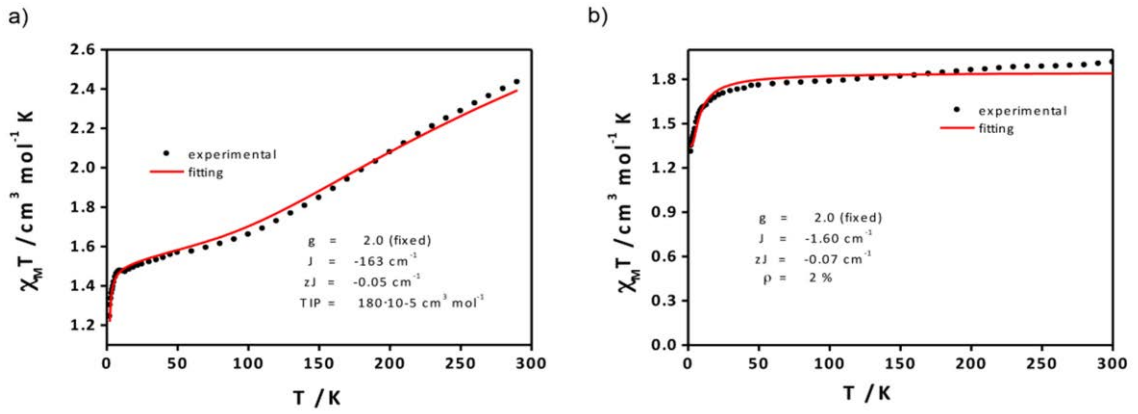

Figure 3.8. Experimental $\chi_M T$ vs T data of systems (a) **2**$_{CuCu}$ and (b) **2**$_{CuZn}$ (●) and fitting (red line) between 2.0 and 300.0 K using a dc external magnetic field of 1 T. Estimated exchange coupling constant values were achieved by the use of PHI[37] and fixing g (2.0) at all the range of temperatures (2.0 – 300 K) and at the highest (50 K to 300 K) with reasonable fittings. To proceed with, systems were described as one paddlewheel unit (Cu^{II} -Cu^{II} (a) and Cu^{II} -Zn^{II} (b)) surrounded by four mononuclear Cu^{II} -cyclam derivate centers, respectively. In 1, J describes the exchange inside the paddle-wheel, *z*J encloses intra/intermolecular interactions among the other centers and TIP has the general meaning. In the case of b, J describes the interaction among the Cu^{II} centre inside the paddlewheel and the surroundings. It was found that J values are in a range of -160 to -190 cm^{-1} for a and of -4 to -2 cm^{-1} for b.

Figure 3.9 shows a proposed mechanism for the formation of these hetero-bimetallic paddlewheel units, which starts with a dynamic cleavage of the η^2 acetate arms on $\mathbf{1}_{\mathbf{CuZn}}$ through the Cu–O bond, induced by the presence of water (first fragment of Figure 3.9). This step triggers the formation of a metaphase where all the pendant arms are equally open (second fragment of Figure 3.9). This metaphase can therefore be seen as "half-empty" paddlewheel units. The transition continues when half of these open arms rearrange to complete again the thermodynamically favorable octahedral coordination around the Cu(II) ions, leaching to the solution half of the Zn(II) ions (third fragment of Figure 3.9). A partial dissociation of the material should occur afterwards in order to compensate the charge unbalance, releasing an equal value of $[Cu–DOTA]^{2-}$ units to the solution. Half of these released Cu(II) ions must be able to complete the holes on the half-formed paddlewheel units, finally forming the hetero-bimetallic clusters found in $\mathbf{2}_{\mathbf{CuZn}}$ (fourth fragment of Figure 3.9). This hypothetic mechanism implies a loss of 41% of the initial weight of the crystals as well as a release of 50% and 25% of the initial Zn(II) and Cu(II) ions, respectively. To follow these parameters, we immersed crystals of $\mathbf{1}_{\mathbf{CuZn}}$ (17.8 mg) in water (5.0 ml) and followed their SC-to-SC transformation to 2_{CuZn}. After 72 hours, the transition was completed, and 9.8 mg of $\mathbf{2}_{\mathbf{CuZn}}$ were collected, corresponding to a weight loss of 45%. In addition, the water solution was analyzed by ICP-OES, and found a Zn(II) and Cu(II) content of

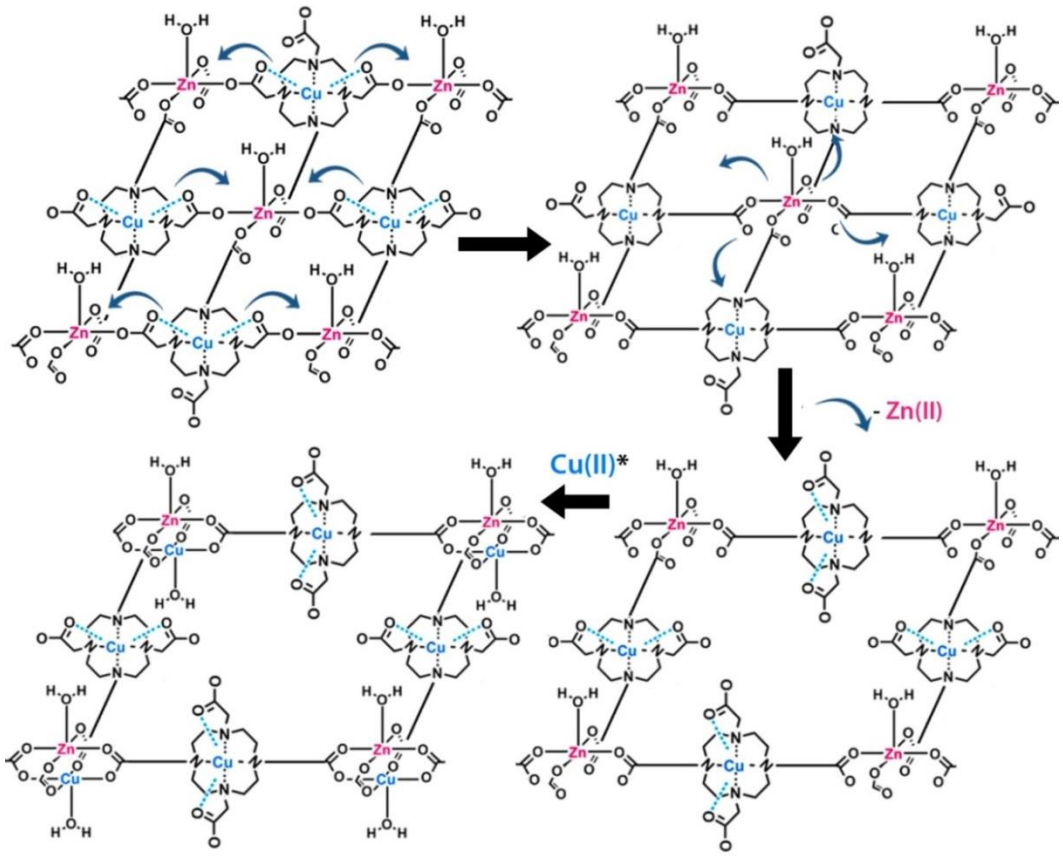

Figure 3.9. Schematic representation of the proposed mechanism. Note that Cu(II)* represents the insertion of Cu(II) coming from the release of Cu–DOTA due to the degradation of the crystal.

1.03 mg (206 ppm) and 0.49 mg (98 ppm), respectively (Section 3.3.4; Table 3.6). These amounts correspond to a weight loss of 51% and 26% of the initial Zn(II) and Cu(II) contents in $\mathbf{1_{CuZn}}$. Altogether, these results evidence the feasibility of our proposed mechanism.

Finally, to expand the variety of hetero-bimetallic paddlewheel units, we reproduced the synthesis of 1_{CuZn} but using nitrate salts of Mn(II), Fe(II)/(III), Co(II), Ni(II), Ag(I) or Pd(II) in the second step. Among these metal ions, we could only confirm the formation of 1_{CuNi} (yield: 71%; obtained as a pure phase, as confirmed by PXRD, EDX, ICP-OES and elemental analysis; See Section 3.3.4.; Tables 3.2-3.5 and Figures 3.11, 3.12). This result seems consistent with the Irving–Williams series for the stability of complexes synthesized from divalent metal ions. Remarkably, we found that the transition $\mathbf{1_{CuNi}} \rightarrow \mathbf{2_{CuNi}}$ was also possible after immersing 1_{CuNi} in water for two months. Here, EDX and ICP-OES analysis also gave a 3:1 Cu(II) : Ni(II) ratio, thus confirming the formation of the hetero-bimetallic Cu(II)–Ni(II) paddlewheel units in $\mathbf{2_{CuNi}}$.

3.2.4 Conclusions

In conclusion, we have shown the unprecedented formation of isostructural CPs that contain hetero-bimetallic paddlewheel units having a 1 : 1 metal ratio inside the cluster. This formation takes place via a water-induced SC–SC transformation from a compact hetero-bimetallic framework built up from connecting Cu–DOTA units through isolated metal ions to a more open framework built up from connecting identical Cu–DOTA units through hetero-bimetallic paddlewheel units. This SC-to-SC transformation was reproduced for two different cases allowing the formation of Cu(II)–Zn(II) and Cu(II)–Ni(II) paddlewheel units. This study illustrates the diversity, richness and beauty of this type of chemistry, from which many new systems remain to be discovered.

3.3. Experimental Part

3.3.1. Materials and Methods

All chemical reagents and solvents were purchased from commercial sources and used as received without further purification. Purity of all bulk materials was confirmed through X-Ray powder diffraction measurements (XRPD) collected on an X'Pert PRO MPD analytical diffractometer (Panalytical at 45 kV and 40mA using Cu Kα radiation (λ= 1.5419 Å) and compared with single crystal simulated patters. Elemental Analyses were performed on a Flash EA 2000 CHNS (Thermo Fisher Scientific) analyser. Metal ratio on the final bulk materials were confirmed through ICP-OES using a Perkin Elmer Optima 4300DV instrument or through EDX measurements on a FEI Quanta 650F Environmental SEM. Gravimetric water sorption measurements were performed at 298 K using a flow of nitrogen, up to relative humidity (RH) of 95% with a DVS-Advantage-1 (Surface Measurements Systems Ltd.). The relative humidity inside the chamber was adjusted by bobbling a carrier gas (N2) in pure water until stream saturated in water (95% RH). The adsorbed moisture was expressed as gwater/gdry sample. Prior to the water adsorption measurements, samples were outgassed each cycle at 120 ºC during 3 hours using a heating rate of 0.5 ºC/min. The EPR spectra were recorded on crystalline powder at 140 K in a Bruker ELEXYS E500 X-band spectrometer equipped with a TE102 microwave cavity, a Bruker variable temperature unit, and a field-frequency (F/F) lock system Bruker ER 033 M. Line positions were determined with an NMR Gaussmeter Bruker ER 035 M. The modulation amplitude was kept well below the line width, and the microwave power was well below saturation. Magnetic susceptibility measurements were performed on polycrystalline samples with a DMS5 Quantum Design susceptometer working in the range 1.8-300.0 K under a magnetic field of 0.1 T. TIP is the temperature-independent paramagnetism. Diamagnetic corrections were estimated from Pascal Tables.

3.3.2. Synthetic methodologies

Synthesis of $\mathbf{1_{CuZn}}$. In a screw capped vial, $CuCl_2 \cdot 2H_2O$ (12.8 mg, 0.075 mmol) and H_4DOTA (30.3 mg, 0.075 mmol) were solved in 4 mL of distilled H_2O under sonication. After 5 minutes, a light-blue precipitate appeared corresponding to the discrete supramolecular complex CuH_2DOTA.[1] $Zn(NO_3)_2 \cdot 6H_2O$ (43,9 mg, 0.15 mmol) solved in 4 mL of DMF was added afterwards. The resulting mixture was heated for 12 hours at 120ºC, obtaining plated-shaped sky blue crystals (28.0 mg, 66% based on H_4DOTA). Crystals were washed three times with 5 mL of DMF and maintained under the same solvent at room temperature. Found C 34.7 %, H 4.7 %, N 10.0 %. $CuZnC_{16}H_{26}N_4O_9$ requires 35.1 %, H 4.8 %, N 10.2 %.

Synthesis of $\mathbf{1}_{CuNi}$. In a screw capped vial, $CuCl_2 \cdot 2H_2O$ (12.8 mg, 0.075 mmol) and H_4DOTA (30.3 mg, 0.075 mmol) were solved in 4 mL of distilled H_2O under sonication. After 5 minutes, $Ni(NO_3)_2 \cdot 6H_2O$ (40.5 mg, 0.15 mmol) solved in 4 mL of DMF was added afterwards. The resulting mixture was heated for 12 hours at 120ºC, obtaining plated-shaped sky blue crystals (30.5 mg, 71% based on H_4DOTA). Crystals were washed three times with 5 mL of DMF and maintained under the same solvent at room temperature. Found C 35.6 %, H 4.9 %, N 10.3 %. $CuNiC_{16}H_{26}N_4O_9$ requires 35.6 %, H 4.9 %, N 10.4 %.

Synthesis of $\mathbf{1}_{CuCu}$. In a screw capped vial, $CuCl_2 \cdot 2H_2O$ (12.8 mg, 0.075 mmol) and H_4DOTA (30.3 mg, 0.075 mmol) were solved in 4 mL of distilled H_2O under sonication. After 5 minutes, $Cu(NO_3)_2 \cdot 2.5H_2O$ (35.7 mg, 0.15 mmol) solved in 4 mL of DMF was added afterwards. The resulting mixture was heated for 12 hours at 120ºC, obtaining plated-shaped sky blue crystals (35.0 mg, 87% based on H_4DOTA). Crystals were washed three times with 5 mL of DMF and maintained under the same solvent at room temperature. 1_{CuCu} can also be synthesized by direct mixture of H_4DOTA and 2 equivalents of $CuCl_2 \cdot 2H_2O$ in a water:DMF mixture and heating at the same temperature. Crystals were washed three times with 5 mL of DMF and maintained under the same solvent at room temperature. Found C 35.0 %, H 4.8 %, N 10.0 %. $Cu_2C_{16}H_{26}N_4O_9$ requires 35.2 %, H 4.8 %, N 10.2 %.

Synthesis of $\mathbf{2}_{CuZn}$. 30 mg of dry crystals of $\mathbf{1}_{CuZn}$ were immersed in 5 mL of distilled water and left undisturbed at room temperature. A change of colour in the crystalline material from sky blue to green was observed at the same time that the solution became blueish. The transition was completed after 72 hours, in which PXRD measurements confirmed phase purity. The material was then washed three times with 10 mL of distilled water, and kept under the same solvent (18 mg). Found C 31.4 %, H 5.2 %, N 9.0 %. $Cu_{1.5}Zn_{0.5}C_{16}H_{26}N_4O_9 \cdot 4H_2O$ requires 31.0 %, H 5.5 %, N 9.0 %.

Synthesis of $\mathbf{2}_{CuNi}$. 30 mg of dry crystals of $\mathbf{1}_{CuNi}$ were immersed in 5 mL of distilled water left undisturbed at room temperature. A change of colour in the crystalline material from blue to green was observed at the same time that the solution became blueish. The transition was completed after 2 months, in which PXRD measurements confirmed phase purity. The material was then washed three times with 10 mL of distilled water, and kept under the same solvent (18 mg). Found C 31.9 %, H 5.9 %, N 9.2 %. $Cu_{1.5}Ni_{0.5}C_{16}H_{26}N_4O_9 \cdot 4H_2O$ requires 31.4 %, H 5.6 %, N 9.1

Synthesis of $\mathbf{2}_{CuCu}$ 30 mg of dry crystals of $\mathbf{1}_{CuCu}$ were immersed in 5 mL of distilled water and left undisturbed at room temperature. A change of colour in the crystalline material from blue to green was observed at the same time that the solution became blueish. The transition was completed after 96 hours, in which PXRD measurements confirmed phase purity. The material

was then washed three times with 10 mL of distilled water, and kept in the same solvent (22 mg). Found C 32.0 %, H 5.8 %, N 9.3 %. $Cu_2C_{16}H_{26}N_4O_9 \cdot 4H_2O$ requires 31.1 %, H 5.6 %, N 9.1 %.

3.3.3. Single-Crystal XRD analysis

Table 3.1. Crystal and structural refinement data for 1_{CuZn} and 2_{CuZn}.

Compound Reference	$\mathbf{1_{CuZn}}$	$\mathbf{2_{CuZn}}$
Chemical Formula	$CuZnC_{16}H_{26}N_4O_9$	$CuZnC_{16}H_{26}N_4O_9 \cdot 4H_2O$
Formula Mass	547.35	619.5
Crystal System	Monoclinic	Monoclinic
Space group	P2/n	$P2_1/c$
a/ Å	10.950(4)	11.560(5)
b/ Å	6.350(4)	16.830(5)
c/ Å	13.610(4)	12.920(5)
α/ °	90	90
β/ °	92.58(12)	110.97(3)
γ/ °	90	90
Unit Cell Volume / $Å^3$	972.2(8)	2347.2(16)
Temperature / K	100	293
Z	2	4
Reflexions Measured	14404	24123
Independent Reflections	1126	4144
Reflections ($I > 2\sigma(I)$)	1065	3593
R_{int}	0.088	0.067
R_1 ($I > 2\sigma(I)$)	0.0413	0.0549
$wR(F^2)$ ($I > 2\sigma(I)$)	0.1095	0.1583
R_1 (all data)	0.0428	0.0616
$wR(F^2)$ (all data)	0.1103	0.1641

CCDC CIF files: CCDC 1505012 (**1_{CuZn}**) and CCDC 1505013 (**2_{CuZn}**)

3.3.4. Characterisation

EDX and ICP-OES metal ratios

Table 3.2. Metal proportion on bimetallic Phase 1 crystals measured by EDX analysis

Material	Cu (At %)	M (At %)
$\mathbf{1}_{CuZn}$	51.90	48.10
$\mathbf{1}_{CuNi}$	50.78	49.22

Table 3.3. Metal proportion on bimetallic Phase 1 crystals measured by ICP-OES analysis

Material	Cu (mg/L)	M (mg/L)
$\mathbf{1}_{CuZn}$	202	210
$\mathbf{1}_{CuNi}$	251	234

Table 3.4. Metal proportion on bimetallic Phase 2 crystals measured by EDX analysis

Material	Cu (At %)	M (At %)
$\mathbf{2}_{CuZn}$	75.05	24.95
$\mathbf{2}_{CuNi}$	74.36	25.64

Table 3.5. Metal proportion on bimetallic Phase 2 crystals measured by ICP-OES analysis

Material	Cu (mg/L)	M (mg/L)
$\mathbf{2}_{CuZn}$	555	187
$\mathbf{2}_{CuNi}$	378	120

Table 3.6. ICP-OES measurements of the transition water after 72 hours.

Initial Material	Exact mass (mg)	V H_2O (mL)	Cu ICP-OES (mg/L)	Zn ICP-OES (mg/L)	Cu/Zn % loss
$\mathbf{1}_{CuZn}$	17.8 mg	5.0 mL	98	206	**26%/51%**

PXRD measurements

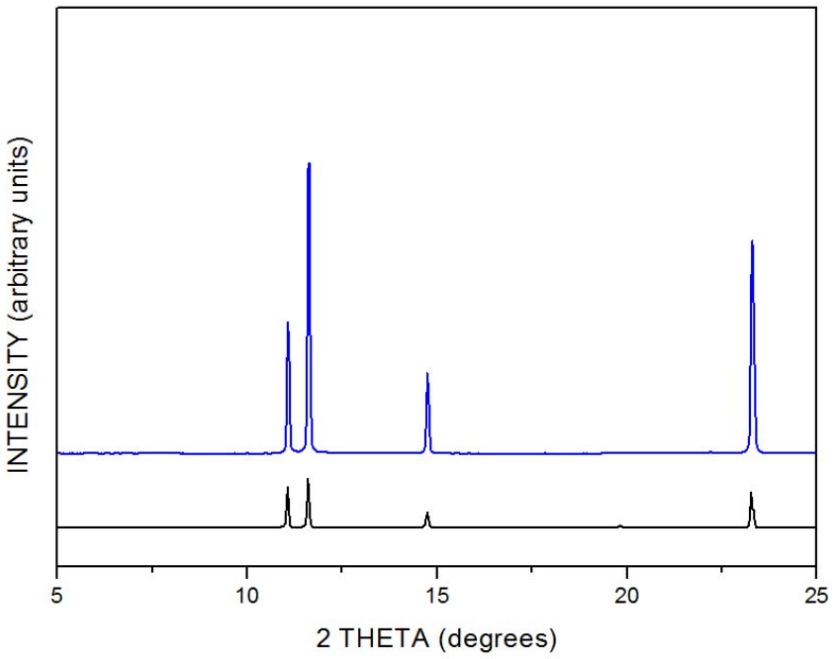

Figure 3.10. XRPD diagrams of simulated (black) and experimental (blue) H_2Cu-DOTA.

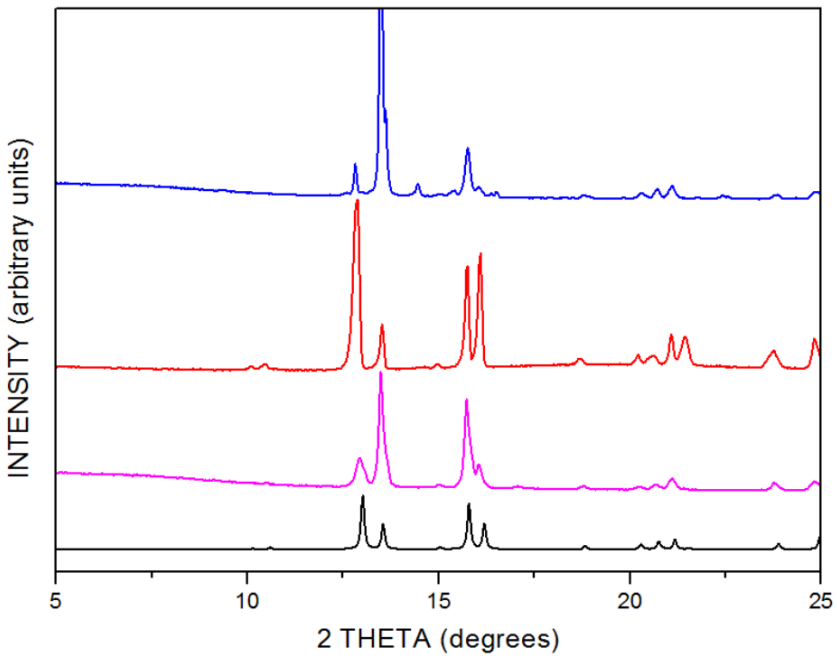

Figure 3.11. XRPD diffractograms of the synthesized $\mathbf{1}_{CuZn}$ (purple), $\mathbf{1}_{CuCu}$ (red) and $\mathbf{1}_{CuNi}$ (blue), as compared to the simulated powder pattern for the crystal structure of $\mathbf{1}_{CuZn}$ (black).

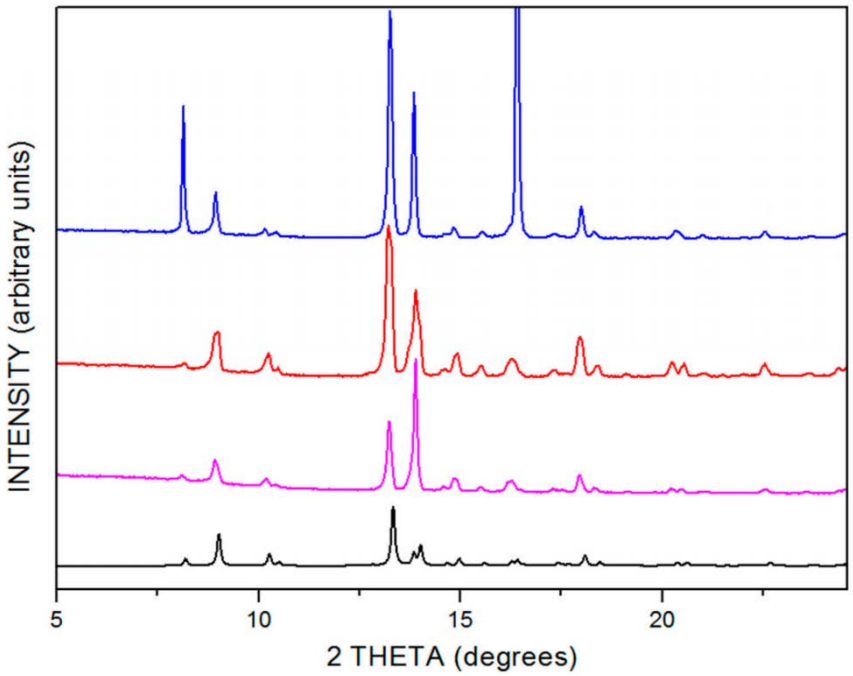

Figure 3.12. XRPD diffractograms of the synthesized $\mathbf{2}_{\mathbf{CuZn}}$ (purple), $\mathbf{2}_{\mathbf{CuCu}}$ (red) and $\mathbf{2}_{\mathbf{CuNi}}$ (blue), as compared to the simulated powder pattern for the crystal structure of $\mathbf{2}_{\mathbf{CuZn}}$ (black).

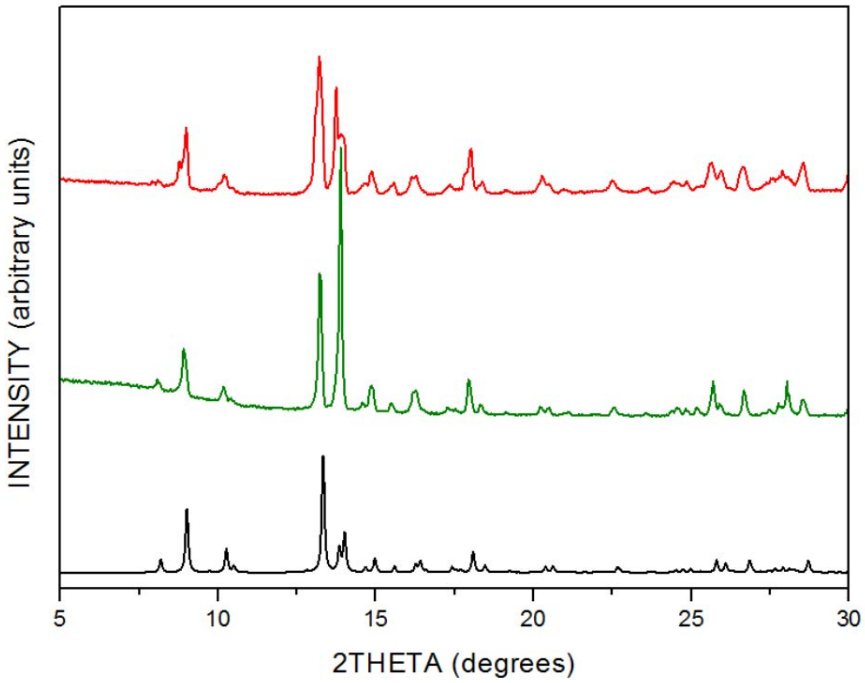

Figure 3.13. XRPD diffractograms of the synthesized $\mathbf{2}_{\mathbf{CuZn}}$ after 6 months immersed in water (green) and after 1 hour immersed in boiling water (red), as compared to the simulated powder pattern for the crystal structure of $\mathbf{2}_{\mathbf{CuZn}}$ (black).

3.3.5. Water uptake measurements

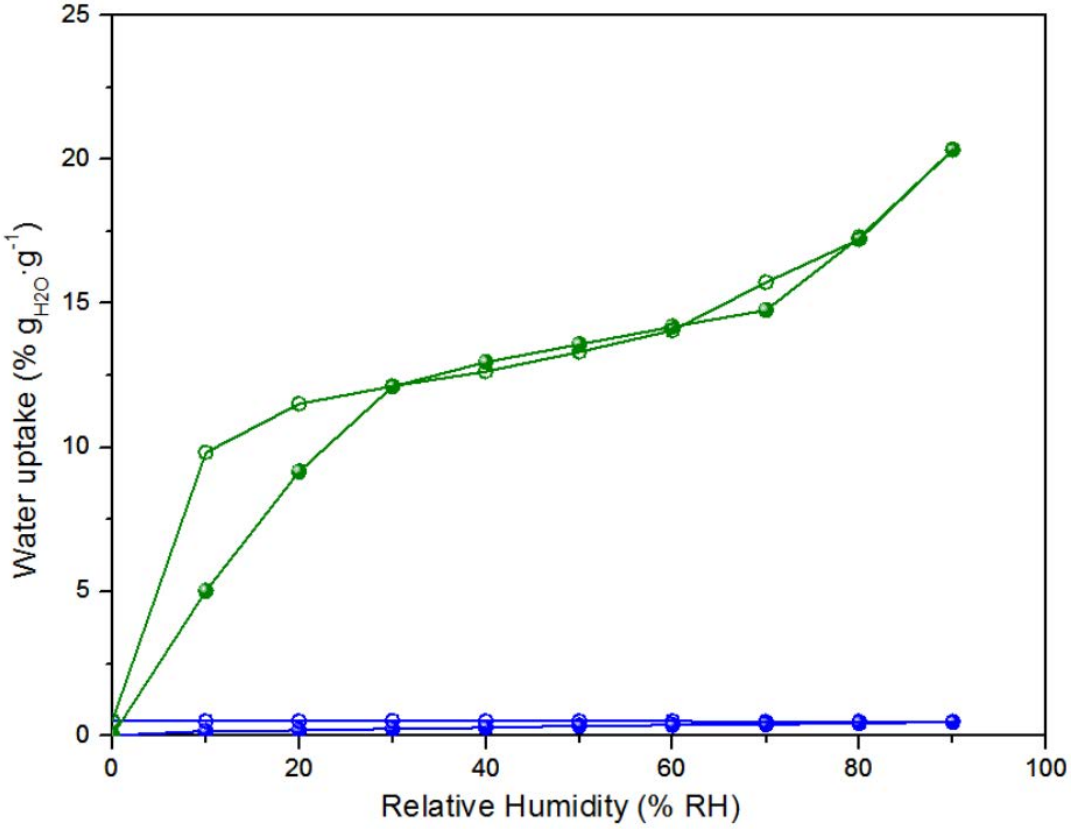

Figure 3.14. Water adsorption isotherm of $\mathbf{1}_{CuZn}$ (blue) and $\mathbf{2}_{CuZn}$ (green).

3.4. References

(1) Janiak, C. *Dalt. Trans.* **2003**, No. 14, 2781.

(2) Kitagawa, S.; Kitaura, R.; Noro, S. *Angew. Chemie Int. Ed.* **2004**, *43* (18), 2334.

(3) Imaz, I.; Rubio-Martínez, M.; García-Fernández, L.; García, F.; Ruiz-Molina, D.; Hernando, J.; Puntes, V.; Maspoch, D. *Chem. Commun.* **2010**, *46* (26), 4737.

(4) Aríñez-Soriano, J.; Albalad, J.; Carné-Sánchez, A.; Bonnet, C. S.; Busqué, F.; Lorenzo, J.; Juanhuix, J.; Terban, M. W.; Imaz, I.; Tóth, É.; Maspoch, D. *Chem. - A Eur. J.* **2016**, *22* (37), 13162.

(5) Zhao, D.; Timmons, D. J.; Yuan, D.; Zhou, H.-C. *Acc. Chem. Res.* **2011**, *44* (2), 123.

(6) Liu, B.-L.; Zang, H.-Y.; Tan, H.-Q.; Wang, Y.-H.; Li, Y.-G. *CrystEngComm* **2016**, *18* (18), 3300.

(7) Jiao, L.; Sun, S.; Meng, X.; Ji, P. *Catalysts* **2019**, *9* (9), 739.

(8) Bu, F.-X.; Hu, M.; Xu, L.; Meng, Q.; Mao, G.-Y.; Jiang, D.-M.; Jiang, J.-S. *Chem. Commun.* **2014**, *50* (62), 8543.

(9) Fluch, U.; McCarthy, B. D.; Ott, S. *Dalt. Trans.* **2019**, *48* (1), 45.

(10) Marreiros, J.; Caratelli, C.; Hajek, J.; Krajnc, A.; Fleury, G.; Bueken, B.; De Vos, D. E.; Mali, G.; Roeffaers, M. B. J.; Van Speybroeck, V.; Ameloot, R. *Chem. Mater.* **2019**, *31* (4), 1359.

(11) Taddei, M.; Wakeham, R. J.; Koutsianos, A.; Andreoli, E.; Barron, A. R. *Angew. Chemie Int. Ed.* **2018**, *57* (36), 11706.

(12) Burrows, A. D.; Frost, C. G.; Mahon, M. F.; Richardson, C. *Chem. Commun.* **2009**, No. 28, 4218.

(13) Liu, B.; Jie, S.; Bu, Z.; Li, B.-G. *RSC Adv.* **2014**, *4* (107), 62343.

(14) Yin, Z.; Wan, S.; Yang, J.; Kurmoo, M.; Zeng, M.-H. *Coord. Chem. Rev.* **2019**, *378*, 500.

(15) Brozek, C. K.; Dincă, M. *Chem. Soc. Rev.* **2014**, *43* (16), 5456.

(16) Evans, J. D.; Sumby, C. J.; Doonan, C. J. *Chem. Soc. Rev.* **2014**, *43* (16), 5933.

(17) Li, W.; Zhang, Y.; Zhang, C.; Meng, Q.; Xu, Z.; Su, P.; Li, Q.; Shen, C.; Fan, Z.; Qin, L.; Zhang, G. *Nat. Commun.* **2016**, *7* (1), 11315.

(18) Grancha, T.; Ferrando-Soria, J.; Zhou, H.-C.; Gascon, J.; Seoane, B.; Pasán, J.; Fabelo, O.; Julve, M.; Pardo, E. *Angew. Chemie Int. Ed.* **2015**, *54* (22), 6521.

(19) Yang, S.; Lin, X.; Blake, A. J.; Walker, G. S.; Hubberstey, P.; Champness, N. R.; Schröder, M. *Nat. Chem.* **2009**, *1* (6), 487.

(20) Yang, S.; Martin, G. S. B.; Titman, J. J.; Blake, A. J.; Allan, D. R.; Champness, N. R.; Schröder, M. *Inorg. Chem.* **2011**, *50* (19), 9374.

(21) Zou, R.; Li, P.-Z.; Zeng, Y.-F.; Liu, J.; Zhao, R.; Duan, H.; Luo, Z.; Wang, J.-G.; Zou, R.; Zhao, Y. *Small* **2016**, *12* (17), 2334.

(22) Matthes, P. R.; Höller, C. J.; Mai, M.; Heck, J.; Sedlmaier, S. J.; Schmiechen, S.; Feldmann, C.; Schnick, W.; Müller-Buschbaum, K. *J. Mater. Chem.* **2012**, *22* (20), 10179.

(23) Brozek, C. K.; Michaelis, V. K.; Ong, T.-C.; Bellarosa, L.; López, N.; Griffin, R. G.; Dincă, M. *ACS Cent. Sci.* **2015**, *1* (5), 252.

(24) Tranchemontagne, D. J.; Mendoza-Cortés, J. L.; O'Keeffe, M.; Yaghi, O. M. *Chem. Soc. Rev.* **2009**, *38* (5), 1257.

(25) Sunderland, T. L.; Berry, J. F. *Dalt. Trans.* **2016**, *45* (1), 50.

(26) Pal, T. K.; Neogi, S.; Bharadwaj, P. K. *Chem. - A Eur. J.* **2015**, *21* (45), 16083.

(27) Gotthardt, M. A.; Schoch, R.; Wolf, S.; Bauer, M.; Kleist, W. *Dalt. Trans.* **2015**, *44* (5), 2052.

(28) Song, X.; Jeong, S.; Kim, D.; Lah, M. S. *CrystEngComm* **2012**, *14* (18), 5753.

(29) Gul-E-Noor, F.; Jee, B.; Mendt, M.; Himsl, D.; Pöppl, A.; Hartmann, M.; Haase, J.; Krautscheid, H.; Bertmer, M. *J. Phys. Chem. C* **2012**, *116* (39), 20866.

(30) Teo, J. M.; Coghlan, C. J.; Evans, J. D.; Tsivion, E.; Head-Gordon, M.; Sumby, C. J.; Doonan, C. J. *Chem. Commun.* **2016**, *52* (2), 276.

(31) Kim, D.; Song, K. S.; Buyukcakir, O.; Yildirim, T.; Coskun, A. *Chem. Commun.* **2018**, *54* (86), 12218.

(32) Aríñez-Soriano, J.; Albalad, J.; Pérez-Carvajal, J.; Imaz, I.; Busqué, F.; Juanhuix, J.; Maspoch, D. *CrystEngComm* **2016**, *18* (22), 4196.

(33) Juanhuix, J.; Gil-Ortiz, F.; Cuní, G.; Colldelram, C.; Nicolás, J.; Lidón, J.; Boter, E.; Ruget, C.; Ferrer, S.; Benach, J.; IUCr. *J. Synchrotron Radiat.* **2014**, *21* (4), 679.

(34) Riesen, A.; Zehnder, M.; Kaden, T. A. *Helv. Chim. Acta* **1986**, *69* (8), 2067.

(35) Viola-Villegas, N.; Doyle, R. P. *Coord. Chem. Rev.* **2009**, *253* (13–14), 1906.

(36) Fontanet, M.; Popescu, A.-R.; Fontrodona, X.; Rodríguez, M.; Romero, I.; Teixidor, F.; Viñas, C.; Aliaga-Alcalde, N.; Ruiz, E. *Chem. - A Eur. J.* **2011**, *17* (47), 13217.

(37) Chilton, N. F.; Anderson, R. P.; Turner, L. D.; Soncini, A.; Murray, K. S. *J. Comput. Chem.* **2013**, *34* (13), 1164.

Chapter 4

Single-crystal-to-single-crystal post-synthetic modification of a Metal-Organic Framework via ozonolysis

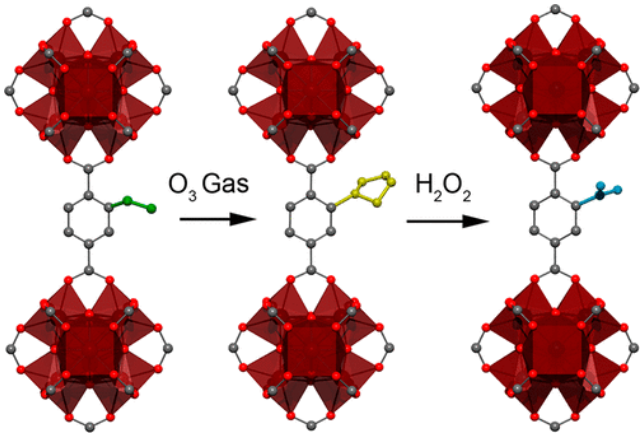

Abstract

In this Chapter, a solid–gas phase, single-crystal-to-single-crystal, post-synthetic modification of a Zr-based metal–organic framework (MOF) is described. Using ozone, the olefin groups of a UiO-66-type MOF are quantitatively transformed into 1,2,4-trioxolane rings, which can then be selectively converted into either aldehydes or carboxylic acids without affecting the framework's integrity.

This Chapter is based on the following publication:

Albalad, J.; Xu, H.; Gándara, F.; Haouas, M.; Martineau-Corcos, C.; Mas-Ballesté, R.; Barnett, S.A.; Juanhuix, J.; Imaz, I.; Maspoch, D. *J. Am. Chem. Soc.,* 2018, **140**, 2028-2031.

4.1. Introduction

As previously stated in Chapter 1, Metal-Organic Frameworks (MOFs) are an ideal platform for applications that entail incorporation of target chemical functionalities onto their pore walls.[1–4] To date, several post-synthetic modification (PSM) methodologies have been developed to introduce different chemical functionalities into preassembled MOFs. These include covalent modification of the organic linkers,[5,6] ligand exchange processes[7–9] and post-synthetic metalations.[10,11] However, the PSM approach presents major drawbacks. The synthetic conditions of post-synthetic covalent modifications typically require long reaction times and high temperatures that many MOFs cannot sustain; and for those MOFs that can resist such conditions, the yields are mostly low to moderate. This is partly because the most common PSM methods are based on solid−liquid phase processes, whereby reaction progress is limited by the diffusion of reagents inside the microporous frameworks to reach the target sites. As the reaction advances, the external MOFs surface gets partially tagged and the freshly-anchored surface groups block access to the pores.[12]

Solvent-less reactivity, particularly solid−gas (S/G) phase reactivity, is a widely explored approach in metallurgy and polymer science. Indeed, reactive gases (e.g., fluorine gas in the steel industry) have been used to quantitatively passivate, cleave, or switch the hydrophobic character of diverse materials since the early 90s.[13–15] However, there is scant precedent on solid−gas phase reactions with MOFs.[16] Such an approach could be used to overcome the previously stated limitations in the post-synthetic functionalization of MOF pores.

This Chapter will develop this path by exploring a proof-of-concept solid-gas PSM in a UiO-66-type MOF. For this, the Ozonolysis Reaction was chosen because of its well-known mechanism[17] and its fast, quantitative conversion rates. Ozone has proven to be a powerful oxidizing reagent for diverse chemistries under mild conditions.[18,19] Out of these reactions, the ozonolysis of alkenes is arguably the most widely studied.[20] Initially used for routine characterization of lipids and natural polymers, it is now employed for selective cleavage of olefinic bonds, as it enables regiospecific formation of carbonyl derivative moieties (aldehydes, ketones or carboxylic acids) in mere minutes. This reaction involves the metastable intermediate 1,2,4-trioxolane (Figure 4.1). Due to their low stability, trioxolane rings are not easy to isolate; however, those that could be isolated have demonstrated to be strong antibacterial and therapeutic agents, especially in the form of ozonated oils or triglycerides.[21] Additionally, trioxolane rings are powerful reaction intermediates, as they can be treated under mild reductive or oxidative conditions to chemoselectively form aldehyde moieties[22] or carboxylic acids,[23] respectively.

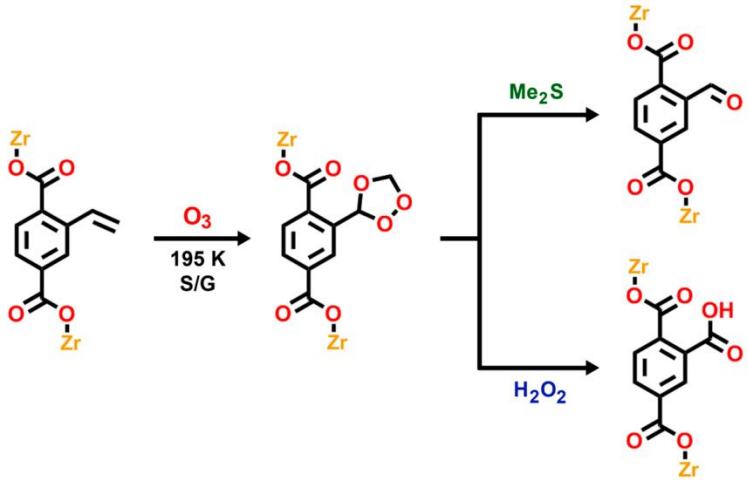

Figure 4.1. Illustrated PSM strategy of an olefin-tagged Zr-based MOF via ozonolysis in a solid-gas fashion.

Hereafter, a solid-gas post-synthetic functionalization of an olefin-tagged UiO-66-type MOF (**ZrEBDC**; EBDC=2-ethenylbenzene-1,4-dicarboxylate) using controlled, S/G ozonolysis is demonstrated. By constantly streaming ozone through the porous structure of ZrEBDC, the pendant ethenyl groups can be quantitatively transformed into stable 1,2,4-trioxolane moieties on the pore walls, with no loss of single-crystallinity. Additionally, the as-obtained moieties could be chemoselectively converted into both aldehyde or carboxylic acid moieties (42% and 100% yield, respectively) by taking advantage of the reactive behaviour of 1,2,4-trioxolane rings.

4.2. Results and Discussion

4.2.1. Establishment of the ozonolysis MOF system – Initial screening

The first milestone of this project was finding the most suitable MOF system for studying how ozone reacts with the metallic clusters and organic linkers within the framework. To this end, several blank tests were performed to known MOF systems with a wide range of chemical environments (Zr-UiO-67,[24] Cr-MIL-101,[25] Al-CAU-10,[26] Zn-MOF-74[27]) without olefinic side-chains in their backbone. Typical ozonolysis conditions widely used in organic chemistry (constant ozone bubbling to a stirred solution of reagents at -78 ºC) were initially explored. Specifically, a constant ozone flux (10 mmol O_3/h) was blown onto a stirred dispersion of the MOF sample in a solvent-assisted fashion. After 30 min, the MOF sample was recovered and characterized by Powder X-ray diffraction (PXRD) and Brunauer–Emmett–Teller (BET) surface area measurements (S_{BET}). Additionally, ^{1}H Nuclear Magnetic Resonance (NMR) analyses were performed to digested MOF samples and to the evaporated supernatant in order to follow any potential degradation in the linkers. From the gathered data, we could observe that both Cr-MIL-101 and Zn-MOF-74 collapsed significantly during the ozonolysis process, as their porosity

profiles and BET surface area (S_{BET}) values suffered a drastic reduction (Figure 4.2 b,c). On the other hand, MOFs with stronger M-COO bonds (*i.e.* Al(III), Zr(IV)) showed no porosity reduction after being exposed to ozone. We attributed this results to the fact that both Al(III) and Zr(IV) MOFs are on their highest oxidation state, thus not being affected by the powerful oxidizing capabilities of ozone. Al-CAU-10H was finally discarded due to partial leeching of its organic linkers during the ozonolysis process. In the end, Zr-based MOFs were chosen as the most suitable system for the study of ozonolysis in MOFs. Indeed, Zr-based MOFs are known to exhibit high thermal and chemical stability, as well as being resistant to aqueous and acidic conditions.[28–30] In our case, Zr-UiO-67 showed no loss in crystallinity or surface area after ozone exposure, as well as no leaching or partial degradation of the linkers.

After spotting the most suitable metal source, the next step focused on selecting the optimal organic linkers for the project. 2-Ethenylbenzene-1,4-dicarboxylic acid (H_2EBDC) was the ligand of choice, as it fulfilled two indispensable requirements; (*i*) the linker presents adequate linear directionality to form UiO-like frameworks when reacting with Zr ions; and (*ii*) the unsaturated moiety is incorporated as a side-pending group and not directly within the MOF backbone, thus not affecting its structural integrity after ozone exposure (Figure 4.3).

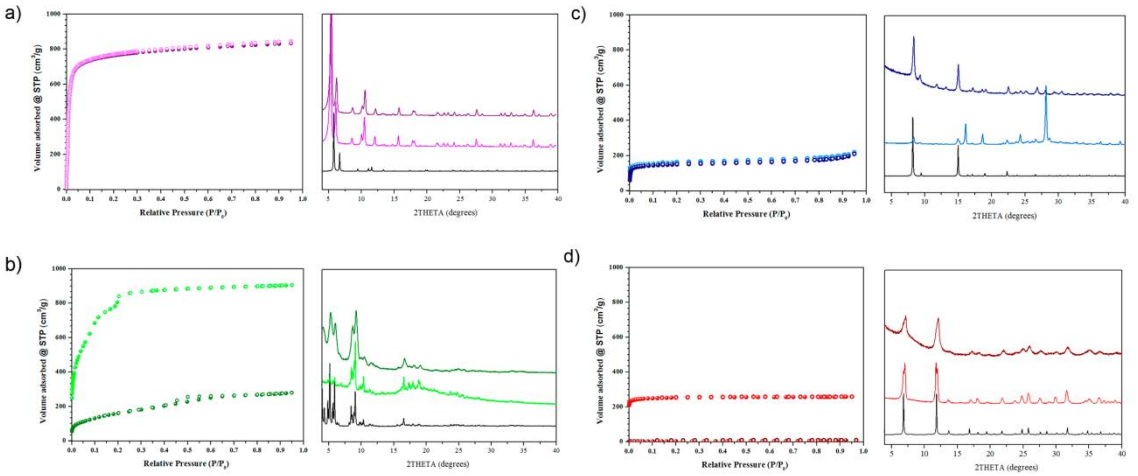

Figure 4.2. N_2 adsorption isotherms (left) and PXRD patterns (right) ordered from top to bottom: simulated PXRD, as-made PXRD and ozonated PXRD from Zr-UiO-67 (a), Cr-MIL-101 (b), Al-CAU-10H (c) and Zn-MOF-74 (d).

4.2.2. Synthesis and characterisation of ZrEBDC

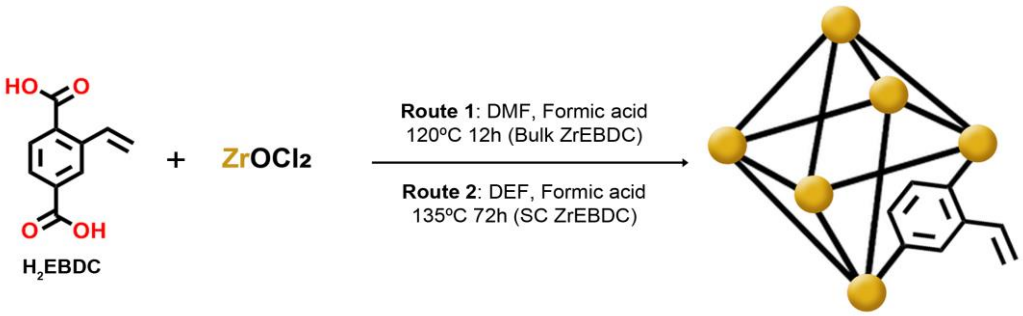

Figure 4.3. Schematic representation of bulk and single-crystal ZrEBDC synthetic pathways.

Bulk ZrEBDC was synthesized by adding an equimolar mixture of H_2EBDC and $ZrOCl_2 \cdot 8H_2O$ into a mixture of DMF and formic acid, and the resulting slurry was then heated at 120 °C (Figure 4.3). After 12 h, the crude solid was washed twice with DMF and acetone, filtered, and activated under vacuum prior to any ozonolysis test. This methodology afforded nanoscaled (20 – 40 nm monitored by Scanning Electron Microscopy (SEM)) spherical architectures in a 92% yield.

Colourless octahedral crystals of ZrEBDC (20 – 40 µm, monitored by SEM) suitable for single-crystal X-Ray diffraction (SCXRD) were obtained by slightly tuning the reaction conditions. After dissolving the two reagents in a 3:1 mixture of DEF/formic acid, the resulting solution was gradually heated from 25 to 135 °C at a heating rate of 5 °C/min for 72 h (Figure 4.3). After cooling down to room temperature, the crystals were recovered and washed with DMF several times. In exchange for the bigger crystal size, this methodology presented poor yields (< 20% based on Zr). The structural elucidation of single-crystal quality ZrEBDC under synchrotron radiation revealed the formation of the archetypical UiO-66-like backbone, consisting on 12-connected zirconium oxoclusters of formula $[Zr_6O_4(OH)_4]^{12+}$ interconnected through bideprotonated $EBDC^{2-}$ linkers in a three-dimensional fashion (Figure 4.4b). In this structure, the olefinic sidechains of the EBDC linkers are pointing inwards toward the pores. Due to the high symmetry of the framework, the atomic positions of the ethenyl side chains were homogeneously distributed at 25% atom occupancy between the four possible positions in EBDC (Figure 4.4c).

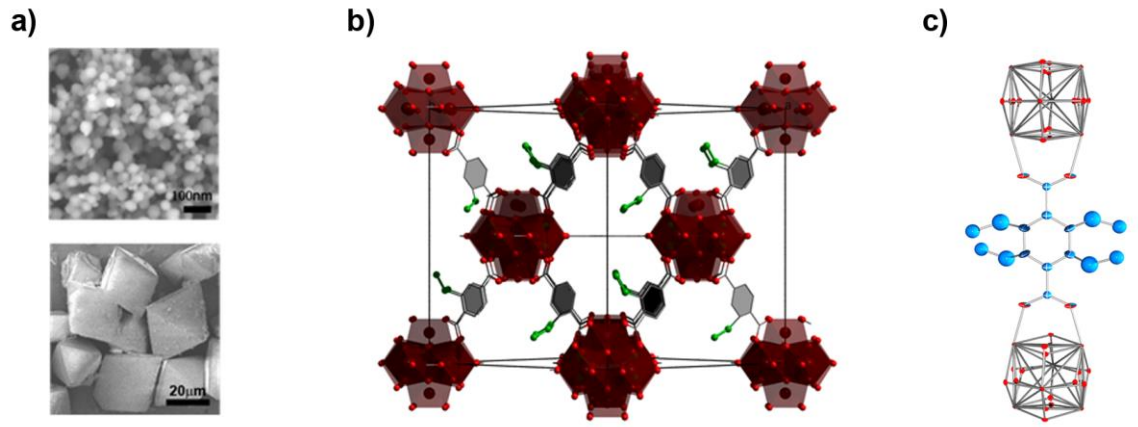

Figure 4.4. (a) SEM microscopy images of bulk ZrEBDC (top) and single-crystal ZrEBDC (bottom). (b) Backbone illustration of the single-crystal structure of ZrEBDC. The olefinic side-chains of the EBDC linkers are highlighted in green. The zirconium oxo-clusters are coloured in maroon red and the aromatic carbons, in grey. (c) ORTEP drawing of EBDC linker as found in the crystal structure of ZrEBDC. The four equivalent ethenyl group positions are distorted.

PXRD measurements confirmed that both bulk and single-crystal ZrEBDC shared the same crystalline phase, in good agreement with the simulated pattern obtained from single-crystal elucidation. For this, the optimization of further ozonolysis tests were performed exclusively with Bulk ZrEBDC, and monitored by routine characterization techniques, such as NMR, PXRD, S_{BET} and Mass Spectrometry (ESI-MS).

4.2.3. Setup optimization for dispersion and solid-gas phase ozonolysis

During the development of this project, two ozonolysis setups were studied: (*i*) A solvent-assisted methodology based on standard ozonolysis procedures widely used in organic chemistry, and (*ii*) a solid-gas phase methodology aimed at exploiting the intrinsic microporosity of MOFs in a solvent-less fashion.

Solvent-assisted setup. Based on the relative stability of ozone under solution, this methodology was rooted on how ozonolysis is routinely performed in organic chemistry laboratories.[31,32] A suitable amount of MOF sample was dispersed in the non-protic solvent of choice (*i.e.* CCl_4, chloroform, acetone, DMF, etc.), placed on a three-neck round-bottom flask and cooled down to either 0 ºC in a water/ice bath, or 195 K in a CO_2/acetone bath. A constant ozone flux (10 mmol O_3/h) was then continuously bubbled through a glass pipette onto the stirred dispersion. After 60 minutes, the MOF sample was recovered and thoroughly washed with acetone. The evolution of the reaction was monitored ^{1}H NMR analysis of the digested sample, and its crystallinity was characterized by PXRD measurements (Figure 4.5). Even though this methodology never achieved a quantitative conversion of the ethenyl moieties (presumably due to ozone's lifetime under the reaction conditions being shorter than its diffusion through the

solvent-filled porous framework[33]), it settled the basis of ozonolysis in MOFs, confirming the partial reactivity of the olefinic groups.

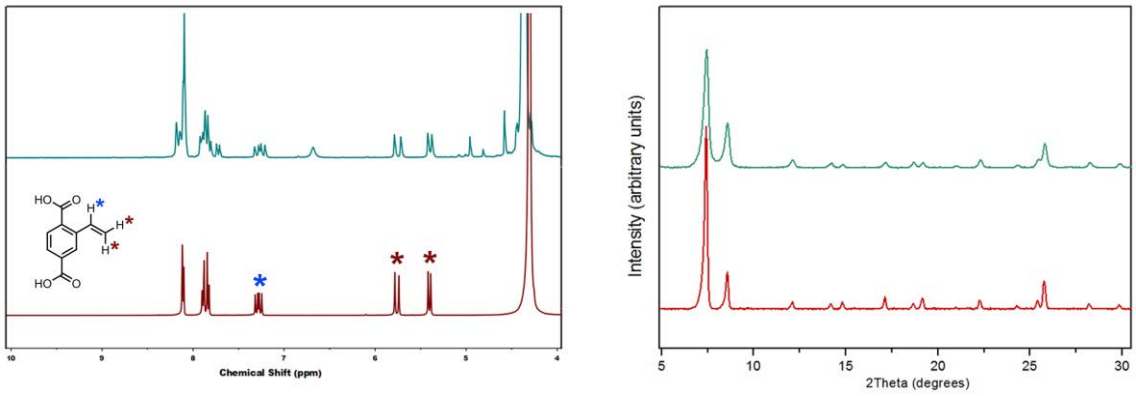

Figure 4.5. Left: ^{1}H NMR spectra of HF-digested (5% in DMSO-d_6) ZrEBDC MOF particles subjected to 1h of solvent-assisted ozonolysis in DMF (blue) compared with as-synthesized ZrEBDC (red). Olefinic signals are marked with a *. Right: PXRD of ZrEBDC (red) and ZrEBDC particles subjected to 1h of solvent-assisted ozonolysis in DMF (blue).

Solid-gas phase setup. In contrast to the poorly efficient solvent-assisted methodology, this setup takes advantage of the intrinsic microporosity MOFs present in the solid state and operates in a solvent-less fashion. Ozone gas is still reactive towards unsaturated moieties, and might react in a solid-gas fashion when diffusing through the framework.[34,35] To this end, the design of a new setup was required. This S/G setup must fulfil the following criteria; (*i*) every part of the setup should be ozone-proof, avoiding both leaking and corrosion; (*ii*) ozone should only take a single pathway, that being through the MOF pores; (*iii*) the setup should allow a proper evacuation of the MOF pores prior to any ozonolysis experiment; and (*iv*) the sample should be kept under the required reaction temperature at all times. Based on this premises, a new setup adapted to small-scale ozonolysis experiments was designed (Figure 4.6a,b) incorporating the following elements:

- Ozone generator
- Desiccation $CaCl_2$ column
- U-shaped Pyrex column, where the sample is horizontally packed
- Temperature bath (CO_2/acetone)
- Aqueous KI trap, acting as colorimetric indicator of free ozone[36]
- Vacuum connection at the end of the set

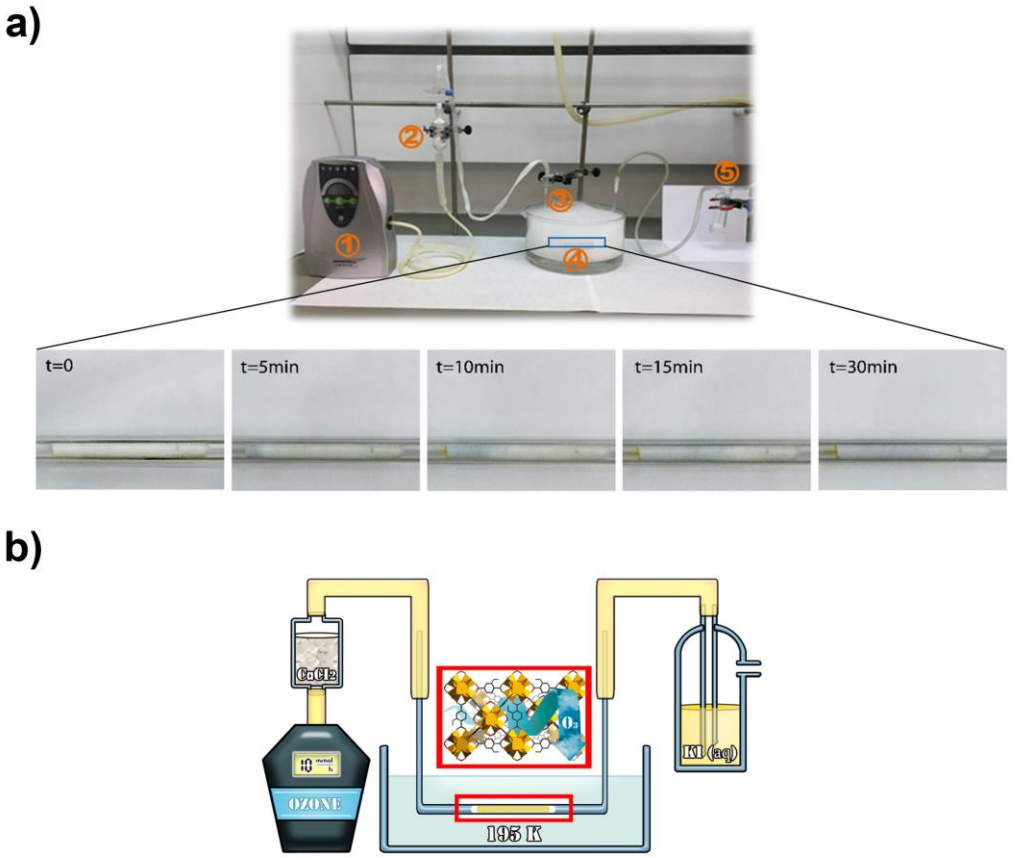

Figure 4.6. Laboratory (a) and schematic (b) representations of the solid-gas ozonolysis setup. (1) Ozonator; (2) $CaCl_2$ dessication column; (3) U-shaped Pyrex tube containing the MOF column; (4) CO_2/acetone bath at -78 ºC (195 K); (5) KI aqueous solution.

In a typical procedure, 50 mg of activated MOF sample (120 ºC vacuum, 12h) were packed inside a 3.4 mm diameter Pyrex tube. Two cotton stoppers were placed around the sample, and the column was bent into a U-shape using a flame torch. One end was directly attached to an ozone generator operating at 10 mmol O_3/h, whereas the other was connected to vacuum. Before the reaction was started, the tube was immersed into a dry ice/acetone bath at −78 °C (195 K) and purged under vacuum for 10 min.

Under these conditions, ozone presents a moderate half-life time and selectively reacts with the unsaturated moieties of the framework. Excessive generation of ozone was avoided by adding an aqueous KI detector to the end of the setup. Once the sample reached the proper temperature, a constant stream of O_3/air, dried through $CaCl_2$, was blown into the column. The stream was maintained until the KI solution changed from colourless to bright yellow (after ∼30 min), which indicated every olefinic side-chain was transformed. The ozone stream was then stopped immediately. The sample, which showed a blue coloration, was left under vacuum for an additional 10 minutes in order to ensure that all the residual unreacted ozone was evacuated from the tube; after this, the sample became white again. The ozonized sample was recovered by

carefully breaking the U-shaped tube and was further characterized by ^{1}H NMR, PXRD and BET measurements.

Through this methodology, quantitative fading of the olefinic NMR signals were achieved in just 30 min of reaction time, without significant crystallinity or surface area losses.

4.2.4 Solid-gas phase ozonolysis of bulk ZrEBDC

Evolution of the reaction followed by HF-digested ^{1}H NMR. 50 mg of activated Bulk ZrEBDC were carefully packed inside a U-shaped column and subjected to S/G Phase ozonolysis following the procedure stated in **4.2.2.** Ozonized samples at different reaction times, from 5 to 30 minutes, were collected. PXRD measurements of every sample confirmed the robustness of the UiO-like framework towards ozone exposure, showing no significant crystallinity loss (Figure 4.7).

In order to gain deeper knowledge on the solid-gas process, the degree of reaction of the olefinic groups was monitored by measuring the ^{1}H NMR spectra of the digested samples (5% HF/DMSO-d_6), and then compared to that of the starting ZrEBDC (Figure 4.7). The spectrum of the unreacted ZrEBDC showed the characteristic peaks of three non-equivalent olefinic protons at δ = 7.29, 5.77, and 5.41 ppm, integrating in a 1:1:1 ratio. In contrast, the spectrum of a fully converted sample (hereafter named **ozo-ZrBDC**) confirmed a quantitative fading of these olefinic signals in approximately 30 minutes of S/G interaction, and presented three new signals at δ = 6.70, 4.90 and 4.55 ppm (Figure 4.7; blue spectrum). The results at intermediate reaction times confirmed a direct correlation between the disappearance of the olefinic signals and the appearance of the new ones: with conversions of 33% at 5 minutes; 52% at 10 minutes; 78% at 15 minutes; and 100% at 30 minutes. However, the newly obtained signals did not match with the expected 1,2,4-trioxolane, as their chemical shifts and integration greatly differ from the theoretical values.

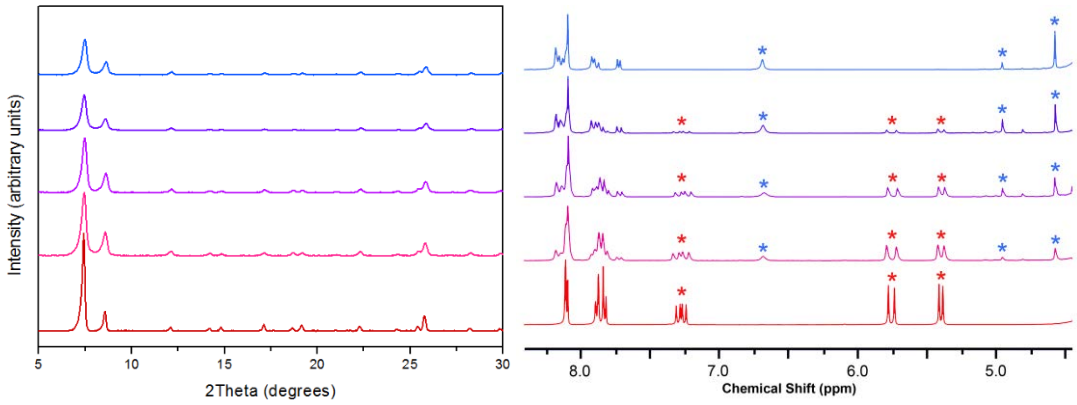

Figure 4.7. Left: PXRD measurements of ZrEBDC samples at different ozonolysis reaction times, from t= 0 minutes (red), t= 5minutes (pink), t= 10 minutes (lavender), t= 15 minutes (purple) and t= 30minutes (blue). Right: ^{1}H NMR spectra of digested ZrEBDC samples at different ozonolysis reaction times, showing a quantitative fading of olefinic signals at 30 minutes.

This experiment clearly shows that, while useful for routine monitoring of the reaction evolution, HF-digested NMR analysis grants little or no information on the real structure of the final product. Three new signals (*) aroused proportionally as the olefinic signals (*) faded, but their integration and chemical shift could not be related to the expected 1,2,4-trioxolane ring. Consequently, several in-depth NMR experiments were required for a proper understanding of the reaction. Such experiments were carried out in close collaboration with the *Institut Lavoisier de Versailles – CNRS*, both in HF-digested and solid-state fashion. 1D-NMR and 2D-NMR spectra (HR-^{1}H NMR, NOESY, DOSY, ^{13}C NMR, DEPT135, HSQC and HMBC) of digested ZrEBDC and ozo-ZrBDC are presented below, with brief explanations and identification of each species (Figures 4.8 - 4.13). A methodical interpretation of all the gathered data suggested that the 1,2,4-trioxolane moiety suffers a chemical transformation under the aggressive MOF digestion conditions, and followed two independent degradation pathways (Scheme 4.1).

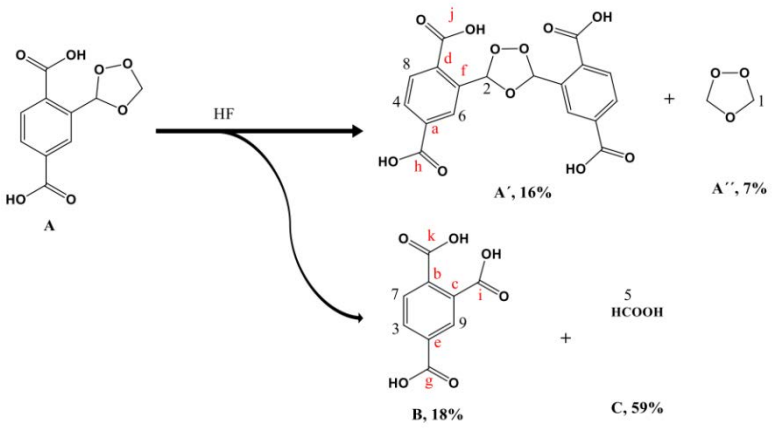

Scheme 4.1. Representation of the species formed after digestion of ozo-ZrBDC with 5% HF in DMSO-*d*$_6$. Carbon atoms with attached protons are labeled with black numbers (1-9) and quaternary carbon atoms, with red letters (a-k).

Four different molecular entities were properly identified in the mixture (DOSY NMR, Figure 4.9). First, two symmetric metathesis products **(cross-ozonation)** of our expected product trioxolane-BDC were identified (A' and A''). Second, two products attributed to the **acid-induced hydrolysis** of trioxolane-BDC (B and C). As previously stated, even though digested NMR analysis did not allow a direct elucidation of our target intermediate, it proved to be an excellent routine characterisation for following the ozonolysis evolution inside the MOF by comparing the olefinic signals versus the combination of two peaks; one at 7.73 ppm (corresponding to H3 of 1,2,4-benzenetricarboxylic acid) and one at 6.70 ppm (attributed to H2 of the trioxolane metathesis product A').

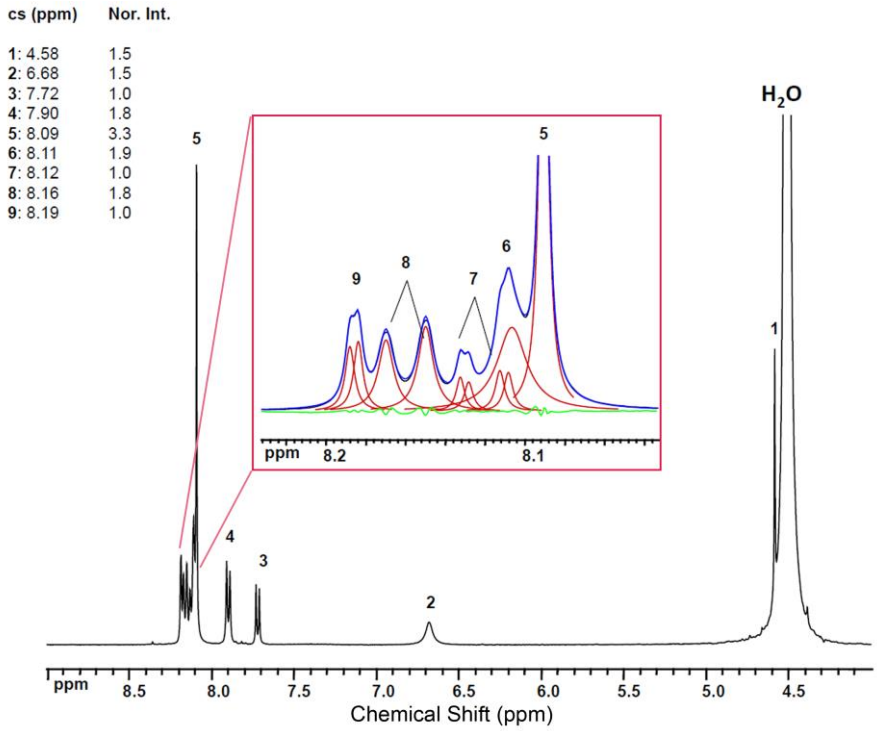

Figure 4.8. [1]H NMR spectrum of digested ozo-ZrBDC in HF/DMSO-d_6, showing nine proton resonances (labelled 1 to 9) corresponding to the 1,2,4-trioxolane derivatives and their decomposition products. An HR inlet spectrum (from 8.04 to 8.23 ppm) focuses on the aromatic region, combined with the fitted peaks (red lines).

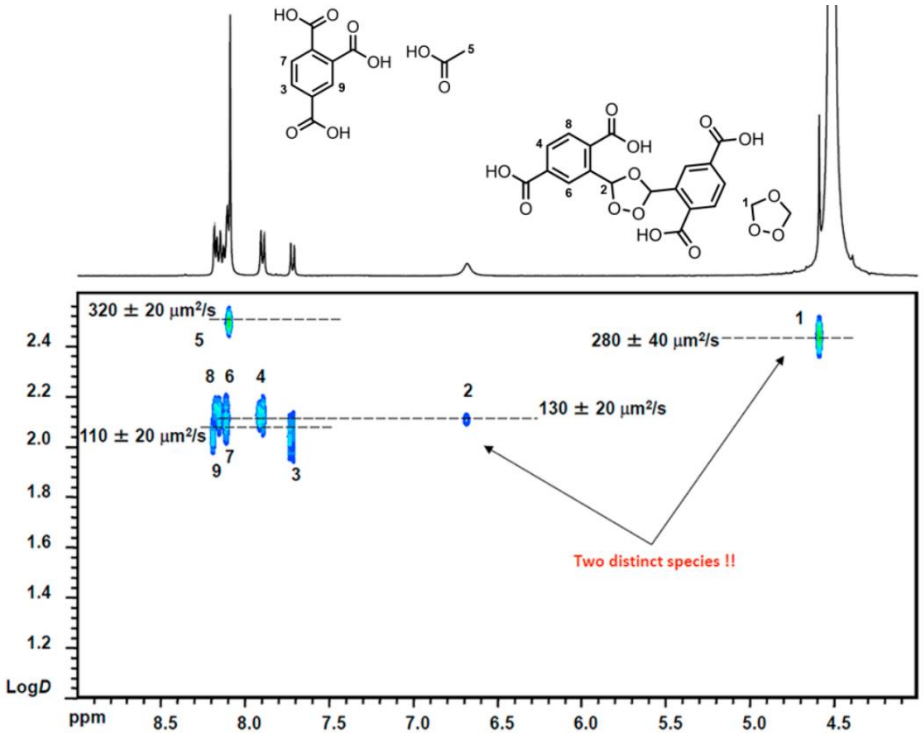

Figure 4.9. DOSY-NMR (Diffusion-Ordered Spectroscopy) spectrum of digested ozo-ZrBDC in HF/DMSO-d_6, showing four resonance entities at four diffusion coefficients. Note that signals 1 and 2, which appear in the range of trioxolane moieties, correspond to two distinct species.

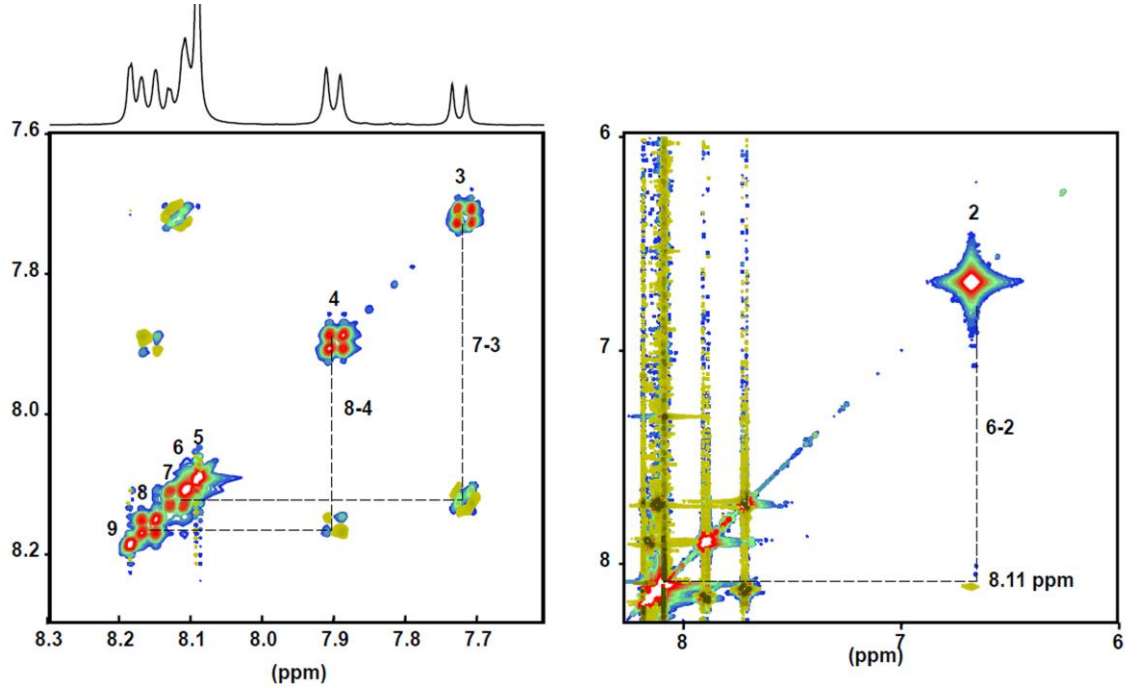

Figure 4.10. ^{1}H NOESY-NMR (Nuclear Overhauser Effect Spectroscopy) spectrum of digested ozo-ZrBDC in HF/DMSO-d_6, showing the spatial proximities between adjacent protons 7 and 3; protons 4 and 8; and protons 2 and 6 over two neighboring bonds.

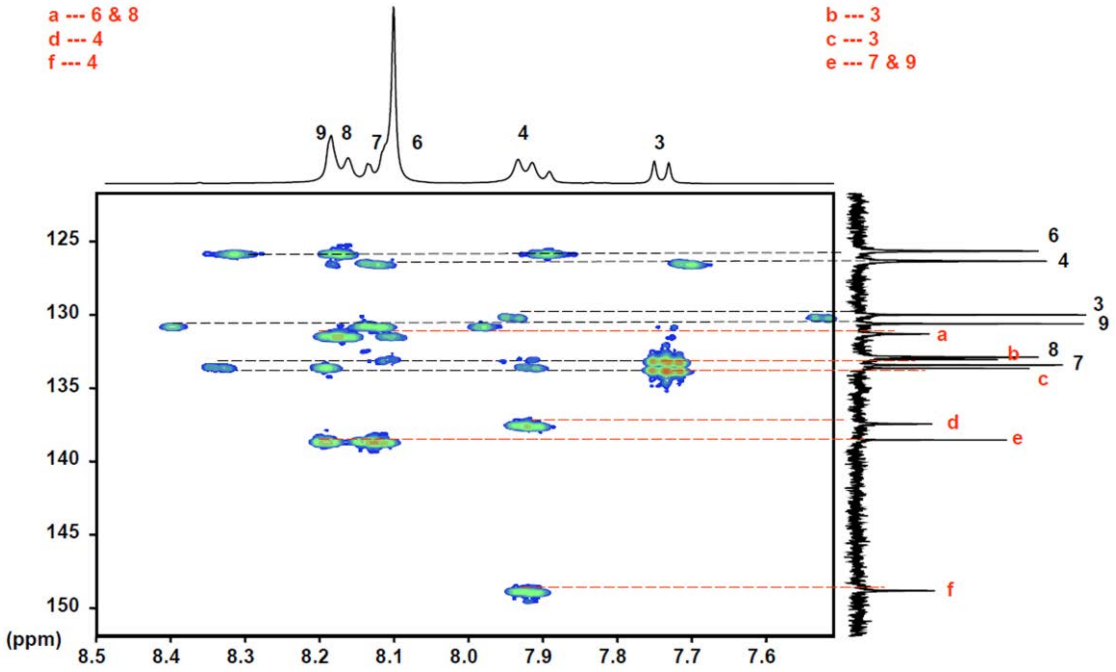

Figure 4.11. ^{13}C{^{1}H} HMBC spectrum of digested ozo-ZrBDC in HF/DMSO-d_6, showing the nine H atoms attached to nine carbon atoms (1-9).

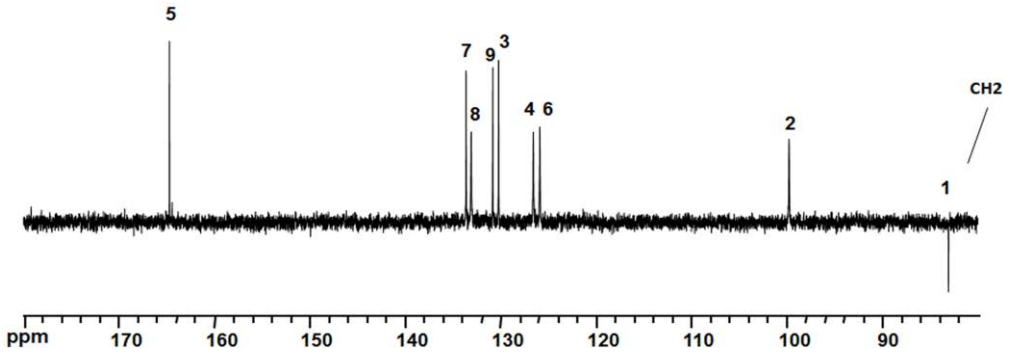

Figure 4.12. $^{13}C\{^{1}H\}$ DEPT135 NMR spectrum of digested ozo-ZrBDC in HF/DMSO-d_6 that enables the differentiation of the CH groups from the CH_2 groups. Note that all carbons, bear one signal, are attached to a single proton.

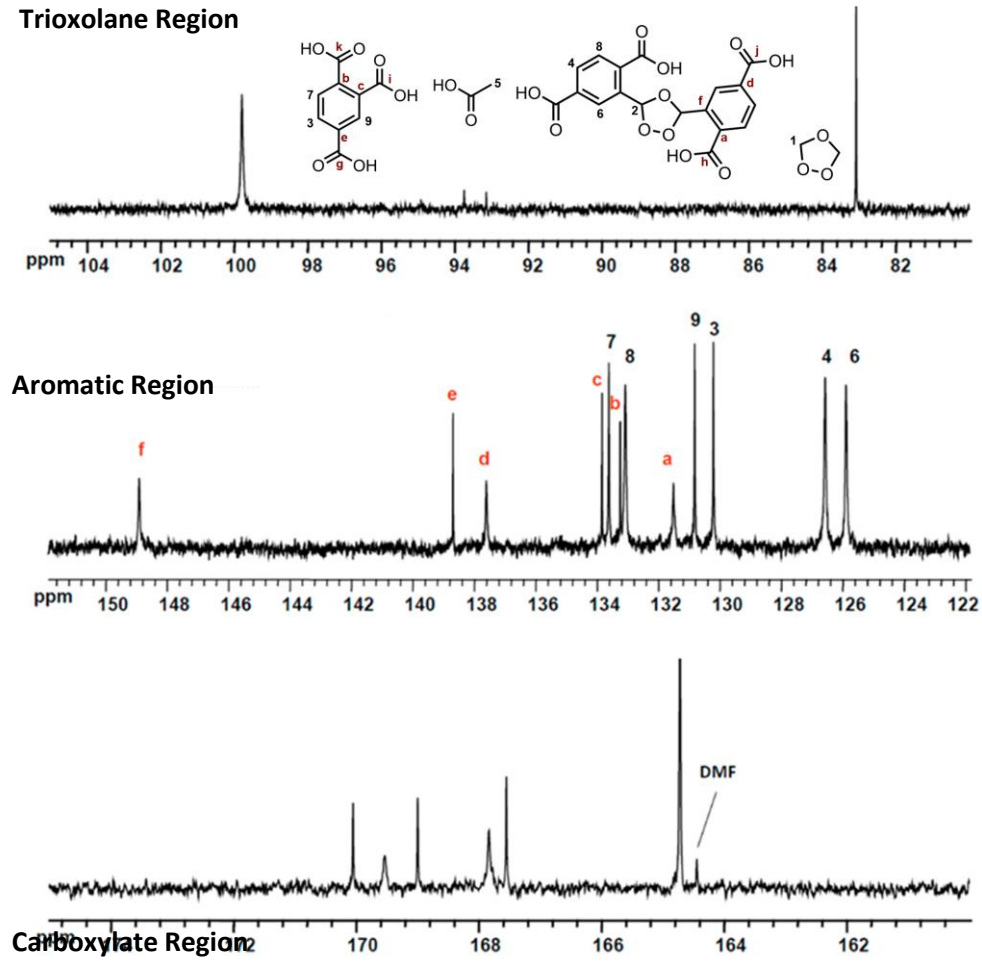

Figure 4.13. $^{13}C\{^{1}H\}$ NMR spectrum of digested ozo-ZrBDC in HF/DMSO-d_6, showing the twenty different carbon atoms labelled 1-9 (C-H) and a-k (quaternary C). The two groups of resonances are differentiated by comparing DEPT135 and polarization experiments.

To gain direct evidence on the 1,2,4-trioxolane formation, solid-state ^{13}C NMR spectra of both ZrEBDC and ozo-ZrBDC were recorded using cross-polarization under magic angle spinning (CP-MAS). The two ^{13}C-peaks of the ethenyl group in ZrEBDC appear at 115.6 and

131.0 ppm (Figure 4.14a, red spectrum). As expected, the spectrum of ozo-ZrBDC lacks these two peaks and shows two new ones, at 93.6 and 101.8 ppm (Figure 4.14a, blue spectrum), which indicated successful conversion of all the olefinic moieties. We then recorded CP-MAS NMR spectra of each product under Polarization Inversion (CPPI),[37] in order to differentiate between carbon sites coupled to protons with contrasted dipolar interaction. In the CPPI spectrum of ozo-ZrBDC (Figure 4.14a, orange spectrum), the resonance at 93.6 ppm is present, whereas that at 101.8 ppm is absent. These observations confirmed the formation of the 1,2,4-trioxalane ring, with the CH_2 peak located at 93.6 ppm and the CH peak, at 101.8 ppm; in agreement with literature data and the expected spectra coming from a 1,2,4-trioxolane.[38,39] We further confirmed this formation by performing a soft-ligand exchange experiment immersing fully ozonated ozo-ZrBDC in a saturated 1,4-BDC DMF solution for seven days at room temperature.[40] Two peaks in solution ^{1}H NMR corresponding to the CH and CH_2 groups of the 1,2,4-trioxolane ring (δ = 5.61 and δ = 4.65 ppm, integrating in a 1:2 ratio) were identified after analysing the evaporated supernatant (Figure 4.14b).

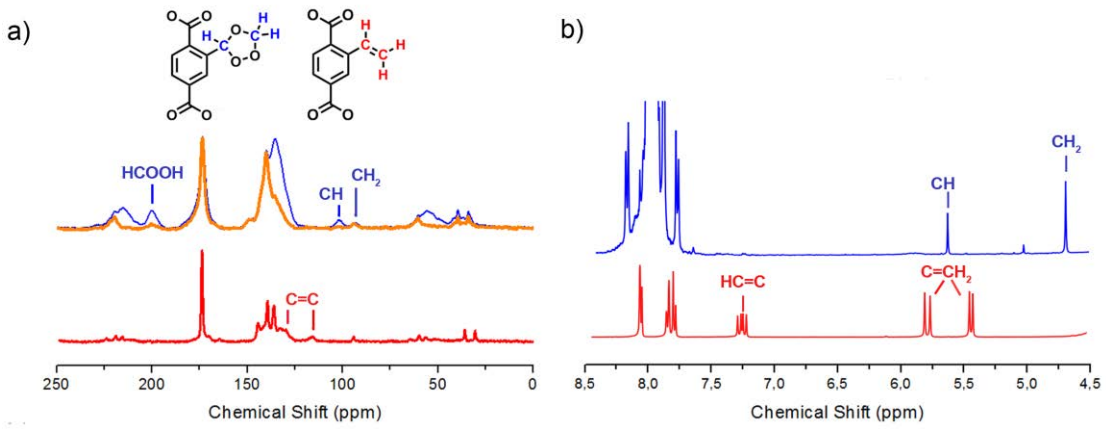

Figure 4.14. (a) Solid-state ^{13}C NMR spectra of ZrEBDC (red: CP-MAS) and ozo-ZrBDC (blue: CP-MAS; orange: CPPI-MAS). (b) ^{1}H NMR spectra after the soft ligand-exchange experiment (blue) versus H_2EBDC (red).

Samples exposed to different ozonation times were also subjected to standard conditions for MOF activation (120 °C, 12 h), and their inner surface area was subsequently measured (see Section 4.3.5). Compared to the initial S_{BET} value for ZrEBDC (1300 m^2/g - see Section 4.3.5.; Figure 4.18), the ozonated samples exhibited decreasingly lower S_{BET} values in function of increasing ozonation time; the value for the fully converted ozo-ZrBDC was 685 m^2/g (Section 4.3.5.; Figure 4.19). Remarkably, this surface area is consistent with a previously reported value for a UiO-66-like MOF with imidazole moieties as pendant groups (S_{BET} = 538 m^2/g).[41]

4.2.5 Solid-gas phase ozonolysis of single-crystal ZrEBDC

After the optimization of the process, we aimed at taking this S/G methodology one step further and proof its efficiency through single-crystal diffraction. SCXRD is arguably one of the most precise characterization techniques at atomic level, defining the electronic density of every atomic position within a crystalline lattice. To this end, SC ZrEBDC was homogeneously mixed with bulk sample and was subjected to S/G ozonolysis at 195 K for 30 min. Mixing SC sample with microcrystalline ZrEBDC proved to be necessary in order to avoid preferential pathways in the ozone flux, forcing it through the material. After confirming a quantitative fading of the olefinic signals in HF-digested NMR measurements, the single crystals were separated by decantation, washed with DMF and analysed under synchrotron radiation. We characterised the ozonolysed crystals of ozo-ZrBDC by SCXRD, which confirmed that they had retained the crystallinity and the UiO-66 framework of the starting MOF (Figure 4.15a).

Analysis of the difference Fourier maps revealed high electron-density within the pores of the framework, which we attributed to the 1,2,4-trioxolane. Due to the high symmetry of the framework, the positions of the 1,2,4- trioxolane groups were statistically disordered, which prevented us from refining their position in the cubic Fm3m space group of ozo-ZrBDC. Nonetheless, in close collaboration with the *Instituto de Ciencia de Materiales de Madrid* (ICMM-CSIC), upon refining the framework atoms (including the defect sites and adsorbed species),[42] we calculated a residual electron-density within the pores of 657 e^- per unit cell, using the program Squeeze.[43] This value was in good agreement with the calculated number of electrons corresponding to the presence of one 1,2,4-trioxolane per organic linker within the unit cell (653 e^-), which is the value obtained when 15% of the linker sites are considered to be defective (as suggested by the single-crystal refinement). To determine the orientation of the 1,2,4-trioxolane groups, we performed an additional single-crystal refinement in the monoclinic C2-space group. Due to the low partial occupancies of the 1,2,4- trioxolane and their positional disorder, rigid body restraints were employed, whereby the conformation of the 1,2,4-trioxolane moiety was obtained from Density Functional Theory (DFT)-based calculations. The 1,2,4-trioxolane rings appeared to be rotated relative to the plane of their corresponding linker phenyl ring, and in all cases oriented toward the inorganic secondary building units (SBUs), at short-contact distances (range: 2.3 to 3.1 Å) between the 1,2,4-trioxolane atoms and the carboxylic groups of the adjacent linkers, in good agreement with the DFT calculations performed in collaboration with the Autonomous University of Madrid (UAM) (Figure 4.15c).

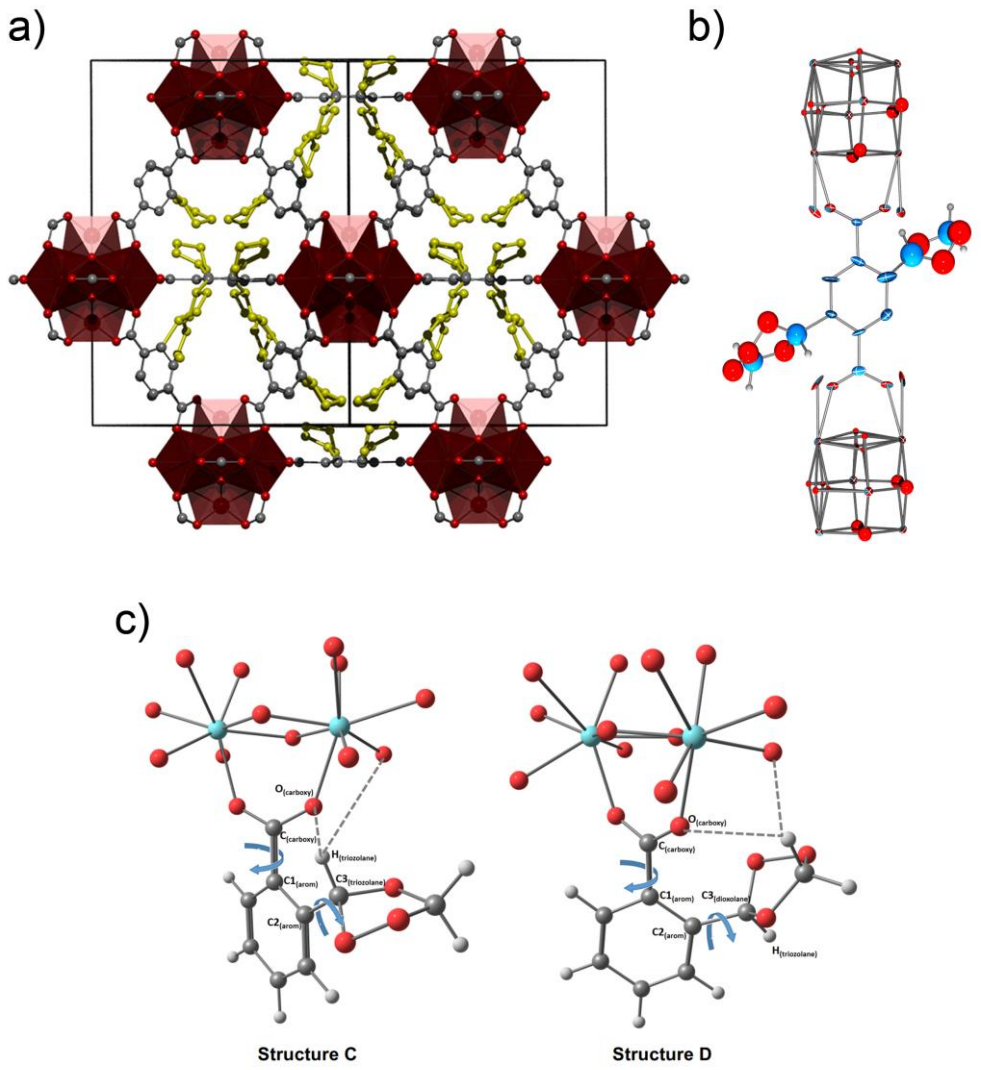

Figure 4.15. Illustration of the single-crystal structure of ozo-ZrBDC across the [1 1 0] direction, highlighting in yellow the disordered 1,2,4-trioxolane moieties. (b) ORTEP drawing of ozo-ZrBDC. (c) Simplified drawings of optimized structure geometries restricting to 180º the values of Zr_a-Zr_b-$C_{(carboxy)}$-$C1_{(atom)}$ dihedral angle. Curved arrows indicate the rotations found accounting for the maximization of H-bond interactions (noted as dashed lines).

4.2.6. Reductive and oxidative work-up procedures of ozo-ZrBDC

Having demonstrated that ozonide rings can be stabilized inside a robust MOF, we next sought to explore the amenability of such rings in ozo-ZrBDC to be selectively reduced into aldehydes or oxidized into carboxylic acids. For the former, ozo-ZrBDC was soaked overnight, with stirring, in an acidic aqueous solution of dimethyl sulphide (Me_2S) as reducing agent, to convert the 1,2,4-trioxolane rings into aldehyde groups in a yield of 40% (Figure 4.16a, left). The mild conditions of the workup did not allow for quantitative conversion of the stabilized trioxolanes, and all attempts to make the reduction more aggressive resulted in undesired formation of carboxylate byproduct. The S_{BET} of this ozo-ZrBDC partially functionalized with aldehyde moieties was 960 m^2/g (see Section 4.3.5.; Figure 4.20). Alternatively, soaking ozo-ZrBDC overnight, with stirring,

in aqueous hydrogen peroxide (H_2O_2) drove oxidative cleavage of the 1,2,4-trioxolane rings to the corresponding carboxylic acids. This transformation was quantitative, as confirmed by ^{1}H NMR analysis (Figure 4.16a, right). In both the aldehyde and carboxylic acid products, the UiO-66-type framework was preserved, as confirmed by PXRD (Figure 4.16b). Furthermore, SCXRD analysis of the crystals resulting from the oxidation pathway (H_2O_2) confirmed that they also retained their single-crystal character. Remarkably, the position of the newly formed carboxylic acid groups could be determined through the refinement of the SCXRD data (Figure 4.16c). In this case, the S_{BET} was found to be 301 m^2/g (see Section 4.3.5; Figure 4.21), which is in good agreement with those reported for this UiO-66-COOH (S_{BET} = 350−400 m^2/g).[44].

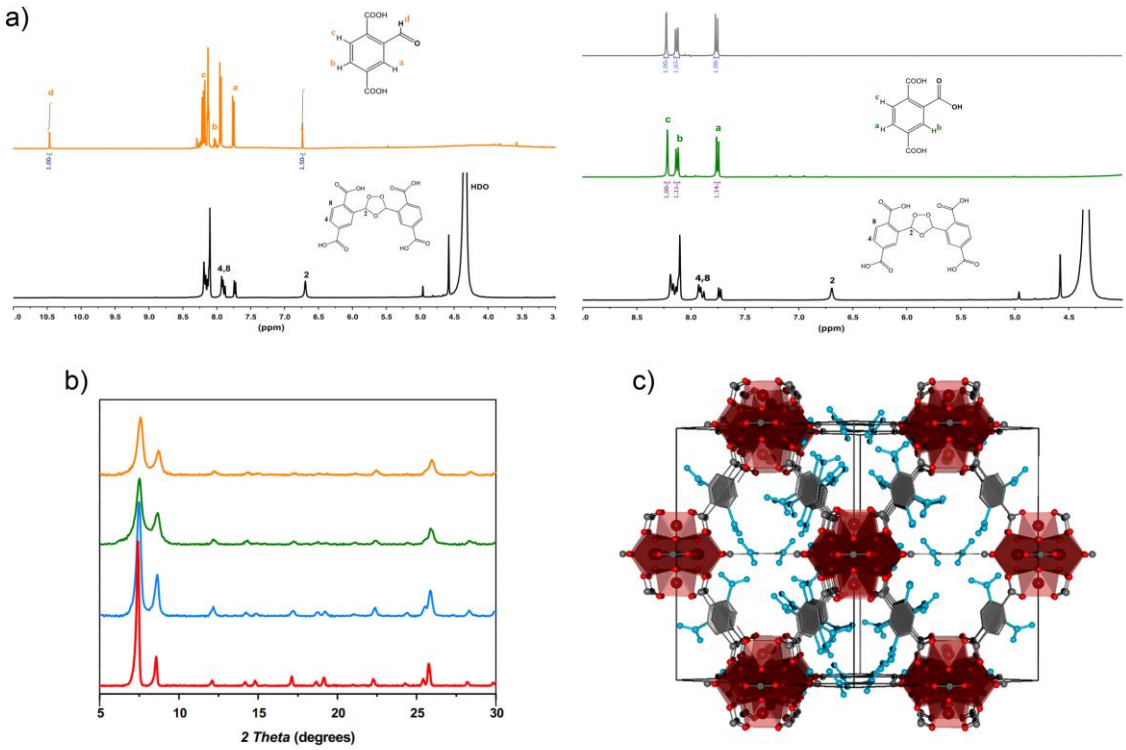

Figure 4.16. (a) ^{1}H NMR spectra of digested reductive work-up (left) and oxidative work-up (right) pathways, compared with ozo-ZrBDC (black). (b) PXRD measurements of ZrEBDC (red), ozo-ZrBDC (blue), ZrBDC-COOH (green) and ozo-ZrBDC partially functionalized with CHO groups (orange).

4.2.7. Conclusions

In summary, we have reported a solvent-less, solid−gas, single-crystal-to-single-crystal, postsynthetic functionalization of a MOF using ozone. Streaming of ozone gas through an olefin-tagged UiO-66-type MOF at −78 °C provided quantitative transformation of the olefins into 1,2,4-trioxolane rings inside the robust MOF framework. When confined inside the MOF pores, this ring proved to be stable under standard heat and vacuum conditions for MOF activation, unlike in solution. Finally, an optimized workup enabled further single-crystal-to-single-crystal

chemistry on these 1,2,4-trioxolane rings: reduction into the corresponding aldehyde or oxidation to the corresponding carboxylic acids, the latter in quantitative yield. We are confident that our methodology will offer new insight into how gas molecules might be exploited for MOF chemistry that transcends common physisorption phenomena.

4.3. Experimental Part

4.3.1. Materials and Methods

Zirconium oxychloride octahydrate ($ZrOCl_2 \cdot 8H_2O$, purity ≥ 99.5%), formic acid (purity >98%), potassium iodide (KI), N,N-diethylformamide (DEF) and anhydrous granular $CaCl_2$ (2-6 mm) were purchased from Sigma-Aldrich Co. N,N-dimethylformamide (DMF) and acetone were obtained from Fisher Chemical. 2-ethenylbenzene-1,4-dicarboxylic acid (purity >97%) was obtained from iChemicals Co. All the reagents and solvents were used without further purification unless otherwise specified. Deionized water was obtained with a Milli-Q® system (18.2 MΩ·cm). Pyrex tubes (outØ5mm x inØ3.4mm; length: 50 cm) were purchased from VIDRASA S.A. The tubes were bent into a U-shape with a flame torch prior to any ozonolysis process. A constant ozone flux was obtained using an ozone generator (model N1668A, 10.4 mmol/h O_3 at room temperature) purchased from Ozonotec.

Powder X-Ray Diffraction (PXRD) patterns were recorded on an X'Pert PRO MPD analytical diffractometer (Panalytical) at 45 kV, 40 mA using Cu K_α radiation (λ = 1.5419 Å). Elemental Analysis measurements were performed on a Flash EA 2000 CHNS (Thermo Fisher Scientific) analyzer. Field-Emission Scanning Electron Microscopy (FE-SEM) images were collected on a FEI Magellan 400L scanning electron microscope at an acceleration voltage of 2.0 KV, using aluminum as support. ^{13}C NMR spectra were recorded on an Bruker Avance 500 NMR spectrometer (static magnetic field of 11.7 T) operating at Larmor frequencies of 500.1 MHz (^1H) or 125.8 MHz(^{13}C). The samples were packed in rotors (o.d.: 4 mm) and analyzed at 10 kHz MAS frequency. ^{13}C chemical shifts were referenced to the carbon signal in TMS at 0 ppm. The Cross-Polarization with Polarization Inversion (CPPI)[37] spectrum of ozo-ZrBDC was recorded using a pulse-inversion duration of 50 μs.^1H step small-phase incremental alternation (SPINAL-64)[45] decoupling was applied during the ^{13}C signal acquisition (~ 80 kHz RF field). Nitrogen adsorption and desorption measurements were done at 77 K using an Autosorb-IQ-AG analyser.

Single-Crystal X-Ray Diffraction (SCXRD) data of ZrEBDC and ZrBDC-COOH were collected at 100(2) K in BL13-XALOC beamline[46] at the ALBA synchrotron, on a single-axis goniometer with a Pilatus 6M detector using a monochromatic X-ray beam (λ = 0.75253 Å and λ = 0.82653 Å, respectively). The data were indexed, integrated and scaled using the XDS program.[47] Absorption corrections were not applied. The ZrEBDC structure was solved by direct methods and subsequently refined by correction of F^2 against all reflections, using SHELXS2013 and SHELXL2013 within the WinGX package and OLEX2.[48,49] Single-crystal diffraction data for ozo-ZrBDC was collected in beamline I19-1 at Diamond Light Source, UK, on a fixed-chi goniometer with a Pilatus 2M detector (silicon (111) monochromatic radiation, λ = 0.6889 Å).[50] Data were processed using XiA.[51] Two different refinements were completed for this sample. In

the first one, the framework's cubic symmetry was maintained, and the residual electron density corresponding to the trioxolane groups was accounted by means of the program Squeeze. In a second refinement, the crystal structure was refined in the C2 space group, in order to refine the position of the trioxolane groups, which were refined as rigid bodies with the use of the FRAG and EADP instructions. The position of the carbon atoms bound to the linker phenyl ring could be readily identified in the difference density maps, and used to set the position of rigid body fragments, whose conformation was obtained from DFT calculations.

All calculations were performed at the DFT level using the M06 functional[52,53] with an ultrafine grid[54] as implemented in Gaussian09. This functional accounts for dispersion interactions and has a good performance on inorganic systems.[55,56] The Zr atom was described by means of an effective core potential SDD for the inner electron and its associated double-ζ basis set for the outer ones,[57] complemented with a set of f-polarisation function.[58] The 6-31G basis set was used for the C atoms, 6- 31G(d) for the O atoms and 6-31G(p,d), for H atoms.[59,60] The two possible structures were fully optimized in gas phase. Both structures were identified as minimum points in the potential energy surface by determining the absence of imaginary frequencies in the Hessian matrix. All energy values correspond to Gibbs energies in kcal mol^{-1}. Structures optimized without any geometrical restriction resulted in folded geometry, which would impose a tension in the solid-state structure that could hardly allow the formation of crystalline samples. Therefore, an additional set of optimizations was carried out restricting to 180º the value of the dihedral angle described by the planes Zr_a-Zr_b-C_a and Zr_b-C_a-C_b. Although unrestricted re-optimization always tends to the folded structure, the energetic difference between restricted an unrestricted was very small. In fact, frequency calculations in all restricted and unrestricted structures resulted only in positive values of frequencies. Therefore, the potential energy surface in the region of calculated geometries was very shallow and all structures found, both folded and straight, can be, as a matter of fact, considered as minimums of energy. The geometries relevant to elucidate the crystal structure are the ones that keep the dihedral angle Zr_a-Zr_b-C_a-C_b value at 180º (Structures **C** and **D** in Figure 14c). Therefore, the following structural discussion is focused on such structures.

The main structural feature distinctive of structures **C** and **D** is the interaction that trioxolane cycle establishes with the $\{Zr_6(RCOO)_{12}(OH)_4O_4\}$ cluster. First, in structure **C** two H-bonding interactions can be described with the proton that corresponds to the fragment O-C(H)-O, one with a H···O(benzoate) distance of 2.24 Å and the other one with a H···O(formiate) distance of 2.41 Å. On the other hand, in structure **D** two H-bonding are established with one of the protons in the fragment O-$C(H)_2$-O, which can be discerned by a H···O(benzoate) distance of 2.66 Å and a H···O(formiate) distance of 2.37 Å. Such multiple supramolecular interactions orientate the triozolane cycle fixing two positions of the rotation trough the $C_{(arom)}$-$CH_{(triozolane)}$

bond: one for structure **C** and another one for structure **D**. Such rotation positions, which can be defined by the dihedral angle $C1_{(arom)}$- $C2_{(arom)}$-$C3_{(triozolane)}$-$H_{(triozolane)}$ (Figure 4.15c; 23º for **C** and 162º for **D**), are two plausible conformations that could be found in the crystal structure. In fact, the crystal structure can be interpreted as a mixture of both situations, which can be found randomly in different positions of the structure. In addition, in order to maximize H-bonding interactions, phenyl groups also rotates around the $C_{(carbox)}$- $C_{(arom)}$ bond. This rotation can be described by the dihedral angle $C1_{(arom)}$- $C2_{(arom)}$- $C_{(carboxy)}$-$O_{(carboxy)}$ (29º for **C** and 36º for **D**). This additional rotation, also associated to the interaction between the metallic cluster and the triozolane cycle, adds an additional uncertainty in the location of carbon atoms in of the phenyl group.

Coordinates of optimized geometries

Structure A

Zr	2.117637000	-2.029536000	-0.669704000
Zr	0.345549000	-1.034259000	2.226930000
O	1.002978000	1.138551000	2.149263000
O	0.695081000	-0.833630000	-1.590741000
O	2.035238000	-0.850242000	1.036972000
O	3.462583000	0.602147000	3.062981000
O	-1.131746000	-3.029185000	-1.908859000
O	1.042601000	-3.681357000	-1.740365000
O	4.815873000	-0.161169000	0.853637000
C	-0.154957000	-3.802433000	-2.134241000
O	1.813696000	-0.727437000	3.895514000
C	2.923461000	-0.120400000	3.952315000
C	5.073605000	-1.329890000	0.439828000
O	-0.924640000	0.093493000	3.689201000
O	3.002428000	-2.111347000	-2.729361000
O	1.201638000	-3.057662000	2.675547000
O	2.344377000	-3.697260000	0.814308000
C	2.962134000	-1.306285000	-3.705976000
C	1.954640000	-3.829633000	2.011724000
O	-1.538286000	-2.239035000	2.468574000
O	-2.563248000	-2.243994000	0.437551000
C	-2.492109000	-2.498226000	1.679450000
O	0.108981000	-2.293211000	0.352438000
Zr	-0.466154000	2.041756000	0.670190000
Zr	1.308834000	1.045021000	-2.224474000
O	2.995668000	0.018641000	-1.104337000
O	-0.785644000	-0.004286000	0.826164000
O	1.360766000	1.714024000	-0.259303000
O	-0.795054000	1.162061000	-1.392235000
O	4.162191000	2.328944000	-0.405253000
O	-3.151303000	0.136555000	-0.704445000
O	-2.662543000	2.117700000	0.274237000
O	2.803148000	3.092708000	1.801160000
O	0.627757000	3.742922000	1.639273000
C	-3.479285000	1.238192000	-0.153681000
O	3.130232000	2.339118000	-2.433842000
C	4.012461000	2.708445000	-1.603991000
C	-4.934616000	1.539529000	-0.051127000
C	1.852185000	3.921340000	1.909771000
O	2.481720000	-0.135040000	-3.730583000
O	-1.451336000	2.069104000	2.689361000
O	0.554498000	3.116668000	-2.634023000
O	-0.584912000	3.762271000	-0.772386000
C	-1.522293000	1.207941000	3.614749000
C	-0.085506000	3.944823000	-1.921476000
O	-0.097363000	0.641742000	-3.925079000
O	-1.749143000	-0.679568000	-3.085240000
C	-5.332731000	2.881746000	-0.074087000
C	-5.906831000	0.524375000	0.027716000
C	-7.258651000	0.873693000	0.033452000

C	-7.647584000	2.211079000	-0.019140000
C	-1.142688000	-0.067667000	-4.013130000
C	-6.683270000	3.218495000	-0.064650000
C	-5.531798000	-0.920489000	0.159223000
C	-6.085270000	-2.913743000	-0.747397000
O	-6.490905000	-1.596025000	0.979759000
O	-6.128882000	-2.945267000	0.682929000
O	-5.621043000	-1.616180000	-1.088527000
Zr	2.914056000	1.026535000	0.929748000
Zr	-1.263588000	-1.012293000	-0.925176000
O	4.304099000	-2.126385000	-0.173962000
H	-0.376003000	-4.696291000	-2.733627000
H	3.480192000	-0.221303000	4.893965000
H	6.094466000	-1.691767000	0.623563000
H	3.411726000	-1.662595000	-4.642854000
H	2.300665000	-4.731776000	2.534393000
H	-3.362019000	-3.011758000	2.113331000
H	2.119308000	4.912897000	2.300108000
H	-2.170531000	1.464169000	4.463750000
H	-0.237990000	4.940319000	-2.360701000
H	-4.566231000	3.648129000	-0.107509000
H	-8.000773000	0.086230000	0.101086000
H	-1.585227000	-0.151975000	-5.014974000
H	-6.982041000	4.260499000	-0.093324000
H	-7.080831000	-3.067594000	-1.179590000
H	-5.382373000	-3.695579000	-1.049531000
H	4.746698000	3.437132000	-1.973862000
H	3.853037000	0.023199000	-1.541615000
H	-1.451426000	1.615942000	-1.930534000
H	-0.177577000	-3.201595000	0.490544000
H	1.072811000	1.584295000	2.999372000
H	-8.701773000	2.466113000	-0.015114000
H	-4.538921000	-1.067926000	0.583906000

Structure B

Zr	2.268416000	-1.679988000	1.094066000
Zr	0.886245000	1.428574000	2.070408000
O	1.149089000	2.430796000	0.050365000
O	0.534664000	-1.759881000	-0.035120000
O	2.290467000	0.390197000	0.949247000
O	3.786734000	2.774547000	0.379940000
O	-0.950247000	-3.031494000	2.088473000
O	1.297700000	-3.371238000	2.210882000
O	4.843379000	0.403454000	-0.358870000
C	0.086755000	-3.687937000	2.401561000
O	2.547934000	2.921009000	2.283717000
C	3.535799000	3.204868000	1.543934000
C	5.214843000	-0.565838000	0.366108000
O	-0.281547000	3.345650000	2.119839000
O	2.783973000	-3.545712000	-0.039829000
O	2.133110000	0.721494000	3.797004000
O	3.018509000	-1.280352000	3.172439000
C	2.438062000	-3.968748000	-1.182207000
C	2.872229000	-0.294744000	3.953774000
O	-0.704558000	1.146125000	3.628501000
O	-2.051075000	-0.528981000	2.879569000
C	-1.719704000	0.389935000	3.684647000
O	0.540513000	-0.805500000	2.277141000
Zr	-0.681565000	1.717708000	-1.094982000
Zr	0.703489000	-1.388156000	-2.069558000
O	2.709238000	-1.063403000	-1.046358000
O	-0.619850000	0.829171000	0.780382000
O	0.985436000	0.632785000	-1.686921000
O	-1.218868000	-0.479421000	-1.278064000
O	3.579164000	0.642479000	-2.920903000
O	-3.242190000	-0.270029000	0.487295000
O	-2.865324000	1.530560000	-0.828887000
O	2.514549000	3.012293000	-2.179959000
O	0.267740000	3.358212000	-2.299587000
C	-3.622766000	0.759485000	-0.147469000
O	2.227330000	-1.024869000	-3.678199000
C	3.164934000	-0.181490000	-3.789032000
C	-5.055782000	1.184661000	-0.086355000

C	1.473924000	3.596981000	-2.602622000
O	1.771143000	-3.359937000	-2.069825000
O	-1.316545000	3.525083000	0.099251000
O	-0.434727000	-0.625835000	-3.840523000
O	-1.316544000	1.377329000	-3.218340000
C	-1.069134000	3.884470000	1.288296000
C	-1.070741000	0.449921000	-4.044300000
O	-0.898558000	-2.948382000	-2.244038000
O	-2.097347000	-2.805446000	-0.318689000
C	-5.262942000	2.571130000	-0.035472000
C	-6.171060000	0.324840000	-0.090007000
C	-7.451736000	0.883434000	-0.021080000
C	-7.646097000	2.259358000	0.071729000
C	-1.821853000	-3.299591000	-1.452500000
C	-6.542837000	3.109202000	0.061341000
C	-6.136075000	-1.172973000	-0.174929000
C	-5.011159000	-2.903734000	0.745148000
O	-5.138536000	-1.646608000	-1.074754000
O	-5.095570000	-3.020816000	-0.680283000
O	-5.825661000	-1.787482000	1.074152000
Zr	2.812326000	1.199889000	-0.888838000
Zr	-1.220955000	-1.147078000	0.886577000
O	4.493262000	-1.449293000	0.916151000
H	-0.085222000	-4.643859000	2.915299000
H	4.256278000	3.923704000	1.957640000
H	6.297613000	-0.660288000	0.526459000
H	2.769316000	-4.983881000	-1.440420000
H	3.446849000	-0.332347000	4.889408000
H	-2.385598000	0.540469000	4.545229000
H	1.638776000	4.422665000	-3.308400000
H	-1.593734000	4.784693000	1.638390000
H	-1.467387000	0.590105000	-5.058979000
H	-4.393222000	3.218582000	-0.074674000
H	-8.311538000	0.220047000	-0.043110000
H	-2.466516000	-4.122592000	-1.787695000
H	-6.675551000	4.183978000	0.115497000
H	-3.982750000	-2.729946000	1.072530000
H	-5.418002000	-3.835119000	1.149465000
H	3.694016000	-0.172774000	-4.751797000
H	3.465791000	-1.489936000	-1.460896000
H	-2.031669000	-0.663576000	-1.762910000
H	0.435255000	-1.135831000	3.174909000
H	1.291238000	3.382395000	0.069515000
H	-8.650930000	2.661666000	0.136660000
H	-7.113507000	-1.547529000	-0.514004000

Structure C

Zr	-2.112561000	-1.997286000	0.779765000
Zr	-0.446819000	-1.103788000	-2.212388000
O	-1.083490000	1.077726000	-2.172094000
O	-0.644846000	-0.789701000	1.609858000
O	-2.087093000	-0.869229000	-0.962343000
O	-3.582179000	0.539500000	-2.970826000
O	1.174735000	-2.997035000	1.917555000
O	-1.011485000	-3.628186000	1.856192000
O	-4.852175000	-0.147022000	-0.690274000
C	0.199854000	-3.752445000	2.203979000
O	-1.979533000	-0.830009000	-3.828684000
C	-3.084996000	-0.213598000	-3.859400000
C	-5.103622000	-1.300291000	-0.232056000
O	0.772358000	-0.030890000	-3.756718000
O	-2.916356000	-2.009462000	2.874483000
O	-1.337238000	-3.131115000	-2.567752000
O	-2.411402000	-3.705288000	-0.645260000
C	-2.829143000	-1.175893000	3.823676000
C	-2.070381000	-3.875971000	-1.852615000
O	1.421023000	-2.327746000	-2.490301000
O	2.528546000	-2.285451000	-0.502984000
C	2.404940000	-2.571066000	-1.733054000
O	-0.146493000	-2.312366000	-0.312922000
Zr	0.454649000	2.006429000	-0.779721000
Zr	-1.213726000	1.113248000	2.209376000
O	-2.953813000	0.072161000	1.187901000

O	0.739699000	-0.045810000	-0.885559000
O	-1.337109000	1.727103000	0.231514000
O	0.861000000	1.183589000	1.292725000
O	-4.126025000	2.371870000	0.470247000
O	3.161111000	0.100937000	0.531258000
O	2.673031000	2.057197000	-0.496213000
O	-2.849003000	3.058684000	-1.809074000
O	-0.663504000	3.692418000	-1.748717000
C	3.487930000	1.199212000	-0.026477000
O	-3.011180000	2.432858000	2.453602000
C	-3.923287000	2.786340000	1.649374000
C	4.938778000	1.531548000	-0.038073000
C	-1.895868000	3.874920000	-1.976976000
O	-2.336150000	-0.009940000	3.793784000
O	1.349537000	1.970759000	-2.840330000
O	-0.421079000	3.188783000	2.526220000
O	0.659169000	3.763989000	0.606977000
C	1.377667000	1.081763000	-3.741221000
C	0.202769000	3.987009000	1.767202000
O	0.254682000	0.747939000	3.865789000
O	1.855852000	-0.619977000	3.003126000
C	5.313405000	2.879039000	0.007921000
C	5.926897000	0.528727000	-0.057207000
C	7.271269000	0.896685000	0.021728000
C	7.636471000	2.239878000	0.098966000
C	1.293093000	0.026192000	3.935221000
C	6.657424000	3.234000000	0.084268000
C	5.578363000	-0.922882000	-0.205302000
C	6.120543000	-2.898175000	0.747296000
O	6.592737000	-1.587727000	-0.964766000
O	6.236102000	-2.940593000	-0.677808000
O	5.605602000	-1.609995000	1.050576000
Zr	-2.943198000	1.019173000	-0.875252000
Zr	1.284490000	-1.010316000	0.873579000
O	-4.317354000	-2.086597000	0.373890000
H	0.435965000	-4.632036000	2.818540000
H	-3.679672000	-0.335786000	-4.774973000
H	-6.134239000	-1.657079000	-0.364121000
H	-3.244848000	-1.498607000	4.787989000
H	-2.445068000	-4.789121000	-2.334870000
H	3.252953000	-3.102447000	-2.188412000
H	-2.169459000	4.857983000	-2.384011000
H	1.990678000	1.308572000	-4.624087000
H	0.382619000	4.993211000	2.170274000
H	4.535123000	3.634201000	-0.008524000
H	8.027637000	0.120186000	0.000963000
H	1.771939000	-0.036143000	4.921856000
H	6.939805000	4.279882000	0.131652000
H	7.097110000	-3.021787000	1.229826000
H	5.423664000	-3.694562000	1.023447000
H	-4.634370000	3.534153000	2.026222000
H	-3.793221000	0.099635000	1.657916000
H	1.535346000	1.644308000	1.802098000
H	0.125821000	-3.226988000	-0.437960000
H	-1.183351000	1.501764000	-3.030287000
H	8.685119000	2.509822000	0.160977000
H	4.612985000	-1.088504000	-0.686939000

Structure D

Zr	-2.274336000	-1.771562000	-0.919469000
Zr	-1.001546000	1.290987000	-2.149731000
O	-1.202744000	2.417012000	-0.187533000
O	-0.494717000	-1.744684000	0.137919000
O	-2.337777000	0.303172000	-0.906860000
O	-3.857067000	2.691176000	-0.423230000
O	0.928364000	-3.121502000	-1.971506000
O	-1.314584000	-3.512885000	-1.966856000
O	-4.830944000	0.352172000	0.510903000
C	-0.106621000	-3.816844000	-2.193810000
O	-2.705187000	2.734262000	-2.386006000
C	-3.666088000	3.047617000	-1.623170000
C	-5.211622000	-0.667999000	-0.135477000
O	0.118311000	3.222714000	-2.371100000

O	-2.702952000	-3.569675000	0.350339000
O	-2.300109000	0.450588000	-3.774712000
O	-3.117316000	-1.522020000	-2.985641000
C	-2.301674000	-3.912382000	1.501643000
C	-3.024366000	-0.586677000	-3.833982000
O	0.533790000	0.937772000	-3.750881000
O	1.948774000	-0.655463000	-2.950599000
C	1.564067000	0.202437000	-3.798690000
O	-0.615371000	-0.943682000	-2.228133000
Zr	0.690563000	1.814948000	0.918002000
Zr	-0.587310000	-1.246782000	2.149835000
O	-2.639410000	-1.026849000	1.194443000
O	0.565698000	0.802035000	-0.888098000
O	-0.925893000	0.739126000	1.651543000
O	1.286836000	-0.357001000	1.219988000
O	-3.464241000	0.778498000	2.995105000
O	3.242565000	-0.226989000	-0.632261000
O	2.856802000	1.660454000	0.551256000
O	-2.486010000	3.115322000	2.058871000
O	-0.243860000	3.508848000	2.060418000
C	3.623432000	0.829899000	-0.045638000
O	-2.048909000	-0.813819000	3.796409000
C	-2.998153000	0.018372000	3.894295000
C	5.073807000	1.203323000	-0.018612000
C	-1.441054000	3.744497000	2.398939000
O	-1.611839000	-3.236143000	2.319936000
O	1.225651000	3.560188000	-0.409972000
O	0.607063000	-0.344532000	3.817338000
O	1.429557000	1.624325000	3.027152000
C	0.922311000	3.834897000	-1.608252000
C	1.232378000	0.751255000	3.922615000
O	1.051706000	-2.758758000	2.362137000
O	2.142862000	-2.738571000	0.369834000
C	5.330225000	2.581602000	-0.085993000
C	6.159768000	0.312435000	0.087894000
C	7.458447000	0.833168000	0.108652000
C	7.703116000	2.199789000	0.004301000
C	1.937721000	-3.154369000	1.548532000
C	6.629061000	3.080782000	-0.092265000
C	6.083228000	-1.181965000	0.189680000
C	4.984294000	-2.912478000	-0.756807000
O	5.035517000	-1.627150000	1.046825000
O	5.002418000	-3.007574000	0.672291000
O	5.818560000	-1.805007000	-1.064999000
Zr	-2.796872000	1.218723000	0.898315000
Zr	1.210335000	-1.163329000	-0.893418000
O	-4.495131000	-1.570629000	-0.660315000
H	0.063441000	-4.799826000	-2.654484000
H	-4.419619000	3.723328000	-2.050565000
H	-6.297949000	-0.792800000	-0.242146000
H	-2.600877000	-4.914863000	1.836997000
H	-3.636858000	-0.695004000	-4.739587000
H	2.193020000	0.311601000	-4.692694000
H	-1.593751000	4.610401000	3.057757000
H	1.406543000	4.723844000	-2.036305000
H	1.667020000	0.965138000	4.908530000
H	4.481666000	3.255677000	-0.132038000
H	8.293198000	0.145677000	0.209442000
H	2.614029000	-3.941951000	1.904787000
H	6.797684000	4.149680000	-0.160630000
H	3.974046000	-2.735863000	-1.134804000
H	5.402747000	-3.852545000	-1.127615000
H	-3.486871000	0.078204000	4.876393000
H	-3.370673000	-1.438802000	1.665353000
H	2.114690000	-0.504351000	1.691988000
H	-0.539870000	-1.327626000	-3.107348000
H	-1.367879000	3.362230000	-0.261273000
H	8.722061000	2.570501000	0.010928000
H	7.033829000	-1.574066000	0.580762000

4.3.2. Synthetic methodologies

Synthesis of bulk ZrEBDC. Bulk ZrEBDC was prepared using an adapted version of a standard solvothermal synthesis.[61] $ZrOCl_2 \cdot 8H_2O$ (2.5 g, 7.8 mmol) was added into a solvent mixture of DMF/formic acid (40 mL/15 mL) in a 100-mL screw-capped jar and sonicated for 15 min. 2-ethenylbenzene-1,4-dicarboxylic acid (H_2EBDC) 1.5 g (7.8 mmol) was added to the solution, which was further sonicated for 15 min. The jar was then transferred to a preheated oven and kept at 120 °C for 12 hours. A white crystalline material was collected and was washed three times with 50 mL of fresh DMF. The bulk particles were rinsed in 150 mL of acetone, which was replaced twice every 12 h. Finally, the solid powder was activated at 120 °C under vacuum for 12 h. (Yield: 2.2 g; 92% based on $ZrOCl_2 \cdot 8H_2O$). Elemental Analysis: Exp. C 32.77%, H 2.40%; Cal. C 32.61%, H 1.77%.

Synthesis of single crystals of ZrEBDC suitable for SCXRD. In a 100 mL Erlenmeyer flask, 240 mg (1.35 mmol) of $ZrOCl_2 \cdot 8H_2O$ and 250 mg (1.30 mmol) of H_2EBDC were dissolved in DEF (40 mL) under sonication. The resulting solution was divided into 20 scintillation vials, to each of which was added formic acid (2 mL). The samples were vortexed to homogenization and placed in an oven before being slowly heated to 135 °C (heating rate: 5 °C /min) for 72 h. Colourless octahedral crystals of ZrEBDC were harvested from the bottom and walls of the vials and treated as the bulk sample. (Yield: 110 mg; 20%).

Solid-gas phase ozonolysis procedure. Activated bulk ZrEBDC (50 mg) was grinded to homogenous powder and mixed with single-crystal ZrEBDC, and the resulting mixture was packed inside of a Pyrex tube stoppered by cotton pellets at both ends. The tube was then bent into a U-shape. A 0.1 M solution of KI was added at the end of the setup to provide a colour-based indicator of ozonolysis progression (from colourless to yellow). Before solid-gas ozonolysis, the sample was vacuumed for 10 min to remove all the residual moisture/solvents. Then, ozone (dried through $CaCl_2$) was steamed into the setup until a deep yellow colour in the KI trap indicated full conversion (ca. 30 min). The bulk column was kept under vacuum for a further 10 min to remove all the unreacted ozone.

Study of the degree of functionalization versus ozonolysis Time. For this study, we systematically studied the ozonolysis using various reaction times (5 min, 10 min, 15 min and 30 min). To this end, the degree of functionalization was monitored by recording the ^{1}H NMR spectra of the digested samples (5% HF/DMSO-d_6), and then compared each one to that of the starting ZrEBDC (see Figure 4.7). The digestion was done by adding 120 µL 5% HF in D_2O to 20 mg of dry ZrEBDC or ozo-ZrBDC powder in a 2 mL Eppendorf tube. The resulting mixture was sonicated for 5 min to afford a slurry, which was treated with 0.5 mL DMSO-d_6 and finally, sonicated for 5 more minutes. The ^{1}H NMR spectrum of the digested ZrEBDC showed the

characteristic peaks of three non-equivalent olefinic protons at δ = 7.29 ppm, δ = 5.77 ppm and δ = 5.41 ppm, integrating in a 1:1:1 ratio (see Figure 4.7, blue spectrum). In contrast, the spectrum of the fully converted ozo-ZrBDC confirmed a quantitative fading of all the olefinic signals in approximately 30 min of solid-gas interaction, together with the appearance of new signals, including two peaks of interest, at δ = 6.70 ppm and δ = 4.58 ppm (see Figure 4.7; red spectrum). These latter signals do not fall within the typical range of chemical shifts for the expected trioxolane moiety,[38,62] nor their relative integration matches the expected 1:2 ratio for the CH and CH_2 protons in the five-membered ring. Due to the instability of trioxolane moiety under aggressive digestion conditions, the fully ozonized linker trioxolane-BDC was subjected to two different degradation pathways. To fully identify these species, the digested ozo-ZrBDC sample was further analysed by 1D-NMR and 2D-NMR (NOESY, DOSY, DEPT135, HSQC and HMBC; see Figures 4.8 - 4.13). After an in-depth analysis of the digested product, four different entities were properly identified in the mixture (see Scheme 4.1 in Section 4.2.3). First, the two, symmetric cross-ozonation products of the target trioxolane-BDC were properly identified (A' and A''). Second, both products of the acid-induced hydrolysis of the initial trioxolane were identified (B and C). Finally, the degree of conversion of the olefinic groups into 1,2,4-trioxolane rings was calculated by comparing the combined integration of two peaks, one at 7.73 ppm (corresponding to H3 of 1,2,4-benzenetricarboxylate) and one at 6.70 ppm (corresponding to H2 of the trioxolane-metathesis product A'), versus the olefinic peak at 5.77 ppm (corresponding to EBCD).

Soft ligand-exchange experiment. ozo-ZrBDC was immersed in a 0.2 M solution of 1,4-benzenedicarboxylic acid in DMF for one week. Afterwards, the supernatant was separated from the crystals by centrifugation and subsequently dried, and the resulting solid was dissolved in deuterated DMSO and analysed by ^{1}H NMR.

Reduction and oxidation work up of ozo-ZrBDC. Fully-converted ozo-ZrBDC (80 mg) was soaked in Me_2S (5% in 0.1M HCl/acetone) and H_2O_2 (10% aqueous solution) and kept under stirring for 12 h.

4.3.3. Single-Crystal XRD analysis

Table 4.1. Crystal and structural refinement data for ZrEBDC, ozo-ZrBDC, ZrBDC-COOH.

Compound	**ZrEBDC**	**ozo-ZrBDC[a]**	**ozo-ZrBDC[b]**	**ZrBDC-COOH**
Empirical formula	$C_{60}O_{40}Zr_6$	$C_{40.8}O_{35}Zr_6$	$C_{44}O_{44.5}H_{4.6}Zr_6$	$Zr_6C_{45.6}O_{48}$
Formula weight	1907.92	1632.27	1792.40	1819.78
Crystal system	Cubic	Cubic	Monoclinic	Cubic
Space group	*Fm-3m*	*Fm-3m*	*C2*	*Fm-3m*
CCDC reference	1589286	1589288	1589287	1589289
Unit cell dimensions				
a (Å)	20.740(4)	20.720(2)	20.747(4)	20.740(4)
b (Å)	20.740(4)	20.720(2)	20.747(4)	20.740(4)
c (Å)	20.740(4)	20.720(2)	14.670(3)	20.740(4)
β (°)			135.00(3)	
v ($Å^3$)	8921.3(1)	8895.0(3)	4465(2)	8921.3(1)
Z	4	4	2	4
F(000)	6272	3155	1729.0	3533
θ range (°)	2.778 – 26.670	2.97 - 72.29	2.97 - 72.29	1.978 - 33.814
Tot., Uniq.Data, R(int)	28302, 513, 0.121	68423, 1636, 0.1208	68694, 27598, 0.1047	29683, 632, 0.058
Final R indices [I/ sigma(I)>2]	R1 = 0.1012 wR2 = 0.2626	R1 = 0.0379 wR2 = 0.1129	R1 = 0.0616 wR2 = 0.1620	R1 = 0.0339 wR2 = 0.1482
Min. and Max. Resd. Dens. [e/$Å^3$]	-3.05, 1.34	-0.5, 1.29	-0.84, 3.19	-0.38, 1.24
GOF	1.243	1.137	1.1015	1.449

a: Data corresponding to refinement not including disorder model for the oxonale groups. Residual electron density in the cavities was accounted with the Platon Squeeze program. Details are copied below.

b: Data corresponding to refinement carried out with a monoclinic cell in order to reduce the number of symmetry equivalent positions of the organic linkers. Note that due to the large correlation of the artificially generated independent positions of the framework atoms, a number of these were isotropically refined, also resulting in higher Rvalues.

4.3.4. Squeeze details of ozo-ZrBDC:

Summary and Remarks: N = NOTE, W = WARNING, E = ERROR

N: Maximum Residue Number Reduced (Round ARU to 0.1 units)
N: No S.U.'s (esd) on observed/calculated parameters.
N: Maximum allowed number of residues reduced
N: DISORDERED structure - ATOMS with Pop. .LT. 1.0 are not moved or as a group.
N: No-Hydrogen atoms in this structure

N: Number of moved primary input atoms: 9
W: Number of (Carbon) Atoms with no sp(x) assignment 1
N: Number of Ignored Lines on INPUT 4
of which blank in column 1 4
N: Number of modified (= #) ATOM labels 2
W: Number of unusual anisotropic displacement parameters 1
N: Total Potential Solvent Accessible Void Vol (SOLV-Map Value) ….. 3466 Ang^3
N: Electron Count Voids / Cell = 657

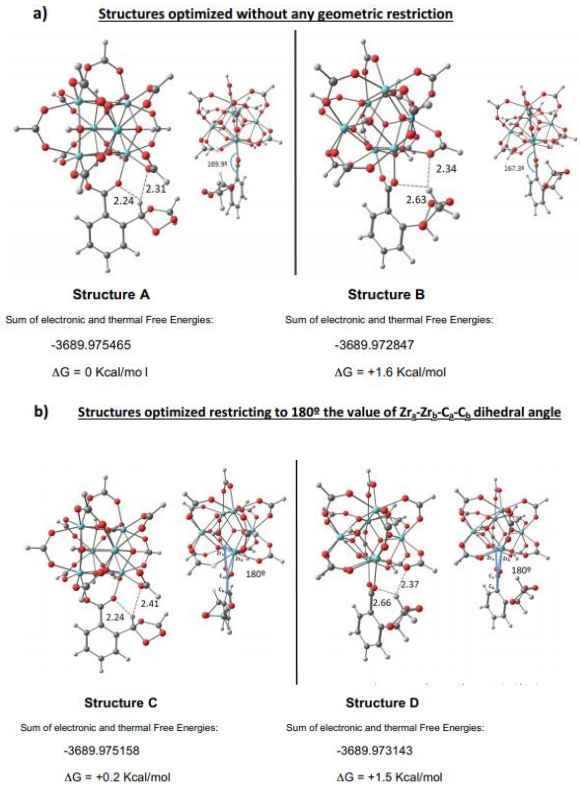

Figure 4.17. (a) Structures A and B: Optimized geometries of model fragment without using any geometric restriction. (b) Structures C and D: Optimized geometries of model fragment fixing to 180º the value of Zr_a-Zr_b-C_a-C_b dihedral angle.

4.3.5. BET measurements

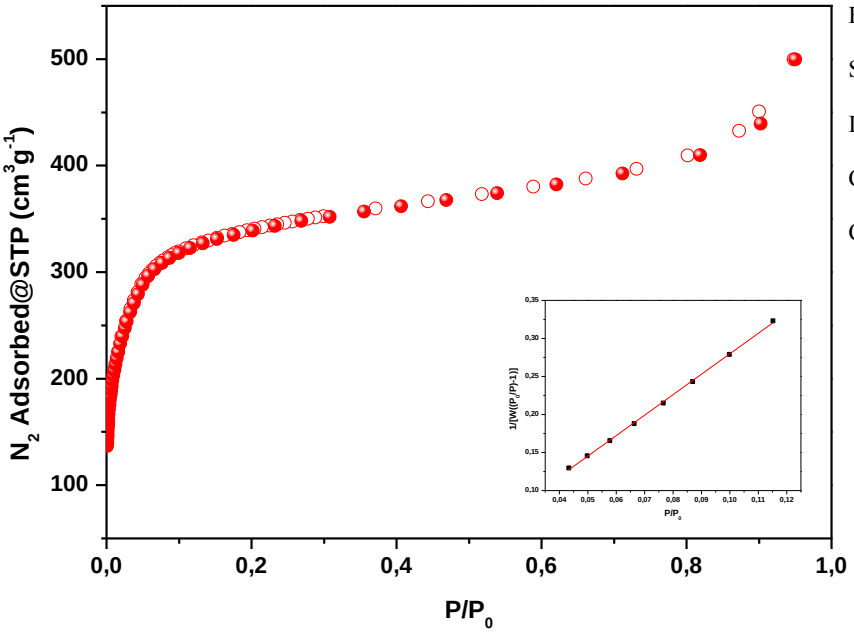

BET surface area: 1298 m²/g

Slope: 2.96 g/cm³ STP

Intercept: 0.0108 g/cm³ STP

Correlation coefficient: r = 0.9996

C constant: 248

Figure 4.18. N_2 adsorption isotherm and BET liner fit for **ZrEBDC**.

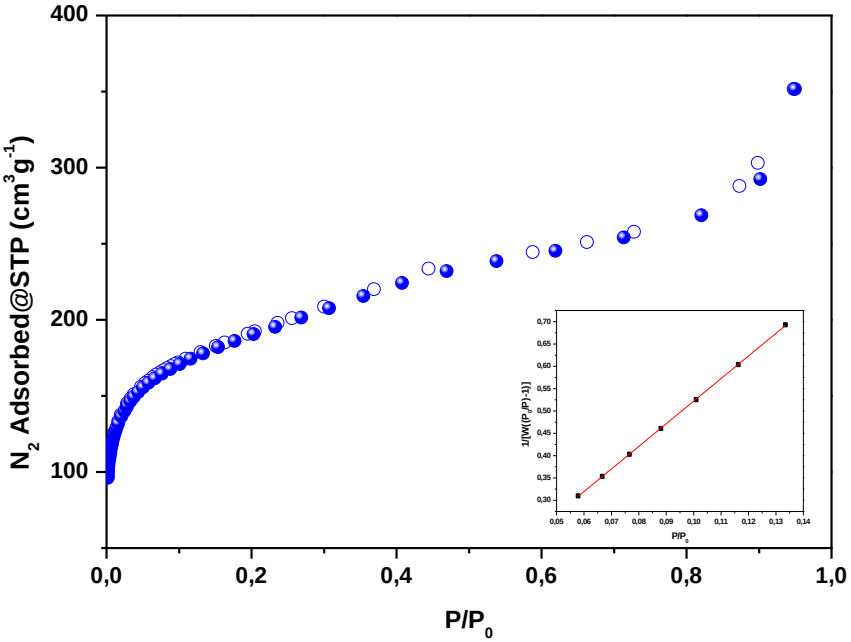

BET surface area: 685 m²/g

Slope: 5.06 g/cm³ STP

Intercept: 0.0159 g/cm³ STP

Correlation coefficient: r = 0.99997

C constant: 318

Figure 4.19. N_2 adsorption isotherm and BET liner fit for **ozo-ZrBDC**.

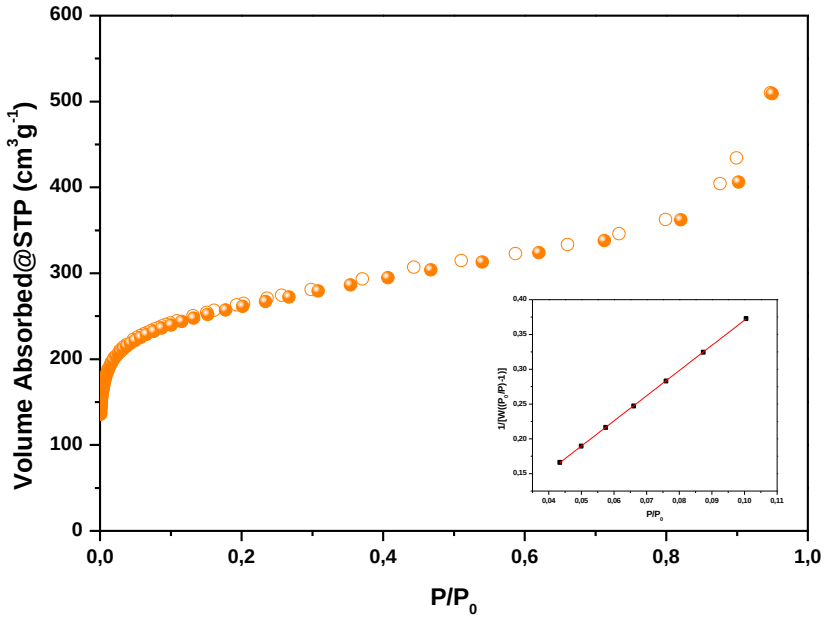

BET surface area: 960 m²/g

Slope: 3.617 g/cm³ STP

Intercept: 0.00886 g/cm³ STP

Correlation coefficient: r = 0.99999

C constant: 409

Figure 4.20. N_2 adsorption isotherm and BET liner fit for **ozo-ZrBDC** partially functionalized with **CHO** groups.

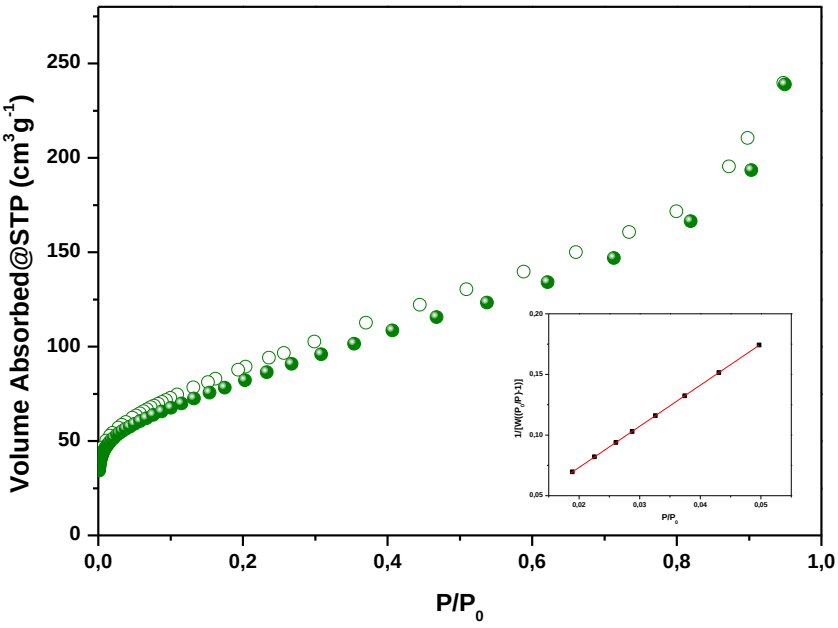

BET surface area: 301 m²/g

Slope: 3.34 g/cm³ STP

Intercept: 0.0054 g/cm³ STP

Correlation coefficient: r = 0.9996

C constant: 622

Figure 4.21. N_2 adsorption isotherm and BET liner fit of **ZrBDC-COOH**.

4.4. References

(1) Wang, Z.; Cohen, S. M. *Chem. Soc. Rev.* **2009**, *38* (5), 1315.

(2) Burrows, A. D.; Cohen, S. M. *CrystEngComm* **2012**, *14* (12), 4095.

(3) Cohen, S. M. *Chem. Rev.* **2012**, *112* (2), 970.

(4) Luo, F.; Wang, M.-S.; Luo, M.-B.; Sun, G.-M.; Song, Y.-M.; Li, P.-X.; Guo, G.-C. *Chem. Commun.* **2012**, *48* (48), 5989.

(5) Morris, W.; Doonan, C. J.; Furukawa, H.; Banerjee, R.; Yaghi, O. M. *J. Am. Chem. Soc.* **2008**, *130* (38), 12626.

(6) Kim, M.; Cahill, J. F.; Prather, K. A.; Cohen, S. M. *Chem. Commun.* **2011**, *47* (27), 7629.

(7) Kim, M.; Cahill, J. F.; Su, Y.; Prather, K. A.; Cohen, S. M. *Chem. Sci.* **2012**, *3* (1), 126.

(8) Liu, C.; Zeng, C.; Luo, T.-Y.; Merg, A. D.; Jin, R.; Rosi, N. L. *J. Am. Chem. Soc.* **2016**, *138* (37), 12045.

(9) Boissonnault, J. A.; Wong-Foy, A. G.; Matzger, A. J. *J. Am. Chem. Soc.* **2017**, *139* (42), 14841.

(10) Bloch, W. M.; Burgun, A.; Coghlan, C. J.; Lee, R.; Coote, M. L.; Doonan, C. J.; Sumby, C. J. *Nat. Chem.* **2014**, *6* (10), 906.

(11) Manna, K.; Zhang, T.; Lin, W. *J. Am. Chem. Soc.* **2014**, *136* (18), 6566.

(12) Wang, Z.; Tanabe, K.; Cohen, S. *Chem. - A Eur. J.* **2010**, *16* (1), 212.

(13) Layer, R. W.; Lattimer, R. P. *Rubber Chem. Technol.* **1990**, *63* (3), 426.

(14) Miki, N.; Maeno, M.; Maruhashi, K.; Nakagawa, Y.; Ohmi, T. *Corros. Sci.* **1990**, *31*, 69.

(15) Harshé, G. *J. Mater. Eng. Perform.* **1992**, *1* (1), 83.

(16) Servalli, M.; Ranocchiari, M.; Van Bokhoven, J. A. *Chem. Commun.* **2012**, *48* (13), 1904.

(17) Criegee, R. *Angew. Chemie Int. Ed. English* **1975**, *14* (11), 745.

(18) Cochran, B. *Synlett* **2015**, *27* (2), 245.

(19) Schiaffo, C. E.; Dussault, P. H. *J. Org. Chem.* **2008**, *73* (12), 4688.

(20) Geletneky, C.; Berger, S. *European J. Org. Chem.* **1998**, *1998* (8), 1625.

(21) Travagli, V.; Zanardi, I.; Valacchi, G.; Bocci, V. *Mediators Inflamm.* **2010**, *2010*, 610418.

(22) Willand-Charnley, R.; Fisher, T. J.; Johnson, B. M.; Dussault, P. H. *Org. Lett.* **2012**, *14* (9), 2242.

(23) Hallen, M. A.; Hallen, H. D. *J. Phys. Chem. C* **2008**, *112*, 2086.

(24) Cavka, J. H.; Jakobsen, S.; Olsbye, U.; Guillou, N.; Lamberti, C.; Bordiga, S.; Lillerud, K. P. *J. Am. Chem. Soc.* **2008**, *130* (42), 13850.

(25) Yang, J.; Zhao, Q.; Li, J.; Dong, J. *Microporous Mesoporous Mater.* **2010**, *130* (1–3), 174.

(26) Reinsch, H.; van der Veen, M. A.; Gil, B.; Marszalek, B.; Verbiest, T.; de Vos, D.; Stock, N. *Chem. Mater.* **2013**, *25* (1), 17.

(27) Nathaniel L. Rosi, †; Jaheon Kim, †,§; Mohamed Eddaoudi, †,∥; Banglin Chen, †,⊥; Michael O'Keeffe, *,‡ and; Omar M. Yaghi*, †. **2005**.

(28) Kandiah, M.; Nilsen, M. H.; Usseglio, S.; Jakobsen, S.; Olsbye, U.; Tilset, M.; Larabi, C.; Quadrelli,

E. A.; Bonino, F.; Lillerud, K. P. *Chem. Mater.* **2010**, *22* (24), 6632.

(29) Piscopo, C. G.; Polyzoidis, A.; Schwarzer, M.; Loebbecke, S. *Microporous Mesoporous Mater.* **2015**, *208*, 30.

(30) Wang, H.-L.; Yeh, H.; Chen, Y.-C.; Lai, Y.-C.; Lin, C.-Y.; Lu, K.-Y.; Ho, R.-M.; Li, B.-H.; Lin, C.-H.; Tsai, D.-H. *ACS Appl. Mater. Interfaces* **2018**, *10* (11), 9332.

(31) Rhoads, C. M.; Farquar, G. R.; Wood, W. F. *J. Chem. Educ.* **1997**, *74* (10), 1220.

(32) Branan, B. M.; Butcher, J. T.; Olsen, L. R. *J. Chem. Educ.* **2007**, *84* (12), 1979.

(33) Wang, H.; Rassu, P.; Wang, X.; Li, H.; Wang, X.; Wang, X.; Feng, X.; Yin, A.; Li, P.; Jin, X.; Chen, S.-L.; Ma, X.; Wang, B. *Angew. Chemie Int. Ed.* **2018**, *57* (50), 16416.

(34) Bouas-laurent, H.; Desvergne, J. P.; Lapouyade, R.; Thomas, J. M. *Mol. Cryst. Liq. Cryst.* **1976**, *32* (1), 143.

(35) Sander, W.; Träubel, M.; Komnick, P. In *Chemical Processes in Atmospheric Oxidation*; Springer Berlin Heidelberg: Berlin, Heidelberg, 1997; pp 200–207.

(36) Byers, D. H.; Saltzman, B. E. *Adv. Chem.* **1959**, *21*, 93.

(37) Wu, X. L.; Zilm, K. W. *J. Magn. Reson. Ser. A* **1993**, *102* (2), 205.

(38) Sega, A.; Zanardi, I.; Chiasserini, L.; Gabbrielli, A.; Bocci, V.; Travagli, V. *Chem. Phys. Lipids* **2010**, *163* (2), 148.

(39) Soriano, N. U.; Migo, V. P.; Matsumura, M. *J. Am. Oil Chem. Soc.* **2003**, *80* (10), 997.

(40) Taddei, M.; Wakeham, R. J.; Koutsianos, A.; Andreoli, E.; Barron, A. R. *Angew. Chemie Int. Ed.* **2018**, *57* (36), 11706.

(41) Liang, J.; Chen, R.-P.; Wang, X.-Y.; Liu, T.-T.; Wang, X.-S.; Huang, Y.-B.; Cao, R. *Chem. Sci.* **2017**, *8* (2), 1570.

(42) Trickett, C. A.; Gagnon, K. J.; Lee, S.; Gándara, F.; Bürgi, H.-B.; Yaghi, O. M. *Angew. Chemie Int. Ed.* **2015**, *54* (38), 11162.

(43) Spek, A. L. *Acta Crystallogr. Sect. C, Struct. Chem.* **2015**, *71* (Pt 1), 9.

(44) Ragon, F.; Campo, B.; Yang, Q.; Martineau, C.; Wiersum, A. D.; Lago, A.; Guillerm, V.; Hemsley, C.; Eubank, J. F.; Vishnuvarthan, M.; Taulelle, F.; Horcajada, P.; Vimont, A.; Llewellyn, P. L.; Daturi, M.; Devautour-Vinot, S.; Maurin, G.; Serre, C.; Devic, T.; Clet, G. *J. Mater. Chem. A* **2015**, *3* (7), 3294.

(45) Fung, B. M.; Khitrin, A. K.; Ermolaev, K. *J. Magn. Reson.* **2000**, *142* (1), 97.

(46) Juanhuix, J.; Gil-Ortiz, F.; Cuní, G.; Colldelram, C.; Nicolás, J.; Lidón, J.; Boter, E.; Ruget, C.; Ferrer, S.; Benach, J.; IUCr. *J. Synchrotron Radiat.* **2014**, *21* (4), 679.

(47) Kissel, L. *Acta Cryst. Sec.A* **1990**, *46*, 170.

(48) Sheldrick, G. M. *Acta Cryst.* **2015**, *C71*, 3.

(49) Sheldrick, G. M.; IUCr. *Acta Crystallogr. Sect. C Struct. Chem.* **2015**, *71* (1), 3.

(50) Allan, D. .; Nowell, H.; Barnett, S.; Warren, M.; Wilcox, A.; Christensen, J.; Saunders, L.; Peach, A.; Hooper, M.; Zaja, L.; Patel, S.; Cahill, L.; Marshall, R.; Trimnell, S.; Foster, A.; Bates, T.; Lay, S.; Williams, M.; Hathaway, P.; Winter, G.; Gerstel, M.; Wooley, R. *Crystals* **2017**, *7* (11), 336.

(51) Winter, G.; IUCr. *J. Appl. Crystallogr.* **2010**, *43* (1), 186.

(52) Zhao, Y.; Truhlar, D. G. *Theor. Chem. Acc.* **2008**, *120* (1–3), 215.

(53) Wheeler, S. E.; Houk, K. N. *J. Chem. Theory Comput.* **2010**, *6* (2), 395.

(54) Cramer, C. J.; Truhlar, D. G. *Phys. Chem. Chem. Phys.* **2009**, *11* (46), 10757.

(55) Zhao, Y.; Truhlar, D. G. *Acc. Chem. Res.* **2008**, *41* (2), 157.

(56) Zhao, Y.; Truhlar, D. G. *Chem. Phys. Lett.* **2011**, *502* (1–3), 1.

(57) Andrae, D.; Häußermann, U.; Dolg, M.; Stoll, H.; Preuß, H. *Theor. Chim. Acta* **1990**, *77* (2), 123.

(58) Ehlers, A. W.; Böhme, M.; Dapprich, S.; Gobbi, A.; Höllwarth, A.; Jonas, V.; Köhler, K. F.; Stegmann, R.; Veldkamp, A.; Frenking, G. *Chem. Phys. Lett.* **1993**, *208* (1–2), 111.

(59) Hehre, W. J.; Ditchfield, R.; Pople, J. A. *J. Chem. Phys.* **1972**, *56* (5), 2257.

(60) Francl, M. M.; Pietro, W. J.; Hehre, W. J.; Binkley, J. S.; Gordon, M. S.; DeFrees, D. J.; Pople, J. A. *J. Chem. Phys.* **1982**, *77* (7), 3654.

(61) Furukawa, H.; Gándara, F.; Zhang, Y.-B.; Jiang, J.; Queen, W. L.; Hudson, M. R.; Yaghi, O. M. *J. Am. Chem. Soc.* **2014**, *136* (11), 4369.

(62) Soriano, N. U.; Migo, V. P.; Matsumura, M. *Chem. Phys. Lipids* **2003**, *126* (2), 133.

Chapter 5

Postsynthetic covalent and coordination functionalisation of Rhodium(II)-based Metal–Organic Polyhedra

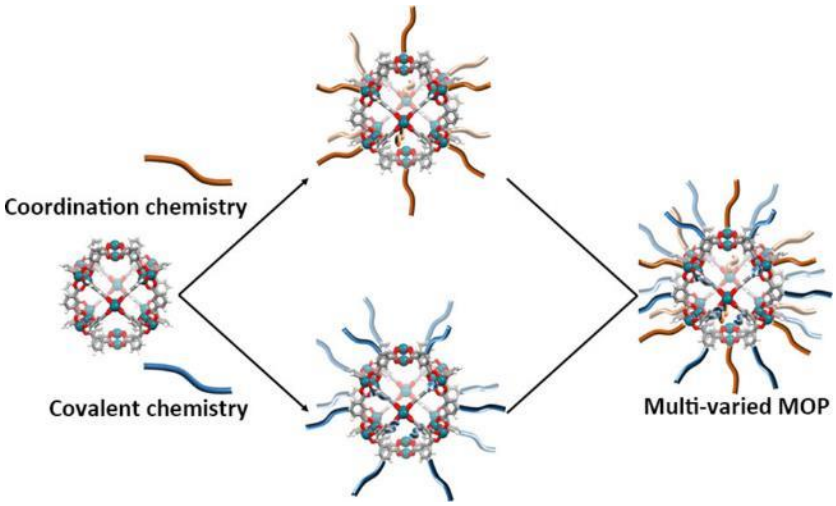

Abstract

This Chapter reports the use of coordination and covalent chemistries to post-synthetically functionalize the external surface of Rh(II)-based cuboctahedral MOPs through their Rh−Rh paddlewheel units or organic linkers, respectively. Specifically, up to 12 N-donor ligands can be coordinated on the periphery of Rh-MOPs, and all 24 organic linkers can be post-synthetically functionalised with esters via covalent chemistry. Both post-synthetic reactions can be synergistically combined to yield doubly functionalized Rh-MOPs, which allowed the modulation of their solubility in a wide range of solvents. Both pathways can potentially be used to engineer Rh-MOPs as scaffolds for applications in delivery, sorption, and catalysis.

This Chapter is based on the following publication:

5.1. Introduction

Ultrasmall inorganic nanoparticles are important because they fill the gap between the molecular and the nanoscale regimes.[1] On this scale, nanoparticles can merge properties of both regimes, such as solubility in different media with high reactivity and unique physicochemical and pharmacokinetic properties.[2–6] Constructed from the self-assembly of metal ions and organic linkers, metal−organic polyhedra (MOPs) fall into this size scale,[7] and as a subclass of molecular cages that can host molecules in solution,[8–11] they are permanently porous in the solid state.[12–16] An archetypical MOP is the cuboctahedron $[M_2(m\text{BDC})_2]_{12}$ (where M = Cu(II), Cr(II), Mo(II), Rh(II), Ru(II), or even heterometallic and *m*BDC =1,3-benzenedicarboxylate), which is ∼2.5 nm in size.[17–21] It is assembled from 12 M(II)−M(II) paddlewheel subunits connected through 24 *m*BDC linkers and has an internal cavity of 1.9 nm that is accessible from eight triangular apertures of 8 Å and six square apertures of 12 Å (Figure 5.1). Practical applications of ultrasmall inorganic nanoparticles demand chemical functionalization of their external surface,[22] as it enables their stabilization and protection, tuning of their hydrophilic/hydrophobic character, and introduction of new functional molecules into them (*e.g.*, to modulate interactions between the nanoparticles and biosystems).[3,23] The latter case is essential for biomedical applications of nanoparticles.[24] As ultrasmall inorganic nanoparticles and MOPs are similarly sized, we reasoned that post-synthetic chemical functionalization of the external surface of MOPs should analogously be crucial for tuning their own properties (*e.g.*, solubility, porosity, etc.) and behaviour in various solution- phase (*e.g.*, delivery systems, adsorbents, catalysis) or solid state (*e.g.*, gas sorption) applications, as well as defining their solubility in diverse solvents. However, to date, post-synthetic functionalization of MOPs has been limited to reactions run under soft conditions,[25,26] such as click chemistry based on strain-promoted azide−alkyne cycloaddition,[27] synthesis of secondary amines or amides from amino-functionalized MOPs,[28–30] or polymerizations based on reverse addition − fragmentation transfer (RAFT) on MOPs functionalized with dithiobenzoate trithioester groups.[31] This is mainly due to the use of chemically unstable MOPs made of highly labile Cu(II)−carboxylate coordination bonds.

This Chapter will focus on a spatially and stoichiometrically controlled post-synthetic modification (PSM) of MOPs via two different site-specific chemistries: coordination chemistry on the metal ions and covalent chemistry on the organic linkers. We selected two robust cuboctahedral Rh(II)-based MOPs: $[Rh_2(m\text{BDC})_2(H_2O)_2]_{12}$ (hereafter named HRhMOP) and $[Rh_2(\text{OH-}m\text{BDC})_2(H_2O)_1(\text{DMA})_1]_{12}$ (hereafter named OHRhMOP; where OH-*m*BDC = 5-hydroxy-1,3-benzenedicarboxylate and DMA = N,N-dimethylacetamide). We chose them for their high microporosity (the BET surface area [S_{BET}] of HRhMOP is 947 m^2/g and that of OHRhMOP is 548 m^2/g) and for their chemical robustness, as they can withstand aggressive reaction conditions, including high temperatures and the presence of strong bases and/or

coordinating molecules. Moreover, these MOPs have two distinct reaction sites (Figure 5.1): their 12 Rh−Rh paddlewheels, each of which has an exohedral axial site that can undergo ligand-exchange reactions, and their 24 organic ligands, which can bear exohedral reactive functional groups (in this case, hydroxyl groups) to enable functionalization of the metal−organic cuboctahedron via covalent chemistry. We have demonstrated spatial control of these modifications by functionalizing both HRhMOP and OHRhMOP with different N-donor ligands (*i.e.* pyridine-, amine-, imidazole-derivatives) and by using the hydroxyl groups of the OH-RhMOP as nucleophiles for synthesis of esters and ethers. Additionally, these two chemistries can be run sequentially or even simultaneously on a single MOP to yield multivariate RhMOPs functionalized with a total of 36 molecules/groups. With this approach, we demonstrate that chemical transformations can be performed on a nanoscale object while preserving all the distinctive features of molecular chemistry, such as the presence of well-defined reactive sites that can be reacted stoichiometrically and characterized at the molecular level by spectroscopic and crystallographic techniques.

5.2. Results and Discussion

5.2.1. Rh(II)-based MOPs – Nanoscaled platforms with well-defined reactive centers

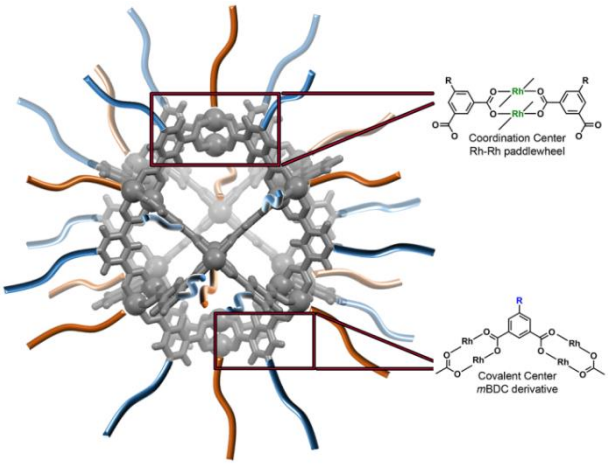

Figure 5.1. Illustration of the crystalline structure of a Rh-based cuboctahedral MOP. Both the coordination- and covalent reactive centers are highlighted.

Metal-Organic Polyhedra (MOPs) are neutrally-charged nanoscopic architectures assembled from metallic ions and bended organic linkers.[32] The obtained zero-dimensional scaffolds (depicted in Figure 5.1) present intrinsic microporosity therein, readily accessible in the solid state. For this reason, MOPs have been used in several application fields such as catalysis,[33] molecular sensing,[34] gas adsorption-separation,[35] drug delivery, [36] or as porous building blocks in the assembly of tridimensional architectures.[37]

Rhodium(II)-based MOPs have been on the spotlight in the last years due to their chemical robustness (relative to their Cu(II) and Pd(II)-based counterparts) and the readily-accessible Rhodium(II) open metal sites (OMS).[38,39] Very recently, RhMOPs have been reported as highly stable potential adsorbents of CO_2 or N_2, and present strong selectivity towards hazardous gases (CO, NO). Representative RhMOPs include

one with a lantern-type (or "super-paddlewheel") structure[34] and one with a cuboctahedron-type structure.[39] The cuboctahedron MOP, assembled from 12 Rh-Rh paddlewheels with 24 *m*BDC linkers, has a molecular formula of $[Rh_2(mBDC)_2]_{12}$, a diameter of 2.5 nm and an accessible internal cavity with a diameter of 1.9 nm (Figure 5.1). Its structure offers two types of windows to the cavity: eight triangular apertures of 8 Å and six square apertures of 12 Å. Still, beyond their strong affinity towards CO and NO adsorption, their practical application is somewhat limited due to the poor processability of the available RhMOPs catalogue (HRhMOP and OHRhMOP). Both HRhMOP and OHRhMOP are synthesised as microcrystalline powder and, despite their molecular behaviour, present almost no solubility in a majority of solvents, thus hindering their potential. However, these cuboctahedral architectures present very interesting features when focusing on their molecular behaviour. Unlike inorganic nanoparticles (INPs)[40] or polymeric nanoparticles (PNPs),[41] which surface is inherently polydisperse, MOPs present a well-defined chemical surface, with symmetrically oriented functional groups and metallic centers. Such limited functionalization, directly evidenced by the amount of linkers forming the scaffold, allows the calculation of a degree of functionalisation by common spectroscopic techniques (NMR, UV-Vis, and ESI-MS/MALDI-TOF) and single-crystal elucidation.

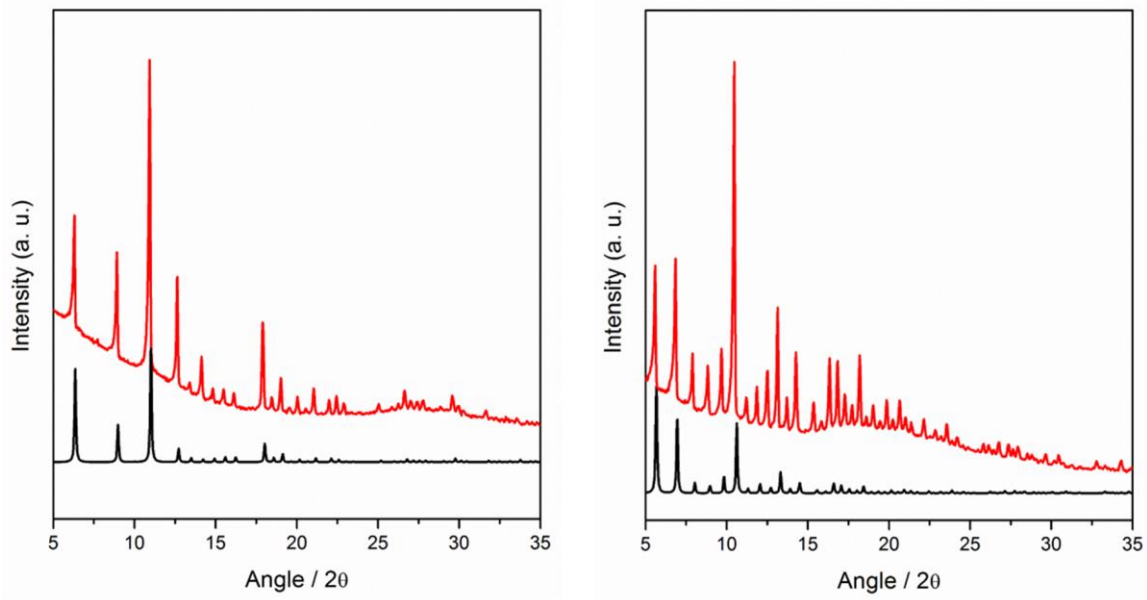

Figure 5.2. Experimental (red) and simulated (black) PXRD of HRhMOP (left) and OHRhMOP (right).

RhMOPs are typically synthesised under solvothermal conditions under the presence of strong inorganic bases in N'N-dimethylacetamide (DMA). Under such aggressive media, the

strong Rh-COO bond starts to gain dynamic behaviour, and slowly gets exchanged by the added linker of choice. After several days, microcrystalline powder of RhMOPs (or single-crystal quality MOP under highly diluted conditions) can be recovered from the mixture and characterised by PXRD measurements (Figure 5.2).

5.2.2. Post-Synthetic Functionalization via coordination chemistry

Isolated Rh−Rh paddlewheel clusters are inert at their equatorial sites but are highly reactive at their axial sites. For instance, they show high affinity toward N-donor ligands,[42] and their reactions with said ligands can be monitored by following the spectroscopic changes of the band centered at 500−600 nm, which corresponds to the $\pi^* \rightarrow \sigma^*$ transitions (λ_{max}) of Rh−Rh bonds.[37] Given this affinity, we envisaged that ligand-exchange reactions at these axial sites would enable functionalization of the surface of Rh-MOPs that contain 12 N-donor ligands. Thus, we selected three chemically distinct N-donor ligands: 4-*tert*butylpyridine (*tert*Py); 4-trifluoromethylpyridine (CF_3-Py), as a source of hydrophobicity; and *L*-proline (*L*-Prol), to make the Rh-MOPs more biocompatible and to confer them with chirality and hydrophilicity. We first tested functionalization of RhMOPs via coordination chemistry by adding *tert*Py (12 molar equivalents [*i.e.,* one per Rh−Rh paddlewheel]) to HRhMOP in N'N-dimethylformamide (DMF) at room temperature. Addition of *tert*Py led to immediate dissolution of the MOP, as indicated by a concomitant colour change from colourless to purple, which is characteristic of the nitrogen coordination to the Rh−Rh paddlewheel clusters. This was a first indication that ligand exchange between the *tert*Py ligands and water molecules had occurred. Thus, we attributed the solubility of the resultant MOP in DMF to the bulky *tert*-butyl groups incorporated onto the surface of HRhMOP, as they would inhibit its aggregation and enable DMF molecules to solvate it. Remarkably, purple crystals suitable for single-crystal X-Ray diffraction analysis (SCXRD) were obtained by exposing the purple solution to diethyl ether vapours for 5 days. SCXRD analysis (performed on the XALOC beamline of the ALBA synchrotron[43]) confirmed functionalization of the outer surface of HRhMOP with 12 *tert*Py ligands (Figure 5.3).

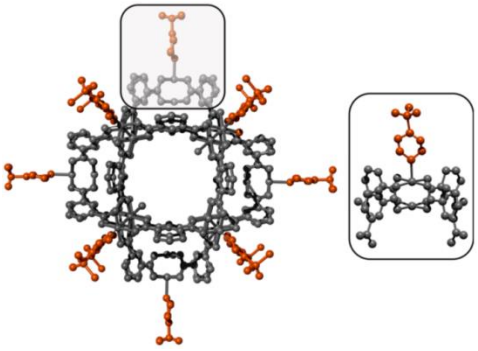

Figure 5.3. Crystalline structure of HRhMOP(*tert*Py). The coordination of *tert*Py to the Rh−Rh axial site is highlighted.

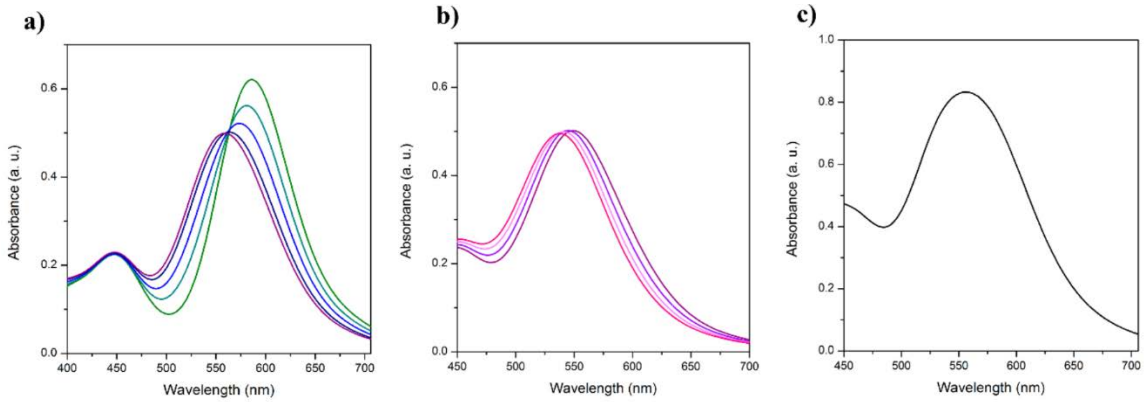

Figure 5.4. (a) UV-Vis spectra of the titration of $Rh_2(OAc)_4$ in DMF (2 mM) with *tert*Py from 0 mol. eq. (green) to 1 mol. eq. (purple). After the addition of 1 mol eq., the adsorption maximum of band I (λ_{max}) is centred at 555 nm. (b) UV-Vis of the titration of $Rh_2(OAc)_4$ in DMF (2 mM) with *tert*Py from 1 mol eq. to 2.5 mol eq. (c) UV-Vis of HRhMOP(*tert*Py) in DMF (0.31 mM). The λ_{max} is 555 nm that indicates that all the dirhodium paddlewheels in the MOP structure are coordinated to one tertPy.

As expected, these *tert*Py ligands were coordinated to the outer axial site of all Rh−Rh paddlewheel units, affording a functionalized Rh-MOP of formula $[Rh_2(mBDC)_2(tertPy)_1(H_2O)_1]_{12}$ (hereafter referred to as HRhMOP(*tert*Py)). Having confirmed the functionalization of the outer surface of HRhMOP via SCXRD, we then established a methodology to follow the ligand exchange. Thanks to the molecular behaviour of Rh-MOPs, it was possible to use routine characterisation techniques based on UV−Vis and ^{1}H NMR spectroscopies (Figure 5.5a,b,c and Figures 5.9 – 5.25). To this end, rhodium acetate $[Rh_2(Ac)_4]$ was used as a model Rh−Rh paddlewheel cluster to first monitor the spectroscopic changes in the UV−Vis spectra caused by the coordination of *tert*Py to it. We found that, upon addition of *tert*Py to a DMF solution of $[Rh_2(Ac)_4]$, λ_{max} shifted from 585 to 555 nm, as the ligand bound to one of the available axial sites. Coordination to the second available axial site induced a further shift of λ_{max} to 538 nm (Figure 5.4). Interestingly, the UV−vis spectrum of HRhMOP(*tert*Py) showed a λ_{max} of 555 nm, matching with the coordination of one *tert*Py ligand to each of the 12 Rh−Rh paddlewheel units (see Section 5.3.4.; Figure 5.9). Further addition of *tert*Py to HRhMOP(*tert*Py) did not cause any additional shift in the λ_{max}, thereby confirming that *tert*Py can only coordinate to the outer part of HRhMOP. Moreover, ^{1}H NMR spectra of HRhMOP(*tert*Py) evidenced coordinated *tert*Py, as indicated by two aromatic peaks (at δ= 9.52 and 8.66 ppm) corresponding to the pyridine moiety and a peak at 1.54 ppm corresponding to the *tert*-butyl groups (Figure 5.5b). Finally, we determined the amount of coordinated *tert*Py ligands by comparing integration of the peaks of the *tert*Py with the peaks ascribed to the *m*BDC ligand of the HRhMOP (δ= 8.10, 7.87, and 7.18 ppm). As expected, the molar ratio of *tert*Py ligands to HRhMOP was 12:1. We then used the two aforementioned techniques to follow the coordination-induced functionalization

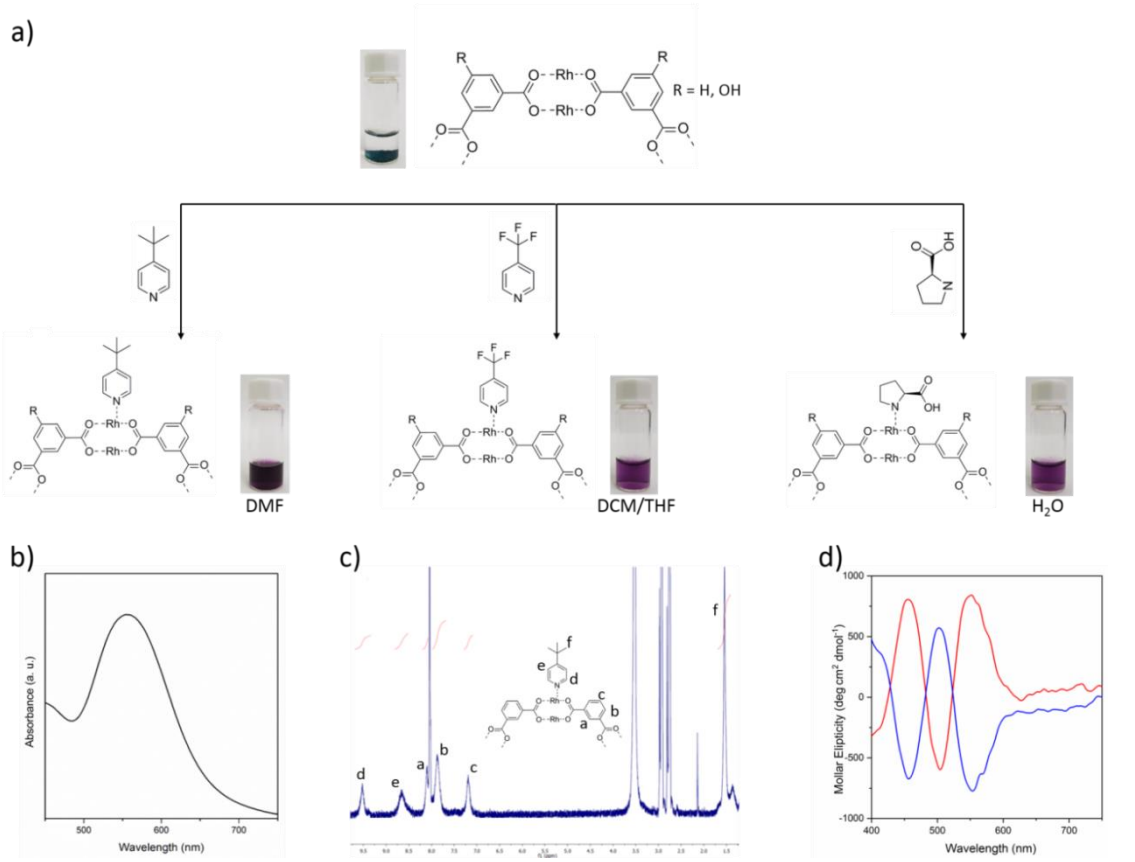

of OHRhMOP with *tert*Py. The reaction was done analogously to HRhMOP and similarly yielded

Figure 5.5. (a) Schematic representation showing the postsynthetic modification of HRhMOP and of OHRhMOP via coordination of N-based ligands at the corresponding dirhodium axial sites. The photographs illustrate the initial dispersion of insoluble HRhMOP or OHRhMOP in DMF, DCM, THF, or H_2O (top), and the purple solutions resulting from postsynthetic functionalization reactions with tertPy (left), CF_3-Py (center), or L-Prol (right). (b) UV−Vis spectrum of HRhMOP (*tert*Py) in DMF showing a λ_{max} at 555 nm. (c) ^{1}H NMR of HRhMOP(tertPy) in DMF-d_7. (d) CD spectra of HRhMOP(L-Prol) (red) and HRhMOP(D-Prol) (blue) in water.

a purple solution upon addition of *tert*Py to a DMF suspension of OHRhMOP. Synthesis of the expected MOP $[Rh_2(OH\text{-}m BDC)_2(tert Py)_1(H_2O)_1]_{12}$ was confirmed by UV−Vis (λ_{max} = 555 nm; Figure 5.9) and ^{1}H NMR (see Section 5.3.5.; Figure 5.16).

Once we had demonstrated that the surface of Rh(II)-based MOPs can be selectively functionalized via coordination chemistry, and that such reactions yield products whose solubility profile differs from that of the starting MOP, we attempted to modify the external surface of both HRhMOP and OHRhMOP to be soluble a wider range of solvents, such as in aprotic organic solvents (e.g., dichloromethane (DCM) and tetrahydrofuran (THF)) or in water. We did this by functionalizing the starting MOPs with either CF_3-Py (for its hydrophobicity) or *L*-Prol (for its hydrophilicity). For the former, we added CF_3-Py to a suspension of HRhMOP crystals in DCM or of OHRhMOP in THF. Instantaneously after addition of CF_3-Py, each suspension became a clear purple solution, giving rise to $[Rh_2(mBDC)_2(CF_3\text{-}Py)_1(H_2O)_1]_{12}$ and $[Rh_2(OH\text{-}m BDC)_2(CF_3\text{-}Py)_1(H_2O)_1]_{12}$, respectively, as determined by UV−Vis (Figure 5.10) and ^{1}H NMR (Figures 5.17, 5.18).

Similarly, we separately functionalized HRhMOP and OHRhMOP with *L*-Prol (again, 12 molar equivalents) by mixing each MOP with *L*-Prol in basic water (pH 10.5). Basic pH was required in order to deprotonate the carboxylate groups in *L*-Prol. In both cases, we observed that, upon addition of *L*-Prol, each suspension became a transparent purple solution, forming $[Rh_2(mBDC)_2(L\text{-prol})_1(H_2O)_1]_{12}$ and $[Rh_2(OH\text{-}mBDC)_2(L\text{-prol})_1(H_2O)_1]_{12}$ respectively, as confirmed by spectroscopic characterisation (Figures 5.19, 5.20).

Functionalisation of MOPs with chiral amino acids is an alternative and straightforward strategy to confer them with chirality.[44,45] To this end, we functionalized HRhMOP and OHRhMOP with either L-Prol or D-Prol. The chirality of the resultant MOPs was studied by circular dichroism (CD) spectroscopy in solution. The enantiomeric MOPs exhibited opposite Cotton effects (Figure 5.5d). Their CD spectra indicated a strong Cotton effect with the crossing wavelengths at 482 and 523 nm near the absorption of the Prol coordinated to the Rh−Rh paddlewheel unit in Rh-MOPs. The shape and magnitude of these Cotton effects clearly reflect the chiral coordination sphere of the Rh−Rh paddlewheel units in the MOPs. Thus, the sign of the CD signal is dictated by the enantiomeric form (*L*- or *D*-) of the proline.

At this point, we had demonstrated that the exterior axial sites of the Rh−Rh paddlewheel units serve as anchoring sites for N-donor ligands and that this reactivity can be used to introduce new functionalities and/or to selectively increase the solubility of Rh-MOPs in organic or aqueous media. The next step was confirming that this post-synthetic pathway was not affecting the intrinsic microporosity of MOPs in the solid state. For this, every 12-functionalized MOP presented above (that is, *tert*Py, CF_3-Py and *L*-Prol versions of HRhMOP and OHRhMOP) was submitted to N_2 sorption tests at 77 K (see section 5.3.7; Figures 5.30 – 5.34). Every functionalized MOP showed a characteristic *Type I* adsorption isotherm, indicating that the inner microporous cavity was preserved. However, as expected, the outer functionalization induced a decrease in their S_{BET} as compared to the parent materials,[46,47] HRhMOP and OHRhMOP, which showed values of 947 m^2/g and 548 m^2/g, respectively. Functionalized HRhMOPs [HRhMOP(*tert*Py), HRhMOP(CF_3-Py) and HRhMOP(L-prol)] showed lower S_{BET} values: 589 m^2/g for HRhMOP(*tert*Py), 675 m^2/g for HRhMOP(CF_3-Py), and 337 m^2/g for HRhMOP (L-Prol). In the case of functionalized OHRhMOPs, a similar trend was observed: 388 m^2/g for OHRhMOP(*tert*Py), 154 m^2/g for OHRhMOP(CF_3-Py), and 64 m^2/g for OHRhMOP(L-Prol).

5.2.3. Post-synthetic functionalization via covalent chemistry

We next looked to a second source of reactive sites for post-synthetic functionalization of MOPs: their organic linkers. Cuboctahedral Rh(II)-based MOPs are assembled from 24 organic linkers.

Accordingly, we considered that if each organic linker had one exohedral reactive functional group, then these MOPs could potentially be functionalized with 24 molecules (*i.e.*, one per linker). We tested our hypothesis by functionalizing OHRhMOP through its 24 hydroxyl groups, using an acyl chloride and an acid anhydride under basic aqueous conditions. The synthesis of esters from acyl chlorides and anhydrides entails a nucleophilic attack to the carboxylic acid derivative by the hydroxyl groups. To increase the nucleophilicity of the hydroxyl groups, these reactions are generally run in the presence of a strong base. Under these conditions, we observe that addition of NaOH (final pH 10.5) to an aqueous suspension of OHRhMOP leads to dissolution of the MOP. This is due to deprotonation of the hydroxyl groups, which renders a negatively charged MOP, hereafter noted as ONaRhMOP. The integrity of ONaRhMOP was confirmed by UV−vis, ^{1}H NMR, and mass spectrometry analysis in basic water, highlighting the high chemical stability of these MOPs (Figures 5.13, 5.21 and 5.26). We then exploited the solubility and nucleophilicity of ONaRhMOP to react it with acryloyl chloride (24 molar equivalents; Figure 5.6). For this, we performed a biphasic reaction by stirring an aqueous solution of ONaRhMOP and diethyl ether containing 1 molar equivalent of acryloyl chloride per phenolate group (*i.e.*, 24 molar equivalent of acryloyl chloride per ONaRhMOP) overnight evolving from 0 °C to room temperature. The reaction product, which was precipitated at the interface after the overnight reaction, was washed with water and methanol (solvent in which unfunctionalized OHRhMOP is soluble), solubilized in DMF (where OHRhMOP is highly insoluble) and analysed by ^{1}H NMR and mass spectrometry (Figures 5.22, 5.27). Both techniques confirmed the quantitative conversion of the phenolate groups into the acrylate ester (hereafter named AcrRhMOP). Indeed, the ^{1}H NMR spectrum of AcrRhMOP evidenced generation of the acrylate ester, as indicated by the appearance of peaks at δ= 6.52, 6.34, and 6.14 ppm corresponding to the three non-equivalent protons of the acryloyl group (Figure 5.22a). The conversion rate was calculated by comparing the integration of the acrylate signals to the integration of the peak at δ= 7.72 ppm, which corresponds to the outer aromatic proton of the OH-*m*BDC ligand. As expected, the molar ratio of acrylate esters per Rh(II)-based MOP was 24:1. In addition, further evidence of the quantitative functionalization with acrylate esters was acquired by matrix-assisted laser desorption/ionization-time-of-flight (MALDI-TOF), which showed a peak at m/z = 8090.5 that matches the molecular formula of the protonated desired fully functionalized Rh-MOP, $[Rh_{24}(Acr\text{-}mBDC)_{24} + H^{+}]^{+}$ (m/z = 8090.9) (see Section 5.3.6, Figure 5.27).

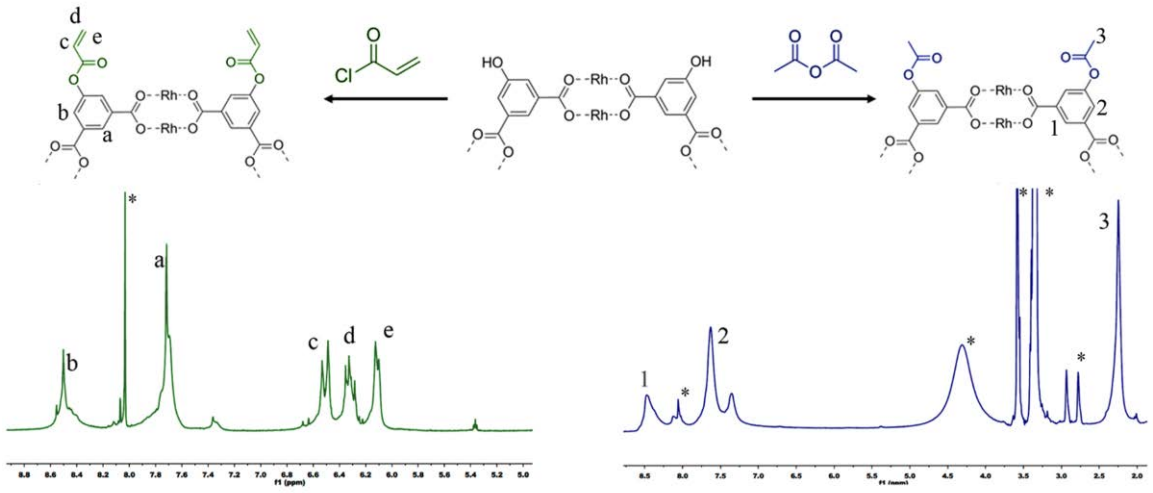

Figure 5.27. Schematic representation showing the covalent post-synthetic functionalization of OHRhMOP via formation of ester linkages. (left, green) ^{1}H NMR of AcrRhMOP in DMF-d_7. (right, blue) ^{1}H NMR of OMetRhMOP in DMF-d_7. Solvent peaks [DMF, MeOH, dioxane and water] are highlighted with an asterisk.

To further evaluate the reactivity of the phenolate groups in ONaRhMOP, we reacted them with acetic anhydride in conditions analogous to those for acryloyl chloride. The as-obtained product was washed with methanol, dissolved in DMF, and then analysed by ^{1}H NMR and mass spectrometry (Figures 5.6, 5.23 and 5.28). In this case, both techniques showed the partial functionalization of the Rh-MOP with acetate ester groups (hereafter named OMetRhMOP). The esterification was confirmed by its ^{1}H NMR spectrum, which showed a new peak at δ= 2.25 ppm, corresponding to the methyl group. The relative intensity of the integrations of the peak at 2.25 ppm and the outer proton of the OH-*m*BDC linker were used to estimate that the conversion rate was *ca.* 75%, meaning that 18 of the available 24 phenolate groups had been converted to esters. This result was confirmed by MALDI-TOF, which showed a peak at m/z = 7968.9, consistent with a partially functionalized RhMOP of formula $[Rh_{24}(OH\text{-}mBDC)_6(OMet\text{-}mBDC)_{18} + H^+]^+$ + DCTB + DMF + MeOH (m/z = 7969.9) (Figure 5.28). Subsequent reactions using more acetic anhydride did not provide any improvement in conversion, suggesting that, under the tested conditions, full conversion of the phenolate groups was precluded due to steric hindrance between the derivatised OMetRhMOP and the acetic anhydride.

With this, the bases on the molecular behaviour of Rh-MOPs were established. The next step aimed at optimizing the combination of both chemistries and enhancing the potential of the approximation.

5.2.4. Post-synthetic dual functionalization via combined coordination and covalent chemistries

Orthogonal anchoring. We next explored the possibility of functionalizing OHRhMOP at its two types of reactive sites (the axial site of the Rh−Rh paddlewheel units and the hydroxyl groups of the organic linkers) using coordination chemistry for the former and covalent chemistry for the latter, reasoning that these two approaches should not be mutually exclusive. We envisaged that combining these chemistries would enable us to functionalize the external surface of these MOPs with a total of 36 functional groups. We demonstrated this by functionalizing AcrRhMOP with 12 tertPy molecules. Addition of tertPy (12 molar equivalents) to a DMF solution of AcrRhMOP caused the solution to immediately change colour from green to purple. The expected product was then confirmed by UV−Vis and ^{1}H NMR as for the previous products (Figure 5.7).

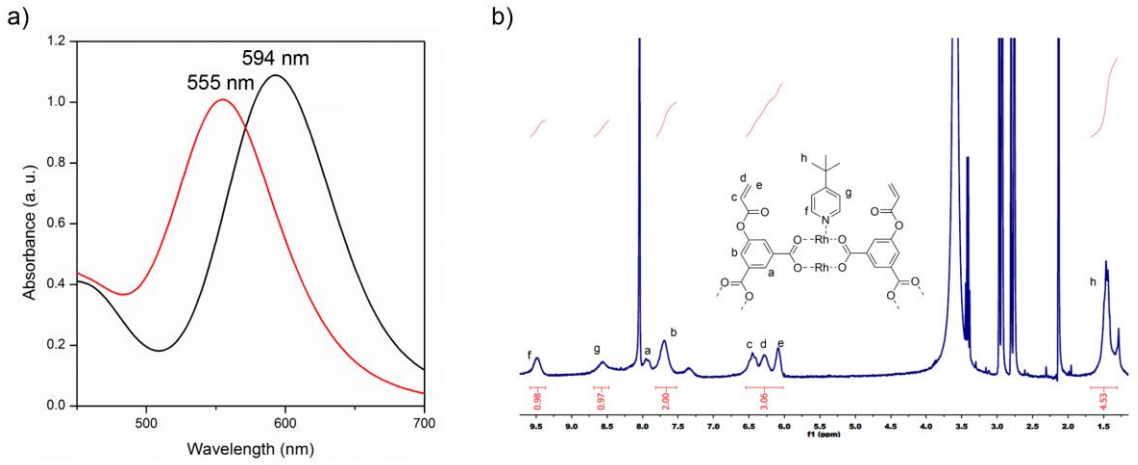

Figure 5.7. (a) UV-Vis spectra of AcrRhMOP in DMF (0.31 mM) before and after the addition of 12 mol eq. of tertPy in black and red, respectively. The λ_{max} shifts from 593 nm to 555 nm indicating the coordination of 12 tertPy molecules per AcrRhMOP. (b) ^{1}H NMR spectra of AcrRhMOP(*tert*Py). The relative integrals of the protons of the acrylate ligand (b, c, d, e) and protons of *tert*Py ligand (f, g, h) show that their molar ratio is 0.5, which gives rise to the following formula: $[Rh_2(Acr\text{-}mBDC)_2(tertPy)_1]_{12}$.

Sequential coordination and covalent chemistries. Once we had confirmed the dual functionalization of OHRhMOP with 12 *tert*Py ligands and 24 esters, we investigated the use of the same two chemistries for functionalizing OHRhMOP by formation of ether linkages. Interestingly, although ester MOP derivatives could be prepared from acyl chlorides or anhydrides at room temperature due to the high reactivity of both functional groups, ethers could not be prepared from halogenated compounds under similar reaction conditions. This result is not surprising, as the standard conditions to alkylate a hydroxyl group with brominated alkanes entails the use of high boiling-point solvents (e.g., DMF) and high temperatures (i.e., above 80 °C) in

the presence of an inorganic base. However, OHRhMOP is not soluble in DMF, which implies that any reaction in this solvent should be carried out under heterogeneous conditions. Unfortunately, the heterogeneous reaction between OHRhMOP and allyl bromide in DMF at 80 °C failed. We reasoned that the close packing of OHRhMOP in the solid state hindered the diffusion of the reagents, thereby preventing conversion of the hydroxyl groups. To overcome this low solubility, we employed dual functionalization to first dissolve the OHRhMOP in DMF by coordinating *tert*Py. Then, the functionalized OHRhMOP(*tert*Py) was reacted in situ with allyl bromide (Figure 5.7). This sequential functionalization was carried out by simply mixing the three components in DMF, and the resulting purple solution was stirred at 80 °C for 12 h. After this period, the MOP was precipitated by diethyl ether, washed with methanol and acetone, and dried under ambient conditions. UV−vis and ^{1}H NMR analyses of the purified product dissolved in DMF confirmed that both types of conversion had occurred. Indeed, the UV−vis spectrum showed the characteristic λ_{max} of 555 nm (Figure 5.8). In addition, the ^{1}H NMR spectrum showed the presence of peaks corresponding to *tert*Py (9.48 and 8.55 ppm for the aromatic protons and 1.36 ppm for the *tert*-butyl group) and to the allyl group (5.91, 5.30, 5.17, and 4.46 ppm). The relative integration between the allyl protons and the aromatic protons of the OH-*m*BDC ligand revealed a conversion degree of 40%. The doubly functionalized Rh-MOP product is referred to hereafter as OallylRhMOP(*tert*Py) (Figure 5.8 and Figure 5.24). Interestingly, the reversible nature of the coordination bond between the Rh−Rh paddlewheel and the *tert*Py ligands enabled us to selectively cleave them after the covalent reaction, leading to their replacement with water. Under aqueous conditions, these cleavage and ligand exchanges occur at a pH below 2.1. Thus, this cleavage was performed by adding one drop of 3 M HCl to a suspension of OallylRhMOP(*tert*Py) in acetone or water, inducing a sudden colour shift in the suspension, from purple to green. This colour change was an indication of the ligand exchange between the *tert*Py and H_2O ligands, which was further corroborated by the UV−vis spectrum, through the expected shift in λ_{max}, from 555 nm to 590 nm (Figure 5.8c). Moreover, the ^{1}H NMR spectrum of the acid-treated MOP confirmed that all the *tert*Py ligands had been cleaved as the integrity of the allyl functionality was preserved, which yielded a new product referred to hereafter as OAllylRhMOP (Figure 5.8b). MALDI-TOF of OAllylRhMOP confirmed its functionalization with allyl groups, showing a peak at *m/z* = 7419.4, which corresponds to the following formula: $[Rh_{24}(OH\text{-}mBDC)_{15}(OAllyl\text{-}mBDC)_9 + H^+]^+$ + DCTB + H_2O (*m/z* = 7418.3) (Figure 5.29). Like with coordinatively-functionalized MOPs, the covalently- or dual-functionalized Rh-MOPs exhibited lower S_{BET} values than the parent MOPs; 410 m^2/g for AcrRhMOP, 120 m^2/g for AcrRhMOP(*tert*Py), and 487 m^2/g for OMetRhMOP. OallylRhMOP was found to be non-porous to N_2 but porous to CO_2 reaching a maximum uptake of 1.15 mmol/g at 1 bar and 298 K (see Section 5.3.7; Figure 5.36.

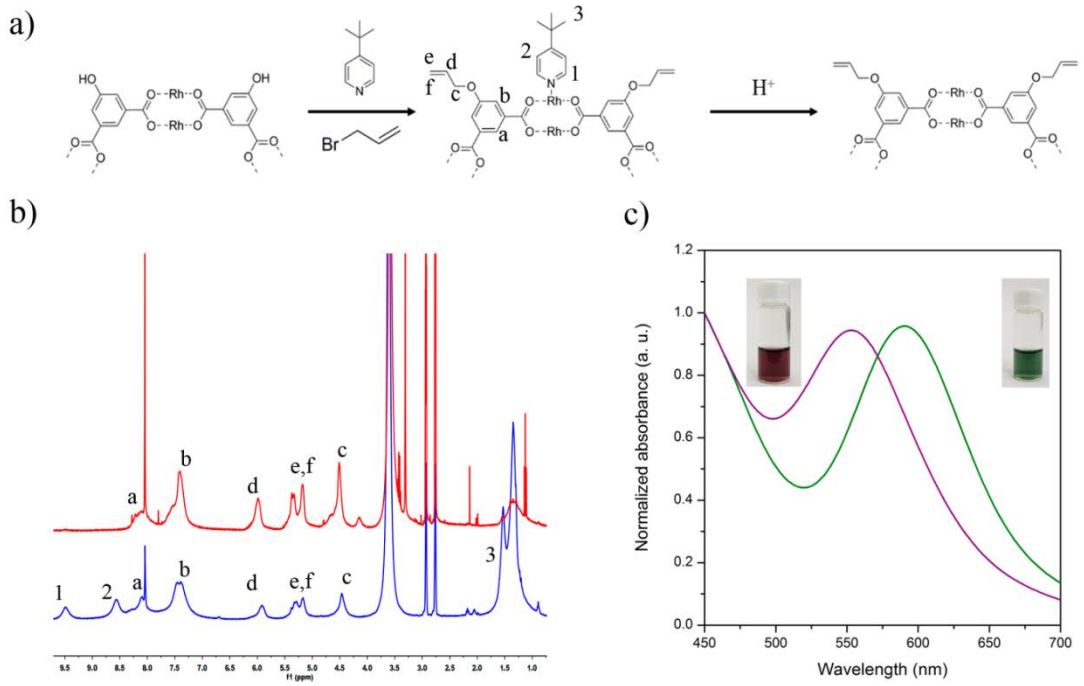

Figure 5.8. (a) Schematic representation showing the sequential coordination−covalent functionalization of OHRhMOP with ether linkages. (b) ^{1}H NMR of OallylRhMOP(*tert*Py) (blue) and OallylRhMOP (red) in DMF-d_7. Solvent peaks (DMF and water) are highlighted with an asterisk. (c) UV−Vis spectra of OallylRhMOP(*tert*Py) (purple) and OallylRhMOP (green) in DMF, showing the shift of λ_{max} from 555 to 590 nm. Inset: Photographs of each solution.

Altogether, these results confirm that, despite the conditions to which functionalized Rh-MOPs were exposed, they retained their intrinsic microporosity in the solid state.

5.2.5. Conclusions

In conclusion, this Chapter has demonstrated postsynthetic functionalization of Rh-based MOPs via two chemistries at two types of reactive sites: coordination chemistry at their Rh−Rh paddlewheel units and covalent chemistry at their organic linkers. Functionalization of the 12 Rh−Rh paddlewheel units was demonstrated by coordinating N-donor ligands, whose relative hydrophobicity dictated the solubility of the resultant products. This coordination approach was also used to confer Rh-MOPs with chirality. Through covalent chemistry, the 24 hydroxyl groups on the organic linkers were converted into esters by reacting them with acyl chlorides or acid anhydrides. The orthogonal reactivity of the Rh−Rh paddlewheel units and the organic linkers enabled us to combine the two chemistries to yield doubly functionalized Rh-MOPs featuring a total of 36 new functional molecules. The possibility of controlling stoichiometrically and spatially the external functionalization of MOPs can provide structurally well-defined nanoscopic platforms for delivery, sorption, and catalytic applications. Once the limited catalogue of available Rh-MOPs is expanded (see Chapter 6), this approach will certainly gain further importance.

5.3. Experimental Part

5.3.1. Materials and Methods

Rhodium acetate, 1,3-benzenedicarboxylic acid, 5-hydroxy-1,3-benzenedicarboxylic acid, acryloyl chloride, acetic anhydride, allyl bromide, *L*- and *D*-Proline and pyridine derivatives (*tert*Py, CF_3-Py) were purchased from Sigma-Aldrich and used as received. Solvents at HPLC grade were purchased from Fischer Chemicals.

Powder X-Ray Diffraction (PXRD) patterns were recorded on an X'Pert PRO MPD analytical diffractometer (Panalytical) at 45 kV, 40 mA using Cu Kα radiation (λ = 1.5419 Å). Nitrogen gas sorption isotherms were measured at 77 and 298 K using an Autosorb-IQ-AG analyzer. UV−vis was measured in an Agilent Cary 4000 and circular dichroism was measured in a J-715 CD spectrophotometer (JASCO), both at room temperature (ca. 25 °C). ^{1}H NMR spectra were acquired in Bruker Advance III 400SB NMR spectrometer. Mass spectrometry (MALDI-TOF) was run in an Applied Biosystems 4700 Proteomics Analyzer operating in positive-ionization mode.

Single-Crystal X-Ray Diffraction (SCXRD) data of HRhMOP(*tert*Py) and OHRhMOP were collected at 100(2) K in BL13-XALOC beamline at the ALBA synchrotron, on a single-axis goniometer with a Pilatus 6M detector using a monochromatic X-ray beam (λ = 0.82656 Å). The data frames were integrated and scaled using XDS software packakge. The structure contains some disorder molecules. Absorption correction was not applied. The structure was solved by direct methods and subsequently refined by correction of F2 against all reflections, using SHELXT2013 and SHELXL2013 within the WinGX package. In HRhMOP(*tert*Py), due to the inherent disorder of the *tert*-butyl group of the 4-*tert*butylpyridine molecules, constraint were applied in these groups and isotropic refinement was applied to these atoms. Both structures contain some disordered molecules. Attempts to adequately model the disordered molecules were unsatisfactory; therefore, the PLATON/SQUEEZE routine was applied to mask out the disordered electron density.

5.3.2. Synthetic methodologies

HRhMOP. 100 mg of $Rh_2(Ac)_4{\cdot}2MeOH$ (0.2 mmol), 160 mg of 1,3-benzenedicarboxylic acid (0.96 mmol), and 105 mg of Na_2CO_3 (1.0 mmol) were dispersed in 7 mL of DMA. The mixture was transferred to a scintillation vial and heated at 100 °C for 48 hours. A microcrystalline powder was separated from the reaction mixture and washed with DMA, EtOH, and MeOH. Finally, microcrystals were kept in acetone overnight and dried at 85 °C under vacuum. Single crystals of HRhMOP were prepared by heating a dispersion of 10 mg of $Rh_2(Ac)_4{\cdot}2MeOH$ (0.02 mmol), 10 mg of 1,3-benzenedicarboxylic acid (0.06 mmol), and 1.5 mg of K_2CO_3 (0.01 mmol) in 1 mL of DMA in a scintillation vial at 100 °C for 48 hours.

OHRhMOP. 100 mg of $Rh_2(Ac)_4 \cdot 2MeOH$ (0.2 mmol), 180 mg of 5-hydroxy-1,3-benzenedicarboxylic acid (0.96 mmol), and 105 mg of Na_2CO_3 (1.0 mmol) were dispersed in 7 mL of DMA. The mixture was transferred to a scintillation vial and heated at 100 °C for 48 h. The resulting OHRhMOP single crystals were washed with DMA and dissolved in MeOH to separate them from Na_2CO_3. The solution was dried under vacuum, and the residue was washed with water and acetone. Finally, the powder was kept in acetone overnight and dried at 85 °C under vacuum.

HRhMOP(*tert*Py). 17 μL of *tert*Py (111 μmol) were added to a dispersion of 60 mg of HRhMOP (9.3 μmol) in 10 mL of DMF. The resulting mixture was sonicated for 5 minutes and then centrifuged at 18,000 rpm for 10 min. The supernatant was collected and precipitated with ether vapours over 5 days to yield single purple crystals. HRhMOP(*tert*Py) crystals were then separated from the mother liquor and washed with ether and acetone. Finally, the sample was kept in acetone overnight and dried at 85 °C under vacuum.

OHRhMOP(*tert*Py). The sample was prepared using the same conditions as for HRhMOP(*tert*Py), except that instead of 17 μL of *tert*Py, 15 μL were used.

HRhMOP(CF_3-Py). 13 μL of CF_3-Py (111 μmol) were added to a dispersion of 60 mg of HRhMOP (9.3 μmol) in 10 mL of dichloromethane. This mixture was sonicated for 5 minutes. Then, it was filtered and the filtrate was evaporated under vacuum. The resulting solid was washed with acetone. Finally, the sample was kept in acetone overnight and dried at 85 °C under vacuum.

OHRhMOP(CF_3-Py). The sample was prepared using the same conditions as for HRhMOP(CF_3-Py), except that instead of using 13 μL of CF_3-Py and dichloromethane as solvent, 12 μL of CF_3-Py was used and THF was the solvent.

HRhMOP(*L*-Prol). A solution of 13 mg of L-Prol (111 μmol) in 1 mL of water at pH 10.5 (pH was adjusted with NaOH) was added to a dispersion of 70 mg of OHRhMOP (9.3 μmol) in 5 mL of water. The resulting mixture was sonicated for 5 minutes, and the solution was centrifuged at 18,000 rpm for 10 min. The supernatant was collected and precipitated with acetone vapours over 10 days to yield purple crystals. HRhMOP(L-Prol) crystals were separated from the mother liquors and washed with acetone. Finally, the sample was kept in acetone overnight and dried at 85 °C under vacuum. Note here that **HRhMOP(*D*-Prol)** was prepared using the same conditions as for HRhMOP(L-Prol), except that instead of *L*-Prol, *D*-Prol was used.

OHRhMOP(*L*-Prol). A solution of 13 mg of *L*-Prol (111 μmol) in 1 mL of water at pH 10.5 (pH was adjusted with NaOH) was added to a dispersion of 70 mg of OHRhMOP (9.3 μmol) in 5 mL of water. The resulting mixture was sonicated for 5 minutes, and the solution was centrifuged at 18,000 rpm for 10 min. The supernatant was collected and precipitated with acetone vapours over

10 days to yield purple crystals. HRhMOP(*L*-Prol) crystals were separated from the mother liquors and washed with acetone. Finally, the sample was kept in acetone overnight and dried at 85 °C under vacuum. Note here that **OHRhMOP(*D*-Prol)** was prepared using the same conditions as for HRhMOP(*L*-Prol), except that instead of *L*-Prol, *D*-Prol was used.

AcrRhMOP. A total of 4.3 mg (105 μmol) of NaOH was added to a dispersion of 30 mg of OHRhMOP (4.4 μmol) in 1 mL of water. After this addition, the OHRhMOP dissolved instantly, due to deprotonation of the phenol groups. Then, a diethyl ether solution containing 8.5 μL of acryloyl chloride (105 μmol) was layered on top of the as-made ONaRhMOP aqueous solution at 0 °C. The biphasic mixture was vigorously stirred overnight at room temperature. Afterwards, a green solid appeared at the interphase; it was isolated and then washed with MeOH and acetone. Finally, the sample was kept in acetone overnight and dried at 85 °C under vacuum.

OMetRhMOP. OMetRhMOP was prepared using the same conditions as for AcrRhMOP, except that instead of using 8.5 μL of acryloyl chloride and diethyl ether as solvent, 15 μL of acetic anhydride (137 μmol) were used and 1,4-dioxane as the solvent.

AcrRhMOP(*tert*Py). 10 mg of AcrRhMOP (1.2 μmol) were dissolved 5 mL of DMF. Then, 100 μL of a 1 mL stock solution of *tert*Py containing 18 μL (120 μmol) was added to the AcrRhMOP solution, causing an immediate colour change from green to purple. AcrRhMOP(*tert*Py) was precipitated by adding diethyl ether. The solid was washed with ether and dried under vacuum.

OAllylRhMOP(*tert*Py). 30 mg of OHRhMOP (4.4 μmol) was dissolved in 2 mL of DMF by adding 10 μL of *tert*Py (66 μmol). Then, 45 mg of K_2CO_3 (316 μmol) was added to the OHRhMOP(*tert*Py) solution. The mixture was stirred at 80 °C for 30 min. Then, 14 μL of allyl bromide (316 μmol) were added, and the resulting mixture was reacted at 80 °C for 24 h. The final purple-reddish solution was centrifuged, and the supernatant was evaporated under vacuum to obtain a purple residue. The crude product was washed with diethyl ether, MeOH, and acetone and dried at 85 °C under vacuum.

OAllylRhMOP. 100 μL of 3 M HCl were added to a dispersion of 20 mg of OAllylRhMOP(*tert*Py) in acetone at room temperature. The purple suspension rapidly became green, indicating decoordination of *tert*Py molecules. The solid was recovered by centrifugation and further washed with water and MeOH. Finally, the sample was kept in acetone overnight and dried at 85 °C under vacuum.

5.3.3. Single-Crystal XRD analysis

Table 5.1. Crystal and structural refinement data for HRhMOP, OHRhMOP and HRhMOP(*tert*Py).

	HRhMOP	OHRhMOP(DMA)$_{12}$	HRhMOP(*tert*Py)
Formula	C_{192} H_{96} O_{120} Rh_{24}	$C_{240}H_{180}N_{12}O_{144}Rh_{24}$	C_{304} N_{12} O_{108} Rh_{24}
Formula Weight	6808.53	8702.78	8017.00
Crystal System	cubic	tetragonal	tetragonal
Space group	Im-3m	I4/m	P4m
a/ Å	27.480(4)	31.080(5)	29.620(4)
b/ Å	27.480(4)	31.080(5)	29.620(4)
c/ Å	27.480(4)	31.250(5)	29.140(4)
α/ º	90	90	90
β/ º	90	90	90
γ/ º	90	90	90
Unit Cell Volume/ Å^3	20752(9)	30187(11)	25566(8)
Temperature (K)	100	100	100
Z	2	2	2
Radiation/ Å	0.826530	0.826530	0.826530
Reflections Measured	28846	194980	166455
Independent Reflections	946	18195	13210
Reflections (I > 2σ (I))	886	15797	8294
R_{int}	0.064	0.024	0.063
R	0.0989	0.0901	0.1207
wR2	0.3305	0.2704	0.3779

CCDC CIF Files: 1883914 (HRhMOP), 1883124 (OHRhMOP) and 1884202 (HRhMOP(*tert*Py).

5.3.4. UV-Vis analysis

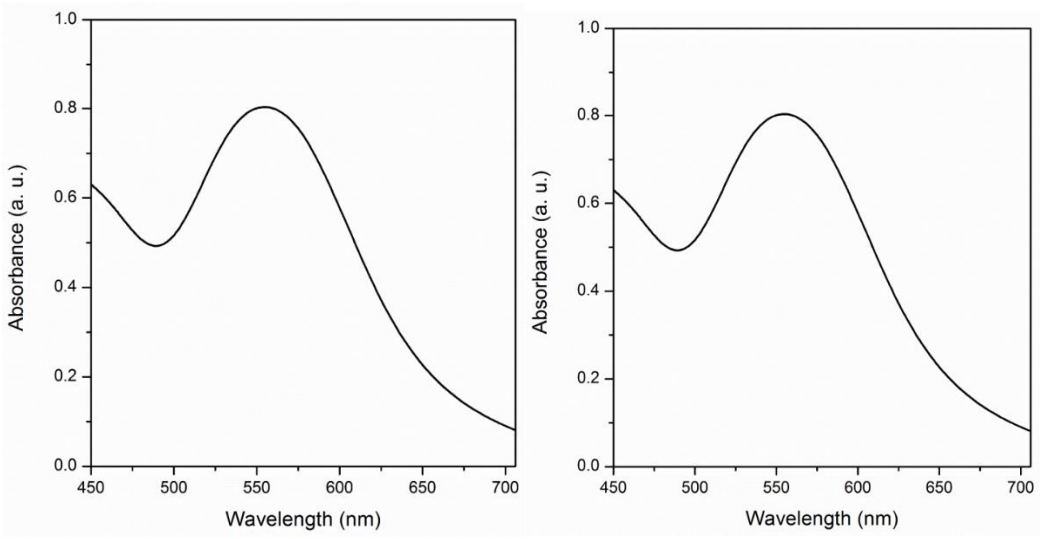

Figure 5.9. UV-Vis of HRhMOP(*tert*Py) (left) and OHRhMOP(*tert*Py) in DMF (0.32 mM). The λ_{max} is 555 nm which indicates that all the dirhodium paddlewheels in the MOP structure are coordinated to one *tert*Py.

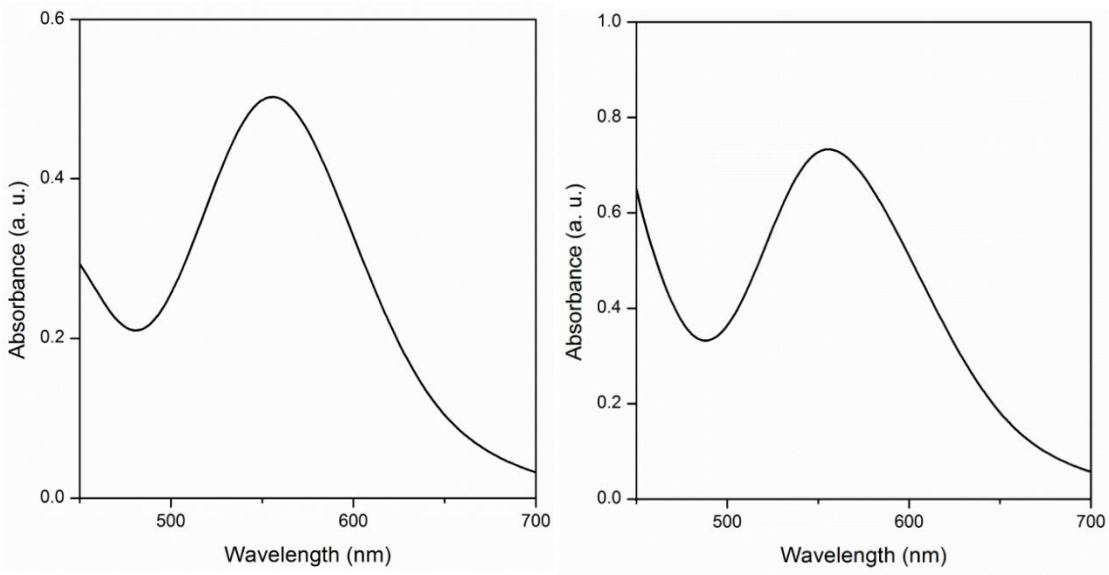

Figure 5.10. UV-Vis of HRhMOP(CF_3-Py) (left) and OHRhMOP(CF_3-Py) (right) in DMF (0.32 mM). The λ_{max} is 555 nm which indicates that all the dirhodium paddlewheels in the MOP structure are coordinated to one CF_3-Py.

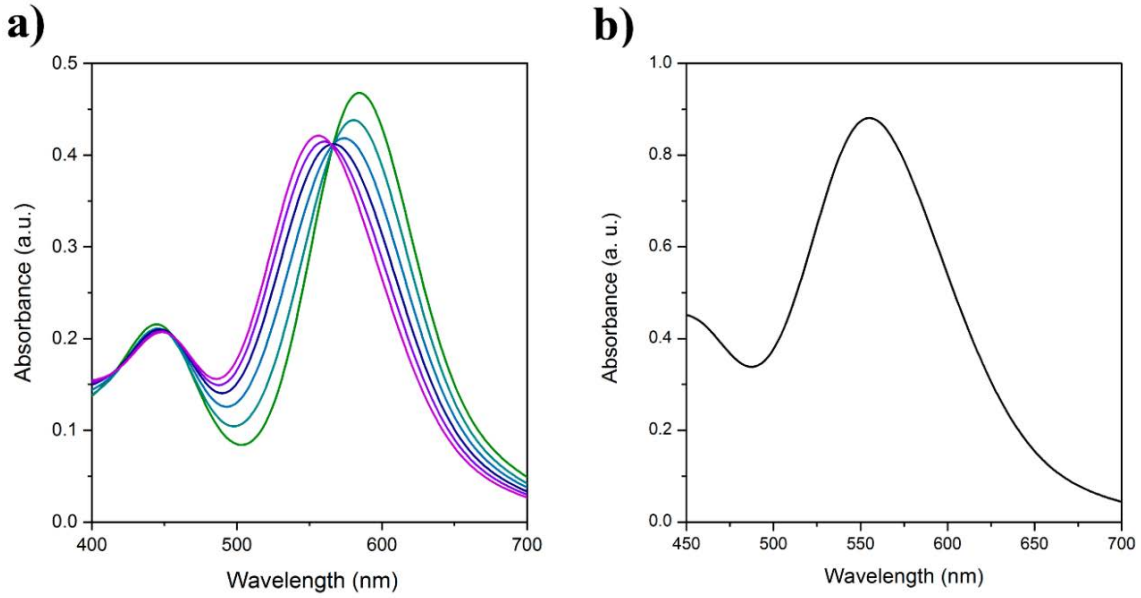

Figure 5.11. (a) UV-Vis spectra of the titration of $Rh_2(OAc)_4$ in water (2 mM) with L-Prol at a pH = 10.5 from 0 mol. eq. (green) to 1 mol. eq. (purple) adding 0.2 mol. eq. of L-Prol per step. After the addition of 1 mol eq., the adsorption maximum of band I (λ_{max}) is centred at 556 nm. (b) UV-Vis of HRhMOP(L-Prol) in water (0.3 mM, pH = 10.5). The λ_{max} is 555 nm that indicates that all the dirhodium paddlewheels in the MOP structure are coordinated to one L-Prol.

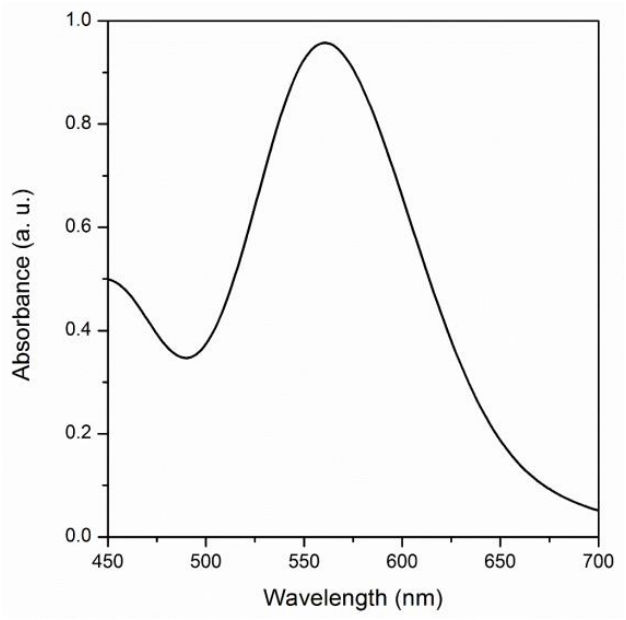

Figure 5.12. UV-Vis of OHRhMOP(L-Prol) in water (0.32 mM, pH = 10.5). The λ_{max} is 560 nm that indicates that all the dirhodium paddlewheels in the MOP structure are coordinated to one L-Prol.

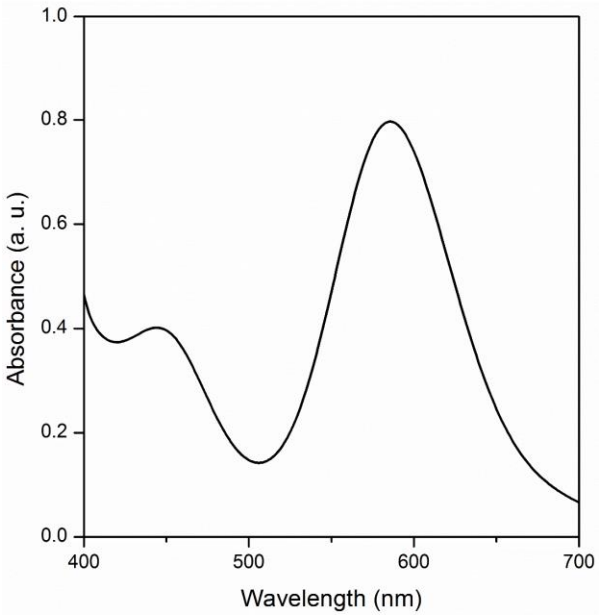

Figure 5.13. UV-Vis spectra of ONaRhMOP in water (0.3 mM). The λ_{max} centred at 586 nm and the presence of a second band centred at 445 confirms the integrity of the dirhodium paddlewheel.

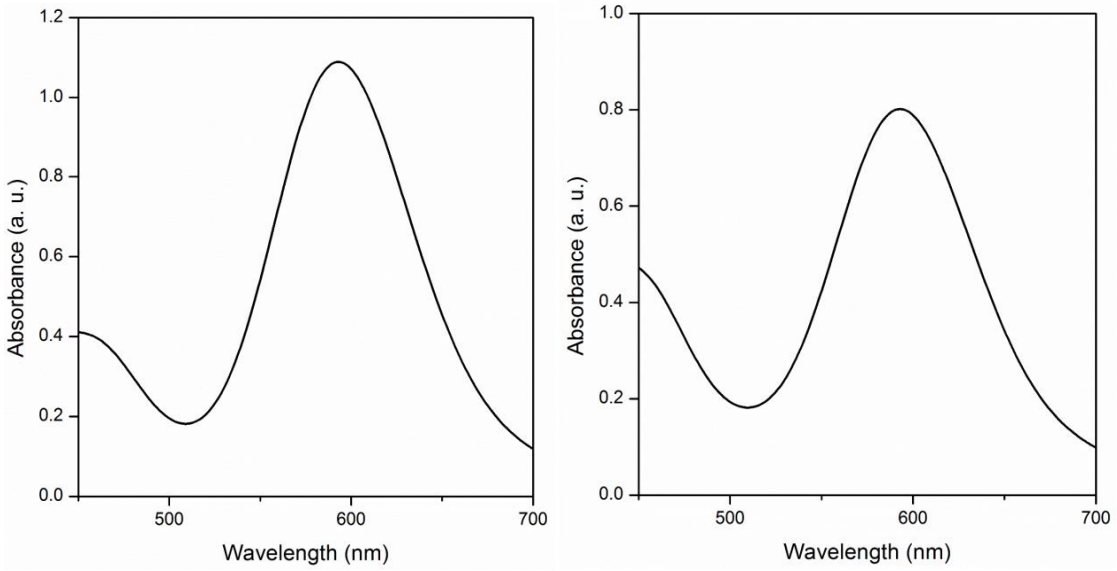

Figure 5.14. (left) UV-Vis of AcrRhMOP in DMF (0.31 mM). λ_{max} is centred at 593 nm. (right) UV-Vis of OMetRhMOP in DMF (0.64 mM). The λ_{max} is centred at 593.

5.3.5. ^{1}H NMR analysis

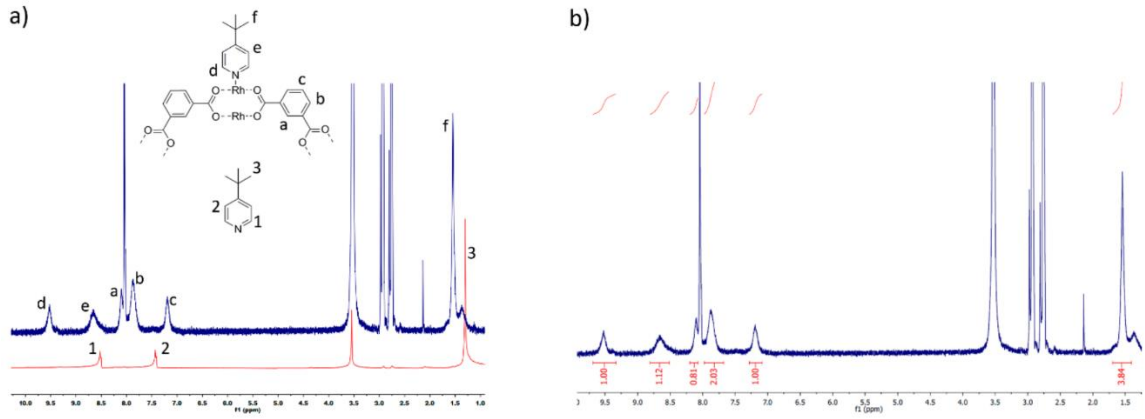

Figure 5.15. (a) Stacked ^{1}H-NMR of HRhMOP(*tert*Py) (blue) and *tert*Py (red) in DMF-d_7 . A shift in the position of the protons of the *tert*Py ligand when coordinated to HRhMOP is observed. (b) ^{1}H-NMR spectra of HRhMOP(*tert*Py) indicating the relative integrals of the assigned proton signals. The molar ratio between bdc and tertPy is 1:0.5, which corresponds to the following formula: $[Rh_2(mBDC)_2(tertPy)_1]_{12}$.

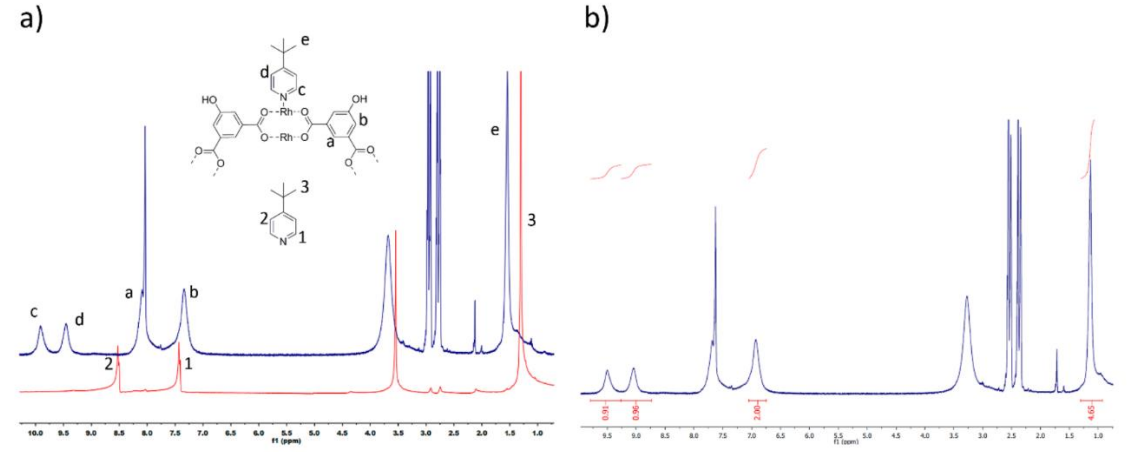

Figure 5.16. (a) Stacked ^{1}H NMR of OHRhMOP(*tert*Py) (blue) and *tert*Py (red) in DMF-d_7. A shift in the position of the protons of the *tert*Py ligand when coordinated to OHRhMOP is observed. (b) ^{1}H NMR spectra of OHRhMOP(*tert*Py) indicating the relative integrals of the assigned proton signals. The molar ratio between OH-*m*BDC and *tert*Py is 1:0.5, which corresponds to the following formula: $[Rh_2(OH\text{-}mBDC)_2(tertPy)_1]_{12}$.

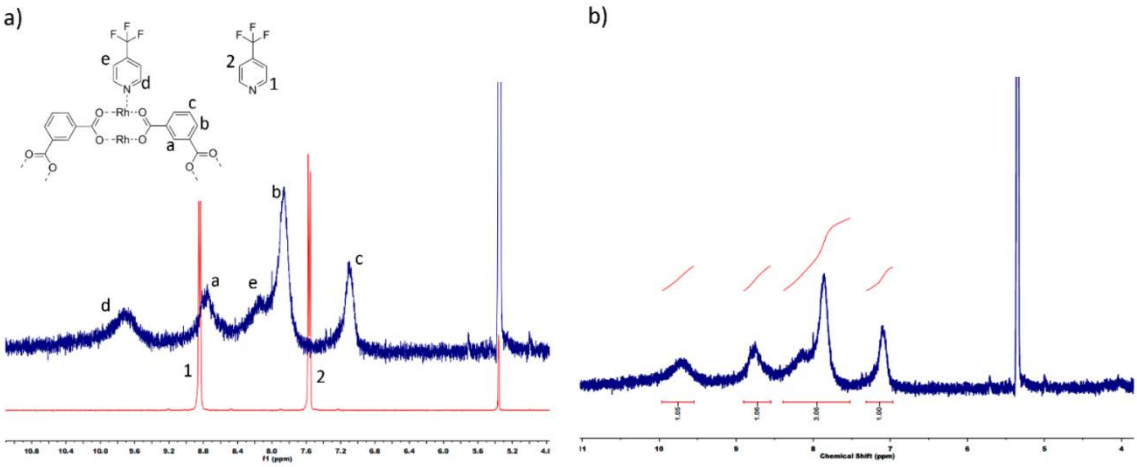

Figure 5.17. (a) Stacked ^{1}H NMR of HRhMOP(CF_3-Py) (blue) and CF_3-Py (red) in DCM-d_2 . A shift in the position of the protons of the CF_3-Py ligand when coordinated to HRhMOP is observed. (b) ^{1}H NMR spectra of HRhMOP(CF_3-Py) in DCM-d_2 indicating the relative integrals of the assigned proton signals. The molar ratio between *m*BDC and CF_3-Py is 1:0.5, which corresponds to the following formula: $[Rh_2(mBDC)_2(CF_3\text{-}Py)_1]_{12}$.

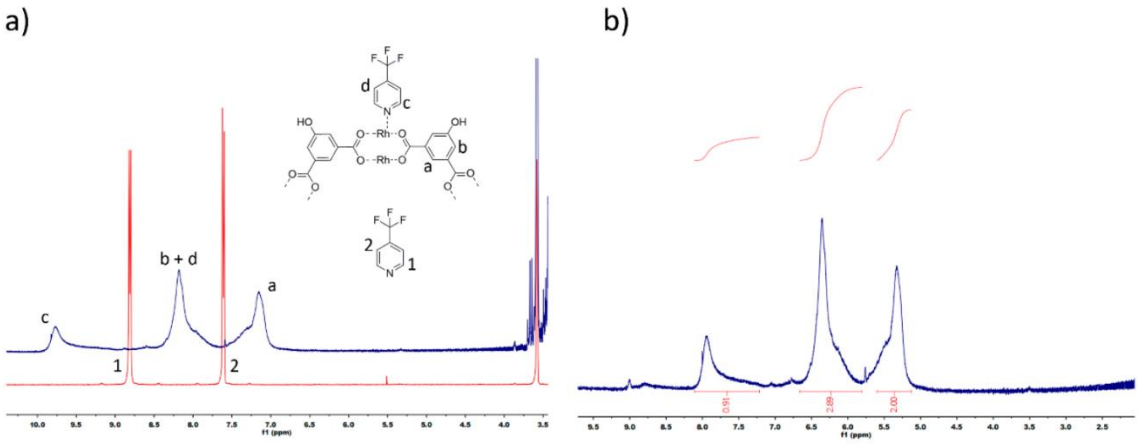

Figure 5.18. (a) Stacked ^{1}H NMR of OHRhMOP(CF_3-Py) (blue) and CF_3-Py (red) in THF-d_8 . A shift in the position of the protons of the CF_3-Py ligand when coordinated to OHRhMOP is observed. (b) ^{1}H NMR spectra of OHRhMOP(CF_3-Py) in THF-d_8 indicating the relative integrals of the assigned proton signals. The molar ratio between *m*BDC and CF_3-Py is 1:0.5, which corresponds to the following formula: $[Rh_2(OH\text{-}mBDC)_2(CF_3\text{-}Py)_1]_{12}$.

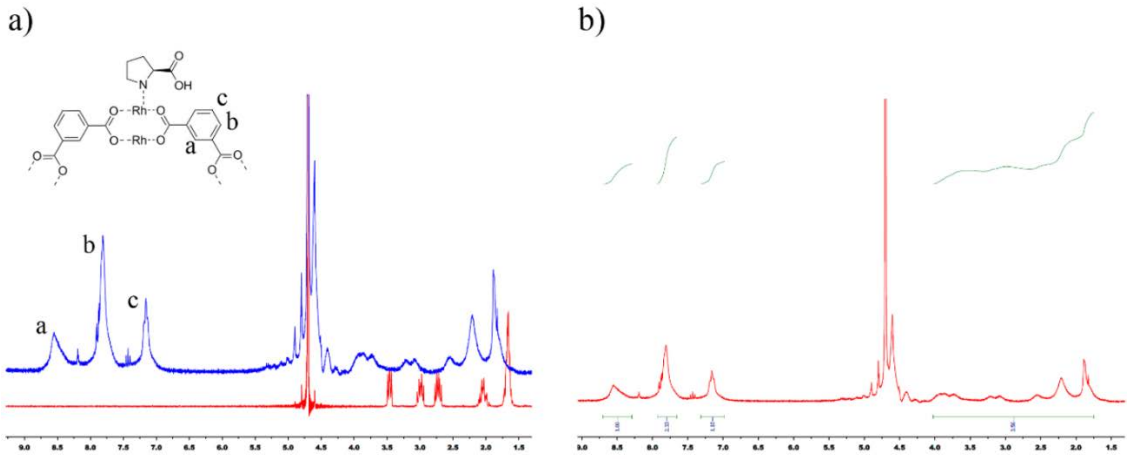

Figure 5.19. Stacked ^{1}H NMR of HRhMOP(L-Prol) (blue) and L-Prol (red) in D_2O at pD = 10.5. A broadening and shifting of the peaks corresponding to the L-Prol is observed, indicating its coordination to the HRhMOP. (b) ^{1}H NMR of HRhMOP(L-Prol) showing the relative integrals of the aromatic protons and the aliphatic protons ascribed to L-Prol. Taking into account that L-Prol has 7 aliphatic protons, the molar ratio between HRhMOP and L-Prol was found to be 1:0.5, giving rise to the following formula: $[Rh_2(mBDC)_2(L\text{-}Prol)_1]_{12}$.

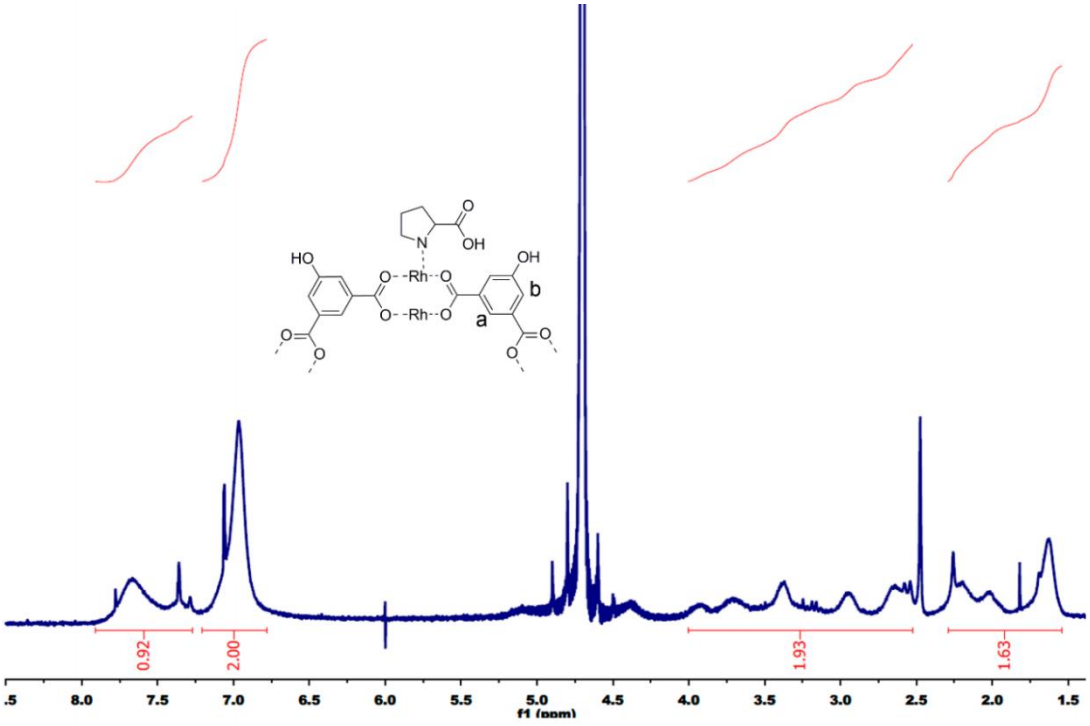

Figure 5.20. ^{1}H NMR of OHRhMOP(L-Prol) in D_2O in pD = 10.3. The relative integrals of the aromatic protons (a and b) and the aliphatic protons ascribed to L-Prol indicate that the molar ration between OH-mBDC and L-Prol is 0.5, giving rise to the following formula: $[Rh_2(OH\text{-}\textit{m}bdc)_2(L\text{-}Prol)_1]_{12}$.

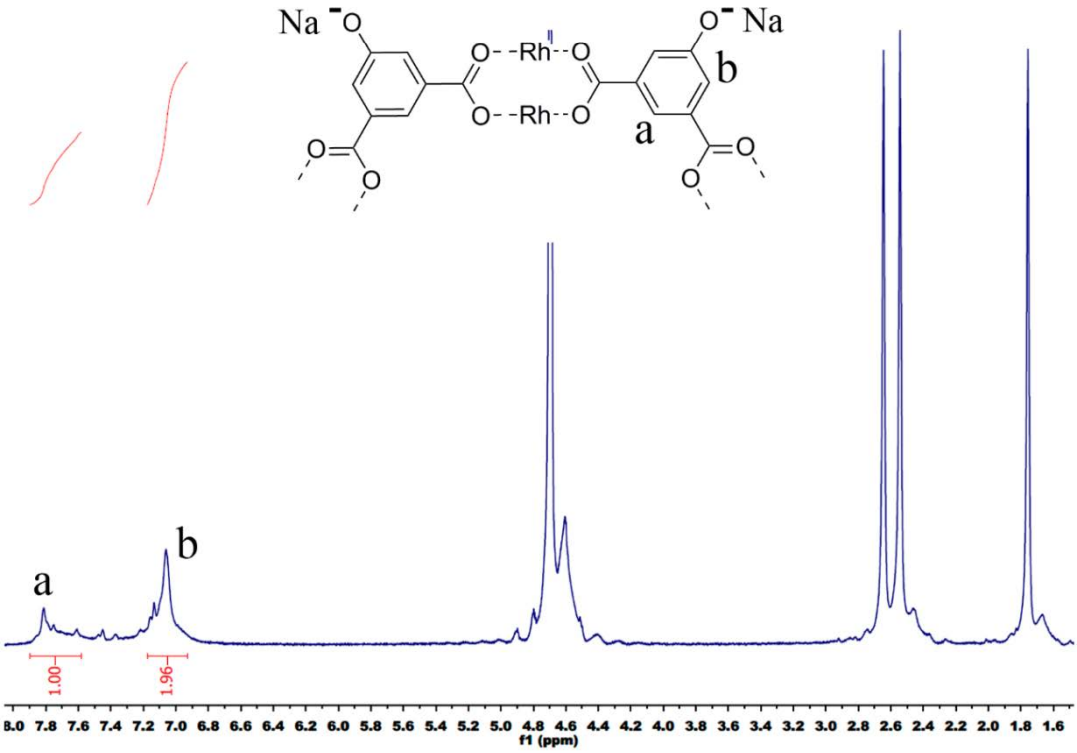

Figure 5.21. ^{1}H NMR of *in situ* formed ONaRhMOP in D_2O. Unassigned picks correspond to DMA and H_2O. The multiplicity of the aromatic protons is attributed to the fact that probably not all phenol groups are deprotonated and therefore, that a mixture of phenol and phenolate groups exists within the Rh-MOP.

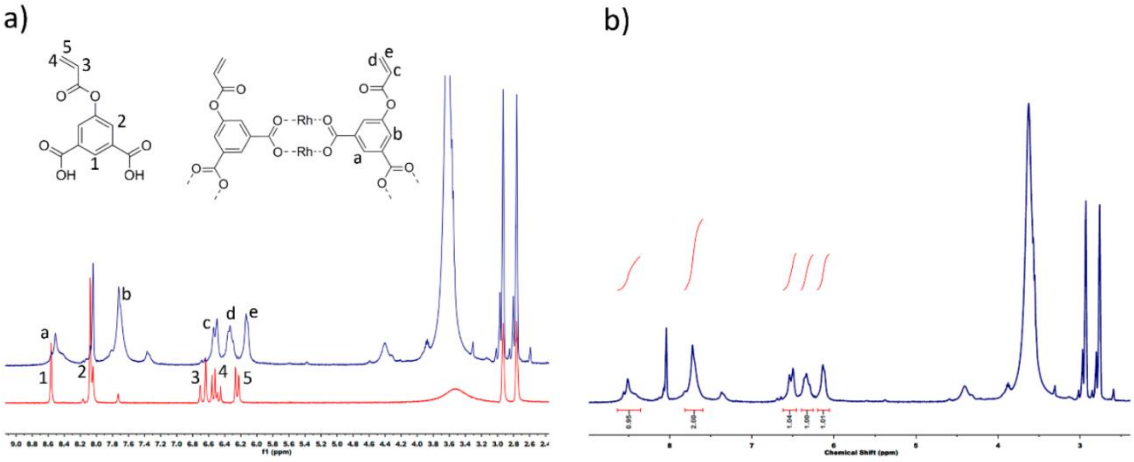

Figure 5.22. (a) Stacked ^{1}H NMR of OAcrRhMOP (blue) and 5-acryloyloxyisophthalic (red). (b) ^{1}H-NMR spectra of OAcrRhMOP indicating the relative integrals of the assigned proton signals. The molar ratio between the aromatic groups and the acrylate protons indicates a full conversion of OH-*m*BDC into the corresponding ester, giving rise to the following formula: $[Rh_2(OAcr\text{-}mBDC)_2]_{12}$.

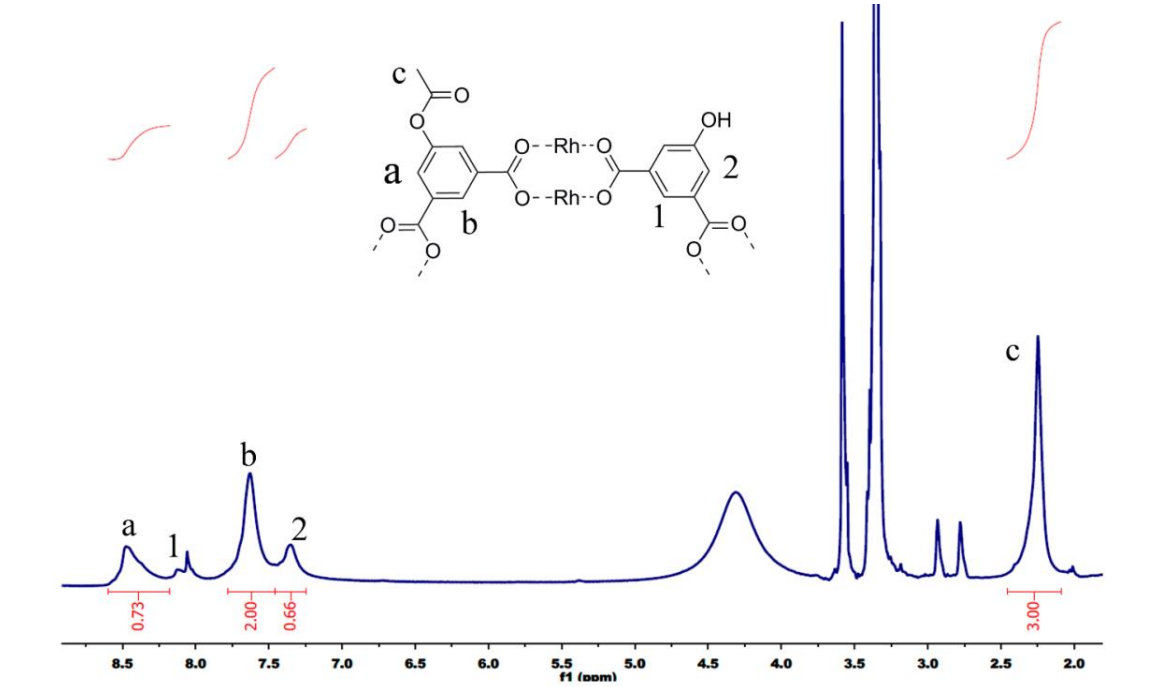

Figure 5.23. ^{1}H NMR of OMetRhMOP in acetone-d_6. Unassigned peaks correspond to water, DMF and acetone. The molar ratio between OH- bdc and the functionalized ligand (COOMet-*m*BDC)) is 0.33, which gives rise to the following formula: $[Rh_{24}(OH\text{-}mBDC)_6(COOMet\text{-}\ mBDC)_{18}]$.

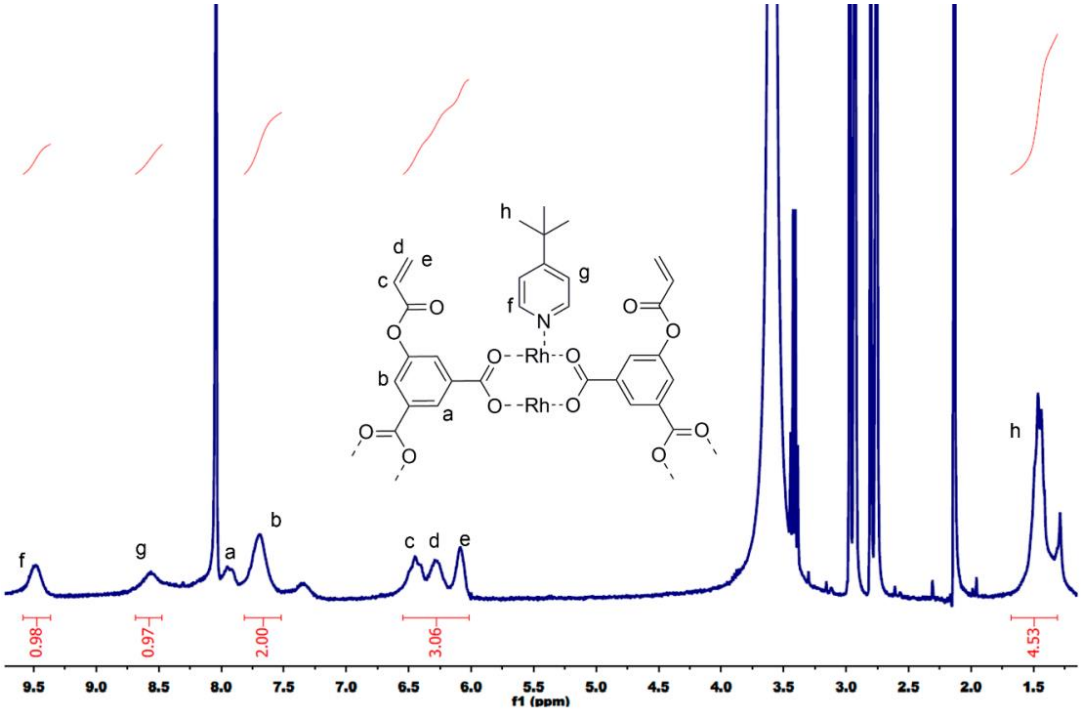

Figure 5.24. ^{1}H NMR spectra of AcrRhMOP(*tert*Py). The relative integrals of the protons of the acrylate ligand (b, c, d, e) and protons of *tert*Py ligand (f, g, h) show that their molar ratio is 0.5, which gives rise to the following formula: $[Rh_2(Acr\text{-}mBDC)_2(tertPy)_1]_{12}$.

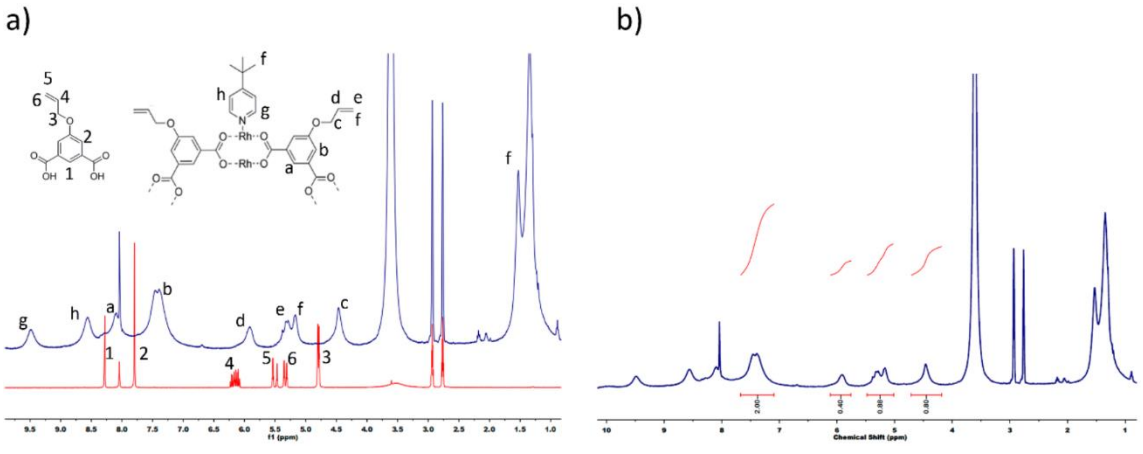

Figure 5.25. (a) Stacked ^{1}H NMR spectra of OallylRhMOP(*tert*Py) (red) and 5-allyloxyisophthalic (red) in DMF-d_7. (b) ^{1}H NMR spectra of OallylRhMOP(*tert*Py) indicating the relative integrals of the assigned proton signals. In order to determine the conversion degree, the relative integrals of the proton **b** and **c** were analysed. Fixing the integral of proton **b** to 2, it follows that the integration of proton c should be 2 if the conversion had been 100%. However, the integration of proton c was 0.8 giving rise to a conversion of 40% with the following formula: $[Rh_2(OH\text{-}mBDC)_{1.2}(Oallyl\text{-}mBDC)_{0.8}]_{12}$.

5.3.6. Mass-Spectrometry (MALDI-TOF) analysis

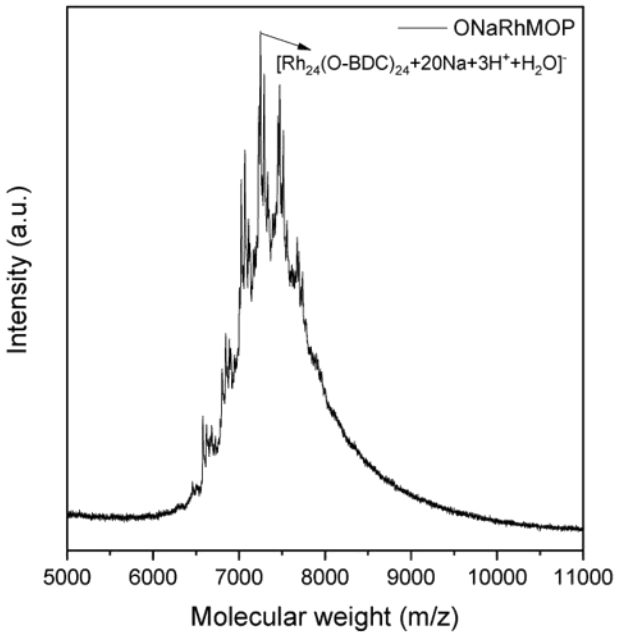

Figure 5.26. MALDI-TOF spectrum of ONaRhMOP. MALDI-TOF spectrum of ONaRhMOP. The weight corresponding to the formula $[Rh_{24}(O\text{-}mBDC)_{24} + 20Na + 3H + H_2O]^-$ has been highlighted: expected = 7247; found = 7246.

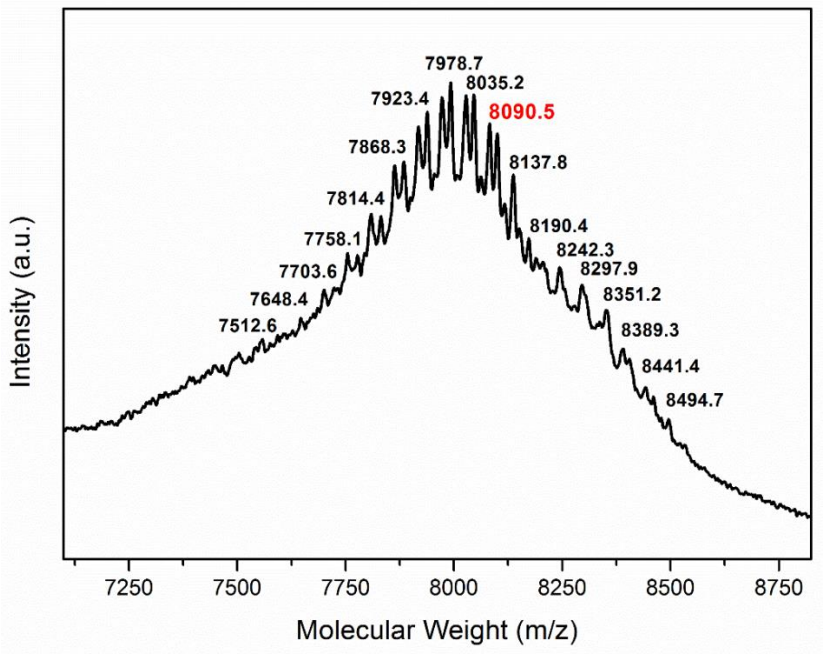

Figure 5.27. MALDI-TOF spectra of OAcrRhMOP. The weight corresponding to the formula $[Rh_{24}(OAcr\text{-}m BDC)_{24} + H]^+$ has been highlighted: expected = 8090.92; found = 8090.5. The other labelled peaks correspond to the loss of acrylates (*m/z* = 55)

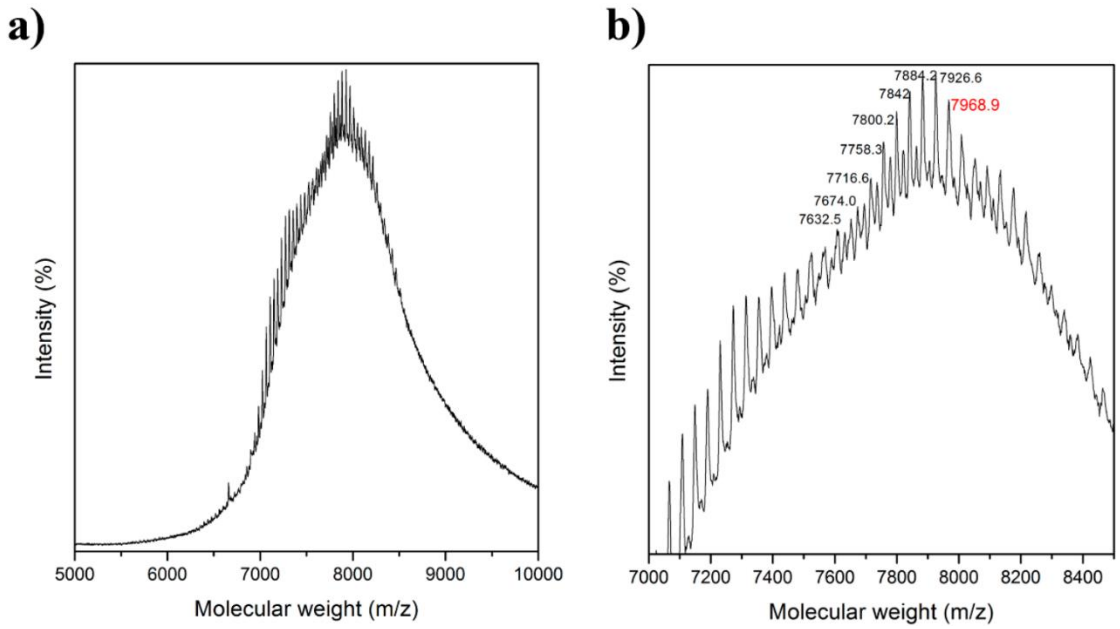

Figure 5.28. (a,b) MALDI-TOF spectra of OMetRhMOP. In (b) the weight corresponding to the formula $[Rh_{24}(OH\text{-}m BDC)_6(COOMet\text{-}bdc)_{18} + H]^+$ + DCTB + DMF + MeOH has been highlighted: expected = 7969.9; found = 7968.3. The other highlighted peaks correspond to the consecutive loses of methyl ester moieties (m/z = 42).

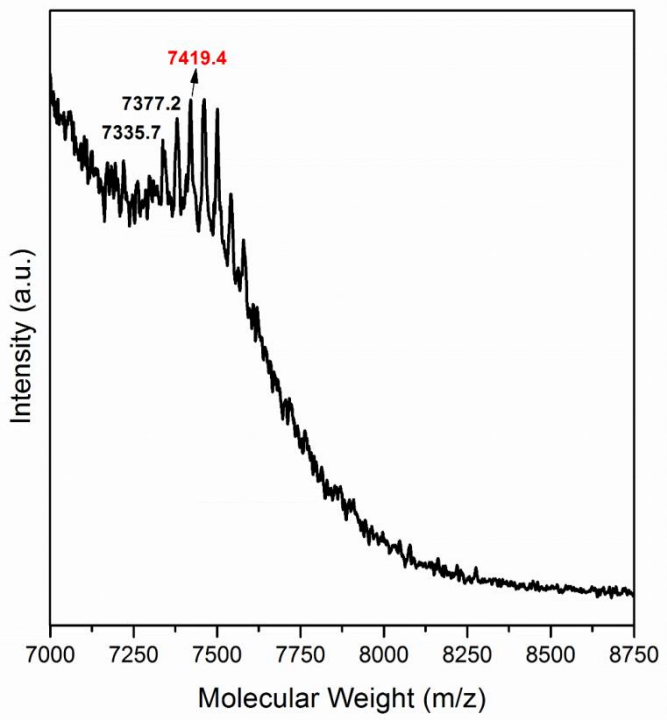

Figure 5.29. MALDI-TOF spectra of OAllyRhMOP. The weight corresponding to the formula $[Rh_{24}(OH\text{-}mBDC)_{15}(OAllyl\text{-}mBDC)_9 + H]^+ + DCTB + H_2O$ has been highlighted: expected = 7418.3; found = 7419.9. The other labelled peaks correspond to the loss of the $CH^2\text{-}CH{=}CH_2$ (*m/z* = 42).

5.3.7. BET measurements

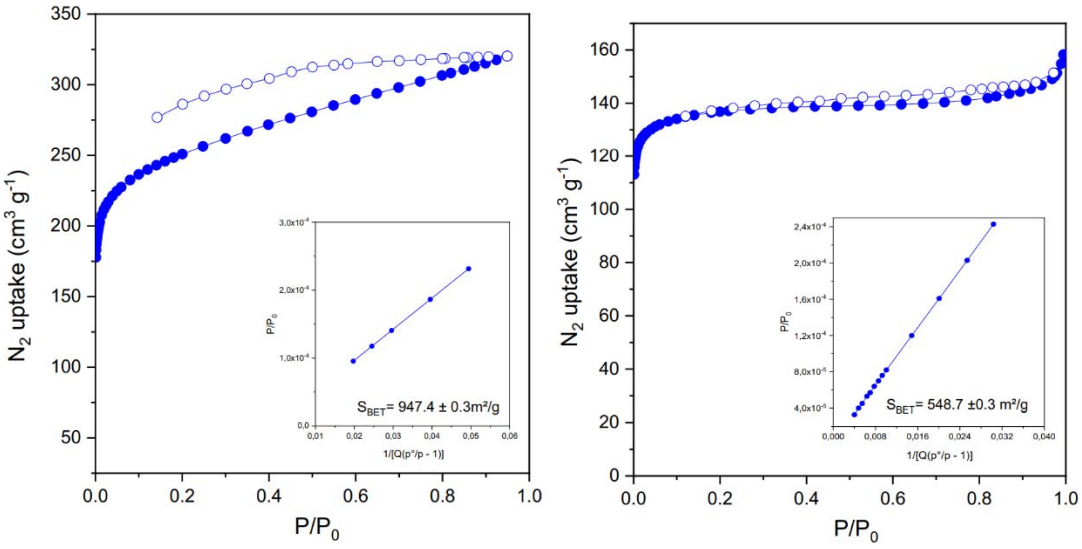

Figure 5.30. N_2 adsorption isotherms of HRhMOP (left) and OHRhMOP (right) at 77 K.

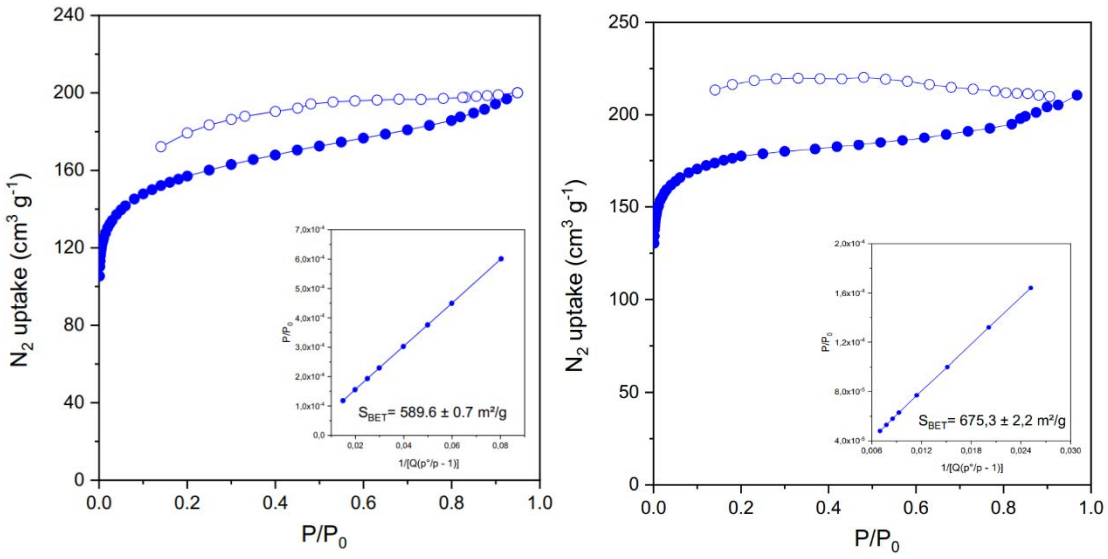

Figure 5.31. N_2 adsorption isotherm of HRhMOP(*tert*Py) (left) and HRhMOP(CF_3-Py) (right) at 77 K.

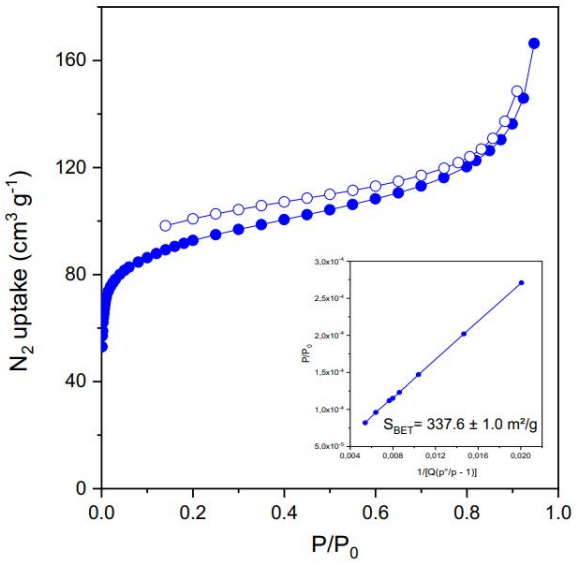

Figure 5.32. N_2 adsorption isotherm of HRhMOP(L-Prol) at 77 K.

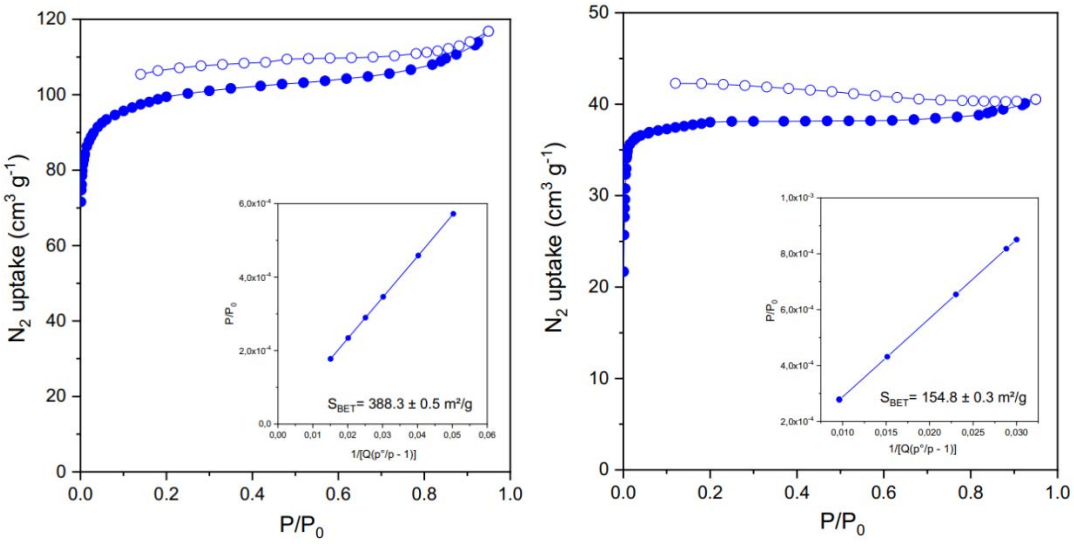

Figure 5.33. N_2 adsorption isotherm of OHRhMOP(*tert*Py) (left) and OHRhMOP(CF_3-Py) (right) at 77 K.

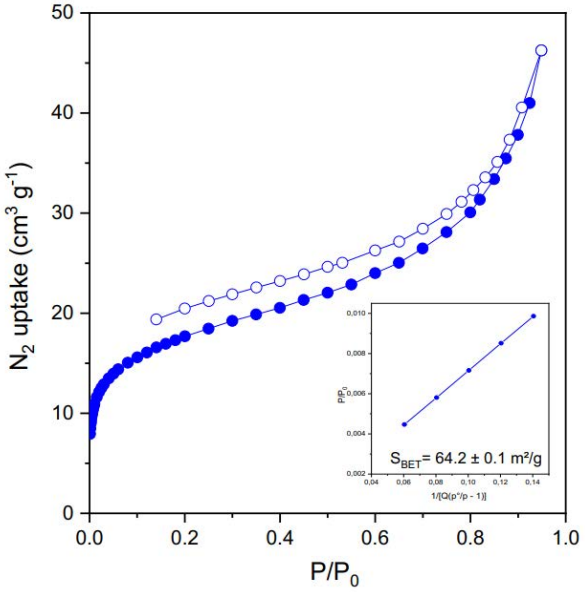

Figure 5.34. N_2 adsorption isotherm of OHRhMOP(L-Prol) at 77 K.

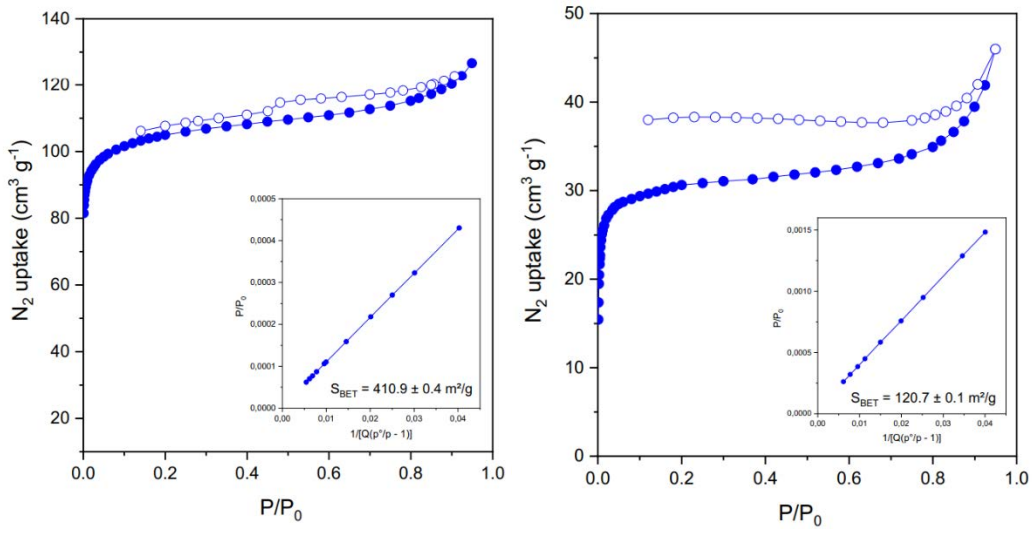

Figure 5.35. N_2 adsorption isotherm of AcrRhMOP (left) and AcrRhMOP(*tert*Py) (right) at 77 K.

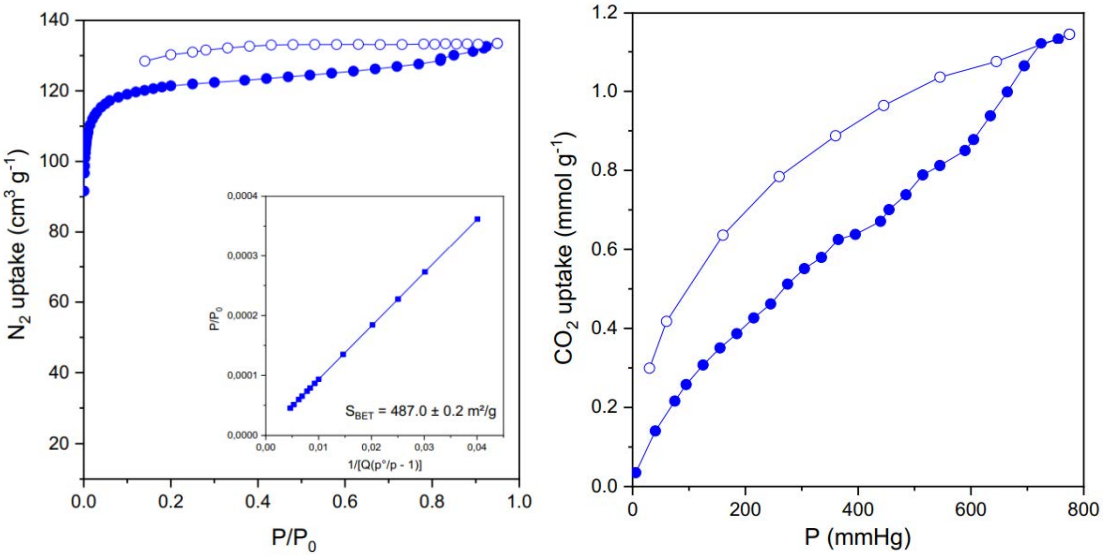

Figure 5.36. N_2 adsorption isotherm of OMetRhMOP at 77 K (left) and CO_2 adsorption isotherm of OAllylRhMOP (right) at RT.

5.4. References

(1) Jin, R.; Zeng, C.; Zhou, M.; Chen, Y. *Chem. Rev.* **2016**, *116* (18), 10346.

(2) Gargas, D. J.; Chan, E. M.; Ostrowski, A. D.; Aloni, S.; Altoe, M. V. P.; Barnard, E. S.; Sanii, B.; Urban, J. J.; Milliron, D. J.; Cohen, B. E.; Schuck, P. J. *Nat. Nanotechnol.* **2014**, *9* (4), 300.

(3) Kim, B. H.; Hackett, M. J.; Park, J.; Hyeon, T. *Chem. Mater.* **2014**, *26* (1), 59.

(4) Liu, Q.; Sun, Y.; Yang, T.; Feng, W.; Li, C.; Li, F. *J. Am. Chem. Soc.* **2011**, *133* (43), 17122.

(5) Ma, K.; Sai, H.; Wiesner, U. *J. Am. Chem. Soc.* **2012**, *134* (32), 13180.

(6) Zarschler, K.; Rocks, L.; Licciardello, N.; Boselli, L.; Polo, E.; Garcia, K. P.; De Cola, L.; Stephan, H.; Dawson, K. A. *Nanomedicine Nanotechnology, Biol. Med.* **2016**, *12* (6), 1663.

(7) Tranchemontagne, D. J.; Ni, Z.; O'Keeffe, M.; Yaghi, O. M. *Angew. Chemie Int. Ed.* **2008**, *47* (28), 5136.

(8) Cullen, W.; Misuraca, M. C.; Hunter, C. A.; Williams, N. H.; Ward, M. D. *Nat. Chem.* **2016**, *8* (3), 231.

(9) Fujita, D.; Ueda, Y.; Sato, S.; Mizuno, N.; Kumasaka, T.; Fujita, M. *Nature* **2016**, *540* (7634), 563.

(10) Zhang, D.; Ronson, T. K.; Nitschke, J. R. *Acc. Chem. Res.* **2018**, *51* (10), 2423.

(11) Cook, T. R.; Stang, P. J. *Chem. Rev.* **2015**, *115* (15), 7001.

(12) Li, J.-R.; Zhou, H.-C. *Nat. Chem.* **2010**, *2* (10), 893.

(13) Rowland, C. A.; Lorzing, G. R.; Gosselin, E. J.; Trump, B. A.; Yap, G. P. A.; Brown, C. M.; Bloch, E. D. *J. Am. Chem. Soc.* **2018**, *140* (36), 11153.

(14) Liu, G.; Ju, Z.; Yuan, D.; Hong, M. *Inorg. Chem.* **2013**, *52* (24), 13815.

(15) Li, J.-R.; Yu, J.; Lu, W.; Sun, L.-B.; Sculley, J.; Balbuena, P. B.; Zhou, H.-C. *Nat. Commun.* **2013**, *4* (1), 1538.

(16) Xing, W.-H.; Li, H.-Y.; Dong, X.-Y.; Zang, S.-Q. *J. Mater. Chem. A* **2018**, *6* (17), 7724.

(17) Eddaoudi, M.; Kim, J.; Wachter, J. B.; Chae, H. K.; O'Keeffe, M.; Yaghi, O. M. *J. Am. Chem. Soc.* **2001**, 123, 4368.

(18) Park, J.; Perry, Z.; Chen, Y.-P.; Bae, J.; Zhou, H.-C. *ACS Appl. Mater. Interfaces* **2017**, *9* (33), 28064.

(19) Ke, Y.; Collins, D. J.; Zhou, H.-C. *Inorg. Chem.* **2005**, 44 (12), 4154.

(20) Furukawa, S.; Horike, N.; Kondo, M.; Hijikata, Y.; Carné-Sánchez, A.; Larpent, P.; Louvain, N.; Diring, S.; Sato, H.; Matsuda, R.; Kawano, R.; Kitagawa, S. *Inorg. Chem.* **2016**, *55* (21), 10843.

(21) Ni, Z.; Yassar, A.; Antoun, T.; Yaghi, O. M. *J. Am. Chem. Soc.* **2005**. 127 (37), 12752.

(22) Boselli, L.; Polo, E.; Castagnola, V.; Dawson, K. A. *Angew. Chemie Int. Ed.* **2017**, *56* (15), 4215.

(23) Jiang, Y.; Huo, S.; Mizuhara, T.; Das, R.; Lee, Y.-W.; Hou, S.; Moyano, D. F.; Duncan, B.; Liang, X.-J.; Rotello, V. M. *ACS Nano* **2015**, *9* (10), 9986.

(24) Ma, K.; Mendoza, C.; Hanson, M.; Werner-Zwanziger, U.; Zwanziger, J.; Wiesner, U. *Chem. Mater.* **2015**, *27* (11), 4119.

(25) Roberts, D. A.; Pilgrim, B. S.; Nitschke, J. R. *Chem. Soc. Rev.* **2018**, *47* (2), 626.

(26) Lu, W.; Yuan, D.; Yakovenko, A.; Zhou, H.-C. *Chem. Commun.* **2011**, *47* (17), 4968.

(27) Zhao, D.; Tan, S.; Yuan, D.; Lu, W.; Rezenom, Y. H.; Jiang, H.; Wang, L.-Q.; Zhou, H.-C. *Adv. Mater.* **2011**, *23* (1), 90.

(28) Brega, V.; Zeller, M.; He, Y.; Peter Lu, H.; Klosterman, J. K. *Chem. Commun.* **2015**, *51* (24), 5077.

(29) Liu, G.; Di Yuan, Y.; Wang, J.; Cheng, Y.; Peh, S. B.; Wang, Y.; Qian, Y.; Dong, J.; Yuan, D.; Zhao, D. *J. Am. Chem. Soc.* **2018**, *140* (20), 6231.

(30) Nam, D.; Huh, J.; Lee, J.; Kwak, J. H.; Jeong, H. Y.; Choi, K.; Choe, W. *Chem. Sci.* **2017**, *8* (11), 7765.

(31) Hosono, N.; Gochomori, M.; Matsuda, R.; Sato, H.; Kitagawa, S. *J. Am. Chem. Soc.* **2016**, *138* (20), 6525.

(32) Vardhan, H.; Yusubov, M.; Verpoort, F. *Coord. Chem. Rev.* **2016**, *306*, 171.

(33) Vardhan, H.; Verpoort, F. *Adv. Synth. Catal.* **2015**, *357* (7), 1351.

(34) Craig, G. A.; Larpent, P.; Kusaka, S.; Matsuda, R.; Kitagawa, S.; Furukawa, S. *Chem. Sci.* **2018**, *9* (31), 6463.

(35) Yan, Y.; Kolokolov, D. I.; da Silva, I.; Stepanov, A. G.; Blake, A. J.; Dailly, A.; Manuel, P.; Tang, C. C.; Yang, S.; Schröder, M. *J. Am. Chem. Soc.* **2017**, *139* (38), 13349.

(36) Zhu, W.; Guo, J.; Ju, Y.; Serda, R. E.; Croissant, J. G.; Shang, J.; Coker, E.; Agola, J. O.; Zhong, Q.; Ping, Y.; Caruso, F.; Brinker, C. J. *Adv. Mater.* **2019**, *31* (12), 1806774.

(37) Carné-Sánchez, A.; Craig, G. A.; Larpent, P.; Hirose, T.; Higuchi, M.; Kitagawa, S.; Matsuda, K.; Urayama, K.; Furukawa, S. *Nat. Commun.* **2018**, *9* (1), 2506.

(38) Kawano, R.; Horike, N.; Hijikata, Y.; Kondo, M.; Carné-Sánchez, A.; Larpent, P.; Ikemura, S.; Osaki, T.; Kamiya, K.; Kitagawa, S.; Takeuchi, S.; Furukawa, S. *Chem* **2017**, *2* (3), 393.

(39) Furukawa, S.; Horike, N.; Kondo, M.; Hijikata, Y.; Carné-Sánchez, A.; Larpent, P.; Louvain, N.; Diring, S.; Sato, H.; Matsuda, R.; Kawano, R.; Kitagawa, S. *Inorg. Chem.* **2016**, *55* (21), 10843.

(40) Giner-Casares, J. J.; Henriksen-Lacey, M.; Coronado-Puchau, M.; Liz-Marzán, L. M. *Mater. Today* **2016**, *19* (1), 19.

(41) Crucho, C. I. C.; Barros, M. T. *Mater. Sci. Eng. C* **2017**, *80*, 771.

(42) Warzecha, E.; Berto, T. C.; Berry, J. F. *Inorg. Chem.* **2015**, *54* (17), 8817.

(43) Juanhuix, J.; Gil-Ortiz, F.; Cuní, G.; Colldelram, C.; Nicolás, J.; Lidón, J.; Boter, E.; Ruget, C.; Ferrer, S.; Benach, J.; IUCr. *J. Synchrotron Radiat.* **2014**, *21* (4), 679.

(44) Chen, L.-J.; Yang, H.-B.; Shionoya, M. *Chem. Soc. Rev.* **2017**, *46* (9), 2555.

(45) Li, S.; Du, X.-S.; Li, B.; Wang, J.-Y.; Li, G.-P.; Gao, G.-G.; Zang, S.-Q. *J. Am. Chem. Soc.* **2018**, *140* (2), 594.

(46) Chen, T.-H.; Wang, L.; Trueblood, J. V.; Grassian, V. H.; Cohen, S. M. *J. Am. Chem. Soc.* **2016**, *138* (30), 9646.

(47) Reiss, P. S.; Little, M. A.; Santolini, V.; Chong, S. Y.; Hasell, T.; Jelfs, K. E.; Briggs, M. E.; Cooper, A. I. *Chem. - A Eur. J.* **2016**, *22* (46), 16547.

Chapter 6

Protection strategies for directionally-controlled synthesis of previously inaccessible Metal-Organic Polyhedra (MOPs): the cases of carboxylate- and amino-functionalized Rh(II)-MOPs

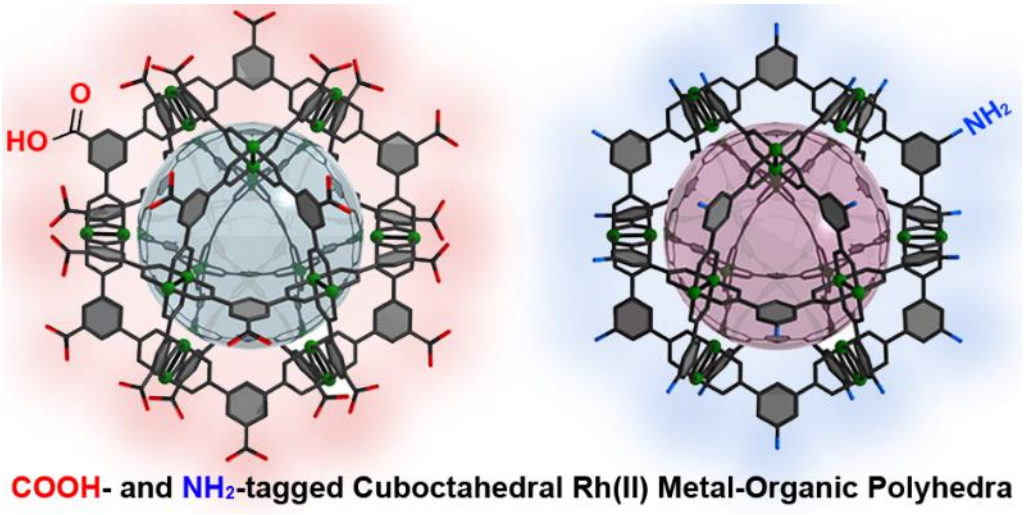

Abstract

This Chapter reports how a strategic use of protecting groups in coordination reactions enables directional inhibition that leads to the synthesis of highly functionalised metal-organic polyhedra (MOPs), rather than extended coordination networks. Using this approach, we were able to functionalise two new porous cuboctahedral Rh(II)-based MOPs with 24 peripheral carboxylic acid groups or 24 peripheral amino groups, expanding the arsenal of existing Rh(II)-based MOPs amenable to surface anchoring.

This Chapter is based on the following publication:

Albalad, J.; Carné-Sánchez, A.; Grancha, T.; Hernández-López, L.; Maspoch D.; *Chem. Commun.,* 2019, **55**, 12785-12788.

6.1. Introduction

Undesired side reactions are arguably the most common limitation any chemical synthesis, either organic or inorganic, faces.[1–5] Even when the simplest synthetic protocol is followed, any minor misstep can lead to wasteful side-products, leading to the costly path of having to start over. Thus, every preparation of delicate molecules must be evaluated at every step in order to eliminate side reactions. Omitting this analysis could lead to reactions in other parts of the molecule, especially on those with multiple functional groups. Thus, a persistent challenge in avoiding side reactions is to ensure that the chemistry in question occurs exclusively at the targeted functional group(s). Functional groups are the reactive sites of a molecule, and it is certainly challenging to restrict a chemical reaction in one group whilst another with similar reactivity remains untouched.[6–8] In these cases, the most common approach is the use of protecting groups (PGs) in order to temporally render an otherwise reactive group into an inert one. Protecting groups act as molecular barriers that covalently bond to a functional group, temporarily removing their reactive behaviour until a further deprotection step takes place.[9] The success of this approach has led to development of a broad arsenal of protecting groups and methodologies for their use, including chemoselective steps for protection and subsequent deprotection of the group(s) whose reactivity is to be temporarily blocked.[10–12] PGs have played an important role in the growth of organic chemistry as a field, as the ability to induce chemoselective and orthogonal reactivity onto polyfunctional molecules opened up unprecedented stepwise reaction pathways for the synthesis of active principles and materials, including polymers[13,14] and peptides[7,8,15–19] with pre-defined sequences of monomers and amino acids.

In coordination chemistry, the use of PGs is less generalized as the reactivity of different functional groups can be controlled by their relative affinity towards metal ions (*e.g.* hard Lewis acids would preferentially react with carboxylates than with amines). This strategy has been successfully employed in the synthesis of multi-varied Metal-Organic Frameworks (MOFs),[20] Metal-Organic Cages[21] and Metal-Organic Polyhedra (MOPs)[22] that present free pending functionalities such as amines, hydroxyls and sulfonate groups, among others. However, there are situations in which these preferential affinities become futile. Not every unreacted functionality can always stand the aggressive media required for the synthesis of coordination assemblies; being due to extra metal-ligand interactions in aggressive conditions, or simply because the functional groups are chemically delicate and amenable to degradation. To this end, few examples of these situations solved through the use of PGs can be found in the literature.[23–26] For example, use of PGs has allowed the introduction of sensitive moieties inside the pore walls, controlling the framework's extension and interpenetration and, in the zero-dimensional field, PGs have allowed to control how Metal-Organic Cages assemble *in situ*.[27] Surprisingly, the most attractive feature of PGs (that is, the stoichiometric control of reactivity) has never been exploited in the

coordination materials field. The directionality of the building blocks plays a major role in the final architecture and dimensionality of the framework. Thus, having a stoichiometric control on the growth step could play an important role to confine at will the degree of extension, from zero-dimensional to 3D.

Herein, we demonstrate how protecting groups can be used to modulate the connectivity of polydentate ligands, which in turn dictates the directional growth of the assembly. We explored this methodology for obtaining previously inaccessible coordination assemblies. Specifically, cuboctahedral Rh(II)-based MOPs with 24 available carboxylic acid (COOH) or amino (NH_2) groups on their periphery were obtained rather than the extended coordination networks that normally form in the absence of protection strategies. As explained in Chapter 5, the synthesis of this class of MOPs entails assembly of 1,3-benzenedicarboxylic acid (mBDC) derivatives and Rh(II)-Rh(II) paddlewheels, in which the 5th position of the mBDC derivative dictates the outer functionality of the MOP.[28] Therefore, chemical limitations can be foreseen when trying to incorporate highly-active functionalities in RhMOPs surface. On one hand, the synthesis of COOH-RhMOP requires use of 1,3,5-benzenetricarboxylic acid (H_3BTC) as the linker. However, as expected, reaction of Rh(II) with H_3BTC tends to form extended coordination networks instead of the desired COOH-RhMOP. This is because the three carboxylic groups react with Rh(II), extending the material uncontrolledly. Consequently, conventional MOP-synthesis conditions (DMA, Na_2CO_3, ~100 °C; detailed synthesis in Section 6.3.2), afford an extended coordination polymer in the form of an amorphous non-porous solid as product (Figures 6.17, 6.18), whereas solvothermal conditions (in methanol) yield a porous coordination polymer.[29] On the other hand, as mentioned in the previous Chapter, Rh(II)–Rh(II) paddlewheel secondary building units (SBUs) present a strong affinity towards free N-donor linkers. For this, the synthesis of an NH_2-functionalised RhMOP is as well unattainable by direct methodologies, unlike with other metal sources.

6.2. Results and Discussion

6.2.1. Protecting groups – From a wide arsenal to the best candidates

We first began our study by carefully selecting the most suitable PG from the available roster.[30] There are myriads of available protection strategies for every functional group. Additionally, most of them offer multiple deprotection pathways to accommodate to the necessities of our targeted molecule.

This project requires very explicit conditions for its successful implementation. The chosen PGs must ensure the following criteria:

(i) Thermal/chemical robustness during the solvothermal MOP synthesis (Na_2CO_3, DMA, 100 ºC)

(ii) Inert behaviour towards free Rhodium metal ions

(iii) Chemoselective or relatively mild deprotection pathways

(iv) Stoichiometric and quantitative protection and/or deprotection steps

(v) Compatibility with free COOH moieties

According to the before-mentioned rules, the selection of a PG for amino moieties was straightforward. The rich chemistry and notorious versatility of NH_2 moieties has led to the generation of a rich reactivity catalogue, including protection/deprotection strategies. There are more documented protective methods for amino groups than for any other moiety, because of how prevalently used they are in peptide chemistry.[19] Among the available PG roster, we selected *tert*-butyloxycarbonyl (Boc) (Figure 6.1) because of its notorious basic stability and compatibility with free COOH groups.

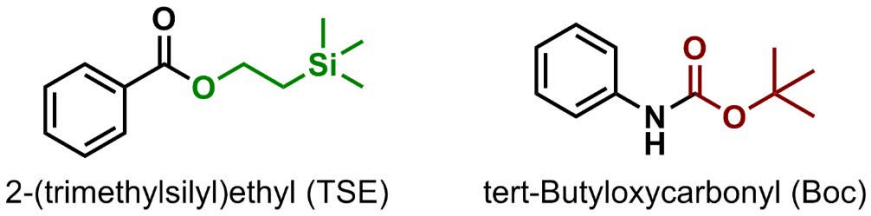

Figure 6.1. Schematic representation of the selected protecting groups.

On the contrary, the synthesis of a COOH-tagged RhMOP requires a stoichiometric protection of 1/3 COOH moieties of H_3BTC, which cannot be obtained in a simple way. There is almost no information on stoichiometric protection/deprotection steps of polycarboxylic acid molecules in the literature, mainly because such steps are never required to be stepwise. The protection of carboxylic acids is usually performed through uncontrolled esterification reactions, whilst the deprotection step is based on non-stoichiometric hydrolysis in basic media to achieve the highest yields. Nevertheless, through an in-depth bibliographic research we were able to spot a stoichiometric deprotection step than involved the use of a less common PG. To this end, we revised the work of Barret *et. al.*,[31] who had previously described a controlled semi-deprotection of a 2-(trimethylsilyl)ethyl-protected (TSE) (Figure 6.1) dicarboxylic acid by stoichiometric addition of fluoride. Since TSE is kinetically stable under basic conditions, we reasoned that it would be suitable for MOP protection.

6.2.2. Symmetrical directional inhibition – The case of COOH-RhMOP

Synthesis of the mono-protected ligand H_2BTC-COOTSE. After selecting TSE as the most suitable PG, we then proceeded with the design of a synthetic methodology for obtaining the TSE mono-protected H_3BTC derivative (hereafter named H_2BTC-COOTSE). The synthetic pathway employed is depicted below in Figure 6.2, and follows a three-step synthetic route (detailed synthetic procedure in Section 6.3.2 – Experimental Part). Such procedure was necessary, as only the TSE deprotection step has proven to be stoichiometrically controllable.

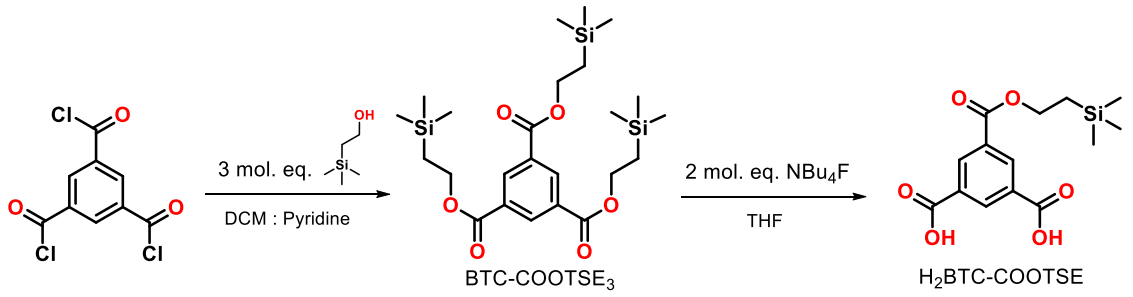

Figure 6.2. Schematic representation of the synthetic procedure for obtaining H_2BTC-COOTSE.

Initially, H_3BTC was converted to its triacyl chloride counterpart *in situ*, through reaction with $SOCl_2$. Then, the triacyl chloride product was reacted with 3 mol. eq. of 2-(trimethylsilyl)ethanol and pyridine to obtain the tri-protected intermediate tris(2-(trimethylsilyl)ethyl)benzene-1,3,5-tricarboxylate (BTC-COOTSE$_3$). Finally, a stoichiometric deprotection of BTC-COOTSE$_3$ was carried out by using 2 mol. eq. of a tetrabutylammonium fluoride (NBu_4F) solution (1.0 M in THF) in two successive additions, followed by a final protonation step. This procedure afforded the mono-protected H_2btc-COOTSE as a fine white powder. The purity and basic media stability of the obtained tri-protected intermediate and H_2BTC-COOTSE were monitored by ^{1}H NMR and ESI-MS (Figures 6.3, 6.4 and 6.5), and no further purification steps were required for the synthesis of RhMOPs.

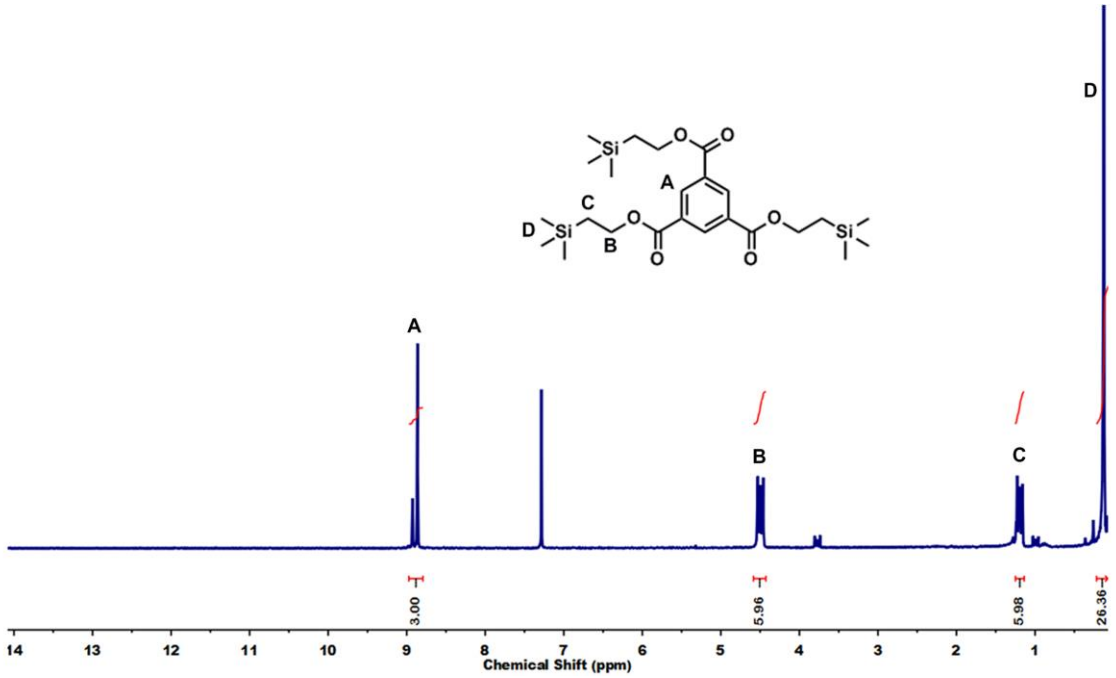

Figure 6.3. ^{1}H NMR spectrum of the tri-protected intermediate BTC-COOTSE$_3$ in CDCl$_3$. The TMS signal (D) is not fully integrable due to the presence of TMS as an internal reference in deuterated solvents.

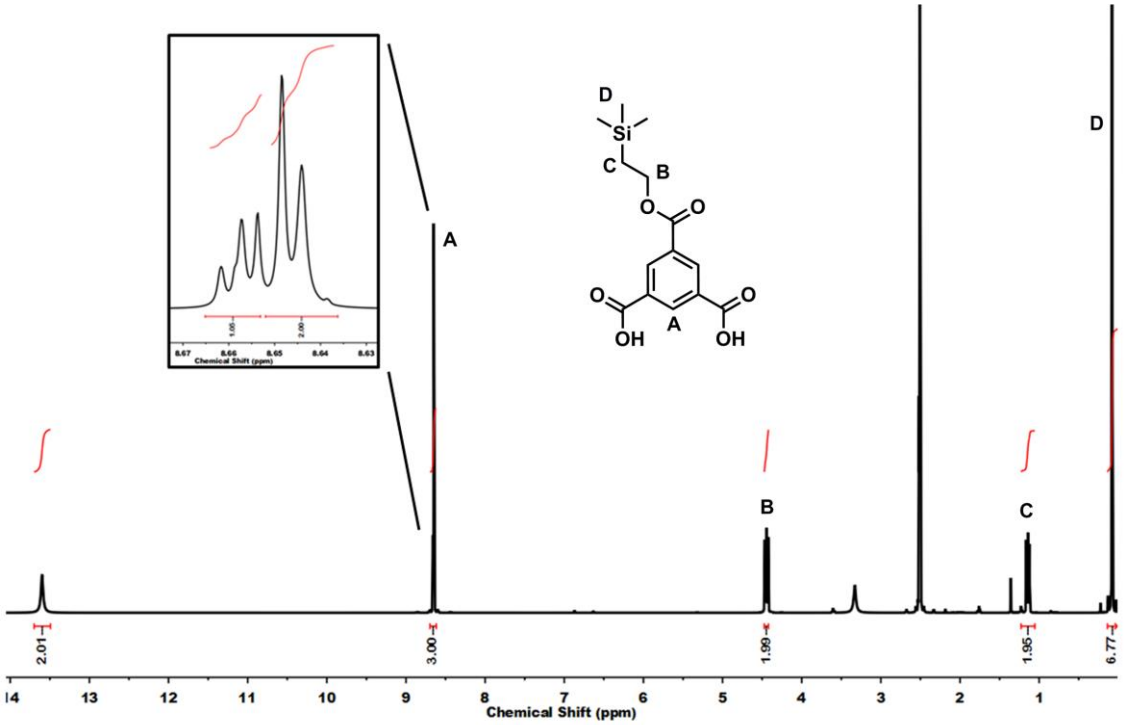

Figure 6.4. ^{1}H NMR spectrum of the mono-protected linker H$_2$BTC-COOTSE in DMSO-*d*$_6$. TMS signal (D) is not fully integrable due to the presence of TMS as an internal reference in deuterated solvents.

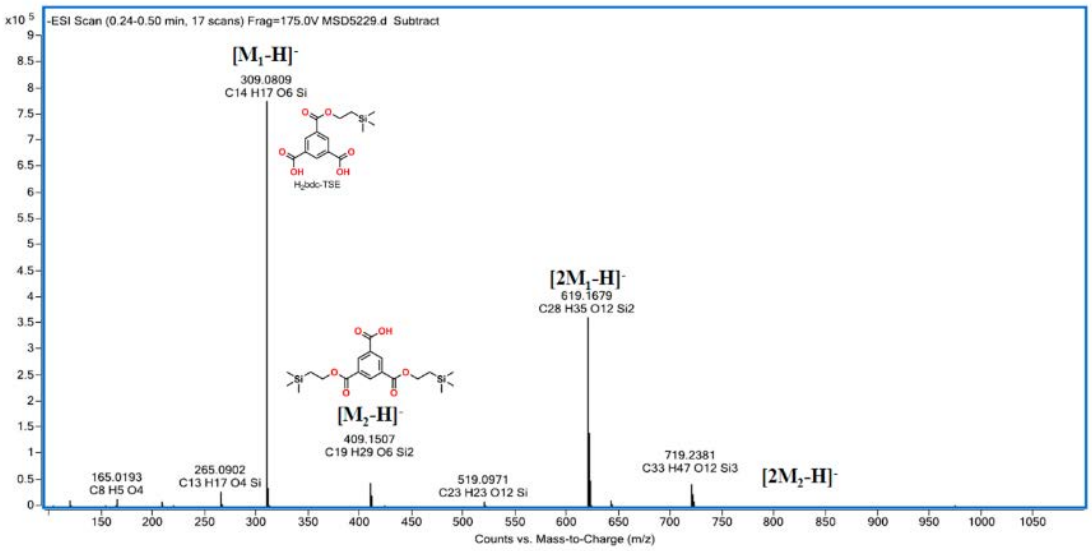

Figure 6.5. ESI-MS spectrum of H_2BTC-COOTSE. Residual traces (<5%) of mono-deprotected linker can be observed.

Synthesis of COOTSE-RhMOP. After properly characterising the linker, we then performed the complexation reaction by mixing H_2BTC-COOTSE with Rhodium acetate in *N'N*-dimethylacetamide (DMA) under solvothermal conditions (100 °C, 48 hours). After separating the residual base by centrifugation, water was used to precipitate out COOTSE-RhMOP from the supernatant, which was obtained as a green solid. The product was sequentially washed with a water:icohol 9:1 mixture and dried under vacuum at 85 ºC. After drying overnight, a final washing step was performed using diethyl ether (Et_2O). Mass Spectrometry (MALDI-TOF) analysis of the washed product in acetone revealed a peak at *m/z* = 9890.3, matching the theoretical value for a cuboctahedral Rh(II)-based MOP of formula $([Rh_{24}(COOTSE\text{-}BDC)_{24}] + H^+)^+$ (expected *m/z*= 9891.5; Figure 6.6a). Additionally, the processability of RhMOPs allowed us to use solution NMR as a fast routine characterisation. ^{1}H NMR of the sample in acetone-d_6 further confirmed the formation of a zero-dimensional architecture featuring 24 TSE protecting groups at its periphery (δ = 8.85, 8.45, 4.35, 1.28, 0.05 ppm) (Figure 6.6b). No residual linker signals were spotted in the spectrum, nor signals of potential degradation of the PGs. Additionally, the integrity of the Rh-Rh paddlewheel SBU was confirmed by UV-Vis and FTIR Spectroscopies (See Section 6.3.3.; Figure 6.19).

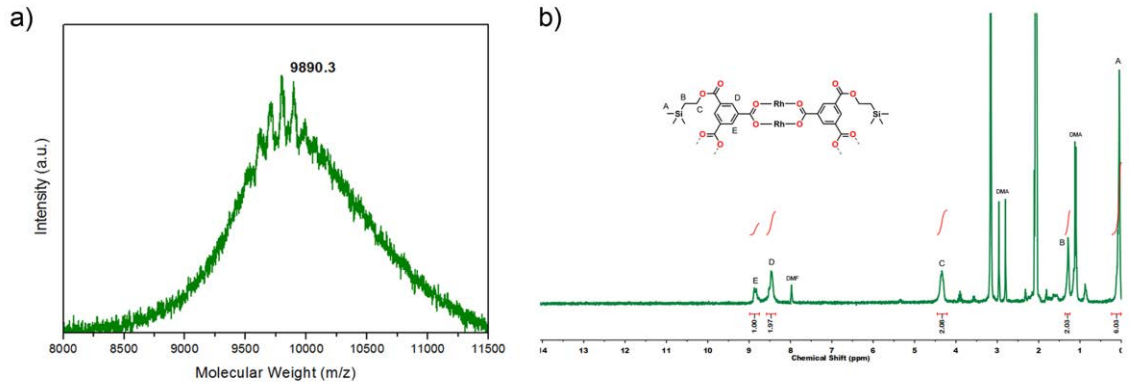

Figure 6.6. a) MALDI-TOF spectra of COOTSE-RhMOP in acetone. The weight corresponding to the formula $[Rh_{24}(TSE\text{-}bdc)_{24} + H^+]^+$ has been highlighted: expected = 9891.5; found = 9890.3. b) ^1H NMR spectrum of COOTSE-RhMOP in acetone-d_6. TMS signal (A) is not fully integrable due to the presence of TMS as an internal reference in deuterated solvents. The chemical shift of the signals is shifted compared with the free linker. No residual H_2btc-COOTSE peaks are observed.

Deprotection step. Next, we did a subsequent deprotection step by reacting a COOTSE-RhMOP solution in THF with 24 mol of a NBu_4F solution (1.0 M in THF) for 6 hours at room temperature. The precipitated product was isolated, washed with THF, Et_2O and water, and finally, dried under vacuum. ^1H NMR (DMSO-d_6) confirmed a quantitative fading of the TSE signals (δ = 0.05 ppm, 1.28 ppm and 4.35 ppm) with the appearance of a new signal at δ = 13.4 ppm, which we attributed to the free COOH groups (Figure 6.7). MALDI-TOF analysis showed a peak at m/z= 7439.4, which matched accordingly with the estimated formula ($[Rh_{24}(COOH\text{-}BDC)_{24}] + H^+)^+$ (expected m/z= 7441.5).

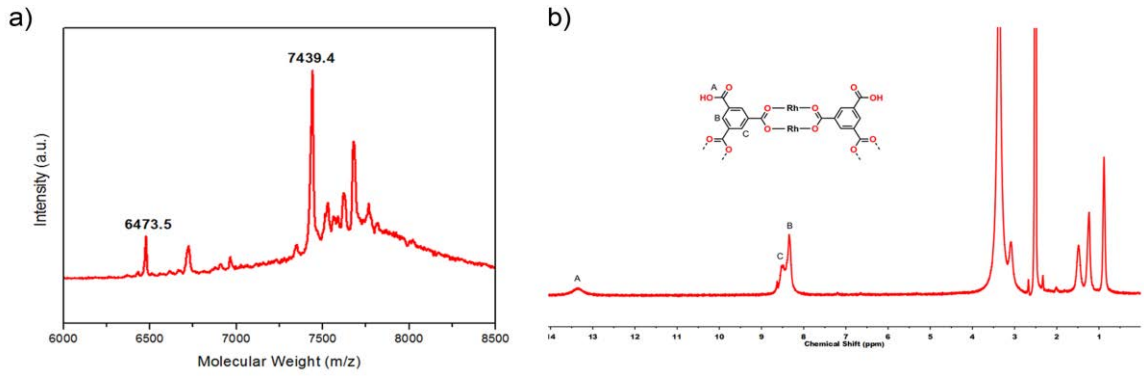

Figure 6.7. ^1H NMR spectrum of COOH-RhMOP in DMSO-d_6. COOH signal is observable at 13.4 ppm, with no residual TSE signals present. MALDI-TOF spectra of COOH-RhMOP in DMF. The weight corresponding to the formula $[Rh_{24}(COOH\text{-}BDC)_{24} + H^+)]^+$ has been highlighted: expected = 7441.5; found = 7439.4. The weight corresponding to the decarboxylation of COOH-RhMOP, with formula $[Rh_{24}(COOH\text{-}BDC)_{24} - 22CO_2 + H^+]^+$ has been highlighted: expected = 6473.3; found = 6473.5.

Porosity measurements of COOTSE- and COOH-RhMOPs. After confirming the phase purity of both COOTSE-RhMOP and COOH-RhMOP, both samples were subjected to gas sorption measurements (N_2, 77 K ; CO_2, RT) after an activation step of 120 ºC for 12 hours. As expected, the deprotection step rendered RhMOPs significantly more porous than the corresponding parent MOPs. Thus, whereas COOTSE-RhMOP was non-porous to N_2, COOH-RhMOP showed a BET surface area (S_{BET}) of 198 $m^2 \cdot g^{-1}$ (See section 6.3.4.; Figure 6.23). Similarly, the CO_2 uptake increased from 0.8 mmol $CO_2 \cdot g^{-1}$ for COOTSE-RhMOP to 2.0 mmol $CO_2 \cdot g^{-1}$ for COOH-RhMOP (Section 6.3.4.; Figure 6.24). The increase of gas uptake observed after the deprotection step is attributed to the removal of the TSE bulky groups from the surface of the Rh(II)-MOP akin to similar examples in which a decrease in surface functionalisation of molecular cages caused a beneficial effect on their porous properties.[32,33]

Single-crystal structural elucidation of COOH-RhMOP. The processable behavior that discrete RhMOPs present enables their crystallization via solvent-induced precipitation methodologies. A concentrated solution of COOH-RhMOP in DMA was subjected to slow diffusion of ether vapours, affording single-crystalline sample that could be structurally resolved in Alba Synchrotron. The as-obtained structure confirmed the presence of 24-oriented COOH moieties symmetrically distributed within the periphery of the MOP (Figure 6.8.).

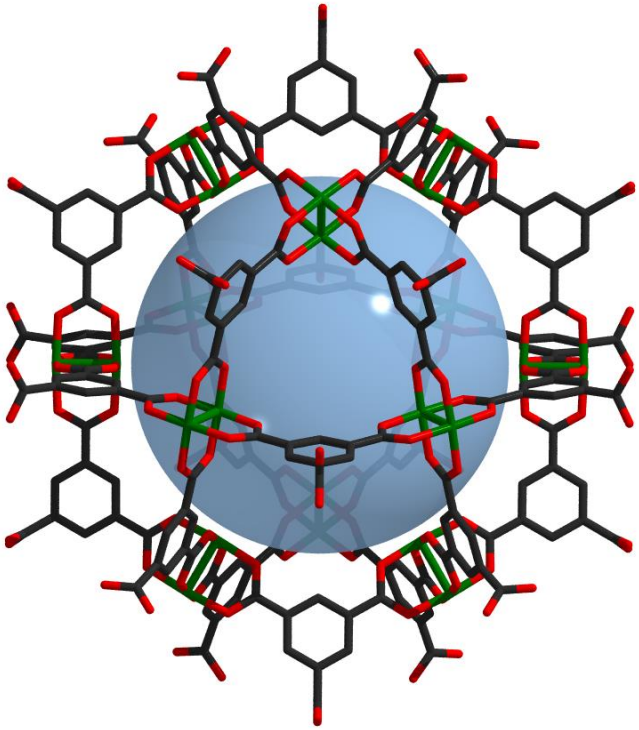

Figure 6.8. Schematic representation of the crystalline structure of COOH-RhMOP, highlighting the 24 free COOH moieties on its periphery. Colour scheme: Rh (green), C (gray), O (red). H atoms omitted for clarity.

COOH-RhMOP aqueous solubility and stability tests. Carboxylic acids typically have moderately low pKa values (*i.e.* pKa = 3 to 5). Therefore, at near-physiological pH, they tend to be deprotonated in solution. Accordingly, COOH-RhMOP dissolved in water upon addition of 1 mol. eq. (*i.e.* 24 mol per MOP) of NaOH (pH = 10.5), rendering a negatively-charged MOP, as evidenced by the Z-potential value derived by Dynamic Light Analysis measurements (Figure 6.9). MALDI-TOF analysis of the solution revealed a peak at *m/z* = 7945.6 (Figure 6.10a), matching the theoretical formula $(Na_{24}[Rh_{24}(OOC\text{-}BDC)_{24}] - 2Na^{+} + H^{+})^{-}$ (expected *m/z* = 7947.0, hereafter called COONa-RhMOP). After confirming the solubility of COOH-RhMOP in basic pH, we ran a pH calibration curve to identify the lowest pH at which the cage would be water soluble. After the addition of 6 mol of NaOH (25% of COOH groups deprotonated), the MOP fully dissolved in water giving a final pH value of pH= 8.2. ^{1}H NMR of the product after it had been in aqueous solution for 7 days did not reveal any signs of scaffold degradation (Figure 6.10b). Additionally, the RhMOP was able to be sequentially precipitated by protonation and dissolved again with addition of base without any significant integrity loss.

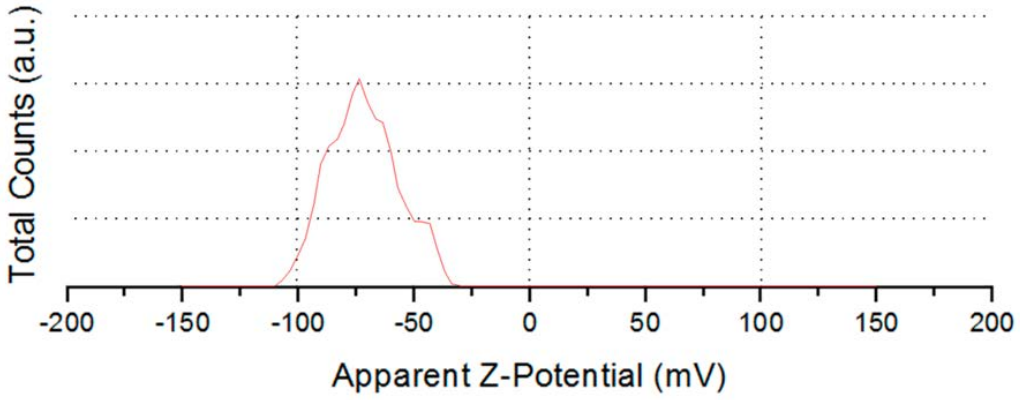

Figure 6.9. Z-Potential measurements of COONa-RhMOP in basic H_2O, confirming a charged specie.

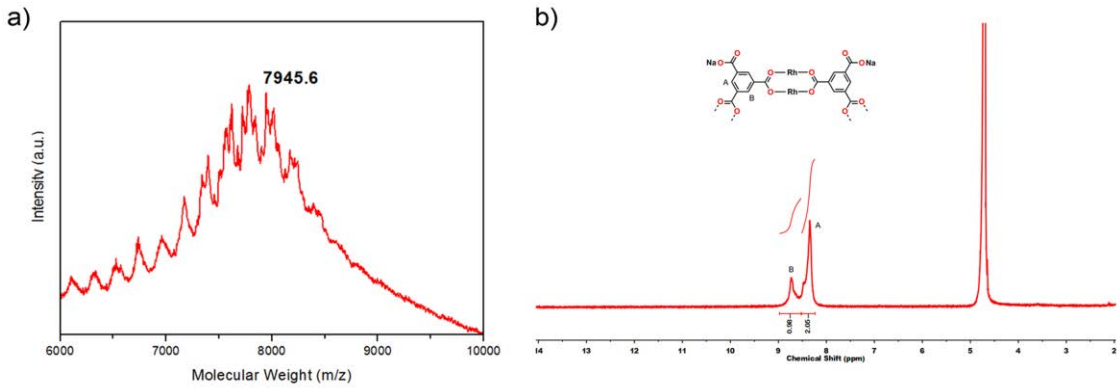

Figure 6.10. a) MALDI-TOF spectrum of COONa-RhMOP. The weight corresponding to the formula $[Rh_{24}(COONa\text{-}BDC)_{24} - 2Na^{+} + H^{+})]^{-}$ has been highlighted: expected = 7947; found = 7945.6. b) ^{1}H NMR spectrum of COONa-RhMOP in D_2O/NaOD (24 mol. eq. vs MOP) dissolved for 7 days.

6.2.3. Orthogonal directional inhibition – The case of NH_2-RhMOP

Inspired by our previous results, we then aimed to extend our MOP-protection chemistry by endeavouring to incorporate functionalities that had previously been inaccessible in Rh-based materials. The strong affinity of Rh(II) paddlewheels towards N-donor groups precludes the synthesis of a NH_2-tagged Rh(II)-based MOP, unlike with other metal sources. Amino groups are among the most exploited functional groups in the literature, owing to their basicity, dominant nucleophilicity and versatility, as they can be transformed into myriad products under diverse conditions. This has led to the generation of a rich catalogue of amine chemistry. Moreover, amino-functionalized materials can exhibit enhanced physicochemical properties and have been thoroughly used in many applications, such as surface anchoring, carbon dioxide capture, water uptake and pollutant removal. For this, we explored the possibility of protecting the reactive NH_2 moiety of 5-aminoisophthalic acid with a suitable protecting group to synthesise the desired RhMOP. Note that as in the formation of COOH-RhMOP, a direct reaction of Rh acetate with 5-aminoisopthalic acid under solvothermal conditions produced an extended coordination network in the form of an amorphous solid. As previously mentioned, we chose *tert*-butyloxycarbonyl (Boc) as our PG, given its excellent stability in basic media and its compatibility with free carboxylates.

Synthesis of the mono-protected ligand H_2BDC-NBoc. The amino-protected linker was synthesised adapting a literature procedure. Briefly, H_2bdc-NBoc was obtained by reacting 5-aminoisophthalic acid with di-*tert*-butyl dicarbonate (Boc_2O) in a mixture (1:1 v/v) of dioxane and 1M NaOH (Figure 6.11). A subsequent addition of a 20% $KHSO_4$ aqueous solution precipitated the linker on its protonated form, and the product was thoroughly washed with water and dried under vacuum. Its phase purity was confirmed by ^{1}H NMR analysis (Figure 6.12).

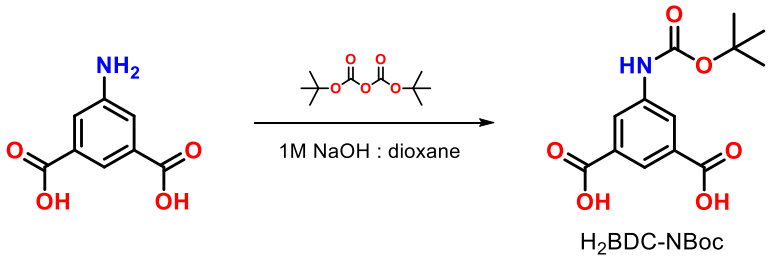

Figure 6.28. Schematic representation of the synthetic procedure for obtaining H_2BTC-COOTSE.

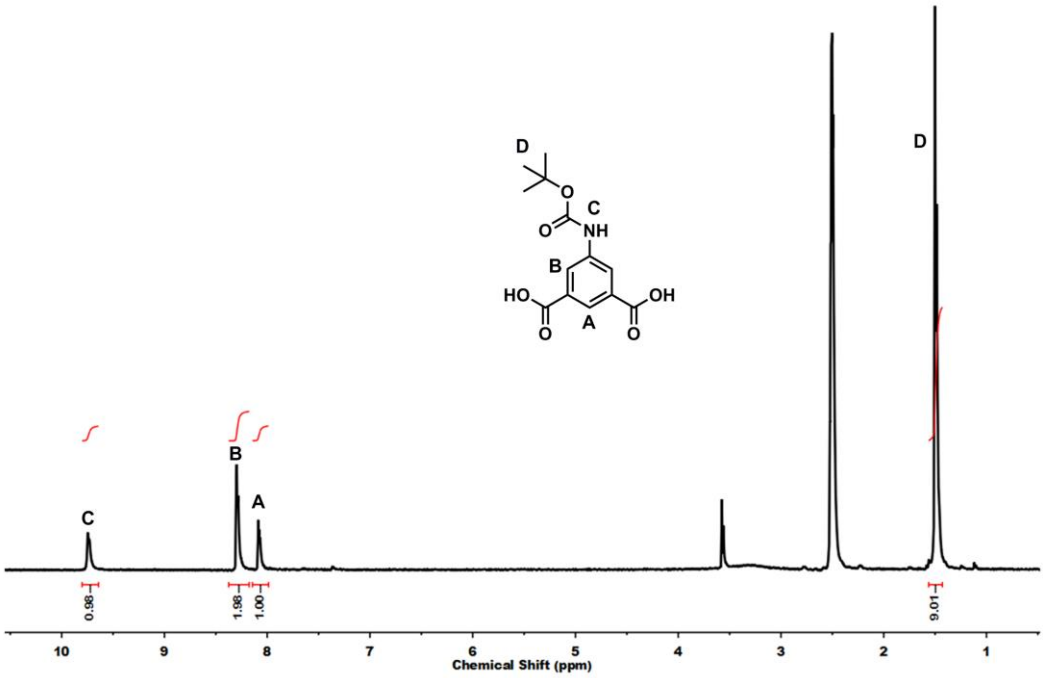

Figure 6.29. ^{1}H NMR spectrum of H_2BDC-NBoc in DMSO-*d*$_6$.

Synthesis of NBoc-RhMOP. The purified H_2BDC-NBoc linker was then reacted with rhodium acetate and Na_2CO_3 in DMA at 100 °C for 48 hours. After that, the residual solids were discarded and the supernatant was precipitated by the addition of diethyl ether. The as-obtained blue product was then washed with a 1M NaOH solution and water and dried under vacuum. The formation and phase purity of NBoc-RhMOP was confirmed by MALDI-TOF (*m/z* = 9110.1; expected 9105.4; Figure 6.13a) and ^{1}H NMR (δ = 9.24, 8.40 and 1.41 ppm) (Figure 6.13b).

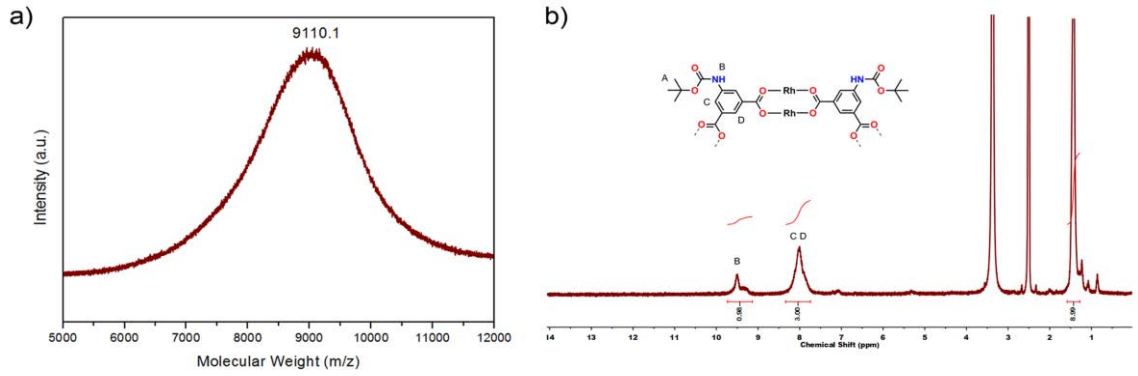

Figure 6.30. a) MALDI-TOF spectra of NBoc-RhMOP in Acetone. The weight corresponding to the formula $[Rh_{24}(NBoc\text{-}BDC)_{24} - NBoc + H^{+}]^{+} + 2H_2O$ has been highlighted: expected = 9105.4; found = 9110.1. b) ^{1}H NMR spectrum of NBoc-RhMOP in DMSO-*d*$_6$. The chemical shift of the signals is shifted compared with the free linker. No residual H_2BDC-NBoc peaks are observed.

Deprotection step(s). Finally, we explored the deprotection of NBoc-RhMOP by following standard procedures deeply employed in organic synthesis. That is, subjecting the RhMOP to stirring it in a solution of trifluoroacetic acid (TFA; 9 mol. eq. vs MOP in dichloromethane) for a few hours in an heterogeneous fashion. UV-Vis and ^{1}H NMR analysis of the obtained supernatant (Figure 6.14a,b) did not reveal any signals of leached 5-aminoisophthalic acid linker nor partial degradation, thereby confirming the robustness of the MOP under the deprotection conditions. The crude product was then neutralised with a triethylamine solution in acetone, washed with methanol and acetone, and characterised by ^{1}H NMR and MALDI-TOF (Figure 6.15).

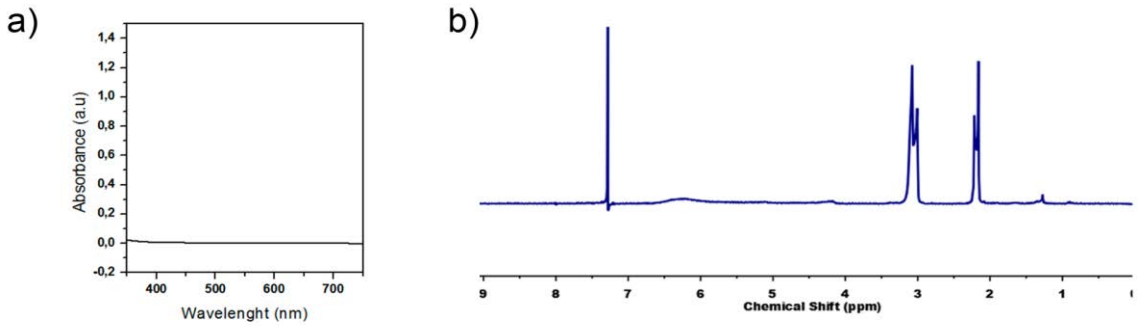

Figure 6.31. a) UV-Vis spectrum and b) ^{1}H NMR spectrum of the TFA-deprotection supernatant.

Both techniques confirmed that the deprotection had been quantitative. Likewise, ^{1}H NMR analysis evidenced generation of free amino moieties in the MOP (δ= 5.32 ppm) and quantitative fading of all the previous NBoc signals (δ= 9.50 ppm and 1.42 ppm) when exploring deprotection steps in more diluted conditions (*i.e.* 3 mol eq. per MOP and 6 mol. eq. per MOP). In addition, MALDI-TOF analysis in DMSO revealed a peak at *m/z* = 6899.2, consistent with the formula of the fully deprotected RhMOP $[Rh_{24}(NH_2\text{-BDC})_{24} + H^+ + DMSO]^+$ (expected m/z= 6895.3; Figure 6.15, navy blue).

Additionally, taking advantage of the processability of RhMOPs in the solid state, we explored an alternative route for the deprotection of NBoc-RhMOP in a solventless fashion, reflecting on the fact that the Boc group can undergo thermolytic deprotection without any reagents, solvents or neutralisation step.[34,35] To this end, we ran a thermogravimetric analysis (TGA) on NBoc-RhMOP to identify the weight-loss attributable to the thermolabile deprotection (Figure 6.16, top). The thermogram clearly showed a step of 24.9% weight-loss in the region between 150 °C to 200 °C, owing to the thermolytic cleavage of 24 Boc groups into CO_2 and isobutylene (25.1% based on theoretical mass). Afterwards, we ran an isothermal

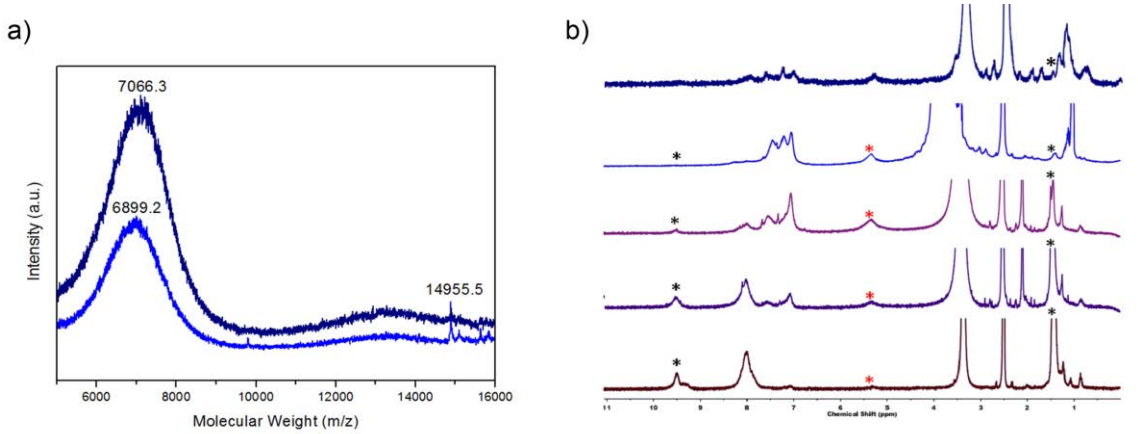

Figure 6.32. a) MALDI-TOF spectra of NH2-RhMOP in DMSO, deprotected through the Thermolabile strategy (navy) and TFA-based strategy (blue). The weight corresponding to the formula [Rh24(NH2-BDC)24 +H+] + DMSO (expected = 6895.3, found = 6899.2) and Rh24(NH2-BDC)24 +H+] + 3DMSO + H2O (expected = 7069.6, found = 7066.3) have been highlighted. Small packings of two NH2-RhMOP units (m/z = 14,955) can start to be observed, due to the strong affinity of Rh paddlewheels for N-donor functional groups. b) 1H NMR spectrum of the TFA-based Deprotection strategy of NBoc-RhMOP (wine) in DMSO-d6. After the addition of 3 mol. eq. (deep purple), 6 mol. eq. (light purple) and 9 mol. eq. of TFA (blue). Fading NBoc signals are highlighted in black (*) and arising NH2 signal in red (*). Thermolabile-deprotected NH2-RhMOP is represented on top (navy).

experiment at 150 °C for 6 hours to confirm that no further degradation of the MOP would occur. After the initial weight loss attributable to solvent loss and the deprotection itself, the curve plateaued until the end of the measurement, thus confirming the robustness of the scaffold (Figure 6.16, bottom). MALDI-TOF analysis of the crude product further confirmed the thermal cleavage, with a peak at *m/z* = 7066.3 matching with the formula $[Rh_{24}(NH_2\text{-}BDC)_{24} + H^+ + H_2O + 3\ DMSO]^+$ (expected m/z= 7066.3) (Figure 6.15a, blue).

Porosity measurements of NBoc- and NH_2-RhMOPs. Analogously to the deprotection of COOTSE-RhMOP, the deprotection of NBoc-RhMOP (either by thermolysis or by treatment with TFA) yielded a product that was more porous than the corresponding starting material. Thus, whereas the S_{BET} of the NBoc-RhMOP was 59 $m^2 \cdot g^{-1}$ (See Section 6.3.4.; Figure 6.26), upon deprotection, the resultant NH_2-RhMOP showed S_{BET} values of 255 $m^2 \cdot g^{-1}$ (thermolysis) or 417 $m^2 \cdot g^{-1}$ (TFA) (Section 6.3.4.; Figure 6.27). We attributed the difference in S_{BET} between these two products to their different morphologies: the thermolytic deprotection of NBoc-RhMOP yields micrometric particles, whereas the TFA-based method yields an amorphous powder composed of aggregated nanoparticles (*ca*. 50 nm) (Figure 6.17).

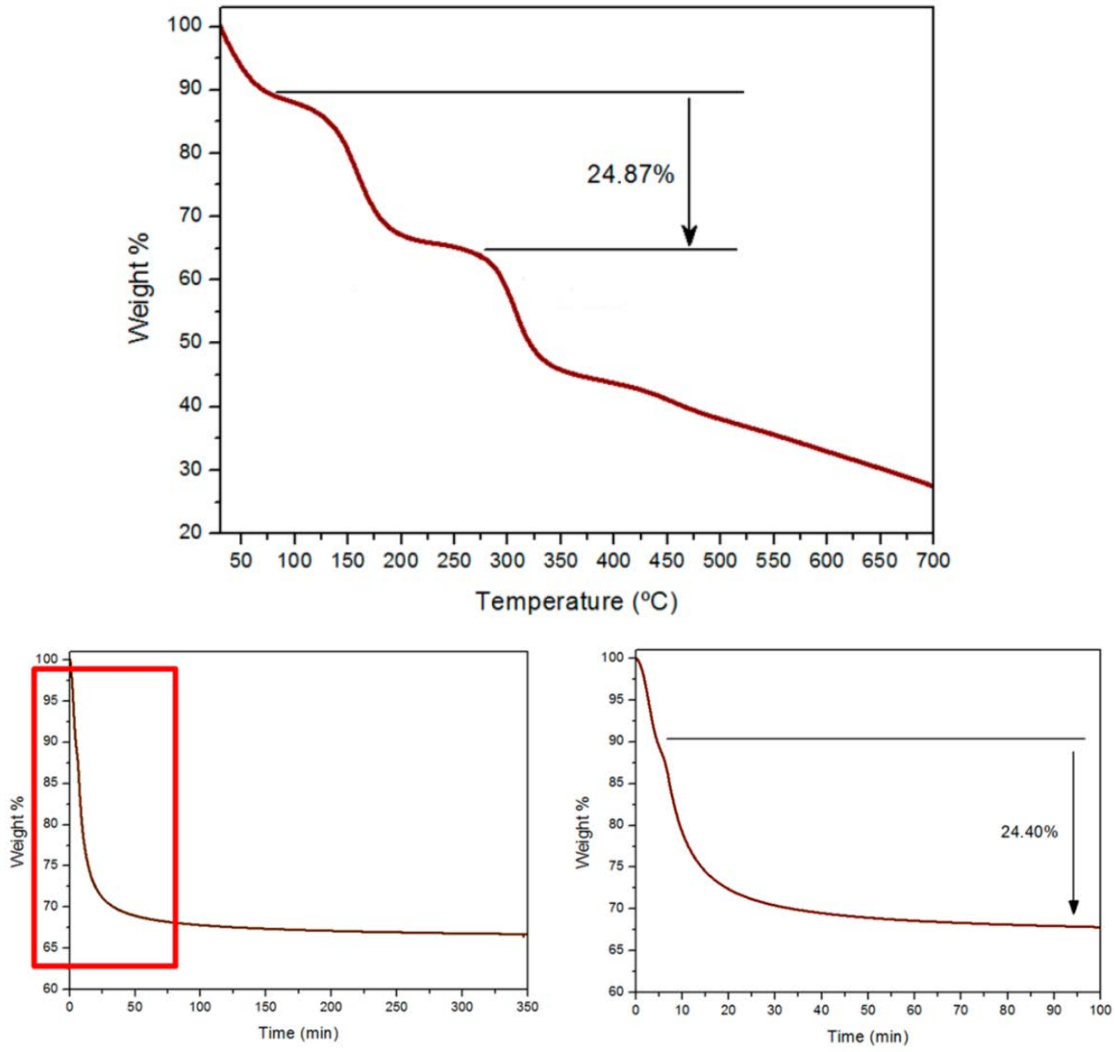

Figure 6.33. (Top) Thermogravimetric Analysis of NBoc-RhMOP, highlighting the 24.87% weight loss attributed to the thermolabile deprotection of 24 Boc groups (Calculated weight loss 25.1%). (Bottom) Isothermal Thermogravimetric Analysis of NBoc-RhMOP at 150 ºC, highlighting the stability of the material after the weight loss attributed to the thermolabile deprotection of 24 Boc groups.

These values echo the previously reported trend that MOPs exhibit greater gas sorption upon miniaturisation.[36] Furthermore, the CO_2 uptake measured at 298 K also increased after deprotection, as depicted in Figures 6.26 and 6.27. Thus, whereas the NBoc-RhMOP adsorbed 0.88 mmol $CO_2 \cdot g^{-1}$, the deprotected products (NH_2-RhMOPs) exhibited uptakes of 1.39 mmol $CO_2 \cdot g^{-1}$ (thermolysis) and 1.52 mmol $CO_2 \cdot g^{-1}$ (TFA) at 1 bar under the same conditions. Remarkably, both the S_{BET} and CO_2 uptake values for these NH_2-RhMOP products are significantly higher than for their Cu(II) analogue (non-porous to N_2; CO_2 uptake = 0.70 mmol $CO_2 \cdot g^{-1}$).[22]

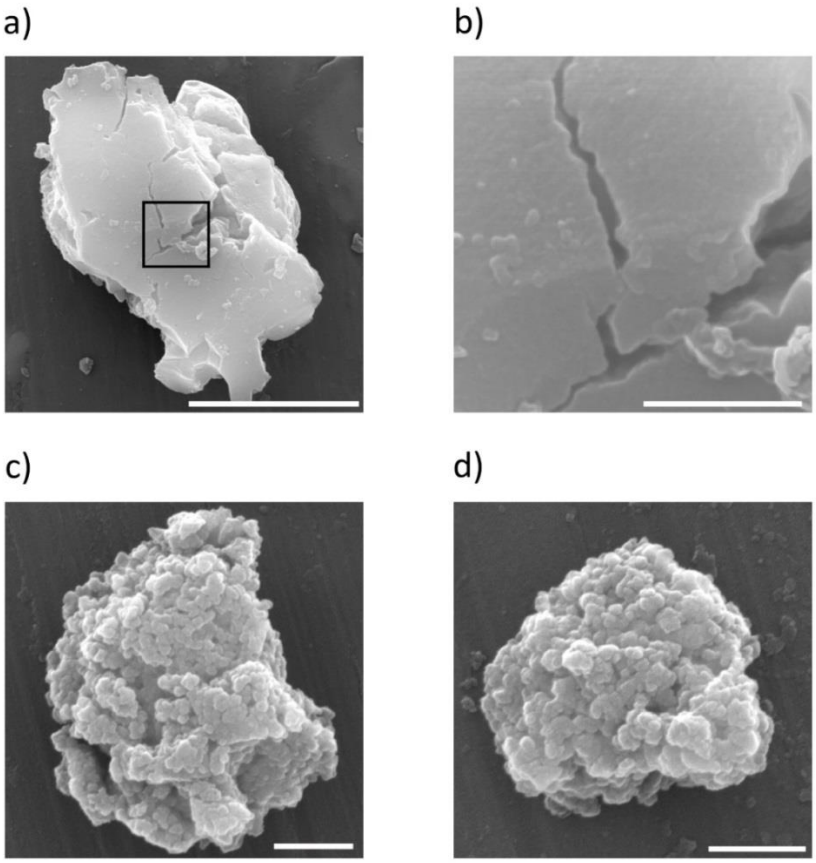

Figure 6.34. a,b) FESEM images of the NH_2-RhMOP obtained by the thermal treatment of the NBoc-RhMOP. b) High magnification image of the highlighted area in a). c,d) FESEM images of the NH_2-MOP obtained after deprotecting the NBoc-RhMOP with TFA. Scale bars = 5 μm (a), 1 μm (b), and 500 nm (c, d).

6.2.3. Conclusions

In conclusion, we have demonstrated strategic use of protecting groups for directionally-controlled coordination chemistry synthesis of Rh(II)-based MOPs with previously inaccessible funcionalities. We firmly believe that our approach is not limited to robust metallic subunits, since relatively mild, chemoselective deprotection steps are used. Using our orthogonal protection/deprotection process, we prepared two new Rh(II)-based MOPs with 24 peripheral COOH or NH_2 moieties, without affecting the structural integrity or microporosity. Owing to their strong processability, the protected Rh(II)-based MOPs can be then deprotected either in solid state or in solution. Moreover, we dissolved COOH-RhMOP in water at near-neutral pH. Interestingly, the presence of 24 directional COOH or NH_2 groups in a zero-dimensional porous scaffold opens up new post-synthetic pathways to take advantage of the well-defined orthogonal reactive sites within a cuboctahedral MOP nanoparticle. Additionally, these free pending groups might be of particular interest for Reticular Chemistry.

6.3. Experimental Part

6.3.1. Materials and Methods

Rhodium acetate, 5-amino-1,3-benzenedicarboxylic acid, di-*tert*-butyl dicarbonate (Boc_2O), 1,3,5-benzenetricarboxylic acid, $SOCl_2$, 2-(trimethylsilyl)ethanol, anhydrous pyridine, trifluoroacetic acid and tetrabutylammonium fluoride (1.0 M in THF) were purchased from Sigma-Aldrich Co. Solvents at HPLC grade were purchased from Fischer Chemical. All the reagents and solvents were used without further purification unless otherwise specified. Deionized water was obtained with a Milli-Q® system (18.2 MΩ·cm).

^{1}H NMR spectra were acquired in a Bruker Avance III 400SB NMR spectrometer. Mass spectrometry (MALDI-TOF) experiments were run in an Applied Biosystems 4700 Proteomics Analyzer operating in positive-ionization mode. UV−Vis spectra were measured in an Agilent Cary 4000 at room temperature (ca. 25 °C). FTIR spectra were recorded in transmission mode on a Bruker Tensor 27 IR equipped with a Golden Gate diamond ATR cell. Elemental analysis measurements were performed using a Flash EA 2000 CHNS, Thermo Fisher Scientific analyser. Thermogravimetric analyses were performed under nitrogen flow using a Pyris TGA8000 with a heating rate of 5 °C min^{-1}. Powder X-ray Diffraction (PXRD) patterns were recorded on an X'Pert PRO MPD analytical diffractometer (Panalytical) at 45 kV, 40 mA using Cu Kα radiation (λ = 1.5419 Å). Nitrogen and CO_2 adsorption isotherms were measured at 77 K and 298 K respectively using an Autosorb-IQ-AG analyzer.

6.3.2. Synthetic methodologies

Synthesis of non-protected blank tests:

BT_Rh-BTC: 20 mg of $Rh_2(acetate)_4 \cdot 2MeOH$ (0.04 mmol), 42 mg of 1,3,5-benzenetricarboxylic acid (0.19 mmol), and 25 mg of Na_2CO_3 (0.2 mmol) were dispersed in 2 mL of DMA. The mixture was transferred to a scintillation vial and heated at 100 °C for 48 h. A green dispersion was obtained and the solid was separated by centrifugation, washed with water, DMA and diethyl ether and dried *in vacuo* to afford BT_Rh-BTC as a green solid.

BT_Rh-NH_2BDC: In a typical procedure, 20 mg of $Rh_2(acetate)_4 \cdot 2MeOH$ (0.04 mmol), 36 mg of 5-aminoisophthalic acid (0.19 mmol), and 25 mg of Na_2CO_3 (0.2 mmol) were dispersed in 2 mL of DMA. The mixture was transferred to a scintillation vial and heated at 100 °C for 48 h. A green dispersion was obtained and the solid was separated by centrifugation, washed with water, DMA and diethyl ether and dried *in vacuo* to afford BT_Rh-NH_2BDC as a dark green powder.

Synthesis of protected organic linkers

***5-((2-(trimethylsilyl)ethoxy)carbonyl)isophthalic acid* (H_2BTC-COOTSE):**

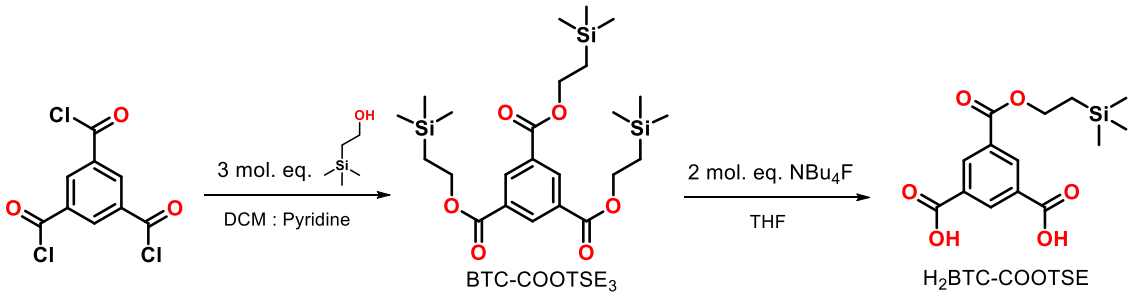

1,3,5-benzenetricarboxyl trichloride was synthesized *in situ* by reacting 1,3,5-benzenetricarboxylic acid with $SOCl_2$. 531 mg (2.0 mmol) of 1,3,5-benzenetricarbonyl trichloride and 730 µL (9.0 mmol) of pyridine were dissolved in 20 mL of dichloromethane. 860 µL (6.0 mmol) of 2-(trimethylsilyl)ethanol were added slowly, and the mixture was stirred at room temperature for 8 hours. The solution was then poured into 100 mL of chloroform, and washed subsequently with a 1 M NH_4Cl aqueous solution, 1 M HCl and water. The organic layer was recovered, dried over $MgSO_4$ and evaporated in vacuum to afford the tri-protected intermediate tris(2-(trimethylsilyl)ethyl)benzene-1,3,5-tricarboxylate (**BTC-COOTSE$_3$**). In a second step, 892.9 mg (1.75 mmol) of BTC-COOTSE$_3$ were dissolved in 7 mL of tetrahydrofuran. 3.5 mL (3.5 mmol, 2 mol. eq.) of tetrabutylammonium fluoride (1.0M solution in THF) were added stepwise in two additions (1.75 mL each) over a period of 5 hours. Then, the obtained yellowish solution was allowed to stir overnight at room temperature. 90 mL of diethyl ether were added, and a white precipitate formed. 20 mL of 1M HCl were added and the mixture was strongly shaked until no residual precipitate was observed. The organic phase was extracted, washed twice with water, dried over $MgSO_4$ and evaporated under vacuum to afford **H_2BTC-COOTSE** as a white powder. No extra purification steps were required for the MOP synthesis.

^{1}H NMR (400 MHz, DMSO-d_6): δ = 8.65 (3H, m); 4.44 (2H, t); 1.14 (3H, t); 0.08 (9H, s). ESI-TOF (m/z) = 309.08 ([L-COOEtTMS$_1$ – H]$^-$

5-((*tert*-butoxycarbonyl)amino)isophthalic acid (H_2BDC-NBoc):

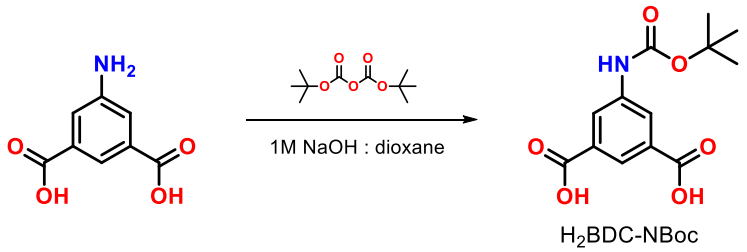

H_2BDC-NBoc

H_2BDC-NBoc was synthesized adapting a literature procedure.[37] 1.80 g (10.0 mmol) of 5-aminoisophtalic acid were dissolved in 20 mL of 1M NaOH and cooled to 0 °C. A solution of 2.40 g (11.0 mmol) of di-*tert*-butyl dicarbonate (Boc_2O) disolved in 20 mL of 1,4-dioxane was added dropwise to the former over 2 hours, and stirred at room temperature overnight. The solvent was subsequently evaporated to half of its initial volume by rotatory evaporation, and the product was precipitated with a 20% $KHSO_4$ aqueous solution up to pH = 3. **H_2BDC-NBoc** was filtered off, washed with water and dried under vacuum.

^{1}H NMR (400 MHz, DMSO-d_6): δ = 9.77 (1H, s br); 8.30 (2H, s); 8.07 (1H, s); 1.49 (9H, s).

Synthesis of protected Metal-Organic Polyhedra

COOTSE-RhMOP: 20 mg of Rh_2(acetate)$_4$·2MeOH (0.04 mmol), 71 mg of H_2btc-COOTSE (0.2 mmol) and 25 mg of Na_2CO_3 (0.2 mmol) were dispersed in 2 mL of DMA. The mixture was then transferred to a scintillation vial and heated at 100 °C for 48 h. A deep green solution was obtained and separated from the residual solids by centrifugation. 20 mL of water were added to the supernatant in order to precipitate the crude product, which was separated by centrifugation, washed with water and dried under vacuum at 85 ºC. Further purification was achieved by sequential washing steps with diethyl ether until no residual linker signals were observed in ^{1}H NMR.

^{1}H NMR (400 MHz, Acetone-d_6): δ = 8.85 (1H, Ar), 8.45 (2H, Ar), 4.35 (2H, CH_2), 1.28 (2H, CH_2), 0.05 (9H, TMS).

NBoc-RhMOP: 100 mg of Rh_2(acetate)$_4$·2MeOH (0.2 mmol), 323 mg of H_2bdc-NBoc (0.98 mmol), and 123 mg of Na_2CO_3 (1.0 mmol) were dispersed in 7 mL of DMA. The mixture was transferred to a scintillation vial and heated at 100 °C for 48 h. A deep green solution was obtained and separated from the residual solids by centrifugation. The supernatant was then precipitated with 150 mL of diethyl ether, washed with a 0.3 M NaOH aqueous solution, water and diethyl ether and dried in vacuo to afford **NBoc-RhMOP** as a blue powder.

^{1}H NMR (400 MHz, DMSO-d_6): δ = 9.24 (1H, NH), 8.40 – 8.05 (3H, Ar), 1.41 (9H, *tert*-Bu).

Deprotection of Metal-Organic Polyhedra

COOH-RhMOP: 50.0 mg (0.0053 mmol) of COOTSE-RhMOP were dissolved in 10 mL of wet tetrahydrofuran. 162 µL (0.162 mmol) of tetrabutylammonium fluoride (1.0 M solution in THF) were added slowly, and the mixture was allowed to stir overnight at room temperature, obtaining a blue precipitate. The supernatant was discarded, and the solid was washed with THF and Et_2O three times. After that, the product was dissolved in 5 mL of water and further precipitated with a dropwise addition of 1M HCl. The solid was recovered by centrifugation, washed with water and dried under vacuum. Further washing and solvent exchange steps with THF and Acetone were performed to the vacuum-dried material.

^{1}H NMR (400 MHz, DMSO-d_6): δ = 13.35 (1H, COO*H*); 8.51-8.33 (3H, Ar).

NH_2-RhMOP. NBoc-RhMOP could be quantitatively deprotected both in solid and solution fashions, hereafter referred as Thermolabile Deprotection and TFA Deprotection, respectively.

Thermolabile deprotection of NBoc-MOP. 25 mg of NBoc-RhMOP were charged into a ceramic pan and charged into a Thermogravimetric Analizer oven. The material was then heated at 150 ºC for 6 hours or until a mass plateau was achieved (expected: 25% weight loss). The sample was then recovered, washed with methanol and acetone and dried under vacuum.

TFA deprotection of NBoc-MOP. 20 mg of NBoc-RhMOP were dispersed into 2 mL of dichloromethane. 36 µL of trifluoroacetic acid (9 mol. eq.) were added and the slurry was stirred at room temperature overnight. The solid was then separated by centrifugation, neutralized with a trimethylamine solution in acetone (44 µL in 2 mL x3), and washed with methanol and acetone.

^{1}H NMR (400 MHz, DMSO-d_6): δ = 7.60 – 6.95 (3H, Ar); 5.35 (2H, NH_2).

6.3.3. Characterisation

Non-protected blank tests

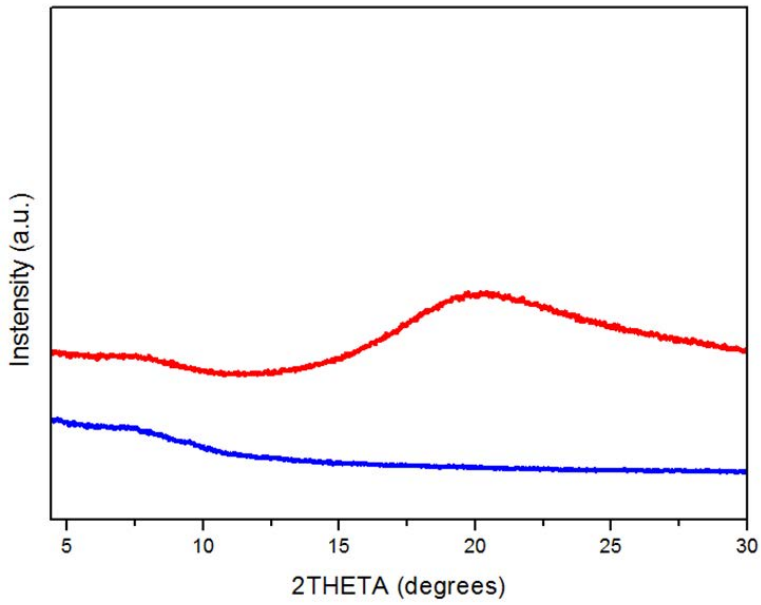

Figure 6.35. PXRD patterns of BT_Rh-NH_2BDC (blue) and BT_RhBTC (red)

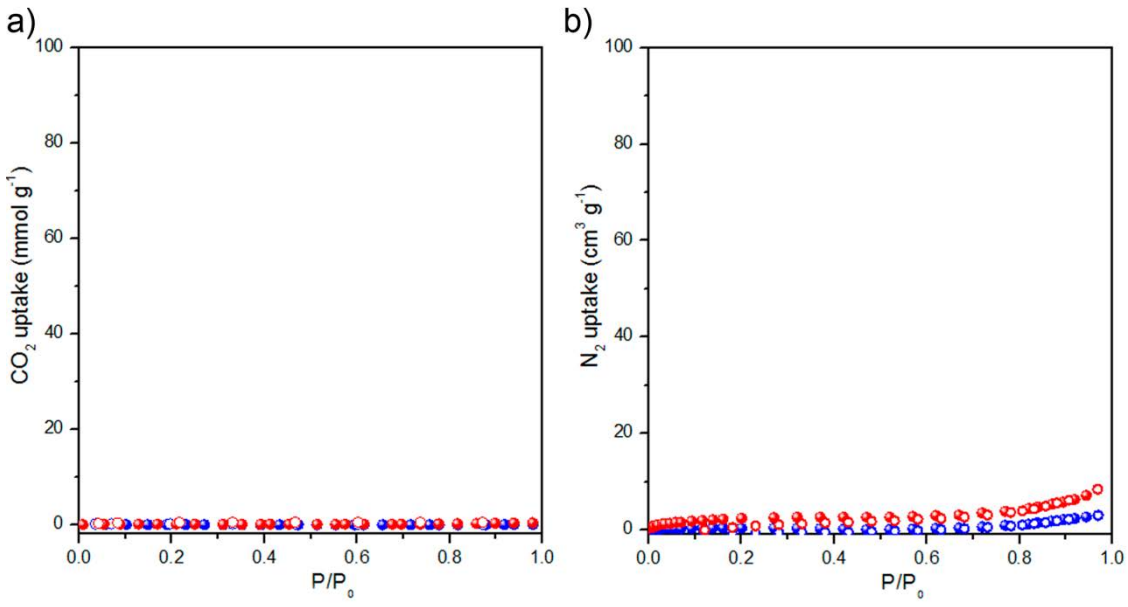

Figure 6.36. a) CO_2 adsorption isotherm at 295 K and b) N_2 adsorption isotherm at 77 K with BET linear fit of BT_Rh-NH_2BDC (blue) and BT_RhBTC (red).

UV-Vis and FTIR spectroscopic characterisation

Protected MOPs

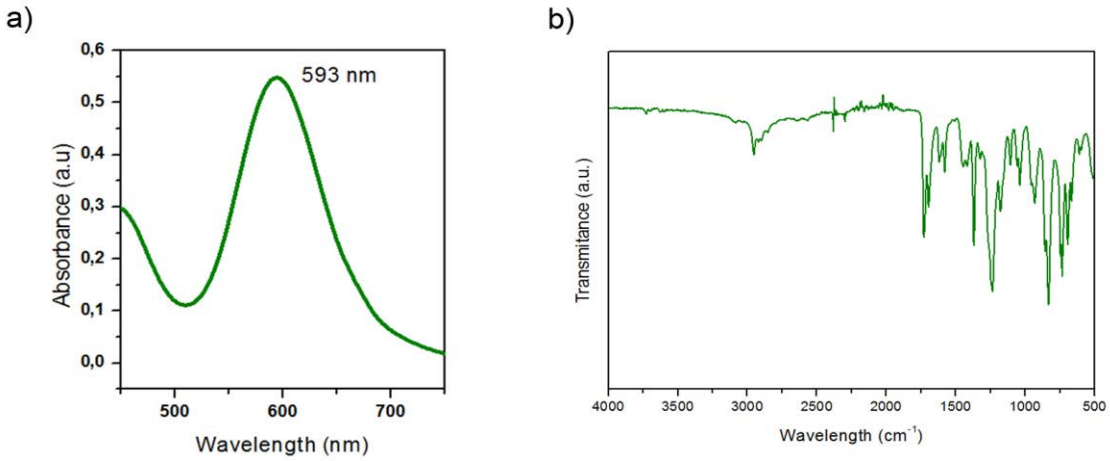

Figure 6.37. a) UV-Vis spectrum of COOTSE-RhMOP in acetone (0.30 mM). λ_{max} is centered at 593 nm. b) FTIR spectrum of COOTSE-RhMOP.

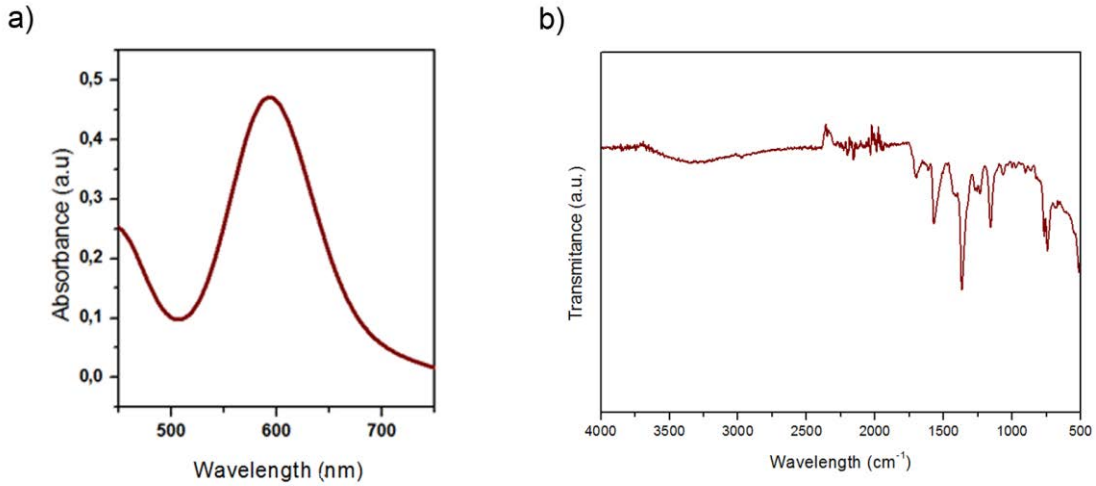

Figure 6.38. a) UV-Vis spectrum of NBoc-RhMOP in Acetone (0.30 mM). λ_{max} is centered at 594 nm. b) FTIR spectrum of NBoc-RhMOP.

Deprotected MOPs

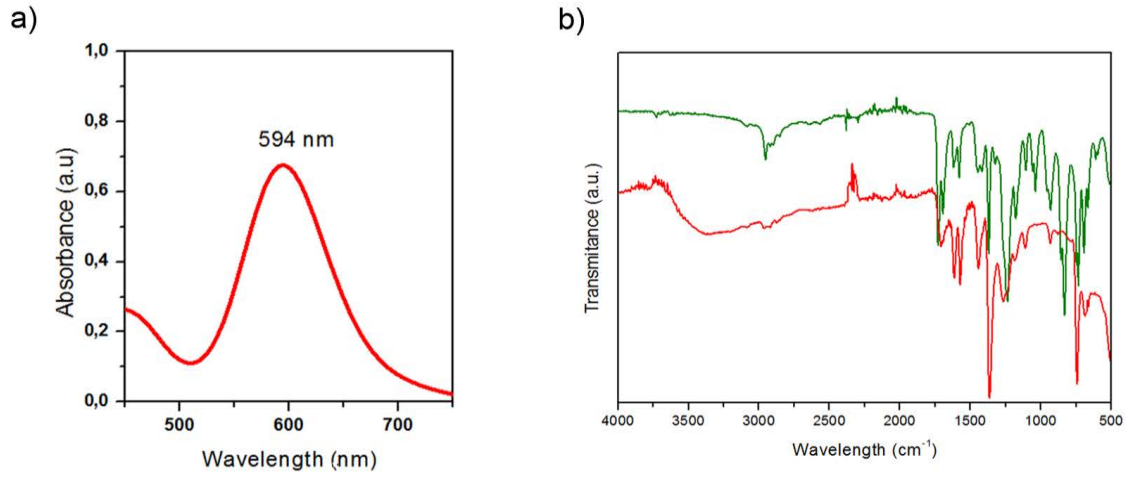

Figure 6.39. a) UV-Vis spectrum of COOH-RhMOP in DMF (0.30 mM). λ_{max} is centered at 594 nm. b) FTIR spectra of COOH-RhMOP (red) in comparison with COOTSE-RhMOP (green).

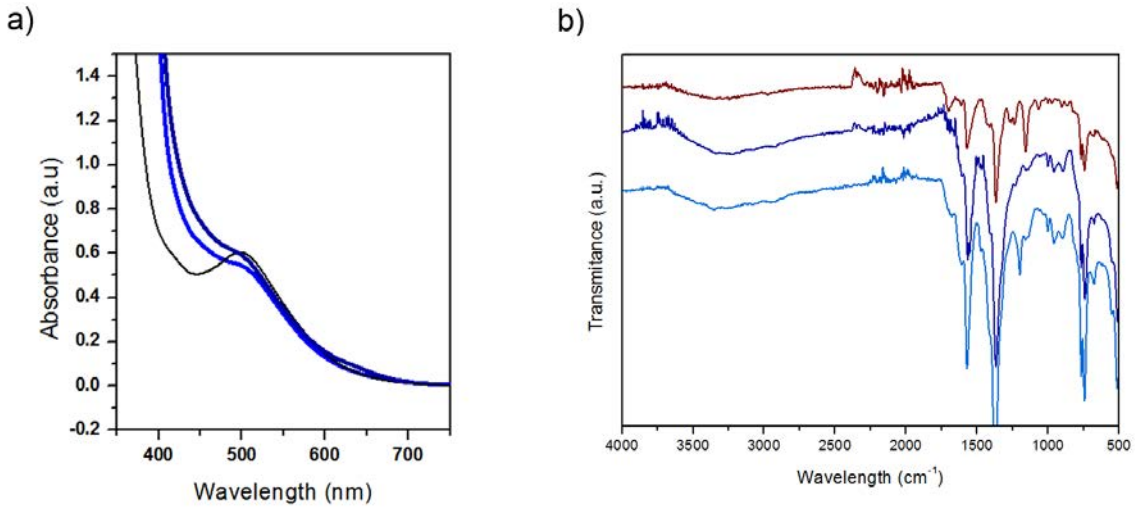

Figure 6.23. a) UV-Vis spectrum of NH_2-RhMOP deprotected by thermolabile (navy) or TFA (blue) in DMSO (0.30 mM). λ_{max} is centered at 501 nm. $Rh_2(Acetate)_4$ in DMSO (0.3 mM) added for reference (Black) to show the strong coordination of DMSO molecules in the axial positions of the paddlewheel.[38,39] b) FTIR spectra of NH_2-RHMOP, deprotected by thermolabile (navy) or TFA (blue) in comparison with NBoc-RhMOP (wine).

6.3.4. BET measurements

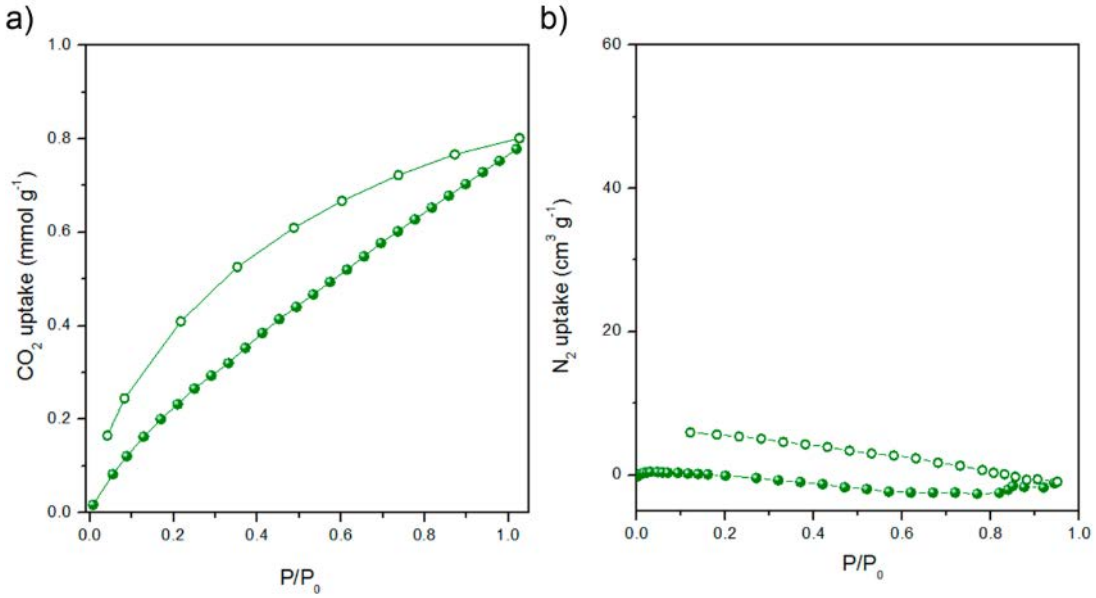

Figure 6.24. a) CO_2 adsorption isotherm at 295 K and b) N_2 adsorption isotherm at 77 K with BET linear fit of COOTSE-RhMOP

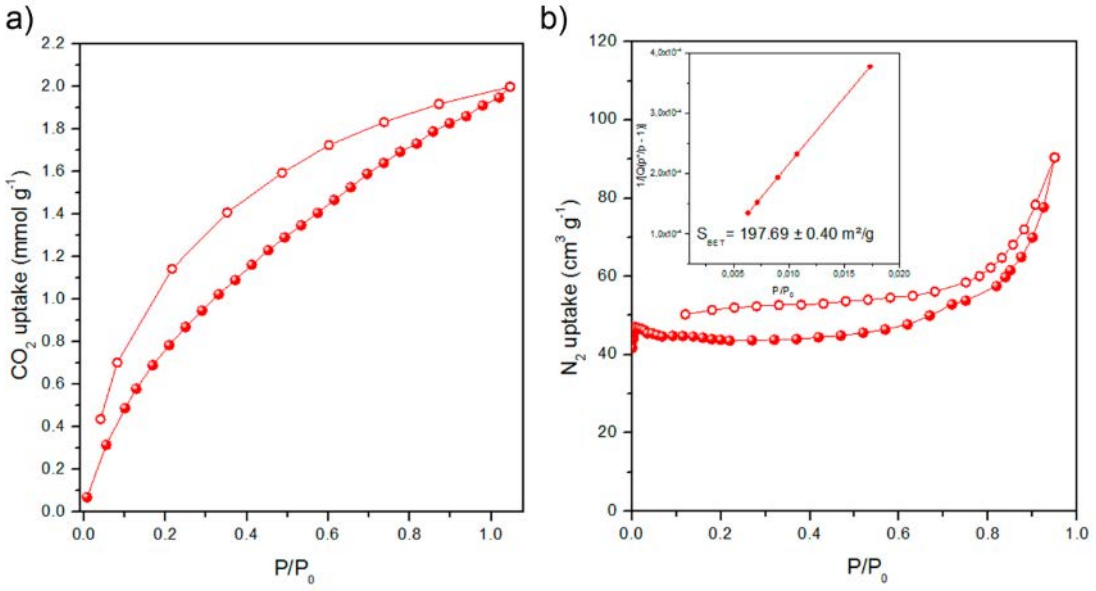

Figure 6.25. a) CO_2 adsorption isotherm at 295 K and b) N_2 adsorption isotherm at 77 K with BET linear fit of COOH-RhMOP

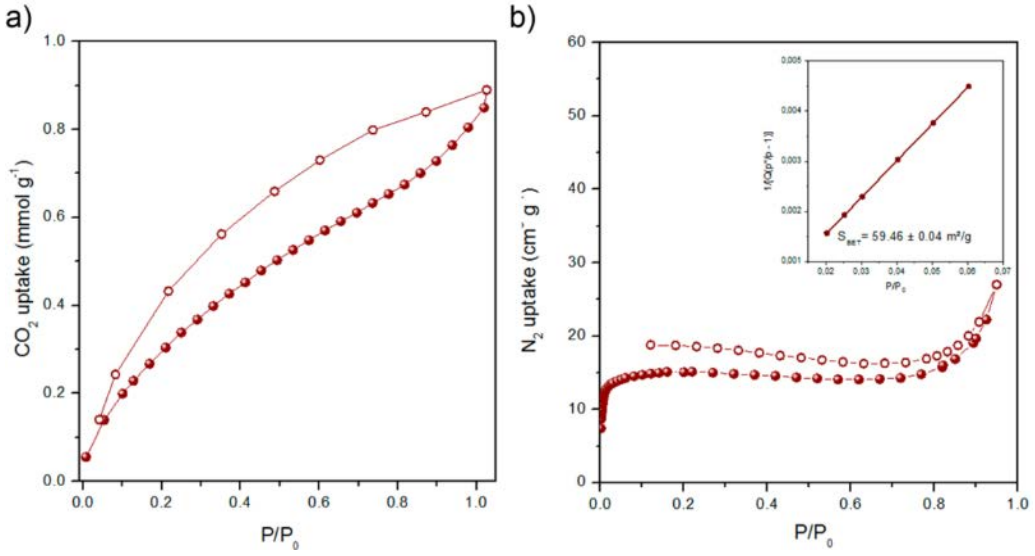

Figure 6.26. a) CO_2 adsorption isotherm at 295 K and b) N_2 adsorption isotherm at 77 K with BET linear fit of NBoc-RhMOP

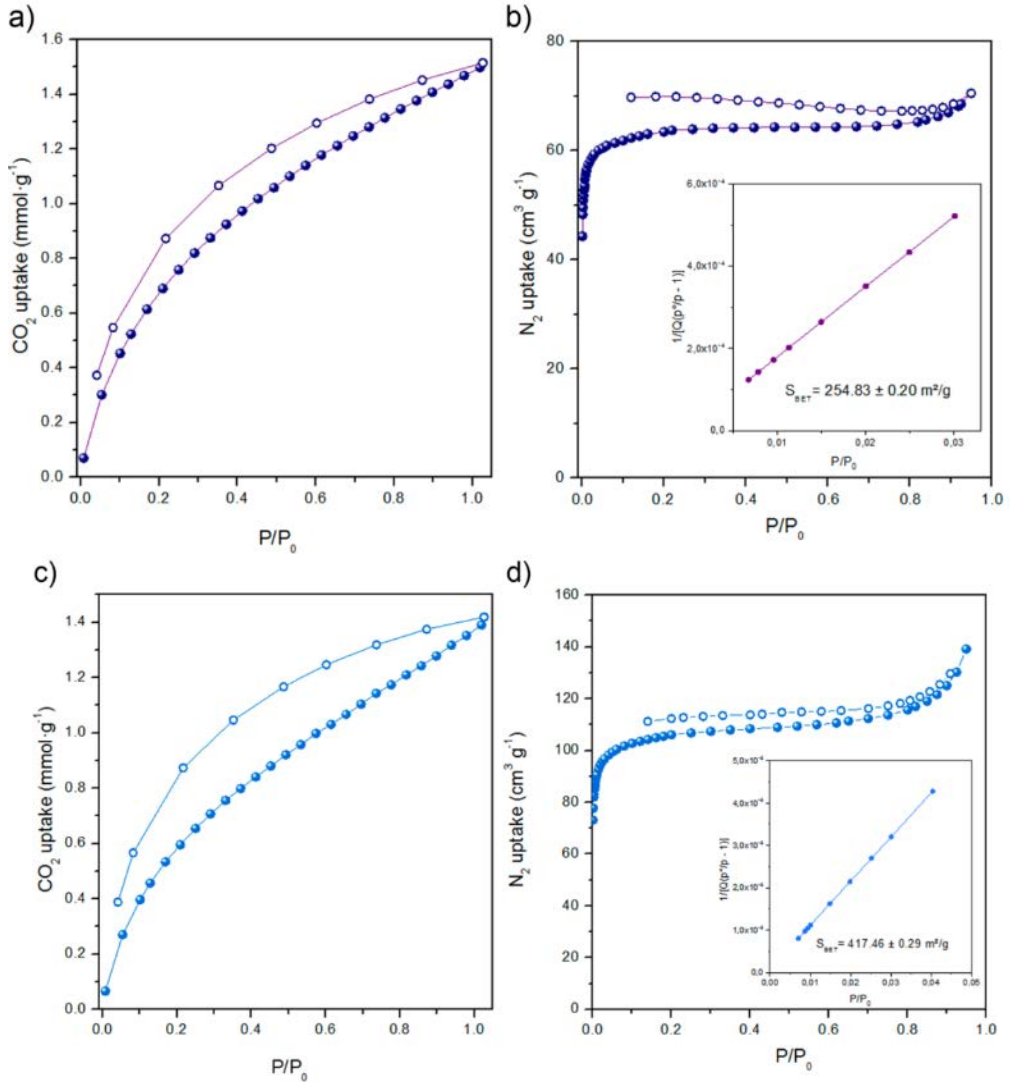

Figure 6.27. a,c) CO_2 adsorption isotherm at 295 K and b,d) N_2 adsorption isotherm at 77 K with BET linear fit of thermolabile-deprotected NH_2-RhMOP (navy) and TFA-deprotected NH_2-RhMOP (blue).

6.4. References

(1) Kurahashi, K.; Takemoto, Y.; Takasu, K. *ChemSusChem* **2012**, *5* (2), 270.

(2) Kuwabara, J.; Fujie, Y.; Maruyama, K.; Yasuda, T.; Kanbara, T. *Macromolecules* **2016**, *49* (24), 9388.

(3) Abel, G. R.; Calabrese, Z. A.; Ayco, J.; Hein, J. E.; Ye, T. *Bioconjug. Chem.* **2016**, *27* (3), 698.

(4) Lei, D.; Lee, D.-C.; Magasinski, A.; Zhao, E.; Steingart, D.; Yushin, G. *ACS Appl. Mater. Interfaces* **2016**, *8* (3), 2088.

(5) Liu, Y.; Wang, L.; Cao, L.; Shang, C.; Wang, Z.; Wang, H.; He, L.; Yang, J.; Cheng, H.; Li, J.; Lu, Z. *Mater. Chem. Front.* **2017**, *1* (12), 2495.

(6) Bloomberg, G. B.; Askin, D.; Gargaro, A. R.; Tanner, M. J. A. *Tetrahedron Lett.* **1993**, *34* (29), 4709.

(7) Abdel-Aal, A.-B. M.; Papageorgiou, G.; Raz, R.; Quibell, M.; Burlina, F.; Offer, J. *J. Pept. Sci.* **2016**, *22* (5), 360.

(8) Toonstra, C.; Amin, M. N.; Wang, L.-X. *J. Org. Chem.* **2016**, *81* (15), 6176.

(9) Bochet, C. G. *Angew. Chemie Int. Ed.* **2001**, *40* (11), 2071.

(10) Eberling, J.; Braun, P.; Kowalczyk, D.; Schultz, M.; Kunz, H. *J. Org. Chem.* **1996**, *61* (8), 2638.

(11) Arjona, O.; Medel, R.; Rojas, J.; Costa, A. M.; Vilarrasa, J. *Tetrahedron Lett.* **2003**, *44* (34), 6369.

(12) Velappan, A. B.; Kogatam, S.; Datta, D.; Srithar, R.; Nanjappan, G.; Debnath, J. *Org. Chem. Front.* **2019**, *6* (14), 2360.

(13) De Alwis Watuthanthrige, N.; Kurek, P. N.; Konkolewicz, D. *Polym. Chem.* **2018**, *9* (13), 1557.

(14) Hiltebrandt, K.; Kaupp, M.; Molle, E.; Menzel, J. P.; Blinco, J. P.; Barner-Kowollik, C. *Chem. Commun.* **2016**, *52* (60), 9426.

(15) Wilson, K. R.; Sedberry, S.; Pescatore, R.; Vinton, D.; Love, B.; Ballard, S.; Wham, B. C.; Hutchison, S. K.; Williamson, E. J. *J. Pept. Sci.* **2016**, *22* (10), 622.

(16) Levengood, M. R.; Zhang, X.; Hunter, J. H.; Emmerton, K. K.; Miyamoto, J. B.; Lewis, T. S.; Senter, P. D. *Angew. Chem. Int. Ed. Engl.* **2017**, *56* (3), 733.

(17) Katayama, H.; Hojo, H. *Org. Biomol. Chem.* **2013**, *11* (26), 4405.

(18) Lapeyre, M.; Leprince, J.; Massonneau, M.; Oulyadi, H.; Renard, P.-Y.; Romieu, A.; Turcatti, G.; Vaudry, H. *Chem. - A Eur. J.* **2006**, *12* (13), 3655.

(19) Isidro-Llobet, A.; Álvarez, M.; Albericio, F. *Chem. Rev.* **2009**, *109* (6), 2455.

(20) Deng, H.; Doonan, C. J.; Furukawa, H.; Ferreira, R. B.; Towne, J.; Knobler, C. B.; Wang, B.; Yaghi, O. M. *Science,* **2010**, *327* (5967), 846.

(21) Roberts, D. A.; Pilgrim, B. S.; Nitschke, J. R. *Chem. Soc. Rev.* **2018**, *47* (2), 626.

(22) Liu, X.; Wang, X.; Bavykina, A. V.; Chu, L.; Shan, M.; Sabetghadam, A.; Miro, H.; Kapteijn, F.; Gascon, J. *ACS Appl. Mater. Interfaces* **2018**, *10* (25), 21381.

(23) Yamada, T.; Kitagawa, H. *J. Am. Chem. Soc.* **2009**, *131* (18), 6312.

(24) Deshpande, R. K.; Minnaar, J. L.; Telfer, S. G. *Angew. Chemie Int. Ed.* **2010**, *49* (27), 4598.

(25) Lun, D. J.; Waterhouse, G. I. N.; Telfer, S. G. *J. Am. Chem. Soc.* **2011**, *133* (15), 5806.

(26) Bryant, M. R.; Ablott, T. A.; Telfer, S. G.; Liu, L.; Richardson, C. *CrystEngComm* **2019**, *21* (1), 60.

(27) McConnell, A. J.; Haynes, C. J. E.; Grommet, A. B.; Aitchison, C. M.; Guilleme, J.; Mikutis, S.; Nitschke, J. R. *J. Am. Chem. Soc.* **2018**, *140* (49), 16952.

(28) Carné-Sánchez, A.; Albalad, J.; Grancha, T.; Imaz, I.; Juanhuix, J.; Larpent, P.; Furukawa, S.; Maspoch, D. *J. Am. Chem. Soc.* **2019**, *141* (9), 4094.

(29) Nickerl, G.; Stoeck, U.; Burkhardt, U.; Senkovska, I.; Kaskel, S. *J. Mater. Chem. A* **2014**, *2* (1), 144.

(30) Greene, T. W.; Wuts, P. G. M. *Protective groups in organic synthesis.*; Wiley-Interscience, 2007.

(31) Barrett, A. G. M.; Hamprecht, D.; James, R. A.; Ohkubo, M.; Procopiou, P. A.; Toledo, M. A.; White, A. J. P.; Williams, D. J. *J. Org. Chem.* **2001,** 66, 2187-2196.

(32) Reiss, P. S.; Little, M. A.; Santolini, V.; Chong, S. Y.; Hasell, T.; Jelfs, K. E.; Briggs, M. E.; Cooper, A. I. *Chem. - A Eur. J.* **2016**, *22* (46), 16547.

(33) Carné-Sánchez, A.; Craig, G. A.; Larpent, P.; Guillerm, V.; Urayama, K.; Maspoch, D.; Furukawa, S. *Angew. Chemie Int. Ed.* **2019**, *58* (19), 6347.

(34) Deshpande, R. K.; Minnaar, J. L.; Telfer, S. G. *Angew. Chemie Int. Ed.* **2010**, *49* (27), 4598.

(35) Lun, D. J.; Waterhouse, G. I. N.; Telfer, S. G. *J. Am. Chem. Soc.* **2011**, *133* (15), 5806.

(36) Carné-Sánchez, A.; Craig, G. A.; Larpent, P.; Hirose, T.; Higuchi, M.; Kitagawa, S.; Matsuda, K.; Urayama, K.; Furukawa, S. *Nat. Commun.* **2018**, *9* (1), 2506.

(37) Bitta, J.; Kubik, S. *Org. Lett.* **2001**, *3* (17), 2637.

(38) Abbasi, A.; Skripkin, M. Y.; Eriksson, L.; Torapava, N. *Dalt. Trans.* **2011**, *40* (5), 1111.

(39) Sharutin, V. V.; Sharutina, O. K.; Senchurin, V. S. *Russ. J. Inorg. Chem.* **2019**, *64* (8), 1025.

Chapter 7

Conclusions

7.1. General Conclusions

The development of this Thesis orbited around overcoming the main limitations on the post-synthetic modification of Metal-Organic Frameworks (MOFs), and transfer the acquired knowledge to the zero-dimensional field. In particular, the main efforts were addressed to dispose the diffusion of reagents from the complex kinetic mechanism that PSM relies on.

First, we showed the potential of exploiting coordination vacancies within the organic linkers to induce a solvent-based restructuration on the inorganic secondary building units of coordination polymers. Thanks to the dynamic nature of the macrocycle-based linkers, the metal-defective SBUs of a compact hetero-bimetallic CP were transformed via a single-crystal-to-single-crystal transformation to a more open framework extended by homogeneously-distributed bimetallic paddlewheel SBUs. This transformation was reproduced for two different cases, which allowed the formation of Cu(II)-Zn(II) and Cu(II)-Ni(II) paddlewheel SBUs. The development of this project presented a major challenge, as the characterisation of almost electronically-identical metals within the same SBU cannot be properly elucidated by SCXRD techniques. With it, the author had its first contact with characterisation techniques based on studies of the magnetic properties of metallic assemblies, such as electronic paramagnetic resonance (EPR) and magnetic susceptibility measurements. These techniques, in combination with induced coupled plasma (ICP-OES) measurements on the sample and supernatant, allowed the postulation of a general mechanism of the transformation, thus completing the study.

Next, this Thesis focused on targeting the organic moieties of Zr(IV)-based MOFs through a solid-gas phase reaction pathway. Specifically, ozone gas was used to transform the olefinic side-chains of an UiO-66-like MOF into the metastable 1,2,4-trioxolane intermediate. For this purpose, we first designed and constructed a new solid-gas setup for properly accommodating MOF sample to the required ozonolysis reaction conditions (*i.e.* -78ºC, vacuum) in the most efficient and safe way. The setup consisted on a U-shaped Pyrex tube in which the MOF sample is packed and blocked by two cotton stoppers. One extreme was connected to an ozonator, whereas the other was directly connected to a vacuum line, creating a fast continuous flow of gas. The tube was then immersed on an acetone/CO_2 bath at -78ºC, temperature in which ozone is known to present moderate lifetime and chemoselectively reacts with unsaturated moieties. By using this setup, we achieved quantitative conversions into 1,2,4-trioxolane moieties in about 30 minutes without requiring any solvent. Remarkably, the metastable 1,2,4-trioxolane ring proved to be stable to heat and vacuum when confined inside the MOF pores. Still, this reaction intermediate proved to be chemically active to both reductive and oxidative reaction pathways, and was selectively converted to aldehyde and carboxylic acid groups in a 42% and 100% yield, respectively. The mild treatment conditions and quantitative yields allowed following the two-

step transformation by SCXRD measurements, an uncommon characterisation technique on organic transformations within MOFs. This long project allowed the author to deepen his knowledge on non-routine nuclear magnetic resonance characterisation techniques, as the bulk screening of the reaction was performed to microcrystalline MOF sample and not on single-crystal quality material. Additionally, the project opened up important collaborations with the Autonomous University of Madrid (UAM) and the Instituto de Ciencia de Materiales de Madrid (ICMM) in regards of conformational simulation and single-crystal elucidation, respectively; and with the CNRS centre in the Université d'Orleans for the in-depth NMR characterisation, from which the author greatly benefited and learned. Additionally, the acquired knowledge in how MOFs interact with ozone lead to the development of a second research project not included in this Thesis (Manuscript presented in Annex 1) widening the solid-gas reactivity approach for MOF chemistry.

Finally, the acquired post-synthetic knowledge, both from self-experience and from bibliographic research, was transferred to the zero-dimensional field targeting Rh(II)-based metal-organic polyhedra (MOPs). MOPs can be seen as soluble metal-organic porous nanoparticles with well-defined reactive sites anchored on their surface. The physicochemical properties of these scaffolds are greatly influenced by the functionalities present of their surface. For this, the post-synthetic modification of their periphery, both by covalent chemistry on the linkers and by coordination chemistry on their unsaturated open-metal sites can be a useful tool in the manipulation, processability and application of these materials. First, two isostructural RhMOPs of formula $[Rh_2(L)_2]_{12}$ (where L= 1,3-benzenedicarboxylic acid (mBDC) and 5-hydroxy-1,3-benzenedicarboxylic acid (OH-mBDC) were synthesised. Both MOPs present 12 oriented Rh-Rh paddlewheel SBUs that can be targeted by N-donor linkers. With it, the solubility of both scaffolds could be reversibly tuned, from highly hydrophilic solvents to hydrophobic ones by coordinatively-anchoring different N-donor linkers (4-(*tert*-butyl)pyridine, 4-(trifluoromethyl)pyridine or L/D-Proline). Next, we were able to proof that the organic linkers within MOPs still present identical chemical reactivity as their free counterparts. Through this, up to 24 directionally-anchored moieties were anchored in the surface of OHRhMOP by using ester and ether linkages. Remarkably, both covalent and coordination PSM are not exclusive and can be operated orthogonally and in tandem fashion anchoring up to 36 directional functional groups to the MOPs periphery, greatly enhancing the applications of the approach. Remarkably, not only dative PSM can be performed on these materials. The use of protecting groups, greatly exploited in organic synthesis, can be incorporated to the MOPs field in order to synthesise otherwise unobtainable scaffolds. Through the use of orthogonal protection/deprotection pathways, two unprecedented RhMOPs with 24 NH2 or COOH groups on their periphery were synthesised. Both MOPs present functional groups with rich chemistries in the covalent and

coordination fields, respectively, thus expanding the horizons for the applications of MOPs. In fact, during the redaction of these Thesis, the first sketches in applying MOP chemistry for specific applications was developed. In this sense, we reported that the hydroxyl-functionalized OHRhMOP can be transferred between immiscible phases by pH changes or by cation-exchange reactions. This phenomenon allowed the transport of coordinatively bound cargoes between immiscible layers, including into solvents in which the cargo was initially insoluble. As a final proof-of-concept, we employed the same MOP to separate a challenging mixture of structurally similar cyclic aliphatic (tetrahydrothiophene) and aromatic (thiophene) compounds (Manuscript embedded in Annex 1).

These results open new opportunities for the exploration and expansion of the post-synthetic modification field in MOFs and MOPs. By overcoming one of the major limitations of the approach, new alternative PSM pathways can be exploited as an effective tool for selectively removing, anchoring and recovering specific fragments of these molecules/frameworks, greatly enhancing the processability (and therefore, application) of these materials.

Glossary

Acronyms and abbreviations

List of Acronyms and abbreviations

2-MIM	2-methylimidazolate
AAS/AES	Atomic absorption/Emission Spectroscopy
acac	Acetylacetonate
AzTC	3,3′,5,5′-azobenzenetetracarboxylate
BDC	1,4-benzenedicarobxylate
BET(S_{BET})	Brunauer, Emmett and Tellerr surface area
BHB	3,3′,3″,5,5′,5″-benzene-1,3,5-triyl-hexabenzoic acid
BIPY	4,4-bipyridine
BPDC	biphenyl-4,4′-dicarboxylate
BPTC	Biphenyl-3,3′,5,5′-tetracarboxylic acid
BPYDC	2,2'-bipyridyldicarboxylic acid
BTAC	Benzene-1,3,5-tri-β-acrylic acid
BTB	1,3,5-tris(4-carboxyphenyl)benzene
BTC	1,3,5-benzenetricarboxylate
BTE	4,4′,4″-[benzene-1,3,5-triyl-tris(ethyne-2,1-diyl)]tribenzoate
CF_3-Py	4-(trifluoromethyl)pyridine
CSD	Cambridge Structural Database
CP	Coordination Polymer
CP-MAS-NMR	Cross-Polarization Magic-Angle Spinning NMR
CPPI	Cross Polarisation with Polarisation Inversion
CVD	Chemical Vapour Deposition
dabco	1,4-diazabicyclo[2.2.2]octane
DEF	N'N-Diethylformamide
DEPT135-NMR	Distortionless Enhancement by Polarization Transfer
DFT	Density Functional Theory
DHTP	2,5-dihydroxy-1,4-benzenedicarboxylic acid
DMA	N'N-Dimethylacetamide
DMF	N'N-Dimethylformamide
DMOF	dabco-pillared MOF
DOE	Department of Energy
DOSY-NMR	Diffusion-Ordered Spectroscopy-NMR
DOTA	1,4,7,10-tetraazacyclododecane-N,N′,N″,N‴-tetraacetate
EA	Elemental Analysis
EBDC	2-Ethenyl-1,4-benzoic acid
EDX	Energy-Dispersive X-ray spectroscopy

EPR	Electronic Paramagnetic Resonance
ESI-MS	Electro-Spray Ionisation Mass Spectroscopy
EXAFS	Extended X-ray Absorption Fine Structure
FTIR	Fourier-Transformance Infrared spectroscopy
HETT	ethyl-substituted truxenetricarboxylic acid
HKUST	Hong Kong University of Science and Technology
HSQC/HMBC	Heteronuclear Single Quantum Coherence / Heteronuclear Multiple Bond Correlation spectroscopy
ICP-OES	Induced Coupled Plasma spectroscopy coupled to Optical Emission Spectrometer
INP	Inorganic Nanoparticle
IRMOF	Isoreticular Metal-Organic Framework
IUPAC	International Union of Pure and Applied Chemistry
MALDI-TOF	Matrix-Assisted Laser Desorption/Ionization coupled to Time-of-flight detector
mBDC	1,3-benzenedicarboxylate
Me_2-BPDC	2,2′-dimethylbiphenyl-4,4′-dicarboxylate
MIL	Materials of the Insitut Lavoisier
MOF	Metal-Organic Framework
MOP	Metal-Organic Polyhedra
MP-11	microperoxidase-11
MTV-MOFs	Multivariative MOF
NBoc	N-(4-*tert*-butyloxy)carbonyl
NH_2-BDC	2-amino-1,4-benzenedicarboxylic acid
NMR	Nuclear Magnetic Resonance
NOESY-NMR	Nuclear Overhauser Spectroscopy
NOTT	Nottingham University
NU	Northwestern University
OH-mBDC	5-hydroxy-1,3-benzenedicarboxylate
PCN	Porous Coordination Network
PCPs	Porous Coordination Polymer
POM	Polyoxometalate
PS	Post-Synthetic
PSEtch	Post-Synthetic Etching
PSLig	Post-Synthetic Ligand modification
PSLE	Post-Synthetic Ligand Exchange
PSLI	Post-Synthetic Ligand Insertion

PSM	Post-Synthetic Modification
PSMet	Post-Synthetic Metalation
PNP	Polymeric Nanoparticle
PXRD	Powder X-Ray Diffraction
PyC	4-pyrazolebenzoic acid
RAFT	reverse addition − fragmentation transfer
RhMOP	Rh(II)-based Metal-Organic Polyhedra
SBU	Secondary Building Unit
SBPDC	4,4′-dibenzoic acid-2,2′-sulfone
SCXRD	Single-Crystal X-Ray Diffraction
SEM	Scanning Electron Microscopy
S/G	Solid/Gas
TATB	4,4',4''-s-triazine-2,4,6-triyl-tribenzoic acid
***tert*Py**	4-*tert*-butylpyridine
TGA	Thermogravimetric Analysis
TPDC	Triphenyldicarboxylate
TSE	2-(trimethylsilyl)ethanol
UiO	University in Oslo
UMCM	University of Michigan Crystalline Material
USTC	University of Science and Technology of China
XANES	X-ray Absorption Near Edge Structure
XRD	X-Ray Diffraction

Annex 1

Publications

List of Publications

The publications related to the main objectives of this PhD Thesis are listed below:

1. **Albalad, J.**; Aríñez-Soriano, J.; Vidal-Gancedo, J.; Lloveras, V.; Juanhuix, J.; Imaz, I.; Aliaga-Alcalde, N; Maspoch D. "Hetero-bimetallic paddlewheel clusters in coordination polymers formed by a water-induced single-crystal-to-single-crystal transformation" *Chem. Commun.,* **2016**, 52, 13397-13400.

2. **Albalad, J.**; Xu, H.; Gándara, F.; Haouas, M.; Martineau-Corcos, C.; Mas-Ballesté, R.; Barnett, S.A.; Juanhuix, J.; Imaz, I.; Maspoch, D. "Single-Crystal-to-Single-Crystal Postsynthetic Modification of a Metal–Organic Framework via Ozonolysis" *J. Am. Chem. Soc.,* **2018**, 140, 2028-2031.

3. Carné-Sánchez, A.; **Albalad, J.**; Grancha, T.; Imaz, I.; Juanhuix, J.; Larpent, P.; Furukawa, S.; Maspoch, D. "Postsynthetic Covalent and Coordination Functionalization of Rhodium(II)-Based Metal–Organic Polyhedra" *J. Am. Chem. Soc.,* **2018**, 141, 4094-4102.

4. **Albalad, J.**; Carné-Sánchez, A.; Grancha, T.; Hernández-López, L.; Maspoch D. "Protection strategies for directionally-controlled synthesis of previously inaccessible metal–organic polyhedra (MOPs): the cases of carboxylate- and amino-functionalised Rh(II)-MOPs *Chem. Commun.,* **2019**, 55, 12785-12788.

The author of this Thesis also contributed his work in the following publications not included in the main body of this Thesis. The files are included in this Annex section.

5. Aríñez-Soriano, J.; **Albalad, J.**; Pérez-Carvajal, J.; Imaz, I.; Busqué, F.; Juanhuix, J.; Maspoch, D. "Two-step synthesis of heterometallic coordination polymers using a polyazamacrocyclic linker" *Cryst. Eng. Comm.* 2016, 22, 4196-4204.

6. Aríñez-Soriano, J.; **Albalad, J.**; Carné-Sánchez, A.; Bonnet, C.S.; Busqué, F.; Lorenzo, J.; Juanhuix, J.; Terban, M.W.; Imaz, I.; Tóth, E.; Maspoch, D. "pH-Responsive Relaxometric Behaviour of Coordination Polymer Nanoparticles Made of a Stable Macrocyclic Gadolinium Chelate" *Chem. Eur. J.,* **2016**, 22, 13162-13170.

7. Aríñez-Soriano, J.; **Albalad, J.**; Vila-Parrondo, C.; Pérez-Carvajal, J.; Rodríguez-Hermida, S.; Cabeza, A.; Juanhuix, J.; Imaz, I.; Maspoch, D. "Single-crystal and humidity-controlled powder

diffraction study of the breathing effect in a metal–organic framework upon water adsorption/desorption" *Chem. Commun.*, **2016**, 52, 7229-7232.

8. Guillerm, V.; Xu, H.; **Albalad, J.**; Imaz, I.; Maspoch, D. "Postsynthetic Selective Ligand Cleavage by Solid–Gas Phase Ozonolysis Fuses Micropores into Mesopores in Metal–Organic Frameworks" *J. Am. Chem. Soc.*, **2018**, 140, 15022-15030.

9. Grancha, T.; Carné-Sánchez, A.; Hernández-López, L.; **Albalad, J.**; Maspoch, D. "Phase Transfer of Rhodium(II)-Based Metal-Organic Polyhedra Bearing Coordinatively-Bound Cargo Enables Molecular Separation" *J. Am. Chem. Soc.,* **2019**, *Accepted Manuscript* (DOI: 10.1021/jacs.9b10403)

ystEngComm

PER

View Article Onl
View Journal | View Issu

rossMark
click for updates

CrystEngComm, 2016, 18,

22nd December 2015,
11th February 2016

039/c5ce02520f

org/crystengcomm

Two-step synthesis of heterometallic coordina polymers using a polyazamacrocyclic linker†

J. Aríñez-Soriano,[a] J. Albalad,[a] J. Pérez-Carvajal,[a] I. Imaz,*[a] F. Busqué,[b] J. Jua and D. Maspoch*[ad]

A new macrocyclic linker 1,4,7,10-tetraazacyclododecane-1,7-bis(4-acetamidobenzoic)-4,10-diac (H_4L1) was synthesized and characterized. This linker was used to create two heterometallic coo polymers following a two-step synthesis. This synthesis consisted of first combining th azamacrocyclic linker with Ni(II) or Mn(II) ions to obtain the corresponding metallomacrocyclic cc showing non-coordinated carboxylic groups. In a second step, these metallated macrocycles were building units to construct two heterometallic Ni(II)–Zn(II) and Mn(II)–Zn(II) coordination polyme combined with Zn(II) ions. In addition, a third Zn(II)–Zn(II) coordination polymer could also be synthe direct mixing of H_4L1 with Zn(II) ions. Interestingly, the Mn(II)–Zn(II) coordination polymer exhibits ible type-I "crystal-to-amorphous transformation" upon water sorption/desorption.

duction

ıation polymers have become an in-depth thread of uring the past few decades mainly because of their potential properties and applications.[1–3] In this field, tegic design of the organic linkers to be used (known *'inker design approach*) has proven critical for tuning ıposition and structure of coordination polymers and, or achieving the desired functionality for a target ion.[4–6] For example, Kitagawa *et al.* designed a lumi- porous coordination polymer-based sensor by using a l derivative of the photoactive 1,4,5,8- ılenediimide.[7] The material showed strong shifting on tted wavelength when different volatile organic com- were adsorbed on the framework. In a similar way, *t al.* designed a porous coordination polymer with ntrolled reversible alteration of its adsorbing proper- ough the design of a photosensitive linker.[8] The con- investigation of new organic linkers is thus essential essing novel coordination polymers with enhanced performances in numerous applications such as in c gas sorption, separation, sensors, pollutant remov antibacterials.

Polyazamacrocycles (cyclen and cyclam derivative family of heteromolecules with high affinity to chelat ions in their cavities due to the preorganization of the ing sites and their kinetic and thermodynamic stab duced by the macrocyclic effect.[9,10] Because of this these macrocyclic ligands have already shown promis ferent fields ranging from contrast agents[11] and catal to sensors.[14] Recently, the functionalization of the amine positions of polyazamacrocycles with pendant a corporating functional groups (*e.g.* carboxylates, amid phosphonates)[15–18] has opened the possibility of usir as multitopic organic linkers. These organic linkers h potential to coordinate a metal ion inside the inne and different ones through these pendant arms, ex the framework and thus forming heterometallic coorc polymers. However, their use as linkers for the synt coordination polymers is to date limited; only a few e of homometallic[19–26] and even less heterometallic[27] cc tion polymers are found in the literature. This sca structures can be attributed to their high degree of fl that makes it difficult to obtain suitable crystals for crystal X-ray diffraction, to their sensitivity to harsh media, and to the tendency of their pendant arms to nate the metal ions within the macrocyclic cavity,[28] promoting the generation of mononuclear compound than coordination polymers.

Herein, we present the stepwise synthesis of metallic coordination polymers using polyazamacroc

Institute of Nanoscience and Nanotechnology (ICN2), CSIC and The Institute of Science and Technology, Campus UAB, Bellaterra, 08193 Spain. E-mail: inhar.imaz@icn.cat, daniel.maspoch@icn.cat
at Autònoma de Barcelona, Departament de Química, 08193 Bellaterra,

chrotron, 08290 Cerdanyola del Vallès, Barcelona, Catalonia, Spain
i Catalana de Recerca i Estudis Avançats (ICREA), 08100 Barcelona,

ic supplementary information (ESI) available: Characterization details allographic views. CCDC 1443836–1443841. For ESI and crystallo- ıta in CIF or other electronic format see DOI: 10.1039/c5ce02520f

organic linkers. Our strategy consists of first preparing complexes of the polyazamacrocycle 1,4,7,10-tetraazacyclododecane-1,7-bis(4-acetamidobenzoic)-4,10-diacetic acid (H_4**L1**) with Mn(II) and Ni(II) ions and then using these metallated macrocycles as building units to create heterometallic coordination polymers. We show that the coordination of these Mn(II)/Ni(II) building units showing free carboxylic groups with Zn(II) ions allows the synthesis of two bimetallic Zn(II)–Mn(II) and Zn(II)–Ni(II) coordination polymers (Scheme 1). We also show that a Zn(II)–Zn(II) coordination polymer could be synthesized by direct mixing of H_4**L1** with Zn(II) ions. Interestingly, the Mn(II)–Zn(II) coordination polymer shows a reversible type-I "crystal-to-amorphous transformation" upon water sorption/desorption.[29]

Experimental

General considerations

tert-Butyl-4-aminobenzoate, bromoacetyl bromide, potassium carbonate and trifluoroacetic acid were purchased from Sigma-Aldrich. DO2AtBu (a.k.a. di-*tert*-butyl-2,2′-(1,4,7,10-tetraazacyclododecane-1,7-diyl)diacetate) was purchased from CheMatech. All solvents were purchased from Fisher Scientific and Scharlab. Solvents and reagents were used as received unless otherwise stated. ^{1}H and ^{13}C NMR spectra of intermediates **1** and **2** were recorded on a Bruker Avance DPX-360 spectrometer operating at 360 and 90 MHz, respectively. ^{1}H and ^{13}C NMR spectra of H_4**L1** were recorded on a Bruker Avance III 400 SB operating at 400 and 100 MHz, respectively. Samples were dissolved in $CDCl_3$ or D_2O after purification. Mass spectra were acquired using a micrOTOF-QII ESI-MS instrument. The purity of all bulk material batches was confirmed by X-ray powder diffraction (XRPD) patterns collected using an X'Pert PRO MPD analytical diffractometer (Panalytical) at 45 kV and 40 mA with Cu Kα radiation (λ = 1.5419 Å) and compared with single crystal simulated patterns. Thermogravimetric analyses were performed under nitrogen flow using an STA 449 F1 Jupiter-Simultaneous TGA-DSC from NETZSCH with a heating rate of 5 °C min^{-1}. IR spectra were recorded in transmission mode on a Bruker Tensor 27FTIR equipped with a Golden Gate diamond ATR cell. Gravimetric water sorption measurements were performed at 298 K using a flow of nitrogen, up to a relative humidity of 90%, using a DVS-Advantage-1 (Surface Measurements Systems). Elemental analysis measurements were performed using a Flash EA 2000 CHNS, Thermo Fisher Scientific analyser.

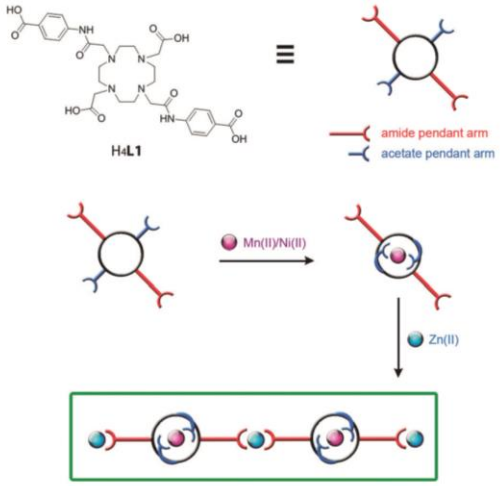

Scheme 1 Illustration showing the two-step strategy used to synthesize heterometallic coordination polymers **6** and **7**.

Synthesis of the linker

Synthesis of 4-*tert*-butyl(2-bromoacetamido)benzoate (1). **1** was synthesized by adapting a literature procedure.[15] Potassium carbonate (4.0 g, 28.8 mmol) was added to a solution of *tert*-butyl-4-aminobenzoate (5.0 g, 26.2 mmol) in dichloromethane (100 mL). The reaction mixture was stirred vigorously and cooled to 0 °C in an ice bath. Bromoacetyl bromide (2.5 mL, 28.8 mmol) was added dropwise afterwards. The reaction mixture was allowed to warm to room temperature and then stirred for 12 h. The resulting mixture was then filtered over Celite®, the solids were discarded and the filtrate was concentrated by evaporation of the solvents under vacuum. Yield: 6.64 g (21.2 mmol, 65%). Found: C 49.8%, H 4.9%, N 4.7%; $C_{13}H_{16}NO_3Br$ requires: C 49.7%, H 5.1%, N 4.5%. ^{1}H NMR (360 MHz, $CDCl_3$): δ = 8.26 (1H, s br, NH), 8.02 (2H, d, $^3J_{H-H}$ = 7.5 Hz, Ar), 7.63 (2H, d, $^3J_{H-H}$ = 7.5 Hz, Ar), 4.07 (2H, s, $BrCH_2$), 1.61 (9H, s, $C(CH_3)_3$). ^{13}C NMR (90 MHz, $CDCl_3$): δ = 164.8 (C=O), 163.1 (C=O), 140.2 (Ar), 130.4 (Ar), 128.3 (Ar), 118.6 (Ar), 80.8 ($C(CH_3)_3$), 29.1 ($C(CH_3)_3$), 27.9 ($BrCH_2$). *m*/*z* (ESI-TOF): 336.02 (100%, $[M + Na]^+$), an appropriate isotope pattern was observed.

Synthesis of 1,4,7,10-tetraazacyclododecane-1,7-bis(4-*tert*-butylacetamidobenzoate)-4,10-bis(*tert*-butylacetate) (2). DO2AtBu (1.09 g, 2.71 mmol) and potassium carbonate (0.94 g, 6.78 mmol) were added to a solution of bromoacetamide **1** (1.78 g, 5.70 mmol) in acetonitrile (50 mL). The reaction mixture was heated under reflux at 85 °C for 72 h. The resulting mixture was then filtered over Celite® to remove the inorganic salts, and the filtrate was concentrated by evaporation of the solvents under vacuum. Finally, the title compound was purified by column chromatography over silica gel, eluting with 13% methanol in dichloromethane, to obtain an analytical sample. Yield: 1.41 g (1.63 mmol, 60%). Found: C 59.2%, H 7.7%, N 9.1%; $C_{46}H_{70}N_6O_{10}Br$ requires: C 58.3%, H 7.6%, N 8.9%. ^{1}H NMR (360 MHz, $CDCl_3$): δ = 7.96 (4H, d, $^3J_{H-H}$ = 7.5 Hz, Ar), 7.65 (2H, d, $^3J_{H-H}$ = 7.5 Hz, Ar), 3.30 (4H, s, $-NCH_2CONH-$), 3.11 (4H, s, $-NCH_2COO-$), 2.96 (8H, s, $-NCH_2CH_2N-$), 2.80 (8H, s, $-NCH_2CH_2N-$), 1.57 (18H, s, $C(CH_3)_3$), 1.38 (18H, s, $C(CH_3)_3$). ^{13}C NMR (90 MHz, $CDCl_3$): δ = 170.4 (CH_2COO^tBu), 169.5 (CH_2CONH), 165.2 ($ArCOO^tBu$), 141.5 (NH–Ar) 130.6 (Ar),

126.9 (*Ar*–COO), 117.4 (Ar), 81.0 ($C(CH_3)_3$), 80.6 ($C(CH_3)_3$), 56.8 (NCH_2CONH), 52.4 (NCH_2COO), 51.8 (NCH_2CH_2N), 48.1 (NCH_2CH_2N), 28.0 ($C(CH_3)_3$), 27.8 ($C(CH_3)_3$). *m/z* (ESI-TOF): 889.50 (100%, $[M + Na]^+$), an appropriate isotope pattern was observed.

Synthesis of 1,4,7,10-tetraazacyclododecane-1,7-bis(4-acetamidobenzoic)-4,10-diacetic acid (H_4L1). Trifluoroacetic acid (15 mL) was added to a solution of **2** (0.96 mmol) in dichloromethane (15 mL). The reaction mixture was stirred at room temperature for 16 h to promote the cleavage of the *tert*-butyl groups. The resulting mixture was evaporated under vacuum at low temperature (30 °C) until dryness. The residue was taken up in methanol, and the solvent was evaporated again. Finally, the residue was dissolved in the minimum amount of methanol and precipitated by addition of diethyl ether to properly recover a pale white solid. To further purify the compound, **H_4L1** (1 g) was dissolved in deionized water (100 mL) and the pH was set to 2.5 by adding concentrated hydrochloric acid to recrystallize the compound. Yield: 1.23 g (2.0 mmol, 91%). Found: C 44.4%, H 7.0%, N 10.3%; $C_{30}H_{38}N_6O_{10}\cdot 8H_2O$ requires: C 45.7%, H 7.2%, N 10.6%. ^{1}H NMR (400 MHz, $CDCl_3$): δ = 7.72 (4H, d, $^3J_{H-H}$ = 7.5 Hz, Ar), 7.37 (4H, d, $^3J_{H-H}$ = 7.5 Hz, Ar), 3.24 (4H, s, NCH_2COO), 2.88 (4H, s, NCH_2CONH), 2.43 (16H, mult., NCH_2CH_2N). ^{13}C NMR (100 MHz, $CDCl_3$): δ = 179.9 (CH_2COO), 174.9 (CH_2CONH), 172.3 (ArCOO), 140.6 (NH–Ar) 132.0 (Ar), 129.8 (*Ar*–COO), 120.6 (Ar), 58.7 (NCH_2CONH), 57.8 (NCH_2COO), 50.5 (NCH_2CH_2N). *m/z* (ESI-TOF): 665.25 (100%, $[H_4L1 + Na]^+$), an appropriate isotope pattern was observed. ν_{max} (FTIR, cm^{-1}): 3222m, 2995w, 2366s, 2341s, 1686s, 1598s, 1535s, 1409s, 1258s, 1170s, 1094s (Scheme 2).

Synthesis of discrete complexes

Synthesis of $[Mn(H_1L1)]\cdot[Na(H_2O)_6]\cdot 4H_2O$ (3). A stirred mixture of **H_4L1** (1.0 g, 1.56 mmol) in water (100 mL) was basified to pH = 8.0 with 1 M sodium hydroxide. Then, manganese chloride (195.8 mg, 1.56 mmol) in water (2 mL) was added dropwise into the previous solution. After this, the pH of the stirred mixture was readjusted again to 8.0, and the mixture was left at room temperature under stirring for 18 h. The pH of the suspension was again adjusted to pH = 12 to precipitate the excess of manganese chloride in the form of insoluble manganese hydroxides. The mixture was filtered, and the solids were discarded. The filtrate was then acidified to pH = 3 with 1 M hydrochloric acid to precipitate **3**. The precipitated complex was centrifuged, the solvent was replaced with fresh deionized water, and the solid was resuspended. This process was repeated twice. Finally, the suspension was filtered, and the pale yellow solid was air-dried. Yield: 1.1 g (1.36 mmol, 87%). Found: C, 45.4%, H 5.7%, N 10.4%; $C_{30}H_{47}N_6O_{16}MnNa$ requires: C 43.6%, H 5.7%, N 10.2%. *m/z* (ESI^-): 694.18 ($[Mn(HL1)]^-$, 100%), an appropriate isotope pattern was observed. ν_{max} (ATR, cm^{-1}): 3222m, 2968w, 2366s, 2341s, 1686s, 1598s, 1535s, 1409s, 1258s, 1170s, 1094s.

Synthesis of $[Ni(H_2L1)]\cdot 2H_2O$ (4). **4** was prepared following the same procedure as for **3**, except that nickel acetate (388 mg, 1.56 mmol) was used as the metal ion precursor, obtaining **4** as a light pink powder. Yield: 352 mg (0.50 mmol, 35%). Found: C 48.0%, H 5.3%, N 11.1%; $C_{30}H_{37}N_6O_{10}Ni\cdot 2H_2O$ requires: C 49.0%, H 5.5%, N 11.4%. *m/z* (ESI^+): 699.19 ($[Ni(H_3L1)]^+$, 100%), an appropriate isotope pattern was observed. ν_{max} (FTIR, cm^{-1}): 3222m, 2995w, 2366s, 2341s, 1686s, 1598s, 1535s, 1409s, 1258s, 1170s, 1094s.

Synthesis of coordination polymers

Synthesis of $[Zn(ZnL1)H_2O]\cdot 3H_2O$ (5). A solution of zinc acetate (85.6 mg, 390 μmol) in distilled water (2 mL) was added dropwise to a solution of **H_4L1** (100 mg, 156 μmol) in 10 mL of pure water, adjusted to pH = 6.7. After 10 minutes, the solution became cloudy leading to the precipitation of a white crystalline powder of **5**. The powder was then collected by centrifugation, washed several times in pure water and maintained on the same solvent. Yield: 47 mg (68 μmol, 47%). Found: C 42.5%, H 5.1%, N 10.1%; $C_{30}H_{36}N_6O_{11}Zn_2\cdot 3H_2O$ requires: C 42.8%, H 5.0%, N 10.0%. ν_{max} (FTIR, cm^{-1}): 3453w, 2927m, 2871m, 1673s, 1595vs, 1550s, 1472w, 1416m, 1371m, 1304s, 1259s, 1203m, 1158s, 1091s, 923s. The experimental *vs.* simulated PXRD pattern can be found in the ESI.†

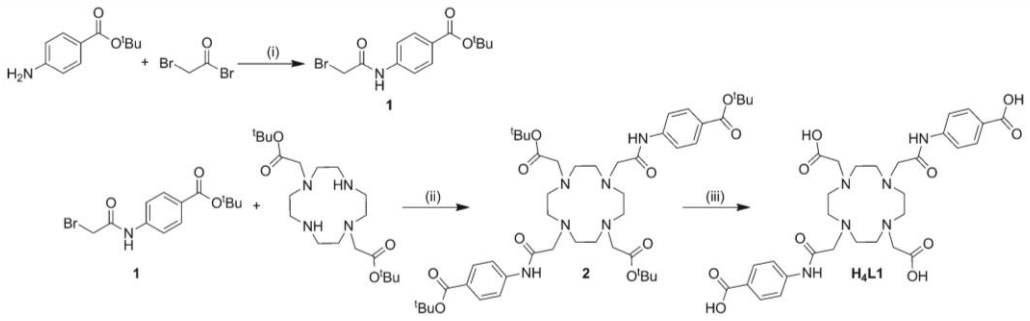

Scheme 2 Synthetic route for the synthesis of **H_4L1**. Reagents and conditions: (i) K_2CO_3, CH_2Cl_2, 0 °C to RT, 12 h; (ii) K_2CO_3, CH_3CN, reflux 85 °C, 72 h + column chromatography, 13% MeOH in CH_2Cl_2; (iii) trifluoroacetic acid, CH_2Cl_2, 16 h.

Synthesis of [Zn(NiL1)H_2O]·8H_2O (6). A mixture of 4 (133 mg, 154 mmol) and zinc acetate (67.6 mg, 308 mmol) in pure distilled water was basified to pH = 6.5 with 1 M NaOH. The solution was allowed to react for 12 h at 85 °C. After this period, plate-shaped crystals of 4 were collected by filtration, washed several times in pure water, and air-dried. Yield: 52.0 mg (74 μmol, 52%). Found: C 39.1%, H 5.8%, N 8.8%; $C_{30}H_{36}N_6O_{11}NiZn·8H_2O$ requires: C 39.0%, H 5.7%, N 9.0%. ν_{max} (FTIR, cm^{-1}): 3342m, 2860w, 1600s, 1529m, 1372s, 1305m, 1260m, 1182m, 1092m, 924m. The experimental *vs.* simulated PXRD pattern can be found in the ESI.†

Synthesis of [Zn(MnL1)H_2O]·9H_2O (7). A solution of zinc acetate (75 mg, 340 μmol) in distilled water (10 mL) was added dropwise to a solution of 3 (10 mL, 136 μmol) in water at room temperature and pH = 8.5. After 10 min, white crystals of 7 were collected by filtration, washed several times in pure water, and air-dried. Yield: 68.6 mg (97 μmol, 68%). Found: C 37.5%, H 5.6%, N 8.6%; $C_{30}H_{36}N_6O_{11}MnZn·9H_2O$ requires: C 38.4%, H 5.8%, N 8.9%. ν_{max} (FTIR, cm^{-1}): 3275m, 2972w, 2872w, 1663w, 1585s, 1540s, 1372s, 1316s, 1260s, 1170m, 1092s, 1003w, 969m. The experimental *vs.* simulated PXRD pattern can be found in the ESI.†

X-Ray crystallography

Refinement and structural information is shown in Table 1. Crystallographic data for 3–5 were collected at 293 K at the I19 beamline at Diamond Synchrotron (λ = 0.6889 Å). These data were indexed, integrated and scaled using CrystalClear software from Rigaku group programs. Absorption correction was performed by using the Multi-Scan method giving max./min. transmission factors of 1.000/0.923 (3), 1.000/0.654 (4), and 1.000/0.448 (5). Crystallographic data for 6 and 7 were collected at 100 K at the XALOC beamline at ALBA Synchrotron (λ = 0.71049 Å). These data were indexed, integrated and scaled using the XDS and IMOSFLM programs.[30] Absorption correction was not applied. Crystallographic data for **H_4L1** was collected at 293 K using a Bruker AXS SMART Apex diffractometer with graphite monochromated Mo-Kα radiation (λ = 0.71073 Å), and it was corrected for Lorentz and polarisation effects. The frames were integrated with the Bruker SAINT software package. Absorption corrections were applied using SADABS giving max./min. transmission factors of 1.000/0.270. The structures were solved by direct methods and subsequently refined by correction of F^2 against all reflections using SHELXS2013 and SHELXL2013 within the WinGX package.[31] All non-hydrogen atoms were refined with anisotropic thermal parameters by full-matrix least-squares calculations on F^2 using SHELXL2013, except for 3, where the oxygen atoms bound to the disordered sodium atom were refined with isotropic thermal parameters. Hydrogen atoms were inserted at calculated positions and constrained with isotropic thermal parameters. The hydrogen atoms of the different hydration water molecules present in all six structures were not located on the Fourier map but were added in the empirical formula to allow accurate determination of the density and absorption coefficient. The structure of 3 contains disordered $[Na(H_2O)_6]^+$. Two sites were identified corresponding to disordered partially occupied sodium atoms (one in a special position) and were refined with occupancy factors of 0.75/0.25. Due to this disorder, the oxygen atoms coordinated to these sodium ions were located and refined

Table 1 Crystallographic data of **H_4L1**, discrete complexes **3** and **4**, and coordination polymers **5**, **6** and **7**

Compound reference	**H_4L1**	**3**	**4**	**5**	**6**	**7**
Chemical formula	$C_{30}H_{38}N_6O_{10}$ ·7H_2O	$C_{30}H_{35}MnN_6O_{10}Na(H_2O)_6$ ·5H_2O	$C_{30}H_{36}N_6NiO_{10}$ ·H_2O	$C_{30}H_{34}N_6O_{11}Zn_2$ ·3H_2O	$C_{30}H_{34}N_6NiO_{11}Zn$ ·8H_2O	$C_{30}H_{34}N_6MnO_{11}Zn$ ·9H_2O
Formula mass	768.66	915.3	717.36	845.37	922.71	918.94
Crystal system	Monoclinic	Monoclinic	Monoclinic	Monoclinic	Monoclinic	Monoclinic
a/Å	13.691(4)	11.730(4)	18.780(4)	10.830(3)	11.360(3)	37.000(4)
b/Å	22.544(4)	19.810(4)	18.110(4)	18.480(3)	22.080(3)	12.500(4)
c/Å	11.572(4)	17.130(4)	9.200(4)	16.550(3)	15.560(3)	18.680(4)
α	90	90	90	90	90	90
β	96.98(4)	105.77(4)	106.22(4)	103.90(4)	90.20(3)	111.40(3)
γ	90	90	90	90	90	90
Unit cell volume	3545.2	3830.7(17)	3004.4(17)	3215.3(13)	3902(14)	8044(4)
Temperature	150	150	150	150	150	150
Space group	*C*2/*c*	*P*21/*c*	*C*2/*c*	*P*21/*n*	*P*21/*n*	*C*2/*c*
Z	4	4	4	4	4	8
Reflections measured	23 208	17 623	5619	8378	111 901	29 802
Independent reflections	3632	8623	2984	3420	5038	4738
Reflections ($I > 2\sigma(I)$)	2885	7786	2077	1497	4415	3765
R_{int}	0.0402	0.0267	0.042	0.117	0.099	0.057
R_1 ($I > 2\sigma(I)$)	0.1019	0.1048	0.0841	0.0951	0.1057	0.1041
w$R(F^2)$ ($I > 2\sigma(I)$)	0.2711	0.2944	0.2394	0.2204	0.3426	0.1171
R_1 (all data)	0.1222	0.1105	0.1095	0.1989	0.1127	0.3237
w$R(F^2)$ (all data)	0.2549	0.3013	0.2671	0.2896	0.3522	0.3450

with different occupancy factors to correlate the different occupancies to the presence of this $[Na(H_2O)_6]^+$ (CCDC 1443836–1443841).

Results and discussion

Crystal structures of H_4L1 and complexes 3 and 4

$H_4L1{\cdot}7H_2O$. Suitable crystals of H_4L1 for single-crystal X-ray diffraction were obtained by diffusion of acidic vapours into a solution of H_4L1 (5 mg mL^{-1}) in water placed in the fridge at 5 °C for one week. The structure was solved and refined in the monoclinic space group $C2/c$. The asymmetric unit was found to contain one half of the macrocyclic H_4L1 lying about a twofold axis, one half of a water molecule (O1W) on another twofold axis and three water molecules in general positions (Fig. 1a), resulting in the overall formula $H_4L1{\cdot}7H_2O$. Charge balance considerations and the location of residual Fourier peaks suggest that H_4L1 is protonated on two of the four central nitrogen atoms (N2 and N2#) and on two of the four carboxylic moieties (O2 and O2#). The macrocycles H_4L1 are linked by hydrogen-bonded interactions between them and water molecules to form 1D chains extending along the *ac* plane (Fig. S9, ESI†). Water molecules act as connectors between two N–H of the amide groups (N3–H···O1W, 2.16 Å; N3–H···O1W, 169°) and between two deprotonated C–O of the acetate pendant arms (O1W···O5, 2.813(0) Å; O1W–O5–C15, 116.84(6)°). In these chains, a deprotonated C–O of the acetate pendant arms also forms hydrogen bonds with a benzene carboxylic acid group (O–H) of the amide pendant arms (O2–H···O4, 1.67 Å; O2–H···O4, 174°).

$[Mn(H_1L1)]{\cdot}[Na(H_2O)_6]{\cdot}4H_2O$ (3). Suitable crystals for single-crystal X-ray diffraction were obtained by slow diffusion of acid vapours into a basic solution of 3 in water (5 mg mL^{-1}, pH = 8.5) at 5 °C for one week. Analysis of these crystals by single crystal X-ray diffraction gave a structure model in the monoclinic space group $P2_1/c$, where the asymmetric unit was found to contain one L1 macrocycle coordinated to a single Mn(II) ion (Fig. 1b) and one disordered $[Na(H_2O)_6]^+$ counterion. The Mn(II) ion is placed within the macrocyclic cavity in a square antiprismatic molecular geometry. The square antiprism has one plane defined by the four aza nitrogen atoms from the macrocyclic core and the other plane defined by O1 and O6 of the amide groups and O4 and O9 of the acetate pendant arms. Mn(II) ion lies 1.324(0) Å above the plane formed by the four aza nitrogen atoms and 1.219(3) Å below the plane defined by the four oxygen atoms. The presence of a Na cation means that 3 must be negatively charged. By comparing the C–O distances of both benzene carboxylic acid groups, it can be noted that the C28–O7 distance (1.319(7) Å) is longer compared to C28–O8 (1.227(5) Å), C17–O2 (1.272(3) Å) and C17–O3 (1.241(1) Å) distances. These differences indicate that O7 is protonated, while the others are not. In the structure, this benzene carboxylic acid group is participating in a hydrogen bond with an acetate pendant arm (O7–H···O4, 1.71 Å; O7–H···O4, 163°) of another complex, while the amide group of the same amide pendant arm is H-bonded with the benzene carboxylic acid group of the non-equivalent amide pendant arm (N6–H···O2, 2.03 Å; N6–H···O2, 162°). Both types of hydrogen bonds define the formation of an H-bonded layer (Fig. S10, ESI†). In these layers, two equivalent protonated benzene carboxylic aromatic rings also form an offset face-to-face π–π interaction with a distance of 3.701(6) Å from centroid to centroid.

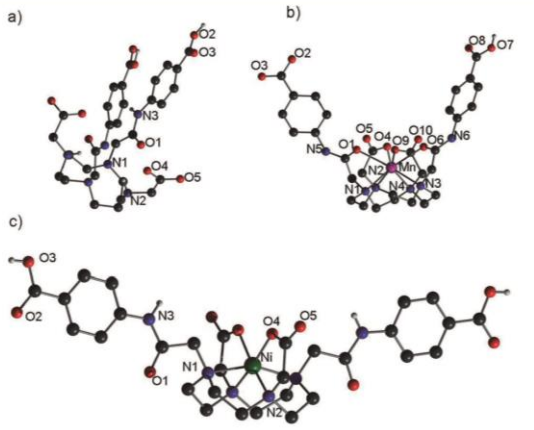

Fig. 1 Ball and stick representation of the crystal structures of (a) H_4L1, (b) 3 and (c) 4. The structures are represented with unique heteroatom labelling. Hydrogen atoms describing the protonation state have been included, and the rest have been omitted for clarity.

$[Ni(H_2L1)]{\cdot}2H_2O$ (4). Crystals of 4 suitable for single-crystal X-ray diffraction were obtained by slow diffusion of acid vapours into a basic solution of 4 in water (5 mg mL^{-1}, pH = 8.5) at 5 °C for one week. The structure was solved and refined in the monoclinic space group $C2/c$, where the asymmetric unit was found to contain one half of the complex with the Ni1 ion lying on a twofold axis. L1 coordinates to a single Ni(II) ion within the macrocyclic cavity in a highly distorted octahedral geometry (Fig. 1c). In this case, the four nitrogen atoms are far from being coplanar, lying at 0.397(4) Å from the average plane. The coordination sphere of Ni(II) is formed by the four aza nitrogen atoms and two equivalent O4 atoms of the acetate pendant arms. Contrary to 3, the oxygen atoms of the amide groups are not involved on any coordination bond, leaving both pendant arms free to rotate. The absence of any counterion and the symmetry equivalence between the two amide pendant arms indicate that both benzene carboxylic acid groups are protonated. These complexes are linked by hydrogen bonds to form layers along the *ac* plane (Fig. S11, ESI†). These layers are created by the typical $R_2^2(8)$ H-bonded dimers formed through the two benzene carboxylic acid groups (O3–H···O2, 1.82 Å; O3–H···O2, 168°) and hydrogen bonds involving N–H of the amide groups and C=O of the acetate pendant arms (N3–H···O5, 1.93 Å; N3–H···O5, 176°). These interactions formed a very compact structure in which only a hydrogen-bonded water molecule

(O1W···O4, 3.022(1) Å; O1W–O4–C15, 132.22(2)°) fits in the asymmetric unit.

Crystal structures of coordination polymers

[Zn(ZnL1)H$_2$O]·3H$_2$O (5). 5 crystallises in the monoclinic space group $P2_1/n$ forming a one-dimensional coordination polymer. Its asymmetric unit contains two Zn(II) ions exhibiting two different coordination environments. Zn1 is chelated within the macrocyclic cavity through the four aza nitrogen atoms, two acetate (O4 and O9) pendant arms and O1 of the amide pendant arm in a capped trigonal prism molecular geometry (Fig. 2a). Zn2 adopts a distorted square pyramidal geometry coordinated to two benzene carboxylate groups in a bidentate (O7 and O8) and monodentate (O2) fashion, one acetate group (O5) that bridges Zn1 and Zn2, and one water molecule (Fig. 2b). The structure of 5 is constructed by the connection of Zn2 ions through three different L1 linkers, forming a double-strand chain in a zigzag conformation that extends along the *b* axis (Fig. 2c and d). The double-strand chains are then connected to each other along the *a* direction through hydrogen bonds (Fig. 2d). These hydrogen bonds (Fig. S12, ESI†) are defined between the uncoordinated amide and the non-bridging acetate group (N6–H···O10, 2.03 Å; N6–H···O10, 160°) and between a water molecule that acts as a connector between the coordinated amide group (N5–H···O2W, 1.91 Å; N5–H···O2W, 169°) and the bidentate benzene carboxylic acid group (O2W···O8, 2.852(1) Å; O2W–O8–C28, 149.13(5)°).

[Zn(NiL1)H$_2$O]·8H$_2$O (6). 6 also crystallises in the monoclinic space group $P2_1/n$, forming a one-dimensional coordination polymer. Its asymmetric unit contains a slightly modified building unit 4 (only the benzene rings are slightly rotated) and one Zn(II) ion connecting these units. As in 4, the Ni(II) ion shows a distorted octahedral geometry coordinated by the four aza nitrogen atoms and O4 and O9 of two acetate pendant arms (Fig. 3a). On the other hand, the Zn(II) ion is tetrahedrally coordinated to two benzene carboxylate groups (O3 and O7) acting both in a monodentate fashion, one O5 of the acetate pendant arm and one water molecule (Fig. 3b). In this structure, each Zn(II) ion connects three different nickelated L1 units creating a double strand chain extending along the [110] and [−110] directions (Fig. 3c and d). The different chains form a cross-linked structure in which the water molecule O2W acts as the connector between two different double-strand chains, forming hydrogen bonds (Fig. S13, ESI†) with one of the amide groups (N6–H···O2W, 2.02 Å; N6–H···O2W, 170°) and one oxygen atom from the benzene carboxylate moiety (O2W···O2, 2.818(1) Å; O2W–O2–C17, 105.58(0)°). In addition, the coordinated water molecule forms a hydrogen bond with the acetate pendant arm (O1W···O10, 2.591(0) Å; O1W–O10–C30, 140.07(4)°).

[Zn(MnL1)H$_2$O]·9H$_2$O (7). 7 crystallises in the monoclinic space group $C2/c$, forming a two-dimensional coordination polymer. The structural model shows a modified building unit 3 and one Zn(II) connecting these units. Indeed, if we compare the initial conformation of the building unit 3 with

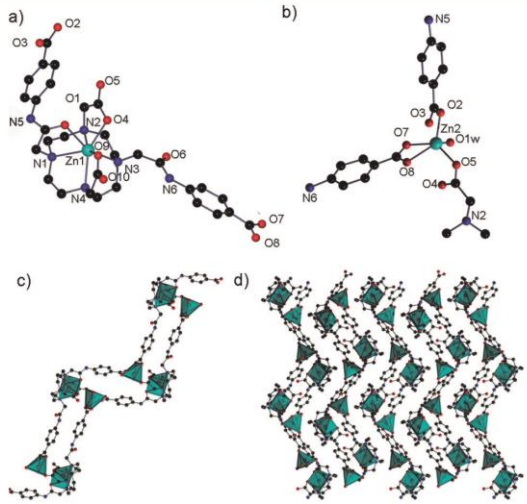

Fig. 2 Ball and stick representation of the crystal structure of 5. (a) Zn1–L1 unit. (b) Zn2 unit. (c) Double strand chain extending along the *b* axis. (d) Packing of the double strand chains viewed along the *b* axis. The sky blue capped trigonal prisms and square pyramids represent the coordination environment of Zn(II) in (c) and (d). H atoms have been omitted for clarity. Atom colour code: Zn, sky blue; C, black-grey; N, blue; O, red.

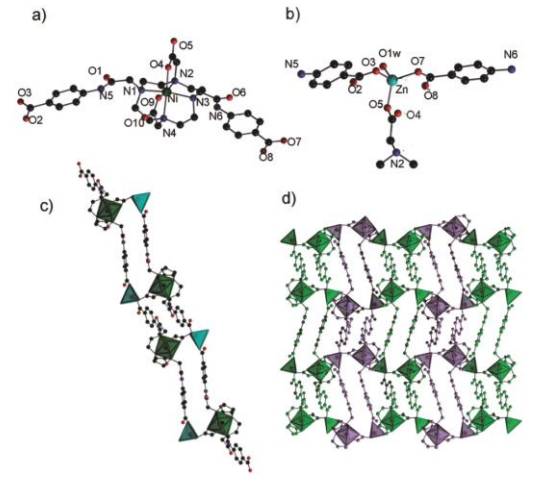

Fig. 3 Ball and stick representation of the crystal structure of 6. (a) Ni–L1 unit. (b) Zn unit. (c) Double strand chain extending along the [110] or [−110] direction. (d) Neighbouring double strand chains viewed along the *a* axis. The green octahedra and sky blue tetrahedra represent the coordination environment of Ni(II) and Zn(II), respectively, in (c). Different chains have been differently coloured in (d). H atoms have been omitted for clarity. Atom colour code: Zn, sky blue; Ni, green; C, black-grey; N, blue; O, red.

that found in 7, a clear difference is that the Mn(II) ion has changed its coordination number from eight to seven. This change leaves one amide pendant arm free to be accommodated in an extended position and, thus, facilitates the coordination of Zn(II) ions with the two benzene carboxylic acid groups. In 7, the Mn(II) ion adopts a capped trigonal prismatic geometry coordinated to the four aza nitrogen atoms, O4 and O9 atoms of two acetate pendant arms and O1 of the amide pendant arm (Fig. 4a). Similar to **6**, the Zn(II) ion is tetrahedrally coordinated to two benzene carboxylate groups (O2 and O7) acting both in a monodentate fashion, one O5 of the acetate pendant arm and one water molecule (Fig. 4b). The coordination structure is built up from connecting each Mn(II)–**L1** unit through three different Zn2 ions (Fig. 4c), forming corrugated layers that grow along the (−101) plane. The different layers are packed in an ABAB sequence connected *via* a water molecule, which directly connects these layers through two hydrogen bond interactions (Fig. S14, ESI†) involving one amide pendant arm (N5–H···O4W, 2.13 Å; N5–H···O4W, 157°) and one benzene carboxylate moiety (O4W···O2, 2.962(4) Å; O4W–O2–C17, 132.79(2)°) and weak contacts through their aliphatic moieties (Fig. 4d and e and Fig. S14, ESI†). As shown in Fig. 4e, the remaining water molecules form independent H-bonded networks that run parallel to the (−101) plane.

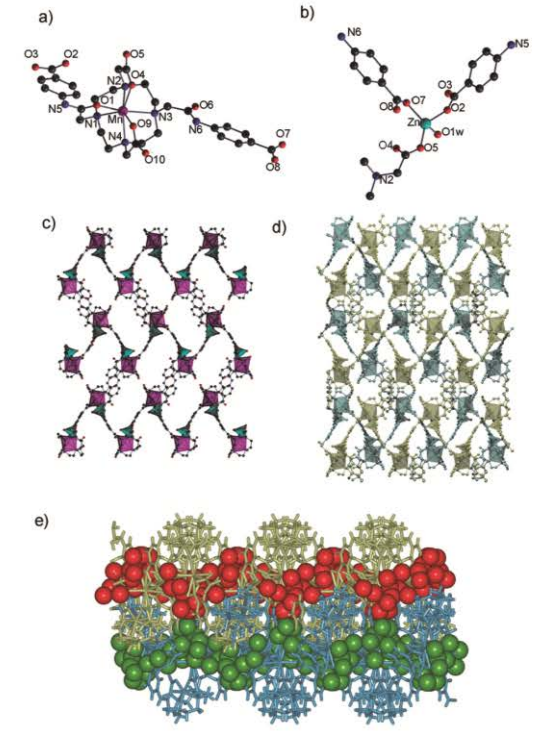

Fig. 4 Ball and stick representation of the crystal structure of **7**. (a) Mn–**L1** unit. (b) Zn unit. (c) Single coordination layer viewed along the *c* axis. (d) Two neighbouring layers viewed along the *c* axis. (e) Two neighbouring corrugated layers viewed along the [101] axis, showing the independent H-bonded network of guest water molecules. The violet capped trigonal prisms and the sky blue tetrahedra represent the coordination environment of Mn(II) and Zn(II) in (c). The two layers in (d) and (e) and the two H-bonded networks of water molecules in (e) have been differently coloured. H atoms have been omitted for clarity. Atom colour code: Zn, sky blue; Mn, violet; C, black-grey; N, blue; O, red.

Structural integrity and water adsorption of 7

The high content of water molecules in the framework of **7** prompted us to investigate its behaviour upon water sorption/desorption. Initially, we performed a thermogravimetric analysis (TGA) on **7**, showing a first weight loss of 21.2% from 20 to 120 °C. This loss was attributed to the loss of all water molecules (19.2%) according to the molecular formula $[Zn(MnL1)H_2O]\cdot 9H_2O$ (Fig. 5a). A second weight loss was found in the temperature range of 340–470 °C corresponding to the decomposition of the framework.

To evaluate the water-vapour sorption properties, **7** was first activated at 120 °C overnight under vacuum, and the activated sample (**7′**) was characterized by TGA and PXRD (Fig. 5a and b). TGA revealed the absence of any weight loss from 20 to 340 °C, confirming that **7′** was free of guest water molecules. On the other hand, the experimental PXRD showed that **7′** becomes an amorphous material after evacuating the water molecules. This behaviour is not unexpected as layers of **7** are three-dimensionally packed *via* hydrogen-bonded water molecules, so that their removal is likely inducing their disordering and loss of crystallinity. Remarkably, the framework of **7** was recovered when **7′** was re-immersed in water or exposed to water vapors (Fig. 5b), as confirmed by

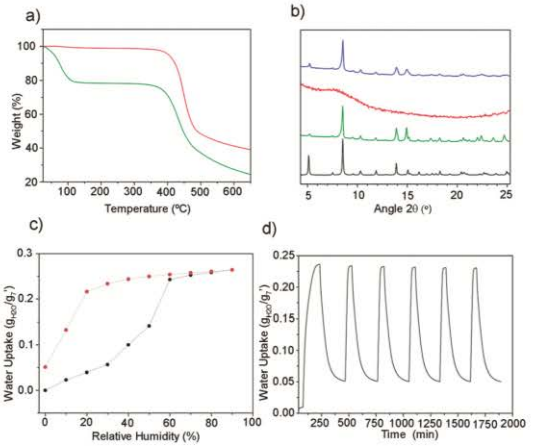

Fig. 5 (a) TGA of **7** (green) and **7′** (red). (b) PXRD patterns of **7**: simulated (black), as made (green), activated under vacuum at 120 °C (red), and activated and immersed in water for 48 h (blue). (c) Water isotherm of **7** at 25 °C. (d) Water sorption/desorption cycles at 60% and 2% RH.

X-ray powder diffraction (XRPD) patterns. This reversible behavior is typical of a type-I "crystal-to-amorphous transformation" as described by Kitagawa *et al.*[29]

Dynamic water sorption measurements performed on 7′ showed an adsorption branch with a sigmoidal shape representative of a type II trend.[32] The water uptake reaches a plateau at a relative humidity (RH) of 60%, achieving an uptake of 0.23 g of H_2O per g of 7′. The maximum water uptake was 0.26 g of H_2O per g of 7′ at a RH of 90%. This weight increase can be attributed to 10 water molecules (calculated on the basis of the dehydrated formula, theoretical = 24%), in agreement with TGA results and the initial hydrated crystal structure. In addition, we observed a hysteresis loop between the adsorption and desorption branches, from which 5.1% in weight was found to be not desorbed. This percentage can be attributed to two water molecules (calculated on the basis of the dehydrated formula, theoretical = 4.7%) that cannot be desorbed without heating this material. We can tentatively ascribe these two water molecules to those that are more strongly bonded in the framework of 7, that is, O1W that is coordinated to the Zn(II) ions (Fig. 4b) and O4W that is responsible for three-dimensionally connecting the coordination layers through several hydrogen bond interactions (Fig. S14, ESI†). In fact, when performing an XRPD of the sample resulting from the desorption process, we could observe a certain degree of crystallinity, thus confirming that this sample shows a certain ordering between layers (Fig. S15, ESI†).

We then performed six water sorption/desorption cycles by alternately exposing the outgassed material to humid (60% RH) and dry (2% RH) environments (Fig. 5d). Remarkably, the maximum uptake at 60% RH (*ca.* 23%) was not significantly modified with the number of cycles, confirming the stability of the material to water sorption/desorption processes. Furthermore, it should be noted that the 5% in weight of water molecules that remains in the material after desorption reduces its working capacity. However, as a counterpart, it makes the cycles narrower, which means that this slightly crystalline material shows a faster response to water sorption than its amorphous analogue 7′.

Conclusions

In conclusion, we have synthesised a tetraazacyclododecane-based linker **H_4L1** and demonstrated its versatility in the formation of two discrete Mn(II) and Ni(II) chelates showing free carboxylic groups. These complexes were further used, in a second step, as metallated building units to create two heterometallic Zn(II)–Ni(II) (6) and Zn(II)–Mn(II) (7) coordination polymers. In addition, a third homometallic Zn(II)-based coordination polymer (5) was synthesized by direct mixing of **H_4L1** with Zn(II) ions. 5 and 6 show extended double strand chains stacked to each other through hydrogen bonds, whereas 7 forms corrugated layers packed in an ABAB fashion also containing independent H-bonded networks of water molecules. Interestingly, this coordination polymer exhibits a reversible type-I "crystal-to-amorphous transformation" upon water sorption/desorption and a plateau uptake of 23% in weight at 60% RH and is stable up to at least six water sorption/desorption cycles.

Acknowledgements

This work was supported by MINECO-Spain through project PN MAT2012-30994. I. I. and J. A. thank MINECO for an RyC contract (RYC-2010-06530) and an FPU predoctoral grant (AP-2010-5934), respectively. ICN2 acknowledges the support of the Spanish MINECO through the Severo Ochoa Centers of Excellence Program, under Grant SEV-2013-0295.

Notes and references

1 G. Férey, *Chem. Soc. Rev.*, 2008, **37**, 191–214.
2 C. Janiak, *Dalton Trans.*, 2003, 2781–2804.
3 S. Kitagawa, R. Kitaura and S. Noro, *Angew. Chem., Int. Ed.*, 2004, **43**, 2334–2375.
4 F. A. Almeida Paz, J. Klinowski, S. M. F. Vilela, J. P. C. Tomé, J. A. S. Cavaleiro and J. Rocha, *Chem. Soc. Rev.*, 2012, **41**, 1088–1110.
5 D. Zhao, D. J. Timmons, D. Yuan and H. C. Zhou, *Acc. Chem. Res.*, 2011, **44**, 123–133.
6 W. Lu, Z. Wei, Z.-Y. Gu, T.-F. Liu, J. Park, J. Park, J. Tian, M. Zhang, Q. Zhang, T. Gentle Iii, M. Bosch and H.-C. Zhou, *Chem. Soc. Rev.*, 2014, **43**, 5561–5593.
7 Y. Takashima, V. M. Martínez, S. Furukawa, M. Kondo, S. Shimomura, H. Uehara, M. Nakahama, K. Sugimoto and S. Kitagawa, *Nat. Commun.*, 2011, **2**, 168.
8 J. Park, D. Yuan, K. T. Pham, J.-R. Li, A. Yakovenko and H.-C. Zhou, *J. Am. Chem. Soc.*, 2012, **134**, 99–102.
9 D. H. Busch, *Acc. Chem. Res.*, 1978, **11**, 392–400.
10 T. Hubin, *Coord. Chem. Rev.*, 2003, **241**, 27–46.
11 F. Benetollo, G. Bombieri, L. Calabi, S. Aime and M. Botta, *Inorg. Chem.*, 2003, **42**, 148–157.
12 R. Cibulka, R. Vasold and B. König, *Chem. – Eur. J.*, 2004, **10**, 6224–6231.
13 C.-S. Jeung, J. B. Song, Y.-H. Kim and J. Suh, *Bioorg. Med. Chem. Lett.*, 2001, **11**, 3061–3064.
14 E. Tamanini, A. Katewa, L. M. Sedger, M. H. Todd and M. Watkinson, *Inorg. Chem.*, 2009, **48**, 319–324.
15 S. J. Ratnakar, M. Woods, A. J. M. Lubag, Z. Kovacs and A. D. Sherry, *J. Am. Chem. Soc.*, 2008, **130**, 6–7.
16 L. M. De León-Rodríguez, S. Viswanathan and A. D. Sherry, *Contrast Media Mol. Imaging*, 2010, **5**, 121–125.
17 J. M. Taylor, R. K. Mah, I. L. Moudrakovski, C. I. Ratcliffe, R. Vaidhyanathan and G. K. H. Shimizu, *J. Am. Chem. Soc.*, 2010, **132**, 14055–14057.
18 D. A. Knight, J. B. Delehanty, E. R. Goldman, J. Bongard, F. Streich, L. W. Edwards and E. L. Chang, *Dalton Trans.*, 2004, 2006–2011.
19 G. Ortiz, S. Brandès, Y. Rousselin and R. Guilard, *Chem. – Eur. J.*, 2011, **17**, 6689–6695.
20 E. Y. Lee and M. P. Suh, *Angew. Chem., Int. Ed.*, 2004, **43**, 2798–2801.

21 C. S. Hawes, S. R. Batten and D. R. Turner, *CrystEngComm*, 2014, **16**, 3737–3748.
22 H.-M. Zhang, H. Wu, Y.-Y. Liu, J. Yang, D.-W. Kang and J.-F. Ma, *CrystEngComm*, 2015, **17**, 1583–1590.
23 C. S. Hawes, Y. Nolvachai, C. Kulsing, G. P. Knowles, A. L. Chaffee, P. J. Marriott, S. R. Batten and D. R. Turner, *Chem. Commun.*, 2014, **50**, 3735–3737.
24 D. Kong, D. G. Medvedev and A. Clearfield, *Inorg. Chem.*, 2004, **43**, 7308–7314.
25 L. V. Tsymbal, Y. D. Lampeka, V. I. Boyko, V. I. Kalchenko, S. V. Shishkina and O. V. Shishkin, *CrystEngComm*, 2014, **16**, 3707–3711.
26 W.-Y. Gao, Y. Niu, Y. Chen, L. Wojtas, J. Cai, Y.-S. Chen and S. Ma, *CrystEngComm*, 2012, **14**, 6115–6117.
27 A. Carné-Sánchez, C. S. Bonnet, I. Imaz, J. Lorenzo, E. Tóth and D. Maspoch, *J. Am. Chem. Soc.*, 2013, **135**, 17711–17714.
28 J. Zagal, M. Páez and J. F. Silva, in *N4-Macrocyclic Metal Complexes*, ed. J. Zagal, F. Bedioui and J.-P. Dodelet, Springer, New York, 2006.
29 S. Kitagawa and K. Uemura, *Chem. Soc. Rev.*, 2005, **34**, 109–119.
30 W. J. Kabsch, *J. Appl. Crystallogr.*, 1993, **26**, 795–800.
31 G. M. Sheldrick, *Acta Crystallogr., Sect. A: Found. Crystallogr.*, 2008, **64**, 112–122.
32 S. Brunauer, *The Adsorption of Gases and Vapors, Vol. 1, Physical Adsorption*, Princeton University Press, Princeton, NJ, 1945.

ChemComm

COMMUNICATION

View Article Online
View Journal | View Issue

Cite this: *Chem. Commun.*, 2016, 52, 7229

Received 7th April 2016,
Accepted 4th May 2016

DOI: 10.1039/c6cc02908f

www.rsc.org/chemcomm

Single-crystal and humidity-controlled powder diffraction study of the breathing effect in a metal–organic framework upon water adsorption/desorption†

Javier Aríñez-Soriano,[a] Jorge Albalad,[a] Christian Vila-Parrondo,[a] Javier Pérez-Carvajal,[a] Sabina Rodríguez-Hermida,[a] Aurelio Cabeza,[b] Jordi Juanhuix,[c] Inhar Imaz*[a] and Daniel Maspoch*[ad]

Herein we report a study on water adsorption/desorption-triggered single-crystal to single-crystal transformations in a MOF, by single-crystal and humidity-controlled powder X-ray diffraction and water-sorption measurements. We identified a gate-opening effect at a relative humidity of 85% upon water adsorption, and a gate-closure effect at a relative humidity of 55 to 77% upon water desorption. This reversible breathing effect between the "open" and the "closed" structures of the MOF involves the cleavage and formation of several coordination bonds.

Research on metal–organic frameworks (MOFs), also known as porous coordination polymers (PCPs), has recently put the spotlight on applications that rely on water-sorption properties. These applications include heat transformation;[1–4] enhancement of CO_2 capture;[5–7] proton conductivity;[8–11] air dehumidification;[12] and water delivery in remote areas.[13] Among the various MOFs that have shown promising water-sorption capabilities,[2,14] the flexible "third-generation" MOFs[15–17] are very interesting because, upon exposure to water at a very specific gate pressure, they can undergo a reversible change from a "closed" structure to an "open" one. Consequently, these MOFs can exhibit stepwise adsorption of water (usually reflected by an S-shape water-sorption isotherm) or behave as water-induced switching materials, which are useful for applications such as heat transformation,[18] sensors[19] and proton conductivity.[20–22] A clear example of this type of flexible MOF is Al-MIL-53-OH,[14,23] which abruptly takes up water at a relative humidity (RH) of roughly 80%, due to a phase transition from its "closed" structure to its "open" one.

To date, very few studies on the breathing effects induced by water sorption in MOFs have been done, and even fewer studies have explored the single crystal-to-single crystal (SC–SC) transformations between the "closed" and "open" structures during water sorption.[24,25] Knowledge on these phase transitions is important for understanding the pertinent water-sorption mechanisms and for developing more efficient MOFs. Much of the work done so far has focused on investigating SC–SC transformations induced by water in dense MOFs—namely, to study the reversible transitions between crystalline states with different proton conductivities.[20–22] Importantly, a case showing a water-induced SC–SC transformation between "closed" and "open" structures was reported by Chen *et al.*, who found a transition between a 5-fold interpenetrated network (the "open" or hydrated structure) and a 6-fold interpenetrated network (the "closed" or dehydrated structure). They proved that these reversible transformations involved coordination bond cleavages and formation in which water molecules intervened.[25] More recently, Morris *et al.* studied the SC–SC transformation of a flexible MOF by using *in situ* temperature-controlled single-crystal diffraction studies. They found that the transition between the hydrated porous phase (which is porous to NO) and the dehydrated non-porous phase involved the reversible breaking and formation of several bonds.[26] Importantly, neither of these two examples has been investigated in terms of water sorption.

Herein, we report a study on water adsorption/desorption-triggered SC–SC transformations in a MOF, by single-crystal and humidity-controlled powder X-ray diffraction and water-sorption measurements. Specifically, we describe the synthesis of a new flexible MOF, of formula $[Mn_2(Gd\text{-}H\text{-}DOTA\text{-}4AmP)(H_2O)_7]\cdot 21H_2O$ (**1**) [where Gd-H_8-DOTA-4AmP is Gd(III)-1,4,7,10-tetraazacyclododecane-1,4,7,10-tetraacetamidomethylene phosphonic acid (Fig. 1a)],[27] which exhibits an S-shape (Type V)[28,29] water isotherm. It abruptly takes up water at a RH of 85%, reaching

[a] *Catalan Institute of Nanoscience and Nanotechnology (ICN2), CSIC and The Barcelona Institute of Science and Technology, Campus UAB, Bellaterra, 08193 Barcelona, Spain. E-mail: inhar.imaz@icn2.cat, daniel.maspoch@icn2.cat*
[b] *Dpto Química Inorgánica, Cristalografía y Mineralogía, Universidad de Málaga, Campus de Teatinos s/n, 29071 Málaga, Spain*
[c] *ALBA Synchrotron, 08290 Cerdanyola del Vallès, Barcelona, Catalonia, Spain*
[d] *Institució Catalana de Recerca i Estudis Avançats (ICREA), 08100 Barcelona, Spain*

† Electronic supplementary information (ESI) available: Experimental section, TGA, PXRD, and water sorption measurements. 1471149 (**1-*op***) and 1471150 (**1-*cp***). For ESI and crystallographic data in CIF or other electronic format see DOI: 10.1039/c6cc02908f

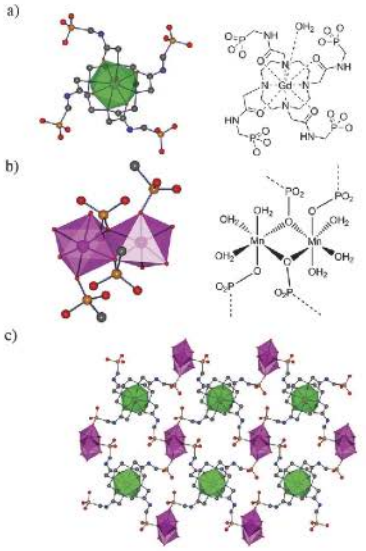

Fig. 1 Crystal structure of **1-*op***. (a) Coordination environment of Gd-H-DOTA-4AmP. (b) Representations of the $[Mn_2(PO_3R)_4(H_2O)_6]$ binuclear building unit. (c) View of a coordination layer along the *b*-axis. Colour code: Gd, green; Mn, pink; P, orange; O, red; N, blue; and C, grey. H atoms have been omitted for clarity.

its total water uptake of 0.4 $g_{water}\ g_1^{-1}$ at a RH of 95%. We used single-crystal X-ray diffraction (SCXRD) and humidity controlled powder X-ray diffraction (PXRD) measurements to determine that the water adsorption/desorption mechanism in **1** involves an SC–SC transition between two different phases: **1-*op*** (**1** open pore) and **1-*cp*** (**1** closed pore). To our knowledge, this is the first-ever reported use of humidity-controlled PXRD measurements on a flexible MOF to understand its water-sorption behaviour in terms of SC–SC transition.

Crystals of **1-*op*** suitable for SCXRD were obtained by the reaction of Gd-H_8-DOTA-4AmP with manganese acetate tetrahydrate in water at room temperature for 10 days (yield: 80%). The structure of **1-*op*** was resolved and refined in the monoclinic space group $P2_1/c$, revealing the formation of a 2-D network of formula $[Mn_2(Gd\text{-}H\text{-}DOTA\text{-}4AmP)(H_2O)_7]\cdot 2H_2O$. The basic unit of **1-*op*** is a binuclear unit of formula $[Mn_2(PO_3R)_4(H_2O)_6]$, in which the two Mn(II) ions are bridged by two O atoms of two phosphonate groups (Fig. 1b). Both Mn(II) centres adopt a distorted octahedral geometry coordinated to three O atoms of phosphonate groups and to three water molecules. In this structure, each binuclear unit is connected to four Gd-H-DOTA-4AmP linkers and each Gd-H-DOTA-4AmP linker is connected to four binuclear Mn(II) units, creating layers extending along the *ac* plane (Fig. 1c). These layers show a corrugated conformation and stack up along the *b*-axis, forming 1-D channels that run along the *a*-axis (Fig. 2). The channels have dimensions of approximately 14.8 Å × 9.5 Å, affording an estimated solvent-accessible void volume of 2657 Å^3, which represents 45% of the total cell volume (5958 Å^3) of **1-*op***. These channels are filled with 21 guest water molecules per formula unit, as confirmed by elemental analysis and thermogravimetric (TGA) analysis (Table S2 and Fig. S1, ESI†).

Interestingly, single crystals of **1-*op*** underwent structural transformations when they were exposed to a dry environment (RH < 40%) for 8 hours. SCXRD performed on the resulting crystals revealed the formation of a new phase, of formula $[Mn_2(Gd\text{-}H\text{-}DOTA\text{-}4AmP)(H_2O)_7]\cdot 5H_2O$ (**1-*cp***), which crystallises in the monoclinic space group $C2/c$. **1-*cp*** is also formed by coordination layers made of binuclear Mn(II) units bridged by Gd-H-DOTA-4AmP linkers. However, compared to **1-*op***, **1-*cp*** showed drastically reduced cell volume (compare 5958 Å^3 (**1-*op***) to 4335 Å^3 (**1-*cp***); 27% reduction), and especially, reduced solvent-accessible volume (from 2657 Å^3 (**1-*op***) to 682 Å^3 (**1-*cp***); 74% reduction). As expected, this reduction makes **1-*cp*** almost non-porous to N_2 (S_{BET} = 30 $m^2\ g^{-1}$) and CO_2 (Fig. S3, ESI†). This reduction is a direct consequence of the transition from the

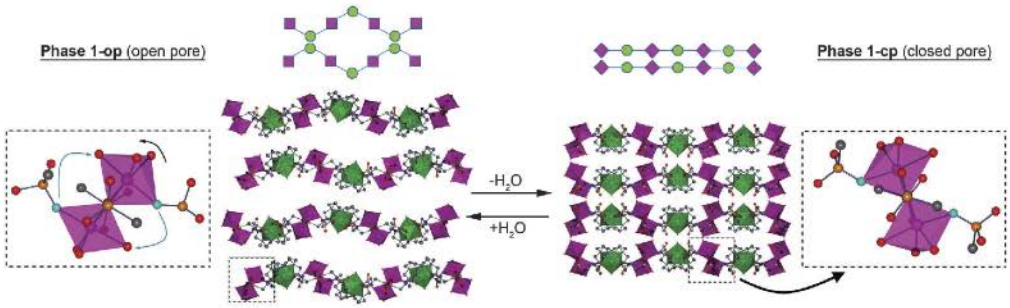

Fig. 2 Schematic representations and views of (top, left) the corrugated coordination layers of **1-*op*** and (top, right) the flatter coordination layers of **1-*cp*** along the *a*-axis. Note that the corrugated layers define the 1D channels, whereas the flat layers close them. (bottom, left) Details of the Mn(II) binuclear subunit in **1-*op*** showing the cleavage/formation of coordination bonds (blue arrows) and the rotation of the subunit (black arrow) during the phase transition. (bottom, right) View of the resulting binuclear subunit in **1-*cp***. Colour code: Gd, green; Mn, pink; P, orange; O, red; N, blue; and C, grey. H atoms have been omitted for clarity.

corrugated conformation of the coordination layers in **1-*op*** to a flatter conformation in **1-*cp***. This change leads to closer packing between the coordination layers along the *b*-axis [*b*-axis is reduced from 19.8 Å (**1-*op***) to 14.5 Å (**1-*cp***)], thereby closing the 1D channels (Fig. 2). This dense packing means that, whilst there is no direct hydrogen bonding between the corrugated layers of **1-*op***, the closest layers in **1-*cp*** form two direct hydrogen bonds between the O3 atom of the phosphonate group and the Mn(II)-bound water molecule O3W (O3W···O3, 2.83 Å) and the O7 atom of the phosphonate group and Gd(III)-bound water molecule O1W (O1W···O7, 2.65 Å; Fig. S4, ESI†). Interestingly, it also involves the removal of sixteen guest water molecules, such that only five guest water molecules remain between the layers of **1-*cp***, as confirmed by elemental analysis and TGA (Table S3 and Fig. S1, ESI†).

A more detailed analysis of the **1-*op*** → **1-*cp*** transformation shows that the transition from the corrugated layers to the flatter layers is promoted by the rotation of the Mn(II) binuclear building unit around the *a* axis (Fig. 2). As illustrated in Fig. 2, this rotation requires the cleavage and formation of two phosphonate–Mn(II) and two water–Mn(II) coordination bonds per binuclear Mn(II) unit. Here, we hypothesise that guest water molecules may participate in this ligand exchange mechanism by coordinating to the Mn(II) ions and forming intermediate species such that two coordinated water molecules would ultimately be replaced with two guest water molecules.[25,30]

To verify the reversibility of this SC–SC transformation, we incubated crystals of **1-*cp*** in water overnight. PXRD analysis of the resulting crystals revealed that the **1-*op*** phase is recovered (Fig. S5, ESI†), demonstrating that the transition **1-*op*** ↔ **1-*cp*** is reversible. As **1-*op*** ↔ **1-*cp*** involves the loss and gain of many water molecules, we then investigated whether **1** shows a gate-opening effect upon water sorption. To this end, we combined water-sorption measurements with PXRD analysis in a humidity-controlled environment (Fig. 3 and 4).[31,32] The collected water isotherm showed different paths between the adsorption and desorption branches. In this isotherm, the water adsorption branch follows a representative type II trend up to a RH of 85%, in which the water uptake is 0.28 $g_{water}\ g_1^{-1}$ or 19 H_2O per formula unit. At this RH, a step appears, changing the trend of the isotherm from type II to type V; behaviour that is characteristic of a gate-opening effect in flexible MOFs (Fig. 3a).[33] This event increases the water uptake up to 0.40 $g_{water}\ g_1^{-1}$ or 28 H_2O per formula unit at a RH of 95%. The presence of this step is in agreement with the transition phase **1-*cp*** → **1-*op*** recorded using humidity-controlled PXRD measurements (Fig. 3b). Indeed, while the characteristic PXRD pattern of **1-*cp*** was observed up to an RH of 80%, the PXRD pattern at a RH of 90% (corresponding to the middle of the step) showed the coexistence of peaks characteristic of both phases. The transition was completed at a RH of 95%, in which the PXRD pattern showed the characteristic pattern of **1-*op***.

The desorption branch also shows a step in the RH range from 70% to 55% (Fig. 4a). This abrupt desorption of water molecules correlates well with humidity-controlled PXRD measurements of the transition **1-*op*** → **1-*cp*** (Fig. 4b).[34] Hence, the PXRD pattern at a RH of 85% is identical to that of **1-*op***, whereas those patterns collected at RHs of 65% and 55% showed the coexistence

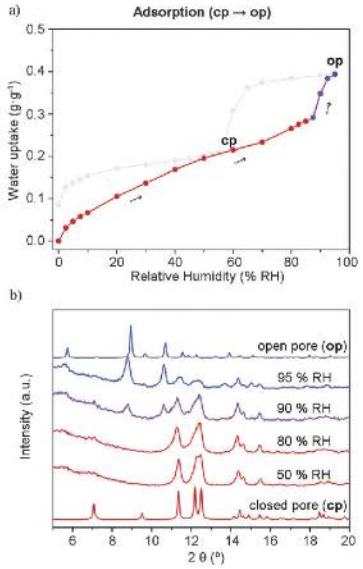

Fig. 3 (a) Adsorption branch of the water isotherm of **1** showing the presence of **1-*cp*** (red), **1-*op*** (blue) and mixed (purple) phases. (b) Humidity-controlled PXRD measurements of **1** at different RH values, showing the presence of **1-*cp*** (red), **1-*op*** (blue) and mixed (purple) phases.

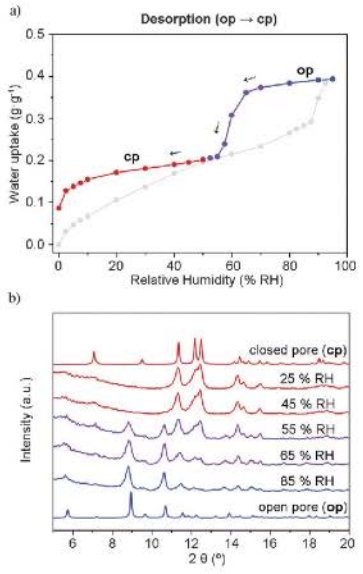

Fig. 4 (a) Desorption branch of the water isotherm of **1** showing the presence of **1-*cp*** (red), **1-*op*** (blue) and mixed (purple) phases. (b) Humidity controlled PXRD measurements of **1** at different RH values, showing the presence of **1-*cp*** (red), **1-*op*** (blue) and mixed (purple) phases.

ks characteristic of both phases. Below a RH of 45%, the pattern is characteristic of **1-*cp***, as confirmed by the lack of ıracteristic peaks of **1-*op*** (*e.g.* 2θ = 9.0° and 10.7°).

then performed four consecutive cycles of water adsorption/ ɔtion to further analyse the reversibility of the water sorption ɜs (Fig. S6, ESI†). Remarkably, the stepwise trend in the rm remained and the maximum uptake (0.40 g_{water} g_1^{-1}) ot significantly different among the cycles, confirming the ty of the material to water sorption/desorption processes inetic study of the phase transition **1-*cp*** → **1-*op***, whereby ***cp*** phase was exposed to an environment having a RH of Fig. S7, ESI†), revealed that the first peaks of the porous appeared in the first 15 minutes, whilst the transition be considered complete after 2.5 hours.

conclusion, we have described the water-induced rever- ɔC–SC transformation of a MOF from a "closed" structure "open" one. This reversible transformation involves the :e and formation of several coordination bonds. We have ı that combining water sorption measurements with -crystal and humidity-controlled powder X-ray diffraction :ovide valuable information on any breathing effects that during the water adsorption/desorption processes. It is that **1** shows gate opening at a RH of 85%, achieving a water uptake of 0.40 g_{water} g_1^{-1}. It also shows a large esis, in which the gate closure occurs at an RH range of %. Furthermore, we have performed kinetics and recycl- studies, showing a total reversibility between the transi- **-*op*** ↔ **1-*cp*** for at least four cycles.

is work was supported by the Spanish MINECO through :t PN MAT2015-65354-C2-1-R and by EU FP7 through ɔo grant agreement no. 615954. I. I. and J. A. thank the ɔO for a RyC grant (RYC-2010-06530) and a FPU predoctoral (AP2010-5934), respectively. J. A. also thanks the Chemistry rogramme of the Universitat Autònoma de Barcelona. A. C. s MINECO and Junta de Andalucía through research :ts MAT2013-41836-R and P12-FQM-1656, respectively. acknowledges the support from the Spanish MINECO ɡh the Severo Ochoa Centres of Excellence Programme, Grant SEV-2013-0295.

es and references

:hrenmann, S. K. Henninger and C. Janiak, *Eur. J. Inorg. Chem.*, 1, 471–474.
:. Henninger, F. Jeremias, H. Kummer and C. Janiak, *Eur. J. Inorg. ɔm.*, 2012, 2625–2634.
Jeremias, A. Khutia, S. K. Henninger and C. Janiak, *J. Mater. ɔm.*, 2012, **22**, 10148–10151.
F. de Lange, K. J. F. M. Verouden, T. J. H. Vlugt, J. Gascon and Kapteijn, *Chem. Rev.*, 2015, **115**, 12205–12250.
E. Soubeyrand-Lenoir, C. Vagner, J. W. Yoon, P. Bazin, F. Y. K. Hwang, C. Serre, J.-S. Chang and P. L. Llewellyn, *J. Am Soc.*, 2012, **134**, 10174–10181.
A. O. Yazaydın, A. I. Benin, S. A. Faheem, P. Jakubczak, J. R. R. Willis and R. Q. Snurr, *Chem. Mater.*, 2009, **21**, 1425–1
Y. F. Chen, R. Babarao, S. I. Sandler and J. W. Jiang, *Langmu* **26**, 8743–8750.
A. Mallick, T. Kundu and R. Banerjee, *Chem. Commun.*, 2(8829–8831.
S. C. Sahoo, T. Kundu and R. Banerjee, *J. Am. Chem. Soc.*, 20 17950–17958.
R. M. P. Colodrero, P. Olivera-Pastor, E. R. Losilla, M. A. G. L. Leon-Reina, M. Papadaki, A. C. McKinlay, R. E. K. D. Demadis and A. Cabeza, *Dalton Trans.*, 2012, **41**, 4045
R. M. P. Colodrero, P. Olivera-Pastor, E. R. Losilla, D. Her Alonso, M. A. G. Aranda, L. Leon-Reina, J. Rius, K. D. D B. Moreau, D. Villemin, M. Palomino, F. Rey and A. Cabeza *Chem.*, 2012, **51**, 7689–7698.
P. Guo, A. G. Wong-Foy and A. J. Matzger, *Langmuir*, 2014, **30**, 19
H. Furukawa, F. Gándara, Y.-B. Zhang, J. Jiang, W. L. Queen Hudson and O. M. Yaghi, *J. Am. Chem. Soc.*, 2014, **136**, 436
J. Canivet, A. Fateeva, Y. Guo, B. Coasne and D. Farrusseng *Soc. Rev.*, 2014, **43**, 5594–5617.
S. Kitagawa and K. Uemura, *Chem. Soc. Rev.*, 2005, **34**, 109–
A. Schneemann, V. Bon, I. Schwedler, I. Senkovska, S. Kas R. A. Fischer, *Chem. Soc. Rev.*, 2014, **43**, 6062–6096.
S. Horike, S. Shimomura and S. Kitagawa, *Nat. Chem.*, 2009, **1**,
C. J. S. K. Henninger, F. Jeremias, J. Ehrenmann, in *Intern Sorption Heat Pump Conference (ISHPC11)*, Padua, 2011, pp. 4
Y. Takashima, V. M. Martínez, S. Furukawa, M. Kondo, S. Shin H. Uehara, M. Nakahama, K. Sugimoto and S. Kitagawa, *Nat. C* 2011, **2**, 168.
S.-S. Bao, N.-Z. Li, J. M. Taylor, Y. Shen, H. Kitagawa an Zheng, *Chem. Mater.*, 2015, **27**, 8116–8125.
M. Sadakiyo, T. Yamada, K. Honda, H. Matsui and H. Ki *J. Am. Chem. Soc.*, 2014, **136**, 7701–7707.
S. Tominaka, F.-X. Coudert, T. D. Dao, T. Nagao and A. K. Che *J. Am. Chem. Soc.*, 2015, **137**, 6428–6431.
A. Shigematsu, T. Yamada and H. Kitagawa, *J. Am. Chem. Soc* **133**, 2034–2036.
T. Zheng, J. M. Clemente-Juan, J. Ma, L. Dong, S.-S. Bao, J. E. Coronado and L.-M. Zheng, *Chem. – Eur. J.*, 2013, **19**, 16394
J.-P. Zhang, Y.-Y. Lin, W.-X. Zhang and X.-M. Chen, *J. Am. Che* 2005, **127**, 14162–14163.
P. K. Allan, B. Xiao, S. J. Teat, J. W. Knight and R. E. Morris *Chem. Soc.*, 2010, **132**, 3605–3611.
F. K. Kalman, M. Woods, P. Caravan, P. Jurek, M. Spiller, G. R. Kiraly, E. Brücher and A. D. Sherry, *Inorg. Chem.*, 20 5260–5270.
N. C. Burtch, H. Jasuja and K. S. Walton, *Chem. Rev.*, 201 10575–10612.
D. Fairen-Jimenez, N. A. Seaton and T. Duren, *Langmuir*, 2(14694–14699.
M. C. Bernini, F. Gándara, M. Iglesias, N. Snejko, E. Gu Puebla, E. V Brusau, G. E. Narda and M. A. Monge, *Chem.* – 2009, **15**, 4896–4905.
D. Fröhlich, S. K. Henninger and C. Janiak, *Dalton Trans.*, 2(15300–15304.
F. Jeremias, D. Fröhlich, C. Janiak and S. K. Henninger, *RS* 2014, **4**, 24073–24082.
S. Brunauer, *The Adsorption of Gases and Vapors Vol I – Physical Ad* Princeton University Press, 1943.
T. K. Maji, G. Mostafa, R. Matsuda and S. Kitagawa, *J. Am Soc.*, 2005, **127**, 17152–17153.

ChemPubSoc Europe

DOI: 10.1002/chem.201602356

CHEMISTRY A European Journal Full Paper

Supramolecular Chemistry

pH-Responsive Relaxometric Behaviour of Coordination Polymer Nanoparticles Made of a Stable Macrocyclic Gadolinium Chelate

Javier Aríñez-Soriano,[a] Jorge Albalad,[a] Arnau Carné-Sánchez,[a] Célia S. Bonnet,[b] Félix Busqué,[c] Julia Lorenzo,[d] Jordi Juanhuix,[e] Maxwell W. Terban,[f] Inhar Imaz,[a] Éva Tóth,*[b] and Daniel Maspoch*[a, g]

Abstract: Lanthanide-containing nanoscale particles have been widely explored for various biomedical purposes, however, they are often prone to metal leaching. Here we have created a new coordination polymer (CP) by applying, for the first time, a stable Gd^{III} chelate as building block in order to prevent any fortuitous release of free lanthanide(III) ion. The use of the Gd-DOTA-4AmP complex as a design element in the CP allows not only for enhanced relaxometric properties (maximum $r_1 = 16.4\ mM^{-1}s^{-1}$ at 10 MHz), but also for a pH responsiveness ($\Delta r_1 = 108\%$ between pH 4 and 6.5), beyond the values obtained for the low molecular weight Gd-DOTA-4AmP itself. The CP can be miniaturised to the nanoscale to form colloids that are stable in physiological saline solution and in cell culture media and does not show cytotoxicity.

Introduction

Magnetic resonance imaging (MRI) is a powerful diagnostic tool in medical science thanks to its non-invasive character and sub-millimetre spatial resolution. This success would not have been possible without the parallel development of contrast agents (CAs), which are substances capable of enhancing the intrinsic contrast of the technique and improve its anatomical resolution.[1] From the 1980s, paramagnetic Gd^{III} chelates have stood out for their excellent properties as CAs and their safe use in comparison to the toxic, free Gd^{III} ions.[2,3] Some of these Gd^{III} chelates (e.g., Dotarem® and Prohance®) are currently commercially available and widely used in clinics. However, these substances are still affected by low sensitivity, lack of selectivity and low retention times, meaning that they are only effective in areas of high bioaccumulation. For this reason, there has been much interest in developing strategies to enhance the performance of this class of CAs.[4] Among the different strategies, a promising one is their nanostructuration, either by using them as building units to make new nanostructured materials or by attaching them onto pre-synthesised nanomaterials.[5] This approach provides the potential advantages of lowering the rotational tumbling of the Gd^{III} chelates, enhancing the payload of Gd^{III} ions per nanoparticle, and increasing the in vivo circulation time. To date, excellent results have been obtained by structuring Gd^{III} chelates in dendrimers,[6] viral capsids,[7] proteins,[8] mesoporous silica,[9] polymeric self-assembled nanoparticles,[10,11] and liposomes.[12]

Nanoscale coordination polymers (CPs) and metal–organic frameworks (MOFs) are an alternative class of materials to be explored for nanostructuring these CAs. Prior to this work, some advances have been done in developing MRI CAs from CPs/MOFs.[13–15] These CAs have mainly been synthesised by the assembly of individual Gd^{III} ions and polycarboxylic organic linkers.[16,17] However, since lanthanide–carboxylate-based CPs/MOFs typically lack stability in water and especially in body fluids, they would degrade when exposed to these media releasing the Gd^{III} ions in their free toxic form. In addition, this lack of stability also prevents detailed relaxometry studies because of the interference of the leached free paramagnetic Gd^{III} ions.

Herein, we present for the first time the incorporation of a Gd^{III} macrocyclic chelate in the structure of a CP by connect-

[a] J. Aríñez-Soriano, J. Albalad, A. Carné-Sánchez, I. Imaz, Prof. D. Maspoch
Catalan Institute of Nanoscience and Nanotechnology (ICN2)
CSIC and The Barcelona Institute of Science and Technology
Campus UAB, Bellaterra, 08193 Barcelona (Spain)
E-mail: daniel.maspoch@icn2.cat

[b] C. S. Bonnet, Prof. É. Tóth
Centre de Biophysique Moléculaire, CNRS, Université d'Orléans
Rue Charles Sadron, 45071, Orléans (France)
E-mail: eva.jakabtoth@cnrs-orleans.fr

[c] Prof. F. Busqué
Departament de Química, Universitat Autònoma de Barcelona
Campus UAB, Bellaterra, 08193 Barcelona (Spain)

[d] Prof. J. Lorenzo
Departament de Bioquímica i Biologia Molecular
Institut de Biotecnologia i Biomedicina (IBB)
Campus UAB, 08193 Bellaterra (Spain)

[e] J. Juanhuix
ALBA Synchrotron, Cerdanyola del Vallès, 08290 Barcelona (Spain)

[f] M. W. Terban
Department of Applied Physics and Applied Mathematics
Columbia University, New York (USA)

[g] Prof. D. Maspoch
ICREA, Pg. Lluís Companys 23, 08010 Barcelona (Spain)

Supporting information for this article is available on the WWW under http://dx.doi.org/10.1002/chem.201602356.

ChemPubSoc Europe

CHEMISTRY A European Journal Full Paper

ing it through Zn^{II} ions. Previous attempts made in our group to build up a CP using a Gd^{III} macrocyclic chelate were focused on using the 1,4,7,10-tetraazacyclododecane-1,4,7,10-tetramethylenephosphonic acid (DOTP).[18] However, we found that the corresponding Gd-DOTP chelate did not react with most of metal ions (e.g., Zn^{II}, Ni^{II}, Co^{II}, Mn^{II}, Fe^{III} and Mg^{II}), presumably because the four phosphonate groups were coordinating the Gd^{III} ions (Scheme 1).[19] In fact, the Gd-DOTP chelate reacted only with Cu^{II} ions,[20] but through a mechanism that involved the replacement of the Gd^{III} by the Cu^{II} inside the DOTP macrocyclic cavity leaving the phosphonate groups free to coordinate to the replaced Gd^{III} ions. In this work, we hypothesize that the introduction of a second functionality in the pendant arms of the macrocyclic ligand applied as linker should ensure the coordination of the Gd^{III} inside the macrocyclic cavity while leaving the phosphonate groups free to coordinate to second metal ions and thus form the CP. For this reason, we have selected 1,4,7,10-tetraazacyclododecane-1,4,7,10-tetraacetamidomethylene phosphonic acid (DOTA-4AmP).[21] In contrast to DOTP, this macrocyclic ligand has two functionalities (amide and phosphonate groups) in each one of the four pendant arms. The four oxygen atoms of the amide groups along with the four ring nitrogen atoms chelate the Gd^{III} ions inside the macrocyclic cavity, thereby allowing the Gd-DOTA-4AmP to have the four phosphonate groups free to coordinate with other metal ions forming CPs (Scheme 1). Importantly, the resultant CPs should also show more stability under aqueous conditions since phosphonates form stronger bonds with metals than carboxylates do.[22] Finally, another potential feature to be considered when using this macrocyclic linker is that, since the Gd-DOTA-4AmP chelate has been already proved to be endowed with pH dependent relaxivities,[21,23] its use could pave the way for the synthesis of nanostructured CPs that, in addition to enhanced CA properties, could behave as a pH-responsive contrast agent.

We demonstrate that bulk crystals of a three-dimensional CP with formula $Zn_{6.5}[Gd_3(H\text{-}DOTA\text{-}4AmP)_2(DOTA\text{-}4AmP)(H_2O)_3]\cdot 18H_2O$ (**1**) are formed when the preformed Gd-DOTA-4AmP chelate is diffused slowly with Zn^{II} ions, whereas increasing the rate of this reaction produced amorphous 90(±30) nm in diameter CP nanoparticles. Here, Zn^{II} ion was selected as the secondary metal ion for a series of key considerations: 1) its stability constant with macrocyclic ligands[24,25] is much lower than that of Gd^{III}[26,27] and lower than those of other metals (e.g., Fe^{III},[28] Cu^{II},[24,25] etc.), preventing a competition with Gd^{III} to occupy the macrocyclic cavity; 2) its toxicity[29] is lower than other metals (e.g., Co^{II},[30,31] Cu^{II},[32,33] etc.), avoiding health risks in the case of disassembly of the structure inside the body; and 3) it is a diamagnetic metal, so the performed relaxivity studies can be interpreted only in terms of the nanostructuration of its building block, the Gd-DOTA-4AmP chelate.[21] Importantly, the colloidal CP nanoparticles we have designed feature a high stability in physiological saline solution and in cell culture media, while they showed an increased r_1 relaxivity of 16 $mM^{-1}s^{-1}$ at 10 MHz (25 °C, pH 7.4) when compared with that of the original Gd-DOTA-4AmP chelate. In addition, they amplify the relaxivity pH response ($\Delta r_1 = 108\%$) that, at intermediate fields (20-40 MHz), doubles the one of the Gd-DOTA-4AmP chelate.

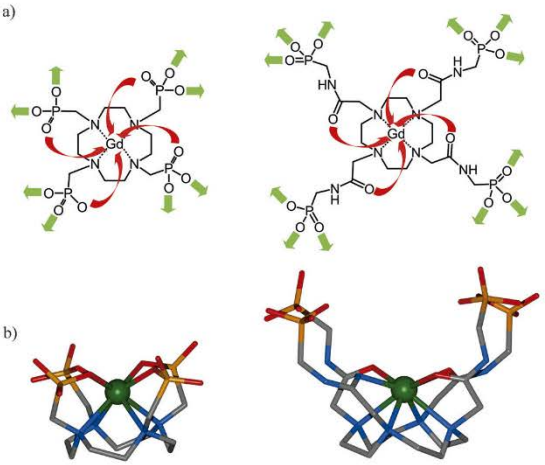

Scheme 1. a) Gd-DOTP (left) and Gd-DOTA-4AmP (right) showing the coordination with Gd^{III} (red arrows) and their potential coordination to a second metal ion (green arrows). b) Three-dimensional conformation of Gd-DOTP (left) and Gd-DOTA-4AmP (right). Colour code: C (grey), N (blue), O (red), P (orange), Gd (green).

Results and Discussion

Synthesis and crystal structure of 1

The macrocyclic ligand DOTA-4AmP was synthesised adapting a procedure reported in the literature.[21] This was then used as a linker to create the crystals of **1** following a two-step synthesis.[34] This synthesis consisted of first combining DOTA-4AmP with Gd^{III} ions to obtain the corresponding metallomacrocyclic complex Gd-DOTA-4AmP showing non-coordinated phosphonic groups. Here, the Gd-DOTA-4AmP was prepared by adding dropwise a solution of gadolinium chloride hexahydrate in water into an aqueous solution of DOTA-4AmP adjusted to pH 10 (using 1 M NaOH) while being stirred at 70 °C. The pH of the mixture was kept at 10 using 1 M NaOH throughout the addition. Then, the mixture was left at 70 °C under stirring for 18 h. Finally, the pH was adjusted to pH 8 by the addition of concentrated HCl. The exact concentration of Gd^{III} ions was determined by ICP-MS, and the final concentration of the GdDOTA-4AmP solution was adjusted to 20 mM by the addition of water. In a second step, an ethanolic solution of zinc acetate was layered onto the aqueous solution of Gd-(DOTA-4AmP). After two weeks, transparent octahedral crystals of **1** suitable for single crystal X-ray diffraction were collected.

Crystal structure of **1** was solved and refined in the tetragonal $P4_2/n$ group (Table S1, in the Supporting Information). The asymmetric unit was found to contain three Gd-DOTA-4AmP units, in which the Gd^{III} ion was confirmed to be chelated inside the macrocyclic cavity. These Gd^{III} ions adopt a capped square antiprismatic geometry coordinated to the four ring ni-

ChemPubSoc Europe

CHEMISTRY A European Journal Full Paper

trogen atoms, the four oxygen atoms of the amide functionalities and one water molecule at the capping position (Figure 1a). On the other hand, Zn^{II} ions adopt a tetrahedral geometry coordinated to four O atoms of the phosphonate groups of the macrocyclic Gd-DOTA-4AmP units. In this structure, the three Gd-DOTA-4AmP of the asymmetric unit have differences in their geometry and coordination modes. According to the notation introduced by Harris et al.[35] (Figure S1a in the Supporting Information), the phosphonate groups of Gd1-DOTA-4AmP and Gd2-DOTA-4AmP show the binding mode [3.111] in one pendant arm and the binding mode [2.110] in the other three arms (Figure 1a and Figure S1b in the Supporting Information). The phosphonate groups of the Gd3-DOTA-4AmP unit adopt the binding mode [3.111] in one arm, [1.100] in another arm, and [2.110] in the two remaining arms (Figure S1b in the Supporting Information).

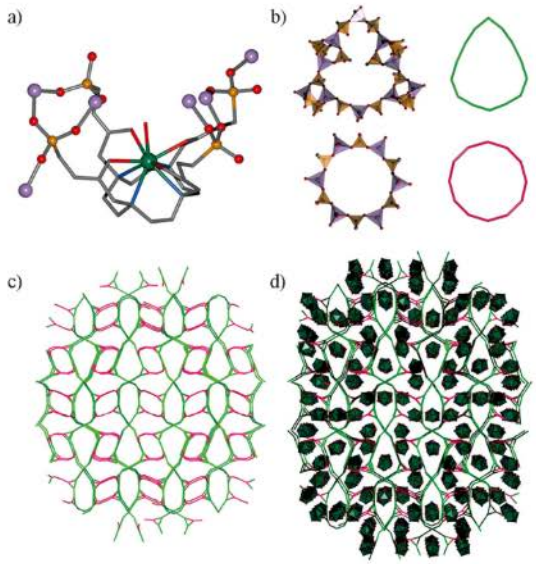

Figure 1. a) Gd-DOTA-4AmP unit found in **1**. b) Egg-shaped 32-membered ring and circular 24-membered ring found in **1**. c) View of the three-dimensional Zn^{II}–PO_3 network resulting from the assembly of the two types of rings along *a* axis. d) Identical view of **1** including the Gd-DOTA-4AmP units. Colour code: C (grey), N (blue), O (red), P (orange), Gd (green), Zn (purple).

Overall, it is very interesting to note that the resulting structure can be analysed in terms of an inorganic framework since the ···Zn^{II}-PO_3-Zn^{II}-PO_3··· linkages extend along the three dimensions. In this framework, the basic units are tri-winged paddle wheel Zn^{II} units, which are formed by two Zn^{II} ions bridged by three phosphonate groups (Figure S2 in the Supporting Information). The assembly of these Zn^{II} units generates two types of $Zn_xP_xO_{2x}$ rings (Figure 1b), one circular 24-membered ring ($Zn_6P_6O_{12}$, 10.9×10.3 Å) and one egg-shaped 32-membered ring ($Zn_8P_8O_{16}$, 16.3×5.6 Å). The size of these rings is relatively larger than other $Zn_xP_xO_{2x}$ rings previously reported.[36] Figure 1c shows the three-dimensional Zn^{II}–PO_3 network resulting from the assembly of these two types of rings. Importantly, the Gd-DOTA-4AmP units are enclosed in the "hypothetical" channel system of this framework, resulting in a more compact structure (Figure 1d) in which guest water molecules are hydrogen-bonded with the oxygen atoms of the different phosphonate groups.

Synthesis and characterisation of the Zn-Gd-DOTA-4AmP nanoparticles

Any attempt to miniaturize **1** and form colloidal crystalline nanoparticles by means of different techniques (e.g., hydrothermal synthesis, fast mixing of reactants, emulsions, etc.) failed. Here, all trials let to the formation of amorphous Zn-Gd-DOTA-4AmP nanoparticles. In fact, by reproducing exactly the same synthesis, but instead of a slow diffusion of both solutions we rapidly mixed them, amorphous Zn-Gd-DOTA-4AmP nanoparticles were immediately formed. These nanoparticles were then purified by centrifugation and washed several times with ethanol and water, and finally redispersed in water. The resulting white colloid showed a good stability (Figure 2a), and the first reversible flocculation traces only appeared after one day. Field-emission scanning (FESEM) and transmission (TEM) electron microscopy images of the colloid demonstrated the formation of rounded nanoparticles (Figure 2b–d and Figure S4 in the Supporting Information) with a size of 90(±30) nm (calculated from TEM images by averaging the diameter of at least 150 particles from images of different areas of the same sample).

To gain more information about the structural–chemical correspondence between Zn-Gd-DOTA-4AmP nanoparticles and

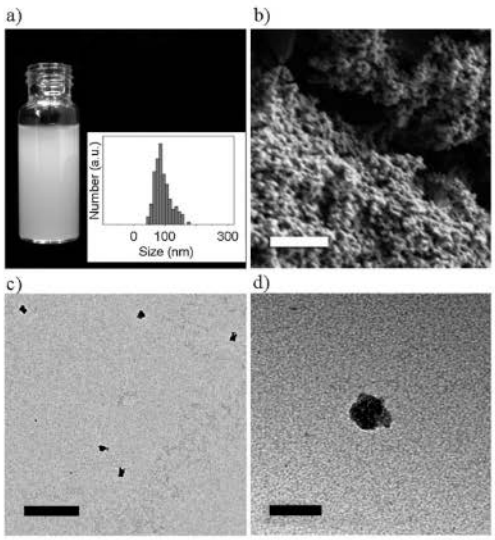

Figure 2. a) Photograph of the colloidal suspension of Zn-Gd-DOTA-4AmP nanoparticles and the size distribution (inset). b) SEM, and c, d) TEM images of Zn-Gd-DOTA-4AmP nanoparticles. Scale bars: b) 1 μm, c) 500 nm, and d) 100 nm.

ChemPubSoc Europe

CHEMISTRY A European Journal Full Paper

the crystalline structure of **1**, we compared the results obtained using different characterisation techniques. First, ICP-MS analysis performed on the nanoparticles showed a Zn/Gd proportion of 2.07, which is consistent with that of the crystalline structure (Zn/Gd = 2.16). This result confirms that the proportion between both metal ions is analogous in both materials. Second, elemental analysis performed on the nanoparticles agreed with the formula $Zn_{6.5}[Gd_3(H\text{-}DOTA\text{-}4AmP)_2(DOTA\text{-}4AmP)(H_2O)_3]\cdot 18H_2O$ (Table S2 in the Supporting Information). Third, both infrared (FT-IR) spectra (Figure S5 in the Supporting Information) and thermogravimetric analysis (TGA; Figure S6, in the Supporting Information) carried out with the nanoparticles and **1** matched. Here, the IR spectra confirm the coordination of the phosphonate groups of Gd-DOTA-4AmP to the Zn^{II} metal ions, as evidenced by the presence of two strong peaks at 1070 and 992 cm^{-1}.[37] TGA showed a first weight loss of 9.1% for **1** and 10.6% for Zn-Gd-DOTA-4AmP nanoparticles in the range 35–275 °C, which was attributed to the loss of all guest water molecules (theoretical = 10.5% considering molecular formula of **1**). Decomposition of **1** and Zn-Gd-DOTA-4AmP nanoparticles occurs in the range of 275–740 °C in a single step (Figure S6 in the Supporting Information). Finally, ^{31}P MAS NMR solid-state measurements using Eu^{III} instead of Gd^{III} (**1** and **1**-Eu are isostructural; see Figure S3 and Figure S5 in the Supporting Information)[38,39] confirmed that the peak shift to higher fields and its widening due to the inclusion of Eu^{III} in the DOTA-4AmP ligand was maintained in the case of Zn-Eu-DOTA-4AmP nanoparticles and in crystals of **1**-Eu. This result confirmed the presence of the lanthanide(III)-DOTA-4AmP unit in both materials (Figure S7 in the Supporting Information).

We also collected X-ray total scattering pair distribution function (PDF) data for both samples. PDF analysis is an excellent technique to access structural information about materials in which disorder or crystallite size broadening effects limit the use of conventional Bragg crystallographic techniques.[40] Because of this, PDF analysis has recently been applied in CP/MOFs to study conformational changes[41] or to identify the correct structural features in MOF nanocrystals.[42] Figure 3 shows the results of these measurements as the PDF, $G(r)$ function of each sample. $G(r)$ provides the real-space probability of finding a pair of atoms at a distance r relative to the average atomic density in an isotropic sample; that is, it is a weighted histogram of atom-atom distances in a structure. The presence of peaks in the case of **1** at $r > 5$ Å (Figure 3a and Figure S8 in the Supporting Information) indicates long-range order and agrees with the Bragg diffraction observed in the PXRD measurements (Figure S3 in the Supporting Information). On the other hand, Zn-Gd-DOTA-4AmP nanoparticles appear diffuse for $r > 5$ Å, demonstrating the loss of long-range order as a consequence of the miniaturisation process. However, careful analysis (using PDFgui software, Figure S9 in the Supporting Information)[43] of the peaks at low distances (r) revealed that **1** and Zn-Gd-DOTA-4AmP nanoparticles present a very similar pattern (Figure 3a). Figure 3 correlates the peak positions of $G(r)$ for both materials with the average atomic distances extracted from the crystalline structure of **1**. Their similarity confirms that the main building blocks forming the crystal structure of **1** are also present in the nanoparticles. The loss of the peak at 5.43 Å shows that disordering may develop between the Gd^{III} ion and the Zn^{II} ion distance upon miniaturisation. Additionally, the presence of two broader features beyond 5 Å (Figure S8 in the Supporting Information) show that a small degree of structural coherence remains up to about 10 Å.

To this end, altogether these techniques confirmed that even though the Zn-Gd-DOTA-4AmP nanoparticles do not show a long-range structural ordering, their composition and chemical connectivity at a short range is comparable to those found in the structure of **1**.

Relaxometric measurements

Reliable relaxometry studies of any material need to be done in a stable nanoparticle colloid. Thus, we first studied the stability of these nanoparticles in physiological saline solution (NaCl, 0.9%). For this, as-synthesised Zn-DOTA-4AmP nanoparticles were first centrifuged and redispersed in water three times and finally redispersed in the medium of study to form a stable colloid. Exposure of this sample to saline solution at pH 5.5, 7.4, and 8.5 and at $T = 37.5$ °C led to negligible leaching of total Gd^{III}: 1.7, 1.2 and 1.8% in the first 10 min, and 3.6, 1.3 and 1.8% after 10 h, as determined by ICP-MS (Figure S10 in the Supporting Information).

The form in which the small amount of Gd^{III} is released during this degradation was studied by mass spectrometry

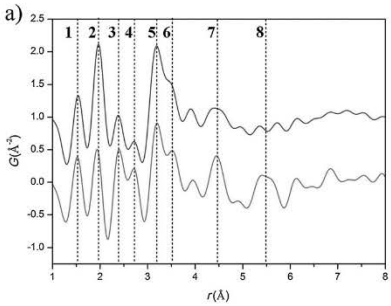

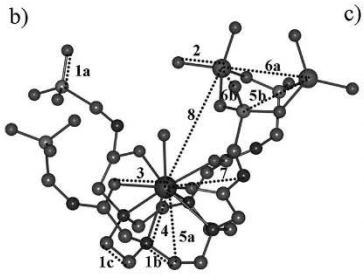

c)

Peak	Peak position (Å)	Contribution to the peak	Distance in 1 (Å)
1	1.50	**1a.** P-O	1.52
		1b. N-C	1.50
		1c. C-C	1.50
2	1.91	Zn-O	1.90
3	2.40	Gd-O	2.37
4	2.60	Gd-N	2.61
5	3.26	**5a.** Gd-C	3.42
		5b. Zn-P	3.17
6	3.60	**6a.** Zn-Zn	3.69
		6b. Zn-O	3.64
7	4.48	Gd-N	4.45
8	5.43	Gd-Zn	5.47

Figure 3. a) Pair distribution function $G(r)$ of **1** (bottom) and Zn-Gd-DOTA-4AmP nanoparticles (top). b) Characteristic distances indicated in the PDF. c) Pair atom correlations contributing to the peaks in the PDF with their corresponding average crystallographic distance in **1**.

ChemPubSoc Europe

CHEMISTRY A European Journal Full Paper

(ESI-TOF) and ^{1}H NMR spectroscopy. To study the former, we analysed the supernatants resulting from the degradation experiments using ESI-TOF. From this analysis, we found species corresponding to $[^{158}$Gd-4H-DOTA-4AmP$]^- = 930.1$,$[^{160}$Gd-4H-DOTA-4AmP$]^- = 932.1$,$[^{157}$Gd-4H-DOTA-4AmP$]^- = 929.1$,$[^{156}$Gd-4H-DOTA-4AmP$]^- = 928.1$ and $[^{155}$Gd-4H-DOTA-4AmP$]^- = 927.1$ (Figure S11 in the Supporting Information), confirming that Gd^{III} ions are still chelated when they are leached. In addition, studying the supernatant resulting from incubating a colloid of Zn-Eu-DOTA-4AmP nanoparticles (strongly relaxing Gd^{III} ions were replaced by Eu^{III} ions that allow for NMR observations; vide supra) to acidic D_2O conditions by ^{1}H NMR further corroborated that lanthanide ions are still chelated during the degradation of the nanoparticles. Indeed, the ^{1}H NMR spectrum showed the presence of the characteristic eight resonances of equal intensity corresponding to the chelate Eu-DOTA-4AmP (Figure S12 in the Supporting Information), but not those signals corresponding to free DOTA-4AmP. These results are in agreement with cytotoxicity assays conducted with two cell lines, Hep G2 and MCF-7. Both cells showed good viability (75% for Hep G2 and for MCF-7) when incubated for 24 h with Zn-Gd-DOTA-4AmP nanoparticles, even at [Gd] = 200 μM. This lack of cytotoxicity for the nanoparticles is attributed to the eventual release of the Gd-DOTA-4AmP species nontoxic to cells instead of the free Gd^{III} ion. Indeed, identical toxicity experiments performed on the Gd-DOTA-4AmP chelate showed that Gd-DOTA-4AmP exhibits similar viabilities (69% for Hep G2 and 67% for MCF-7). Clearly, the lack of cytotoxicity does not guarantee in vivo nontoxicity. Also, the presence of phosphonate groups often drives to bone accumulation of such agents.[44] Nevertheless, they still might be helpful in small animal studies without causing acute toxicity, as it has been evidenced by the successful use of Gd-DOTA-4AmP for pH-mapping of mouse kidney[45] or rat glioma.[46]

Relaxometry properties were investigated by ^{1}H nuclear magnetic relaxation dispersion (NMRD) profiles in the frequency range 10 kHz $\leq \nu \leq$ 400 MHz using a colloidal suspension of the Zn-Gd-DOTA-4AmP nanoparticles in saline solution. The suspension was stable throughout the measurement without addition of surfactants or thickeners that can interfere. The relaxivity r_1 profiles as a function of the magnetic field at pH 7.4 at 25 °C and 50 °C show an increase at intermediate magnetic fields, reaching a maximum of r_1 at 10 MHz and 25 °C (r_1 = 16 $mM^{-1}s^{-1}$; Figure 4). This is characteristic of slowly rotating species and enables to reach more than two times higher relaxivities than that of the discrete Gd-DOTA-4AmP complex at the same field and temperature (r_1 = 7.4 $mM^{-1}s^{-1}$). Figure 4 also shows that the relaxivity slightly decreases with temperature, conversely to what was observed for the previously reported CAMOF-1,[18] where mean proton exchange was the limiting factor. The temperature-dependence of the relaxivities of Zn-Gd-DOTA-4AmP nanoparticles indicates that the relaxivity is not limited by proton exchange.

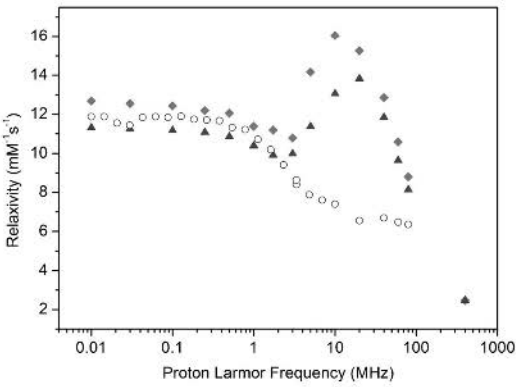

Figure 4. NMRD profiles of a colloidal suspension of Zn-Gd-DOTA-4AmP nanoparticles in saline solution (NaCl 0.9%) at pH 7.4 at 25 °C (light grey diamond) and at 50 °C (dark grey triangle) and Gd-DOTA-4AmP complex in saline solution (NaCl 0.9%) at pH 7.4 at 25 °C (empty circle).

pH-dependent relaxometric study

The pH dependence of r_1 of Zn-Gd-DOTA-4AmP nanoparticles was studied at 20 MHz in the pH range between 4 and 10 (Figure 5a). This pH range was selected to avoid leaching of either Gd-DOTA-4AmP or Zn^{II} ions. Indeed, the release is less than 3.0% in weight at 4 < pH < 10, however a burst release of the complex was observed at pH ≤ 4, indicating a fast degradation of the nanoparticles below pH 4 (Figure 5b). In consequence, relaxometric data were collected in the pH range 4–10 by starting with a colloidal suspension of these nanoparticles in saline solution at pH 7.4 and with a Gd^{III} concentration of 5.4 mM. The pH was stepwise lowered to 4 and then increased to 10 by the addition of small quantities of hydrochloric acid and sodium hydroxide, respectively, after which the pH and T_1 were immediately measured. The concentration of Gd^{III} was corrected after each addition of concentrated acid/base to calculate r_1. Identical r_1 values were obtained when starting the measurements from a colloidal suspension with a pH initially set at 4 and raising it with sodium hydroxide, confirming the reversibility of the pH dependence of Zn-Gd-DOTA-4AmP nanoparticles. The plotted data have the shape of an asymmetric inverted parabola (Figure 5a). The r_1 values steeply increase from pH 4 (r_1 = 7.9 $mM^{-1}s^{-1}$) to pH 6 (maximum r_1 = 16.4 $mM^{-1}s^{-1}$), then steadily decrease reaching a value of r_1 = 8 $mM^{-1}s^{-1}$ at pH 10. For direct comparison, we also repeated the pH dependence study for the Gd-DOTA-4AmP complex.[21] The r_1 values increase from pH 4 (r_1 = 4.8 $mM^{-1}s^{-1}$) up to pH 6 (maximum r_1 = 5.8 $mM^{-1}s^{-1}$), followed by a decrease to reach a minimum at pH 9 (r_1 = 3.9 $mM^{-1}s^{-1}$). As Figure 5a evidences, the use of the nanoparticle amplifies the pH-dependent relaxivity changes at this frequency. Indeed, for Zn-Gd-DOTA-4AmP nanoparticles, the difference between the maximum (r_1 = 16.4 $mM^{-1}s^{-1}$; pH 6) and the minimum (7.9 $mM^{-1}s^{-1}$; pH 4) relaxivity values corresponds to a factor of two (Δr_1 = 108%), while for Gd-DOTA-4AmP, the difference between the maximum (r_1 = 5.8 $mM^{-1}s^{-1}$) and the minimum (r_1 = 3.9 $mM^{-1}s^{-1}$) is a factor of 1.5. This is nevertheless a slightly smaller amplifica-

ChemPubSoc Europe

CHEMISTRY A European Journal Full Paper

tion than what has been observed for Gd-DOTA-4AmP conjugated to a G5-PAMAM dendrimer ($\Delta r_1 = -122\%$ between pH 6 and 9).[47] Evidently, the amplification of the pH response by nanoscale systems such as our CP or the G5-PAMAM dendrimer operates only at intermediate fields, where the effect of slow rotation on proton relaxivity is observable.

Sherry and co-workers showed with potentiometric and relaxometric studies that the phosphonates of the pendant arms were responsible of the unique pH-responsive behaviour of Gd-DOTA-4AmP.[21] They concluded that the protons of the Gd^{III}-bound water molecule undergo a prototropic exchange with the bulk solvent which is catalysed by the phosphonate groups located close enough to the coordinated water. In particular, they could derive that the diprotonated complex has the maximal effect on the measured relaxivity and was responsible for the relaxivity peak at pH 6.3. They have also shown that converting these phosphonate groups to phosphonate esters eliminates the pH responsive behaviour.[48]

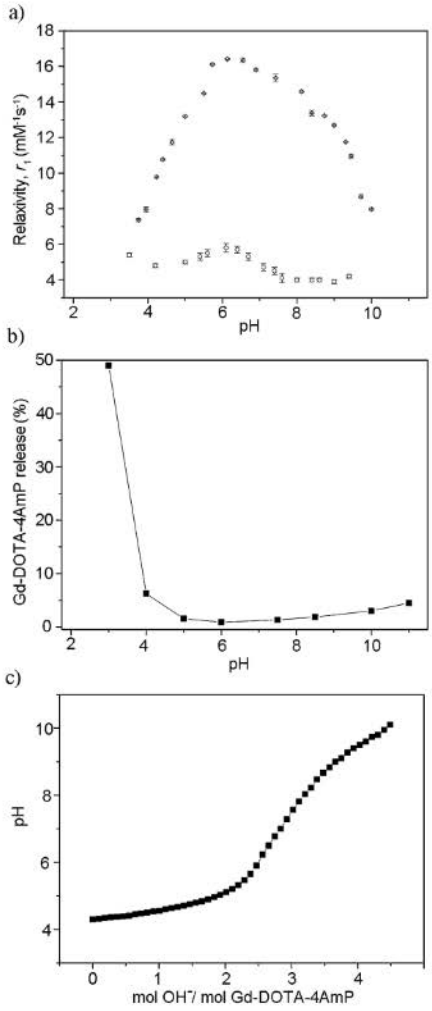

Figure 5. a) pH dependence of the relaxivity of a colloidal suspension of Zn-Gd-DOTA-4AmP nanoparticles (filled diamond) and Gd-DOTA-4AmP complex (empty circle) measured at 20 MHz (25 °C). b) Gd-DOTA-4AmP release (wt.%) for Zn-Gd-DOTA-4AmP nanoparticles at the pH range of study. c) Potentiometric titration of a colloidal suspension of Zn-Gd-DOTA-4AmP nanoparticles.

It is remarkable that the pH dependence profile of the relaxivity is preserved when Gd-DOTA-4AmP is part of a coordination polymer framework, despite the fact that most of the phosphonate oxygens are involved in coordination bonds to the Zn^{II} cations. We have proved that the coordination polymer is not destroyed in the pH range 4–10 (see above). We can thus hypothesize that three possible mechanisms could account for the pH responsiveness of the nanoparticles, which can take place simultaneously. First, the pH dependence in the nanoparticles can be attributed to non-coordinating phosphonate groups on the surface of the nanoparticles. Second, intrinsic defects of any framework could also assure the presence of a number of non-coordinating phosphonate groups also in the interior of the nanoparticles. Finally, it has been described that coordinated oxygen atoms of the phosphonate groups can also accept protons,[49] making possible their protonation and the catalysis of the prototropic water exchange on the Gd^{III} centres as formulated by Sherry.

By potentiometry, Sherry et al. determined four protonation constants for the monomer Gd-DOTA-4AmP complex, which are log $K_{H1-4} = 7.20$, 6.47, 6.03 and 5.36, respectively.[21] In order to gain some information about the protonation scheme of the Zn-Gd-DOTA-4AmP nanoparticles, we have titrated a solution of the nanoparticles (5.4 mM in Gd^{III}) by adding increasing amounts of 1 M NaOH. The titration curve shows that protonation occurs in a larger range (pH 4 to 10, Figure 5c) than what was observed for the monomer, which is not surprising as many protonation sites are in close proximity, and the Zn-Gd-DOTA-4AmP nanoparticle is expected to behave as a polyelectrolyte. This implies that the protonation of one site strongly influences the protonation of neighbouring sites. As a result, the protonation steps extend on a larger pH range, instead of being characterised by discrete protonation constants. This site-binding model explains the characteristic broadening of the titration curve of polyelectrolytes with respect to the one of a corresponding monoprotic acid or base.[50]

Although it is impossible to extract protonation constants from the titration curve, it unambiguously indicates that in average, there are several protonation sites per Gd-DOTA-4AmP unit in the nanoparticles. It implies that protonation occurs also within the interior of the framework. This is an interesting finding since it shows that these nanoparticles can accept a large quantity of protons without the destruction of the coordination polymeric network. We note that metal coordination of protonated phosphonate oxygens has been previously reported.[49] Based on these results, we can conclude that the possibility to protonate the phosphonate oxygens even within the nanoparticles explains why the pH-dependent relaxivities are retained.

ChemPubSoc Europe

CHEMISTRY A European Journal Full Paper

Conclusions

We have created a bimetallic Zn^{II}- and Gd^{III}-based coordination polymer (CP) by using, for the first time, a macrocyclic chelate (Gd-DOTA-4AmP) as building block. This design element warrants stable complexation of the lanthanide ion, even in case of partial disassembly of the polymeric network. This coordination polymer can miniaturised to the nanometer scale (90(±30) nm) to form stable colloids, preserving its structural coherence up to about 10 Å. The colloid is stable in saline solution at physiological pH, in cell culture media; and it does not show cytotoxicity. The Zn-Gd-DOTA-4AmP nanoparticle has a maximum r_1 relaxivity of 16.4 $mM^{-1}s^{-1}$ at pH 6 and 10 MHz. It retains the pH-dependence profile of the monomer in the pH range 4–10, with a double relaxivity response to pH change ($\Delta r_1 = 108\%$) as compared to the monomer Gd-DOTA-4AmP ($\Delta r_1 = 50\%$). Furthermore, we have demonstrated by potentiometric measurements that the Zn-Gd-DOTA-4AmP CP nanoparticles behave as a polyelectrolyte, accepting several protons per Gd-DOTA-4AmP unit without destroying the CP framework.

This proof-of-concept study shows that Gd^{III}-chelates can serve as building blocks to create stable MOFs/CP. Such systems can be explored to enhance the relaxivity or pH dependence properties in view of their potential use in MRI diagnostics.

Experimental Section

General considerations

All chemical reagents and solvents were purchased from commercial sources and used as received without further purification. NMR spectra were recorded on a Bruker Avance DPX-250 spectrometer and Bruker AMX-400 Wide Bore for liquid and solid-state samples, respectively. Mass spectra were acquired on a micrOTOF-QII ESI-MS instrument. Purity of all bulk material batches was confirmed by X-ray powder diffraction (XRPD) patterns collected on an X'Pert PRO MPD analytical diffractometer (Panalytical) at 45 kV, 40 mA by using $Cu_{K\alpha}$ radiation ($\lambda = 1.5419$ Å), and compared with single-crystal simulated patterns. Thermogravimetric analyses were performed under nitrogen flow using a STA 449 F1 Jupiter-Simultaneous TGA-DSC from NETZSCH with a heat rate of 5 °C min^{-1}. IR spectra were recorded in transmission mode on a Bruker Tensor 27FTIR equipped with a Golden Gate diamond ATR cell. Elemental analysis measurements were performed on a Flash EA 2000 CHNS, Thermo Fisher Scientific analyser. Inorganic elemental analysis measurements were performed on an ICP-MS 7500ce, Agilent Technologies. Scanning electron microscope images were acquired on a FEI Quanta 650F working at an accelerating voltage of 2 kV and a beam current of 50 pA. Transmission electron microscope images were acquired on a JEOL JEM-1400 working at an accelerating voltage of 120 kV.

Synthesis of Gd-DOTA-4AmP and Eu-DOTA-4AmP

First, a solution of DOTA-4AmP (354 mg, 396 μmol) in water (8 mL) was prepared and the pH was adjusted to 10 by cautious addition of 1 M NaOH. Then, a solution of gadolinium chloride hexahydrate was prepared (147 mg, 396 μmol) in water (2 mL). Gadolinium chloride solution was added dropwise into the stirring DOTA-4AmP solution which was warmed at 70 °C. The pH of the stirring mixture was kept at 10 by addition of concentrated NaOH (1 M) during the addition process. Note that, after each addition of gadolinium chloride into the DOTA-4AmP solution, a white precipitate appears at first, but it is dissolved after some minutes, indicating that Gd-DOTA-4AmP is being formed. The absence of free Gd^{III} in the stirring mixture was also monitored by xylenol orange test.[51] The addition of gadolinium chloride was stopped after the xylenol test showed the persistent presence of free gadolinium. Then, the mixture was left at 70 °C under stirring for 18 h. Finally, the pH was adjusted to pH 8 by the addition of concentrate HCl. The exact concentration of Gd^{III} ions was determined by ICP-MS, and the final concentration of the Gd-DOTA-4AmP solution was adjusted to 20 mM by the addition of water. The same procedure was followed for the synthesis of Eu-DOTA-4AmP but using europium chloride hexahydrate instead of gadolinium chloride.

Synthesis of 1 and 1-Eu

A solution of zinc acetate dihydrate in ethanol (4 mL, 11.3 mM) was carefully layered onto a Gd-DOTA-4AmP aqueous solution (4 mL, 5.2 mM) in a 9 mL glass vial. This glass vial containing the liquid diffusion was capped and left undisturbed at room temperature for two weeks. After that, transparent octahedral crystals of **1** appeared on the walls and at the bottom of the vial. To recover crystals of **1**, the liquid phase was exchanged by fresh EtOH/water mixture (50:50) and the vials were sonicated in an ultrasounds bath at 0 °C to detach the crystals from the glass walls. The process was repeated two more times, and the crystals were finally kept under pure water. The same procedure was followed for the synthesis of **1**-Eu but using an aqueous solution of Eu-DOTA-4AmP instead of Gd-DOTA-4AmP.

Synthesis of Zn-Gd-DOTA-4AmP and Zn-Eu-DOTA-4AmP nanoparticles

A solution of zinc acetate dihydrate in ethanol (4 mL, 11.3 mM) was rapidly added onto a Gd-DOTA-4AmP aqueous solution (4 mL, 5.2 mM) under stirring (900 rpm) at room temperature. Immediately after this addition, the appearance of a white solid was observed, and the mixture was left stirring for 12 h. To recover Zn-Gd-DOTA-4AmP nanoparticles, the solid was precipitated by centrifugation (44 000 RCF, 10 min) and washed four times with EtOH/water mixture (50:50) and finally redispersed in pure water. The same procedure was followed for the synthesis of Zn-Eu-DOTA-4AmP nanoparticles but using an aqueous solution of Eu-DOTA-4AmP instead of Gd-DOTA-4AmP.

X-ray crystallography

Crystallographic data for **1** were collected at 100 K at XALOC beamline[52] at ALBA synchrotron ($\lambda = 0.88557$ Å). These data were indexed, integrated and scaled using XDS program.[53] Absorption correction was not applied. The structure was solved by direct methods[54] and subsequently refined by correction of F^2 against all reflections using SHELXS2013 and SHELXL2013 within the WinGX package.[55] All non-hydrogen atoms were refined with anisotropic thermal parameters by full-matrix least-squares calculations on F^2 using SHELXL2013. Hydrogen atoms were inserted at calculated positions and constrained with isotropic thermal parameters. The hydrogen of the crystal lattice water molecules present in the structure were not located on Fourier map, but were added in the empirical formula to allow accurate determination of density and

ChemPubSoc Europe

CHEMISTRY
A European Journal
Full Paper

absorption coefficient. CCDC 1471203 contains the supplementary crystallographic data for this paper. These data are provided free of charge by The Cambridge Crystallographic Data Centre.

Total X-ray scattering PDF measurements

Total scattering X-ray PDF experiments were performed at the National Synchrotron Light Source II (NSLS-II) on beamline 28-ID at Brookhaven National Laboratory. The miniaturised sample (shown) was measured using the rapid acquisition pair distribution function (RaPDF) technique[56] with an X-ray energy of 65.7107 keV (= 0.188682 Å). A Perkin–Elmer 2D at panel detector (2048×2048 pixels and 200×200 μm pixel size) was mounted orthogonal to the beam path with a sample-to-detector distances of 300.785 mm. The raw 2D data were azimuthally integrated and converted to 1D intensity versus the magnitude of the scattering vector Q ($Q = 2\pi\sin(\theta)/\lambda$) using xPDFsuite[57] then corrected, normalised and Fourier transformed to obtain the PDF, $G(r)$, using PDFgetX3.[58] A Ni standard was measured to calibrate the experimental setup with xPDF suite and fit with an FCC Ni model in PDFgui[45] to determine the instrumental resolution effects on the PDF, $Q_{damp} = 0.033039$ Å^{-1} and $Q_{broad} = 0.013760$ Å^{-1}. Both miniaturised and crystalline (shown) samples were measured on a subsequent date with an X-ray energy of 67.3910 keV (=0.183977 Å) and a detector distance of 207.6170 mm, giving instrumental resolution effects $Q_{damp} = 0.043902$ Å^{-1} and $Q_{broad} = 0.017594$ Å^{-1}. The separate measurements of the miniaturised samples were consistent, but with better statistics collected on the former.

Cytotoxicity assays

Human breast-cancer cells (MCF-7) and human hepatocellular carcinoma cells (HepG2) were obtained from the American Type Culture Collection (ATCC, Manassas, VA, USA). The cells were routinely cultured with DMEM F12 or DMEM (Invitrogen) containing 10% (v/v) heat-inactivated foetal bovine serum (FBS), at 37 °C in a humidified 5% CO_2 atmosphere. Growth inhibitory effects on cell lines were measured by the XTT (sodium 2,3,-bis(2-methoxy-4-nitro-5-sulfophenyl)-5-[(phenylamino)-carbonyl]-2*H*-tetrazolium inner salt) assay. Cells were plated at a density of 4×103 cells per well in 100 μL of culture medium in 96-well plates, and cultured. After 24 h incubation cells were treated with different concentrations of Gd-DOTA-4AmP and Zn-Gd-DOTA-4AmP nanoparticles during 24 h and then, 20 μL of XTT was added. After 2 h, the colour formed was quantified with a spectrophotometric plate reader at 490 nm by a microplate reader (Victor3). The percentage of cell viability was calculated by dividing the average absorbance of the cells treated with the complex by that of the control. Each sample was tested in quadruplicate.

Relaxometry measurements

Proton NMRD profiles were recorded on a Stelar SMARTracer fast field cycling relaxometer (0.01–10 MHz) and a Bruker WP80 NMR electromagnet adapted to variable field measurements (20–80 MHz) and controlled by a SMARTracer PC NMR console. The temperature was monitored by a VTC91 temperature control unit and maintained by a gas flow. The temperature was determined by previous calibration with a Pt resistance temperature probe. The longitudinal relaxation rates ($1/T_1$) were determined in physiological saline solution (NaCl, 0.9%) for colloidal suspensions of Zn-Gd-DOTA-4AmP nanoparticles ([Gd] = 5.0–5.4 mM).

Acknowledgements

This work was supported by the MINECO-Spain through projects PN MAT2012-30994. I.I. and J.A.S. thank the MINECO for a RyC contract and a predoctoral FPU grant, respectively. J.A. is grateful to the Generalitat de Catalunya for a predoctoral FI grant. ICN2 is supported by the Spanish MINECO through the Severo Ochoa Centers of Excellence Program, under Grant SEV-2013-0295. M.T. acknowledges support from the US Department of Energy NEUP #DE-NE 0000746 and S. J. L. Billinge for helpful discussion. Use of the National Synchrotron Light Source II, Brookhaven National Laboratory, was supported by the US Department of Energy, Office of Science, Office of Basic Energy Sciences, under Contract No. DE-SC0012704. E.T. and C.S.B. acknowledge financial support of the Ligue contre le Cancer (France).

Keywords: chelates · contrast agents · coordination polymers · gadolinium · relaxometry

[1] A. S. Merbach, L. Helm, É. Tóth, *The Chemistry of Contrast Agents in Medical Magnetic Resonance Imaging*, Wiley, **2013**.
[2] P. Caravan, J. J. Ellison, T. J. McMurry, R. B. Lauffer, *Chem. Rev.* **1999**, *99*, 2293–2352.
[3] S. Aime, M. Botta, E. Terreno, *Adv. Inorg. Chem.* **2005**, *57*, 173–237.
[4] E. Terreno, D. D. Castelli, A. Viale, S. Aime, *Chem. Rev.* **2010**, *110*, 3019–3042.
[5] M. Botta, L. Tei, *Eur. J. Inorg. Chem.* **2012**, 1945–1960.
[6] J. Zhu, Z. Xiong, M. Shen, X. Shi, *RSC Adv.* **2015**, *5*, 30286–30296.
[7] J. Min, H. Jung, H.-H. Shin, G. Cho, H. Cho, S. Kang, *Biomacromolecules* **2013**, *14*, 2332–2339.
[8] M. B. Winter, P. J. Klemm, C. M. Phillips-Piro, K. N. Raymond, M. A. Marletta, *Inorg. Chem.* **2013**, *52*, 2277–2279.
[9] G. Zhang, J. Gao, J. Qian, L. Zhang, K. Zheng, K. Zhong, D. Cai, X. Zhang, Z. Wu, *ACS Appl. Mater. Interfaces* **2015**, *7*, 14192–14200.
[10] C. Diaferia, E. Gianolio, P. Palladino, F. Arena, C. Boffa, G. Morelli, A. Accardo, *Adv. Funct. Mater.* **2015**, *25*, 7003–7016.
[11] L. M. Randolph, C. L. M. LeGuyader, M. E. Hahn, C. M. Andolina, J. P. Patterson, R. F. Mattrey, J. E. Millstone, M. Botta, M. Scadeng, N. C. Gianneschi, *Chem. Sci.* **2016**, *7*, 4230–4236.
[12] K. Zhang, M. Liu, X. Tong, N. Sun, L. Zhou, Y. Cao, J. Wang, H. Zhang, R. Pei, *Biomacromolecules* **2015**, *16*, 2618–2623.
[13] J. Della Rocca, W. Lin, *Eur. J. Inorg. Chem.* **2010**, 3725–3734.
[14] J. Della Rocca, D. Liu, W. Lin, *Acc. Chem. Res.* **2011**, *44*, 957–968.
[15] P. Horcajada, T. Chalati, C. Serre, B. Gillet, C. Sebrie, T. Baati, J. F. Eubank, D. Heurtaux, P. Clayette, C. Kreuz, *Nat. Mater.* **2010**, *9*, 172–178.
[16] W. J. Rieter, K. M. L. Taylor, H. An, W. Lin, W. Lin, *J. Am. Chem. Soc.* **2006**, *128*, 9024–9025.
[17] K. M. L. Taylor, A. Jin, W. Lin, *Angew. Chem. Int. Ed.* **2008**, *47*, 7722–7725; *Angew. Chem.* **2008**, *120*, 7836–7839.
[18] A. Carné-Sánchez, C. S. Bonnet, I. Imaz, J. Lorenzo, E. Tóth, D. Maspoch, *J. Am. Chem. Soc.* **2013**, *135*, 17711–17714.
[19] F. Avecilla, J. A. Peters, C. F. G. C. Geraldes, *Eur. J. Inorg. Chem.* **2003**, 4179–4186.
[20] C. F. G. C. Geraldes, M. P. M. Marques, B. de Castro, E. Pereira, *Eur. J. Inorg. Chem.* **2000**, 559–565.
[21] F. K. Kalmán, M. Woods, P. Caravan, P. Jurek, M. Spiller, G. Tircsó, R. Kiraly, E. Brücher, A. D. Sherry, *Inorg. Chem.* **2007**, *46*, 5260–5270.
[22] K. J. Gagnon, H. P. Perry, A. Clearfield, *Chem. Rev.* **2012**, *112*, 1034–1054.
[23] G. V. Martinez, X. Zhang, M. L. García-Martín, D. L. Morse, M. Woods, A. D. Sherry, R. J. Gillies, *NMR Biomed.* **2011**, *24*, 1380–1391.
[24] E. T. Clarke, A. E. Martell, *Inorg. Chim. Acta* **1991**, *190*, 27–36.
[25] S. Chaves, R. Delgado, J. J. R. F. Da Silva, *Talanta* **1992**, *39*, 249–254.
[26] X. Wang, T. Jin, V. Comblin, A. Lopez-Mut, E. Merciny, J. F. Desreux, *Inorg. Chem.* **1992**, *31*, 1095–1099.

[27] K. Kumar, C. A. Chang, L. C. Francesconi, D. D. Dischino, M. F. Malley, J. Z. Gougoutas, M. F. Tweedle, *Inorg. Chem.* **1994**, *33*, 3567–3575.
[28] E. T. Clarke, A. E. Martell, *Inorg. Chim. Acta* **1991**, *190*, 37–46.
[29] G. J. Fosmire, *Am. J. Clin. Nutr.* **1990**, *51*, 225–227.
[30] J. R. Curtis, G. C. Goode, J. Herrington, L. E. Urdaneta, *Clin. Nephrol.* **1976**, *5*, 61–65.
[31] C. L. Evans, *Br. J. Pharmacol. Chemother.* **1964**, *23*, 455–475.
[32] R. P. Singh, S. Kumar, R. Nada, R. Prasad, *Mol. Cell. Biochem.* **2006**, *282*, 13–21.
[33] L. Gaetke, *Toxicology* **2003**, *189*, 147–163.
[34] J. Ariñez-Soriano, J. Albalad, J. Pérez-Carvajal, I. Imaz, F. Busqué, J. Juanhuix, D. Maspoch, *CrystEngComm* **2016**, *18*, 4196–4204.
[35] R. A. Coxall, S. G. Harris, D. K. Henderson, S. Parsons, P. A. Tasker, R. E. P. Winpenny, *J. Chem. Soc. Dalton Trans.* **2000**, 2349–2356.
[36] R. Fu, X. Huang, S. Hu, S. Xiang, X. Wu, *Inorg. Chem.* **2006**, *45*, 5254–5256.
[37] S. Drumel, P. Janvier, P. Barboux, M. Bujoli-Doeuff, B. Bujoli, *Inorg. Chem.* **1995**, *34*, 148–156.
[38] L. Di Bari, G. Pescitelli, A. D. Sherry, M. Woods, *Inorg. Chem.* **2005**, *44*, 8391–8398.
[39] R. S. Dickins, D. Parker, J. I. Bruce, D. J. Tozer, *Dalton Trans.* **2003**, 1264–1271.
[40] S. J. L. Billinge, T. Egami, *Underneath the Bragg Peaks*, 2nd ed., Pergamon, **2012**.
[41] P. K. Allan, K. W. Chapman, P. J. Chupas, J. A. Hriljac, C. L. Renouf, T. C. A. Lucas, R. E. Morris, *Chem. Sci.* **2012**, *3*, 2559–2564.
[42] M. I. Mohideen, P. K. Allan, K. W. Chapman, J. A. Hriljac, R. E. Morris, *Dalton Trans.* **2014**, *43*, 10438–10442.
[43] C. L. Farrow, P. Juhas, J. W. Liu, D. Bryndin, E. S. Božin, J. Bloch, T. Proffen, S. J. L. Billinge, *J. Phys. Condens. Matter* **2007**, *19*, 335219.
[44] T. Vitha, V. Kubícek, P. Hermann, L. Vander Elst, R. N. Muller, Z. I. Kolar, H. T. Wolterbeek, W. A. P. Breeman, I. Lukes, J. A. Peters, *J. Med. Chem.* **2008**, *51*, 677–683.
[45] N. Raghunand, C. Howison, A. D. Sherry, S. Zhang, R. J. Gillies, *Magn. Reson. Med.* **2003**, *49*, 249–257.
[46] M. L. Garcia-Martin, G. V. Martinez, N. Raghunand, A. D. Sherry, S. Zhang, R. J. Gillies, *Magn. Reson. Med.* **2006**, *55*, 309–315.
[47] M. M. Ali, M. Woods, P. Caravan, A. C. L. Opina, M. Spiller, J. C. Fettinger, A. D. Sherry, *Chem. Eur. J.* **2008**, *14*, 7250–7258.
[48] Z. Shanrong, W. Kuangcong, D. Sherry, *Invest. Radiol.* **2001**, *36*, 82–86.
[49] G. Guerrero, J. G. Alauzun, M. Granier, D. Laurencin, P. H. Mutin, *Dalton Trans.* **2013**, *42*, 12569–12585.
[50] G. J. M. Koper, M. Borkovec, *Polymer (Guildf).* **2010**, *51*, 5649–5662.
[51] A. Barge, G. Cravotto, E. Gianolio, F. Fedeli, *Contrast Media Mol. Imaging* **2006**, *1*, 184–188.
[52] J. Juanhuix, F. Gil-Ortiz, G. Cuní, C. Colldelram, J. Nicolás, J. Lidón, E. Boter, C. Ruget, S. Ferrer, J. Benach, *J. Synchrotron Radiat.* **2014**, *21*, 679–689.
[53] W. Kabsch, *J. Appl. Crystallogr.* **1993**, *26*, 795–800.
[54] L. Palatinus, G. Chapuis, *J. Appl. Crystallogr.* **2007**, *40*, 786–790.
[55] G. M. Sheldrick, *Acta Crystallogr. Sect. A* **2008**, *64*, 112–122.
[56] P. J. Chupas, X. Qiu, J. C. Hanson, P. L. Lee, C. P. Grey, S. J. L. Billinge, *J. Appl. Crystallogr.* **2003**, *36*, 1342–1347.
[57] X. Yang, P. Juhas, C. L. Farrow, S. J. L. Billinge, *arXiv* **2015**, 1402.3163v3.
[58] P. Juhás, T. Davis, C. L. Farrow, S. J. L. Billinge, *J. Appl. Crystallogr.* **2013**, *46*, 560–566.

Received: May 17, 2016
Published online on August 4, 2016

ChemComm

COMMUNICATION

View Article Online
View Journal | View Issue

Cite this: *Chem. Commun.*, 2016, 52, 13397

Received 20th September 2016,
Accepted 21st October 2016

DOI: 10.1039/c6cc07653j

www.rsc.org/chemcomm

Hetero-bimetallic paddlewheel clusters in coordination polymers formed by a water-induced single-crystal-to-single-crystal transformation†

Jorge Albalad,[a] Javier Aríñez-Soriano,[a] José Vidal-Gancedo,[bc] Vega Lloveras,[bc] Jordi Juanhuix,[d] Inhar Imaz,*[a] Núria Aliaga-Alcalde[be] and Daniel Maspoch*[ae]

Herein we report a water-induced single-crystal to single-crystal transformation that involves the formation of hetero-bimetallic paddlewheel clusters in coordination polymers. Through this transformation, which involves the cleavage and formation of different coordination bonds, two different Cu(II)–Zn(II) and Cu(II)–Ni(II) paddlewheel units exhibiting a 1:1 metal ratio were created.

Coordination polymers (CPs), including porous metal–organic frameworks (MOFs), exhibit a very rich organic–inorganic chemistry that makes possible their structural and compositional design for myriad applications.[1–5] This design is mostly succeeded through the careful choice of the building blocks (that is, the organic linker and the metal ion),[6–8] or by inducing post-synthetic modifications onto pre-synthesized systems.[9–12] To date, most of these post-synthetic modifications have been made on organic linkers.[13] However, increasing interest is recently focused on exchanging metal ions in inorganic units using post-synthetic metalation (PSM) pathways.[14,15] The latter strategy allows the creation of more "exotic" hetero-metallic inorganic units in CPs that can optimize, for example, their stability,[16] gas sorption,[17,18] catalytic activity,[19] luminescence[20] and magnetic properties.[21]

Among all potential clusters present in the literature of CPs/MOFs,[22] the paddlewheel unit is probably one of the best candidates for the study of the above-mentioned metalation processes due to its centrosymmetric character and structural simplicity. This cluster is relatively easy to synthesize using a wide range of metal sources, including Cu, Ni, Zn, Co, Mn, Cd, Ru, or even Bi-Rh,[23] among others. Based on it, some advances have already been made in the PSM of paddlewheel units in CPs.[19,24,25] For example, Cu(II) ions were introduced into the paddlewheel units of HKUST-1 by starting with a pure Zn(II)-HKUST-1 sample and making PSM with $Cu(NO_3)\cdot 2.5H_2O$.[26] Also, different metal ions such as Cu(II), Ni(II) and Co(II) were exchanged in CPs made of Zn(II)-paddlewheel units.[24] However, the governing factors of PSM are still uncertain and a successful insertion of a specific metal ion is usually achieved using empirical trial-and-error methodologies, provoking also uncontrolled substitutions in which the exact spatial disposition adopted by the new ions is unclear.[27]

Another approach for designing novel heterometallic clusters (and in particular, hetero-bimetallic paddlewheel clusters) in a more controlled way should be their formation during the CP synthesis. Using this approach, Kleist *et al.* synthesized HKUST-1 made of paddlewheel units containing Cu(II) and Ru(III).[25] However, the content of Ru(III) in this HKUST-1 was very low, meaning that only 9% of the units should potentially be hetero-bimetallic units. To our knowledge, there is only one example of pure hetero-bimetallic paddlewheel units with a 1:1 metal ratio obtained using this strategy.[28] Doonan *et al.* successfully showed the formation of discrete polyhedra made of Pd(II)–M(II) (where M is Zn, Cu and Ni) paddlewheel units starting from preformed bimetallic acetates as reagents.

Herein we show the formation of hetero-bimetallic Cu(II)–Zn(II) and Cu(II)–Ni(II) paddlewheel clusters exhibiting a 1:1 metal ratio in two isostructural CPs (hereafter called $\mathbf{2_{CuZn}}$ and $\mathbf{2_{CuNi}}$). These CPs are made from water-induced single-crystal-to-single-crystal (SC–SC) transformations of preformed hetero-bimetallic CPs (hereafter called $\mathbf{1_{CuZn}}$ and $\mathbf{1_{CuNi}}$) that do not contain the paddlewheel units.

$\mathbf{1_{CuZn}}$ was initially obtained through a two-step synthesis.[29] In the first step, the macrocyclic Cu–DOTA complex was precipitated by mixing $CuCl_2\cdot 2H_2O$ (0.075 mmol) and 1,4,7,10-tetraazacyclododecane-1,4,7,10-tetraacetic acid (H_4DOTA; 0.075 mmol) in water (4 mL) under sonication for 5 min at room temperature (Fig. S1, ESI†). In the second step, a DMF solution (4 mL)

[a] *Catalan Institute of Nanoscience and Nanotechnology (ICN2), CSIC and The Barcelona Institute of Science and Technology, Campus UAB, Bellaterra, Spain. E-mail: inhar.imaz@icn2.cat, daniel.maspoch@icn2.cat*
[b] *Institut de Ciència de Materials de Barcelona (ICMAB-SCIC), Bellaterra, Spain*
[c] *CIBER-BBN, Barcelona, Spain*
[d] *ALBA Synchrotron, 08290 Cerdanyola del Vallès, Barcelona, Catalonia, Spain*
[e] *ICREA, Pg. Lluís Companys 23, 08010 Barcelona, Spain*

† Electronic supplementary information (ESI) available: The experimental section, ICP-OES, EDX, XRPD, and water sorption measurements. CCDC 1505012 ($\mathbf{1_{CuZn}}$) and CCDC 1505013 ($\mathbf{2_{CuZn}}$). For ESI and crystallographic data in CIF or other electronic format see DOI: 10.1039/c6cc07653j

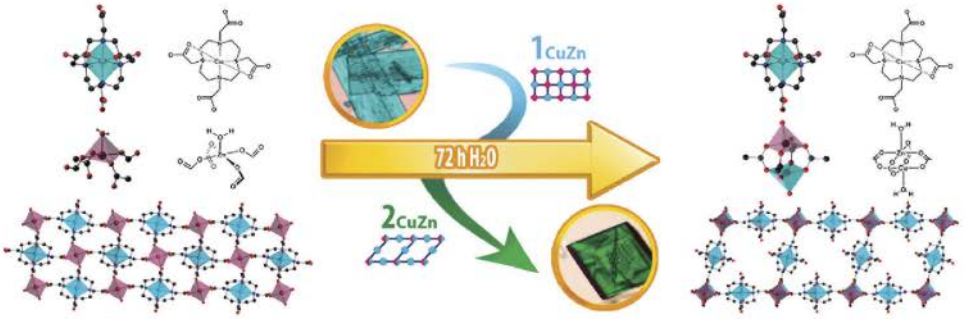

Fig. 1 Schematic representation of the water-triggered transition from $\mathbf{1}_{CuZn}$ to $\mathbf{2}_{CuZn}$. For both sides: (top) Representation of the Cu–DOTA illustrating the octahedral coordination geometry (blue octahedron); (middle) representation of the square-based pyramidal coordination geometry of Zn(II) ions in $\mathbf{1}_{CuZn}$ (purple tetrahedron), which is transformed to a hetero-bimetallic Cu(II)–Zn(II) paddlewheel unit in $\mathbf{2}_{CuZn}$ (purple tetrahedron for Zn(II) and blue tetrahedron for Cu(II)); and (bottom) 2-D frameworks of $\mathbf{1}_{CuZn}$ (left) and $\mathbf{2}_{CuZn}$ (right).

containing $Zn(NO_3)\cdot 6H_2O$ (0.15 mmol) was added to the aqueous solution containing the precipitated Cu–DOTA complex under stirring. This mixture was then transferred to high temperature capped vials and allowed to react at 120 °C, from which plate-shaped sky blue crystals suitable for single-crystal X-Ray diffraction (SCXRD) were collected after 12 hours (yield: 66%; obtained as a pure phase, as confirmed by elemental analysis, energy-dispersive X-ray spectroscopy (EDX), inductively coupled plasma optical emission spectrometry (ICP-OES) and X-ray powder diffraction (XRPD); Tables S2, S3 and Fig. S2, ESI†). $\mathbf{1}_{CuZn}$ crystallized in the monoclinic $P2/n$ symmetry group with the formula $[ZnCu(DOTA)(H_2O)]$ (Table S1, ESI†). A closer analysis of $\mathbf{1}_{CuZn}$ revealed the formation of a 2-D framework extended along the ac plane (Fig. 1, left-bottom). In these layers, Cu(II) ions are accommodated inside the macrocyclic cavity adopting a distorted octahedral geometry coordinated to the cyclen subunit and to two of the acetate arms (Fig. 1, left-top). These two arms act as bidentate bridges (η_2) between the Cu(II) and Zn(II) ions. Zn(II) extends the framework into a square-based pyramid motif (Fig. 1, left-middle) using not only the two η_2 bridge carboxylate arms along the a axis but also the open η_1 arms along the perpendicular c axis. The coordination environment around Zn(II) is completed with the presence of a water molecule (O_1W) crowning the axial position of the pyramid. The different layers are packed in an AAA sequence connected *via* hydrogen bonds between O_1W and the non-coordinated oxygen atoms in the η_1 carboxylate arms of a subsequent layer (Fig. S3, ESI†). Remarkably, the resulting framework is compact, meaning that there are no guest solvent molecules in the structure.

Because the neighboring Cu(II) and Zn(II) cannot be discriminated by SCXRD owing to their similar scattering power, the location of Cu(II) ions in $\mathbf{1}_{CuZn}$ was further investigated by electron paramagnetic resonance (EPR). To study the former, we performed measurements on $\mathbf{1}_{CuZn}$ and compared with that of the discrete macrocyclic complex Cu–DOTA.[30] As expected, Cu–DOTA showed the characteristic EPR spectrum of a Cu(II) complex with an elongated octahedral geometry (Fig. 2a). The $g_\parallel$ and $g_\perp$ values were 2.290 and 2.083, respectively (see the EPR simulation in Fig. S4, ESI†).

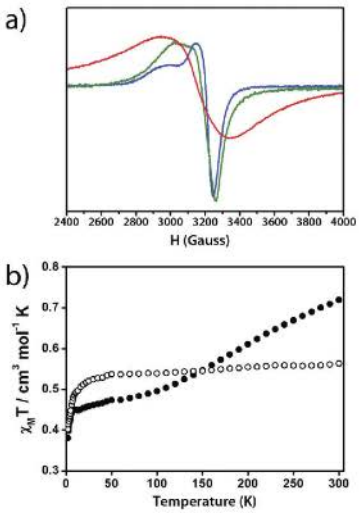

Fig. 2 (a) EPR spectra of Cu–DOTA (blue), $\mathbf{1}_{CuZn}$ (green) and $\mathbf{1}_{CuCu}$ (red). An octahedral environment around Cu(II) ions can be attributed to the initial heterometallic phase. (b) Experimental $\chi_M T$ *vs.* T data of systems $\mathbf{2}_{CuCu}$ (●) and $\mathbf{2}_{CuZn}$ (○) between 2.0 K and 300.0 K using a dc external magnetic field of 1 T.

Importantly, the EPR spectrum of $\mathbf{1}_{CuZn}$ was very similar to that of Cu–DOTA, with $g_\parallel$ and $g_\perp$ values of 2.240 and 2.085, respectively (see the EPR simulation in Fig. S5, ESI†). This similarity confirmed that indeed the Cu(II) ions reside inside the macrocyclic cavities in $\mathbf{1}_{CuZn}$, and that the Zn(II) ions bridge these Cu–DOTA units. It is important to highlight here that this evidence is also in good agreement with the reported Cu/Zn association constants with H_4DOTA ($\log K_d$ = 22.72 and 18.70 for Cu–DOTA and Zn–DOTA, respectively).[31] Finally, to discard the presence of Cu(II) ions in the metal positions responsible for bridging the macrocyclic complexes, we finally compared our previous spectra with that obtained for the isostructural homometallic

$\mathbf{1_{CuCu}}$. Note here that $\mathbf{1_{CuCu}}$ was prepared under the same conditions as for $\mathbf{1_{CuZn}}$, except that instead of $Zn(NO_3)\cdot 6H_2O$ in the second synthetic step, we used $Cu(NO_3)_2\cdot 2.5H_2O$ (yield: 87%; obtained as a pure phase, as confirmed by elemental analysis and XRPD; Fig. S2, ESI†). In this case, the EPR spectrum was quite different, exhibiting a broad line with a g value of 2.128 (Fig. 2a). Since Cu(II) ions in $\mathbf{1_{CuCu}}$ adopt not only an elongated octahedral geometry but also a square pyramidal geometry, these results confirmed the absence of Cu(II) ions outside the macrocycle in $\mathbf{1_{CuZn}}$.

Crystals of $\mathbf{1_{CuZn}}$ (and also of $\mathbf{1_{CuCu}}$) were thermodynamically unstable in their reaction medium, undergoing a spontaneous SC–SC transition when left undisturbed for weeks. Moreover, this SC–SC transformation could be accelerated when dry crystals of $\mathbf{1_{CuZn}}$ were soaked in pure distilled water without any addition of external metal sources for 72 hours (96 hours for $\mathbf{1_{CuCu}}$; Fig. S6 and S7, ESI†). Remarkably, the resulting prism-shaped green crystals of $\mathbf{2_{CuZn}}$ were suitable for SCXRD. $\mathbf{2_{CuZn}}$ crystallized in the $P2_1/c$ symmetry group showing a theoretical formula of $[Zn_xCu_{2-x}(DOTA)(H_2O)]\cdot 4H_2O$ (note here that Cu(II) and Zn(II) cannot be differentiated by SCXRD; Table S1, ESI†). $\mathbf{2_{CuZn}}$ shows a 2D framework (Fig. 1, right-bottom) in which the Cu(II) ions also reside in the macrocyclic cavity adopting the same distorted octahedral geometry (Fig. 1, right-top). However, unlike in $\mathbf{1_{CuZn}}$, the closed pendant arms do not contribute to extending the coordination layers. Instead, the coordination layers in $\mathbf{2_{CuZn}}$ are expanded along the ab plane through the open arms forming $M_2(COO)_4$ paddlewheel clusters (Fig. 1, right-middle). The different layers are then stacked in an ABA′B′ sequence forming 1-D channels along the c axis, which are filled with guest water molecules (Fig. S8, ESI†). Interestingly, $\mathbf{2_{CuZn}}$ was stable in water for at least 6 months (Fig. S9, ESI†), and their guest water molecules could be removed and re-adsorbed without affecting the integrity of the open-framework (Fig. S10 and S11, ESI†). Indeed, water adsorption measurements showed a standard Type I isotherm with a water uptake of 0.12 $g_{water}\ g_{\mathbf{2_{CuZn}}}^{-1}$ at 30% RH, which corresponds to 4.2 water molecules. The isotherm shows then a plateau from 25% to 65% RH and, after that, $\mathbf{2_{CuZn}}$ gained hydrophilicity adsorbing up to 0.21 $g_{water}\ g_{\mathbf{2_{CuZn}}}^{-1}$.

To obtain more details of the composition of $\mathbf{2_{CuZn}}$, we then analyzed it using EDX and ICP-OES (Tables S4 and S5, ESI†). Surprisingly, the multiple measurements carried out using both techniques never suggested an equal proportion ($x = 1$) of Cu(II) and Zn(II) ions but always a precise 3 : 1 Cu(II) : Zn(II) ratio (or $x = 0.5$). These results lead to a final formula of $[Zn_{0.5}Cu_{1.5}(DOTA)(H_2O)]\cdot 4H_2O$ for $\mathbf{2_{CuZn}}$. Thus, considering that the metal position inside the macrocycle is occupied by Cu(II), the two metal positions of the paddlewheel units must be occupied by a 1 : 1 mixture of Cu(II) and Zn(II) ions.

To further confirm the formation of the bimetallic 1 : 1 Zn(II) : Cu(II) paddlewheel units, we performed magnetic susceptibility measurements on both $\mathbf{2_{CuZn}}$ and $\mathbf{2_{CuCu}}$ (Fig. 2b). If the hetero-bimetallic Cu(II)–Zn(II) units are formed, the paramagnetic Cu(II) ions located inside the macrocycles and those forming the paddlewheel units should be magnetically weakly coupled with only appreciable intermolecular magnetic interactions at the lowest temperatures. In contrast, strong antiferromagnetic interactions are expected if homometallic Cu(II)–Cu(II) paddlewheel units are present in $\mathbf{2_{CuZn}}$. Indeed, homometallic Cu(II)–Cu(II) paddlewheel units display a rather strong antiferromagnetic behavior, providing exchange coupling constants of J values between $-200\ cm^{-1}$ and $-1000\ cm^{-1}$.[32] With this in mind, solid-state variable-temperature (1.8–300.0 K) dc magnetic susceptibility data of polycrystalline samples of $\mathbf{2_{CuZn}}$ and $\mathbf{2_{CuCu}}$ using a 1.0 T field were collected. Their magnetic behaviors are depicted in Fig. 2b as plots of $\chi_M T$ *vs.* T. In both cases, TIP corrections were performed by adding $-60 \times 10^{-6}\ cm^3\ mol^{-1}\ K$ per Cu(II) unit. The $\chi_M T$ values at 300 K were 0.72 $cm^3\ mol^{-1}\ K$ for $\mathbf{2_{CuCu}}$ and 0.56 $cm^3\ mol^{-1}\ K$ for $\mathbf{2_{CuZn}}$, which are in good agreement with those expected for one and a half independent Cu(II) centers in $\mathbf{2_{CuCu}}$ (0.74 $cm^3\ mol^{-1}\ K$) and for one Cu(II) center in $\mathbf{2_{CuZn}}$ (0.55 $cm^3\ mol^{-1}\ K$); considering a g value of 2.00 in both cases. As expected, the $\chi_M T$ values of $\mathbf{2_{CuCu}}$ rapidly decreased upon cooling, consistent with the presence of strong antiferromagnetic coupling between the two Cu(II) ions forming the homometallic paddlewheel units ($J = -163\ cm^{-1}$, see fitting in Fig. S12, ESI†). In quite contrast, the $\chi_M T$ values for $\mathbf{2_{CuZn}}$ remained almost constant all over the temperatures, and slightly decreased below 25 K. This behavior is characteristic of a system that is weakly coupled, as expected for a $\mathbf{2_{CuZn}}$ system built up from hetero-bimetallic Cu(II)–Zn(II) paddlewheel units.

Fig. 3 shows a proposed mechanism for the formation of these hetero-bimetallic paddlewheel units, which starts with a dynamic cleavage of the η_2 acetate arms on $\mathbf{1_{CuZn}}$ through the Cu–O bond, induced by the presence of water (first fragment of Fig. 3). This step triggers the formation of a metaphase where all the pendant arms are equally open (second fragment of Fig. 3). This metaphase can therefore be seen as "half-empty" paddlewheel units. The transition continues when half of these open arms rearrange to complete again the thermodynamically favorable octahedral coordination around the Cu(II) ions, leaching to the solution half of the Zn(II) ions (third fragment of Fig. 3). A partial dissociation of the material should occur afterwards in

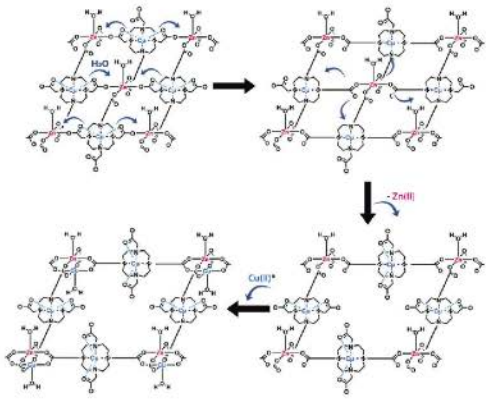

Fig. 3 Schematic representation of the mechanism. Note that Cu(II)* represents the insertion of Cu(II) coming from the release of Cu–DOTA due to the degradation of the crystal.

› compensate the charge unbalance, releasing an equal value DOTA]^{2} units to the solution. Half of these released Cu(II) ıust be able to complete the holes on the half-formed wheel units, finally forming the hetero-bimetallic clusters in $\mathbf{2_{CuZn}}$ (fourth fragment of Fig. 3). This hypothetic ıism implies a loss of 41% of the initial weight of the ; as well as a release of 50% and 25% of the initial Zn(II) ı(II) ions, respectively. To follow these parameters, we ıed crystals of $\mathbf{1_{CuZn}}$ (17.8 mg) in water (5.0 ml) and followed ⁻SC transformation to $\mathbf{2_{CuZn}}$. After 72 hours, the transition npleted, and 9.8 mg of $\mathbf{2_{CuZn}}$ were collected, corresponding eight loss of 45%. In addition, the water solution was d by ICP-OES, and found a Zn(II) and Cu(II) content of g (206 ppm) and 0.49 mg (98 ppm), respectively. These ts correspond to a weight loss of 51% and 26% of the initial ıd Cu(II) contents in $\mathbf{1_{CuZn}}$. Altogether, these results evidence ıibility of our proposed mechanism.

ılly, to expand the variety of hetero-bimetallic paddle- units, we reproduced the synthesis of $\mathbf{1_{CuZn}}$ but using salts of Mn(II), Fe(II)/(III), Co(II), Ni(II), Ag(I) or Pd(II) in the step. Among these metal ions, we could only confirm mation of $\mathbf{1_{CuNi}}$ (yield: 71%; obtained as a pure phase, as ıed by XRPD, EDX, ICP-OES and elemental analysis; S2, S3 and Fig. S2, ESI†). This result seems consistent ıe Irving–Williams series for the stability of complexes ıized from divalent metal ions. Remarkably, we found ıe transition $\mathbf{1_{CuNi}} \rightarrow \mathbf{2_{CuNi}}$ was also possible after ıing $\mathbf{1_{CuNi}}$ in water for two months (Fig. S5, ESI†). Here, ıd ICP-OES analysis also gave a 3 : 1 Cu(II) : Ni(II) ratio ; S4 and S5, ESI†), thus confirming the formation of the bimetallic Cu(II)–Ni(II) paddlewheel units in $\mathbf{2_{CuNi}}$.

onclusion, we have shown the unprecedented formation ructural CPs that contain hetero-bimetallic paddlewheel ıaving a 1 : 1 metal ratio inside the cluster. This for- takes place *via* a water-induced SC–SC transformation compact hetero-bimetallic framework built up from ting Cu–DOTA units through isolated metal ions to a ›pen framework built up from connecting identical Cu- ınits through hetero-bimetallic paddlewheel units. This transformation was reproduced for two different cases ıg the formation of Cu(II)–Zn(II) and Cu(II)–Ni(II) paddle- units. This study illustrates the diversity, richness and of this type of chemistry, from which many new systems to be discovered.

work was supported by the Spanish MINECO (projects I2015-65354-C2-1-R and MAT2013-47869-C4-2-P), DGI grant (CTQ2013-40480-R), the Catalan AGAUR (project 2014-SGR- 2014-SGR-17), and the ERC under the EU FP7 (ERC-Co). J. A. thanks the Generalitat de Catalunya for a FI fellowship B 00449). ICN2 and ICMAB acknowledge the support of the ı MINECO through the Severo Ochoa Centres of Excellence nme, under Grants SEV-2013-0295 and SEV-2015-0496. The ; thank Dr N. Clos from the Serveis Cientifico-Tècnics of the ity of Barcelona for her assistance.

Notes and references

1 C. Janiak, *Dalton Trans.*, 2003, 2781–2804.
2 S. Kitagawa, R. Kitaura and S. Noro, *Angew. Chem., Int. Ed.*, 2(2334–2375.
3 K. M. Fromm, *Angew. Chem., Int. Ed.*, 2009, **48**, 4890–4891.
4 D. Zhao, D. J. Timmons, D. Yuan and H. C. Zhou, *Acc. Che* 2011, **44**, 123–133.
5 B.-L. Liu, H.-Y. Zang, H.-Q. Tan, Y.-H. Wang and Y.-G. Li, *C Comm*, 2016, **18**, 3300–3305.
6 X. Zhang, Z. Zhang, J. Boissonnault and S. M. Cohen, *Commun.*, 2016, **52**, 8585–8588.
7 F. A. Almeida Paz, J. Klinowski, S. M. F. Vilela, J. P. C. J. A. S. Cavaleiro and J. Rocha, *Chem. Soc. Rev.*, 20 1088–1110.
8 A. J. Fletcher, K. M. Thomas and M. J. Rosseinsky, *J. Soli Chem.*, 2005, **178**, 2491–2510.
9 A. Béziau, S. A. Baudron, G. Rogez and M. W. Hosseini, *Inorg.* 2015, **54**, 2032–2039.
10 S. Yang, L. Liu, J. Sun, K. M. Thomas, A. J. Davies, M. W. A. J. Blake, A. H. Hill, A. N. Fitch, C. C. Tang and M. Sc *J. Am. Chem. Soc.*, 2013, **135**, 4954–4957.
11 M. H. Mir, L. L. Koh, G. K. Tan and J. J. Vittal, *Angew. Chem.,* 2010, **49**, 390–393.
12 M. R. Warren, S. K. Brayshaw, A. L. Johnson, S. Schiffers Raithby, T. L. Easun, M. W. George, J. E. Warren and S. *Angew. Chem., Int. Ed.*, 2009, **48**, 5711–5714.
13 G. Tuci, A. Rossin, X. Xu, M. Ranocchiari, J. A. van Bol L. Luconi, I. Manet, M. Melucci and G. Giambastiani, *Chem.* 2013, **25**, 2297–2308.
14 C. K. Brozek and M. Dincă, *Chem. Soc. Rev.*, 2014, **43**, 5456–
15 J. D. Evans, C. J. Sumby and C. J. Doonan, *Chem. Soc. Rev.*, 2(5933–5951.
16 T. Grancha, J. Ferrando-Soria, H. C. Zhou, J. Gascon, B. J. Pasán, O. Fabelo, M. Julve and E. Pardo, *Angew. Chem., I* 2015, **54**, 6521–6525.
17 S. Yang, X. Lin, A. J. Blake, G. S. Walker, P. Hubberstey Champness and M. Schröder, *Nat. Chem.*, 2009, **1**, 487–493.
18 S. Yang, G. S. B. Martin, J. J. Titman, A. J. Blake, D. R. Allar Champness and M. Schröder, *Inorg. Chem.*, 2011, **50**, 9374–9
19 R. Zou, P. Z. Li, Y. F. Zeng, J. Liu, R. Zhao, H. Duan, J. G. Wang, R. Zou and Y. Zhao, *Small*, 2016, **12**, 2334–2343
20 P. R. Matthes, C. J. Hoeller, M. Mai, J. Heck, S. J. Sed S. Schmiechen, C. Feldmann, W. Schnick and K. Mueller-Busc *J. Mater. Chem.*, 2012, **22**, 10179–10187.
21 C. K. Brozek, V. K. Michaelis, T.-C. Ong, L. Bellarosa, N. R. G. Griffin and M. Dincă, *ACS Cent. Sci.*, 2015, **1**, 252–260.
22 D. J. Tranchemontagne, J. L. Mendoza-Cortés, M. O'Keeffe an Yaghi, *Chem. Soc. Rev.*, 2009, **38**, 1257–1283.
23 T. L. Sunderland and J. F. Berry, *Dalton Trans.*, 20 50–55.
24 T. K. Pal, S. Neogi and P. K. Bharadwaj, *Chem. – Eur. J.*, 2(16083–16090.
25 M. A. Gotthardt, R. Schoch, S. Wolf, M. Bauer and W. Kleist, *Trans.*, 2015, **44**, 2052–2056.
26 X. Song, S. Jeong, D. Kim and M. S. Lah, *CrystEngComm*, 2(5753–5756.
27 F. Gul-E-Noor, B. Jee, M. Mendt, D. Himsl, A. Pöppl, M. Har J. Haase, H. Krautscheid and M. Bertmer, *J. Phys. Chem. C* **116**, 20866–20873.
28 J. M. Teo, C. J. Coghlan, J. D. Evans, E. Tsivion, M. Head-G C. J. Sumby and C. J. Doonan, *Chem. Commun.*, 2015, **52**, 27
29 J. Aríñez-Soriano, J. Albalad, J. Pérez-Carvajal, I. Imaz, F. I J. Juanhuix and D. Maspoch, *CrystEngComm*, 2016, **37**, 191–
30 A. Riesen, M. Zehnder and T. a Kaden, *Helv. Chim. Acta*, 19 2067–2073.
31 N. Viola-Villegas and R. P. Doyle, *Coord. Chem. Rev.*, 200 1906–1925.
32 M. Fontanet, A. R. Popescu, X. Fontrodona, M. Roc I. Romero, F. Teixidor, C. Viñas, N. Aliaga-Alcalde and E *Chem. – Eur. J.*, 2011, **17**, 13217–13229.

NAL OF THE AMERICAN CHEMICAL SOCIETY

e-Crystal-to-Single-Crystal Postsynthetic Modification of a l–Organic Framework via Ozonolysis

.balad,[†,#] Heng Xu,[†,#] Felipe Gándara,[‡] Mohamed Haouas,[§] Charlotte Martineau-Corc Mas-Balleste,[∇] Sarah A. Barnett,[⊥] Judith Juanhuix,[¶] Inhar Imaz,[*,†] and Daniel Maspo

nstitute of Nanoscience and Nanotechnology (ICN2), CSIC and The Barcelona Institute of Science and Tec UAB, Bellaterra, 08193 Barcelona, Spain

Science Factory, Instituto de Ciencia de Materiales de Madrid (ICMM), Consejo Superior de Investigaciones Calle Sor Juana Inés de la Cruz, 3, 28049 Madrid, Spain

avoisier de Versailles, CNRS, UVSQ, Université Paris-Saclay, 45 Avenue des Etats-Unis, 78035 Versailles Ced

CEMHTI UPR3079, Université d'Orléans, F-45071 Orléans, France

c Chemistry Department, Universidad Autónoma de Madrid, Madrid 28049, Spain

l Light Source, Harwell Science and Innovation Campus, Didcot, Oxfordshire OXII ODE, United Kingdom

nchrotron, Cerdanyola del Vallès, 08290 Barcelona, Spain

Pg. Lluís Companys 23, 08010 Barcelona, Spain

porting Information

ACT: We describe solid–gas phase, single-crystal-e-crystal, postsynthetic modifications of a metal–framework (MOF). Using ozone, we quantitatively med the olefin groups of a UiO-66-type MOF into oxolane rings, which we then selectively converted ner aldehydes or carboxylic acids.

l–organic frameworks (MOFs) are crystalline terials that comprise organic linkers and metal ers. For the past two decades, they have attracted for their exceptional porosity and structural diversity.[1] neir inherent crystallinity and porosity, MOFs are an orm for applications that entail incorporation of target functionalities onto their pore walls.[2−4] To date, nethodologies have been developed to introduce chemical functionalities into preassembled MOFs. clude covalent modification of the organic linkers,[5] change processes[6] and postsynthetic metalations.[7,8] the synthetic conditions of postsynthetic covalent ons typically require long reaction times and high res that many MOFs cannot sustain; and for those t can resist such conditions, the yields are only low to This is partly because the methods are based on id phase processes, whereby reaction progress is y the diffusion of reagents inside the porous ts to reach the target sites, especially for MOFs rfaces are already partially tagged, as the surface ock access to the pores.[9]

-less reactivity, particularly solid–gas phase reactivity, ly explored approach in metallurgy and polymer ndeed, reactive gases (e.g., fluorine gas in the steel have been used to quantitatively passivate, cleave, or e hydrophobic character of diverse materials.[10] there is scant precedent on solid–gas phase reactions with MOFs.[11] We reasoned that such an approach used to overcome the aforementioned limitation synthetic functionalization of MOF pores. Here, v strate this concept by reporting transformation of groups of a UiO-66-type MOF into 1,2,4-trioxo which we then selectively converted into either al carboxylic acids.

Ozone has proven to be a powerful oxidizing diverse chemistries under mild conditions.[12,13] reactions, ozonolysis of alkenes is arguably the m studied.[14,15] Initially used for routine characterizatic and natural polymers, it is now employed for selecti of olefinic bonds, as it enables regio-specific fo aldehydes, ketones or carboxylic acids in mere mi reaction involves the metastable intermediate 1,2,4 Due to their low stability, trioxolane rings are n isolate; however, those that have been are strong a and therapeutic agents, especially in the form of oz or triglycerides. Moreover, trioxolane rings can be tre mild reductive or oxidative conditions to form moieties[16] or carboxylic acids,[12] respectively.

Here, we report postsynthetic functionalization of olefin-tagged UiO-66-type MOF, **ZrEBDC**, using solid–gas phase ozonolysis. We selected it because this type exhibit high thermal and chemical stabili resistant to aqueous and acidic conditions. Addit chose 2-ethenylbenzene-1,4-dicarboxylic acid (H_2EB organic ligand because it is a simple and robust link reactive sites other than its olefin-tagged pendant a 1a). We demonstrate that, by constantly stream through **ZrEBDC**, the pendant alkene group quantitatively transformed into stable 1,2,4-trioxolan on the pore walls, with no loss of single-crystallinity.

Received: December 6, 2017
Published: January 24, 2018

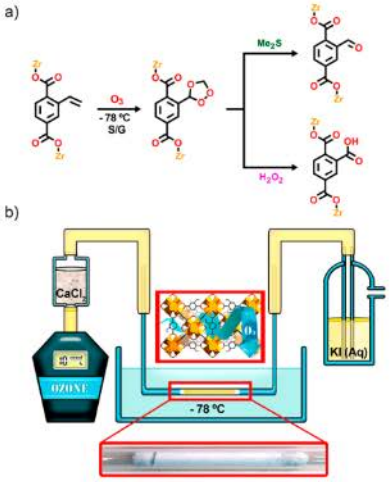

Figure 1. (a) Scheme of the postsynthetic modifications performed with **ZrEBDC**. (b) Scheme of the setup used for the ozonolysis of **ZrEBDC**. Bottom: photo of the tube containing the crystals.

optimized workup conditions enabled cleavage of these 1,2,4-trioxolane rings to selectively form aldehydes or carboxylic acids (Figure 1a).

Bulk **ZrEBDC** was synthesized by adding an equimolar mixture of H_2EBDC and $ZrOCl_2 \cdot 8H_2O$ into a mixture of DMF and formic acid, and the resulting slurry was then heated at 120 °C. After 12 h, the crude solid was washed twice with DMF and acetone, filtered, and activated under vacuum prior to any ozonolysis test. Colorless octahedral crystals of **ZrEBDC** suitable for single-crystal X-ray diffraction (SCXRD) were obtained by dissolving the two reagents in a 3:1 mixture of DEF/formic acid, and then heating the resulting solution from 25 to 135 °C (heating rate = 5 °C/min) for 72 h (Figure S2). The crystal structure of **ZrEBDC** revealed the formation of the archetypical UiO-66-like backbone, in which the olefinic side-chains of the EBDC linkers point inward toward the pores (Figures S3, S4).

In a typical ozonolysis experiment, activated **ZrEBDC** (50 mg) was packed inside a 3.4 mm diameter Pyrex tube (Figure 1b, Figure S1). Two cotton stoppers were added around the sample, and the tube was bent into a U-shape using a flame torch. One end was directly attached to an ozone generator, whereas the other was connected to vacuum. Before the reaction was started, the tube was immersed into a dry ice/acetone bath at −78 °C and purged under vacuum for 10 min. Under these conditions, ozone presents a moderate half-life and selectively reacts with unsaturated moieties. Excessive generation of ozone was avoided by adding an aqueous KI detector to the end of the setup. Once the sample had reached the proper temperature, a constant stream of O_3/air (10 mmol O_3/h, dried through $CaCl_2$) was blown into the reaction from one end of the tube. The stream was maintained until the KI solution changed from colorless to bright yellow (after ~30 min), which indicated that all the olefins had been transformed. The ozone stream was then stopped immediately. The sample, which showed a blue color, was left under vacuum for an additional 10 min to ensure that all the residual unreacted ozone was evacuated from inside the tube; after this, the sample became white again.

We characterized the ozonolyzed crystals (hereafter called **ozo-ZrBDC**) by SCXRD, which confirmed that they had retained the crystallinity and the UiO-66 framework of the starting MOF (Figure 2a). Analysis of the difference Fourier

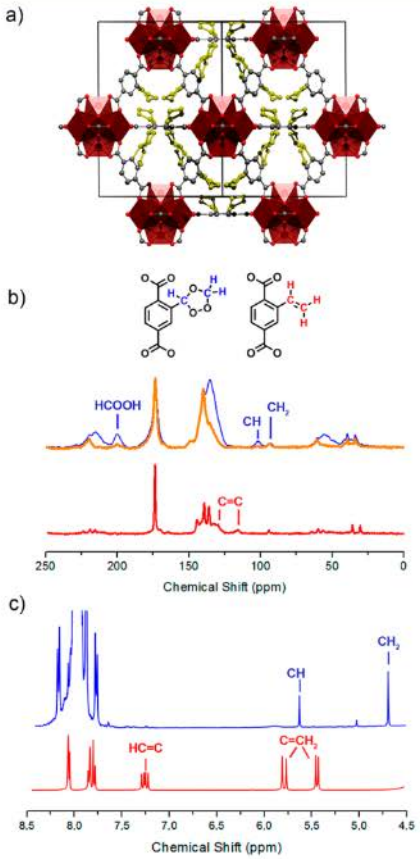

Figure 2. (a) Illustration of the single-crystal structure of **ozo-ZrBDC** across the [110] direction, highlighting the disordered 1,2,4-trioxolane moieties (yellow). (b) Solid-state ^{13}C NMR spectra of **ZrEBDC** (red: CPMAS) and **ozo-ZrBDC** (blue: CPMAS; orange: CPPI-MAS). (c) ^1H NMR spectra after the ligand-exchange experiment (blue) and H_2EBDC (red).

maps revealed high electron-density within the pores of the framework, which we attributed to the 1,2,4-trioxolane. Due to the high symmetry of the framework, the positions of the 1,2,4-trioxolane groups were statistically disordered, which prevented us from refining their position in the cubic $Fm\bar{3}m$ space group of **ozo-ZrBDC**. Nonetheless, upon refining the framework atoms (including the defect sites and adsorbed species),[17] we calculated a residual electron-density within the pores of 657 e^- per unit cell, using the program Squeeze.[18] This value is in good agreement with the calculated number of electrons corresponding to the presence of one 1,2,4-trioxolane per organic linker within the unit cell (653 e^-), which is the value obtained when 15% of the linker sites are considered to be defective (as suggested by our single-crystal refinement). To determine the orientation of the 1,2,4-trioxolane groups, we performed an additional single-crystal refinement in the monoclinic *C*2-space

DOI: 10.1021/jacs.7b12913
J. Am. Chem. Soc. 2018, 140, 2028−2031

group. Due to the low partial occupancies of the 1,2,4-trioxolane and their positional disorder, rigid body restraints were employed, whereby the conformation of the 1,2,4-trioxolane moiety was obtained from DFT based calculations. The 1,2,4-trioxolane rings appeared to be rotated relative to the plane of their corresponding linker phenyl ring, and in all cases oriented toward the inorganic SBUs, at short-contact distances (range: 2.3 to 3.1 Å) between the 1,2,4-trioxolane atoms and the carboxylic groups of the adjacent linkers, in good agreement with DFT calculations (Figure 2a).

To further confirm the presence of the 1,2,4-trioxolane groups, we compared solid-state ^{13}C NMR spectra, recorded in cross-polarization under magic-angle spinning (CPMAS), of the starting **ZrEBDC** and the **ozo-ZrBDC**. The two ^{13}C-peaks of the ethenyl group in **ZrEBDC** appear at 115.6 and 131.0 ppm (Figure 2b, red spectrum). As expected, the spectrum of **ozo-ZrBDC** lacks these two peaks and shows two new ones, at 93.6 and 101.8 ppm (Figure 2b, blue spectrum), which indicated successful conversion of all the olefinic moieties. We then recorded CPMAS-NMR spectra of each product under Polarization Inversion (CPPI),[19] in order to differenciate between carbon sites coupled to protons with contrasted dipolar interaction. In the CPPI spectrum of **ozo-ZrBDC** (Figure 2b, orange spectrum), the resonance at 93.6 ppm is present, whereas that at 101.8 ppm is absent. These observations confirmed the formation of the 1,2,4-trioxalane ring, with the CH_2 peak located at 93.6 ppm and the CH peak, at 101.8 ppm; in agreement with literature data[20] and the solution study shown in the Supporting Information. We further confirmed this formation by performing a soft-ligand exchange experiment (Supporting Information), from which two peaks in solution ^1H NMR corresponding to the CH and CH_2 groups of the 1,2,4-trioxolane ring (δ = 5.61 and δ = 4.65 ppm, integrating in a 1:2 ratio) were identified (Figure 2c).

To gain further insight into the ozonolysis reaction, we systematically studied it using various reaction times (5, 10, 15, and 30 min). To this end, the degree of conversion of the olefinic groups into 1,2,4-trioxolane rings was monitored by measuring the ^1H NMR spectra of the digested samples (5% HF/DMSO-d_6), and then compared to that of the starting **ZrEBDC** (Section S4). The spectrum of the digested **ZrEBDC** showed the characteristic peaks of three nonequivalent olefinic protons at δ = 7.29, 5.77, and 5.41 ppm, integrating in a 1:1:1 ratio. In contrast, the spectrum of the fully converted **ozo-ZrBDC** confirmed a quantitative fading of these olefinic signals in approximately 30 min of solid−gas interaction. It also confirmed the formation of four byproducts (two symmetric trioxolane-metathesis products, 1,2,4-benzenetricarboxylate, and formic acid; Scheme S1) in solution coming from exposing the released 1,2,4-trioxolane-containing linker under aggressive acidic conditions.[14] The results at intermediate reaction times confirmed a direct correlation between the disappearance of the olefinic signals and the appearance of the new ones: with conversions of 33% at 5 min; 52% at 10 min; 78% at 15 min; and 100% at 30 min (as previously confirmed by CPMAS-^{13}C NMR).

Samples exposed to different ozonation times were also subjected to standard conditions of MOF-activation (120 °C, 12 h), and their inner surface area was subsequently measured (Figure S25). Compared to the initial S_{BET} value for **ZrEBDC** (1300 m^2/g; Figure S24), the ozonated samples exhibited decreasingly lower S_{BET} values in function of increasing ozonation time; the value for the fully converted **ozo-ZrBDC** was 685 m^2/g. Remarkably, this surface area is consistent with a previously reported value for a UiO-66-like MOF with imidazole moieties as pendant groups (S_{BET} = 538 m^2/g).[21]

Having demonstrated that ozonide rings can be stabilized inside a robust MOF, we next sought to explore the amenability of such rings in **ozo-ZrBDC** to be selectively reduced into aldehydes or oxidized into carboxylic acids (Figure 1a). For the former, **ozo-ZrBDC** was soaked overnight, with stirring, in an acidic aq. solution of dimethyl sulfide (Me_2S) as reducing agent, to convert the 1,2,4-trioxolane rings into aldehyde groups in a yield of 40% (Figure S20). The mild conditions of the workup did not allow for quantitative conversion of the stabilized trioxolanes, and all attempts to make the reduction more aggressive resulted in undesired formation of carboxylate byproduct. The S_{BET} of this **ozo-ZrBDC** partially functionalized with aldehyde moieties was 960 m^2/g (Figure S26). Alternatively, soaking **ozo-ZrBDC** overnight, with stirring, in aq. hydrogen peroxide (H_2O_2) drove oxidative cleavage of the 1,2,4-trioxolane rings to the corresponding carboxylic acids. This transformation was quantitative, as confirmed by ^1H NMR analysis (Figure S21). In both the aldehyde and carboxylic acid products, the UiO-66-type framework was preserved, as confirmed by powder XRD (Figure S23). Furthermore, SCXRD analysis of the crystals resulting from the aggressive oxidation confirmed that they also retained their single-crystal character. Remarkably, the position of the newly formed carboxylic acid groups could be determined through the refinement of the SCXRD data (Figure 3). In this case, the S_{BET} was found to be 301 m^2/g (Figure S27), which is in good agreement with those reported for this UiO-66-COOH (S_{BET} = 350−400 m^2/g).[22]

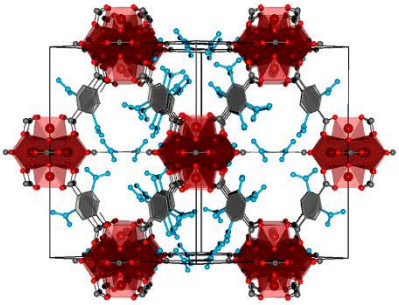

Figure 3. Illustration based on the single-crystal structure of **ZrBDC-COOH** across the [110] direction, highlighting the disordered −COOH moieties (blue).

In summary, we have reported a solvent-less, solid−gas, single-crystal-to-single-crystal, postsynthetic functionalization of a MOF using ozone. Streaming of ozone gas through an olefin-tagged UiO-66-type MOF at −78 °C provided quantitative transformation of the olefins into 1,2,4-trioxolane rings inside the robust MOF framework. When confined inside the MOF pores, this ring proved to be stable under standard heat and vacuum conditions for MOF activation, unlike in solution. Finally, an optimized workup enabled further single-crystal-to-single-crystal chemistry on these 1,2,4-trioxolane rings: reduction into the corresponding aldehyde or oxidation to the corresponding carboxylic acids, the latter in quantitative yield. We are confident that our methodology will offer new

DOI: 10.1021/jacs.7b12913
J. Am. Chem. Soc. 2018, 140, 2028−2031

insight into how gas molecules might be exploited for MOF chemistry that transcends common physisorption phenomena.

■ ASSOCIATED CONTENT

Supporting Information

The Supporting Information is available free of charge on the ACS Publications website at DOI: 10.1021/jacs.7b12913.

Experimental details, DFT calculations, NMR spectra and crystal structures (PDF)
Data for $0.25(C_{204}O_{123.2}Zr_{24})$, $2.67(O_3)$ (CIF)
Data for $0.5(C_{81.6}O_{64}Zr_{12})$, $1.98(O_3)$ (CIF)
Data for $0.5(C_{88}H_{9.2}O_{73.6}Zr_{12})$, $2.57(O_3)$ (CIF)
Data for $0.25(C_{182.4}O_{171.2}Zr_{24})$, $47.62(O_{0.11})$ (CIF)

■ AUTHOR INFORMATION

Corresponding Authors

*inhar.imaz@icn2.cat
*daniel.maspoch@icn2.cat

ORCID

Felipe Gándara: 0000-0002-1671-6260
Charlotte Martineau-Corcos: 0000-0003-1887-1042
Rubén Mas-Ballesté: 0000-0003-1988-8700
Inhar Imaz: 0000-0002-0278-1141
Daniel Maspoch: 0000-0003-1325-9161

Author Contributions

#J.A. and H.X. contributed equally.

Notes

The authors declare no competing financial interest.

■ ACKNOWLEDGMENTS

This work was supported by EU-FP7-ERC-Co-615954, the Spanish MINECO (projects PN MAT2015-65354-C2-1-R and CTQ2015-64561-R), and the Catalan AGAUR (project 2014 SGR 80). It was also funded by the CERCA Program/Generalitat de Catalunya. J.A. and H.X. acknowledge the Generalitat de Catalunya for FI fellowships. C.M.C. thanks the Institut Universitaire de France (IUF) for financial support. We also thank for the award of beamtime at Diamond through rapid access mode, visit number mt18409-1, and for the allocation of computer time at the Centro de Computación Científica at the Universidad Autónoma de Madrid (CCC-UAM). ICN2 acknowledges the support of MINECO through the Severo Ochoa Centers of Excellence Program, under Grant SEV-2013-0295.

■ REFERENCES

(1) (a) Janiak, C. *Dalt. Trans.* **2003**, *14*, 2781. (b) Kitagawa, S.; Kitaura, R.; Noro, S. *Angew. Chem., Int. Ed.* **2004**, *43*, 2334.
(2) Wang, Z.; Cohen, S. M.; Stern, C. L.; Hupp, J. T.; Li, J.; Uribe-Romo, F. J.; Chae, H. K.; O'Keeffe, M.; Yaghi, O. M.; Chaudret, B.; Fischer, R. A. *Chem. Soc. Rev.* **2009**, *38*, 1315.
(3) Burrows, A. D.; Cohen, S. M. *CrystEngComm* **2012**, *14*, 4095.
(4) Cohen, S. M. *Chem. Rev.* **2012**, *112*, 970.
(5) (a) Morris, W.; Doonan, C. J.; Furukawa, H.; Banerjee, R.; Yaghi, O. M. *J. Am. Chem. Soc.* **2008**, *130*, 12626. (b) Kim, M.; Cahill, J. F.; Prather, K. A.; Cohen, S. M. *Chem. Commun.* **2011**, *47*, 7629. (c) Morris, W.; Doonan, C. J.; Yaghi, O. M. *Inorg. Chem.* **2011**, *50*, 6853. (d) Luan, Y.; Qi, Y.; Gao, H.; Andriamitantsoa, R. S.; Zheng, N.; Wang, G.; Čejka, J.; Valenzano, L.; Lamberti, C.; Lillerud, K. P.; Bordigaa, S. *J. Mater. Chem. A* **2015**, *3*, 17320.
(6) (a) Boissonnault, J. A.; Wong-Foy, A. G.; Matzger, A. J. *J. Am. Chem. Soc.* **2017**, *139*, 14841. (b) Kim, M.; Cahill, J. F.; Su, Y.; Prather, K. A.; Cohen, S. M. *Chem. Sci.* **2012**, *3*, 126. (c) Liu, C.; Zeng, C.; Luo, T.-Y.; Merg, A. D.; Jin, R.; Rosi, N. L. *J. Am. Chem. Soc.* **2016**, *138*, 12045.
(7) Bloch, W. M.; Burgun, A.; Coghlan, C. J.; Lee, R.; Coote, M. L.; Doonan, C. J.; Sumby, C. J. *Nat. Chem.* **2014**, *6*, 906.
(8) Manna, K.; Zhang, T.; Lin, W. *J. Am. Chem. Soc.* **2014**, *136*, 6566.
(9) Wang, Z.; Tanabe, K.; Cohen, S. M. *Chem. - Eur. J.* **2010**, *16*, 212.
(10) (a) Layer, R. W.; Lattimer, R. P. *Rubber Chem. Technol.* **1990**, *63*, 426. (b) Miki, N.; Maeno, M.; Maruhashi, K.; Nakagawa, Y.; Ohmi, T. *Corros. Sci.* **1990**, *31*, 69. (c) Harshé, G. *J. Mater. Eng. Perform.* **1992**, *1*, 83.
(11) Servalli, M.; Ranocchiari, M.; Van Bokhoven, J. A.; Long, J. R.; Lillerud, K. P.; Tilset, M.; Fischer, R. W.; Fischer, R. A. *Chem. Commun.* **2012**, *48*, 1904.
(12) Cochran, B. *Synlett* **2016**, *27*, 245.
(13) Schiaffo, C. E.; Dussault, P. H. *J. Org. Chem.* **2008**, *73*, 4688.
(14) Criegee, R. *Angew. Chem., Int. Ed. Engl.* **1975**, *14*, 745.
(15) Geletneky, C.; Berger, S. *Eur. J. Org. Chem.* **1998**, *1998*, 1625.
(16) Willand-Charnley, R.; Fisher, T. J.; Johnson, B. M.; Dussault, P. H. *Org. Lett.* **2012**, *14*, 2242.
(17) Trickett, C. A.; Gagnon, K. J.; Lee, S.; Gándara, F.; Bürgi, H.-B.; Yaghi, O. M. *Angew. Chem., Int. Ed.* **2015**, *54*, 11162.
(18) Spek, A. L. *Acta Crystallogr., Sect. C: Struct. Chem.* **2015**, *71*, 9.
(19) Wu, X.; Zilm, K. W. *J. Magn. Reson., Ser. A* **1993**, *102*, 205.
(20) (a) Soriano, N. U.; Migo, V. P.; Matsumura, M. *Chem. Phys. Lipids* **2003**, *126*, 133. (b) Sega, A.; Zanardi, I.; Chiasserini, L.; Gabbrielli, A.; Bocci, V.; Travagli, V. *Chem. Phys. Lipids* **2010**, *163*, 148.
(21) Liang, J.; Chen, R.-P.; Wang, X.-Y.; Liu, T.-T.; Wang, X.-S.; Huang, Y.-B.; Cao, R. *Chem. Sci.* **2017**, *8*, 1570.
(22) Ragon, F.; Campo, B.; Yang, Q.; Martineau, C.; Wiersum, A. D.; Lago, A.; Guillerm, V.; Hemsley, C.; Eubank, J. F.; Vishnuvarthan, M.; Taulelle, F.; Horcajada, P.; Vimont, A.; Llewellyn, P. L.; Daturi, M.; Devautour-Vinot, S.; Maurin, G.; Serre, C.; Devic, T.; Clet, G. *J. Mater. Chem. A* **2015**, *3*, 3294.

DOI: 10.1021/jacs.7b12913
J. Am. Chem. Soc. 2018, 140, 2028−2031

JACS JOURNAL OF THE AMERICAN CHEMICAL SOCIETY
Article
Cite This: J. Am. Chem. Soc. 2018, 140, 15022−15030
pubs.acs.org/JACS

Postsynthetic Selective Ligand Cleavage by Solid−Gas Phase Ozonolysis Fuses Micropores into Mesopores in Metal−Organic Frameworks

Vincent Guillerm,[†] Heng Xu,[†] Jorge Albalad,[†] Inhar Imaz,*[,†] and Daniel Maspoch*[,†,§]

[†]Catalan Institute of Nanoscience and Nanotechnology (ICN2), CSIC and The Barcelona Institute of Science and Technology, Campus UAB, Bellaterra, 08193 Barcelona, Spain

[§]ICREA, Pg. Lluís Companys 23, 08010 Barcelona, Spain

Supporting Information

ABSTRACT: Herein we report a novel, ozone-based method for postsynthetic generation of mesoporosity in metal−organic frameworks (MOFs). By carefully selecting mixed-ligand Zr-**fcu**-MOFs based on organic ligand pairs in which one ligand has ozone-cleavable olefin bonds and the other ligand is ozone-resistant, we were able to selectively break the cleavable ligand via ozonolysis to trigger fusion of micropores into mesopores within the MOF framework. This solid−gas phase method is performed at room-temperature, and, depending on the cleavable ligand used, the resultant ligand-fragments can be removed from the ozonated MOF by either washing or sublimation. Compared to the corresponding highly microporous starting MOFs, the highly mesoporous product MOFs exhibit radically distinct gas sorption properties.

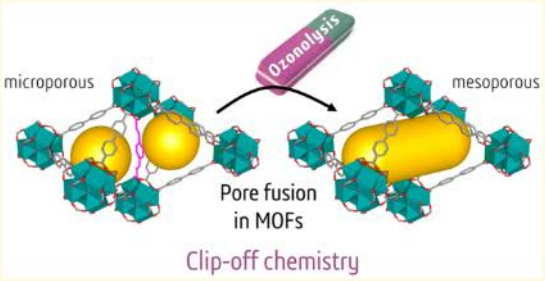

INTRODUCTION

Since the advent of metal−organic frameworks (MOFs) in the late 1990s,[1] these porous materials have shown promise for critical applications[2] such as gas storage,[3] catalysis,[4] drug delivery,[5] thermal energy storage,[6] sensors,[7] etc. MOFs have become benchmark materials for adsorption, surpassing most traditional adsorbents for hydrogen storage,[3a] methane storage,[3b] CO_2/N_2 separation,[8] etc. By marrying the advantages of the inorganic and organic chemistries, MOFs exhibit both polyfunctionality and a high degree of tunability, as well as the opportunity to postfunctionalize them.[9] Among the main advantage of this tunability is the possibility to perform reticular chemistry[1d,10] through ligand functionalization, length/width[10g] variation, and/or metal ion substitution, which enables strategic design and synthesis of materials for specific applications.

A remaining challenge in MOF chemistry is the creation of mesoscale cavities, which are necessary for increased storage capacity, encapsulation of large molecules, etc. Reticular chemistry strategies to surpass previous limits on pore size and cavity diameter include increasing the distance between the organic molecular building blocks and using longer or wider organic ligands.[10e,11] However, many of the most well-known MOFs are associated with self-dual nets (**pcu**: MOF-5,[1c] IRMOFs (isoreticular metal-organic framework) series,[1d] MXFSIX MOFs[12]) or nets that can easily interpenetrate upon ligand elongation (**tbo**: HKUST-1 (Hong Kong University of Science and Technology),[1e,13] **fcu**: UiO-66 (Universitetet i Oslo),[14] **acs**: MIL-88's (Material Institute Lavoisier),[15] etc.). To avoid this problem, researchers have developed platforms based on topologies that cannot interpenetrate, such as IRMOFs-74[10e] and **rht**-MOFs,[16] which, thanks to the design of very ambitious organic ligands, currently hold porosity records.[10e,11b,d]

Regrettably, systematic access to MOFs exhibiting hierarchical porosity from the micro- to the mesorange remains a challenge, as it currently demands use of complex organic ligands that are not commercially available.[11c,17] Although MOFs were initially considered as structurally ideal, defect-free materials, numerous recent studies have highlighted the non-negligible level of structural defects and irregularities in these materials, which strongly influence their porosity and catalytic properties.[17e,18] These findings suggest that access to hierarchically porous materials would require rational control over the structural defects within MOFs. Unfortunately, to date, only a few methods for generating and controlling such defects have emerged. One such strategy is to use large amounts of monotopic agents (known as *modulators*) in competition with the required polytopic ligand corresponding to the targeted MOFs.[14b,19] Alternatively, rational design strategies such as transversal reticular chemistry also have proven invaluable for generating MOFs with ordered defects.[10g] However, there are very few reports on engineering of defects and control of

Received: September 7, 2018
Published: October 13, 2018

DOI: 10.1021/jacs.8b09682
J. Am. Chem. Soc. 2018, 140, 15022−15030

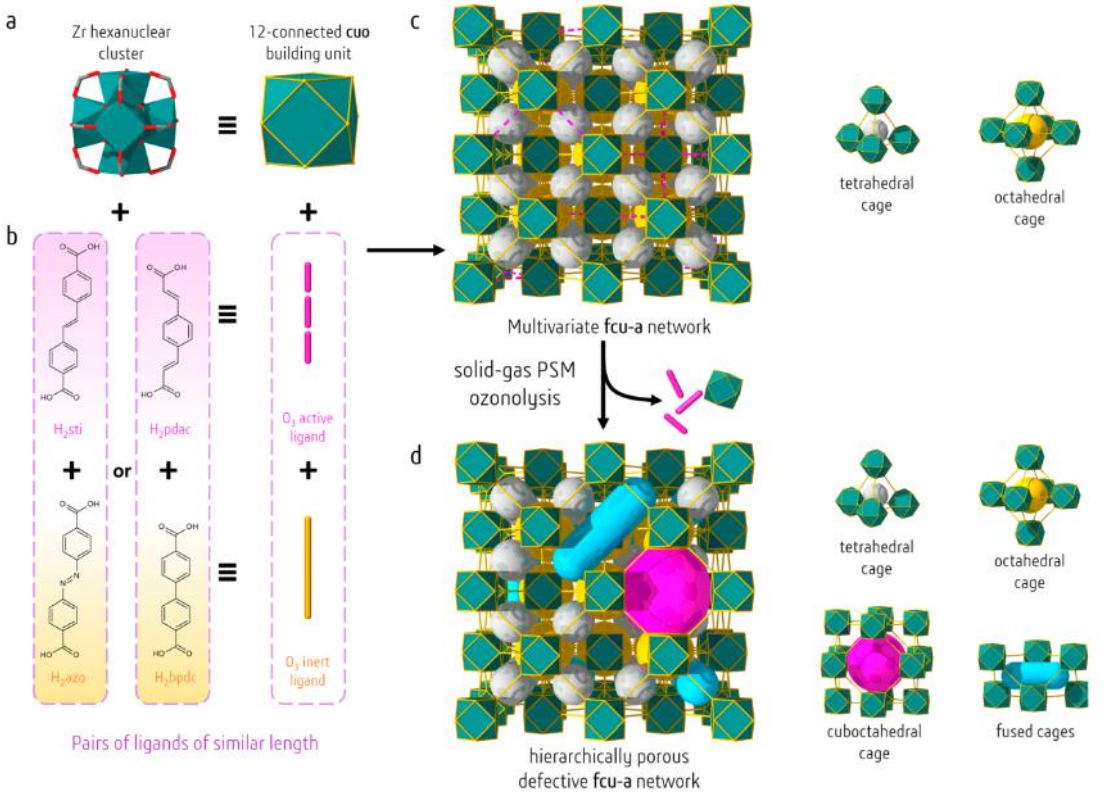

Figure 1. Postsynthetic modification of multivariate Zr-**fcu**-MOFs via solid−gas ozonolysis. Reaction of a) 12-connected hexanuclear clusters (**cuo** molecular building blocks) with b) pairs of organic ligands that are similar in length but show opposite reactivity to ozone (H_2sti and H_2azo or H_2pdac and H_2bpdc) yields. c) Multivariate MOFs with the **fcu** topology and two types of cages. Postsynthetic modification of the resultant MOFs through ligand cleavage by solid−gas ozonolysis results in d) Zr-**fcu**-MOFs with a defective network that exhibits hierarchical porosity generated upon fusion of micropores into larger pores (up to the mesoscale).

hierarchical porosity with commercially available and/or moderately sized ligands,[17e,18e,20] and some of the existing methods require harsh chemical or thermal treatments.

Our group recently reported the first solid−gas phase covalent postsynthetic modification of a MOF: under mild conditions, we achieved quantitative conversion of the constituent olefin groups in single crystals of UiO-66-like MOF into trioxolane moieties, aldehydes, and/or carboxylates without compromising the crystallinity.[21] Encouraged by the stability of the MOFs under these conditions, we envisioned exploiting this solid−gas phase ozonolysis[22] method to cleave and remove selected organic ligands within MOFs. We hypothesized and later confirmed (*vide infra*) that ligands containing nonterminal olefin groups could be split into several parts (Scheme S1). When implemented in MOFs, these ligands can be selectively broken and subsequently removed from the framework, to provide an original and controllable method for postsynthetic fusion of micropores into mesopores.

Herein we report application of our postsynthetic strategy to selectively and quantitatively cleave and remove the organic ligands in two multivariate (MTV)[23] Zr-**fcu**-MOFs (Figure 1), thereby affecting their adsorption performance in gas uptake. By controlling the ozone inert/active ratio of ligands in these MOFs, we were able to control the final number of defects in their structures.

RESULTS AND DISCUSSION

Zr-fcu-azo/sti System. *System Validation.* Our ligand-removal strategy is only amenable to MOFs based on ligand pairs that exhibit the following characteristics: similar shape and length; similar reactivity under given reaction conditions; and opposite reactivity to ozone (Figure 1b). To this end, we selected two dicarboxylic acids: 4,4′-azobenzene dicarboxylic acid (H_2azo) and 4,4′-stilbene dicarboxylic acid (H_2sti) (with lengths ≈ 13.3 Å). The reactivity of each ligand to ozone was initially tested in solution, in *N,N′*-dimethylformamide (DMF), which was used to avoid $\pi-\pi$ stacking of the ligands and to facilitate access of the ozone molecules to the olefin groups. Interestingly, the two acids showed diametric responses to ozone: H_2azo was unreactive, whereas H_2sti was fully converted into terephthalic acid (H_2bdc) and formylbenzoic acid (Hfba) (Scheme S1, Figure S18).

Having confirmed the suitability of H_2azo and H_2sti as a ligand pair, we then decided to choose an appropriate MOF for testing. We selected the robust Zr-**fcu**-MOF platform, which had already proven amenable to postsynthetic modification and ozone resistant.[9b,d,21,24] Thus, we embarked on the synthesis of the resultant MOFs (Zr-**fcu**-azo[25] and Zr-**fcu**-sti[26]) and testing of their response to ozonolysis. Both MOFs were synthesized by suspending $ZrCl_4$ and the corresponding

DOI: 10.1021/jacs.8b09682
J. Am. Chem. Soc. 2018, 140, 15022−15030

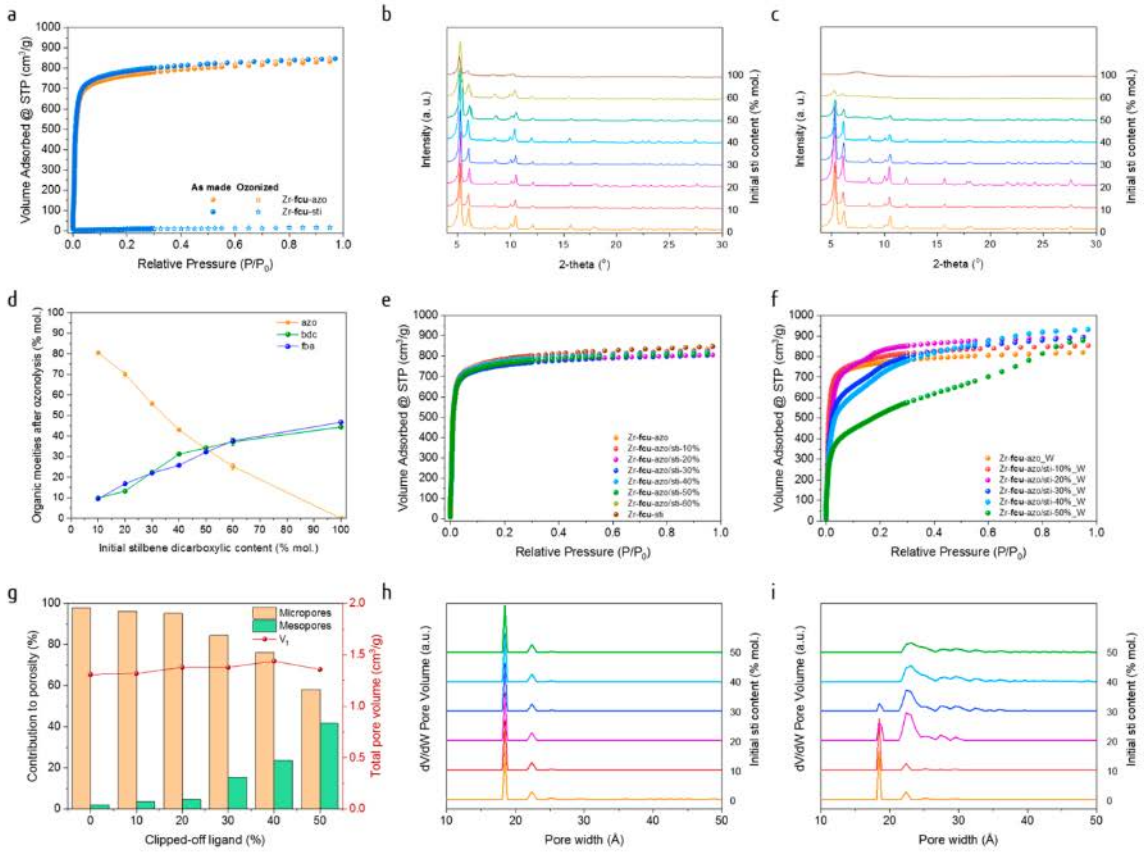

Figure 2. a) N_2 sorption isotherms for Zr-**fcu**-azo and Zr-**fcu**-sti before and after ozonolysis. b) PXRD diagrams for Zr-**fcu**-azo/sti-*X*%. c) PXRD diagrams for ozonated (OZ), washed Zr-**fcu**-azo/sti-*X*%. d) Remaining organic moieties in Zr-**fcu**-azo/sti-*X*%_OZ, as derived from ^{1}H NMR spectra of digested samples. e) N_2 sorption isotherms (77 K) for Zr-**fcu**-azo/sti-*X*%. f) N_2 sorption isotherms (77 K) for ozonated Zr-**fcu**-azo/sti-*X* % after washing (denoted here by "_W"). g) Change in total pore volume and in the relative contribution of microporosity and mesoporosity to total uptake, in Zr-**fcu**-azo/sti-*X*%_OZ after washing, as calculated with the Dubinin−Radushkevich equation. h) Pore size distribution estimated by DFT (density functional theory) for Zr-**fcu**-azo/sti-*X*%. i) Pore size distribution estimated by DFT for ozonated, washed Zr-**fcu**-azo/sti-*X*%.

dicarboxylic ligand in DMF, in the presence of HCl and L-proline, and then heating the resulting mixture at 120 °C overnight in a scintillation vial. The resulting crystals (of Zr-**fcu**-azo or Zr-**fcu**-sti) were washed with DMF and then subjected to solvent exchange with acetone. As expected, N_2 sorption isotherms collected at 77 K confirmed comparable Brunauer−Emmett−Teller areas (A_{BET}) of 3025 m^2/g for Zr-**fcu**-azo and 3065 m^2/g for Zr-**fcu**-sti (Figure 2a). When submitted to ozone treatment for 30 min, Zr-**fcu**-azo retained its crystallinity and porosity, whereas Zr-**fcu**-sti collapsed into an amorphous, nonporous solid due to cleavage of all the ligands of the framework (Figures 2a, S2, S9).

*Synthesis and Porosity of Zr-**fcu**-azo/sti-X%.* To prepare multivariate Zr-**fcu**-MOFs containing specific ratios of azo/sti (ranging from 90:10 to 40:60), we used similar synthetic conditions as for Zr-**fcu**-azo but partially replaced the H_2azo with the appropriate amount of H_2sti. The phase purity of the resulting single crystals of Zr-**fcu**-azo/sti-*X*% ($X \approx 10$, 20, 30, 40, 50, or 60 stilbene molar percentage) was confirmed by powder X-ray diffraction (PXRD; Figure 2b). The crystals varied in color from bright orange to colorless (Figure S1) according to their constituent azo/sti ratio, which was confirmed by proton nuclear magnetic resonance (^{1}H NMR) of digested crystals (Figure S19, Tables S1, S3). Finally, N_2 sorption analysis performed at 77 K showed comparable uptake and type I isotherm for all different activated samples (Figure 2e). Indeed, all apparent A_{BET} values ranged from 3000 m^2/g to 3065 m^2/g, and total pore volumes ranged from 1.24 cm^3/g to 1.28 cm^3/g (Table 1). As expected, and similarly to reported values for comparable MOF systems,[18e] the pore size distributions (PSD (pore size distribution), Figure 2h) of all Zr-**fcu**-azo/sti-*X*% are comparable: with a main pore population of ca. 18.4 Å attributed to the intrinsic porosity of the framework and a minor population of larger pores of ca. 22.4 Å attributed to some modulator related defects.

*Ozonolysis of Zr-**fcu**-azo/sti-X%.* To selectively break the sti ligands, we packed ca. 50 mg of Zr-**fcu**-azo/sti-*X*% into a L-shaped glass tube, connected on one side to the ozonator (through a $CaCl_2$ humidity trap) and, on the other side, to a vacuum pump (through a KI trap), to ensure a continuous flow of ozone through the column. The reaction was run at room temperature for 30 min. The ozonated Zr-**fcu**-azo/sti-*X*%

DOI: 10.1021/jacs.8b09682
J. Am. Chem. Soc. 2018, 140, 15022−15030

Table 1. Apparent BET Area, Micropore Volume, and Total Pore Volume of Zr-fcu-azo/sti-X%, before and after Ozonolysis and Washing

	starting MOF			ozonated and washed MOF		
initial% sti	A_{BET} (m^2/g)	V_μ (cm^3/g)	V_t (cm^3/g)	A_{BET} (m^2/g)	V_μ (cm^3/g)	V_t (cm^3/g)
0	3025	1.26	1.29	3030	1.24	1.27
10	3060	1.25	1.28	3115	1.27	1.32
20	3045	1.23	1.25	3130	1.31	1.38
30	3000	1.11	1.24	2680	1.17	1.38
40	3040	1.23	1.27	2580	1.10	1.44
50	3065	1.23	1.26	1860	0.79	1.36
60	3015	1.22	1.26	985	0.42	0.75
100	3065	1.26	1.31		nonporous	

materials maintained their high crystallinity after ozonolysis, as confirmed by PXRD (Figures S2–S10). ^{1}H NMR of digested, Zr-**fcu**-azo/sti-X%_OZ confirmed the full conversion of sti into bdc and fba for all samples (Figure S20, Table S4). The 1:1 bdc/fba ratio observed for all Zr-**fcu**-azo/sti-X%_OZ also indicated the stoichiometric character of the reaction (Figures 2d, 3a). As expected, based on our preliminary results with Zr-**fcu**-azo, the content of azo ligand in the framework was not affected by ozonolysis, thus confirming its high selectivity toward olefin bonds.

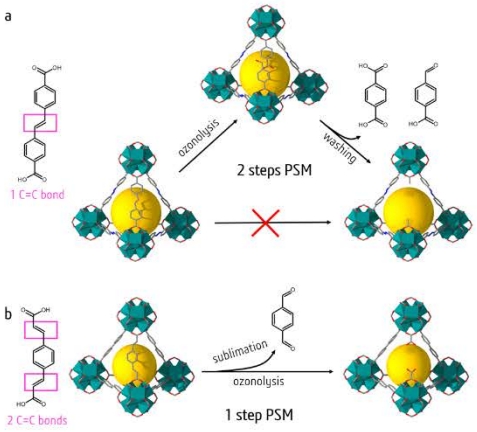

Figure 3. Postsynthetic generation of mesoporosity in MOFs. a) In Zr-**fcu**-azo/sti MOFs, removal of the sti ligand requires two steps: ozonolysis (to break the ligand) and washing. b) In contrast, in Zr-**fcu**-bpdc/pdac MOFs, removal of the pdac ligand requires only one step: ozonolysis (to break the ligand) and concomitant sublimation (to remove the central core). This is made possible by the two olefin groups in this ligand.

*Washing of Zr-**fcu**-azo/sti-X%_OZ.* To remove the organic and inorganic fragments trapped in the pores of the Zr-**fcu**-azo/sti-X%_OZ, we washed the ozonated crude product in a 0.5 M solution of acetic acid in DMF. The washed samples did not exhibit any marked difference in crystallinity compared to the corresponding crude products, as confirmed by PXRD (Figure S10), with one exception: Zr-**fcu**-azo/sti-60%_OZ. The washing step revealed that the latter had indeed lost crystallinity, which we attributed to a partial collapse of its framework upon loss of 60% of its ligands via ozonolysis. In all cases, ^{1}H NMR (Figures S21, S22 and Tables S5, S6) of the washed Zr-**fcu**-azo/sti-X% revealed the absence of fba and the persistence of some bdc, which could not be fully removed (repeated washing did not remove any additional bdc).

*Porosity Properties of Washed, Ozonated Zr-**fcu**-azo/sti-X%.* After confirming that in the washed, ozonated Zr-**fcu**-azo/sti-X%, all the sti ligands had been broken (Figure S20), most of the resulting organic fragments had washed out (Figure S21), and the high crystallinity had remained (Figure S10c), we submitted these materials to N_2 sorption tests at 77 K (Figure 2f, Table 1). As expected, Zr-**fcu**-azo/sti-10% performed very similarly to the preozonated material, showing only slightly higher values for apparent A_{BET} (3115 m^2/g vs 3060 m^2/g) and total pore volume (1.32 cm^3/g vs 1.28 cm^3/g). Based on the Dubinin–Radushkevich (DR) equation,[27] the relative proportion of microporosity to the total pore volume was estimated to be 96% (Figure 2g). Although the washed ozonated Zr-**fcu**-azo/sti-20% showed a nearly identical value for this parameter (95%), its isotherm exhibited a shoulder/step characteristic from bigger pores, giving insights into the modified nature of the microporosity. The isotherms for the washed ozonated Zr-**fcu**-azo/sti-30% and Zr-**fcu**-azo/sti-40% did not show the type I shape of the isotherms of the corresponding starting MOFs, but rather they exhibited a small hysteresis on the desorption branch, characteristic of mesoporosity (Figures S29, S30). Notably, ozonolysis treatment reduced the apparent A_{BET}: for the washed ozonated Zr-**fcu**-azo/sti-30%, 2680 m^2/g (vs 3000 m^2/g) and for the washed ozonated Zr-**fcu**-azo/sti-40%, 2580 m^2/g (vs 3040 m^2/g) (Table 1). However, in both cases, this decrease was offset by a major increase in the proportion of pores with mesoscale dimensions, as derived from the DR equation (Figure 2g and Table S9): for the washed ozonated Zr-**fcu**-azo/sti-30%, 15% (vs 2%) and for the washed ozonated Zr-**fcu**-azo/sti-40%, 24% (vs 3%). Likewise, the total pore volume also increased in both cases: for the washed ozonated Zr-**fcu**-azo/sti-30%, 1.36 cm^3/g (vs 1.24 cm^3/g) and for the washed ozonated Zr-**fcu**-azo/sti-40%, 1.44 cm^3/g (vs 1.27 cm^3/g). Similar results were observed in the washed ozonated Zr-**fcu**-azo/sti-50%, which exhibited the most extreme change relative to the corresponding starting MOF: the contribution of the mesoporosity reached 42% of the total porosity (Figure 2g and Table S9), and the hysteresis characteristic from mesoporosity was clearly visible (Figure S31); consequently, its A_{BET} was only 1860 m^2/g (vs 3065 m^2/g). Note that additional washing treatment did not affect the sorption properties (Figure S40a), excluding the hypothesis of structural etching sometimes observed through chemical treatment.[18e,28]

The modification of the micro- vs mesoporosity ratio was also reflected by studying the PSD (Figure 2i). If no noticeable change was observed for the washed ozonated Zr-**fcu**-azo, a subtle appearance of pores of ca. 25 Å and above was noted for the washed ozonated Zr-**fcu**-azo/sti-10%. The washed ozonated Zr-**fcu**-azo/sti-20% and -30% showed a clear decrease of the initial main pore size of ca. 18.4 Å and an increase of the second population at ca. 22.4 Å, confirming that micropores are merged into wider pores. For these two samples, the formation of pores bigger than 25 Å was also visible. Finally, the initial main pores of ca. 18.4 Å completely vanished in washed and ozonated Zr-**fcu**-azo/sti-40% and -50%. In these cases, the pores were mainly observed at ca. 22.4 Å and spread over a wide range up to 50 Å. Albeit nonobserved through PXRD, the pore population centered at 22.4 Å could be attributed to the existence of nonordered **reo**

DOI: 10.1021/jacs.8b09682
J. Am. Chem. Soc. 2018, 140, 15022−15030

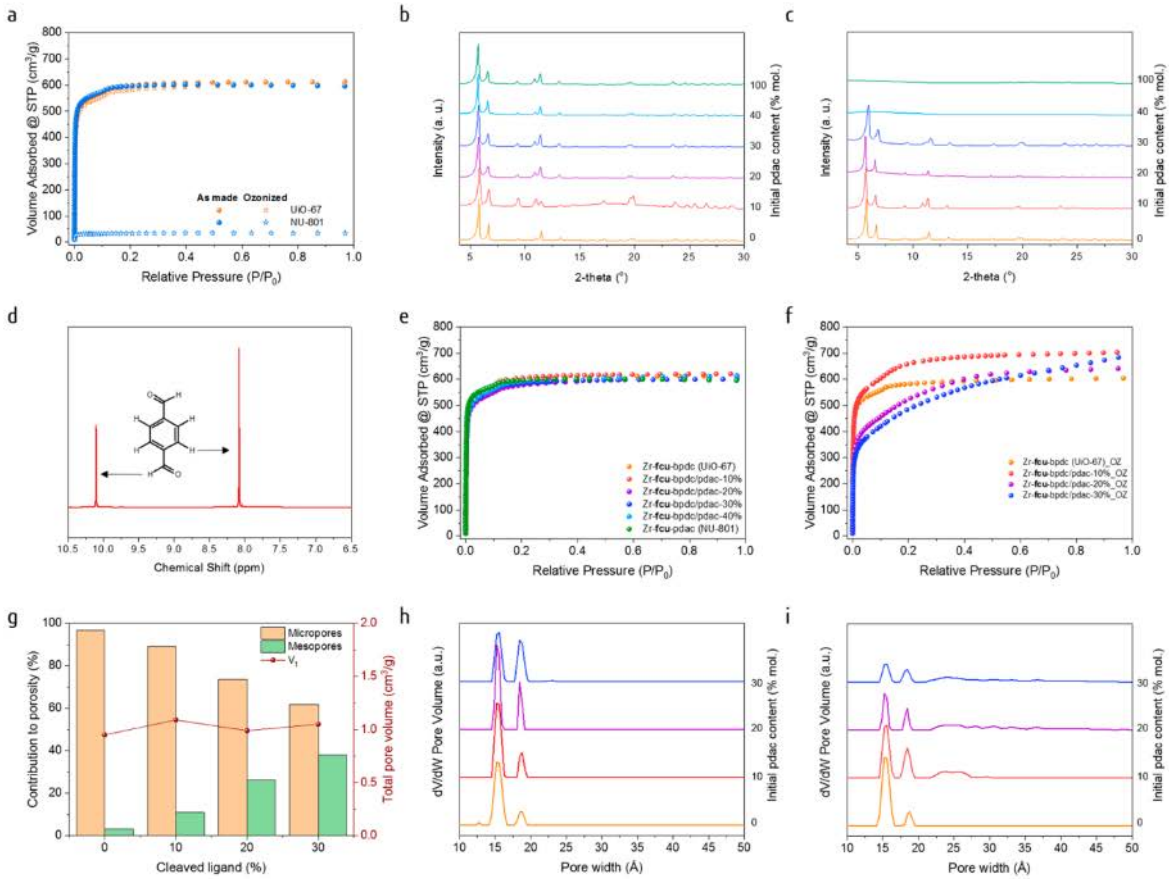

Figure 4. a) N_2 sorption isotherms for UiO-67 and NU-801 before and after ozonolysis. b) PXRD diagrams for Zr-**fcu**-bpdc/pdac-*X*%. c) PXRD diagrams for Zr-**fcu**-bpdc/pdac-*X*%_OZ. d) ^{1}H NMR spectra of the sublimated terephthalaldehyde recovered by heating at 85 °C under vacuum after ozonolysis. e) N_2 sorption isotherms (77 K) for Zr-**fcu**-bpdc/pdac-*X*%. f) N_2 sorption isotherms (77 K) for Zr-**fcu**-bpdc/pdac-*X*%_OZ. g) Plot showing the overall stability of the total pore volume and evolution of the relative contribution of mesoporosity vs microporosity to total uptake, in Zr-**fcu**-bpdc/pdac-*X*%_OZ, as calculated with the Dubinin−Radushkevich equation. h) Pore size distribution estimated by DFT for Zr-**fcu**-bpdc/pdac-*X*%. i) Pore size distribution estimated by DFT for Zr-**fcu**-bpdc/pdac-X_OZ%.

motifs, resulting from the removal of inorganic clusters, as hypothesized in some comparable systems.[18e]

Zr-fcu-bpdc/pdac System. Based on these pioneering results, we envisioned extending our method to a more challenging system. We considered that 4,4′-biphenyldicarboxylic acid (H_2bpdc) and 1,4-phenylenediacrylic acid (H_2pdac), found in the two Zr-**fcu**-MOFs UiO-67 and NU-801, would be a suitable ligand pair, given their geometric (length ≈ 11.3 Å) and chemical properties (*vide supra*). A particularity of H_2pdac is its two olefin bonds (Figure 3b), which we reasoned would enable cutting of the ligand into three distinct parts, rather than two, as in H_2sti (Scheme S2, Figure S23). In addition, we hypothesized that removal of the central part of the ligand could generate terephthalaldehyde, which could be sublimated under vacuum at moderate temperature -for example, during ozonolysis and/or during a classical presorption activation procedure (Figure 3). That turned out to be correct and, by obviating the washing step, represented a major improvement to our method.

*Synthesis of Zr-**fcu**-bpdc/pdac-X%.* Multivariate Zr-**fcu**-MOFs containing specific ratios of bpdc/pdac, from 100:0 (UiO-67)[14,29] to 0:100 (NU-801),[19b,30] were prepared from mixtures of $ZrCl_4$, H_2bpdc, and H_2pdac dissolved in DMF in the presence of trifluoroacetic acid (tfa) and heated at 120 °C for 72 h in a scintillation vial. The samples were washed with DMF overnight and then soaked in toluene for 3 days. The phase purity of the single crystals of Zr-**fcu**-bpdc/pdac-*X*% (*X* ≈ 10, 20, 30, 40% pdac molar percentage) was confirmed by PXRD (Figure 4b), ^{1}H NMR of digested crystals (Figure S24, Table S7), and N_2 sorption analysis performed at 77 K (Figure 4e and Table 2). The sorption isotherms for Zr-**fcu**-bpdc/pdac-*X*% were comparable (2210 $m^2/g < A_{BET} < 2310$ m^2/g and 0.92 $cm^3/g < V_t < 0.96$ cm^3/g). We observed a slight shoulder at a P/P_0 value of ca. 0.1, which we attributed to a higher number of initial defects in the structure, likely due to our use of a slightly different synthetic procedure than for Zr-**fcu**-azo/sti-*X*%. This is in fact reflected by the estimation of the PSD (Figure 4h), in which all samples presented two main contributions at ca. 15.2 and 18.4 Å; the bigger size being attributed (similarly as for Zr-fcu-azo/sti system, *vide supra*) to modulator-related defects.

DOI: 10.1021/jacs.8b09682
J. Am. Chem. Soc. 2018, 140, 15022−15030

: Zr-fcu-bpdc/pdac-X%, before and after
s

starting MOF			ozonated MOF		
A_{BET} (m^2/g)	V_μ (cm^3/g)	V_t (cm^3/g)	A_{BET} (m^2/g)	V_μ (cm^3/g)	V_t (cm^3/g)
2250	0.91	0.93	2305	0.92	0.95
2295	0.95	0.96	2400	0.97	1.09
2210	0.91	0.95	1870	0.73	0.99
2245	0.93	0.94	1730	0.65	1.05
2265	0.93	0.95		nonporous	
2310	0.92	0.92		nonporous	

ysis of Zr-fcu-bpdc/pdac-X%. Analogously to the MOF pair (*vide supra*), the crystallinity and porosity were unaffected by ozonolysis (Figures 4a, S11), but f the pdac ligands in NU-801 led to collapse of its and loss of its crystallinity and porosity (Figures 4a, ng demonstrated this, we proceeded with ozonolysis fcu-bpdc/pdac-X% MOFs. ^{1}H NMR of all Zr-fcu-X%_OZ highlighted the absence of any remaining d (Figures S25, Table S8). Moreover, after the Zr-pdac-X%_OZ were activated at 85 °C, a white solid ered in the cold trap (77 K) placed between the the pump. This solid was confirmed by ^{1}H NMR to halaldehyde (Figure 4d), which, after cleavage of were able to directly extract from the framework via n, as anticipated.

of Zr-fcu-bpdc/pdac-X%_OZ. To investigate the emoving the central core of pdac on the porosity of -bpdc/pdac-X%_OZ, we performed N_2 sorption ts on these MOFs (Figure 4f, Table 2). Upon terephthalaldehyde from the backbone of Zr-fcu--10%, the porosity was enhanced, as demonstrated ease in the apparent A_{BET} (from 2295 m^2/g to 2400 this sample, besides the evolution of microporous ne (V_μ) (from 0.95 cm^3/g to 0.97 cm^3/g) not being a more pronounced shoulder in the isotherm a transformation of the microporosity. The of some mesoporosity was revealed by the DR with a contribution of 11% (vs 1%) to the total n contrast, upon further removal of pdac pillars, from lc/pdac-20%_OZ and Zr-fcu-bpdc/pdac-30%_OZ, nt A_{BET} decreased sharply: for Zr-fcu-bpdc/pdac-(A_{BET} = 1870 m^2/g vs 2210 m^2/g) and for Zr-fcu--30%_OZ (A_{BET} = 1730 m^2/g vs 2245 m^2/g). The croporosity for Zr-fcu-bpdc/pdac-20%_OZ (V_μ = g vs 0.91 cm^3/g) and for Zr-fcu-bpdc/pdac-30%_OZ cm^3/g vs 0.93 cm^3/g) was offset by a major increase portion of pores with mesoscale dimensions, as m the DR equation (Figure 4g, Table S10): for Zr-pdac-20%_OZ, 26% (vs 4%) and for Zr-fcu-bpdc/_OZ, 38% (vs 1%). Likewise, the total pore volume y increased in both cases: for Zr-fcu-bpdc/pdac-20% cm^3/g (vs 0.95 cm^3/g) and for Zr-fcu-bpdc/pdac-1.05 cm^3/g (vs 0.94 cm^3/g). As expected, Zr-fcu--40%, which, upon ozonation, lost its crystallinity 5) due to structural collapse caused by removal of ligands, was nonporous. Overall, the change in the Zr-fcu-bpdc/pdac-X% paralleled that of Zr-fcu-. However, in the former, these changes occurred at greater number of defects in the starting MOFs.

The estimation of the PSD in this system also cor evolution of the porosity toward mesopores (Figure ozonolysis of UiO-67 did not affect the pore syst pristine MOF, the appearance of pores distribute 21.6 and 27.4 Å was clearly visible for the ozonat bpdc/pdac-10%, -20%, and -30%. In addition, the main pore populations decreased in ozonated Zr pdac-20% and Zr-fcu-bpdc/pdac-30%. In these samples, the porosity population was extended up Å, further confirming the fusion of micropores mesopores.

CONCLUSIONS

In conclusion, we have developed a selective and c method for postsynthetic modification of MOF p ozonolysis. Through removal of organic ligands, ou causes micropores to fuse into larger (mesoscale) controlled fashion and without any loss in total p selectively breaks the olefin bonds in organic ligan affecting other organic moieties and can be applie reaction times (ca. 30 min) under mild conditi temperature). Moreover, we have demonstrated th ysis can be used as a novel tool to selectively re recover, specific fragments of molecules/framewor solid−gas manipulation.

EXPERIMENTAL SECTION

Materials and Instruments. *Reagents.* 4,4′-Stilbene acid (H_2sti), 4,4′-biphenyldicarboxylic (H_2bpdc), and 4,4′-dicarboxylic acid (H_2azo) were purchased from T Acetic acid, 1,4-phenylenediacrylic acid (H_2pdac), trifluor (tfa), zirconium chloride ($ZrCl_4$), L-proline, hydroc potassium iodide, and anhydrous granular $CaCl_2$ (2−6 purchased from Sigma-Aldrich (Merck). *N*,*N*-Dimethy (DMF) and acetone were obtained from Fisher Chemi was purchased from Acros Organics. All the reagents a were used as received. Pyrex tubes (ext Ø = 7 mm; in Ø length = 150 mm) were purchased from Vidrasa S.A. The bent into an L-shape with a flame torch.

Optical Microscopy images were captured by a Observer Z1m optical microscope.

PXRD diagrams were recorded on an X'Pert PRO MP diffractometer (Panalytical) at 45 kV, 40 mA using CuKα = 1.5406 Å).

^{1}H NMR spectra were recorded on a Bruker Avance spectrometer (static magnetic field: 11.7 T) operating frequencies of 400 MHz (^{1}H).

Ozonolysis treatment was performed using an ozon (N1668A from Ozonotec) generating a constant flow of 1 at room temperature.

Volumetric N_2 sorption isotherms were collected at using an ASAP 2020 HD (Micromeritics). Tempe controlled by using a liquid nitrogen bath. Total pore was calculated at P/P_0 = 0.95, and microporous volum calculated using the Dubinin−Radushkevich equation distribution was estimated using a density functional th model (N_2 − cylindrical pores−oxide surface) impleme Microactive 4.00 software with a regularization factor of

Synthesis. *Synthesis of Zr-fcu-azo/sti-X%.* 4,4′-Stilbe ylic acid (H_2sti, 0.44-*x* mmol) and azobenzene-4,4′-dicar (H_2azo, *x* mmol) were suspended in 10 mL of DMF and s 30 min in a 23 mL scintillation vial. Then 5 mL of a DMI $ZrCl_4$ (105 mg, 0.45 mmol), L-proline (250 mg, 2.17 mn μL of conc. HCl was transferred into the vial and vortexe

crystals of Zr-**fcu**-azo/sti-X% (see the Supporting
n for more details about the H_2azo:H_2sti ratio in this

's of Zr-fcu-bpdc/pdac-X%. $ZrCl_4$ (200 mg, 0.86 mmol), nediacrylic acid (H_2pdac, *x* mmol), and biphenyl-4,4′- c acid (H_2bpdc, y mmol) were dissolved by sonication in DMF in the presence of tfa (1 mL) in a 23 mL scintillation heating at 120 °C for 72 h, colorless octahedral crystals of c/pdac-*X*% were obtained (see the Supporting Information etails about the H_2bpdc/H_2pdac ratio in the synthesis).

Activation. *Activation of Zr-fcu-azo/sti-X%.* Crystals of 'sti-*X*% were soaked in 15 mL of DMF (refreshed after 4 en subjected to solvent exchange in 15 mL of acetone after 4 h). The supernatant was removed after decantation, ystals were dried at 65 °C. Sample purity was verified by ure 2b), and experimental azo/sti ratios were analyzed by f the digested samples (Figure S19, Table S3). Crystals of 'sti-*X*% were then transferred into a glass sorption cell and under dynamic vacuum at 85 °C prior to sorption s.

on of Zr-fcu-bpdc/pdac-X%. Crystals of Zr-**fcu**-bpdc/ ere soaked in 10 mL of DMF for 24 and then subjected to hange for 72 h in 20 mL of toluene (refreshed twice per supernatant was removed by filtration. The sample purity d by PXRD (Figure 4b), and the experimental bpdc/pdac analyzed by ^{1}H NMR of the digested samples (Figure S24, Crystals of Zr-**fcu**-bpdc/pdac-*X*% were then transferred sorption cell and activated under dynamic vacuum at 85 sorption experiments.

ysis Treatment. *Ozonolysis of the Organic Ligands.* In a cedure, 30 mg of the H_2azo, H_2sti, H_2bpdc, or H_2pdac was lispersed in 20 mL of DMF. The solution was then to a 50 mL three-necked round-bottom flask and was) °C using an ice−water bath. A constant ozone flux was the solution through a glass pipet for 30 min under ıe crude reaction was then allowed to warm up to room e, and the solvent was removed *in vacuo*. The crude residue ed and analyzed by ^{1}H NMR. ^{1}H NMR analysis confirmed haracter of H_2azo and H_2bpdc, while revealing complete within 30 min, of the active linkers H_2sti and H_2pdac.

'sis of Zr-fcu-azo/sti-X% and Zr-fcu-bpdc/pdac_X%. A Zr-**fcu**-azo/sti-*X*% or Zr-**fcu**-azo/sti-*X*% (50 mg to 100 aded over a cotton stopper in an L-shaped Pyrex tube. The vas connected to the solid−gas postsynthetic modification urged under vacuum for 5 min. The ozone gas flow (10.4 vas passed through the MOF column for 30 min. After 1−2 ueous potassium iodide solution turned yellow, indicating MOF column had been exposed to oz1 atm. The recovered 'sti-*X*%_OZ or Zr-**fcu**-bpdc/pdac-*X*%_OZ samples were racterized by PXRD (Figures S10b, S17b) and ^{1}H NMR 20, S25, Tables S4, S8).

Acid Wash. About 50 mg of Zr-**fcu**-azo/sti-*X*%_OZ was r a few seconds in 20 mL of a 0.5 M acetic acid solution in left at room temperature for 24 h. The supernatant was nd analyzed by ^{1}H NMR after decantation (Figure S22, The crystals were washed twice with 20 mL of acetone. ıe was removed after decantation, and the crystals were 5 °C. The sample purity was verified by PXRD (Figure the experimental organic content was analyzed by ^{1}H ıe digested samples (Figures S21, Table S5). Crystals of ınated Zr-**fcu**-azo/sti-*X*% were then transferred into a glass ll and activated under dynamic vacuum at 85 °C prior to ɔn experiments. Note that the Zr-**fcu**-bpdc/pdac-*X*% d not require this additional treatment to reveal their sity potential (Figures 3, S40b).

estion Methodology. In a typical procedure, 10 mg of placed in an Eppendorf tube, to which 120 μL of a 5% aq. n was added. The mixture was sonicated for 15 min, and urry was placed in a 110 °C sand bath inside a fume hood

DMSO-d$_6$ without any need for addition of acid. Note with standard digestion methodologies were not suc when using the same quantities of HF and solvent. T evaporation step is crucial for proper sample digestion. N digested solutions obtained with our methodology did nc specific (e.g., HF-resistant) PTFE NMR tubes.

■ ASSOCIATED CONTENT

Supporting Information

The Supporting Information is available free of ch ACS Publications website at DOI: 10.1021/jacs.8b

Detailed synthetic procedures, microscopy, NMR, additional sorption data (PDF)

■ AUTHOR INFORMATION

Corresponding Authors

*inhar.imaz@icn2.cat

*daniel.maspoch@icn2.cat

ORCID

Vincent Guillerm: 0000-0003-3460-223X

Jorge Albalad: 0000-0001-5850-6723

Inhar Imaz: 0000-0002-0278-1141

Daniel Maspoch: 0000-0003-1325-9161

Notes

The authors declare no competing financial intere

■ ACKNOWLEDGMENTS

This work was supported by the Spanish MINEC PN MAT2015-65354-C2-1-R), the Catalan AGAU 2014 SGR 80), and the ERC under the EU-FP7 615954). It was also funded by the CERCA P Generalitat de Catalunya. ICN2 acknowledges the the Spanish MINECO through the Severo Ochoa Excellence Programme, under Grant SEV-2013- thanks the Generalitat de Catalunya for a Beatri fellowship (2014 BP-B 00155) (Marie Curie Fell funded project ITHACA). J.A. and H.X. ackno Generalitat de Catalunya for FI fellowships.

■ REFERENCES

(1) (a) Subramanian, S.; Zaworotko, M. J. Porous Solic [Zn(4,4′-bpy)$_2$(SiF$_6$)]$_n$·xDMF, a Single Framework Coordination Polymer with Large Square Channels. *A Int. Ed. Engl.* **1995**, *34* (19), 2127−2129. (b) Kondo, M T.; Matsuzaka, H.; Kitagawa, S.; Seki, K. Three- Framework with Channeling Cavities for Small Molecu 4′-bpy)$_3$(NO$_3$)$_4$]·xH$_2$O}$_n$ (M = Co, Ni, Zn). *Angew. C Engl.* **1997**, *36* (16), 1725−1727. (c) Li, H.; Eddaoudi, M M.; Yaghi, O. M. Design and synthesis of an exceptional highly porous metal-organic framework. *Nature* **1999**, 276−279. (d) Eddaoudi, M.; Kim, J.; Rosi, N.; Vodak, D. O'Keeffe, M.; Yaghi, O. M. Systematic Design of Pc Functionality in Isoreticular MOFs and Their Applicatior Storage. *Science* **2002**, *295* (5554), 469−472. (e) Chui, S M. F.; Charmant, J. P. H.; Orpen, A. G.; Williams, I. D. functionalizable nanoporous material [Cu$_3$(TMA)$_2$(H$_2$O **1999**, *283* (5405), 1148−1150.

(2) Themed issue: Metal-Organic Frameworks: (a) *Ch* Zhou, H. C., Kitagawa, S., Eds.; **2014**, *43* (5), 5415−61 issue: Metal-Organic Frameworks: (b) *Chem. Rev.* Zhou, J. R., Yaghi, O. M., Eds.; **2012**, *112* (2), 673−1268. T Metal-Organic Frameworks: (c) *Chem. Soc. Rev.* Long, J. M., Eds.; **2009**, *38* (5), 1201−1508.

(b) He, Y.; Zhou, W.; Qian, G.; Chen, B. Methane storage ganic frameworks. *Chem. Soc. Rev.* **2014**, *43* (16), 5657–
umida, K.; Rogow, D. L.; Mason, J. A.; McDonald, T. M.; .; Herm, Z. R.; Bae, T.-H.; Long, J. R. Carbon Dioxide Metal–Organic Frameworks. *Chem. Rev.* **2012**, *112* (2),

sseng, D.; Aguado, S.; Pinel, C. Metal–Organic Frame- portunities for Catalysis. *Angew. Chem., Int. Ed.* **2009**, *48* –7513.
ajada, P.; Gref, R.; Baati, T.; Allan, P. K.; Maurin, G.; P.; Férey, G.; Morris, R. E.; Serre, C. Metal–Organic s in Biomedicine. *Chem. Rev.* **2012**, *112* (2), 1232–1268.
nge, M. F.; Verouden, K. J. F. M.; Vlugt, T. J. H.; Gascon, , F. Adsorption-Driven Heat Pumps: The Potential of ganic Frameworks. *Chem. Rev.* **2015**, *115* (22), 12205–

, L. E.; Leong, K.; Farha, O. K.; Allendorf, M.; Van Duyne, p, J. T. Metal–Organic Framework Materials as Chemical iem. Rev. **2012**, *112* (2), 1105–1125.
bkhout, Y.; Guillerm, V.; Eddaoudi, M. Low concentration re using physical adsorbents: Are metal–organic frame- ming the new benchmark materials? *Chem. Eng. J.* **2016**, 397.
ohen, S. M. Postsynthetic Methods for the Functionaliza- tal-Organic Frameworks. *Chem. Rev.* **2012**, *112* (2), 970– Kim, M.; Cohen, S. M. Discovery, development, and tation of Zr(iv)-based metal–organic frameworks. *Crys-* **2012**, *14* (12), 4096–4104. (c) Bloch, W. M.; Burgun, A.; . J.; Lee, R.; Coote, M. L.; Doonan, C. J.; Sumby, C. J. snapshots of post-synthetic metallation chemistry in nic frameworks. *Nat. Chem.* **2014**, *6*, 906. (d) Garibay, en, S. M. Isoreticular synthesis and modification of with the UiO-66 topology. *Chem. Commun.* **2010**, *46* –7702.
Yaghi, O. M.; O'Keeffe, M.; Ockwig, N. W.; Chae, H. K.; M.; Kim, J. Reticular synthesis and the design of new *Nature* **2003**, *423* (6941), 705–714. (b) Chae, H. K.; M.; Kim, J.; Hauck, S. L.; Hartwig, J. F.; O'Keeffe, M.; M. Tertiary Building Units: Synthesis, Structure, and a Metal–Organic Dendrimer Framework (MODF-1). *J. Soc.* **2001**, *123* (46), 11482–11483. (c) Eddaoudi, M.; B.; Li, H. L.; Chen, B. L.; Reineke, T. M.; O'Keeffe, M.; M. Modular chemistry: Secondary building units as a basis ign of highly porous and robust metal-organic carboxylate s. *Acc. Chem. Res.* **2001**, *34* (4), 319–330. (d) Eddaoudi, , J.; O'Keeffe, M.; Yaghi, O. M. Cu_2[o-Br- $)_2]_2(H_2O)_2\cdot(DMF)_8(H_2O)_2$: A Framework Deliberately To Have the NbO Structure Type. *J. Am. Chem. Soc.* **2002**, 376–377. (e) Deng, H.; Grunder, S.; Cordova, K. E.; ; Furukawa, H.; Hmadeh, M.; Gándara, F.; Whalley, A. C.; sahina, S.; Kazumori, H.; O'Keeffe, M.; Terasaki, O.; . F.; Yaghi, O. M. Large-Pore Apertures in a Series of nic Frameworks. *Science* **2012**, *336* (6084), 1018–1023. wa, H.; Cordova, K. E.; O'Keeffe, M.; Yaghi, O. M. The and Applications of Metal-Organic Frameworks. *Science* (6149), 1230444. (g) Guillerm, V.; Grancha, T.; Imaz, I.; .; Maspoch, D. Zigzag Ligands for Transversal Design in Chemistry: Unveiling New Structural Opportunities for ganic Frameworks. *J. Am. Chem. Soc.* **2018**, *140* (32), 57.
Li, P.; Vermeulen, N. A.; Malliakas, C. D.; Gómez- D. A.; Howarth, A. J.; Mehdi, B. L.; Dohnalkova, A.; N. D.; O'Keeffe, M.; Farha, O. K. Bottom-up construction tructure in a porous uranium-organic crystal. *Science* **2017**,), 624–627. (b) Farha, O. K.; Eryazici, I.; Jeong, N. C.; G.; Wilmer, C. E.; Sarjeant, A. A.; Snurr, R. Q.; Nguyen, S. n, A. Ö.; Hupp, J. T. Metal-Organic Framework Materials

Serre, C.; Millange, F.; Dutour, J.; Surblé, S.; Margi chromium terephthalate-based solid with unusually volumes and surface area. *Science* **2005**, *309* (5743), (d) Guillerm, V.; Weseliński, Ł. J.; Belmabkhout, Y.; C D'Elia, V.; Wojtas, Ł.; Adil, K.; Eddaoudi, M. Dis introduction of a (3,18)-connected net as an ideal bluep design of metal-organic frameworks. *Nat. Chem.* **2014**, *6* 680.
(12) (a) Seki, K.; Takamizawa, S.; Mori, W. Desig Adsorption Property of a Three-Dimensional Coordinati with a Stable and Highly Porous Framework. *Chem. Let* (4), 332–333. (b) Nugent, P.; Belmabkhout, Y.; Burd, S. A. J.; Luebke, R.; Forrest, K.; Pham, T.; Ma, S.; Space, B.; Eddaoudi, M.; Zaworotko, M. J. Porous materials w adsorption thermodynamics and kinetics for CO_2 separat **2013**, *495* (7439), 80–84.
(13) Sun, D.; Ma, S.; Ke, Y.; Collins, D. J.; Zhou, Interweaving MOF with High Hydrogen Uptake. *J. Am.* **2006**, *128* (12), 3896–3897.
(14) (a) Cavka, J. H.; Jakobsen, S.; Olsbye, U.; G Lamberti, C.; Bordiga, S.; Lillerud, K. P. A new zirconiu building brick forming metal organic frameworks with stability. *J. Am. Chem. Soc.* **2008**, *130* (42), 13850–13851. A.; Roy, P.; Godt, A.; Lippke, J.; Waltz, F.; Wiebcke, M.; Modulated Synthesis of Zr-Based Metal–Organic Framew Nano to Single Crystals. *Chem. - Eur. J.* **2011**, *17* (24), 6
(15) (a) Serre, C.; Mellot-Draznieks, C.; Surblé, S.; Aud Filinchuk, Y.; Férey, G. Role of solvent-host interactions very large swelling of hybrid frameworks. *Science* **2007**, 1828–1831. (b) Dan-Hardi, M.; Chevreau, H.; Devic, T.; P.; Maurin, G.; Férey, G.; Popov, D.; Riekel, C.; Wuttke, J.-C.; Vimont, A.; Boudewijns, T.; de Vos, D.; Serr Interpenetration Ensures Rigidity and Permanent Porosity Flexible Hybrid Solid. *Chem. Mater.* **2012**, *24* (13), 2486
(16) Eubank, J. F.; Nouar, F.; Luebke, R.; Cairns, A. J.; Alkordi, M.; Bousquet, T.; Hight, M. R.; Eckert, J.; E Georgiev, P. A.; Eddaoudi, M. On Demand: The Singular Ideal Blueprint for the Construction of a Metal–Organic (MOF) Platform. *Angew. Chem., Int. Ed.* **2012**, *51* (4 10103.
(17) (a) Sonnauer, A.; Hoffmann, F.; Froeba, M.; Duppel, V.; Thommes, M.; Serre, C.; Férey, G.; Stock, N. in a Chromium 2,6-Naphthalenedicarboxylate Open- Structure with MIL-101 Topology. *Angew. Chem., Int. E* (21), 3791–3794. (b) Koh, K.; Wong-Foy, A. G.; Matz Crystalline Mesoporous Coordination Copolymer with H porosity. *Angew. Chem., Int. Ed.* **2008**, *47* (4), 677–680. (Wang, K.; Su, J.; Liu, T.-F.; Park, J.; Wei, Z.; Bosch, M.; A.; Zou, X.; Zhou, H.-C. A Highly Stable Zeotype M Zirconium Metal–Organic Framework with Ultralarge Po *Chem., Int. Ed.* **2015**, *54* (1), 149–154. (d) Serra-Crespo, Fernandez, E. V.; Gascon, J.; Kapteijn, F. Synthesis and ization of an Amino Functionalized MIL-101(Al): Sep Catalytic Properties. *Chem. Mater.* **2011**, *23* (10), (e) Feng, L.; Yuan, S.; Zhang, L.-L.; Tan, K.; Li, J.-L.; Liu, L.-M.; Zhang, P.; Han, Y.; Chabal, Y. J.; Zhou, H.- Hierarchical Pores by Controlled Linker Thermolysis in Metal–Organic Frameworks. *J. Am. Chem. Soc.* **2018**, *140* 2372.
(18) (a) Cliffe, M. J.; Wan, W.; Zou, X.; Chater, P. A.; Kl Tucker, M. G.; Wilhelm, H.; Funnell, N. P.; Coudert, F.-X A. L. Correlated defect nanoregions in a metal–organic *Nat. Commun.* **2014**, *5*, 4176. (b) Bunck, D. N.; Dichtel, W Linker Strategies for Organic Framework Functionalizati *Eur. J.* **2013**, *19* (3), 818–827. (c) Park, J.; Wang, Z. U.; Chen, Y.-P.; Zhou, H.-C. Introduction of Functionalized to Metal–Organic Frameworks via Metal–Ligand–Frag

. J.; Kang, J. K.; Yaghi, O. M. Heterogeneity within Order of a Porous Metal−Organic Framework. *J. Am. Chem. Soc.* 31), 11920−11923. (e) Yuan, S.; Zou, L.; Qin, J.-S.; Li, J.; Feng, L.; Wang, X.; Bosch, M.; Alsalme, A.; Cagin, T.;). Construction of hierarchically porous metal−organic through linker labilization. *Nat. Commun.* **2017**, *8*, 15356. ².; Bueken, B.; De Vos, D. E.; Fischer, R. A. Defect-Metal−Organic Frameworks. *Angew. Chem., Int. Ed.* **2015**, 234−7254. (g) Bradshaw, D.; El-Hankari, S.; Lupica-L. Supramolecular templating of hierarchically porous nic frameworks. *Chem. Soc. Rev.* **2014**, *43* (16), 5431− iang, W.; Coghlan, C. J.; Ragon, F.; Rubio-Martinez, M.; o, D. M.; Babarao, R. Defect engineering of UiO-66 for H_2O uptake − a combined experimental and simulation *n Trans.* **2016**, *45* (11), 4496−4500.

Wißmann, G.; Schaate, A.; Lilienthal, S.; Bremer, I.; A. M.; Behrens, P. Modulated synthesis of Zr-fumarate *oporous Mesoporous Mater.* **2012**, *152*, 64−70. (b) Gutov, ina, S.; Escudero-Adán, E. C.; Shafir, A. Modulation by s: Toward Superior Control in the Synthesis of Zirconium anic Frameworks. *Chem. - Eur. J.* **2016**, *22* (38), 13582− Marshall, R. J.; Hobday, C. L.; Murphie, C. F.; Griffin, S. n, C. A.; Moggach, S. A.; Forgan, R. S. Amino acids as ient modulators for single crystals of zirconium and tal-organic frameworks. *J. Mater. Chem. A* **2016**, *4* (18), . (d) Øien, S.; Wragg, D.; Reinsch, H.; Svelle, S.; Bordiga, i, C.; Lillerud, K. P. Detailed Structure Analysis of Atomic nd Defects in Zirconium Metal−Organic Frameworks. *th Des.* **2014**, *14* (11), 5370−5372. (e) Trickett, C. A.; . J.; Lee, S.; Gándara, F.; Bürgi, H.-B.; Yaghi, O. M. Molecular Level Characterization of Defects in UiO-66 *gew. Chem., Int. Ed.* **2015**, *54* (38), 11162−11167.

Yue, Y.; Qiao, Z.-A.; Fulvio, P. F.; Binder, A. J.; Tian, C.; elson, K. M.; Zhu, X.; Dai, S. Template-Free Synthesis of l Porous Metal−Organic Frameworks. *J. Am. Chem. Soc.* (26), 9572−9575. (b) Yue, Y.; Fulvio, P. F.; Dai, S. l Metal−Organic Framework Hybrids: Perturbation-anofusion Synthesis. *Acc. Chem. Res.* **2015**, *48* (12), . (c) Sun, L.-B.; Li, J.-R.; Park, J.; Zhou, H.-C. : Template-Directed Assembly of Mesoporous Metal− ameworks. *J. Am. Chem. Soc.* **2012**, *134* (1), 126−129. H.; Li, J.-R.; Wang, K.; Han, T.; Tong, M.; Li, L.; Xie, Y.; u, D.; Zhong, C. An in situ self-assembly template strategy paration of hierarchical-pore metal-organic frameworks. *un.* **2015**, *6*, 8847. (e) Qiu, L.-G.; Xu, T.; Li, Z.-Q.; Wang, Jiang, X.; Tian, X.-Y.; Zhang, L.-D. Hierarchically Micro-orous Metal−Organic Frameworks with Tunable Porosity. *m., Int. Ed.* **2008**, *47* (49), 9487−9491. (f) Zhao, Y.; Han, B.; Song, J.; Li, J.; Wang, Q. Metal−Organic Nanospheres with Well-Ordered Mesopores Synthesized Liquid/CO_2/Surfactant System. *Angew. Chem., Int. Ed.*), 636−639. (g) Cao, S.; Gody, G.; Zhao, W.; Perrier, S.; Ducati, C.; Zhao, D.; Cheetham, A. K. Hierarchical is porosity in metal−organic frameworks templated from lock co-oligomer micelles. *Chem. Sci.* **2013**, *4* (9), 3573− Wee, L. H.; Wiktor, C.; Turner, S.; Vanderlinden, W.; .; Bajpe, S. R.; Houthoofd, K.; Van Tendeloo, G.; De Kirschhock, C. E. A.; Martens, J. A. Copper Benzene ate Metal−Organic Framework with Wide Permanent Stabilized by Keggin Polyoxometallate Ions. *J. Am. Chem.* 34 (26), 10911−10919. (i) Shen, K.; Zhang, L.; Chen, X.; ng, D.; Han, Y.; Chen, J.; Long, J.; Luque, R.; Li, Y.; Chen, l macro-microporous metal-organic framework single *ence* **2018**, *359* (6372), 206−210.

lad, J.; Xu, H.; Gándara, F.; Haouas, M.; Martineau-Mas-Ballesté, R.; Barnett, S. A.; Juanhuix, J.; Imaz, I.;). Single-Crystal-to-Single-Crystal Postsynthetic Modifica-

2016, *140* (6), 2028−2031.

(22) (a) Geletneky, C.; Berger, S. The Mechanism of Revisited by ^{17}O-NMR Spectroscopy. *Eur. J. Org. Chem.* (8), 1625−1627. (b) Criegee, R. Mechanism of Ozonol *Chem., Int. Ed. Engl.* **1975**, *14* (11), 745−752.

(23) Deng, H.; Doonan, C. J.; Furukawa, H.; Ferreira, R. J.; Knobler, C. B.; Wang, B.; Yaghi, O. M. Multiple Functic of Varying Ratios in Metal-Organic Frameworks. *Science* (5967), 846−850.

(24) (a) Marshall, R. J.; Forgan, R. S. Postsynthetic Mod Zirconium Metal-Organic Frameworks. *Eur. J. Inorg. C* *2016* (27), 4310−4331. (b) Ragon, F.; Campo, B.; Martineau, C.; Wiersum, A. D.; Lago, A.; Guillerm, V.; H Eubank, J. F.; Vishnuvarthan, M.; Taulelle, F.; Horcajada, A.; Llewellyn, P. L.; Daturi, M.; Devautour-Vinot, S.; I Serre, C.; Devic, T.; Clet, G. Acid-functionalized UiO-66 and their evolution after intra-framework cross-linking features and sorption properties. *J. Mater. Chem. A* **2** 3294−3309.

(25) (a) Yang, Q.; Guillerm, V.; Ragon, F.; Wiersı Llewellyn, P. L.; Zhong, C.; Devic, T.; Serre, C.; Maur storage and CO_2 capture in highly porous zirconium metal-organic frameworks. *Chem. Commun.* **2012**, *48* (9833. (b) Hobday, C. L.; Marshall, R. J.; Murphie, C. F. Richards, T.; Allan, D. R.; Düren, T.; Coudert, F.-X.; Fo Morrison, C. A.; Moggach, S. A.; Bennett, T. D. A Compu Experimental Approach Linking Disorder, High-Pressur and Mechanical Properties in UiO Frameworks. *Angew. Ch* **2016**, *55* (7), 2401−2405.

(26) Marshall, R. J.; Richards, T.; Hobday, C. L.; Mur Wilson, C.; Moggach, S. A.; Bennett, T. D.; For Postsynthetic bromination of UiO-66 analogues: alte flexibility and mechanical compliance. *Dalton Trans.* **201** 4132−4135.

(27) Dubinin, M. M.; Zaverina, E. D.; Radushkev Sorbtsiya, I. Struktura Aktivnykh Uglei 0.1. Issledovanie Organicheskikh Parov. *Zh. Fiz. Khim.* **1947**, *21* (11), 135

(28) Avci, C.; Ariñez-Soriano, J.; Carné-Sánchez, A.; G Carbonell, C.; Imaz, I.; Maspoch, D. Post-Synthetic Aniso Chemical Etching of Colloidal Sodalite ZIF Crystals. *An Int. Ed.* **2015**, *54* (48), 14417−14421.

(29) Guillerm, V.; Ragon, F.; Dan-Hardi, M.; Vishnuvarthan, M.; Campo, B.; Vimont, A.; Clet, G.; Maurin, G.; Férey, G.; Vittadini, A.; Gross, S.; Serre, C. isoreticular, highly stable, porous zirconium oxide based m frameworks. *Angew. Chem., Int. Ed.* **2012**, *51* (37), 9267−

(30) Gomez-Gualdron, D. A.; Gutov, O. V.; Krungle Borah, B.; Mondloch, J. E.; Hupp, J. T.; Yildirim, T.; Fa Snurr, R. Q. Computational Design of Metal−Organic I Based on Stable Zirconium Building Units for Storage and Methane. *Chem. Mater.* **2014**, *26* (19), 5632−5639.

JACS JOURNAL OF THE AMERICAN CHEMICAL SOCIETY
Article
Cite This: J. Am. Chem. Soc. 2019, 141, 4094−4102
pubs.acs.org/JACS

Postsynthetic Covalent and Coordination Functionalization of Rhodium(II)-Based Metal−Organic Polyhedra

Arnau Carné-Sánchez,[*,†,#] Jorge Albalad,[†,#] Thais Grancha,[†,#] Inhar Imaz,[†] Judith Juanhuix,[‡] Patrick Larpent,[§] Shuhei Furukawa,[*,§,⊥] and Daniel Maspoch[*,†,∥]

[†]Catalan Institute of Nanoscience and Nanotechnology (ICN2), CSIC and The Barcelona Institute of Science and Technology, Campus UAB, Bellaterra, 08193 Barcelona, Spain

[‡]ALBA Synchrotron, Cerdanyola del Vallès, 08290 Barcelona, Spain

[§]Institute for Integrated Cell-Material Science (WPI-iCeMS), Kyoto University, Yoshida, Sakyo-ku, Kyoto 606-8501, Japan

[⊥]Department of Synthetic Chemistry and Biological Chemistry, Graduate School of Engineering, Kyoto University, Katsura, Nishikyo-ku, Kyoto 615-8510, Japan

[∥]ICREA, Pg. Lluís Companys 23, 08010 Barcelona, Spain

Supporting Information

ABSTRACT: Metal−organic polyhedra (MOP) are ultrasmall (typically 1−4 nm) porous coordination cages made from the self-assembly of metal ions and organic linkers and are amenable to the chemical functionalization of its periphery; however, it has been challenging to implement postsynthetic functionalization due to their chemical instability. Herein, we report the use of coordination chemistries and covalent chemistries to postsynthetically functionalize the external surface of ≈2.5 nm stable Rh(II)-based cuboctahedra through their Rh−Rh paddlewheel units or organic linkers, respectively. We demonstrate that 12 N-donor ligands, including amino acids, can be coordinated on the periphery of Rh-MOPs. We used this reactivity to introduce new functionalities (e.g., chirality) to the MOPs and to tune their hydrophilic/hydrophobic characteristics, which allowed us to modulate their solubility in diverse solvents such as dichloromethane and water. We also demonstrate that all 24 organic linkers can be postsynthetically functionalized with esters via covalent chemistry. In addition, we anticipate that these two types of postsynthetic reactions can be combined to yield doubly functionalized Rh-MOPs, in which a total of 36 new functional molecules can be incorporated on their surfaces. Likewise, these chemistries could be synergistically combined to enable covalent functionalization of MOPs through new linkages such as ethers. We believe that both reported postsynthetic pathways can potentially be used to engineer Rh-MOPs as scaffolds for applications in delivery, sorption, and catalysis.

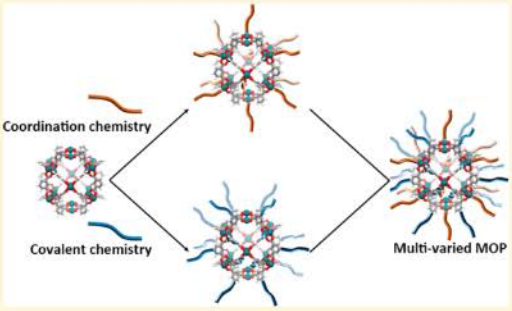

INTRODUCTION

Ultrasmall inorganic nanoparticles are important because they fill the gap between the molecular and the nanoscale regimes.[1] On this scale, nanoparticles can merge properties of both regimes, such as solubility in different media with high reactivity and unique physicochemical and pharmacokinetic properties.[2−6] Constructed from the self-assembly of metal ions and organic linkers, metal−organic polyhedra (MOP) fall into this size scale,[7] and as a subclass of molecular cages[8−11] that can host molecules in solution, they are permanently porous in the solid state.[12−16] An archetypical MOP is the cuboctahedron $[M_2(m\text{-bdc})_2]_{12}$ (where M = Cu(II), Cr(II), Mo(II), Rh(II), Ru(II), or even heterometallic and *m*-bdc = 1,3-benzenedicarboxylate), which is ~2.5 nm in size.[17] It is assembled from 12 M(II)−M(II) paddlewheel units connected through 24 *m*-bdc linkers and has an internal cavity of 1.9 nm that is accessible from eight triangular apertures of 8 Å and six square apertures of 12 Å.

Practical applications of ultrasmall inorganic nanoparticles demand chemical functionalization of their external surface,[18] as it enables their stabilization and protection, tuning of their hydrophilic/hydrophobic character, and introduction of new functional molecules into them (e.g., to modulate interactions between the nanoparticles and biosystems).[19,20] The latter case is essential for biomedical applications of nanoparticles.[21]

As ultrasmall inorganic nanoparticles and MOPs are similarly sized, we reasoned that postsynthetic chemical functionalization of the external surface of MOPs should analogously be crucial for tuning their own properties (e.g., solubility, porosity, etc.) and behavior in various solution-

Received: December 20, 2018
Published: February 5, 2019

DOI: 10.1021/jacs.8b13593
J. Am. Chem. Soc. 2019, 141, 4094−4102

phase (e.g., delivery systems, adsorbents, catalysis) or solid-state (e.g., gas sorption) applications, as well as defining their solubility in diverse solvents. However, to date, postsynthetic functionalization of MOPs has been limited to reactions run under soft conditions,[22] such as click chemistry based on strain-promoted azide–alkyne cycloaddition,[23] synthesis of secondary amines or amides from amino-functionalized MOPs,[24−26] or polymerizations based on reverse addition–fragmentation transfer (RAFT) on MOPs functionalized with dithiobenzoate trithioester groups.[27] This is mainly due to the use of chemically unstable MOPs made of highly labile Cu(II)–carboxylate coordination bonds.

Herein, we report spatially and stoichiometrically controlled postsynthetic functionalization of MOPs via two different site-specific chemistries: coordination chemistry on the metal ions and covalent chemistry on the organic linkers. We selected two robust cuboctahedral Rh(II)-based MOPs: $[Rh_2(bdc)_2(H_2O)_2]_{12}$ (hereafter named HRhMOP) and $[Rh_2(OH\text{-}bdc)_2(H_2O)_1(DMA)_1]_{12}$ (hereafter named OHRh-MOP; where OH-bdc = 5-hydroxy-1,3-benzenedicarboxylate and DMA = *N*,*N*-dimethylacetamide) (Figure 1a). We chose them for their high microporosity (the BET surface area [S_{BET}] of HRhMOP is 947 m^2/g and that of Rh-OH-MOP is 548 m^2/g) and for their chemical robustness, as they can withstand aggressive reaction conditions, including high temperatures and the presence of strong bases and/or coordinating molecules. Moreover, these MOPs have two distinct reaction sites (Figure 1b): their 12 Rh–Rh paddlewheels, each of which has an exohedral axial site that can undergo ligand-exchange reactions, and their 24 organic ligands, which can bear exohedral reactive functional groups (in this case, hydroxyl groups) to enable functionalization of the metal–organic cuboctahedron via covalent chemistry. We have demonstrated spatial control of these modifications by functionalizing both HRhMOP and OHRhMOP with different N-donor ligands and by using the hydroxyl groups of the OHRhMOP as nucleophiles for synthesis of esters and ethers. Finally, we have determined that these two chemistries can be run sequentially or even simultaneously on a single MOP to yield multivariate Rh-MOPs functionalized with a total of 36 molecules/groups (Figure 1b). With this approach, we demonstrated that chemical transformations can be performed on a nanoscale object while preserving all the distinctive features of molecular chemistry, such as the presence of well-defined reactive sites that can be reacted stoichiometrically and characterized at the molecular level by spectroscopic and crystallographic techniques.

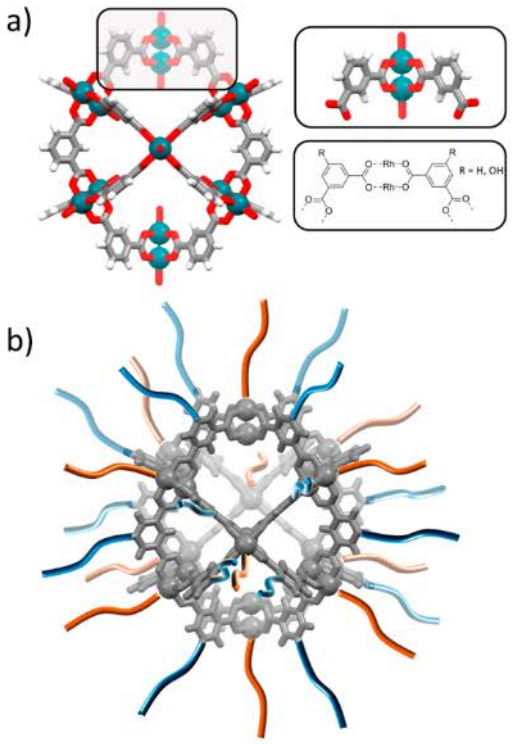

Figure 1. (a) Structure of a cuboctahedron Rh-MOP, highlighting the coordination and composition of the Rh–Rh paddlewheel units. Color key: green, rhodium; red, oxygen; gray, carbon; white, hydrogen. (b) Illustration of a cuboctahedron Rh-MOP functionalized on the 12 dirhodium paddlewheels through coordination chemistry (in orange) and on the 24 organic linkers through covalent chemistry (in blue).

RESULTS AND DISCUSSION

Postsynthetic Functionalization via Coordination Chemistry. Isolated Rh–Rh paddlewheel clusters are inert at their equatorial sites but are highly reactive at their axial sites. For instance, they show high affinity toward N-donor ligands,[28] and their reactions with said ligands can be monitored by following the spectroscopic changes of the band centered at 500–600 nm, which corresponds to the $\pi^* \rightarrow \sigma^*$ transitions (λ_{max}) of Rh–Rh bonds.[29] Given this affinity, we envisaged that ligand-exchange reactions at these axial sites would enable functionalization of the surface of Rh-MOPs that contain 12 N-donor ligands. Thus, we selected three chemically distinct N-donor ligands (Figure 2a): 4-*tert*-butylpyridine (tertPy); 4-trifluoromethylpyridine (CF_3-Py), as a source of hydrophobicity; and L-proline (L-Prol), to make the Rh-MOPs more biocompatible and to confer them with chirality and hydrophilicity.

We first tested functionalization of Rh-MOPs via coordination chemistry by adding tertPy (12 molar equiv [i.e., one per Rh–Rh paddlewheel]) to HRhMOP in dimethylformamide (DMF) at room temperature (Figure 2a). Addition of tertPy led to immediate dissolution of the MOP, as indicated by a concomitant color change from colorless to purple, which is characteristic of the nitrogen coordination to the Rh–Rh paddlewheel clusters (Figure 2a). This was a first indication that ligand exchange between the tertPy ligands and water molecules had occurred. Thus, we attributed the solubility of the resultant MOP in DMF to the bulky *tert*-butyl groups incorporated onto the surface of HRhMOP, as they would inhibit its aggregation and enable DMF molecules to solvate it.

Remarkably, purple crystals suitable for single-crystal X-ray diffraction analysis (SCXRD) were obtained by exposing the purple solution to diethyl ether vapors for 5 days. SCXRD analysis (performed on the XALOC beamline of the ALBA synchrotron[30]) confirmed functionalization of the outer surface of HRhMOP with 12 tertPy ligands (Figure 3a). As expected, these tertPy ligands were coordinated to the outer axial site of all Rh–Rh paddlewheel units, affording a functionalized Rh-MOP of formula

DOI: 10.1021/jacs.8b13593
J. Am. Chem. Soc. 2019, 141, 4094−4102

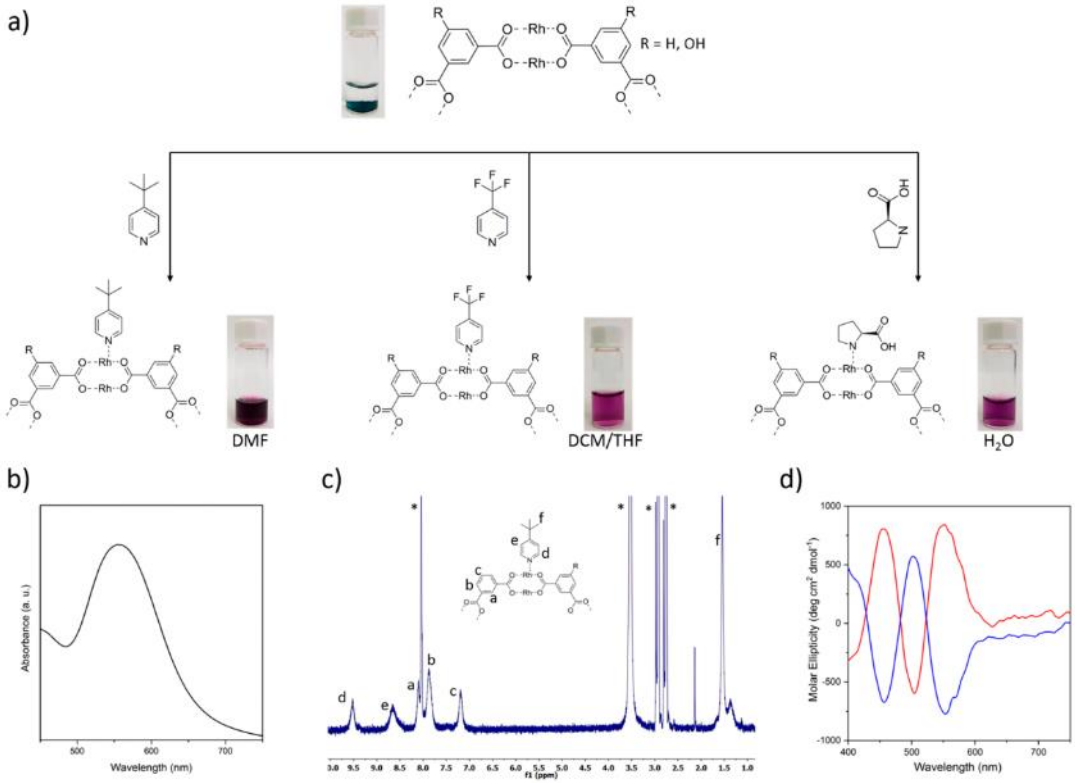

Figure 2. (a) Schematic representation showing the postsynthetic modification of HRhMOP and of OHRhMOP via coordination of N-based ligands at the corresponding dirhodium axial sites. The photographs illustrate the initial dispersion of insoluble HRhMOP or OHRhMOP in DMF, DCM, THF, or H_2O (top), and the purple solutions resulting from postsynthetic functionalization reactions with tertPy (left), CF_3-Py (center), or L-Prol (right). (b) UV−vis spectrum of HRhMOP (tertPy) in DMF showing a λ_{max} at 555 nm. (c) ^{1}H NMR of HRhMOP (tertPy) in DMF-d_7. Solvent peaks (DMF and water) are labeled with an asterisk. (d) CD spectra of HRhMOP (L-Prol) (red) and HRhMOP (D-Prol) (blue) in water.

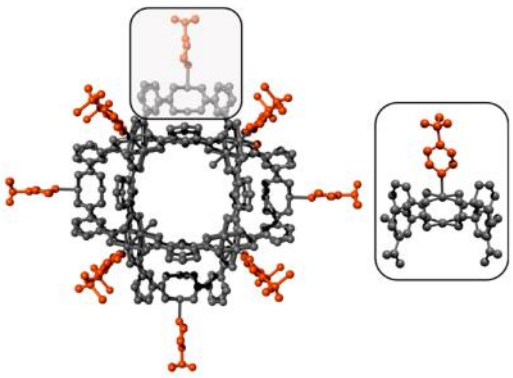

Figure 3. Crystalline structure of HRhMOP(tertPy). The coordination of tertPy to the Rh−Rh axial site is highlighted.

$[Rh_2(bdc)_2(tertPy)_1(H_2O)_1]_{12}$ (hereafter referred to as HRhMOP(tertPy)).

Having confirmed the functionalization of the outer surface of HRhMOP via SCXRD, we then established a methodology to follow the ligand exchange, based on UV−vis and ^{1}H NMR spectroscopies (Figure 2b,c and Figures S3 and S4). To this end, $[Rh_2(Ac)_4]$ (where Ac is acetate) was used as a model Rh−Rh paddlewheel cluster to first monitor the spectroscopic changes in the UV−vis spectra caused by the coordination of tertPy to it. We found that, upon addition of tertPy to a DMF solution of $[Rh_2(Ac)_4]$, λ_{max} shifted from 585 to 555 nm, as the ligand bound to one of the available axial sites. Coordination to the second available axial site induced a further shift of λ_{max} to 538 nm (Figure S3). Interestingly, the UV−vis spectrum of HRhMOP (tertPy) showed a λ_{max} of 555 nm, matching with the coordination of one tertPy ligand to each of the 12 Rh−Rh paddlewheel units (Figure 2b). Further addition of tertPy to HRhMOP(tertPy) did not cause any additional shift in the λ_{max}, thereby confirming that tertPy can only coordinate to the outer part of HRhMOP. Moreover, ^{1}H NMR spectra of HRhMOP(tertPy) evidenced coordinated tertPy, as indicated by two aromatic peaks (at 9.52 and 8.66 ppm) corresponding to the pyridine moiety and a peak at 1.54 ppm corresponding to the *tert*-butyl groups (Figure 2c). Finally, we determined the amount of coordinated tertPy ligands by comparing integration of the peaks of the tertPy with the peaks ascribed to the bdc ligand of the HRhMOP (8.10, 7.87, and 7.18 ppm) (Figure S4). As expected, the molar ratio of tertPy ligands to HRhMOP was 12:1.

We then used the two aforementioned techniques to follow the coordination-induced functionalization of OHRhMOP with tertPy. The reaction was done analogously to HRhMOP

DOI: 10.1021/jacs.8b13593
J. Am. Chem. Soc. 2019, 141, 4094−4102

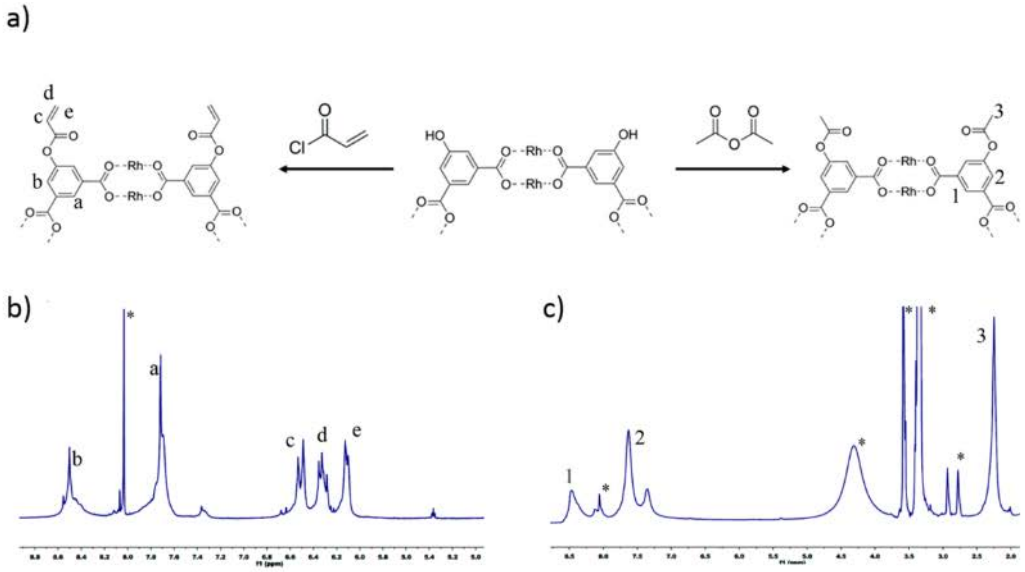

Figure 4. (a) Schematic showing the covalent postsynthetic functionalization of OHRhMOP via formation of ester linkages. (b) ^{1}H NMR of AcrRhMOP in DMF-d_7. (c) ^{1}H NMR of OMetRhMOP in DMF-d_7. Solvent peaks [DMF in (b) and DMF, MeOH, dioxane and water in (c)] are highlighted with an asterisk.

and similarly yielded a purple solution upon addition of tertPy to a DMF suspension of OHRhMOP. Synthesis of the expected MOP $[Rh_2(OH\text{-}bdc)_2(tertPy)_1(H_2O)_1]_{12}$ was confirmed by UV−vis (λ_{max} = 555 nm; Figure S5) and ^{1}H NMR (Figure S6).

Once we had demonstrated that the surface of Rh-based MOPs can be selectively functionalized via coordination chemistry, and that such reactions yield products whose solubility profile differs from that of the starting MOP, we attempted to synthesize variants of HRhMOP and OHRhMOP that would be soluble in aprotic organic solvents (e.g., dichloromethane and tetrahydrofuran) and in water. We did this by functionalizing the starting MOPs with either CF_3-Py (for its hydrophobicity) or L-Prol (for its hydrophilicity). For the former, we added CF_3-Py to a suspension of HRhMOP crystals in dichloromethane (DCM) or of OHRhMOP in tetrahydrofuran (THF) (Figure 2a). Instantaneously after addition of CF_3-Py, each suspension became a clear purple solution, giving rise to $[Rh_2(bdc)_2(CF3\text{-}Py)_1(H_2O)_1]_{12}$ and $[Rh_2(bdc\text{-}OH)_2(CF_3\text{-}Py)_1(H_2O)_1]_{12}$, respectively, as determined by UV−vis and ^{1}H NMR (Figure S7−S10).

Similarly, we separately functionalized HRhMOP and OHRhMOP with L-Prol (again, 12 molar equiv) by mixing each MOP with L-Prol in basic water (pH 10.5). In both cases, we observed that, upon addition of L-Prol, each suspension became a transparent purple solution, forming $[Rh_2(H\text{-}bdc)_2(L\text{-}prol)_1(H_2O)_1]_{12}$ and $[Rh_2(OH\text{-}bdc)_2(L\text{-}prol)_1(H_2O)_1]_{12}$ respectively, as confirmed by spectroscopic characterization (Figures S11−S14).

Functionalization of MOPs with chiral amino acids is an alternative and straightforward strategy to confer them with chirality.[31] To this end, we functionalized HRhMOP and OHRhMOP with either L-Prol or D-Prol. The chirality of the resultant MOPs was studied by circular dichroism (CD) spectroscopy in solution. The enantiomeric MOPs exhibited opposite Cotton effects (Figures 2d and S15). Their CD spectra indicated a strong Cotton effect with the crossing wavelengths at 482 and 523 nm near the absorption of the Prol coordinated to the Rh−Rh paddlewheel unit in Rh-MOPs. The shape and magnitude of these Cotton effects clearly reflect the chiral coordination sphere of the Rh−Rh paddlewheel units in the MOPs. Thus, the sign of the CD signal is dictated by the enantiomeric form (L- or D-) of the proline.

At this point, we had demonstrated that the exterior axial sites of the Rh−Rh paddlewheel units serve as anchoring sites for N-donor ligands and that this reactivity can be used to introduce new functionalities and/or to selectively increase the solubility of Rh-MOPs in organic or aqueous media while preserving their intrinsic porosity (vide infra).

Postsynthetic Functionalization via Covalent Chemistry. We next looked to a second source of reactive sites for postsynthetic functionalization of MOPs: their organic linkers. Cuboctahedral Rh(II)-based MOPs are assembled from 24 organic linkers. Accordingly, we considered that if each organic linker had one exohedral reactive functional group, then these MOPs could potentially be functionalized with 24 molecules (i.e., one per linker). We tested our hypothesis by functionalizing OHRhMOP through its 24 hydroxyl groups, using an acyl chloride and an acid anhydride under basic aqueous conditions.

The synthesis of esters from acyl chlorides and anhydrides entails nucleophilic attack to the carboxylic acid derivative by hydroxyl groups. To increase the nucleophilicity of the hydroxyl groups, these reactions are generally run in the presence of a strong base. Under these conditions, we observe that addition of NaOH (final pH 10.5) to an aqueous suspension of OHRhMOP leads to dissolution of the MOP. This is due to deprotonation of the hydroxyl groups, which renders a negatively charged MOP, hereafter noted as ONaRhMOP. The integrity of ONaRhMOP was confirmed by UV−vis, ^{1}H NMR, and mass spectrometry analysis in basic

DOI: 10.1021/jacs.8b13593
J. Am. Chem. Soc. 2019, 141, 4094−4102

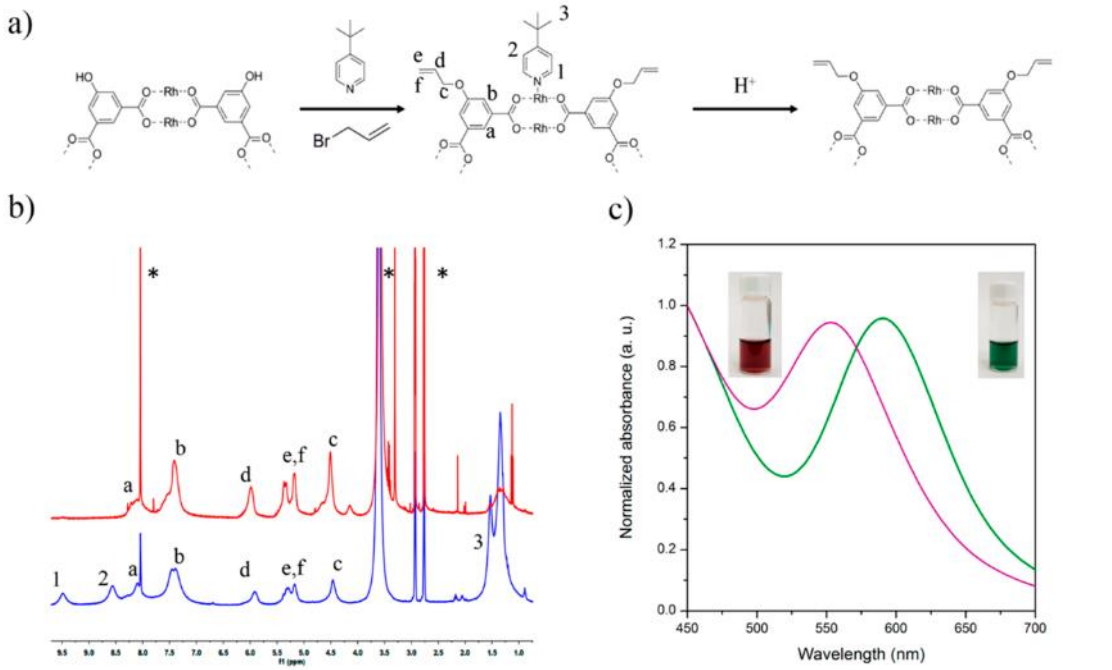

Figure 5. (a) Schematic showing the sequential coordination−covalent functionalization of OHRhMOP with ether linkages. (b) ^{1}H NMR of OallylRhMOP(tertPy) (blue) and OallylRhMOP (red) in DMF-d_7. Solvent peaks (DMF and water) are highlighted with an asterisk. (c) UV−vis spectra of OallylRhMOP (tertPy) (purple) and OallylRhMOP (green) in DMF, showing the shift of λ_{max} from 555 to 590 nm. Inset: Photographs of each solution.

water, highlighting the high chemical stability of these MOPs (Figure S16−S18).

We then exploited the solubility and nucleophilicity of ONaRhMOP to react it with acryloyl chloride (24 molar equiv; Figure 4a,b). For this, we performed a biphasic reaction by stirring an aqueous solution of ONaRhMOP and diethyl ether containing 1 molar equiv of acryloyl chloride per phenolate group (i.e., 24 molar equiv of acryloyl chloride per ONaRhMOP) overnight evolving from 0 °C to room temperature. The reaction product, which was precipitated at the interface after the overnight reaction, was washed with water and methanol and solubilized in DMF and analyzed by ^{1}H NMR and mass spectrometry (Figure 4b and Figures S19 and S20). Both techniques confirmed the quantitative conversion of the phenolate groups into the acrylate ester (hereafter named AcrRhMOP). Indeed, the ^{1}H NMR spectrum of AcrRhMOP evidenced generation of the acrylate ester, as indicated by the appearance of peaks at 6.52, 6.34, and 6.14 ppm corresponding to the three protons of the acryloyl group. The conversion rate was calculated by comparing the integration of the acrylate signals to the integration of the peak at 7.72 ppm, which corresponds to the outer aromatic proton of the OH-bdc ligand. As expected, the molar ratio of acrylate esters per Rh(II)-based MOP was 24:1. In addition, further evidence of the quantitative functionalization with acrylate esters was acquired by matrix-assisted laser desorption/ionization-time-of-flight (MALDI-TOF), which showed a peak at m/z = 8090.5 that matches the molecular formula of the protonated desired fully functionalized Rh-MOP, $[Rh_2(Acr\text{-}bdc)_2 + H^+]^+$ (m/z = 8090.9).

To further evaluate the reactivity of the phenolate groups in ONaRhMOP, we reacted it with acetic anhydride in conditions analogous to those for acryloyl chloride. The reaction solid was washed once with methanol, dissolved in DMF, and then analyzed by ^{1}H NMR and mass spectrometry (Figure 4c and Figures S22 and S23). In this case, both techniques showed the partial functionalization of the Rh-MOP with acetate ester groups (hereafter named OMetRhMOP). The esterification was confirmed by the ^{1}H NMR spectrum, which showed a new peak at 2.25 ppm, corresponding to the methyl group. The relative intensity of the integrations of the peak at 2.25 ppm and the outer proton of the OH-bdc was used to estimate that the conversion rate was ca. 75%, meaning that 18 of the available 24 phenolates had been converted to esters. This result was confirmed by MALDI-TOF, which showed a peak at m/z = 7968.9, consistent with a partially functionalized Rh-MOP of formula $[Rh_{24}(OH\text{-}bdc)_6(OMet\text{-}bdc)_{18} + H]^+$ + DCTB + DMF + MeOH (m/z = 7969.9). Subsequent reactions using more acetic anhydride did not provide any improvement in conversion, suggesting that, under the tested conditions, full conversion of the phenolate groups was precluded due to steric hindrance between the derivatized OMetRhMOP and the acetic anhydride.

Postsynthetic Dual Functionalization via Combined Coordination and Covalent Chemistries. We next explored the possibility of functionalizing OHRhMOP at its two types of reactive sites (the axial site of the Rh−Rh paddlewheel units and the hydroxyl groups of the organic linkers) using coordination chemistry for the former and covalent chemistry for the latter, reasoning that these two approaches should not be mutually exclusive. We envisaged that combining these

DOI: 10.1021/jacs.8b13593
J. Am. Chem. Soc. 2019, 141, 4094−4102

these MOPs with a total of 36 functional groups. We ted this by functionalizing AcrRhMOP with 12 lecules. Addition of tertPy (12 molar equiv) to a ution of AcrRhMOP caused the solution to ly change color from green to purple. The expected as then confirmed by UV−vis and ^{1}H NMR as for as products (Figures S25 and S26).

ve had confirmed the dual functionalization of OP with 12 tertPy ligands and 24 esters, we ed the use of the same two chemistries for zing OHRhMOP by formation of ether linkages. ly, although esters could be prepared from acyl or anhydrides at room temperature due to the high of both functional groups, ethers could not be rom halogenated compounds under similar reaction . This result is not surprising, as the standard to alkylate a hydroxyl group with brominated tail use of high boiling-point solvents (e.g., DMF) emperatures (i.e., above 80 °C) in the presence of an base. However, OHRhMOP is not soluble in DMF, olies that any reaction in this solvent should be t under heterogeneous conditions. Unfortunately, geneous reaction between OHRhMOP and allyl DMF at 80 °C failed. We reasoned that the close OHRhMOP in the solid state hindered the diffusion gents, thereby preventing conversion of the hydroxyl

rcome this low solubility, we employed dual zation to first dissolve the OHRhMOP in DMF by g tertPy (vide supra). Then, the functionalized P (tertPy) was reacted in situ with allyl bromide). This sequential functionalization was carried out mixing the three components in DMF, and the urple solution was stirred at 80 °C for 12 h. After , the MOP was precipitated by diethyl ether, washed anol and acetone, and dried under ambient .

and ^{1}H NMR analyses of the purified product n DMF confirmed that both types of conversion had ndeed, the UV−vis spectrum showed the character- of 555 nm (Figure 5c). In addition, the ^{1}H NMR showed the presence of peaks corresponding to 8 and 8.55 ppm for the aromatic protons and 1.36 e *tert*-butyl group) and to the allyl group (5.91, 5.30, 4.46 ppm). The relative integration between the allyl nd the aromatic protons of the OH-bdc ligand conversion degree of 40%. The doubly function- MOP product is referred to hereafter as OallylRhMOP-tertPy) (Figures 5b and S27).

ngly, the reversible nature of the coordination bond he Rh−Rh paddlewheel and the tertPy ligands s to selectively cleave them after the covalent eading to their replacement with water. Under nditions, this cleavage and ligand exchange occur at w 2.1. Thus, this cleavage was performed by adding of 3 M HCl to a suspension of OallylRhMOP-tertPy in acetone or water, inducing a sudden color shift in sion, from purple to green. This color change was an of the ligand exchange between the tertPy and H_2O hich was further corroborated by the UV−vis through the expected shift in λ_{max}, from 555 nm gure 5c). Moreover, the ^{1}H NMR spectrum of the been cleaved as the integrity of the allyl functio preserved, which yielded a new product referred to h OAllyl RhMOP (Figure 5b). MALDI-TOF of Rh-O confirmed its functionalization with allyl groups, peak at m/z = 7419.4, which corresponds to the formula: $[Rh_{24}(OH\text{-}bdc)_{15}(OAllyl\text{-}bdc)_9 + H]^+ + H_2O$ (m/z = 7418.3) (Figure S28).

Porosity of Functionalized Rh-MOPs. Finally, that functionalized Rh-MOPs maintain their porous in the solid state, we submitted all these materi sorption tests at 77 K (Figures S29−S40). All a functionalized Rh-MOPs showed a type I adsorption indicating that the inner microporous cavity was despite the postsynthetic modifications. Howeve pected,[32,33] we found that the outer functionaliza Rh-MOPs induced a decrease in their S_{BET} as compa parent materials, HRhMOP and OHRhMOP, whi the highest BET surface areas (S_{BET}), with values c 548 m^2/g, respectively. Functionalized HRhMOP lower S_{BET} values: 675 m^2/g for HRhMOP(CF_3-Py), for HRhMOP(tertPy), and 337 m^2/g for HRhMOP In the case of functionalized OHRhMOPs, a similar observed: 154 m^2/g for OHRhMOPs (CF_3-Py), 38 OHRhMOPs(tertPy), and 64 m^2/g for OHRhMOP Finally, the covalently functionalized Rh-MOPs ex S_{BET} of 410 m^2/g for AcrRhMOP, 120 m^2/g for Ac (tertPy), and 487 m^2/g for OMetRhMOP. OallylRh found to be nonporous to N_2 but porous to CO_2 maximum uptake of 1.15 mmol/g at 1 bar an Altogether, these results confirm that, despite the co which functionalized Rh-MOPs were exposed, the their intrinsic microporosity in the solid state.

■ CONCLUSIONS

In conclusion, we have demonstrated postsynthetic alization of Rh-based MOPs via two chemistries at tw reactive sites: coordination chemistry at thei paddlewheel units and covalent chemistry at the linkers. Functionalization of the 12 Rh−Rh paddlew was demonstrated by coordinating N-donor ligan relative hydrophobicity dictated the solubility of th products. This coordination approach was also used Rh-MOPs with chirality. Through covalent chemist hydroxyl groups on the organic linkers were conv esters by reacting them with acyl chlorides or acid a The orthogonal reactivity of the Rh−Rh paddlewhee the organic linkers enabled us to combine the two c to yield doubly functionalized Rh-MOPs featuring a new functional molecules. We believe that the stoi cally and spatially controlled functionalization of *I* provide structurally well-defined nanoscopic plat delivery, sorption, and catalytic applications.

■ EXPERIMENTAL SECTION

Materials and Instruments. Rhodium acetate, 1,3 carboxylic acid, 5-hydroxy-1,3-benzenedicarboxylic aci chloride, acetic anhydride, and allyl bromide were purc Sigma-Aldrich and used as received. Solvents at HPLC purchased from Fischer Chemicals.

Powder X-ray Diffraction (PXRD) patterns were reco X'Pert PRO MPD analytical diffractometer (Panalytical) a mA using Cu Kα radiation (λ = 1.5419 Å). Nitrogen g

as measured in a J-715 CD spectrophotometer (JASCO), ɔm temperature (ca. 25 °C). ^{1}H NMR spectra were Bruker Avance III 400SB NMR spectrometer. Mass y (MALDI-TOF) was run in an Applied Biosystems 4700 Analyzer operating in positive-ionization mode.

s of Rh-MOPs. *HRhMOP.* One hundred milligrams of $_4$·2MeOH (0.2 mmol), 160 mg of isophthalic acid (0.96 105 mg of Na_2CO_3 (1 mmol) were dispersed in 7 mL of nixture was transferred to a scintillation vial and heated at 48 h. A microcrystalline powder was separated from the ture and washed with DMA, EtOH, and MeOH. Finally, s were kept in acetone overnight and dried at 85 °C under gle crystals of Rh-H-MOP were prepared by heating a f 10 mg of Rh_2(acetate)$_4$·2MeOH (0.02 mmol), 10 mg of dicarboxylic acid (0.06 mmol), and 1.5 mg of K_2CO_3) in 1 mL of DMA in a scintillation vial at 100 °C for 48 h.

P. One hundred milligrams of Rh_2(acetate)$_4$·2MeOH 180 mg of 5-hydroxy-1,3-benzenedicarboxylic acid (0.96 105 mg of Na_2CO_3 (1 mmol) were dispersed in 7 mL of nixture was transferred to a scintillation vial and heated at 48 h. The resulting OHRhMOP single crystals were DMA and dissolved in MeOH to separate them from ıe solution was dried under vacuum, and the residue was ı water and acetone. Finally, the powder was kept in rnight and dried at 85 °C under vacuum.

(tertPy). Seventeen microliters of tertPy (111 μmol) was lispersion of 60 mg of HRhMOP (9.3 μmol) in 10 mL of resulting mixture was sonicated for 5 min and then at 18000 rpm for 10 min. The supernatant was collected ated with ether vapors over 5 days to yield single purple hMOP(tertPy) crystals were then separated from the ɔr and washed with ether and acetone. Finally, the sample ıcetone overnight and dried at 85 °C under vacuum. Note MOP(tertPy) was prepared using the same conditions as P(tertPy), except that instead of 17 μL of tertPy, 15 μL

(CF_3-Py). Thirteen microliters of CF_3-Py (111 μmol) was lispersion of 60 mg of HRhMOP (9.3 μmol) in 10 mL of hane. This mixture was sonicated for 5 min. Then, it was the filtrate was evaporated under vacuum. The resulting ashed with acetone. Finally, the sample was kept in rnight and dried at 85 °C under vacuum. Note here that (CF_3-Py) was prepared using the same conditions as for ertPy), except that instead of using 13 μL of tertPy and hane as solvent, 12 μL of tertPy was used and THF was

(L-Prol). A solution of 13 mg of L-Prol (111 μmol) in 1 at pH 10.5 (pH was adjusted with NaOH) was added to of 60 mg of HRhMOP (9.3 μmol) in 5 mL of water. The xture was sonicated for 5 min, and the solution was at 18000 rpm for 10 min. The supernatant was collected ated with acetone vapors over 10 days to yield purple hMOP(L-Prol) crystals were separated from the mother washed with acetone. Finally, the sample was kept in rnight and dried at 85 °C under vacuum. Note here that ɔ-Prol) was prepared using the same conditions as for .-Prol), except that instead of L-Prol, we used D-Prol. The ɔl was also used to obtain OHRhMOP(L-Prol) and (D-Prol).

P. A total of 4.3 mg (105 μmol) of NaOH was added to a f 30 mg of OHRhMOP (4.4 μmol) in 1 mL of water. ıddition, the OHRhMOP dissolved instantly, due to ɔn of the phenol groups. Then, a diethyl ether solution .5 μL of acryloyl chloride (105 μmol) was layered on top .de ONaRhMOP aqueous solution at 0 °C. The biphasic s vigorously stirred overnight at room temperature. green solid appeared at the interphase; it was isolated ıshed with MeOH and acetone. Finally, the sample was

for AcrRhMOP, except that instead of using 8.5 μL chloride and diethyl ether as solvent, 15 μL of acetic anh μmol) was used and 1,4-dioxane was the solvent.

AcrRhMOP(tertPy). Ten milligrams of AcrRhMOP (1.: dissolved 5 mL of DMF. Then, 100 μL of a 1 mL stock tertPy containing 18 μL (120 μmol) was added to the R solution, causing an immediate color change from gree AcrRhMOP(tertPy) was precipitated by adding diethyl solid was washed with ether and dried under vacuum.

OAllylRhMOP(tertPy). Thirty milligrams of OHRh μmol) was dissolved in 2 mL of DMF by adding 10 μ (66 μmol). Then, 45 mg of K_2CO_3 (316 μmol) was adde OH-MOP(tertPy) solution. The mixture was stirred at 8 min. Then, 14 μL of allyl bromide (316 μmol) was adc resulting mixture was reacted at 80 °C for 24 h. The reddish solution was centrifuged, and the supernatant wa under vacuum to obtain a purple residue. The crude washed with diethyl ether, MeOH, and acetone and dri under vacuum.

OAllylRhMOP. One hundred microliters of 3 M HCl v a dispersion of 20 mg of OAllylRhMOP(tertPy) in acet temperature. The purple suspension rapidly became gree decoordination of tertPy. The solid was recovered by ce and further washed with water and MeOH. Finally, the kept in acetone overnight and dried at 85 °C under vac

■ ASSOCIATED CONTENT

Supporting Information

The Supporting Information is available free of cha ACS Publications website at DOI: 10.1021/jacs.8b

PXRD, ^{1}H NMR, UV−vis, MALDI-TOF, ar data (PDF)

Single-crystal X-ray data for HRhMOI 1883914) (CIF)

Single-crystal X-ray data for OHRhMOI 1883124) (CIF)

Single-crystal X-ray data for HRhMOP(tertP 1884202) (CIF)

■ AUTHOR INFORMATION

Corresponding Authors

*arnau.carne@icn2.cat

*shuhei.furukawa@icems.kyoto-u.ac.jp

*daniel.maspoch@icn2.cat

ORCID

Jorge Albalad: 0000-0001-5850-6723

Inhar Imaz: 0000-0002-0278-1141

Judith Juanhuix: 0000-0003-3728-8215

Shuhei Furukawa: 0000-0003-3849-8038

Daniel Maspoch: 0000-0003-1325-9161

Author Contributions

#A.C.-S., J.A., and T.G. contributed equally.

Notes

The authors declare no competing financial interes

■ ACKNOWLEDGMENTS

The authors thank Ms. Nao Horike, Dr. Mio K Nicolas Louvain, and Dr. Gavin Craig for their works on the synthesis of OH-RhMOP. This supported by the Spanish MINECO (Projects PN 65354-C2-1-R), the Catalan AGAUR (Project 201 and the ERC under the EU-FP7 (ERC-Co 615954).

ıpported by the Severo Ochoa program from the INECO (Grant No. SEV-2017-0706). A.C.S. and c the Spanish MINECO for Juan de la Cierva (IJCI-2016-29802 and FJCI-2017-31598). J.A. ges the Generalitat de Catalunya for an FI This study was supported by JSPS KAKENHI 18H01995 (Kiban B) and 17H05367 (Coordina-netry). iCeMS is supported by the World Premier al Research Initiative (WPI), MEXT, Japan.

ɛENCES

.; Zeng, C.; Zhou, M.; Chen, Y. Atomically Precise etal Nanoclusters and Nanoparticles: Fundamentals and es. *Chem. Rev.* **2016**, *116*, 10346.

. D. J.; Chan, E. M.; Ostrowski, A. D.; Aloni, S.; Altoe, M. rd, E. S.; Sanii, B.; Urban, J. J.; Milliron, D. J.; Cohen, B. P. J. Engineering bright sub-10-nm upconverting for single-molecule imaging. *Nat. Nanotechnol.* **2014**, *9*,

. H.; Hackett, M. J.; Park, J.; Hyeon, T. Characterization, ion of Ultra-small Nanoparticles. *Chem. Mater.* **2014**, *26*,

.; Sun, Y.; Yang, T.; Feng, W.; Li, C.; Li, F. Sub-10 nm Lanthanide-Doped NaLuF4 Upconversion Nanocrystals Bioimaging in Vivo. *J. Am. Chem. Soc.* **2011**, *133*, 17122.

.; Sai, H.; Wiesner, U. Ultra-small Sub-10 nm Near-orescent Mesoporous Silica Nanoparticles. *J. Am. Chem.* *34*, 13180.

ler, K.; Rocks, L.; Licciardello, N.; Boselli, L.; Polo, E.; .; De Cola, L.; Stephan, H.; Dawson, K. A. Ultra-small anoparticles: State-of-the-art and perspectives for bio-lications. *Nanomedicine* **2016**, *12*, 1663.

ıemontagne, D. J.; Ni, Z.; O'Keeffe, M.; Yaghi, O. M. ıemistry of Metal−Organic Polyhedra. *Angew. Chem., Int.* *7*, 5136.

, W.; Misuraca, M. C.; Hunter, C. A.; Williams, N. H.; . Highly efficient catalysis of the Kemp elimination in the ubic coordination cage. *Nat. Chem.* **2016**, *8*, 231.

D.; Ueda, Y.; Sato, S.; Mizuno, N.; Kumasaka, T.; Fujita, mbly of tetravalent Goldberg polyhedra from 144 small . *Nature* **2016**, *540*, 563.

g, D.; Ronson, T. K.; Nitschke, J. R. Functional Capsules ponent Self-Assembly. *Acc. Chem. Res.* **2018**, *51*, 2423.

c, T. R.; Stang, P. J. Recent Developments in the and Chemistry of Metallacycles and Metallacages via n. *Chem. Rev.* **2015**, *115*, 7001.

R.; Zhou, H.-C. Bridging-ligand-substitution strategy for ion of metal−organic polyhedra. *Nat. Chem.* **2010**, *2*, 893.

ınd, C. A.; Lorzing, G. R.; Gosselin, E. J.; Trump, B. A.; A.; Brown, C. M.; Bloch, E. D. Methane Storage in -Based Porous Coordination Cages. *J. Am. Chem. Soc.* 11153.

ɜ.; Ju, Z.; Yuan, D.; Hong, M. In Situ Construction of a n Zirconocene Tetrahedron. *Inorg. Chem.* **2013**, *52*,

R.; Yu, J.; Lu, W.; Sun, L.-B.; Sculley, J.; Balbuena, P.; Porous materials with pre-designed single-molecule traps ective adsorption. *Nat. Commun.* **2013**, *4*, 1583.

. W.-H.; Li, H.-Y.; Dong, X.-Y.; Zang, S.-Q. Robust nal Zr-based metal−organic polyhedra for high proton and selective CO2 capture. *J. Mater. Chem. A* **2018**, *6*,

Eddaoudi, M.; Kim, J.; Wachter, J. B.; Chae, H. K.; .; Yaghi, O. M. Porous Metal−Organic Polyhedra: 25 Å ron Constructed from 12 Cu2(CO2)4 Paddle-Wheel cks. *J. Am. Chem. Soc.* **2001**, *123*, 4368. (b) Park, J.; Perry, .-P.; Bae, J.; Zhou, H.-C. Chromium(II) Metal−Organic

2017, *9*, 28004. (c) Ke, T.; Collins, D. J.; Zhou, H.-C. S Structure of Cuboctahedral and Anticuboctahedral Cages 12 Quadruply Bonded Dimolybdenum Units. *Inorg. Che* 4154. (d) Furukawa, S.; Horike, N.; Kondo, M.; Hijikata Sánchez, A.; Larpent, P.; Louvain, N.; Diring, S.; Sato, H R.; Kawano, R.; Kitagawa, S. Rhodium−Organic Cubc Porous Solids with Strong Binding Sites. *Inorg. Chem* 10843. (e) Young, M. D.; Zhang, Q.; Zhou, H.-C. M polyhedra constructed from dinuclear ruthenium paddlew *Chim. Acta* **2015**, *424*, 216. (f) Teo, J. M.; Coghlan, C. J.; Tsivion, E.; Head-Gordon, M.; Sumby, C. J.; Doonan, C bimetallic metal−organic polyhedra. *Chem. Commun.* **20**

(18) Boselli, L.; Polo, E.; Castagnola, V.; Dawson, K. A. Biomolecular Ultra-small Nanoparticle Interactions. *An* *Int. Ed.* **2017**, *56*, 4215.

(19) Jiang, Y.; Huo, S.; Mizuhara, T.; Das, R.; Lee, Y.-W Moyano, D. F.; Duncan, B.; Liang, X.-J.; Rotello, V. M. T of Size and Surface Functionality on the Cellular Uptak nm Gold Nanoparticles. *ACS Nano* **2015**, *9*, 9986.

(20) Kim, B. H.; Hackett, M. J.; Park, J.; Hyeon, T Characterization, and Application of Ultrasmall Nanopar *Mater.* **2014**, *26*, 59.

(21) Ma, K.; Mendoza, C.; Hanson, M.; Werner-Zw Zwanziger, J.; Wiesner, U. Control of Ultra-small Sub-10 Functionalized Fluorescent Core−Shell Silica Nanoparticl Water. *Chem. Mater.* **2015**, *27*, 4119.

(22) (a) Roberts, A. D.; Pilgrim, B. S.; Nitschke, J. R. Co Assembly Modification in Metallosupramolecular Chem *Soc. Rev.* **2018**, *47*, 626. (b) Lu, W.; Yuan, D.; Yakovenk H.-C. Surface Functionalization of Metal-Organic Pol Homogeneous Cyclopropanation Catalysis. *Chem. Commu* 4968.

(23) Zhao, D.; Tan, S.; Yuan, D.; Lu, W.; Rezenom, Y. H Wang, L.-Q.; Zhou, H.-C. Surface Functionalization Coordination Nanocages Via Click Chemistry and Their in Drug Delivery. *Adv. Mater.* **2011**, *23*, 90.

(24) Brega, V.; Zeller, M.; He, Y.; Lu, H. P.; Klosterman Responsive Metal−Organic Lantern Cages in Solut *Commun.* **2015**, *51*, 5077.

(25) Liu, G.; Di Yuan, Y.; Wang, J.; Cheng, Y.; Peh, S. B Qian, Y.; Dong, J.; Yuan, D.; Zhao, D. Process-Tracing S Postassembly Modification of Highly Stable Zirconi Organic Cages. *J. Am. Chem. Soc.* **2018**, *140*, 6231.

(26) Nam, D.; Huh, J.; Lee, J.; Kwak, J. H.; Jeong, H. Y Choe, W. Cross-Linking Zr-based Metal−Organic Polyhe Synthetic Polymerization. *Chem. Sci.* **2017**, *8*, 7765.

(27) Hosono, N.; Gochomori, M.; Matsuda, R.; Sato, H S. Metal−Organic Polyhedral Core as a Versatile Divergent and Convergent Star Polymer Synthesis. *J.* *Soc.* **2016**, *138*, 6525.

(28) Warzecha, E.; Berto, T. C.; Berry, J. F. A Coordination to the C−H Amination Catalyst Rh Structural and Spectroscopic Study. *Inorg. Chem.* **2015**,

(29) Carné-Sánchez, A.; Craig, G. A.; Larpent, P.; Higuchi, M.; Kitagawa, S.; Matsuda, K.; Urayama, K.; H Self-assembly of metal−organic polyhedra into sup polymers with intrinsic microporosity. *Nat. Commun.* **20**

(30) Juanhuix, J.; Gil-Ortiz, F.; Cuni, G.; Colldelram, C. Lidon, J.; Boter, E.; Ruget, C.; Ferrer, S.; Benach, J. Deve Optics and Performance at BL13-XALOC, the Mac Crystallography Beamline at the Alba Synchrotron. *J.* *Radiat.* **2014**, *21*, 679.

(31) (a) Chen, L.-J.; Yang, H.-B.; Shionoya, M. C losupramolecular Architectures. *Chem. Soc. Rev.* **2017** (b) Li, S.; Du, X.-S.; Li, B.; Wang, J.-Y.; Li, G.-P.; Gao, S.-Q. Atom-Precise Modification of Silver(I) Thiolate Clu Ligand Substitution: A New Approach to Generation Functionality and Chirality. *J. Am. Chem. Soc.* **2018**, *140*

(32) Chen, T.-H.; Wang, L.; Trueblood, J. V.; Grassian, V. H.; Cohen, S. M. Poly(isophthalic acid)(ethylene oxide) as a Macromolecular Modulator for Metal–Organic Polyhedra. *J. Am. Chem. Soc.* **2016**, *138*, 9646.
(33) Reiss, P. S.; Little, M. A.; Santolini, V.; Chong, S. Y.; Hasell, T.; Jelfs, K. E.; Briggs, M. E.; Cooper, A. I. Periphery-Functionalized Porous Organic Cages. *Chem. - Eur. J.* **2016**, *22*, 16547.

DOI: 10.1021/jacs.8b13593
J. Am. Chem. Soc. 2019, 141, 4094–4102

ChemComm

COMMUNICATION

View Article Online
View Journal | View Issue

Cite this: Chem. Commun., 2019, 55, 12785

Received 10th September 2019,
Accepted 1st October 2019

DOI: 10.1039/c9cc07083d

rsc.li/chemcomm

Protection strategies for directionally-controlled synthesis of previously inaccessible metal–organic polyhedra (MOPs): the cases of carboxylate- and amino-functionalised Rh(II)-MOPs†

Jorge Albalad, [a] Arnau Carné-Sánchez, *[a] Thais Grancha, [a] Laura Hernández-López [a] and Daniel Maspoch *[ab]

Herein we report that strategic use of protecting groups in coordination reactions enables directional inhibition that leads to synthesis of highly functionalised metal–organic polyhedra (MOPs), rather than of the extended coordination networks. Using this approach, we functionalised two new porous cuboctahedral Rh(II)-based MOPs with 24 peripheral carboxylic acid groups or 24 peripheral amino groups.

Undesired side reactions are the most common limitation in chemical synthesis.[1–4] Even when the simplest protocol is followed, any minor misstep can lead to wasteful side-products, leading to the costly path of having to start over. A persistent challenge in avoiding side reactions is to ensure that the chemistry in question occurs exclusively at the targeted functional group(s).[5–7] This has led to development of a broad arsenal of protecting groups and methods for their use, including separate steps for protection and subsequent deprotection of the group(s) whose reactivity is to be temporarily blocked.[8] In Organic Chemistry, protecting groups confer polyfunctional molecules with chemoselective and orthogonal reactivity, opening up unprecedented reaction pathways for synthesis of active principles, including polymers and peptides with pre-defined sequences of monomers[9,10] and amino acids.[6,7,11–15] In Coordination Chemistry, protecting groups have proven essential for introducing sensitive moieties inside the pore walls of metal–organic frameworks (MOFs)[16,17] and/or for controlling the framework interpenetration of MOFs.[18]

Herein, we report that protecting groups can also be used to synthesise previously inaccessible coordination assemblies: specifically, we have developed chemistry to prepare functionalised porous metal–organic polyhedra (MOPs) rather than the extended coordination networks that normally form in the absence of protection strategies. Fig. 1 illustrates our strategy for synthesising a cuboctahedral Rh(II)-based MOP with 24 available carboxylic acid

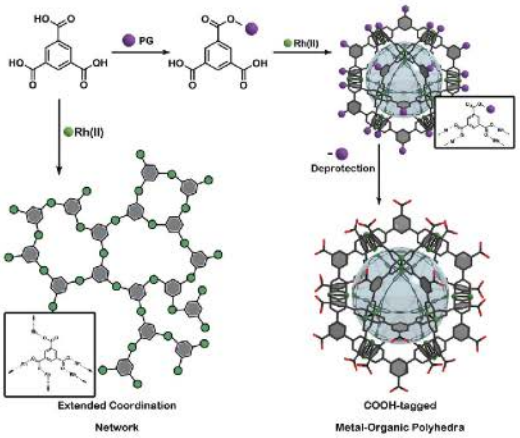

Fig. 1 Scheme of the protecting group strategy to synthesise a COOH-tagged cuboctahedral Rh(II)-based MOP.

moities located at its periphery (hereafter called COOH-RhMOP). The synthesis of this class of MOPs entails assembly of 1,3-benzenedicarboxylic acid (H_2bdc) derivatives and Rh(II)–Rh(II) paddlewheels, in which the 5-position of the bdc derivative dictates the outer functionality of the MOP.[19] Accordingly, the synthesis of COOH-RhMOP requires use of 1,3,5-benzenetricarboxylic acid (H_3btc) as the linker. However, as expected, reaction of Rh(II) with H_3btc tends to form extended coordination networks instead of the desired COOH-RhMOP. This is because the three carboxylic groups react with Rh(II), extending the material uncontrolledly. Consequently, conventional MOP-synthesis conditions (DMA, Na_2CO_3, ~100 °C; detailed synthesis in ESI†), afford an extended coordination polymer in the form of an amorphous solid as product (Fig. S1 and S2, ESI†), whereas solvothermal conditions (in methanol) yield a porous coordination polymer.[20]

Our protection strategy comprises three steps. Firstly, one of the three carboxylic groups of the linker 1,3,5-benzenetricarboxylic acid (H_3btc) is protected, which provides stoichiometric control

[a] Catalan Institute of Nanoscience and Nanotechnology (ICN2), CSIC and The Barcelona Institute of Science and Technology, Campus UAB, Bellaterra, 08193 Barcelona, Spain. E-mail: arnau.carne@icn2.cat, daniel.maspoch@icn2.cat
[b] ICREA, Pg. Lluís Companys 23, 08010 Barcelona, Spain

† Electronic supplementary information (ESI) available. See DOI: 10.1039/c9cc07083d

over the coordination of two of the three chemically equivalent COOH functionalities in H_3btc. Secondly, the protected linker is reacted with Rh acetate, such that the aforementioned stereochemical control hinders the extension of the coordination network, thereby favouring the formation of the zero-dimensional MOP. Finally, chemoselective deprotection of the protected COOH affords COOH-RhMOP, in which 24 carboxylic acid moities are accommodated at its periphery.

We began our study by carefully selecting an appropriate protecting group. We sought one that would be sufficiently robust to endure the conditions for the Rh(II) MOPs synthesis (*i.e.*, strong basic media and temperatures of up to 100 °C) and be amenable to quantitative and chemoselective deprotection. To this end, we revisited the work of Barrett *et al.*, who had previously described a controlled semi-deprotection of a 2-(trimethylsilyl)ethyl-protected (TSE) dicarboxylic acid by stoichiometric addition of fluoride.[21] Since TSE is kinetically stable under basic conditions, we reasoned that it would be suitable for MOP protection.

We first synthesised the mono-protected H_2btc-COOTSE acid derivative, using a three-step route (Fig. 2; detailed synthesis in ESI†). Initially, H_3btc was converted to its triacyl chloride counterpart *in situ*, through reaction with $SOCl_2$. Then, the triacyl chloride product was reacted with 3 mol. eq. of 2-(trimethylsilyl)ethanol and pyridine to obtain the tri-protected intermediate tris(2-(trimethylsilyl)ethyl)benzene-1,3,5-tricarboxylate (btc-COOTSE$_3$). Finally, stoichiometric deprotection of btc-COOTSE$_3$, using 2 mol. eq. of a tetrabutylammonium fluoride solution (1.0 M in tetrahydrofuran) in two successive additions, followed by a final protonation step, afforded the mono-protected H_2btc-COOTSE. The purity of the obtained tri-protected intermediate and the mono-protected H_2btc-COOTSE were monitored by ^{1}H NMR and ESI-MS (Fig. S3–S5, ESI†), and no further purification steps were required for the synthesis of COOH-RhMOP.

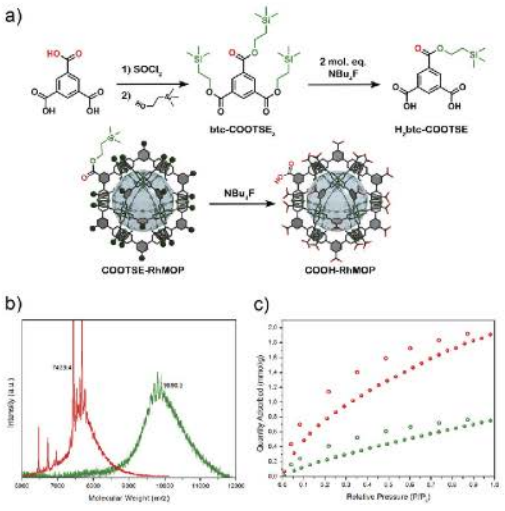

Fig. 2 (a) Scheme of the strategy used to synthesise COOH-RhMOP. (b) MALDI-TOF of COOTSE-RhMOP (green) and COOH-RhMOP (red). (c) CO_2 adsorption isotherm at 298 K of COOTSE-RhMOP (green) and COOH-RhMOP (red).

We then performed the complexation reaction by mixing the mono-protected H_2btc-COOTSE linker with Rh acetate in *N′N*-dimethylacetamide (DMA) under solvothermal conditions (100 °C, 48 hours). Water was used to precipitate out COOTSE-RhMOP from the supernatant, which was a green solid. The product was sequentially washed and finally, dried under vacuum. MALDI-TOF analysis revealed a peak at m/z = 9890.3, matching the theoretical value for a cuboctahedral Rh(II) based MOP of formula $([Rh_{24}(COOTSE\text{-}bdc)_{24}] + H^+)^+$ (expected m/z = 9891.5; Fig. 2b, Fig. S6, ESI†). Additionally, ^{1}H NMR (acetone-d_6) further confirmed the formation of a zero-dimensional architecture featuring 24 TSE protecting groups at its periphery (δ = 8.85, 8.45, 4.35, 1.28, 0.05 ppm) (Fig. S7, ESI†).

Next, we did a subsequent deprotection step by reacting COOTSE-RhMOP with 24 mol of a tetrabutylammonium fluoride solution (1.0 M in tetrahydrofurane) for 6 hours. The precipitated product was isolated, washed with diethyl ether, 1.0 M HCl and water, and finally, dried under vacuum. ^{1}H NMR (DMSO-d_6) confirmed quantitative fading of the TSE signals (at δ = 0.05 ppm, 1.28 ppm and 4.35 ppm) with appearance of a new signal at δ = 13.4 ppm, which we attributed to the free COOH groups (Fig. S9, ESI†). MALDI-TOF analysis showed a peak at m/z = 7439.4 (Fig. 3b and Fig. S10, ESI†), which matched accordingly with the estimated formula $([Rh_{24}(COOH\text{-}bdc)_{24}] + H^+)^+$ (expected m/z = 7441.5). As expected, the deprotection step rendered these MOPs significantly more porous than the corresponding parent MOPs. Thus, whereas COOTSE-RhMOP was non-porous to N_2, COOH-RhMOP showed a BET surface area (S_{BET}) of 198 $m^2\ g^{-1}$ (Fig. S11 and S12, ESI†). Similarly, the CO_2 uptake increased from 0.8 mmol $CO_2\ g^{-1}$ for COOTSE-RhMOP to 2.0 mmol $CO_2\ g^{-1}$ for COOH-RhMOP (Fig. 2c). The increase of gas uptake observed after the deprotection step is attributed to the removal of the TSE bulky groups from the surface of the Rh(II)-MOP akin to similar examples in which a decrease in surface functionalisation of molecular cages caused a beneficial effect on their porous properties.[22]

Carboxylic acids typically have moderately low pKa values (*i.e.*, pK_a = 3 to 5). Therefore, at near physiological pH, they tend to be deprotonated. Accordingly, COOH-RhMOP dissolved in water upon addition of 1 mol. eq. (*i.e.*, 24 mol per MOP) of NaOH (pH = 10.5), rendering a negatively-charged MOP, as evidenced by the z-potential value derived by Dynamic Light Analysis measurements (Fig. S14, ESI†). MALDI-TOF analysis of the solution revealed a peak at m/z = 7945.6 (Fig. S15, ESI†), matching the theoretical formula $([Na_{24}[Rh_{24}(OOC\text{-}bdc)_{24}]\text{-}2Na^+ + H^+)$ (expected m/z = 7947.0). After confirming the solubility of COOH-RhMOP in basic pH, we ran a pH calibration curve to identify the lowest pH at which the cage would be water soluble. After the addition of 6 mol of NaOH (25% of COOH groups deprotonated), the MOP fully dissolved in water, giving a final pH value of pH = 8.2. ^{1}H NMR of the product after it had been in aqueous solution for 7 days did not reveal any signs of scaffold degradation (Fig. S16, ESI†).

Inspired by our previous results, we then aimed to extend our MOP-protection chemistry by endeavouring to incorporate

functionalities that had previously been inaccessible in Rh-based materials. The strong affinity of Rh(II) paddlewheels towards N-donor groups precludes the synthesis of a NH_2-tagged Rh(II)-based MOP, unlike with other metal sources. Amino groups are among the most exploited functional groups in the literature, owing to their basicity, dominant nucleophilicity and versatility, as they can be transformed into myriad products under diverse conditions. This has led to the generation of a rich catalogue of amine chemistry. Moreover, amino-functionalized materials can exhibit enhanced physicochemical properties and have been thoroughly used in many applications, such as surface anchoring, carbon dioxide capture, water uptake and pollutant removal.[23,24]

We explored the possibility of protecting the reactive NH_2 moiety of 5-aminoisophthalic acid with a suitable protecting group to synthesise the desired MOP. Note that, as in the formation of COOH-RhMOP, direct reaction of Rh acetate with 5-aminoisopthalic acid under the same reaction conditions produced an extended coordination network in the form of an amorphous solid (Fig. S1 and S2, ESI†). As protecting group, we chose *tert*-butyloxycarbonyl (Boc), given its excellent stability in basic media and its compatibility with free carboxylates. Thus, we synthesised a Boc-protected version of the linker (H_2bdc-NBoc) by reacting 5-aminoisophthalic acid with di-*tert*-butyldicarbonate (Boc_2O) in a mixture (1 : 1 v/v) of dioxane and 1 M NaOH (Fig. 3 and Fig. S18, ESI†).[25] This linker was then reacted with Rh acetate and Na_2CO_3 in DMA at 100 °C for 48 hours. The solids were discarded, and the supernatant was precipitated with diethyl ether and washed with a 1 M NaOH solution and water. The formation of NBoc-RhMOP was confirmed by MALDI-TOF (m/z = 9110.1; expected 9105.4) and ^{1}H NMR (δ = 9.24, 8.40 and 1.41 ppm) (Fig. 3b and Fig. S19 S20, ESI†).

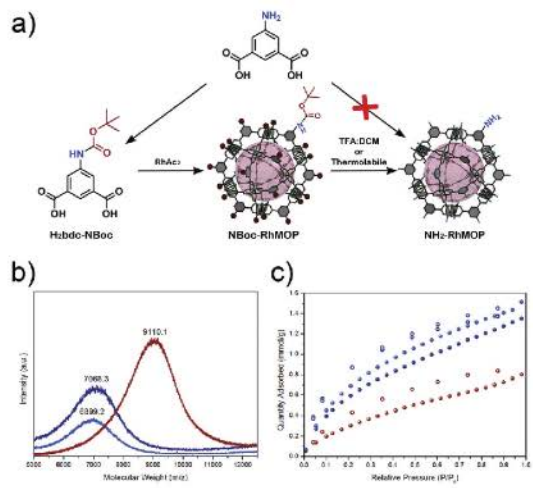

Fig. 3 (a) Scheme of the strategy used to synthesise NH_2-RhMOP. (b) MALDI-TOF spectra of the NBoc-RhMOP (red) and the NH_2-RhMOP prepeared by thermolysis (navy) or by the TFA based deprotection (blue). (c) CO_2 adsorption isotherm at 298 K of the NBoc-RhMOP (red) and the NH_2-RhMOP prepeared by thermolysis (navy) or by the TFA based deprotection (blue).

Finally, we deprotected the NBoc-RhMOP by following a standard procedure of stirring it in a solution of trifluoroacetic acid (TFA; 9 mol. eq. *vs.* MOP) in the dichloromethane for a few hours. ^{1}H NMR and UV-vis analysis of the obtained supernatant (Fig. S22 and S23, ESI†) did not reveal any signals of leached 5-aminoisophthalic acid linker or partial degradation, thereby confirming the robustness of the MOP under the deprotection conditions. The crude product was then neutralised with a triethylamine solution in acetone, washed with methanol and acetone, and characterised by ^{1}H NMR and MALDI-TOF (Fig. 3b and Fig. S24, S25, ESI†). Both techniques confirmed that the deprotection had been quantitative. Likewise, ^{1}H NMR analysis evidenced generation of free amino moieties in the MOP (δ = 5.32 ppm) and quantitative fading of all the previous NBoc signals (δ = 9.50 ppm and 1.42 ppm). In addition, MALDI-TOF analysis in DMSO revealed a peak at m/z = 6899.2 consistent with the formula of the fully deprotected Rh-MOP $[Rh_{24}(NH_2\text{-bdc})_{24} + H^+ + DMSO]^+$ (expected m/z = 6895.3).

Next, we explored an alternative route for the deprotection of NBoc-RhMOP in the solid state, reflecting on the fact that the Boc group can undergo thermolabile deprotection without any reagents, solvents or neutralisation step.[17,26] To this end, we ran a thermogravimetric analysis (TGA) on NBoc-RhMOP to identify the weight-loss attributable to the thermolabile deprotection (Fig. S26, ESI†). The thermogram clearly showed a step of 24.9% weight-loss in the region between 150 °C to 200 °C, owing to the thermolytic cleavage of 24 Boc groups in CO_2 and isobutylene (25.1% based on theoretical mass). Afterwards, we ran an isothermal experiment at 150 °C for 6 hours to confirm that no further degradation of the MOP would occur. After the initial weight loss attributable to solvent loss and the deprotection itself, the curve plateaued until the end of the measurement, thus confirming the robustness of the scaffold (Fig. S27, ESI†). MALDI-TOF analysis of the crude product further confirmed the thermolytic cleavage, with a peak at m/z = 7066.3 matching with the formula $[Rh_{24}(NH_2\text{-bdc})_{24} + H^+ + H_2O + 3DMSO]^+$ (expected m/z = 7066.3) (Fig. 3b and Fig. S25, ESI†).

Analogously to the deprotection of COOTSE-RhMOP, the deprotection of NBoc-RhMOP (either by thermolysis or by treatment with TFA) yielded a product that was more porous than the corresponding starting material. Thus, whereas the S_{BET} of the NBoc-RhMOP was 59 $m^2\ g^{-1}$, upon deprotection, the resultant NH_2-RhMOP showed S_{BET} values of 255 $m^2\ g^{-1}$ (thermolysis) or 417 $m^2\ g^{-1}$ (TFA) (Fig. S29 and S30, ESI†). We attributed the difference in S_{BET} between these two products to their different morphologies: the thermolytic deprotection of NBoc-RhMOP yields micrometric particles (Fig. S31, ESI†), whereas the TFA-based method yields an amorphous powder composed of aggregated nanoparticles (*ca.* 50 nm). These values echo the previously reported trend that MOPs exhibit greater gas sorption upon miniaturisation.[27] Furthermore, the CO_2 uptake measured at 298 K also increased after deprotection, as depicted in Fig. 3c. Thus, whereas the NBoc-RhMOP adsorbed 0.88 mmol $CO_2\ g^{-1}$, the deprotected products (NH_2-RhMOPs) exhibited uptakes of 1.39 mmol $CO_2\ g^{-1}$ (thermolysis) and 1.52 mmol $CO_2\ g^{-1}$ (TFA) at 1 bar under the same conditions (Fig. 2c).

Remarkably, both the S_{BET} and CO_2 uptake values for these NH_2-RhMOP products are significantly higher than for their Cu(II) analogue (non-porous to N_2; CO_2 uptake = 0.70 mmol CO_2 g^{-1}).[28]

In conclusion, we have demonstrated strategic use of protecting groups for directionally-controlled coordination chemistry synthesis of Rh(II)-based MOPs with previously inaccessible functionalities. Using our orthogonal protection/deprotection process, we prepared two new Rh(II)-based MOPs with 24 peripheral COOH or NH_2 moieties, without affecting the structural integrity or microporosity. Owing to their strong processability, the protected Rh(II)-based MOPs can be then deprotected either in solid state or in solution. Moreover, we dissolved COOH-RhMOP in water at near-neutral pH. Interestingly, the presence of 24 directional COOH or NH_2 groups in a zero-dimensional porous scaffold might be of particular interest for Reticular Chemistry.

This work was supported by the Spanish MINECO (Projects RTI2018-095622-B-I00), the Catalan AGAUR (Project 2017 SGR 238), the ERC, under the EU-FP7 (ERC-Co 615954), and the CERCA Program/Generalitat de Catalunya. ICN2 is supported by the Severo Ochoa programme from the Spanish MINECO (Grant No. SEV-2017-0706). A. C. S. and T. G. thank the Spanish MINECO for Juan de la Cierva fellowships (IJCI-2016-29802 and FJCI-2017-31598). J. A. acknowledges the Generalitat de Catalunya for an FI fellowship (2016FI B 00449).

Conflicts of interest

The authors declare that there are no conflicts of interest in this publication.

Notes and references

1 D. Lei, D.-C. Lee, A. Magasinski, E. Zhao, D. Steingart and G. Yushin, *ACS Appl. Mater. Interfaces*, 2016, **8**, 2088–2096.
2 Y. Liu, L. Wang, L. Cao, C. Shang, Z. Wang, H. Wang, L. He, J. Yang, H. Cheng, J. Li and Z. Lu, *Mater. Chem. Front.*, 2017, **1**, 2495–2510.
3 S. Li, H. Cai, J. He, H. Chen, S. Lam, T. Cai, Z. Zhu, S. J. Bark and C. Cai, *Bioconjugate Chem.*, 2016, **27**, 2315–2322.
4 J. Kuwabara, Y. Fujie, K. Maruyama, T. Yasuda and T. Kanbara, *Macromolecules*, 2016, **49**, 9388–9395.
5 G. B. Bloomberg, D. Askin, A. R. Gargaro and M. J. A. Tanner, *Tetrahedron Lett.*, 1993, **34**, 4709–4712.
6 A.-B. M. Abdel-Aal, G. Papageorgiou, R. Raz, M. Quibell, F. Burlina and J. Offer, *J. Pept. Sci.*, 2016, **22**, 360–367.
7 C. Toonstra, M. N. Amin and L.-X. Wang, *J. Org. Chem.*, 2016, **81**, 6176–6185.
8 C. G. Bochet, *Angew. Chem., Int. Ed.*, 2001, **40**, 2071–2073.
9 N. De Alwis Watuthanthrige, P. N. Kurek and D. Konkolewicz, *Polym. Chem.*, 2018, **9**, 1557–1561.
10 K. Hiltebrandt, M. Kaupp, E. Molle, J. P. Menzel, J. P. Blinco and C. Barner-Kowollik, *Chem. Commun.*, 2016, **52**, 9426–9429.
11 K. R. Wilson, S. Sedberry, R. Pescatore, D. Vinton, B. Love, S. Ballard, B. C. Wham, S. K. Hutchison and E. J. Williamson, *J. Pept. Sci.*, 2016, **22**, 622–627.
12 M. R. Levengood, X. Zhang, J. H. Hunter, K. K. Emmerton, J. B. Miyamoto, T. S. Lewis and P. D. Senter, *Angew. Chem., Int. Ed.*, 2017, **56**, 733–737.
13 H. Katayama and H. Hojo, *Org. Biomol. Chem.*, 2013, **11**, 4405–4413.
14 M. Lapeyre, J. Leprince, M. Massonneau, H. Oulyadi, P.-Y. Renard, A. Romieu, G. Turcatti and H. Vaudry, *Chem. – Eur. J.*, 2006, **12**, 3655–3671.
15 A. Isidro-Llobet, M. Álvarez and F. Albericio, *Chem. Rev.*, 2009, **109**, 2455–2504.
16 T. Yamada and H. Kitagawa, *J. Am. Chem. Soc.*, 2009, **131**, 6312–6313.
17 D. J. Lun, G. I. N. Waterhouse and S. G. Telfer, *J. Am. Chem. Soc.*, 2011, **133**, 5806–5809.
18 R. K. Deshpande, J. L. Minnaar and S. G. Telfer, *Angew. Chem., Int. Ed.*, 2010, **49**, 4598–4602.
19 A. Carné-Sánchez, J. Albalad, T. Grancha, I. Imaz, J. Juanhuix, P. Larpent, S. Furukawa and D. Maspoch, *J. Am. Chem. Soc.*, 2019, **141**, 4094–4102.
20 G. Nickerl, U. Stoeck, U. Burkhardt, I. Senkovska and S. Kaskel, *J. Mater. Chem. A*, 2014, **2**, 144–148.
21 A. G. M. Barrett, D. Hamprecht, R. A. James, M. Ohkubo, P. A. Procopiou, M. A. Toledo, A. J. P. White and D. J. Williams, *J. Org. Chem.*, 2001, **66**, 2187–2196.
22 (*a*) P. S. Reiss, M. A. Little, V. Santolini, S. Y. Chong, T. Hasell, K. E. Jelfs, M. E. Briggs and A. I. Cooper, *Chem. – Eur. J.*, 2016, **22**, 16547–16553; (*b*) A. Carné-Sánchez, G. A. Craig, P. Larpent, V. Guillerm, K. Urayama, D. Maspoch and S. Furukawa, *Angew. Chem., Int. Ed.*, 2019, **58**, 6347–6350.
23 H. Liu, L. Chen and J. Ding, *RSC Adv.*, 2016, **6**, 48884–48895.
24 R. W. Flaig, T. M. Osborn Popp, A. M. Fracaroli, E. A. Kapustin, M. J. Kalmutzki, R. M. Altamimi, F. Fathieh, J. A. Reimer and O. M. Yaghi, *J. Am. Chem. Soc.*, 2017, **139**, 12125–12128.
25 J. Bitta and S. Kubik, *Org. Lett.*, 2001, **3**, 2637–2640.
26 R. K. Deshpande, J. L. Minnaar and S. G. Telfer, *Angew. Chem., Int. Ed.*, 2010, **49**, 4598–4602.
27 A. Carné-Sánchez, G. A. Craig, P. Larpent, T. Hirose, M. Higuchi, S. Kitagawa, K. Matsuda, K. Urayama and S. Furukawa, *Nat. Commun.*, 2018, **9**, 2506.
28 X. Liu, X. Wang, A. V. Bavykina, L. Chu, M. Shan, A. Sabetghadam, H. Miro, F. Kapteijn and J. Gascon, *ACS Appl. Mater. Interfaces*, 2018, **10**, 21381–21389.

JACS JOURNAL OF THE AMERICAN CHEMICAL SOCIETY
Article
Cite This: J. Am. Chem. Soc. XXXX, XXX, XXX−XXX
pubs.acs.org/JACS

Phase Transfer of Rhodium(II)-Based Metal−Organic Polyhedra Bearing Coordinatively Bound Cargo Enables Molecular Separation

Thais Grancha,[†] Arnau Carné-Sánchez,*[,†] Laura Hernández-López,[†] Jorge Albalad,[†] Inhar Imaz,[†] Judith Juanhuix,[∥] and Daniel Maspoch*[,†,‡]

[†]Catalan Institute of Nanoscience and Nanotechnology (ICN2), CSIC and The Barcelona Institute of Science and Technology, Campus UAB, Bellaterra, 08193 Barcelona, Spain
[∥]ALBA Synchrotron, 08290 Cerdanyola del Vallès, Barcelona, Spain
[‡]ICREA, Pg. Lluís Companys 23, 08010 Barcelona, Spain

Supporting Information

ABSTRACT: The transfer of nanoparticles between immiscible phases can be driven by externally triggered changes in their surface composition. Interestingly, phase transfers can enhance the processing of nanoparticles and enable their use as vehicles for transporting molecular cargo. Herein we report extension of such phase transfers to encompass porous metal−organic polyhedra (MOPs). We report that a hydroxyl-functionalized, cuboctahedral Rh(II)-based MOP can be transferred between immiscible phases by pH changes or by cation-exchange reactions. We demonstrate use of this MOP to transport coordinatively bound cargo between immiscible layers, including into solvents in which the cargo is insoluble. As proof-of-concept that our phase-transfer approach could be used in chemical separation, we employed Rh(II)-based MOPs to separate a challenging mixture of structurally similar cyclic aliphatic (tetrahydrothiophene) and aromatic (thiophene) compounds. We anticipate that transport of coordinatively bound molecules will open new avenues for molecular separation based on the relative coordination affinity that the molecules have for the Rh(II) sites of MOP.

INTRODUCTION

Phase transfer has gained importance in the synthesis, functionalization, and application of nanomaterials, especially those of inorganic nanoparticles (NPs).[1] Many applications of NPs demand transfer of as-synthesized NPs from polar to nonpolar solvents and *vice versa*. For example, biomedical applications demand water-soluble NPs,[2] whereas processing of NPs for optoelectronic applications often involves nonpolar organic solvents.[3] These phase transfers are typically achieved by selective modulation of the hydrophilicity/hydrophobicity of NPs upon *in situ* modification of their surface composition. Such modifications can be driven by external stimuli, including changes in pH,[4] light,[5] ionic strength[6] or temperature,[7] electrostatic interactions,[8] or ligand-exchange reactions.[9] *In situ* tuning of solubility via external triggers has been recently extended to cationic metal−organic[10,11] and organic cages,[12] whose phase transfer is usually driven by counteranion exchange. Given the rich host−guest chemistry of such cages, their transfer between phases has shown promise as a method to transport cargo between two immiscible phases.

Herein we report the phase transfer of metal−organic polyhedra (MOPs),[13−19] a neutral class of metal−organic cages that arise from the self-assembly of metal ions or clusters linked through carboxylate organic ligands and that exhibit permanent porosity between organic and aqueous media and *vice versa*. To this end, we selected the cuboctahedral Rh(II)-based MOP of formula $[Rh_2(OH\text{-}bdc)_2(H_2O)(DMA)]_{12}$ (hereafter called OHRhMOP, where OH-bdc = 5-hydroxy-1,3-benzenedicarboxylate and DMA = *N*,*N*-dimethylacetamide),[20] whose outer surface is functionalized with 24 hydroxyl groups (Figure 1a). We discovered that the reversible and quantitative protonation/deprotonation of the peripheral hydroxyl groups can be triggered by changing the pH, which induces a change in solubility that enables transfer of the Rh(II)-MOP between immiscible phases. Further, we found that once the anionic Rh(II)-MOP is generated, a second reversible phase transfer can occur, via cation exchange. We anticipated that these two phase-transfer phenomena could be sequentially coupled via a triphasic solvent system, in which spontaneous phase transfer triggered by cation exchange would drive the (normally nonspontaneous) pH-mediated phase transfer. Finally, we combined the reversible phase transfer of the MOP with the coordination capabilities of its 12 Rh−Rh

Received: September 26, 2019
Published: October 24, 2019

DOI: 10.1021/jacs.9b10403
J. Am. Chem. Soc. XXXX, XXX, XXX−XXX

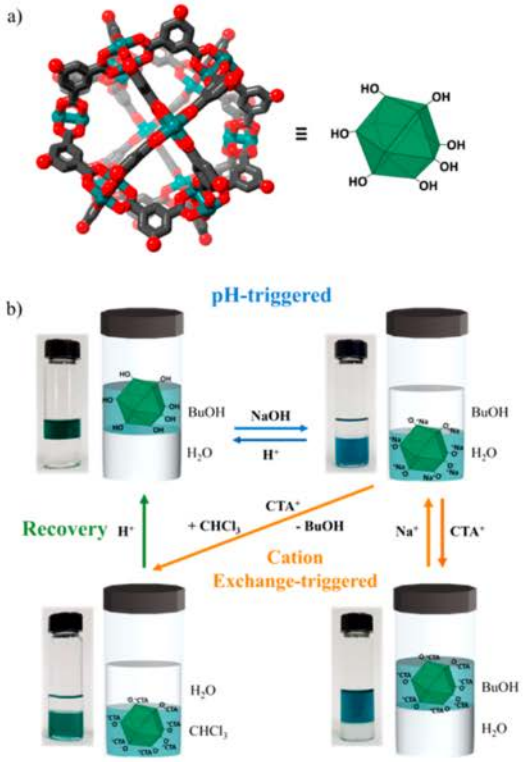

Figure 1. Crystalline structure of OHRhMOP.[20] Color key: green, rhodium; red, oxygen; gray, carbon. Hydrogen atoms and solvent molecules have been omitted for clarity. (b) Schematic representation of Rh(II)-MOPs during pH change-triggered (blue) or cation exchange-triggered (orange) phase transfers and upon recovery after precipitation with diethyl ether and subsequent dissolution in 1-butanol (green). The photographs illustrate the biphasic systems of the corresponding phase transfers.

paddlewheel units[21,22] to transport coordinatively bound cargo between immiscible liquids, including into liquids in which the cargo is not soluble. As proof-of-concept, we combined the selective coordination chemistry of the Rh(II) sites to the phase-transfer phenomena of Rh(II)-MOPs to separate a challenging mixture of a cyclic aliphatic molecule (tetrahydrothiophene) and its corresponding aromatic analogue (thiophene). Rh(II)-MOPs can thus behave as a kind of "molecular nanoparticle" combining the properties of NPs (e.g., high density of surface functionalization) and molecules (e.g., stoichiometric transformation on well-located reactive sites and solubility), opening up novel avenues for molecular transport and separation.

■ RESULTS AND DISCUSSION

pH-Triggered Phase Transfer. We began our study by transferring OHRhMOP from an organic phase to an aqueous phase using a simple acid/base reaction (Figure 1b; SI, Video S1). To this end, we prepared a biphasic system of a solution of OHRhMOP in 1-butanol and an aqueous solution containing NaOH. The phase transfer was partial when left spontaneously to occur (SI, Figure S1), whereas shaking the biphasic system for 5 s induced a complete transfer of the OHRhMOP to the aqueous phase. Since OHRhMOP contains 24 hydroxyl groups that can be deprotonated by base, we studied the transfer efficiency (TE) in function of the molar equivalents (molar equiv) of NaOH added to the aqueous phase. The TE was quantified by means of ultraviolet−visible spectroscopy (UV−vis) measurements on the aqueous phase after phase transfer (SI, Figures S1−S3). Using 24 molar equiv of NaOH in the aqueous phase (which gave a pH of ca. 11.5) provided a TE of 100%, whereas use of fewer than 24 molar equiv gave only partial transfer. These results corroborated a phase-transfer mechanism whereby quantitative deprotonation of the hydroxyl groups renders a fully deprotonated, water-soluble Rh(II)-MOP of formula $Na_{24}[Rh_2(O\text{-}bdc)_2]_{12}$ (hereafter named ONaRhMOP). The formation of ONaRhMOP was confirmed by ^1H NMR, energy-dispersive X-ray spectroscopy (EDX), and inductively coupled plasma optical emission spectrometry (ICP-OES) (SI, Figures S4, S5 and Table S1).

Next, we explored the reversibility of the phase transfer, observing complete reversibility upon addition of trifluoroacetic acid (TFA) to the 1-butanol phase (Figure 1b). We determined that 36 molar equiv of TFA are necessary to complete the transfer from water to 1-butanol, and 36 molar equiv of NaOH are necessary to move the Rh(II)-MOP back into water. The reversible transfer could be repeated up to 10 cycles with an overall TE of 78%, estimated by comparing the maximum absorbance value in the UV−vis spectra of OHRhMOP in the 1-butanol phase before the first transfer had begun and after the 10 cycles had been completed (SI, Figures S6, S7 and Table S2). These results confirmed that pH changes enable phase transfer through formation of (neutral) OHRhMOP or (anionic) ONaRhMOP. The integrity of these Rh(II)-MOPs under the above-mentioned basic and acidic conditions was confirmed 24 h after each phase transfer through UV−vis, dynamic light scattering (DLS), and matrix-assisted laser desorption/ionization (time-of-flight analyzer) mass spectroscopy (MALDI-TOF) (SI, Figures S8−S10).

Cation Exchange-Triggered Phase Transfer. Having demonstrated that reversible phase transfer of Rh(II)-MOP between 1-butanol and water could be achieved by changing the pH, we then evaluated whether phase transfer of ONaRhMOP could be achieved through cation exchange. To this end, a 1-butanol solution containing cetyltrimethylammonium bromide (CTAB) was layered on top of an aqueous solution of ONaRhMOP, and the resulting biphasic system was shaken for 5 s (Figure 1b; SI, Video S1). UV−vis of the aqueous phase showed that 48 molar equiv of CTAB ensured the quantitative transfer of ONaRhMOP from the water to the 1-butanol (SI, Figures S13 and S14). Complete transfer was further corroborated by ICP-OES, which revealed the absence of Rh(II) ions in the aqueous phase (SI, Table S3). The Rh(II)-MOP that had entered the 1-butanol was precipitated out by addition of diethyl ether and then isolated. Characterization of this solid by EDX, ^1H NMR, and ICP-OES (SI, Figures S15−S18 and Table S4) revealed formation of Rh(II)-MOP of formula $CTA_{24}[Rh_2(O\text{-}bdc)_2]_{12}$ (hereafter referred to as OCTARhMOP), in which all the Na^+ cations of the previous Rh(II)-MOP had been replaced by CTA^+ cations. These results confirmed that the phase transfer could be driven by cation exchange. Moreover, the stability of OCTARhMOP 24 h after the phase transfer in 1-butanol was confirmed through UV−vis (SI, Figure S19). Remarkably, replacing the CTA^+ cations with Na^+ cations enabled reverse transfer (Figure 1b): addition of 480 molar equiv of NaCl to the

DOI: 10.1021/jacs.9b10403
J. Am. Chem. Soc. XXXX, XXX, XXX−XXX

aqueous phase (10 times the concentration of CTAB) pushed the Rh(II)-MOP from the 1-butanol back into the water (Figure 1b; SI, video S1, Figures S20–S22).

Encouraged by our results with cation exchange-triggered phase transfer, we investigated whether this method could enable transfer of ONaRhMOP from water to less polar solvents, including aprotic organics solvents such as chloroform. To this end, an aqueous solution of ONaRhMOP was layered on top of a chloroform solution containing CTAB. Remarkably, the transfer from water to chloroform through the formation of OCTARhMOP (Figure 1b; SI, Figure S23) occurred spontaneously; indeed, shaking of the biphasic system was not even required. In this case, 96 CTAB molar equiv were necessary to complete the phase transfer, as confirmed by UV–vis, ICP-OES, EDX, and ^{1}H NMR (SI, Figures S23–S28 and Tables S5 and S6). Again, the stability of OCTARhMOP chloroform solution 24 h after the phase transfer in chloroform was confirmed by UV–vis (SI, Figure S29). Furthermore, as addition of NaCl to the water phase did not enable the corresponding reverse transfer, we attempted to recover the parent OHRhMOP by protonating OCTARhMOP with TFA (Figure 1b). The ^{1}H NMR spectrum of the precipitated solid after addition of TFA did not contain any peaks corresponding to CTA^+ counter-cations, thereby confirming recovery of the initial OHRhMOP, which could be redissolved in 1-butanol (SI, Figure S30).

Coupling the Two Phase-Transfers: A Triphasic Solvent System. Unlike the spontaneous phase transfer of OHRhMOP between water and chloroform that is triggered by cation exchange, the phase transfer of OHRhMOP between 1-butanol and water triggered by pH changes requires shaking. Therefore, to build an autonomous system in which Rh(II)-MOP could be spontaneously transferred through immiscible liquid phases solely via external chemical stimuli, we investigated the possibility of sequentially coupling the two phase transfers into a single system. Accordingly, we prepared a triphasic solvent system (1-butanol/water/chloroform), which we used to test whether OHRhMOP would spontaneously cross from the 1-butanol into the chloroform phase (via the aqueous phase). The system comprised three layers, listed here by increasing density: a 1-butanol solution of OHRhMOP; an aqueous layer containing 24 molar equiv of NaOH and sodium chloride (5%, w/w); and a chloroform layer containing 96 molar equiv of CTAB (Figure 2). After 48 h, OHRhMOP was found and characterized in the chloroform phase, confirming that combining the two phase-transfers provides an autonomous system (SI, Figure S32). We reasoned that the spontaneous phase transfer between water and chloroform triggered by cation exchange drives the pH-mediated phase transfer between water and 1-butanol, thus obviating the need for shaking.

Cargo Transport. We reasoned that, since the transfer of OHRhMOP between immiscible liquid phases requires only modification of its 24 surface hydroxyl groups, then the 12 exohedral axial sites of the Rh–Rh paddlewheel clusters would remain accessible for functionalization via coordination chemistry.[21,23] Accordingly, we envisaged that said clusters could be used to bind cargo (via coordination bonds) to the surface of the OHRhMOP and that the resultant cargo-loaded OHRhMOP could then be transferred between phases. An example of possible cargo is N-donor ligands, which strongly coordinate to such clusters and whose coordination can be readily followed, either by the naked eye or by monitoring

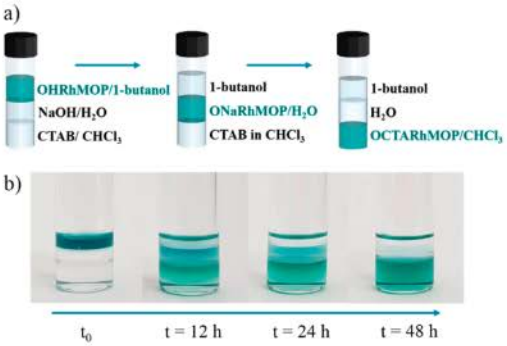

Figure 2. (a) Scheme showing the composition of the triphasic system and the subsequent phase transfers that spontaneously occurred. (b) Photographs showing the changes in the triphasic system over time.

spectroscopic changes of the band centered at λ_{max} = 500–600 nm, which corresponds to the $\pi^* \rightarrow \sigma^*$ transitions of the Rh–Rh bond.[24,25]

As proof-of-concept that OHRhMOP could deliver cargo via phase transfer, we chose 4-aminopyridine (aminopyridine) as test cargo, considering that each OHRhMOP could coordinate 12 aminopyridine molecules to form the loaded product (hereafter called OHRhMOP(aminopyridine)). This loading ratio was confirmed by single-crystal X-ray diffraction (Figure 3a) and UV–vis (λ_{max} shifted to 554 nm; SI, Figure S33). As biphasic solvent systems, we chose water/chloroform and water/1-butanol, as aminopyridine is insoluble in chloroform and only slightly soluble in 1-butanol.

To test the transport of OHRhMOP(aminopyridine) from water to either chloroform or 1-butanol, we first prepared an aqueous solution of ONaRhMOP containing 12 molar equiv of aminopyridine. Formation of ONaRhMOP(aminopyridine) was confirmed by UV–vis (λ_{max} = 555 nm) and ^{1}H NMR (SI, Figures S34–S37). Note that ONaRhMOP-(aminopyridine) could also be prepared from phase transfer of OHRhMOP in 1-butanol to a basic aqueous solution containing aminopyridine (Figure 3b; SI, Video S2). After formation of purple ONaRhMOP(aminopyridine), two biphasic systems were prepared: water/chloroform (containing 96 molar equiv of CTAB) and water/1-butanol (containing 48 molar equiv of CTAB). Complete transfer of ONaRhMOP-(aminopyridine) to chloroform upon exchange of Na^+ ions with CTA^+ ions occurred spontaneously (Figure 2b; SI, Figure S40), whereas in 1-butanol, complete transfer required that the system be shaken for 5 s (SI, Figure S38 and Video S2). In each case, transfer was further confirmed by UV–vis and ^{1}H NMR spectra (SI, Figures S38–S41).

We next explored cargo transfer in the opposite direction, from 1-butanol to water, using 4-pyridinylboronic acid (PBA), an N-donor ligand that is insoluble in water, as cargo. Thus, a 1-butanol solution of OHRhMOP was treated with 12 molar equiv of PBA, and the solution rapidly changed from green to purple. These spectroscopic changes were followed by UV–vis, which revealed a shift in λ_{max}, from 596 to 554 nm (SI, Figure S42), which evidenced coordination of OHRhMOP to 12 molecules of PBA. A biphasic system was then prepared with the 1-butanol solution on top of a basic water layer. After shaking for 5 s, transfer of OHRhMOP(PBA) to the aqueous

DOI: 10.1021/jacs.9b10403
J. Am. Chem. Soc. XXXX, XXX, XXX–XXX

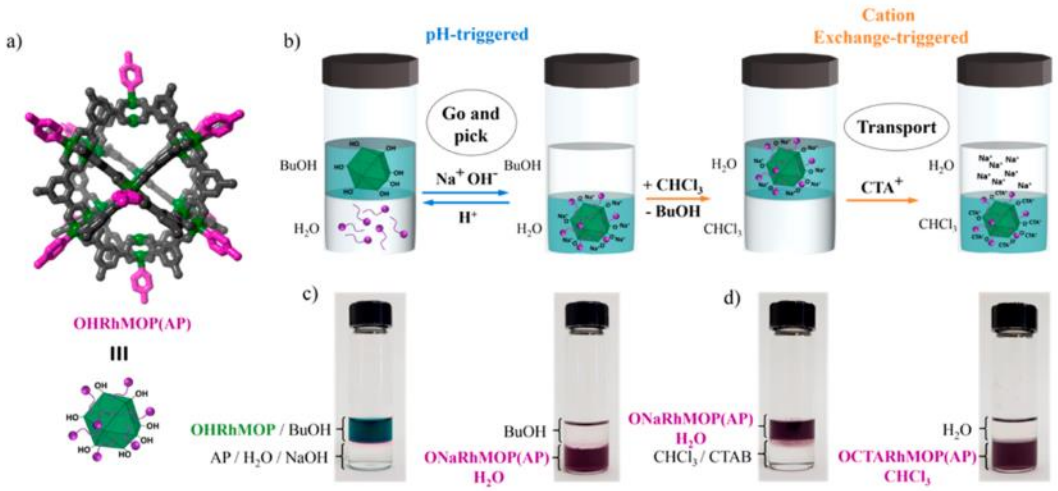

Figure 3. (a) Crystalline structure of OHRhMOP(aminopyridine). Color key: green, rhodium; gray, OH-bdc ligands; purple: aminopyridine molecules coordinated to the Rh(II) axial site. Hydrogen atoms and solvent molecules have been omitted for clarity. (b) Scheme representing loading of OHRhMOP with aminopyridine via pH-driven phase transfer from 1-butanol to water driven by pH and subsequent cation exchange to trigger a second phase transfer, thus delivering the aminopyridine-loaded Rh-MOP into chloroform. (c) Photographs of the biphasic systems BuOH/OHRhMOP and aminopyridine/basic water before and after the phase transfers. (d) Photographs of the biphasic systems ONaRhMOP(aminopyridine)/water and $CHCl_3$/CTAB before and after the phase transfers.

phase by deprotonation of the Rh(II)-MOP was complete, as confirmed by UV−vis and ^{1}H NMR (SI, Figures S43−S46).

Finally, we explored the amenability of OHRhMOP to transport larger molecules into solvents in which they are not soluble. To this end, we chose as cargo neutral red (NR), a phenazine-based dye with available N-donor sites capable of coordinating to the axial sites of the Rh−Rh paddlewheels (SI, Scheme S1). Since NR is soluble in 1-butanol but not in basic water or chloroform, we investigated its transport by two consecutive phase transfers: first, from 1-butanol to basic water and, second, from basic water to chloroform. The maximum number of NR molecules that OHRhMOP could transport to the basic aqueous phase was assessed (Figure 4a). Thus, solutions of OHRhMOP in 1-butanol were separately treated with different amounts of NR (from 1 molar equiv to 12 molar equiv). The resultant solutions were independently layered on top of basic water, the resulting biphasic systems were shaken for 5 s, and finally, the fraction of NR that had been transferred into each aqueous phase was quantified by UV−vis of the 1-butanol phase (SI, Table S7). As depicted in Figure 4b, each OHRhMOP could transport up to four NR molecules into the aqueous phase. Furthermore, UV−vis analysis of the aqueous phases revealed that the molecular transport is driven by coordination of NR to Rh(II)-MOP (SI, Figure S49). Next, the aqueous phase containing the ONaRhMOP(NR) complex was layered on top of a chloroform phase containing CTAB. The ONaRhMOP(NR) was spontaneously and quantitatively transferred into the chloroform phase, having been mediated by cation exchange (SI, Figure S50).

Role of Rh(II)-MOP in Cargo Transport. Since, in our approach, the transport of cargo requires its coordinative anchoring to the outer Rh(II) sites of the paddle-wheels, we sought to investigate whether the Rh(II)-MOP would offer any advantage over the analogous paddle-wheel Rh(II) complex that constitutes the MOP scaffold. Accordingly, we synthesized the neutral Rh(II) paddle-wheel [Rh^{II}_2(4-hydroxybenzoate)$_4$]

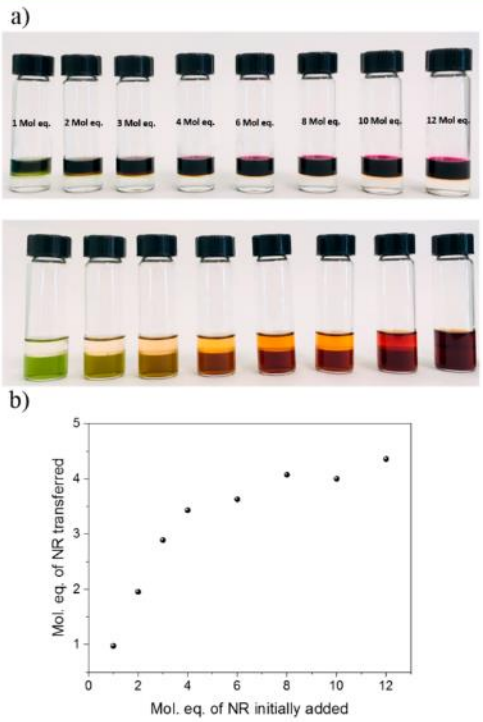

Figure 4. (a) Photographs of the biphasic systems containing OHRhMOP and NR in 1-butanol and basic water before (top) and after (bottom) shaking. (b) Amount of NR (in molar equiv) transferred in each experiment.

DOI: 10.1021/jacs.9b10403
J. Am. Chem. Soc. XXXX, XXX, XXX−XXX

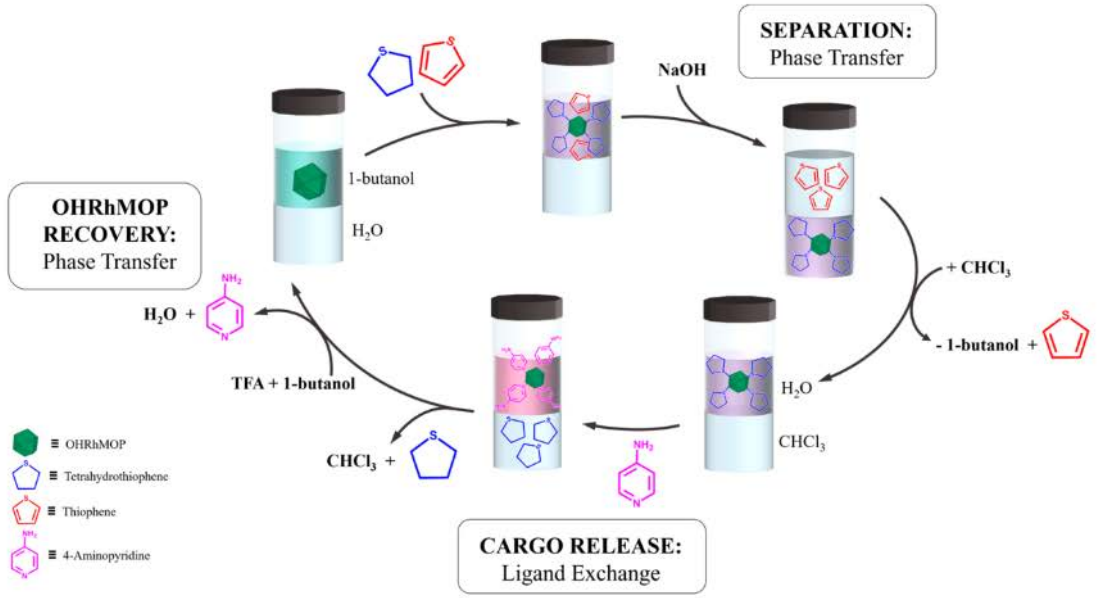

Figure 5. Scheme illustrating the application of phase transfer of Rh(II)-MOPs for molecular separation. Selective coordination of Rh(II)-MOP to tetrahydrothiophene in 1-butanol and further phase transfer to the aqueous phase enable the separation. A subsequent ligand-exchange reaction with aminopyridine triggers the release of tetrahydrothiophene, which is recovered in the $CHCl_3$ phase. Finally, a second phase transfer, triggered by addition of TFA, regenerates the MOP by transferring it to the 1-butanol phase and releasing the aminopyridine into the aqueous layer.

by adapting a literature procedure[26] (SI, Figure S51) and then investigated its phase-transfer performance. Initially, we found that this Rh(II) dimer was insoluble in 1-butanol, thus preventing the pH-triggered phase transfer between 1-butanol and water. We attributed the high solubility of OHRhMOP in various long-chain aliphatic alcohols—including in 1-octanol—to the higher density of hydroxyl groups (up to 24 per MOP) at its outer surface.

Next, we investigated the phase transfer of $[Rh^{II}_2(4\text{-hydroxybenzoate})_4]$ from water to chloroform via cation exchange. First, we dissolved the dimeric cluster in water by adding a stoichiometric amount of NaOH to deprotonate its four hydroxyl groups, which provided the corresponding sodium salt. However, all attempts to transfer this sodium complex from water to chloroform by exchanging Na^+ with CTA^+ failed (SI, Figure S53). Although spectroscopic characterization demonstrated that the Na^+ counterions of the Rh(II) complex had been replaced by CTA^+, the transfer did not occur in less polar solvents (e.g., chloroform). In fact, in cases of poor solubility, a green solid precipitated out into the interphase (SI, Figures S53 and S54). On the basis of these results, we concluded that the paddle-wheel-based Rh(II) dimer does not undergo the same phase transfers that we had observed for OHRhMOP. This finding demonstrated the importance of concentrating several negative charges (in this case, 24 per MOP unit) or hydrophobic moieties at the MOP periphery to facilitate phase transfer—and by extension, cargo transport—between immiscible solvents.

Molecular Separation through Phase Transfer of Rh(II)-MOPs. Having transported diverse molecules between immiscible liquids by combining the coordination capability of Rh(II)-MOP with the phase transfers, we envisaged that selective coordination chemistry of Rh(II) centers could be exploited to separate physicochemically similar molecules that differ only in their affinity toward Rh(II) centers. We considered separation of a cyclic aliphatic compound from its corresponding aromatic counterpart, which is typically challenging due to their physicochemical similarity.[27,28] Specifically, we postulated that the different basicity of aliphatic and aromatic heterocycles could be exploited to separate them via phase transfers of OHRhMOP.

As proof-of-concept for separation by phase transfer using Rh(II)-MOP, we chose the pair tetrahydrothiophene and thiophene (Figure 5). Note that, although we have previously reported examples of N-donor cargo, Rh(II) ions also show excellent affinity toward S-donor ligands.[29] Thus, we exploited the difference in reactivity between the sulfur atom in tetrahydrothiophene, which serves as a basic site, and that in thiophene, whose electron pairs are significantly delocalized in the π ring system, thus precluding any bonding to the Rh(II) acidic site (SI, Figure S55). We prepared a 1-butanol solution of OHRhMOP (1 mol equiv), thiophene (12 mol equiv), and tetrahydrothiophene (12 molar equiv). Note that these compounds are soluble in 1-butanol but not in water. This solution was then layered on top of an aqueous solution of NaOH (24 molar equiv). After shaking for 5 s, the OHRhMOP and tetrahydrothiophene transferred into the aqueous phase, whereas the (noncoordinating) thiophene remained in the 1-butanol layer. These results were supported by UV–vis and ^1H NMR (SI, Figures S58 and S59).

We then explored release of the tetrahydrothiophene through ligand exchange based on the differential affinity of Rh(II) sites toward different functional groups. Given that Rh(II) ions preferentially bond to pyridines over thioethers,[29] we targeted the exchange of the coordinated tetrahydrothiophene with aminopyridine. Hence, 12 molar equiv of

DOI: 10.1021/jacs.9b10403
J. Am. Chem. Soc. XXXX, XXX, XXX−XXX

IOP−tetrahydrothiophene, leading to a rapid change rom violet to pink. UV analysis of the aqueous phase d after the addition of aminopyridine revealed a shift (565 nm → 555 nm), which confirmed the ion of 12 molecules of aminopyridine to ONaRh-, Figure S60). ^{1}H NMR of the aqueous phase further l the formation of ONaRhMOP−aminopyridine (SI, 61). Consequently, tetrahydrothiophene was released cted into a $CDCl_3$ layer, whose ^{1}H NMR spectrum pure tetrahydrothiophene without any trace of e (SI, Figure S62). Note that without the use of idine, addition of chloroform to the ONaRhMOP− othiophene aqueous solution did not trigger tetrahy- ene release, further corroborating the requirement l exchange (SI, Figure S63).

we explored recovery of the original OHRhMOP ONaRhMOP−aminopyridine aqueous solution via nentioned pH-mediated phase transfer. We prepared c system with the aqueous solution and 1-butanol g TFA. After shaking for 5 s, the protonated OP was found and characterized in the 1-butanol hereas the released aminopyridine remained in the phase (SI, Figure S64).

ICLUSIONS

e demonstrated phase transfer of Rh(II)-MOPs water and organic phases by pH changes and by change. Although protonation/deprotonation enables and reversible phase transfer from 1-butanol to xchange between hydrophilic and hydrophobic ations can drive the opposite phase transfer, from k into 1-butanol (or into chloroform). Moreover, we igned a triphasic solvent system in which the pH- iggered and cation-exchange-triggered phase transfers uentially coupled to yield an autonomous transfer m. A unique feature of our phase-transfer system that it combines the functional groups of the organic responsible for shuttling the Rh(II)-MOP across e liquids) and available axial sites of the Rh(II) heels (reactive toward ligand exchange reactions) in a their relative position and stoichiometry are precisely Thus, the surface of the OHRhMOP shows two lities that present orthogonal reactivity and that can for different purposes and synergistically combined. ure enables combining the phase transfer behavior of OP with its ability to coordinate up to 12 anchored s as cargo, thus enabling shuttling of diverse N-donor etween immiscible liquids, including into solvents in e cargo is insoluble. Moreover, we confirmed that go could be delivered from 1-butanol to basic water form, through two sequential phase transfers. Such a m of molecular transport is not based on host−guest tion but on coordination chemistry, opening novel ies in the field of molecular separation. To ate use of our approach in chemical separation selective coordination, we exploited the coordination of Rh(II)-MOP to separate an aliphatic heterocycle rothiophene) from its aromatic analogue (thio- We showed that the coordination hierarchy of Rh(II) les the release of tetrahydrothiophene through ligand with aminopyridine and that OHRhMOP can be ed after the separation and release processes. We are environments in which they are not naturally soluble, subsequent release via external chemical stimuli, w utile in diverse practical applications such as separation, pollutant removal, and catalysis.

EXPERIMENTAL SECTION

Materials and Instruments. Rhodium acetate, 1,3-l carboxylic acid, 5-hydroxy-1,3-benzenedicarboxylic acic hydroxide, tetrabutylammonium bromide (TBAB), benzylt monium bromide (BTBAB), dodecyltrimethylammonium (DTAB), cetyltrimethylammonium bromide (dioctadecyldimethylammonium bromide (DODAB), tetrao nium bromide (TOAB), 4-aminopyridine, 4-pyridinylbor trifluoroacetic acid, deuterium chloride, sodium chloride, n 4-hydroxylbenzoic acid, thiophene, and tetrahydrothiopl purchased from Sigma-Aldrich and used as received. S HPLC grade were purchased from Fisher Chemicals.

UV−vis spectra were measured in an Agilent Cary 400 temperature (ca. 25 °C). ^{1}H NMR spectra were acquired i Avance III 400SB NMR spectrometer at "Servei d'Análisi from the Autonomous University of Barcelona (UAB). Th solutions were prepared following the same procedure. R mg of sample was dissolved in a mixture of 500 μL of DM 20 μL of DCl. The mixture was heated to 100 °C for 8 h. electron microscopy (SEM)-EDX was performed in a SE 650 FEM. ICP-OES was performed in a PerkinElme 4300DV at "Servei d'Análisi Química" from UAB. Mass sp (MALDI-TOF) measurements were performed in a MALDI TOF/TOF (ABSCIEX, 2010). The matrix use case was *trans*-2-[3-(4-*tert*-butylphenyl)-2-methyl-2-prope malononitrile for neutral Rh(II)-MOPs and sinapinic acid f Rh-MOPs. Neutral Rh(II)-MOPs were measured in posit and anionic Rh(II)-MOPs were measured in negative mode Z-potential data were acquired in a Zetasizer Nano ZS.

ASSOCIATED CONTENT

Supporting Information

The Supporting Information is available free of charg ACS Publications website at DOI: 10.1021/jacs.9b1(

Single-crystal X-ray diffraction of OHI (aminopyridine) (CCDC 1914907) and detai syntheses and the phase-transfer procedures UV−vis, ICP-OES, MALDI-TOF, DLS, Z-pote EDX data (PDF)

Supporting movie (AVI)

Supporting movie (AVI)

X-ray crystallographic data (CIF)

AUTHOR INFORMATION

Corresponding Authors

*arnau.carne@icn2.cat

*daniel.maspoch@icn2.cat

ORCID

Thais Grancha: 0000-0001-9591-1058

Arnau Carné-Sánchez: 0000-0002-8569-6208

Jorge Albalad: 0000-0001-5850-6723

Inhar Imaz: 0000-0002-0278-1141

Judith Juanhuix: 0000-0003-3728-8215

Daniel Maspoch: 0000-0003-1325-9161

Notes

The authors declare no competing financial interest.

:k was supported by the Spanish MINECO (project -095622-B-I00), the Catalan AGAUR (project 2017 8), and the ERC under the EU-FP7 (ERC-Co It was also funded by the CERCA Program/ :at de Catalunya. ICN2 is supported by the Severo rogram from the Spanish MINECO (Grant No. SEV-)6). A.C.S. and T.G. thank the Spanish MINECO for la Cierva fellowships (IJCI-2016-29802 and FJCI-)98). J.A. acknowledges the Generalitat de Catalunya fellowship.

ERENCES

, J.; Lee, J. Y.; Ying, J. Y. Phase Transfer and Its Applications :chnology. *Chem. Soc. Rev.* **2011**, *40*, 1672.
ıalet, X. Quantum Dots for Live Cells, in Vivo Imaging, and :s. *Science* **2005**, *307*, 538.
'asaki, Y.; Supran, G. J.; Bawendi, M. G.; Bulović, V. e of Colloidal Quantum-Dot Light-Emitting Technologies. *nics* **2013**, *7*, 13.
a, Y.; Morita, C.; Endo, H.; Kondo, T.; Kawai, T. Reversible nsfer and Fractionation of Au Nanoparticles by pH Change. *mmun.* **2010**, *46*, 9206.
, L.; You, M.; Wu, C.; Han, D.; Öçsoy, I.; Chen, T.; Chen, W. Reversible Phase Transfer of Nanoparticles Based on chable Host−Guest Chemistry. *ACS Nano* **2014**, *8*, 2555.
ards, E. W.; Chanana, M.; Wang, D.; Möhwald, H. Stimuli- e Reversible Transport of Nanoparticles Across Water/Oil . *Angew. Chem., Int. Ed.* **2008**, *47*, 320.
, X.; Ma, H.; Huang, S.; Pan, W.; Zhang, X.; Tian, F.; Gao, g, Y.; Luo, J. Aqueous−Organic Phase-Transfer of Highly ld, Silver, and Platinum Nanoparticles and New Route for n of Gold Nanofilms at the Oil/Water Interface and on ports. *J. Phys. Chem. B* **2006**, *110*, 12311.
J.; Alvarez, J.; Ong, W.; Román, E.; Kaifer, A. E. Phase of Hydrophilic, Cyclodextrin-Modified Gold Nanoparticles form Solutions. *J. Am. Chem. Soc.* **2001**, *123*, 11148.
ins, D. I.; Caruso, F. Spontaneous Phase Transfer of culate Metals from Organic to Aqueous Media. *Angew. : Ed.* **2001**, *40*, 3001.
mmet, A. B.; Hoffman, J. B.; Percástegui, E. G.; Mosquera, D. J.; Bolliger, J. L.; Nitschke, J. R. Anion Exchange Drives : Phase Transfer of Coordination Cages and Their Cargo. *J. ı. Soc.* **2018**, *140*, 14770.
mmet, A. B.; Nitschke, J. R. Directed Phase Transfer of an age and Encapsulated Cargo. *J. Am. Chem. Soc.* **2017**, *139*,

ang, S.-Y.; Kochovski, Z.; Lee, H.-C.; Lu, Y.; Zhang, H.; ; Sun, J.-K.; Yuan, J. Ionic Organic Cage-Encapsulating nsferable Metal Clusters. *Chem. Sci.* **2019**, *10*, 1450.
laoudi, M.; Kim, J.; Wachter, J. B.; Chae, H. K.; O'Keeffe, ıi, O. M. Porous Metal−Organic Polyhedra: 25 Å edron Constructed from 12 Cu2(CO2)4 Paddle-Wheel Blocks. *J. Am. Chem. Soc.* **2001**, *123*, 4368.
J.-R.; Zhou, H.-C. Bridging-Ligand-Substitution Strategy for ration of Metal−organic Polyhedra. *Nat. Chem.* **2010**, *2*,

J.-R.; Yu, J.; Lu, W.; Sun, L.-B.; Sculley, J.; Balbuena, P. B.; -C. Porous Materials with Pre-Designed Single-Molecule CO2 Selective Adsorption. *Nat. Commun.* **2013**, *4*, 1538.
o, J. M.; Coghlan, C. J.; Evans, J. D.; Tsivion, E.; Head- M.; Sumby, C. J.; Doonan, C. J. Hetero-Bimetallic Metal− olyhedra. *Chem. Commun.* **2016**, *52*, 276.
rk, J.; Perry, Z.; Chen, Y.-P.; Bae, J.; Zhou, H.-C. n(II) Metal−Organic Polyhedra as Highly Porous Materials. . *Mater. Interfaces* **2017**, *9*, 28064.
Qian, Y.; Dong, J.; Yuan, D.; Zhao, D. Process-Tracing Stu Postassembly Modification of Highly Stable Zirconium Organic Cages. *J. Am. Chem. Soc.* **2018**, *140*, 6231.
(19) Rowland, C. A.; Lorzing, G. R.; Gosselin, E. J.; Trur Yap, G. P. A.; Brown, C. M.; Bloch, E. D. Methane S Paddlewheel-Based Porous Coordination Cages. *J. Am. C* **2018**, *140*, 11153.
(20) Carné-Sánchez, A.; Albalad, J.; Grancha, T.; Imaz, I.; J.; Larpent, P.; Furukawa, S.; Maspoch, D. Postsynthetic Cov Coordination Functionalization of Rhodium(II)-Based Organic Polyhedra. *J. Am. Chem. Soc.* **2019**, *141*, 4094.
(21) Carné-Sánchez, A.; Craig, G. A.; Larpent, P.; Guil Urayama, K.; Maspoch, D.; Furukawa, S. A Coordinative S Method to Fabricate Soft Porous Materials from Insolub Organic Polyhedra. *Angew. Chem., Int. Ed.* **2019**, *58*, 6347.
(22) Carné-Sánchez, A.; Craig, G. A.; Larpent, P.; H Higuchi, M.; Kitagawa, S.; Matsuda, K.; Urayama, K.; Fur Self-Assembly of Metal−organic Polyhedra into Supra Polymers with Intrinsic Microporosity. *Nat. Commun.* **2018**
(23) Furukawa, S.; Horike, N.; Kondo, M.; Hijikata, Y Sánchez, A.; Larpent, P.; Louvain, N.; Diring, S.; Sato, H.; R.; Kawano, R.; Kitagawa, S. Rhodium−Organic Cuboct Porous Solids with Strong Binding Sites. *Inorg. Chem.* 10843.
(24) Warzecha, E.; Berto, T. C.; Berry, J. F. Axia Coordination to the C−H Amination Catalyst Rh2(I Structural and Spectroscopic Study. *Inorg. Chem.* **2015**, *54*,
(25) Dennis, A. M.; Howard, R. A.; Bear, J. L. The Rea Tetra-μ-acetatodirhodium(II) with Selected Di- and Tr Substituted Pyridines and Imidazole Ligands. *Inorg. Chim. A* *66*, 31.
(26) Sveshnikov, N. N.; Dickman, M. H.; Pope, M. T. Bis sulfoxide-S)tetrakis(μ-p-hydroxybenzoato-O:O')dirhod tetrakis(l-butyrato-O:O')bis(dimethylsulfoxide-S)dirhodium rystal ethanol disolvate. *Acta Crystallogr., Sect. C: Crys Commun.* **2000**, *56*, 1193.
(27) Garcia-Villaluenga, J. P.; Tabe-Mohammadi, A. A revi separation of benzene/cyclohexane mixtures by perv processes. *J. Membr. Sci.* **2000**, *169*, 159.
(28) Jie, K.; Zhou, Y.; Li, E.; Zhao, R.; Huang, F. Sepa Aromatics/Cyclic Aliphatics by Nonporous Adaptive Crystals. *Angew. Chem., Int. Ed.* **2018**, *57*, 12845.
(29) Kitchens, J.; Bear, J. L. A Study of some Rhodium(II Adducts. *J. Inorg. Nucl. Chem.* **1969**, *31*, 2415.